



UNIVERSITY *of the*
WESTERN CAPE

**DESIGN AND SYNTHESIS OF NEW SCAFFOLDS AS
ANTIPROLIFERATIVE AGENTS AND POTENTIAL HSP90 INHIBITORS**

By

Yusuf Adeyemi Adegoke

A Thesis Submitted in Fulfillment of the Requirements
for the Degree of

DOCTOR OF PHILOSOPHY

In

PHARMACEUTICAL SCIENCES

in the School of Pharmacy of the University of the Western cape

Supervisor: Professor Denzil R. Beukes

May 2020

<http://etd.uwc.ac.za/>

DECLARATION

I declare that “design and synthesis of new scaffolds as antiproliferative agents and potential hsp90 inhibitors” is my original research work and it has not been submitted for any degree or examination in any other university and that all the sources I have used or quoted have been indicated and acknowledged by complete references.

Yusuf Adeyemi Adegoke

Date: 19-04-2020

Signed....Y. A. Adegoke



ACKNOWLEDGEMENT

My sincere appreciation goes to my supervisor Prof. Denzil R. Beukes for his mentorship, support and guidance, especially during some difficult times. I acknowledge with gratitude the kind of researcher I have become under your stewardship, thank you Prof.

I would like to express my profound gratitude to the following people who have contributed towards the successful completion of this research.

- Prof. Edith Antunes for her mentorship, NMR training and assistance in running the NMR experiments.
- Prof. Adrienne Edkins, Dr. Jo anne de le Mare and the support team Abir Chakraborty, Kelly Schwartz, Deborah Kajewole and Nyeleti Vukea from Rhodes University for conducting the biological assays.
- Prof Vinesh Maharaj from the University of Pretoria for recording the HR-ESIMS data.
- Prof. Jacques Joubert for his support and training on molecular docking studies.
- Mr. Yunus Kippie and Ms. Audrey Rampling for their timely technical support with equipment and assistance in procurement of chemicals and reagents.

To my fellow marine biodiscovery research group members, thank you for promoting a conducive work environment for learning and the fun times outside the lab are wonderful memories I would cherish for life. My friends; Semir Damisa, Ayodeji Egunlusi and Dr. David Oluwole, thank you all for your support and kindness. A big thank you to Ireen Denya and the members of drug design research group UWC (the J.J. guys) for sharing and being amazing colleagues.

To my parents and my siblings, thank you for your prayers, unconditional love and for believing in me. I'm grateful for having you.

Finally, I say Alhamdulillah rabbi alamin.

To my parents Mr. I.A. Adegoke and Mrs. M.A. Adegoke,
my sisters Mujeedah and Fasilat,
and my triplet brothers Sheu and Muritala.

The logo of the University of the Western Cape, featuring a classical building facade with six columns and a pediment.

UNIVERSITY *of the*
WESTERN CAPE

TABLE OF CONTENTS

DECLARATION	ii
ACKNOWLEDGEMENT	iii
LIST OF FIGURES	ix
LIST OF SCHEMES	xii
LIST OF TABLES	xiv
LIST OF ABBREVIATIONS	xvi
ABSTRACT	xix
Chapter 1: Introduction	1
1.1 The burden of cancer	2
1.2 Discovery of anticancer drugs from natural sources.....	2
1.3 Rationale, Aim and Objectives	4
1.4 Thesis overview	5
References.....	6
Chapter 2: Literature review	8
2.1 Development of anticancer drugs from natural products.....	9
2.2 Natural product derived microtubule-targeting anticancer agents and their synthetic analogues.....	9
2.2.1 Colchicine binding domain agents.....	10
2.2.2 Vinca binding domain agents.....	12
2.2.3 Taxane binding domain agents	16
2.3 Natural product derived heat shock protein 90 inhibitors and their synthetic derivatives as anticancer agents.....	17
2.3.1 N-terminal Inhibitors	19
2.3.2 C-terminal Inhibitors.....	21
2.3.3 Other compounds	24
2.4 Concluding remarks	25
References.....	26

Chapter 3: Synthesis and antiproliferative activity of cyclopenta[*b*]indole derivatives 35

3.1	Introduction.....	36
3.1.1	Naturally occurring and synthetic cyclopenta[<i>b</i>]indoles	36
3.1.2	Biosynthesis of simple cyclopenta[<i>b</i>]indoles.....	38
3.1.3	Synthesis of the cyclopenta[<i>b</i>]indole skeleton – a short review	40
3.1.4	Synthetic approach to cyclopenta[<i>b</i>]indole derivatives – this study.....	47
3.2	Results and discussion	48
3.2.1	Spectroscopic analysis of the compounds 3.32a	51
3.2.2	<i>In vitro</i> antiproliferative study	57
3.2.3	<i>In silico</i> predictions of the physicochemical and drug-likeness of the synthesized compounds.....	58
3.3	Conclusion	61
3.4	Experimental	61
3.4.1	General experimental details.....	61
3.4.2	General Japp-Klingemann procedure	62
3.4.3	Synthesis of 4-benzyloxy aniline (3.321)	63
3.4.4	Compounds	63
3.4.5	Biological assay	68
References	70

Chapter 4: Synthesis and antiproliferative activity of arylidene cyclopenta[*b*]indol-3-one derivatives..... 74

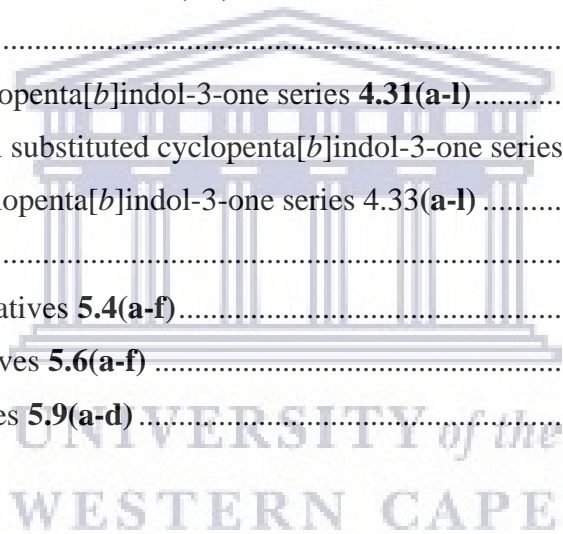
4.1	Introduction.....	75
4.1.1	Cytotoxic compounds containing the arylidene indanone/chalcone-core	75
4.1.2	Synthesis of arylidene/benzylidene derivatives	79
4.1.3	Synthetic approach to arylidene cyclopenta[<i>b</i>]indol-3-one derivatives – this study	80
4.2	Results and discussion	81
4.2.1	Physical properties of arylidene cyclopenta[<i>b</i>]indol-3-ones.....	86
4.2.2	Spectroscopic analysis of synthesized compounds 4.31d , 4.32d, and 4.33d.....	87
4.2.3	Biological evaluation	100
4.3	Conclusion	112

4.4	General experimental details.....	112
4.4.1	Materials	112
4.4.2	General procedure for the Claisen-Schmidt reaction.....	112
4.4.3	Pyridinium chloride salt formation	113
4.4.4	Compounds	113
4.4.5	Biological assay	131
4.4.6	Molecular docking	132
	References.....	133

Chapter 5: Synthesis and antiproliferative activity of prenylated diketopiperazine, barbituric acid and purine derivatives as analogues of sargaquinoic acid and potential Hsp90 inhibitors..... 137

5.1	Introduction.....	138
5.1.1	Interaction of sargaquinoic acid with Hsp90	139
5.1.2	Aim of this study.....	140
5.2	Results and discussion	140
5.2.1	Rationale for the synthesis of diketopiperazine, barbituric acid and theophylline derivatives.....	140
5.2.2	Synthesis of diketopiperazine, barbituric acid and theophylline analogues	141
5.2.3	Physical properties of the synthesized SQA analogues	144
5.2.4	Spectroscopic analysis of the compounds.....	145
5.2.5	Biological evaluation	158
5.3	Conclusion	173
5.4	General experimental details.....	173
5.4.1	Materials	173
5.4.2	Synthesis of 1,4-diacetylpiperazine-2,5-dione (5.2).....	173
5.4.3	General protocol for synthesis of (1-acetyl-3-arylidene-piperazine-2,5-dione) derivatives 5.4(a-f)	174
5.4.4	General procedure for the preparation of barbiturates 5.6(a-f)	174
5.4.5	General procedure for the synthesis of compound 5.9(a-d)	174
5.4.6	Compounds	174
5.4.7	Biological Assays.....	182

5.4.8	Molecular docking	182
	References	183
Chapter 6: Conclusion.....		188
6.1	General summary	189
6.2	Limitation of the study.....	191
6.3	Recommendation for future study	191
Supplementary data.....		192
Chapter 3.....		193
	Cyclopenta[<i>b</i>]indole derivatives 3.32(a-l)	193
Chapter 4.....		217
	Phenyl substituted cyclopenta[<i>b</i>]indol-3-one series 4.31(a-l)	217
	3,4,5-trimethoxyphenyl substituted cyclopenta[<i>b</i>]indol-3-one series 4.32(a-l)	243
	Pyridyl substituted cyclopenta[<i>b</i>]indol-3-one series 4.33(a-l)	270
Chapter 5.....		295
	Diketopiperazine derivatives 5.4(a-f)	296
	Barbituric acid derivatives 5.6(a-f)	309
	Theophylline derivatives 5.9(a-d)	322



LIST OF FIGURES

- Figure 2.1 Polymerization of microtubules.
- Figure 2.2 Structures of colchicine domain binding agents.
- Figure 2.3 Structures of selected vinca alkaloids.
- Figure 2.4 Structure of dolastatin 10, TZT-1027 and brentuximab vedotin.
- Figure 2.5 Structure of halichondrin B and eribulin mesylate.
- Figure 2.6 Structures of paclitaxel, docetaxel and cabazitaxel.
- Figure 2.7 Structures of epothilones A, epothilone B and azoepothilone B (Ixempra®).
- Figure 2.8 The functional domains of Hsp90.
- Figure 2.9 Structures of ansamycin analogues.
- Figure 2.10 Structures of radicicol and its derivatives.
- Figure 2.11 Structures of natural coumarin antibiotics.
- Figure 2.12 Structures synthetic coumarin analogues.
- Figure 2.13 Structures of derrubone and (-)-epigallocatechin gallate (EGCG).
- Figure 3.1 Selected biologically active cyclopenta[*b*]indoles.
- Figure 3.2 General structure of the target tetrahydrocyclopenta[*b*]indol-3-one core.
- Figure 3.3 Summary of compounds synthesized.
- Figure 3.4 ¹H NMR spectrum of compound **3.32a** (400 MHz, DMSO-d₆).
- Figure 3.5 ¹³C NMR spectrum of compound **3.32a** (100 MHz, DMSO-d₆).
- Figure 3.6 DEPT-135 NMR spectrum of compound **3.32a**.
- Figure 3.7 A section of the HSQC spectrum of **3.32a** showing the correlations of the aromatic protons to the corresponding carbon atoms.
- Figure 3.8 A section of HSQC spectrum of **3.32a** showing the methylene protons correlations to the corresponding carbon atoms.
- Figure 3.9 COSY and HMBC correlations of compound **3.32a**.
- Figure 3.10 A section of the HMBC spectrum showing correlations from the methylene protons to the unsaturated ketone and confirming attachment to the cyclopentanone to the indole ring with correlations from C-1 and C-2 to C-11 and C-12.
- Figure 4.1 Development of indole derivatives of indanocine as potential anticancer agents.
- Figure 4.2 α,β -unsaturated ketone moiety in arylidene indanones and chalcone.

- Figure 4.3 Selected cytotoxic natural chalcones.
- Figure 4.4 Synthetic, cytotoxic chalcones.
- Figure 4.5 Synthetic and cytotoxic arylidene/benzylidene indanones.
- Figure 4.6 Summary of compounds synthesized (phenyl substituted **4.31** series).
- Figure 4.7 Summary of compounds synthesized (3,4,5-trimethoxyphenyl substituted **4.32** series).
- Figure 4.8 Summary of compounds synthesized (pyridyl substituted **4.33** series).
- Figure 4.9 ^1H NMR spectrum of compound **4.31d** (400 MHz, DMSO-d₆).
- Figure 4.10 ^{13}C NMR spectrum of compound **4.31d** (100 MHz, DMSO-d₆).
- Figure 4.11 DEPT-135 NMR spectrum of compound **4.31d**.
- Figure 4.12 COSY and HMBC correlations for compound **4.31d**.
- Figure 4.13 1D selective NOESY NMR spectrum of compound **4.31d**.
- Figure 4.14 ^1H NMR spectrum of compound **4.32d** (400 MHz, DMSO-d₆).
- Figure 4.15 ^{13}C NMR spectrum of compound **4.32d** (100 MHz, DMSO-d₆).
- Figure 4.16 DEPT-135 NMR spectrum of compound **4.32d**.
- Figure 4.17 ^1H NMR spectrum of compound **4.33d** (400 MHz, DMSO-d₆).
- Figure 4.18 ^{13}C NMR spectrum of compound **4.33d** (100 MHz, DMSO-d₆).
- Figure 4.19 DEPT-135 NMR spectrum of compound **4.33d**.
- Figure 4.20 1D selective NOESY NMR spectrum of compound **4.33d**.
- Figure 4.21 A section of ^1H NMR spectra of **4.31d**, **4.32d** and **4.33d** showing H-5, and H-14.
- Figure 4.22 Non-linear regression curves for the antiproliferative activity of compound **4.33a** against the cell lines. IC₅₀ values greater than 250 μM were recorded as non-toxic.
- Figure 4.23 Tubulin-Colchicine active site (left) and 2D interaction map showing the binding interactions of colchicine with the ligand coloured in yellow.
- Figure 4.24 Tubulin-Colchicine active site (left) and 2D interaction map showing the binding interactions of combretastatin A-4 (bottom) with the ligand coloured in yellow.
- Figure 4.25 Tubulin-Colchicine active site (left) and 2D interaction map showing the binding interactions of **4.33a** (top) and Indanocine (bottom) with the ligand coloured in yellow.
- Figure 5.1 Data showing the results of a pull-down assay testing the interaction between Hsp90 and Hop (Moyo, 2013).

- Figure 5.2 The design of sargaquinoic acid analogues.
- Figure 5.3 ^1H NMR spectrum of compound **5.4c** (400 MHz, DMSO-d₆).
- Figure 5.4 ^{13}C NMR spectrum of compound **5.4c** (100 MHz, DMSO-d₆).
- Figure 5.5 HSQC NMR spectrum of compound **5.4c** (400 MHz, DMSO-d₆).
- Figure 5.6 COSY and HMBC correlations of compound **5.4c**.
- Figure 5.7 1D selective NOESY NMR spectrum of compound **5.4c**.
- Figure 5.8 ^1H NMR spectrum of compound **5.6e** (400 MHz, DMSO-d₆).
- Figure 5.9 ^{13}C NMR spectrum of compound **5.6e** (100 MHz, DMSO-d₆).
- Figure 5.10 HSQC NMR spectrum of compound **5.6e** (400 MHz, DMSO-d₆) showing the aromatic region.
- Figure 5.11 COSY and HMBC correlations of compound **5.6e**.
- Figure 5.12 ^1H NMR spectrum of compound **5.9d** (400 MHz, DMSO-d₆).
- Figure 5.13 ^{13}C NMR spectrum of compound **5.9d** (100 MHz, DMSO-d₆).
- Figure 5.14 HSQC NMR spectrum of compound **5.9d** (400 MHz, DMSO-d₆) showing some of the ^1H – ^{13}C correlations.
- Figure 5.15 COSY and HMBC correlations of compound **5.9d**.
- Figure 5.16 Non-linear regression curves for the antiproliferative activities of compound **5.9c** against the cell lines. IC_{50} values greater than 250 μM were recorded as non-toxic.
- Figure 5.17 Non-linear regression curves for the antiproliferative activities of compound **5.9d** against the cell lines.
- Figure 5.18 3D and 2D showing the binding interactions of SQA with Hsp90 geldanamycin-binding domain, the compounds are coloured yellow in the active site.
- Figure 5.19 3D and 2D showing the binding interactions of **5.4f** (top), **5.6f** (middle) and **5.9a** (bottom) with Hsp90 geldanamycin-binding domain, the compounds are coloured yellow in the active site.
- Figure 5.20 3D and 2D showing the binding interactions of **5.9c** (top) and **5.9d** (bottom) with Hsp90 geldanamycin-binding domain, the compounds are coloured yellow in the active site.
- Figure 5.21 Western blot analyses showing bands for Hsp90 α , CDK4, Hsp70/Hsc70 and HOP/STIP1 upon treatment with the set of compounds.
- Figure 5.22 Western blot analysis of the dose-dependent inhibition of Hsp90 α .

LIST OF SCHEMES

- Scheme 3.1 Proposed biosynthesis of Nostodione A (3.1).
- Scheme 3.2 Chen and co-workers' proposed biosynthetic pathway of cyclopenta[*b*]indole.
- Scheme 3.3 A plausible biosynthetic pathway of cyclopenta[*b*]indole.
- Scheme 3.4 Synthesis of cyclopenta[*b*]indoles *via* Fischer indolization (Berger & Corraz, 1977).
- Scheme 3.5 Synthesis of cyclopenta[*b*]indole *via* Friedel-crafts acylation reaction (Cui et al., 2004).
- Scheme 3.6 Reformatsky reaction/Dieckmann condensation (Palmieri & Petrini, 2007).
- Scheme 3.7 Palladium-catalysed tandem Heck–Suzuki synthesis of cyclopenta[*b*]indole (Ekebergh et al., 2015).
- Scheme 3.8 Rhodium-Catalyzed synthesis of cyclopenta[*b*]indole (Wu et al., 2017).
- Scheme 3.9 Tandem Au(I)-catalysed rearrangement/Nazarov synthesis of cyclopenta[*b*]indole (Scarpi et al., 2016).
- Scheme 3.10 Synthesis of cyclopenta[*b*]indoles *via* Nazarov cyclization of 1,4-pentadien-3-ols (Wang et al., 2016).
- Scheme 3.11 Synthesis of polysubstituted cyclopenta[*b*]indoles *via* relay gold (i)/Brønsted acid catalysis (Dhiman & Ramasastry, 2015).
- Scheme 3.12 Synthesis of cyclopenta[*b*] indole *via* Catalytic C–H bond functionalization with palladium (II) (Ferreira & Stoltz, 2003).
- Scheme 3.13 Synthesis of cyclopenta[*b*]indoles *via* Gold (I)-catalyzed dearomative Rautenstrauch rearrangement (Zi et al., 2015).
- Scheme 3.14 Japp-Klingemann/Fischer synthesis of cycloalka[*b*]indoles.
- Scheme 3.15 General mechanism of the Japp-Klingemann/Fischer synthesis of cycloalka[*b*]indoles.
- Scheme 3.16 Synthesis of cyclopenta[*b*]indole analogues.
- Scheme 4.1 Aldol condensation of indanone with aromatic aldehydes.
- Scheme 4.2 Palladium-nanoparticle catalyzed domino reaction (Saha et al., 2018).
- Scheme 4.3 General mechanism of Claisen-Schmidt synthesis of the arylidene cyclopenta[*b*]indol-3-one derivatives.

- Scheme 4.4 Claisen-Schmidt condensation of cyclopenta[*b*]indol-3-one with substituted aromatic aldehydes.
- Scheme 5.1 Synthesis of 1-acetyl-3-arylidene-piperazine-2,5-dione derivatives.
- Scheme 5.2 Synthesis of barbituric acid derivatives *via* Knoevenagel condensation.
- Scheme 5.3 Synthesis of prenylated theophylline derivatives.



UNIVERSITY *of the*
WESTERN CAPE

LIST OF TABLES

Table 2.1	The hallmarks of cancer.
Table 3.1	Physical parameters of the synthesized compounds 3.32a-l .
Table 3.2	NMR data for compound 3.32a (400 MHz for ^1H and 100 MHz for ^{13}C , DMSO- d_6).
Table 3.3	Antiproliferative activity of compounds 3.32(a-l) against HCC70 cells.
Table 3.4	<i>In silico</i> physicochemical properties and drug-likeness of the synthesized compounds.
Table 3.5	<i>In silico</i> predicted bioactivity of the synthesized compounds.
Table 4.1	Physical parameters of arylidene cyclopenta[<i>b</i>]indol-3-one.
Table 4.2	NMR data for compound 4.31d (400 MHz for ^1H and 100 MHz for ^{13}C , DMSO- d_6).
Table 4.3	NMR data for compound 4.32d (400 MHz for ^1H and 100 MHz for ^{13}C , DMSO- d_6).
Table 4.4	NMR data for compound 4.33d (400 MHz for ^1H and 100 MHz for ^{13}C , DMSO- d_6).
Table 4.5	Percentage cell viability relative to DMSO at 25 μM of synthesized compounds against HCC70 cancer cells.
Table 4.6	Antiproliferative activities of the selected compounds against three cancer cell lines and normal human cell line.
Table 4.7	The binding energies and intermolecular interactions of the compounds.
Table 4.8	<i>In silico</i> physicochemical of arylidene cyclopenta[<i>b</i>]indol-3-ones.
Table 5.1	NMR data for compound 5.4c (400 MHz for ^1H and 100 MHz for ^{13}C , DMSO- d_6).
Table 5.2	NMR data for compound 5.6e (400 MHz for ^1H and 100 MHz for ^{13}C , DMSO- d_6).
Table 5.3	NMR data for compound 5.9d (400 MHz for ^1H and 100 MHz for ^{13}C , CDCl_3).
Table 5.4	Physical parameters of the synthesized compounds.
Table 5.5	Percentage cell viability relative to DMSO at 25 μM of synthesized compounds against HCC70 cancer cells.
Table 5.6	IC50 values of the selected compounds.

Table 5.7 In silico physicochemical properties and drug-likeness of the synthesized compounds.

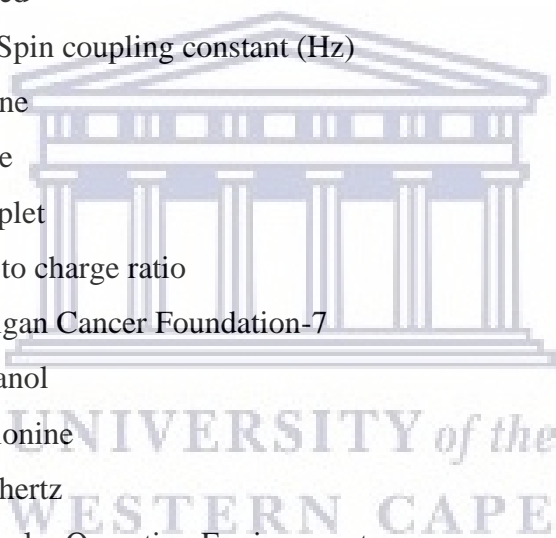
Table 5.8 The binding energies and intermolecular interactions of the compounds.



LIST OF ABBREVIATIONS

^{13}C NMR	Carbon Nuclear Magnetic Resonance
17-AAG	17- <i>N</i> -allylamino-17-demethoxygeldanamycin
17-DMAG	17-Dimethylaminoethylamino-17-demethoxygeldanamycin
^1H NMR	Proton Nuclear Magnetic Resonance
Ala	Alanine
Asn	Asparagine
br s	Broad singlet
CDCl_3	Deuterated chloroform
CDK4	Cyclin-dependent kinase 4
COSY	Correlation Spectroscopy
Cys	Cysteine
d	Doublet
DCM	Dichloromethane
dd	Doublet of doublets
DDQ	2,3-Dichloro-5,6-dicyano-1,4-benzoquinone
DEPT-135	Distortionless Enhancement by Polarization Transfer-135
DMAPP	Dimethylallyl diphosphate
DMF	Dimethylformamide
DMSO-d_6	Deuterated dimethyl sulfoxide
DNA	Deoxyribonucleic Acid
EtOAc	Ethyl acetate
EtOH	Ethanol
FDA	Food and Drug Administration
GLOBOCAN	Global Cancer Statistics
Gly	Glycine
HMBC	Heteronuclear Multiple Bond Correlation
Hop	Hop Hsp70/Hsp90 organising protein
HR-ESIMS	High Resolution Electrospray Ionization Mass Spectrum
HRMS	High Resolution Mass Spectrometry

Hsc70	Heat shock cognate protein 70 kDa
HSF1	Heat shock factor 1
Hsp27	Heat shock protein 27 kDa
Hsp40	Heat shock protein 40 kDa
Hsp70	Heat shock protein 70 kDa
Hsp90	Heat shock protein 90 kDa
HSQC	Heteronuclear Single Bond Correlation
Hz	Hertz
IARC	International Agency for Research on Cancer
IC ₅₀	Inhibitory Concentration 50 %
IR	Infrared
<i>J</i>	Spin-Spin coupling constant (Hz)
Leu	Leucine
Lys	Lysine
m	Multiplet
m/z	Mass to charge ratio
MCF-7	Michigan Cancer Foundation-7
MeOH	Methanol
Met	Methionine
MHz	Megahertz
MOE	Molecular Operating Environment
NMR	Nuclear Magnetic Resonance
NMSC	Nonmelanoma Skin Cancer
NOESY	Nuclear Overhauser enhancement spectroscopy
ppm	Parts per million
RDC	Radical
RMSD	Root mean square deviation
s	Singlet
Ser	Serine
SQA	Sargaquinoic acid
STIP1	Stress induced phosphoprotein 1



t	Triplet
td	Triplet of doublets
THF	Tetrahydrofuran
Thr	Threonine
TLC	Thin Layer Chromatography
Tyr	Tyrosine
UPLCMS	Ultra Performance Liquid Chromatography-Mass Spectrometry
UV	Ultra Violet
Val	Valine
VBL	Vinblastine
VCR	Vincristine
VCR	Vincristine
VDS	Vindesine
VFL	Vinflumine
VNL	Vinorelbine
δ	Chemical shift (ppm)



UNIVERSITY *of the*
WESTERN CAPE

ABSTRACT

Natural products have been an important source of drugs and novel lead compounds in drug discovery. Their unique scaffolds have led to the synthesis of derivatives that continue to give rise to medically relevant agents. Thus, natural product-inspired drugs represent a significant proportion of drugs in the market and with several more in development. Cancer is among the leading public health problems and a prominent cause of death globally. Chemotherapy has been important in the management of this disease even though side effects that arise due to lack of selectivity is still an issue. This has led to the development of anticancer drugs that target cancer-specific structures such as proteins or enzymes that promote cancer progression. The microtubule inhibitors (antimitotics) arrest mitotic cells at the G2-M phase leading to apoptosis of cancer cells. Currently, natural product derived antimitotics such as the vinca alkaloids are available for clinical use. The 90 kDa heat shock protein 90 (Hsp90) regulates the folding and stabilization of many oncogenic proteins that promote cell proliferation and signaling pathways. Hsp90 became a promising target in anticancer drug development following the discovery of the ability of geldanamycin and novobiocin to disrupt the folding machinery of Hsp90, however, no Hsp90 inhibitor has made it to the clinic.

The main purpose of this study was to design and synthesize new compounds as antiproliferative agents that target mitosis and the function of heat shock proteins (e.g. Hsp90). The cyclopenta[*b*]indole scaffold has been found in some microorganisms and plants, and it has been shown to affect the function of heat shock proteins. Hence, we embarked on the synthesis of a series of cyclopenta[*b*]indoles in three steps *via* Japp-Klingemann reaction and Fischer-indole reactions. The most active compound from this group exhibited antiproliferative activity with an IC₅₀ value of 6.9 μM against HCC70 cancer cells.

In an attempt to further increase the activity of this series of compounds, we synthesised their arylidene cyclopenta[*b*]indol-3-one derivatives. Arylidene indanone analogues such as indanocine; an antimitotic compound, display potent activity against a range of cancer cells. The most active arylidene cyclopenta[*b*]indol-3-one derivative displayed selective antiproliferative activity against HCC70 cancer cells with an IC₅₀ of 10.2 μM. Molecular docking studies provided some evidence of the affinity and binding interactions of these compounds with colchicine binding site of tubulin.

Sargaquinoic acid, a marine natural product first isolated from the brown alga *Sargassum serratifolium*, demonstrated moderate activity against Hsp90. Hence we designed and synthesized a series of diketopiperazine, barbituric acid and purine derivatives as analogues of sargaquinoic acid. The most potent compound showed antiproliferative activity with an IC₅₀ value of 1.4 μM against HeLa cells and western blot analysis showed inhibition of Hsp90 through the degradation of CDK4 client protein without overexpression of Hsp70. The compounds designed and synthesized here provide useful lead structures for the further development of antimitotic and Hsp90 inhibitors.



Chapter 1

Introduction



UNIVERSITY *of the*
WESTERN CAPE

1.1 The burden of cancer

The term “cancer” describes a number of diseases in which abnormal cells grow beyond control and can ultimately infiltrate other parts of the body (de Mesquita et al., 2009). Although there is no clear cause of some cancers, certain factors such as inherited genetic mutations, immune conditions, tobacco use and excessive alcohol intake have been implicated in the development of cancer (Bray et al., 2018). The continuous burden of cancer as a prominent world problem is of great concern. According to GLOBOCAN estimates for 2018, 18.1 million new cancer cases, [17.0 million excluding nonmelanoma skin cancer (NMSC)] and 9.6 million cancer deaths (9.5 million excluding NMSC) was estimated worldwide based on the statistics provided by the International Agency for Research on Cancer (IARC). An aging and growing world population together with a decline in mortalities of stroke and coronary heart disease places cancer as one of the leading causes of death (Bray et al., 2018).

In the United States, early diagnosis and improved treatment have improved survival rates for all cancers compared to the 1960s. However, the type of cancer, stage and time of diagnosis are determining factors in cancer survival (American Cancer Society, 2019). In spite of higher incident rates for all cancers in economically developed countries the percentage mortality relative, to incidence, is higher in less developed countries. Late detection and poor management of the disease are the major factors responsible for the disparity (Jemal et al., 2011).

There are different approaches for the treatment of various types of cancer, amongst which are chemotherapy, radiotherapy or surgery. Depending on the stage or severity at the time of diagnosis; these treatment modalities may be combined (American Cancer Society, 2019). The major advantage of chemotherapy over radiotherapy and surgery is the ability to reach target sites. However, the shortcoming of systemic delivery of anticancer drugs is toxicity (Bhosle & Hall, 2009).

1.2 Discovery of anticancer drugs from natural sources

For centuries, humans have used natural products in the form of crude extracts in traditional medicine for the treatment of several kinds of diseases (Petrovska, 2012). Natural products are secondary metabolites produced by terrestrial, marine and microorganisms. The need to adapt to living under extreme conditions, for protection against predation and competition, and for nutrients

drove the evolution of biochemical pathways to the production of secondary metabolites. These secondary metabolites are capable of producing pharmacological actions due to the fact they have evolved to bind and interact with biological targets (drug targets) (Newman & Cragg, 2012; Cragg & Newman, 2013).

The general process for industrial, natural product-based drug discovery follows a few well-defined steps. Firstly, libraries of natural product extracts or fractions are screened for activity against a specific target. Upon identification of a hit, the compound is isolated and its structure elucidated through various spectroscopic techniques, and further biological studies are conducted to recognize specific targets (Koehn & Carter 2005).

Natural products became prominent in anticancer drug discovery in mid-20th century following the discovery of actinomycin D, an antitumor antibiotic drug used in treatment of pediatric tumours (DeVita & Chu, 2008). The vinca alkaloids vincristine and vinblastine, and cytarabine were also discovered around that time and gave the much needed attention to natural products as a source of drugs and novel lead molecules (DeVita & Chu, 2008). In general, more than 60% of current anticancer drugs are natural products or derived from natural sources (Newman & Cragg, 2016). Among the recently FDA approved anticancer drugs from natural origin are trabectedin (Yondelis®) used for the treatment of soft tissue sarcoma and ovarian cancer, eribulin mesylate (Halaveri®) indicated for metastatic breast cancer and plitidepsin (Aplidin®) used for the treatment of multiple myeloma, leukaemia and lymphoma (Haber & Spaventi, 2017).

Although many anticancer drugs have saved many lives, toxicity due to lack of selectivity is a major problem. This often leads to unwanted side effects such as fever, constipation, nausea and vomiting (Moudi et al., 2013).

Another problem associated with the use of anticancer agents is the development of resistance which is the ability of cancer cells to develop tolerance to chemotherapy (Housman et al., 2014). This phenomenon can be categorized into two mechanisms. Primary resistance results from the inability of a tumour to respond to the drug from the beginning, this may be due to poor penetration of the drug or genetic changes in the tumour (Bhosle & Hall, 2009). On the other hand, secondary or acquired resistance occurs after the cells come into contact with the drug. This is due to several acquired mechanisms such as adjustment of repair mechanism or upsurge in drug inactivation (Bhosle & Hall, 2009).

In summary, the discussion above highlights the importance of cancer as a growing health threat and the prominent role that natural products have historically played in the discovery of anticancer drugs. However, the lack of selectivity of anticancer drugs and the development of resistance to these drugs highlights the critical need for new anticancer agents.

1.3 Rationale, Aim and Objectives

Despite the relevance of chemotherapy as an important component in cancer management, its success has been flawed due to lack of selectivity which leads to undesirable side effects which arise from toxicity. For this reason, the continuous search for improved and selective anticancer agents is crucial.

Hence, the aim of this research project was to design and synthesize new scaffolds as antiproliferative agents which could target mitosis and the function of heat shock proteins (e.g. Hsp90).

Taking inspiration from previously reported anticancer natural products based on the cyclopenta[*b*]indole scaffold and the prenylated quinone, sargaquinoic acid, we defined the following objectives:

- To synthesize a series cyclopenta[*b*]indole derivatives
- To expand the cyclopenta[*b*]indole scaffold by incorporating the arylidene moiety derivatives as indanocine analogues
- To synthesize diketopiperazine, barbituric acid and purine derivatives as analogues of sargaquinoic acid
- To evaluate the antiproliferative activities of synthesized compounds
- The in silico prediction of the ADME and pharmacokinetic properties of the synthesized compounds.
- To investigate the binding affinity and interactions of the synthesized compounds with tubulin polymerase and Hsp90 alpha by molecular docking.

1.4 Thesis overview

Chapter one presents the context of cancer as an important disease while chapter two provides a concise review of natural product-derived microtubule targeting agents and Hsp90 inhibitors as attractive molecular targets in cancer drug development. Chapter three provides a report on synthesis and antiproliferative studies of cyclopenta[*b*]indole derivatives. The synthesis, antiproliferative evaluation and assessment of the potential of arylidene cyclopenta[*b*]indol-3-one derivatives as potential tubulin polymerization inhibitors by molecular docking is described in chapter four. In chapter five, an account of design, synthesis and biological studies of diketopiperazine, barbituric acid and purine derivatives as potential Hsp90 inhibitors are reported. Finally, chapter six presents the total findings and recommendations for future studies.



References

- American Cancer Society. (2019). Cancer Facts & Figures 2019 [PDF file]. <https://www.cancer.org/content/dam/cancer-org/research/cancer-facts-and-statistics/annual-cancer-facts-and-figures/2019/cancer-facts-and-figures-2019.pdf> (accessed November 20, 2019).
- Bhosle, J., & Hall, G. (2009). Principles of cancer treatment by chemotherapy. *Surgery (Oxford)*, 27(4), 173-177.
- Bray, F., Ferlay, J., Soerjomataram, I., Siegel, R. L., Torre, L. A., & Jemal, A. (2018). Global cancer statistics 2018: GLOBOCAN estimates of incidence and mortality worldwide for 36 cancers in 185 countries. *CA: A Cancer Journal for Clinicians*, 68(6), 394-424.
- Cragg, G. M., & Newman, D. J. (2013). Natural products: A continuing source of novel drug leads. *Biochimica et Biophysica Acta - General Subjects*, 1830(6), 3670-3695.
- de Mesquita, M. L., de Paula, J. E., Pessoa, C., de Moraes, M. O., Costa-Lotufo, L. V., Grougnet, R., Michel, S., Tillequin, F., & Espindola, L. S. (2009). Cytotoxic activity of Brazilian Cerrado plants used in traditional medicine against cancer cell lines. *Journal of Ethnopharmacology*, 123(3), 439-445.
- DeVita, V. T., & Chu, E. (2008). A history of cancer chemotherapy. *Cancer Research*, 68(21), 8643-8653.
- Haber, V. E., & Spaventi, R. (2017). Discovery and development of novel drugs. *Progress in Molecular and Subcellular Biology*, 55, 91-104.
- Housman, G., Byler, S., Heerboth, S., Lapinska, K., Longacre, M., Snyder, N., & Sarkar, S. (2014). Drug resistance in cancer: an overview. *Cancers*, 6(3), 1769-1792.
- Jemal, A., Bray, F., Center, M. M., Ferlay, J., Ward, E., & Forman, D. (2011). Global cancer statistics. *CA: A Cancer Journal for Clinicians*, 61(2), 69-90.
- Koehn, F. E., & Carter, G. T. (2005). The evolving role of natural products in drug discovery. *Nature Reviews Drug Discovery*, 4(3), 206-220.
- Moudi, M., Go, R., Yien, C. Y. S., & Nazre, M. (2013). Vinca alkaloids. *International Journal of Preventive Medicine*, 4(11), 1231-1235.

Newman, D. J., & Cragg, G. M. (2012). Natural products as sources of new drugs over the 30 years from 1981 to 2010. *Journal of Natural Products*, 75(3), 311-335.

Newman, D. J., & Cragg, G. M. (2016). Natural Products as Sources of New Drugs from 1981 to 2014. *Journal of Natural Products*, 79(3), 629-661.

Petrovska, B. B. (2012). Historical review of medicinal plants' usage. *Pharmacognosy Reviews*, 6(11), 1-5.



Chapter 2

Literature review

UNIVERSITY *of the*
WESTERN CAPE

2.1 Development of anticancer drugs from natural products

In contrast to the early anticancer drugs that induce DNA damage and therefore lack discrimination between cancer cells and normal cells, recent drugs are intended to be more selective to cancer cells and hence should show reduced toxicity (Kumar et. al., 2017). This is based on the knowledge of signal transduction pathways and pathogenesis of cancer that provides molecular targets for chemotherapeutic drug development (Padma, 2015).

The unique chemical space and complex structures offered by natural products present an opportunity for drug development by optimizing their structures to enhance biological activities (Khandelwal et al., 2016). Hence, the focus of this review will be on the development of natural and synthetic analogues of microtubule-targeting anticancer drugs otherwise known as antimetabolic agents and the promising heat shock protein 90 inhibitors derived from natural products.

2.2 Natural product derived microtubule-targeting anticancer agents and their synthetic analogues

Tubulins are spherical proteins consisting of α - and β -tubulin dimers which form the building blocks for the microtubular cytoskeleton. Microtubules are crucial for various cell functions such as cell division and maintenance (Jordan & Wilson, 2004). The heterodimers of α - and β -tubulin assemble to form the microtubule and then polymerize into a long-standing microtubule (Figure 2.1) (Bhattacharya & Cabral 2004; Jordan & Wilson, 2004). Therefore, obstructing the aggregation of tubulins or impeding their segregation could prompt cell cycle arrest in the G2-M phase and development of defective mitotic spindles. This process prevents cell division, making tubulins a target for anticancer drug development (Bukhari, 2017; Kaur et. al., 2014).

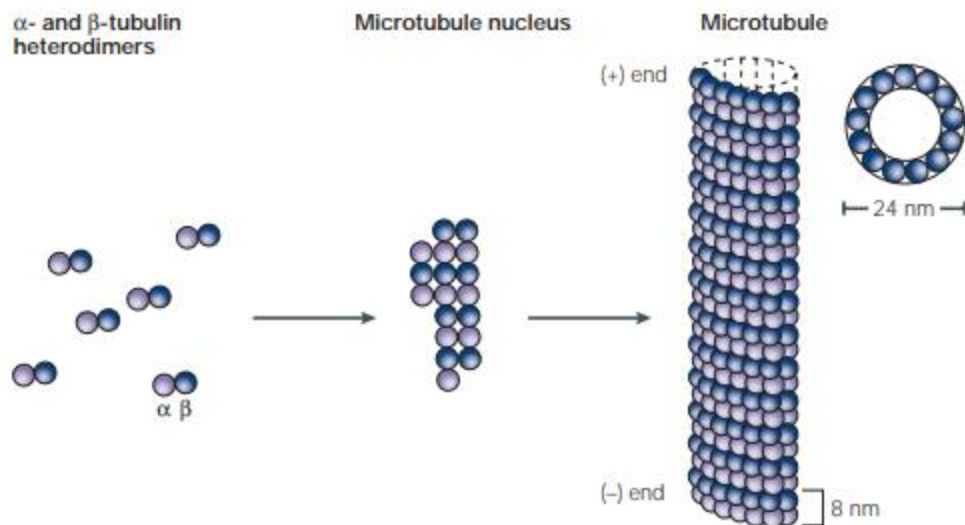


Figure 2.1 Polymerization of microtubules (Jordan & Wilson 2004).

Drugs targeting microtubules can be classified into two classes based on their mechanism of action. Tubulin polymerization inhibitors obstruct stabilization of tubulin by binding to either the vinca binding or colchicine binding site. Tubulin depolymerization agents prevent destabilization of tubulin and they bind to the taxane binding site (Kaur et. al., 2014; Field et. al., 2013).

2.2.1 Colchicine binding domain agents

Colchicine (**2.1**) is a natural product isolated from *Colchicum autumnale*. The plant extract was traditionally used for the treatment of gout. Colchicine the main substance from the plant extract is currently indicated for gout. Although colchicine binds to tubulin its toxicity prevented its clinical application in cancer therapy (Hastie 1991). Structural activity relationship studies revealed that the three methoxy groups on ring A of colchicine is important for tubulin binding affinity and obstruction of tubulin polymerization (Shi et al., 1998). In spite of its failed anticancer application, colchicine has served as a lead in the design of other potential anticancer agents (Kumar et al., 2017). The novel *N*-acetylcolchinol (**2.2**) is a synthetic analogue of colchicine and vascular targeting agent leading to tumour necrosis and vascular stoppage against solid tumours (Beerepoot et al., 2006).

Combretastatins are natural stilbenes isolated from *Combretum caffrum*, a South African willow tree (Pettit et al., 1987a). These compounds exhibited good cytotoxicity against leukaemia P388 cells and inhibits tubulin polymerization at the colchicine binding site. Combretastatin A-4 (**2.3**)

was the most potent with about 5-fold higher activity than Combretastatin A-1 (**2.4**) (Pettit et al., 1987a; Pettit et al., 1987b).

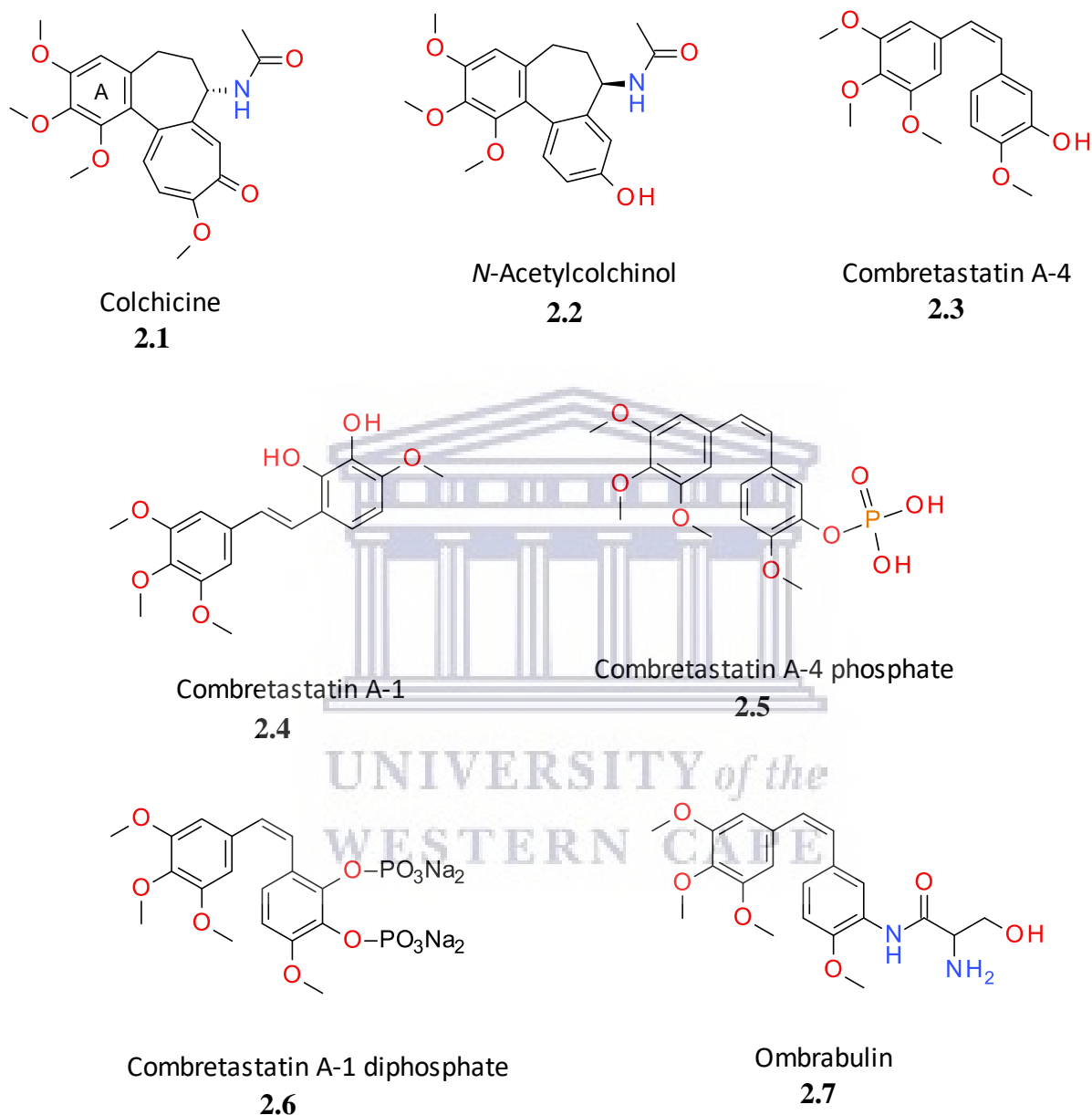


Figure 2.2 Structures of colchicine domain binding agents.

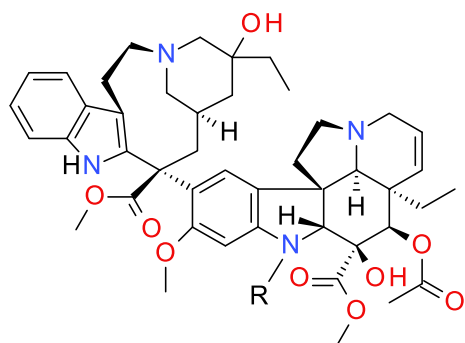
Similar to colchicine, it was demonstrated that 3,4,5-trimethoxy substituents (A ring) are crucial for binding affinity at the colchicine binding site of tubulin (Woods et al., 1995). Due to the poor solubility of combretastatin A-4, a synthetic prodrug (**2.5**) was synthesized that has completed

phase II clinical trials (Pettit et al., 1995; Young & Chaplin 2004). Combretastatin A-1 diphosphate (**2.6**) showed manageable side effects in patients with solid tumours in phase I clinical trials. For this reason, it was recommended for a phase II clinical trials (Patterson et al. 2012). In phase III clinical trials of ombrabulin (**2.7**) a synthetic derivative of combretastatin A-4 used in combination with cisplatin exhibited a uniform safety profile and occurrence of bone marrow suppression against soft-tissue sarcomas (Blay et al., 2015).

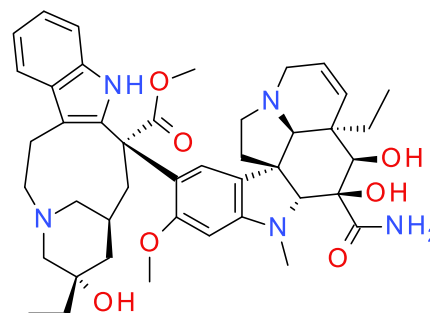
2.2.2 Vinca binding domain agents

The natural vinca alkaloids (Figure 2.3) vincristine (VCR) **2.8** and vinblastine (VBL) **2.9** were originally isolated in the 1950s from the *Catharanthus roseus*, commonly known as Madagascar periwinkle. These alkaloids interfere with mitosis through binding and interaction with microtubules (Himes 1991). Historically, extracts of this plant were used in the treatment of wounds, gastric ulceration, hemorrhage and hyperglycemia. Later on, studies showed that certain fractions of the plant extract caused myelosuppression and peripheral granulocytopenia in rats (Gidding et al., 1999). Including their synthetic derivatives (Figure 2.3) vindesine (VDS) **2.10**, vinorelbine (VNL) **2.11** and the most recent vinflumine (VFL) **2.12**, the vinca alkaloids are used in the treatment of lymphomas, carcinomas and solid tumours. In addition to their useful application, these compounds also possess adverse side effects such as peripheral neuropathy and hepatotoxicity among others (Moudi et al., 2013).

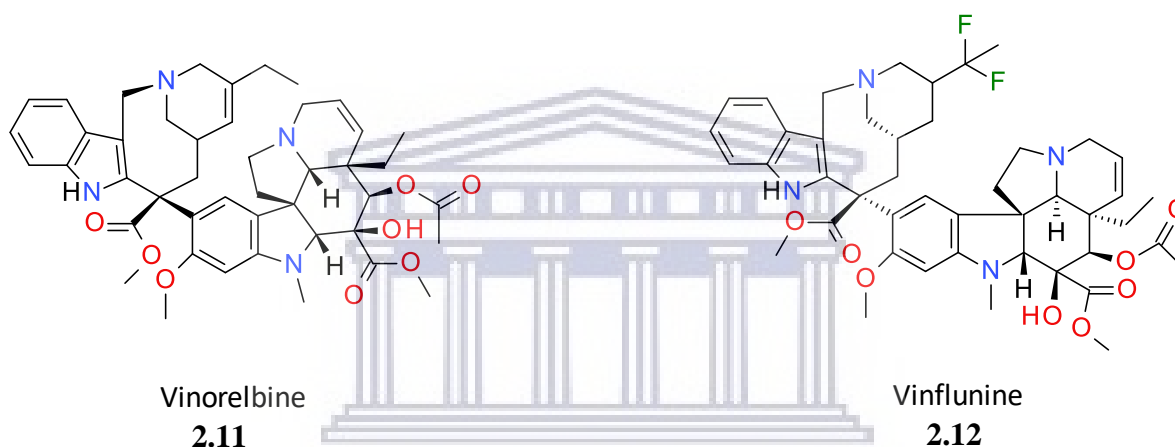
UNIVERSITY of the
WESTERN CAPE



2.8 Vincristine; R = CHO
2.9 Vinblastine; R = CH₃



Vindesine
2.10



Vinorelbine
2.11

Vinflunine
2.12

Figure 2.3 Structures of selected vinca alkaloids.

Dolastatin 10 (**2.13**) is a peptide, first isolated from the sea hare, *Dolabella auricularia*. Its cytotoxicity is also a result of its ability to hinder tubulin polymerization. The synthetic derivative TZT-1027 (**2.14**) shares the same mode of action with the parent compound but with improved antitumour activity (Natsume et al., 2000). Dolastatin 10 was discontinued in phase II clinical trials as a single agent due to low therapeutic activity in patients with hormone refractory metastatic adenocarcinoma, platinum-sensitive ovarian carcinoma recurrence and neurotoxicity (Banerjee et al., 2008). Minor side effects such as fatigue, alopecia, nausea and constipation were observed in phase II clinical trial of TZT-1027 in patients with advanced or metastatic soft-tissue sarcomas who were previously treated with anthracyclines (Patel et al., 2006). Brentuximab vedotin (Adcetris®) (**2.15**) is a CD30-specific antibody drug, co-developed by Seattle Genetics and Millennium Pharmaceuticals (Newman & Cragg, 2017). It was accomplished by connecting anti-

CD30 antibody (cAC10) through a linker with the dolastatin analogue; monomethyl auristatin E (MMAE) (Newman & Cragg, 2017). This drug was approved for the treatment of relapsed Hodgkin lymphoma and systemic anaplastic large cell lymphoma (ALCL) by the FDA in 2011. (Senter & Sievers, 2012).

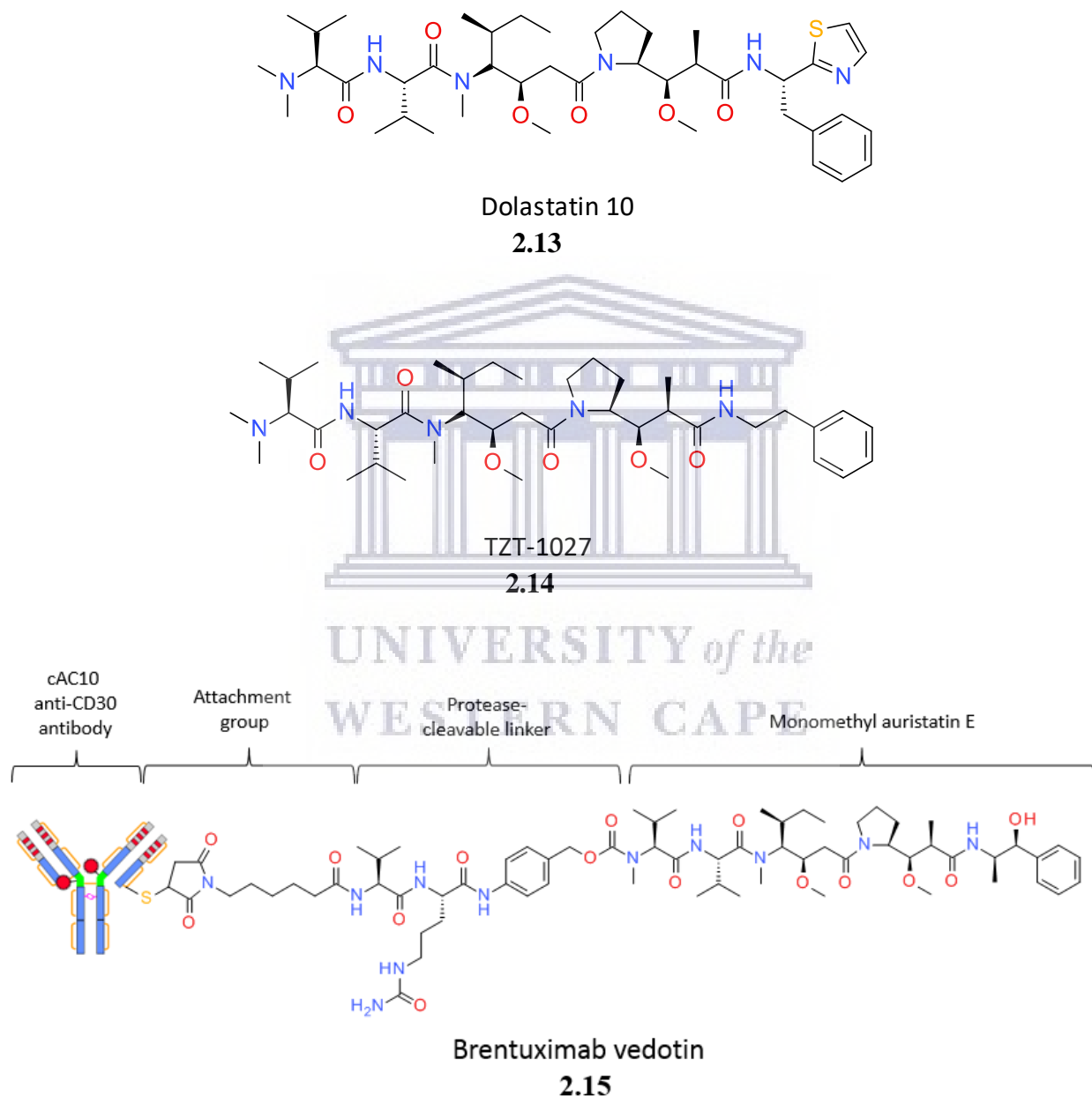


Figure 2.4 Structures of dolastatin 10, TZT-1027 and brentuximab vedotin.

Halichondrin B (**2.16**) is a potent antitumour polyether macrolide first isolated from *Halichondrin okadai*, a Japanese marine sponge (Hirata & Uemura 1986). Later on, it was discovered that other sponges such as: *Axinella* sp, *Phakellia carteri*, and *Lissondendryx* sp produce this natural product (Towle et al., 2001). Halichondrin B binds to the vinca domain as a non-competitive inhibitor to vinblastine and obstructs mitosis by inhibition of tubulin polymerization (Bai et al., 1991). Despite its potent cytotoxicity, it was only obtained in small quantity from the sponges which slowed down its clinical evaluation. Fortunately, the Kishi group achieved the total synthesis of Halichondrin B (Aicher et al., 1992) which provided the platform for its synthetic analogues (Yeung, 2011). The less complex analogue; Eribulin mesylate (Havalen®) (**2.17**) was identified and retained the potency of the parent compound. It was approved for the treatment of metastatic breast cancer by the FDA in 2010, and EMA in 2011 (Huyck et al., 2011).

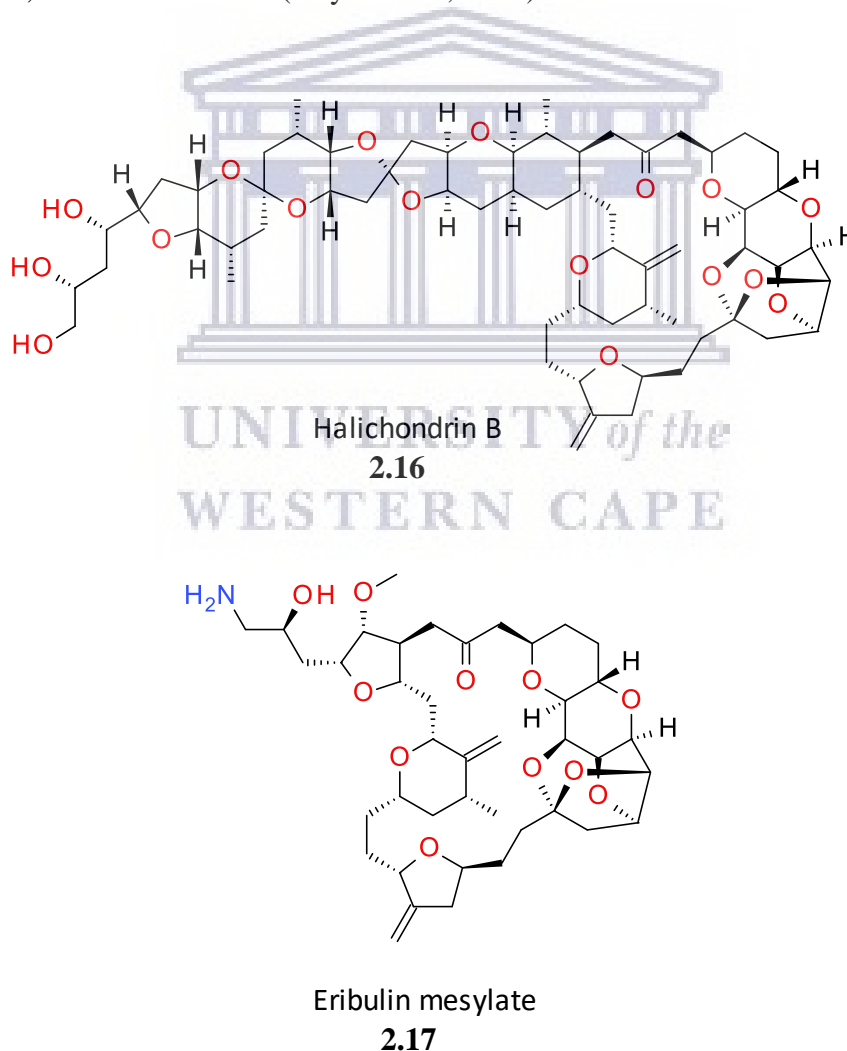


Figure 2.5 Structures of halichondrin B and eribulin mesylate.

2.2.3 Taxane binding domain agents

Paclitaxel (Taxol®) (**2.18**) is a metabolite from the bark of the pacific yew, *Taxus brevifolia*. The FDA approved its clinical application against breast and ovarian cancers in the early 1990s. Its mode of action also involves stabilizing polymerization of microtubules. Besides its success, aqueous solubility and dose-limiting toxicity were the major shortcomings. Solubilizing agents were required to improve bioavailability but also resulted in adverse side effects (Safavy et al., 1999). When compared to paclitaxel, docetaxel (Taxotere®) (**2.19**) a semi-synthetic analogue exhibited a broader range of activity that included non-small cell lung cancer. Although these two important drugs have been approved for over two decades, multidrug resistance remains a major challenge (Gueritte, 2001). The affinity of first generation taxanes to P-glycoprotein has been associated with the development of resistance, however, semi-synthetic cabazitaxel (Jevtana®) (**2.20**) exhibits poor affinity for the multi-drug resistance protein and is thus effective against docetaxel-resistant tumours (Ojima et al., 2016).

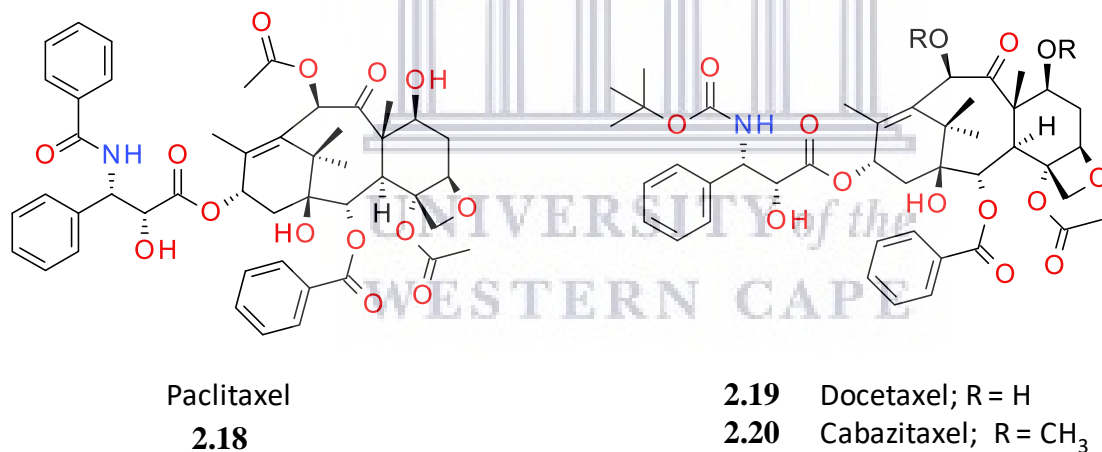


Figure 2.6 Structures of paclitaxel, docetaxel and cabazitaxel.

The epothilones are not taxanes but their mechanism of action is expressed in binding to the taxane binding site of tubulin, thus they are also microtubule stabilizers. Epithothilones A (**2.21**) and B (**2.22**) are natural products first isolated from the myxobacterium *Sorangium cellulosum* (Gerth et al., 1996). Neither compound was effective in *in-vivo* antitumour studies, however, the semi-synthetic lactam analogue of epothilone B, azoepothilone B (Ixempra®) was synthesized and displayed potent activity against a variety of tumour cells (Hunt, 2009). Although its water

solubility is an advantage over paclitaxel, neurological toxicity is one of its disadvantages (de Jonge & Verweij, 2005). Azoepothilone B (**2.23**) was approved in 2007 by the FDA for clinical use as a single agent in treatment of metastatic or locally advanced breast cancer that is unresponsive to other drugs such as taxanes or anthracycline (Hunt, 2009).

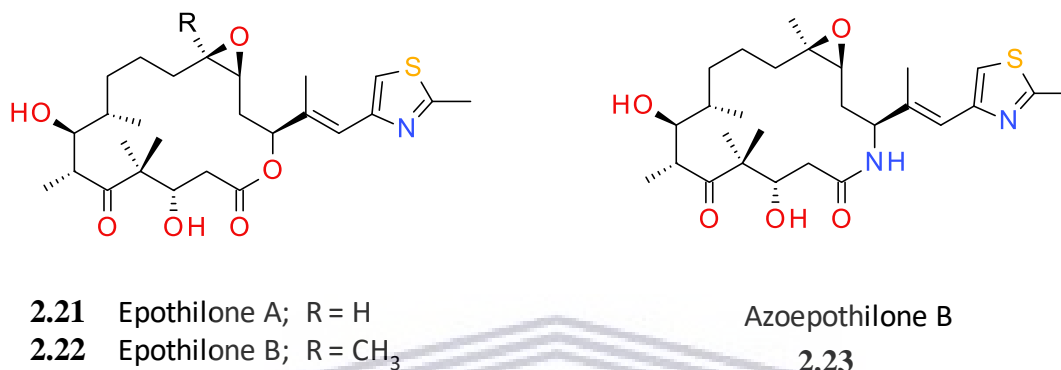


Figure 2.7 Structures of eपोthilones A, eपोthilone B and azoepothilone B (Ixempra®).

2.3 Natural product derived heat shock protein 90 inhibitors and their synthetic derivatives as anticancer agents

The 90 kDa heat shock proteins (Hsp90) are molecular chaperones responsible for growth, folding and stabilization of oncogenic signal transduction proteins. These proteins are otherwise known as Hsp90 client proteins and they include; kinases (EGF-R and Her-2), Akt/PKB, c-MET, ErbB2, HSF-1 and so on (Blagg & Kerr, 2006; Zhang & Burrows, 2004). The malignant progression of cancer has been shown to be dependent on Hsp90 client proteins and they function to ensure the attainment of the hallmarks of cancer (Table 2.1) (Hanahan & Weinberg, 2000). For cancer to maintain its malignancy, it requires the over-expression of heat shock proteins that compensates by refolding denatured proteins that resulted from cellular stress (Blagg & Kerr, 2006). The expression of Hsp90 is reported to be up to 10-fold in cancer cells compared to normal cells. Consequently, inhibition of Hsp90 leads to degradation of the client proteins. As such, it has become a target in chemotherapeutic drug development due to the dependence of multiple oncogenes on Hsp90 for survival and maturation (Zhao & Blagg 2013; Zhang et al., 2017).

Table 2.1 The hallmarks of cancer (Garg et al., 2016).

Hallmarks of Cancer	Hsp90 Client Protein(s)
Sustaining proliferative signaling	Raf-1, AKT, Her2, MEK, Bcr-Abl
Evading growth suppressors	Plk, Wee1, Myc1, CDK4, CDK6, Myt1
Resisting cell death	NF- κ , AKT, p53, c-MET, Apaf-1, Survivin
Enabling replicative immortality	Telomerase (h-Tert)
Inducing angiogenesis	HIF-1 α , VEGFR, PI3K/AKT, RTKs, flt-3
Activating invasion and metastasis	c-MET, SSDF-1, MMP-2
Deregulated cellular energetics	ARNT, ARRB1, HIF-1 α , HMG1, SREBF1
Avoiding immune destruction	IRAK3
Tumour-promoting inflammation	IL-6, IL-8, IRAK1, IRAK2, IRAK3
Genome instability and mutation	FANCA, MAFG, NEK8

Human Hsp90 exists as four isoforms; the Hsp90 α (inducible) and Hsp90 β (constitutional) are the cytoplasmic isoforms while glucose related protein 94 (GRP94) and tumour necrosis factor receptor associated protein 1 (TRAP-1) are the endoplasmic reticulum and mitochondrial isoforms respectively, (Blagg & Kerr, 2006).

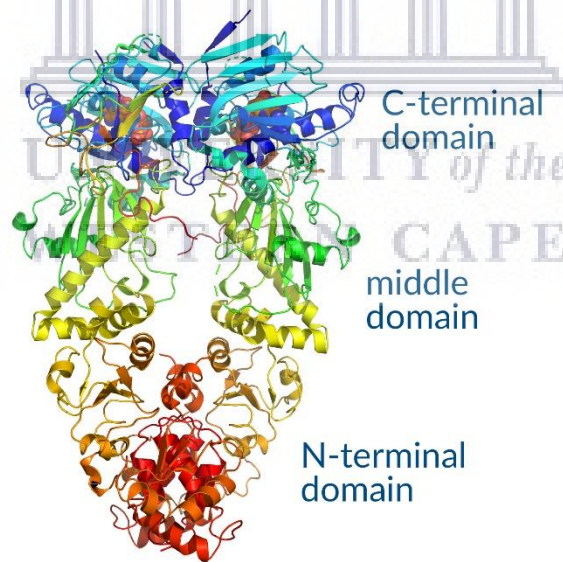


Figure 2.8 The functional domains of Hsp90 (photograph accessed from <https://www.caymanchem.com/news/molecular-chaperones-in-control-of-the-heat-shock-response>).

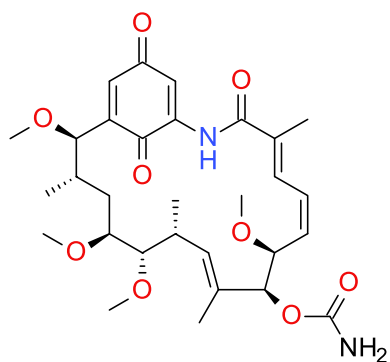
Each Hsp90 monomer consists of three operational domains; N-terminal domain, middle domain and C-terminal domain (Figure 2.8). The N-terminal domain is the ATP binding pocket, while the

charged middle domain is associated with the binding of co-chaperones and linkage of both termini, and C-terminal domain is the nucleotide binding site responsible for dimerization (Harris et al., 2004; Pearl & Prodromou, 2006). The N-terminal inhibitors such as geldanamycin and radicicol exert their activity by hindrance of ATP-catalysed hydrolysis, this is achieved by competitive binding to the N-terminal ATP-binding site (Jadhav et al., 2009).

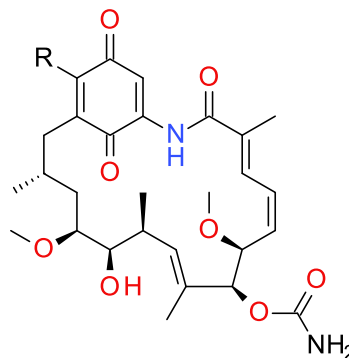
2.3.1 N-terminal Inhibitors

2.3.1.1 Ansamycin derivatives

Herbimycin A (2.24) and geldanamycin (GDM) (2.25) are benzoquinone ansamycin metabolites isolated from *Streptomyces* bacteria and they both exhibit potent antitumour activity (Sasaki et al., 1979; Uehara et al., 1988). The antitumour activity of GDM was initially thought to have resulted from tyrosine kinase inhibition. However, further biological studies revealed its binding to the N-terminal ATP-binding site of Hsp90 and disrupting its folding machinery (Whitesell et al., 1994). This makes Hsp90 a potential anticancer drug target and GDM the first Hsp90 inhibitor (Patel et al., 2004). Although GDM showed a promising therapeutic potential, hepatotoxicity led to its discontinuation in clinical trials (Supko et al., 1995). A semi-synthetic derivative of geldanamycin 17-AAG (2.26) was developed to address its liver toxicity. In the *in vivo* studies, growth inhibition of prostate tumours and Hsp90 client protein inhibition was reported at non-toxic doses, and was subsequently recommended for clinical trials (Solit et al., 2002). Limitations such as dose-dependent toxicity, solubility and bioavailability were some of the challenges encountered in the clinical trial of 17-AAG (Sausville et al., 2003). An effort to address the problem was the addition of *N,N*-dimethyl-1,2-ethanediamine to 17-AAG to produce the water-soluble derivative of GDM; 17-DMAG (2.27), however, its clinical trial was terminated in 2008 (Biamonte et al., 2009).



Herbimycin A
2.24



- 2.25 Geldanamycin; R = OCH₃
 2.26 17-AAG; R = NHCH₂CH₂
 2.27 17-DMAG; R = NH(CH₂)₂N(CH₃)₂

Figure 2.9 Structures of ansamycin analogues.

2.3.1.2 Resorcylic acid lactone derivatives

Radicalol (RDC) (2.28) is a natural resorcylic lactone originally isolated from the fungus, *Monosporium bonorden*. Similar to GDM, radicalol competes with ATP for the N-terminal ATP-binding site and interferes with the functions of Hsp90 and thus became the first non-benzoquinone ansamycin compound to target Hsp90 (Schulte et al., 1998). Radicalol exhibited potent *in vitro* antiproliferative activity, however, it was inactive in animal models (Soga et al., 2003). It was suggested that the lack of *in vivo* activity could be due to its epoxide functionality (Lei & Danishefsky, 2008). Danishefsky and colleagues synthesized cycloproparadicicol (2.29) by replacing the epoxide with a cyclopropane ring to produce a potentially shelf-stable drug with improved pharmacokinetics (Yamamoto et al, 2003, Yang et al., 2004). It exhibited potent antiproliferative activity with an IC₅₀ value of 49 nM against MCF-7 and 68% tumour suppression in preliminary *in vivo* studies (Lei & Danishefsky, 2008).

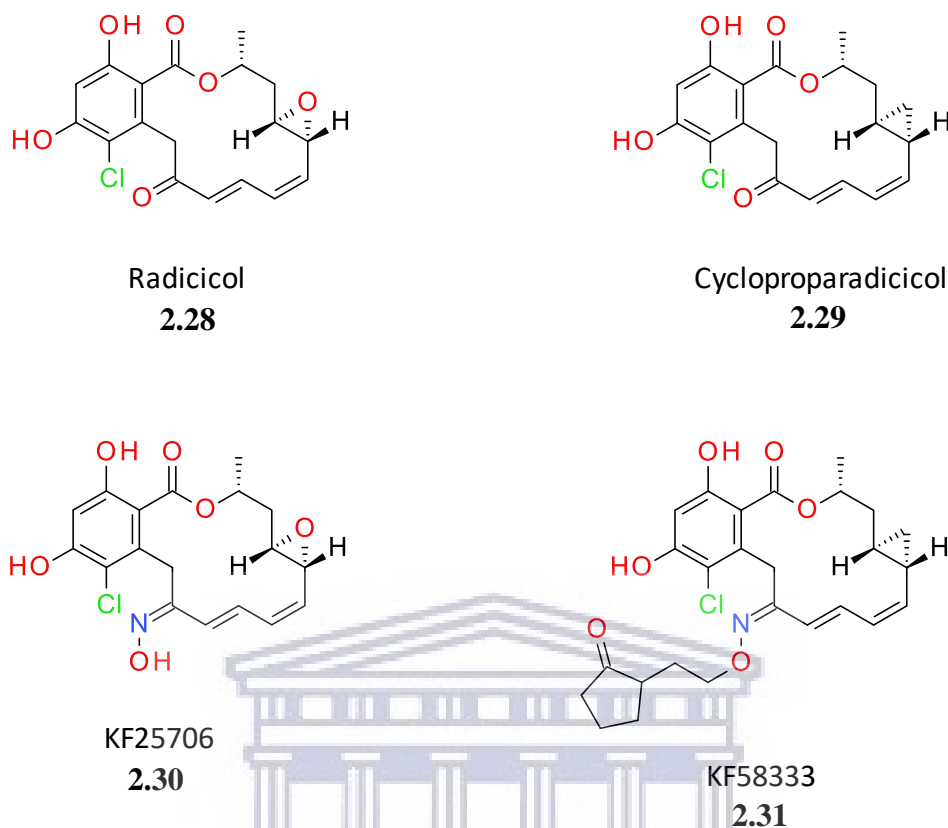


Figure 2.10 Structures of radicicol and its derivatives.

The oxime-derivatives of radicicol, compounds **2.30** and **2.31**, displayed potent *in vivo* antitumour activity with no severe renal or hepatotoxicity. Nevertheless, no clinical studies have been reported on these compounds (Soga et al., 2003).

The clinical progress of the N-terminal inhibitors encountered a setback due to resistance and metastasis, this is attributed to the induction of heat shock response leading to increase in expression of Hsp27, Hsp70, Hsp40, and Hsp90 thus providing chemoprotective effects needed for progression and maturation of oncogenic proteins (Whitesell et al., 2012; Montoir et al., 2016).

2.3.2 C-terminal Inhibitors

The C-terminal domain was first reported by Söti and colleagues (1998), however, the co-crystal structure of a ligand bound to this domain is unavailable (Amolins & Blagg, 2009). In 2000, Necker and colleagues demonstrated the binding of novobiocin to the non-ATP binding site and caused disruption of the Hsp90 complex in a way related to the N-terminal inhibitors. In addition,

the interaction is competitive due to the implication of other co-chaperone and affinity for N-terminal inhibitors (Marcu et al., 2000a; Marcu et al., 2000b). This discovery put the Hsp90 C-terminal domain in the spotlight for anticancer drug development. Furthermore, the C-terminal domain binders are the only cancer agents whose exhibition of cytotoxicity from folding machinery disruption affects all cancer hallmarks (Amolins & Blagg, 2009).

2.3.2.1 Coumarin analogues

Novobiocin (**2.32**), chlorobiocin (**2.33**) and coumermycin A1 (**2.34**) (Figure 2.11) are natural coumarin antibiotics isolated from numerous *Streptomyces* species (Donnelly & Blagg, 2008) and are well known for their antimicrobial properties (Hooper et al., 1982). *In vitro* studies showed the direct interaction of these coumarin antibiotics with Hsp90 leading to client protein degradation (Marcu et al., 2000b). Despite the poor oncogenic protein kinase degradation effect of novobiocin, there was no induction of heat shock response which is detrimental to N-terminal inhibitors (Zhao et al., 2015). This provided a great opportunity for design and synthesis of novobiocin- analogues which targets the C-terminal domain (Montoir et al., 2016). With the proof of concept of the C-terminal domain established, several studies were conducted to understand the structure-activity relationship (SAR) of novobiocin and thus synthesize simpler analogues with improved activity (Le Bras et al., 2007; Kusuma et al., 2014; Zhao et al., 2015; Montoir et al., 2016).

UNIVERSITY of the
WESTERN CAPE

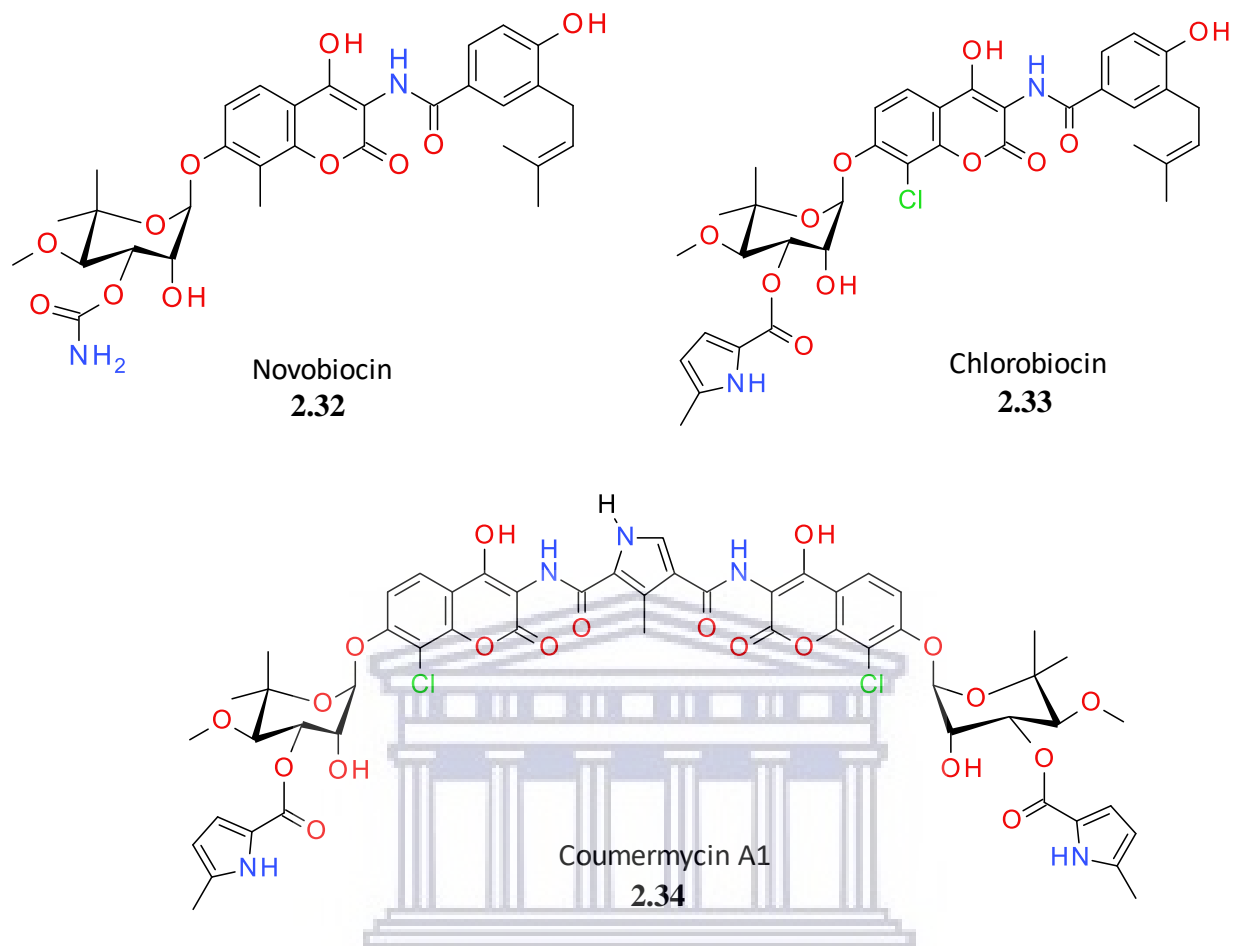


Figure 2.11 Structures of natural coumarin antibiotics.

Blagg and colleagues were able to design and synthesize improved novobiocin derivatives DNH2 and KU174. The rationale for the synthesis of these compounds was conceived from their understanding of the SAR of novobiocin (Yu et al., 2005; Donnelly et al., 2008). With DNH2, the amide side chain (moiety) was retained, a removal of hydroxyl group from the coumarin core and the replacement of the carbamoyl group with a hydroxyl on the sugar moiety. DNH2 manifests potent Hsp90 inhibition by inducing degradation of ErbB2 and p53 clients in SkBr3 breast cancer cells at $\sim 0.5 \mu\text{M}$ (Burlison et al., 2006). KU675 is another novobiocin modified analogue which manifests potent cytotoxicity against prostate cancer cells. Besides Hsp90 inhibition and selectivity for Hsp90 α isoform, it binds to co-chaperone Hsc70 and reduced the expression of Hsc70 clients. Also, there was no induction of the heat shock response (Liu et al., 2015).

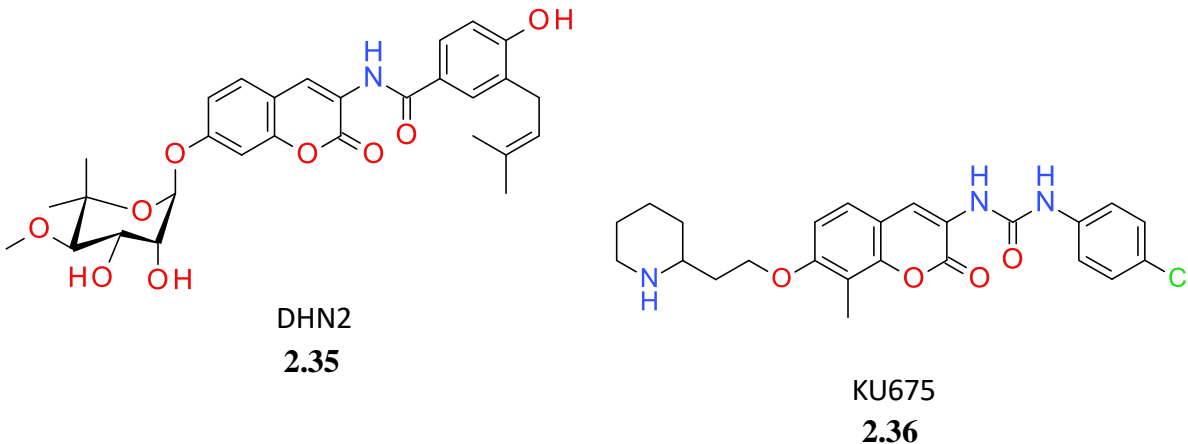
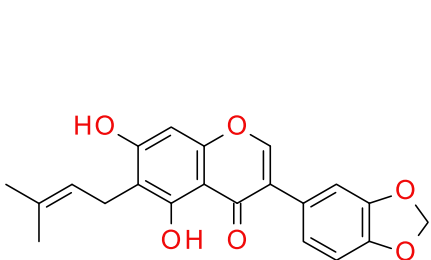


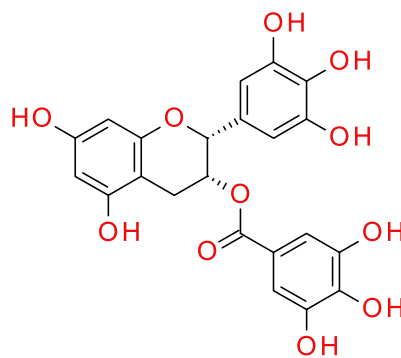
Figure 2.12 Structures synthetic coumarin analogues.

2.3.3 Other compounds

Derrubone (**2.37**) is a flavonoid isolated from *Debrria robusta*, an Indian tree (East et al., 1969). Its biological potential was discovered by high-throughput screening of a natural product library and it showed good antiproliferative activity against MCF-7 and SkBr3 cell lines. Derrubone actively disrupts refolding and induced Her2 degradation (Hadden et al., 2007). The polyphenol; (-)-Epigallocatechin gallate (EGCG) (**2.38**) found in green tea is known to exhibit biological activities such as antioxidant, antimicrobial, and cancer chemopreventive activities (Zaveri, 2006). Previous studies showed inhibition of aryl hydrocarbon receptor in a partial association with Hsp90 (Palermo et al., 2005). Later on, direct binding of EGCG near the C-terminal domain and a decrease in expression of Hsp90 client proteins in a dose-dependent manner was reported (Yin et al., 2008).



Derrubone
2.37



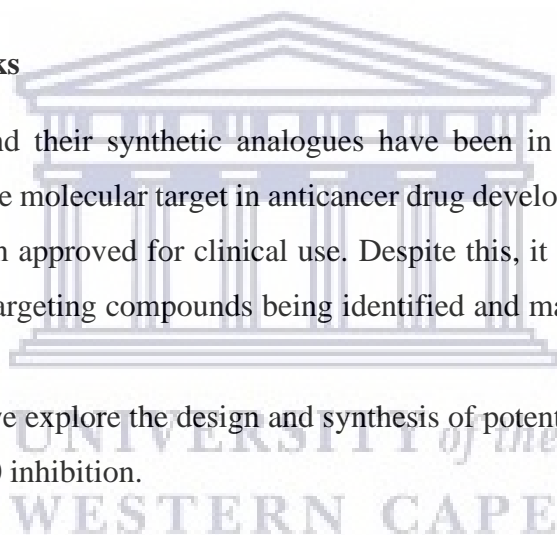
(-)-Epigallocatechin-3-gallate (EGCG)
2.38

Figure 2.13 Structures of derrubone and (-)-epigallocatechin gallate (EGCG).

2.4 Concluding remarks

The natural antimicrobials and their synthetic analogues have been in use for decades and the microtubule remains a viable molecular target in anticancer drug development. On the other hand, no Hsp90 inhibitor has been approved for clinical use. Despite this, it is a promising target with several fascinating Hsp90 targeting compounds being identified and many are still under clinical evaluation.

In the following chapters, we explore the design and synthesis of potential anticancer compounds targeting mitosis and Hsp90 inhibition.



References

Aicher, T. D., Buszek, K. R., Fang, F. G., Forsyth, C. J., Jung, S. H., Kishi, Y., Matelich, M.C., Scola, P.M., Spero, D.M., & Yoon, S. K. (1992). Total synthesis of halichondrin B and norhalichondrin B. *Journal of the American Chemical Society*, 114(8), 3162-3164.

Amolins, M. W., & Blagg, B. S. J. (2009). Natural product inhibitors of Hsp90: potential leads for drug discovery. *Mini Reviews in Medicinal Chemistry*, 9(2), 140-152.

Bai, R. L., Paull, K. D., Herald, C. L., Malspeis, L., Pettit, G. R., & Hamel, E. (1991). Halichondrin B and homohalichondrin B, marine natural products binding in the vinca domain of tubulin. Discovery of tubulin-based mechanism of action by analysis of differential cytotoxicity data. *Journal of Biological Chemistry*, 266(24), 15882-15889.

Banerjee, S., Wang, Z., Mohammad, M., Sarkar, F. H., & Mohammad, R. M. (2008). Efficacy of selected natural products as therapeutic agents against cancer. *Journal of Natural Products*, 71(3), 492-496.

Beerepoot, L. V., Radema, S. A., Witteveen, E. O., Thomas, T., Wheeler, C., Kempin, S., & Voest, E. E. (2006). Phase I clinical evaluation of weekly administration of the novel vascular-targeting agent, ZD6126, in patients with solid tumors. *Journal of Clinical Oncology*, 24(10), 1491-1498.

Bhattacharya, R., & Cabral, F. (2004). A ubiquitous β -tubulin disrupts microtubule assembly and inhibits cell proliferation. *Molecular Biology of the Cell*, 15(7), 3123-3131.

Biamonte, M. A., Van de Water, R., Arndt, J. W., Scannevin, R. H., Perret, D., & Lee, W. C. (2009). Heat shock protein 90: inhibitors in clinical trials. *Journal of Medicinal Chemistry*, 53(1), 3-17.

Blagg, B. S., & Kerr, T. D. (2006). Hsp90 inhibitors: small molecules that transform the Hsp90 protein folding machinery into a catalyst for protein degradation. *Medicinal Research Reviews*, 26(3), 310-338.

Blay, J. Y., Pápai, Z., Tolcher, A. W., Italiano, A., Cupissol, D., López-Pousa, A., Chawla, S.P., Bompas, E., Babovic, N., Penel, N., & Isambert, N. (2015). Ombrabulin plus cisplatin versus placebo plus cisplatin in patients with advanced soft-tissue sarcomas after failure of anthracycline

and ifosfamide chemotherapy: a randomised, double-blind, placebo-controlled, phase 3 trial. *The Lancet Oncology*, 16(5), 531-540.

Bukhari, S. N. A., Kumar, G. B., Revankar, H. M., & Qin, H. L. (2017). Development of combretastatins as potent tubulin polymerization inhibitors. *Bioorganic Chemistry*, 72, 130-147.

Burlison, J. A., Neckers, L., Smith, A. B., Maxwell, A., & Blagg, B. S. (2006). Novobiocin: redesigning a DNA gyrase inhibitor for selective inhibition of hsp90. *Journal of the American Chemical Society*, 128(48), 15529-15536.

de Jonge, M., & Verweij, J. (2005). The epothilone dilemma. *Journal of Clinical Oncology*, 23(36), 9048-9050.

Donnelly, A. C., Mays, J. R., Burlison, J. A., Nelson, J. T., Vielhauer, G., Holzbeierlein, J., & Blagg, B. S. (2008). The design, synthesis, and evaluation of coumarin ring derivatives of the novobiocin scaffold that exhibit antiproliferative activity. *The Journal of Organic Chemistry*, 73(22), 8901-8920.

Donnelly, A., & Blagg, B. S. (2008). Novobiocin and additional inhibitors of the Hsp90 C-terminal nucleotide-binding pocket. *Current Medicinal Chemistry*, 15(26), 2702-2717.

East, A. J., Ollis, W. D., & Wheeler, R. E. (1969). Natural occurrence of 3-aryl-4-hydroxycoumarins. Part I. Phytochemical examination of *Derris robusta* (roxb.) benth. *Journal of the Chemical Society C: Organic*, (3), 365-374.

Field, J. J., Díaz, J. F., & Miller, J. H. (2013). The binding sites of microtubule-stabilizing agents. *Chemistry & Biology*, 20(3), 301-315.

Garg, G., Khandelwal, A., & Blagg, B. S. (2016). Anticancer inhibitors of Hsp90 function: beyond the usual suspects. *Advances in Cancer Research*, 129, 51-88.

Gerth, K., Bedorf, N., HÖFLE, G., Irschik, H., & Reichenbach, H. (1996). Epothilons A and B: antifungal and cytotoxic compounds from *Sorangium cellulosum* (Myxobacteria). *The Journal of Antibiotics*, 49(6), 560-563.

Gidding, C. E., Kellie, S. J., Kamps, W. A., & de Graaf, S. N. (1999). Vincristine revisited. *Critical Reviews in Oncology/Hematology*, 29(3), 267-287.

Gueritte, F. (2001). General and recent aspects of the chemistry and structure activity relationships of taxoids. *Current Pharmaceutical Design*, 7(13), 1229-1249.

Hadden, M. K., Galam, L., Gestwicki, J. E., Matts, R. L., & Blagg, B. S. (2007). Derrubone, an inhibitor of the Hsp90 protein folding machinery. *Journal of Natural Products*, 70(12), 2014-2018.

Hanahan, D., & Weinberg, R. A. (2000). The hallmarks of cancer. *Cell*, 100(1), 57-70.

Harris, S. F., Shiau, A. K., & Agard, D. A. (2004). The crystal structure of the carboxy-terminal dimerization domain of htpG, the *Escherichia coli* Hsp90, reveals a potential substrate binding site. *Structure*, 12(6), 1087-1097.

Hastie, S. B. (1991). Interactions of colchicine with tubulin. *Pharmacology & Therapeutics*, 51(3), 377-401.

Himes, R. H. (1991). Interactions of the catharanthus (Vinca) alkaloids with tubulin and microtubules. *Pharmacology & Therapeutics*, 51(2), 257-267.

Hirata, Y., & Uemura, D. (1986). Halichondrins-antitumor polyether macrolides from a marine sponge. *Pure and Applied Chemistry*, 58(5), 701-710.

Hooper, D. C., Wolfson, J. S., McHugh, G. L., Winters, M. B., & Swartz, M. N. (1982). Effects of novobiocin, coumermycin A1, clorobiocin, and their analogs on *Escherichia coli* DNA gyrase and bacterial growth. *Antimicrobial Agents and Chemotherapy*, 22(4), 662-671.

Hunt, J. T. (2009). Discovery of ixabepilone. *Molecular Cancer Therapeutics*, 8(2), 275-281.

Huyck, T. K., Gradishar, W., Manuguid, F., & Kirkpatrick, P. (2011). Eribulin mesylate. *Nature Reviews Drug Discovery*, 10, 173-174.

Jadhav, V. D., Duerfeldt, A. S., & Blagg, B. S. (2009). Design, synthesis, and biological activity of bicyclic radester analogues as Hsp90 inhibitors. *Bioorganic & Medicinal Chemistry Letters*, 19(24), 6845-6850.

Jordan, M. A., & Wilson, L. (2004). Microtubules as a target for anticancer drugs. *Nature Reviews Cancer*, 4(4), 253-265.

Kaur, R., Kaur, G., Gill, R. K., Soni, R., & Bariwal, J. (2014). Recent developments in tubulin polymerization inhibitors: an overview. *European Journal of Medicinal Chemistry*, 87, 89-124.

Khandelwal, A., Crowley, V. M., & Blagg, B. S. (2016). Natural product inspired N-terminal Hsp90 inhibitors: from bench to bedside?. *Medicinal Research Reviews*, 36(1), 92-118.

Kumar, A., Sharma, P. R., & Mondhe, D. M. (2017). Potential anticancer role of colchicine-based derivatives: an overview. *Anti-Cancer Drugs*, 28(3), 250-262.

Kumar, B., Singh, S., Skvortsova, I., & Kumar, V. (2017). Promising targets in anti-cancer drug development: recent updates. *Current Medicinal Chemistry*, 24(42), 4729-4752.

Kusuma, B. R., Khandelwal, A., Gu, W., Brown, D., Liu, W., Vielhauer, G., Holzbeierlein, J., & Blagg, B. S. (2014). Synthesis and biological evaluation of coumarin replacements of novobiocin as Hsp90 inhibitors. *Bioorganic & Medicinal Chemistry*, 22(4), 1441-1449.

Le Bras, G., Radanyi, C., Peyrat, J. F., Brion, J. D., Alami, M., Marsaud, V., Stella, B., & Renoir, J. M. (2007). New novobiocin analogues as antiproliferative agents in breast cancer cells and potential inhibitors of heat shock protein 90. *Journal of Medicinal Chemistry*, 50(24), 6189-6200.

Lei, X., & Danishefsky, S. J. (2008). Efficient synthesis of a novel resorcyclide as anticancer agent based on Hsp90 inhibition. *Advanced Synthesis & Catalysis*, 350(11-12), 1677-1681.

Liu, W., Vielhauer, G. A., Holzbeierlein, J. M., Zhao, H., Ghosh, S., Brown, D., Lee, E., & Blagg, B. S. (2015). KU675, a concomitant heat-shock protein inhibitor of Hsp90 and Hsc70 that manifests isoform selectivity for Hsp90 α in prostate cancer cells. *Molecular Pharmacology*, 88(1), 121-130.

Marcu, M. G., Chadli, A., Bouhouche, I., Catelli, M., & Neckers, L. M. (2000a). The heat shock protein 90 antagonist novobiocin interacts with a previously unrecognized ATP-binding domain in the carboxyl terminus of the chaperone. *Journal of Biological Chemistry*, 275(47), 37181-37186.

Marcu, M. G., Schulte, T. W., & Neckers, L. (2000b). Novobiocin and related coumarins and depletion of heat shock protein 90-dependent signaling proteins. *Journal of the National Cancer Institute*, 92(3), 242-248.

Montoir, D., Barillé-Nion, S., Tonnerre, A., Juin, P., Duflos, M., & Bazin, M. A. (2016). Novel 1, 6-naphthyridin-2 (1H)-ones as potential anticancer agents targeting Hsp90. *European Journal of Medicinal Chemistry*, 119, 17-33.

Moudi, M., Go, R., Yien, C. Y. S., & Nazre, M. (2013). Vinca alkaloids. *International Journal of Preventive Medicine*, 4(11), 1231-1235.

Natsume, T., Watanabe, J. I., Tamaoki, S., Fujio, N., Miyasaka, K., & Kobayashi, M. (2000). Characterization of the interaction of TZT-1027, a potent antitumor agent, with tubulin. *Japanese Journal of Cancer Research*, 91(7), 737-747.

Newman, D. J., & Cragg, G. M. (2017). Current status of marine-derived compounds as warheads in anti-tumor drug candidates. *Marine Drugs*, 15(4), 99-118.

Ojima, I., Lichtenthal, B., Lee, S., Wang, C., & Wang, X. (2016). Taxane anticancer agents: a patent perspective. *Expert Opinion on Therapeutic Patents*, 26(1), 1-20.

Padma, V. V. (2015). An overview of targeted cancer therapy. *BioMedicine*, 5(4), 1-6.

Palermo, C. M., Westlake, C. A., & Gasiewicz, T. A. (2005). Epigallocatechin gallate inhibits aryl hydrocarbon receptor gene transcription through an indirect mechanism involving binding to a 90 kDa heat shock protein. *Biochemistry*, 44(13), 5041-5052.

Patel, K., Piagentini, M., Rascher, A., Tian, Z. Q., Buchanan, G. O., Regentin, R., Hu, Z., Hutchinson, C.R., & McDaniel, R. (2004). Engineered biosynthesis of geldanamycin analogs for Hsp90 inhibition. *Chemistry & Biology*, 11(12), 1625-1633.

Patel, S., Keohan, M. L., Saif, M. W., Rushing, D., Baez, L., Feit, K., & Anderson, S. (2006). Phase II study of intravenous TZT-1027 in patients with advanced or metastatic soft-tissue sarcomas with prior exposure to anthracycline-based chemotherapy. *Cancer*, 107(12), 2881-2887.

Patterson, D. M., Zweifel, M., Middleton, M. R., Price, P. M., Folkes, L. K., Stratford, M. R., Ross, P., Halford, S., Peters, J., Balkissoon, J., & Chaplin, D. J. (2012). Phase I clinical and

pharmacokinetic evaluation of the vascular-disrupting agent OXi4503 in patients with advanced solid tumors. *Clinical Cancer Research*, 18(5), 1415-1425.

Pearl, L. H., & Prodromou, C. (2006). Structure and mechanism of the Hsp90 molecular chaperone machinery. *Annual Review of Biochemistry*, 75, 271-294.

Pettit, G. R., Cragg, G. M., & Singh, S. B. (1987b). Antineoplastic agents, 122. Constituents of *Combretum caffrum*. *Journal of Natural Products*, 50(3), 386-391.

Pettit, G. R., Singh, S. B., Niven, M. L., Hamel, E., & Schmidt, J. M. (1987a). Isolation, structure, and synthesis of combretastatins A-1 and B-1, potent new inhibitors of microtubule assembly, derived from *Combretum caffrum*. *Journal of Natural Products*, 50(1), 119-131.

Pettit, G. R., Temple C., Narayanan, V. L., Varma, R., Simpson, M. J., Boyd, M. R., Rener G.A., & Bansal, N. (1995). Antineoplastic agents 322. synthesis of combretastatin A-4 prodrugs. *Anti-Cancer Drug Design*, 10(4), 299-309.

Safavy, A., Raisch, K. P., Khazaeli, M. B., Buchsbaum, D. J., & Bonner, J. A. (1999). Paclitaxel derivatives for targeted therapy of cancer: toward the development of smart taxanes. *Journal of Medicinal Chemistry*, 42(23), 4919-4924.

Sasaki, K., Yasuda, H., & Onodera, K. (1979). Growth inhibition of virus transformed cells *in vitro* and antitumor activity *in vivo* of geldanamycin and its derivatives. *The Journal of Antibiotics*, 32(8), 849-851.

Sausville, E. A., Tomaszewski, J. E., & Ivy, P. (2003). Clinical development of 17-allylamino, 17-demethoxygeldanamycin. *Current Cancer Drug Targets*, 3(5), 377-383.

Schulte, T. W., Akinaga, S., Soga, S., Sullivan, W., Stensgard, B., Toft, D., & Neckers, L. M. (1998). Antibiotic radicicol binds to the N-terminal domain of Hsp90 and shares important biologic activities with geldanamycin. *Cell Stress & Chaperones*, 3(2), 100-108.

Senter, P. D., & Sievers, E. L. (2012). The discovery and development of brentuximab vedotin for use in relapsed Hodgkin lymphoma and systemic anaplastic large cell lymphoma. *Nature Biotechnology*, 30(7), 631-637.

Shi, Q., Chen, K., Morris-Natschke, S. L., & Lee, K. H. (1998). Recent progress in the development of tubulin inhibitors as antimetabolic antitumor agents. *Current Pharmaceutical Design*, 4(3), 219-248.

Soga, S., Shiotsu, Y., Akinaga, S., & Sharma, S. V. (2003). Development of radicicol analogues. *Current Cancer Drug Targets*, 3(5), 359-369.

Solit, D. B., Zheng, F. F., Drobnyak, M., Münster, P. N., Higgins, B., Verbel, D., Heller, G., Tong, W., Cordon-Cardo, C., Agus, D.B., & Scher, H. I. (2002). 17-Allylamino-17-demethoxygeldanamycin induces the degradation of androgen receptor and HER-2/neu and inhibits the growth of prostate cancer xenografts. *Clinical Cancer Research*, 8(5), 986-993.

Sóti, C., Radics, L., Yahara, I., & Csermely, P. (1998). Interaction of vanadate oligomers and permolybdate with the 90-kDa heat-shock protein, Hsp90. *European Journal of Biochemistry*, 255(3), 611-617.

Supko, J. G., Hickman, R. L., Grever, M. R., & Malspeis, L. (1995). Preclinical pharmacologic evaluation of geldanamycin as an antitumor agent. *Cancer Chemotherapy and Pharmacology*, 36(4), 305-315.

The functional domains of Hsp90 <https://www.caymanchem.com/news/molecular-chaperones-in-control-of-the-heat-shock-response> (accessed January 10, 2020).

Towle, M. J., Salvato, K. A., Budrow, J., Wels, B. F., Kuznetsov, G., Aalfs, K. K., Welsh, S., Zheng, W., Seletsky, B.M., Palme, M.H., & Habgood, G. J. (2001). *In vitro* and *in vivo* anticancer activities of synthetic macrocyclic ketone analogues of halichondrin B. *Cancer Research*, 61(3), 1013-1021.

Uehara, Y., Murakami, Y., Suzukake-Tsuchiya, K. A. Y. O. K. O., Moriya, Y., Sano, H., Shibata, K., & Omura, S. (1988). Effects of herbimycin derivatives on src oncogene function in relation to antitumor activity. *The Journal of Antibiotics*, 41(6), 831-834.

Whitesell, L., Mimnaugh, E. G., De Costa, B., Myers, C. E., & Neckers, L. M. (1994). Inhibition of heat shock protein HSP90-pp60v-src heteroprotein complex formation by benzoquinone ansamycins: essential role for stress proteins in oncogenic transformation. *Proceedings of the National Academy of Sciences*, 91(18), 8324-8328.

Whitesell, L., Santagata, S., & Lin, N. U. (2012). Inhibiting HSP90 to treat cancer: a strategy in evolution. *Current Molecular Medicine*, 12(9), 1108-1124.

Woods, J. A., Hadfield, J. A., Pettit, G. R., Fox, B. W., & McGown, A. T. (1995). The interaction with tubulin of a series of stilbenes based on combretastatin A-4. *British Journal of Cancer*, 71(4), 705-711.

Yamamoto, K., Garbaccio, R. M., Stachel, S. J., Solit, D. B., Chiosis, G., Rosen, N., & Danishefsky, S. J. (2003). Total synthesis as a resource in the discovery of potentially valuable antitumor agents: cycloproparadicicol. *Angewandte Chemie International Edition*, 42(11), 1280-1284.

Yang, Z. Q., Geng, X., Solit, D., Pratilas, C. A., Rosen, N., & Danishefsky, S. J. (2004). New efficient synthesis of resorcinylic macrolides *via* ynolides: establishment of cycloproparadicicol as synthetically feasible preclinical anticancer agent based on Hsp90 as the target. *Journal of the American Chemical Society*, 126(25), 7881-7889.

Yeung, B. K. (2011). Natural product drug discovery: the successful optimization of ISP-1 and halichondrin B. *Current Opinion in Chemical Biology*, 15(4), 523-528.

Yin, Z., Henry, E. C., & Gasiewicz, T. A. (2008). (-)-Epigallocatechin-3-gallate is a novel Hsp90 inhibitor. *Biochemistry*, 48(2), 336-345.

Young, S. L., & Chaplin, D. J. (2004). Combretastatin A4 phosphate: background and current clinical status. *Expert Opinion on Investigational Drugs*, 13(9), 1171-1182.

Yu, X. M., Shen, G., Neckers, L., Blake, H., Holzbeierlein, J., Cronk, B., & Blagg, B. S. (2005). Hsp90 inhibitors identified from a library of novobiocin analogues. *Journal of the American Chemical Society*, 127(37), 12778-12779.

Zaveri, N. T. (2006). Green tea and its polyphenolic catechins: medicinal uses in cancer and noncancer applications. *Life Sciences*, 78(18), 2073-2080.

Zhang, C., Wang, X., Liu, H., Zhang, M., Geng, M., Sun, L., Shen, A., & Zhang, A. (2017). Design, synthesis and pharmacological evaluation of 4, 5-diarylisoxazols bearing amino acid residues within the 3-amido motif as potent heat shock protein 90 (Hsp90) inhibitors. *European Journal of Medicinal Chemistry*, 125, 315-326.

Zhang, H., & Burrows, F. (2004). Targeting multiple signal transduction pathways through inhibition of Hsp90. *Journal of Molecular Medicine*, 82(8), 488-499.

Zhao, H., & Blagg, B. S. (2013). Novobiocin analogues with second-generation noviose surrogates. *Bioorganic & Medicinal Chemistry Letters*, 23(2), 552-557.

Zhao, H., Garg, G., Zhao, J., Moroni, E., Girgis, A., Franco, L. S., Singh, S., Colombo, G., & Blagg, B. S. (2015). Design, synthesis and biological evaluation of biphenylamide derivatives as Hsp90 C-terminal inhibitors. *European Journal of Medicinal Chemistry*, 89, 442-466.



Chapter 3

Synthesis and antiproliferative activity of cyclopenta[*b*]indole derivatives

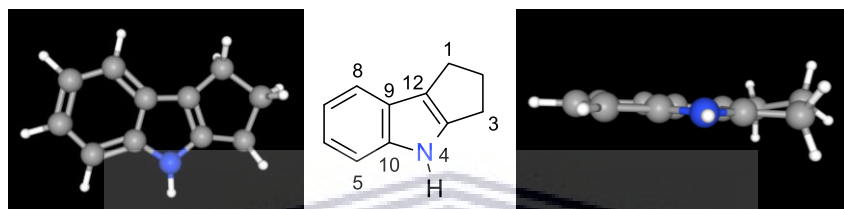


UNIVERSITY *of the*
WESTERN CAPE

3.1 Introduction

The cyclopenta[*b*]indole scaffold is present in several biologically active natural products and synthetic compounds. In this chapter, we briefly review natural and synthetic cyclopenta[*b*]indole derivatives. This is followed by a discussion of the synthesis and antiproliferative activity of a series of new substituted cyclopenta[*b*]indole compounds.

3.1.1 Naturally occurring and synthetic cyclopenta[*b*]indoles



The indole motif is a common scaffold in many medicinal compounds and natural products (Chadha & Silakari, 2017), however, simple, naturally occurring cyclopenta[*b*]indole derivatives are less common. Although the more complex, fungal derived indole diterpenes, represented by the alkaloids paspaline, penitrems, janthitrems, have been extensively studied (Harrison et al., 1995), we have focused our attention on the simpler cyclopenta[*b*]indole alkaloids (Figure 3.1). Some biologically active representatives of this class include nostodione A (**3.1**), a natural product isolated from the cyanobacterium *Nostoc commune* (Kobayashi et al., 1994) and a precursor to the natural product scytonemin. The related indole **3.2** has been shown to inhibit specific melanoma kinases, which makes it a good candidate for targeting skin cancer (Ekebergh et al., 2015). In addition, its characteristic cell permeability and fluorescence permit cellular visualization (Ekebergh et al., 2015). The bruceollines (e.g. **3.3**) are antiplasmodial natural products isolated from the plant *Brucea mollis*, which is used as a herbal remedy with antiparasitic activity (Dethe & Kumar 2015).

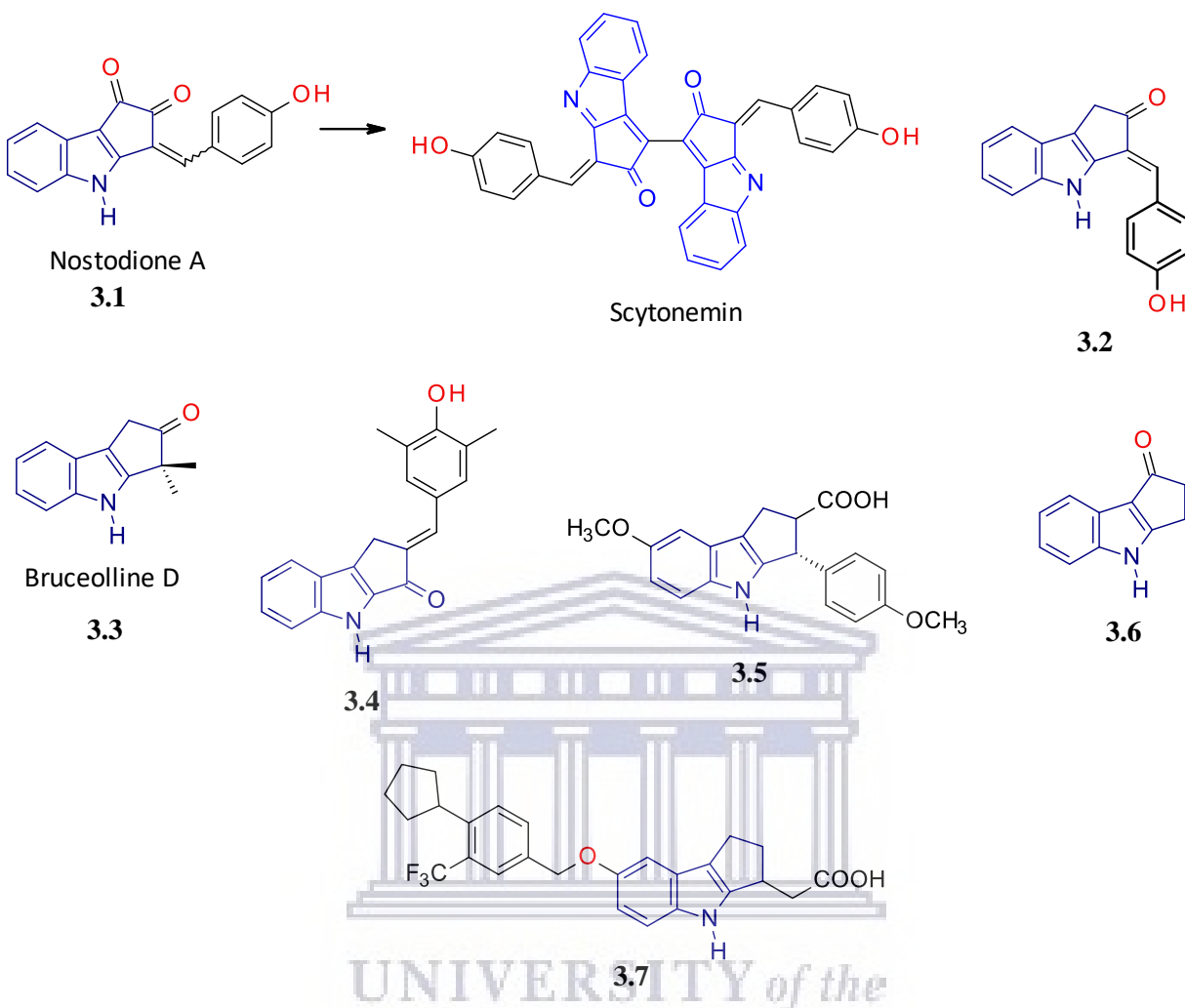
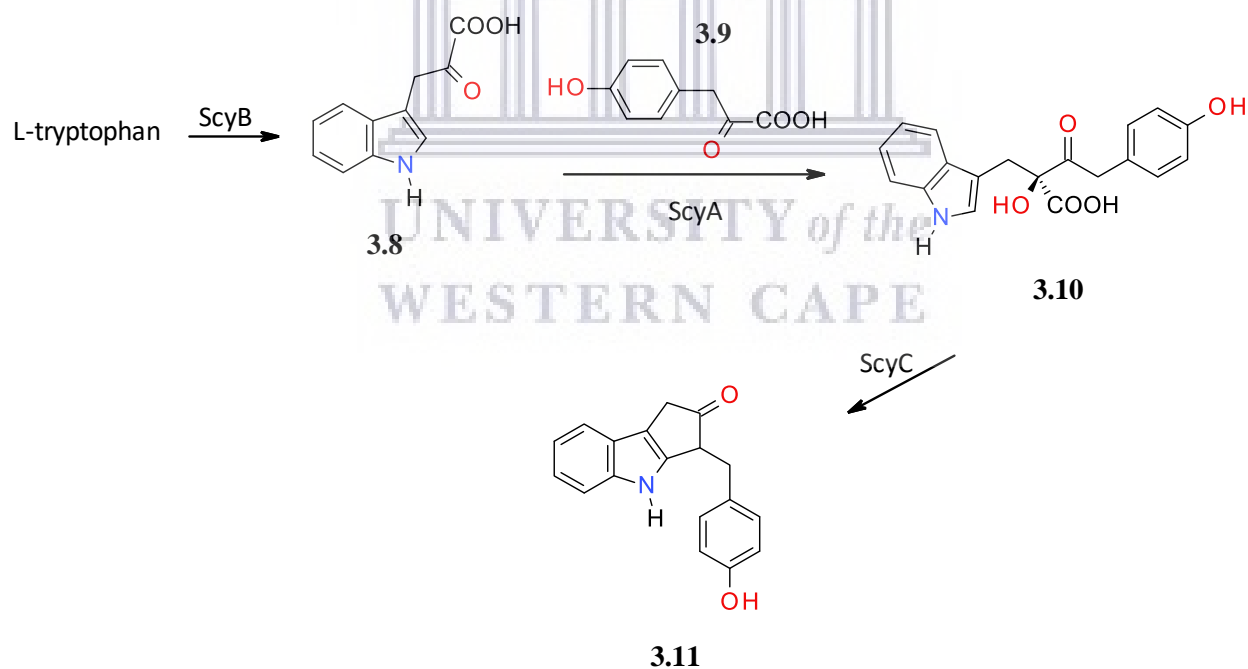


Figure 3.1 Selected biologically active cyclopenta[*b*]indoles.

The synthetic cyclopenta[*b*]indoles such as the alkylidene derivatives **3.4** display antiproliferative activity through binding to tubulin (Tunbridge et al., 2013). Tumour growth inhibition has been reported for compound **3.5** (Santos et al., 2016) while indole **3.6** up-regulated chaperone expression to reduce polyQ aggregation in neuronal differentiated TBP/Q79 cells and was proposed to have therapeutic potential in spinocerebellar ataxia type 17 (SCA17) treatment (Kung et al., 2014). Compound **3.7** was reported to be selective agonist of sphingosine 1-phosphate (S1P1) receptor which may be useful as a potential treatment of autoimmune diseases such as multiple sclerosis (Buzard et al., 2014). The encouraging biological activities, especially antimitotic activity and effect on chaperones, of this small group of compounds, make them useful lead compounds for further investigation.

3.1.2 Biosynthesis of simple cyclopenta[*b*]indoles

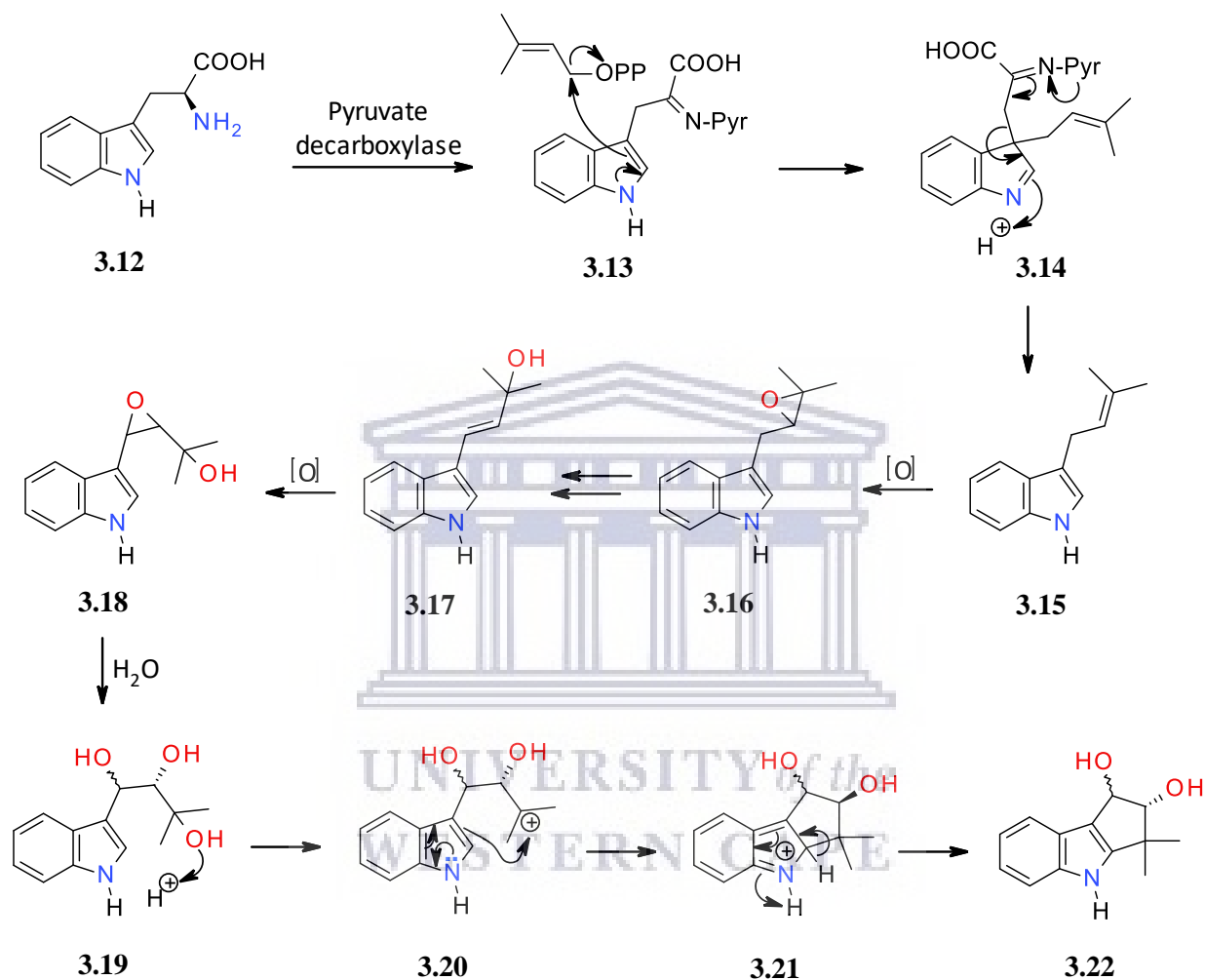
It is tempting to propose that simple cyclopentanone indoles may be biosynthesized *via* deamination and cyclization of tryptophan, however, this is not the case. Nostodione A (**3.1**) has been proposed as a precursor in the biosynthesis of the UV-absorbing natural product, scytonemin (Soule et al., 2009). Scytonemin was demonstrated to have resulted from the transcription of gene clusters of aromatic amino acids after exposure to UV radiation; an adaptive defense mechanism against UV radiation (Gerwick et al., 2009). Two enzymes were proposed to be involved in the conversion of *L*-tryptophan to indole-3-pyruvic acid (**3.8**) which, in turn, couples with *p*-hydroxyphenylpyruvic acid (**3.9**) (Balskus & Walsh, 2008). A third enzyme catalyzes the cyclization and decarboxylation to form the scytonemin monomer **3.11** (Scheme 3.1) (Balskus & Walsh, 2009). It was assumed that **3.11** could undergo oxidative dimerization to form scytonemin, although further investigation into ScyC is required for its characterization and mechanism (Balskus & Walsh, 2009).



Scheme 3.1 Proposed biosynthesis of Scytonemin monomer (**3.11**).

In 2011, Chen and colleagues proposed a biosynthetic pathway for bruceolline natural products (Chen et al., 2011). The authors proposed that the action of pyruvate decarboxylase on tryptophan

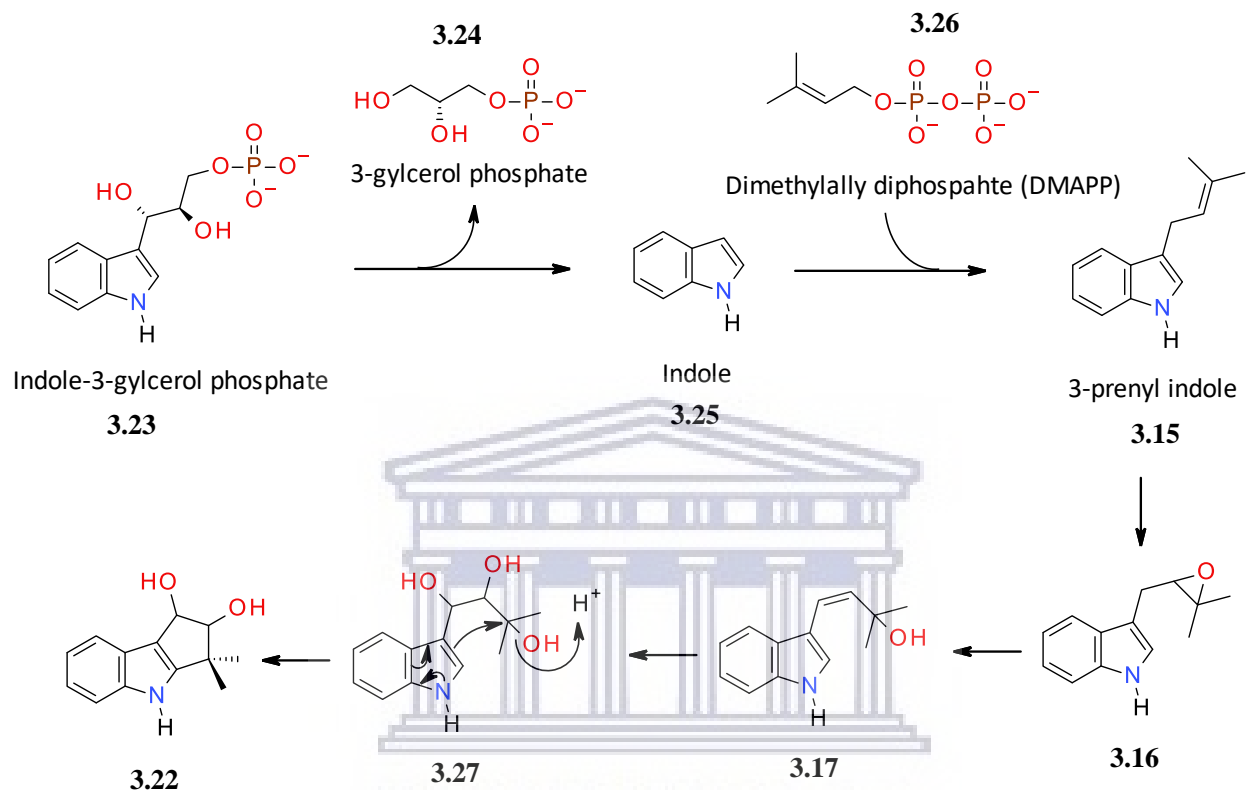
gave rise to the intermediate **3.13** followed by the addition of the prenyl chain by dimethylallyl diphosphate (DMAPP). Epoxidation of 3-prenyl indole followed a series of steps leading to dehydroxylation and cyclization to afford for cyclopenta[*b*]indole (**3.22**) (Scheme 3.2).



Scheme 3.2 Chen and co-workers' proposed biosynthetic pathway of cyclopenta[*b*]indole.

In view of the presented pathway (Scheme 3.2), we proposed another plausible biosynthesis of the cyclopenta[*b*]indoles *via* the shikimic pathway (Scheme 3.3). A transformation of indole-3-glycerol phosphate to indole, prenylation of indole can be achieved by the addition of DMAPP catalyzed by prenyltransferase to generate 3-prenyl indole (**3.15**). A subsequent epoxidation followed by dehydrogenation and dihydroxylation, and the intermediate **3.27** cyclizes leading to the formation of cyclopenta[*b*]indole. Both pathways share some similarities, however, our

proposal was motivated by the report on the biosynthesis of indole **3.25** from indole-3-glycerol phosphate (**3.23**) (Kriechbaumer et al., 2008) and the direct prenylation of indole.

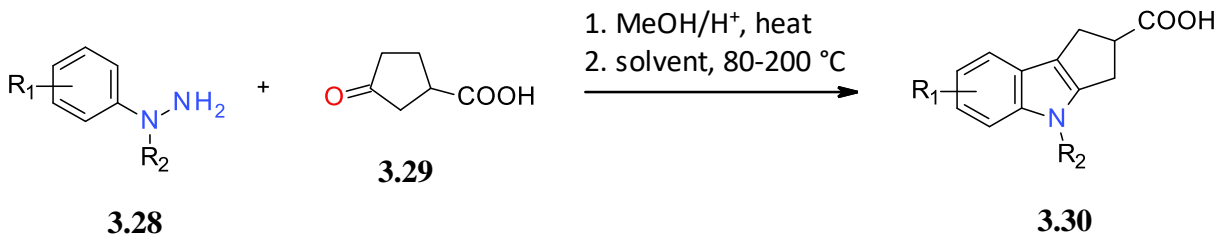


Scheme 3.3 A plausible biosynthetic pathway of cyclopenta[*b*]indole.

3.1.3 Synthesis of the cyclopenta[*b*]indole skeleton – a short review

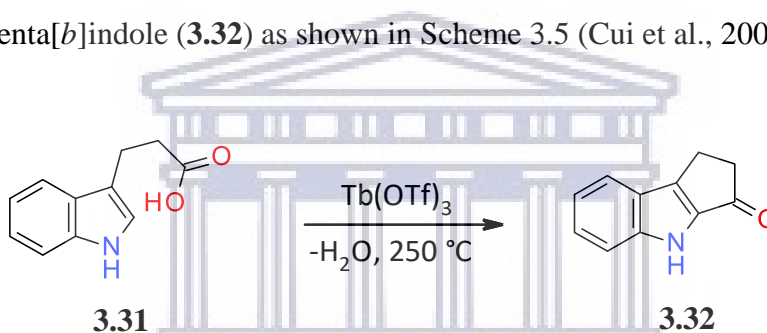
As a result of the increasing biological relevance of this heterocyclic compound, many approaches are being employed in the synthesis of the cyclopenta[*b*]indole scaffold.

Some of the earliest reported syntheses of cyclopenta[*b*]indoles used the Fischer indole synthesis. Berger and Corraz (1977) used this reaction (Scheme 3.4) to synthesize a range of cyclopenta[*b*]indoles with anti-inflammatory activity. They reacted an appropriately substituted phenylhydrazine (**3.28**) with a substituted cyclopentanone (**3.29**) under acidic conditions to give the intermediate hydrazone which was subsequently cyclized at elevated temperature to give the substituted cyclopenta[*b*]indole derivatives (**3.30**) (Berger & Corraz, 1977).



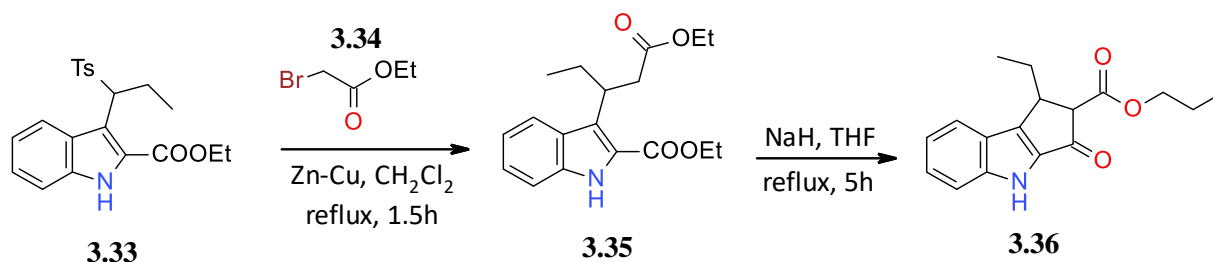
Scheme 3.4 Synthesis of cyclopenta[*b*]indoles *via* Fischer indolization (Berger & Corraz, 1977).

Cui and co-workers utilized terbium(III) trifluoromethanesulfonate ($\text{Tb}(\text{OTf})_3$) catalyzed Friedel–Crafts reaction for the synthesis cyclopenta[*b*]indole from 3-arylpropionic acids (e.g. **3.31**). This dehydrative cyclization was achieved in the presence of a Lewis acid at 250 °C in chlorobenzene to produce cyclopenta[*b*]indole (**3.32**) as shown in Scheme 3.5 (Cui et al., 2004).



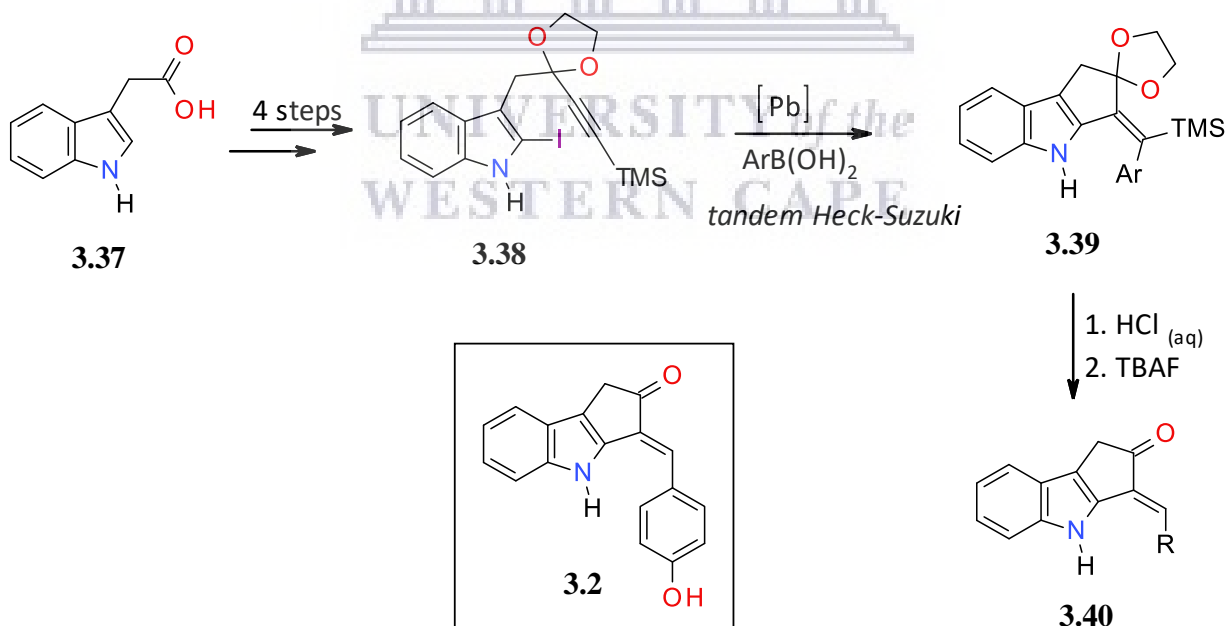
Scheme 3.5 Synthesis of cyclopenta[*b*]indole *via* Friedel-Crafts acylation reaction (Cui et al., 2004).

In 2007, Palmieri & Petrini employed the Reformatsky reaction/Dieckmann condensation to synthesize the cyclopenta[*b*]indole scaffold (Scheme 3.6). They discovered that the reactivity of sulfonyl indole **3.33** was inadequate for a successful reaction when zinc metal and iodine catalyst were used as Reformatsky reagents. Therefore, activated zinc-copper coupled in dichloromethane were later used to condense sulfonyl indole with α -halo ester **3.34** under reflux to obtain the diester **3.35**. This was then converted to a β -keto ester **3.36** *via* intramolecular Dieckmann condensation using NaH in THF (Palmieri & Petrini, 2007).



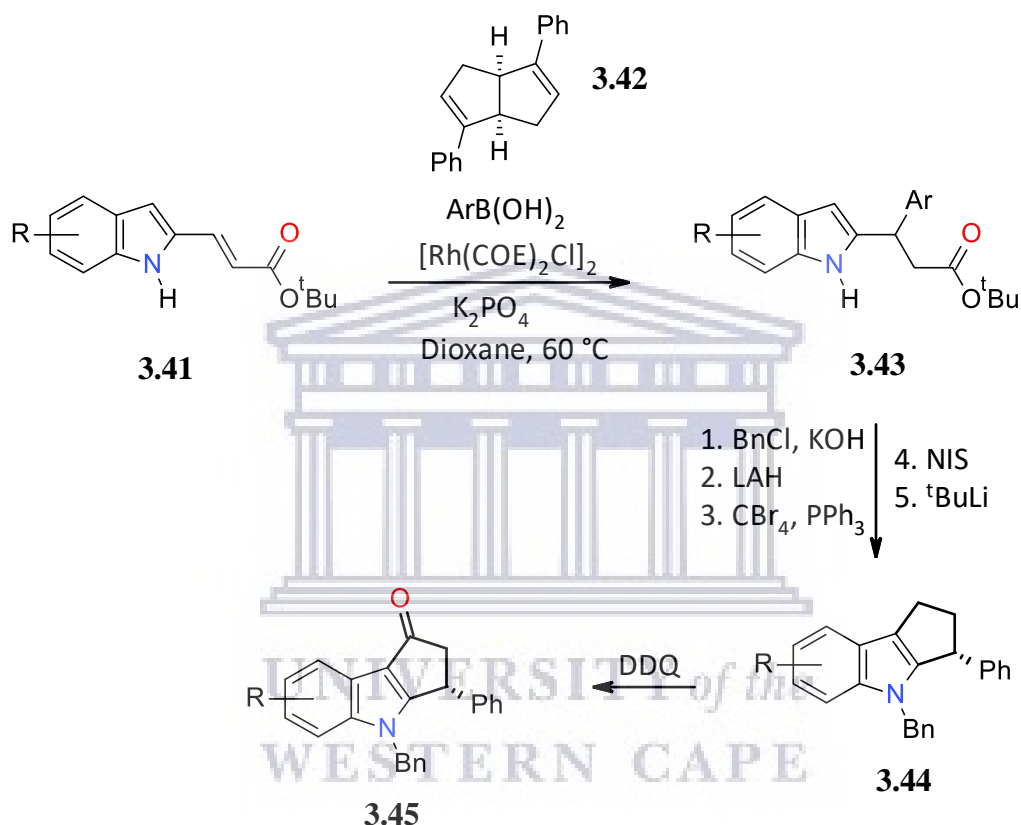
Scheme 3.6 Reformatsky reaction/Dieckmann condensation (Palmieri & Petrini, 2007).

Ekebergh and colleagues synthesized a series of 3-arylidene-cyclopenta[*b*]indol-2-ones **3.40** via a palladium-catalysed tandem Heck–Suzuki reaction (Scheme 3.7). Compound **3.2** was identified from this group of compounds due to its ability to inhibit BRAF, V600E, IRAK4, Aurora A and Aurora B, as well as its cytotoxicity in peripheral blood mononucleated cells (PBMC). Compound **3.2** also possesses a fluorescent property that enabled it for cellular visualization. In four steps, indole-3-acetic acid (**3.37**) was transformed into the indole intermediate **3.38**. Tandem Heck–Suzuki reaction afforded the dihydrocyclopenta[*b*]indole (**3.39**) which was converted to the target cyclopenta[*b*]indol-2-one (**3.40**) under acidic conditions (Ekebergh et al., 2015).



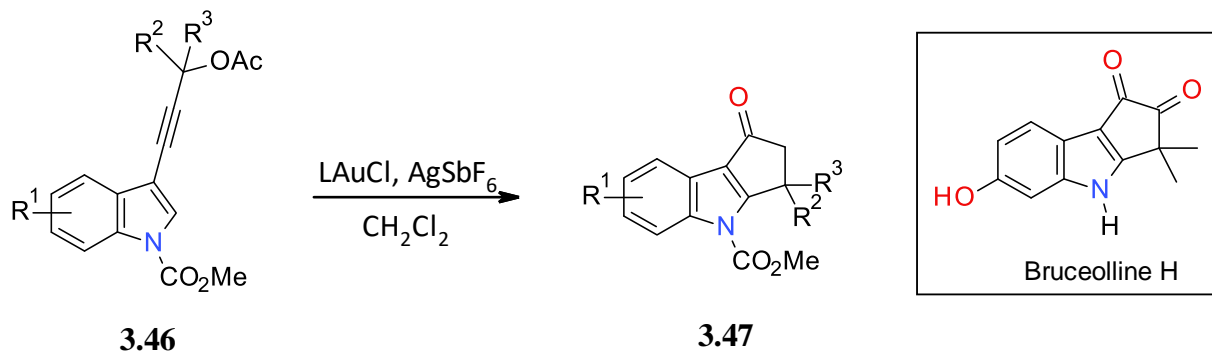
Scheme 3.7 Palladium-catalysed tandem Heck–Suzuki synthesis of cyclopenta[*b*]indole (Ekebergh et al., 2015).

In 2017, Wu and colleagues developed a rhodium-catalysed asymmetric approach (Scheme 3.8) to obtain 3-(1H-indol-2-yl)-3-arylpropanoates (**3.43**) in high enantioselectivity and good yield by arylation of 2-indolyl acrylate **3.41** and aryl boronic acids. In a series of steps, the β -arylpropanoates **3.43** were converted into cyclopenta[*b*]indole (**3.44**). The fused systems were functionalized by oxidation using DDQ to obtain cyclopenta[*b*]indol-1-one (**3.45**).



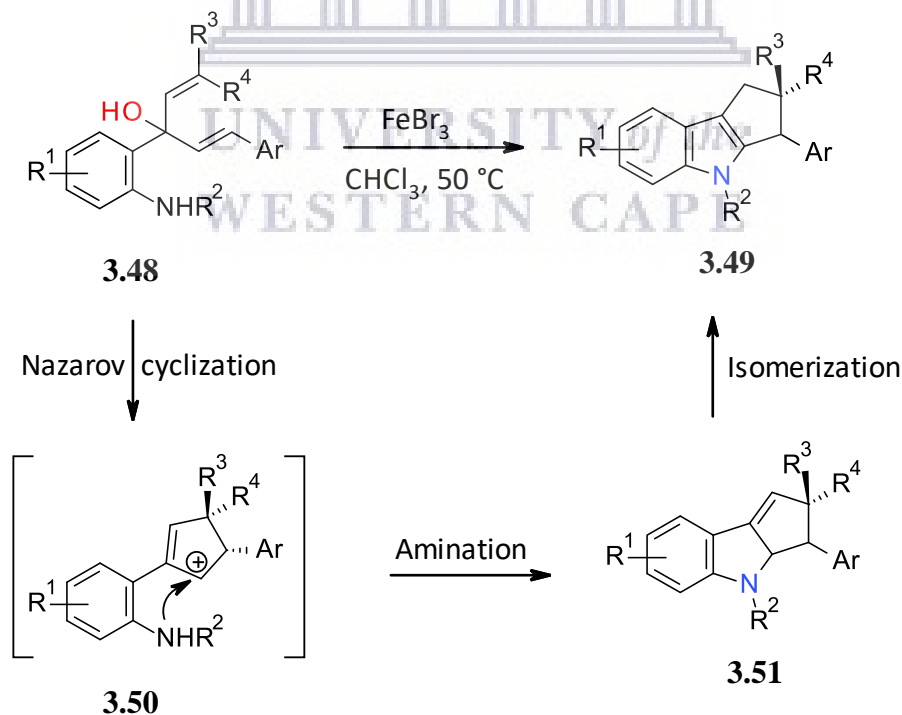
Scheme 3.8 Rhodium-Catalyzed synthesis of cyclopenta[*b*]indole (Wu et al., 2017).

Scarpi and co-workers developed a tandem Au(I)-catalysed rearrangement/Nazarov method to synthesize cyclopenta[*b*]indol-1-ones in good yields (Scheme 3.9). This was achieved through the cyclization of enynyl acetates **3.46** to obtain the target compound **3.47**. The process involves gold(I)-catalyzed [3,3]-sigmatropic rearrangement of the propargylic acetate and Nazarov cyclization to obtain the cyclopenta[*b*]indol-1-ones. The potential of this synthetic method was demonstrated in the total synthesis of the natural and bioactive compound, bruceolline H (Scarpi et al., 2016).



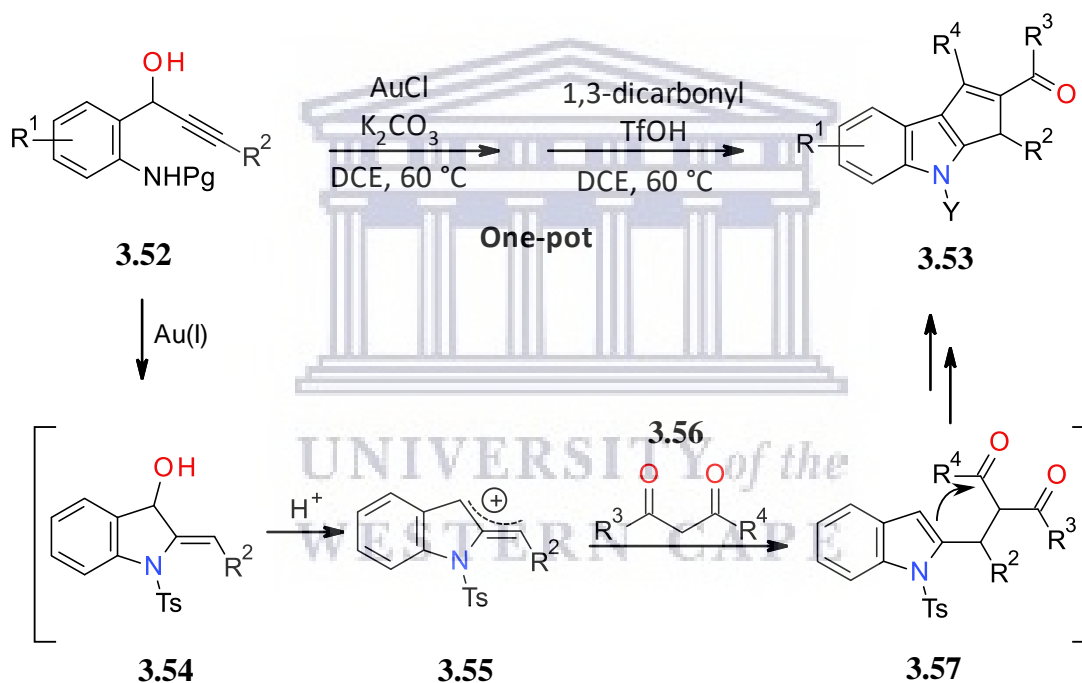
Scheme 3.9 Tandem Au(I)-catalysed rearrangement/Nazarov synthesis of cyclopenta[*b*]indole (Scarpi et al., 2016).

In 2016, Wang and co-workers reported the first Lewis acid-catalyzed intramolecular cyclization of 1,4-pentadien-3-ols (**3.48**) to generate cyclopenta[*b*]indoles (**3.49**). Pentadien-3-ols (**3.48**) in the presence of iron(III) bromide catalyst undergoes a Nazarov cyclization to produce allylic cation intermediate **3.50** and subsequently undergoes intramolecular amination to generate regioisomers **3.51**, and then isomerize to establish a range of cyclopenta[*b*]indoles (Scheme 3.10) (Wang et al., 2016).



Scheme 3.10 Synthesis of cyclopenta[*b*]indoles *via* Nazarov cyclization of 1,4-pentadien-3-ols (Wang et al., 2016).

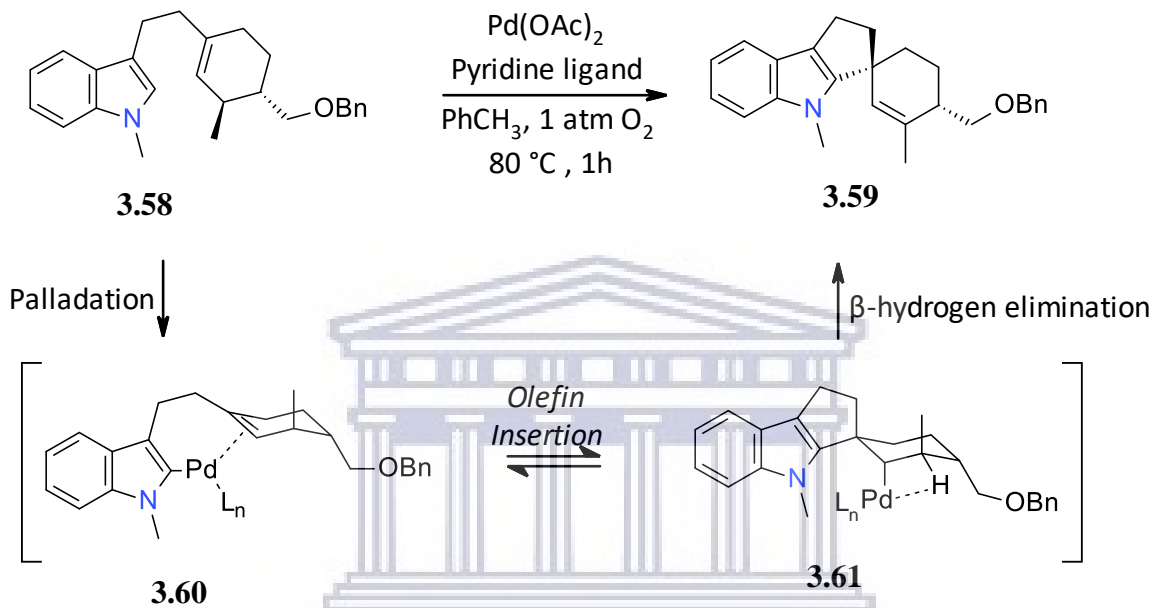
Dhiman and Ramasastry demonstrated a catalytic gold(I)/Brønsted acid-mediated one-pot tandem reaction (Scheme 3.11) for the conversion of 1-(2-aminophenyl)prop-2-ynols (**3.52**) to 1,2,3-trisubstituted cyclopenta[*b*]indoles (**3.53**). The authors' proposed mechanism was the generation of the indolines **3.54** from **3.52**. This was followed by acid-mediated reaction of indolylmethyl cations **3.55** with 1,3-dicarbonyl, and subsequent intramolecular aldol-type reactions to obtain the cyclopenta[*b*]indoles. The authors reported that the first reaction to generate **3.54** failed when Au(I) or Ag(I) salts alone or a combination with Au(I) and silver-based Lewis acids were used. However, a combination of Au(I) with a base (K_2CO_3) was discovered to be efficient (Dhiman & Ramasastry, 2015).



Scheme 3.11 Synthesis of polysubstituted cyclopenta[*b*]indoles via relay gold (i)/Brønsted acid catalysis (Dhiman & Ramasastry, 2015).

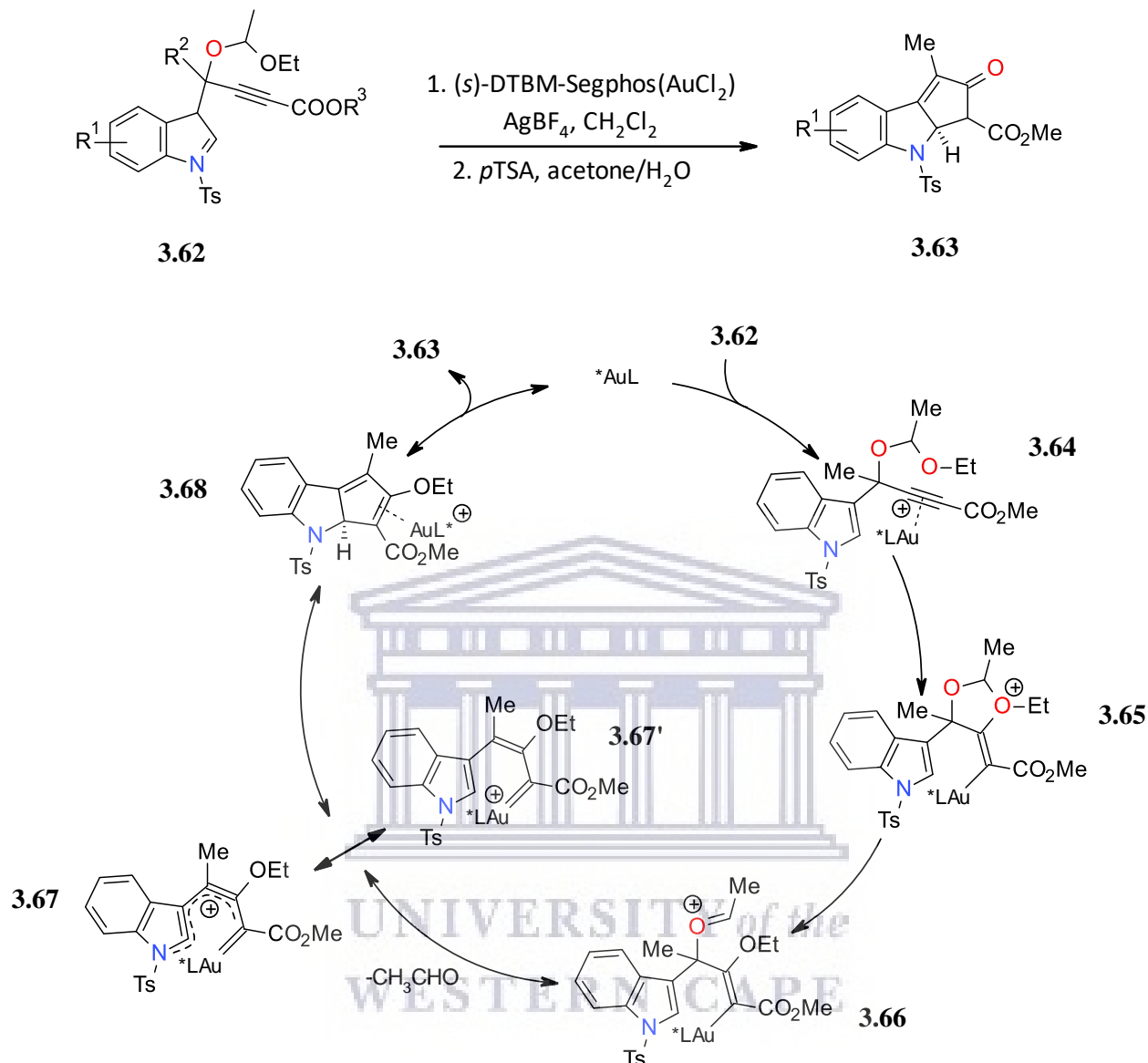
In 2003, Ferreira & Stoltz reported an interesting palladium catalysed and aerobic cyclization of indole (Scheme 3.12). Although the oxidative cyclization was achieved with $Pd(OAc)_2$ catalyst and pyridine under oxygen, the yield obtained was considerably lower compared to other oxidative reaction reports. To maximize the conversion of indoles **3.58** to cyclopenta[*b*]indole **3.59**, they optimized the reaction conditions by (i) the use of high-boiling point polar solvent such as *tert*-

amyl alcohol; (ii) addition of acetic acid as cosolvent to reduce oxidative decomposition of the product from the elongated oxygen contact and (iii) introduction of pyridine as ligand which led to a more reactive palladium catalyst. Regarding the mechanism; an initial palladation was proposed, followed by olefin insertion and finally β -hydrogen elimination (Ferreira & Stoltz, 2003).



Scheme 3.12 Synthesis of cyclopenta[*b*] indole *via* Catalytic C–H bond functionalization with palladium (II) (Ferreira & Stoltz, 2003).

Zi and colleagues reported a dearomative Rautenstrauch rearrangement of cyclopenta[*b*]indoles (Scheme 3.13). This method involves the direct conversion of propargyl acetals **3.62** to cyclopenta[*b*]indoles **3.63** *via* cationic (*S*)-DTBM-Segphosgold(I) catalysis (Zi et al., 2015). The proposed mechanism entails an anti-attack of the ethoxy ether resulting in the formation of oxonium species **3.65**. The extrusion of acetaldehyde from acyclic oxocarbenium **3.66** generates substituted 1-aminopentadienyl intermediate **3.67**. Subsequent imino-Nazarov cyclization of **3.67** gives rise to **3.68**, and in the end hydrolyses to **3.63** (Zi et al., 2015).



Scheme 3.13 Synthesis of cyclopenta[*b*]indoles via Gold (I)-catalyzed dearomative Rautenstrauch rearrangement (Zi, et al., 2015).

3.1.4 Synthetic approach to cyclopenta[*b*]indole derivatives – this study

In this study, we were interested in exploring the effect of both electron-donating and electron-withdrawing substituents on the biological activity of the cyclopenta[*b*]indol-3-one scaffold (Figure 3.2). In order to achieve this, we required a relatively simple synthetic procedure that could accommodate these substituents. Although several reactions are available to construct this ring system (Section 3.1.3), we considered the Japp-Klingeman modification of the classical Fischer

indole synthesis to be the most suitable. This reaction can essentially be done in two steps and “one pot” using a range of commercially available anilines.

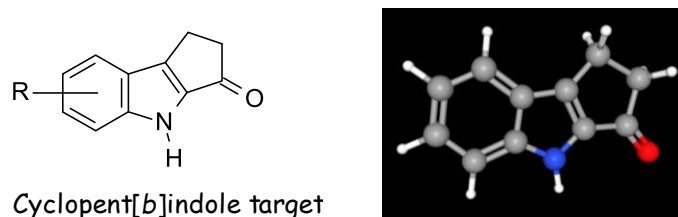
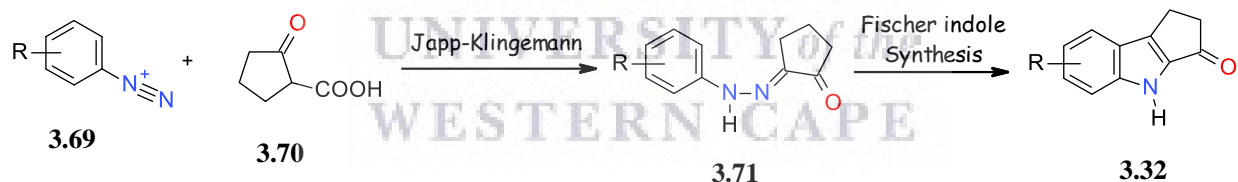


Figure 3.2 General structure of the target tetrahydrocyclopenta[*b*]indol-3-one core.

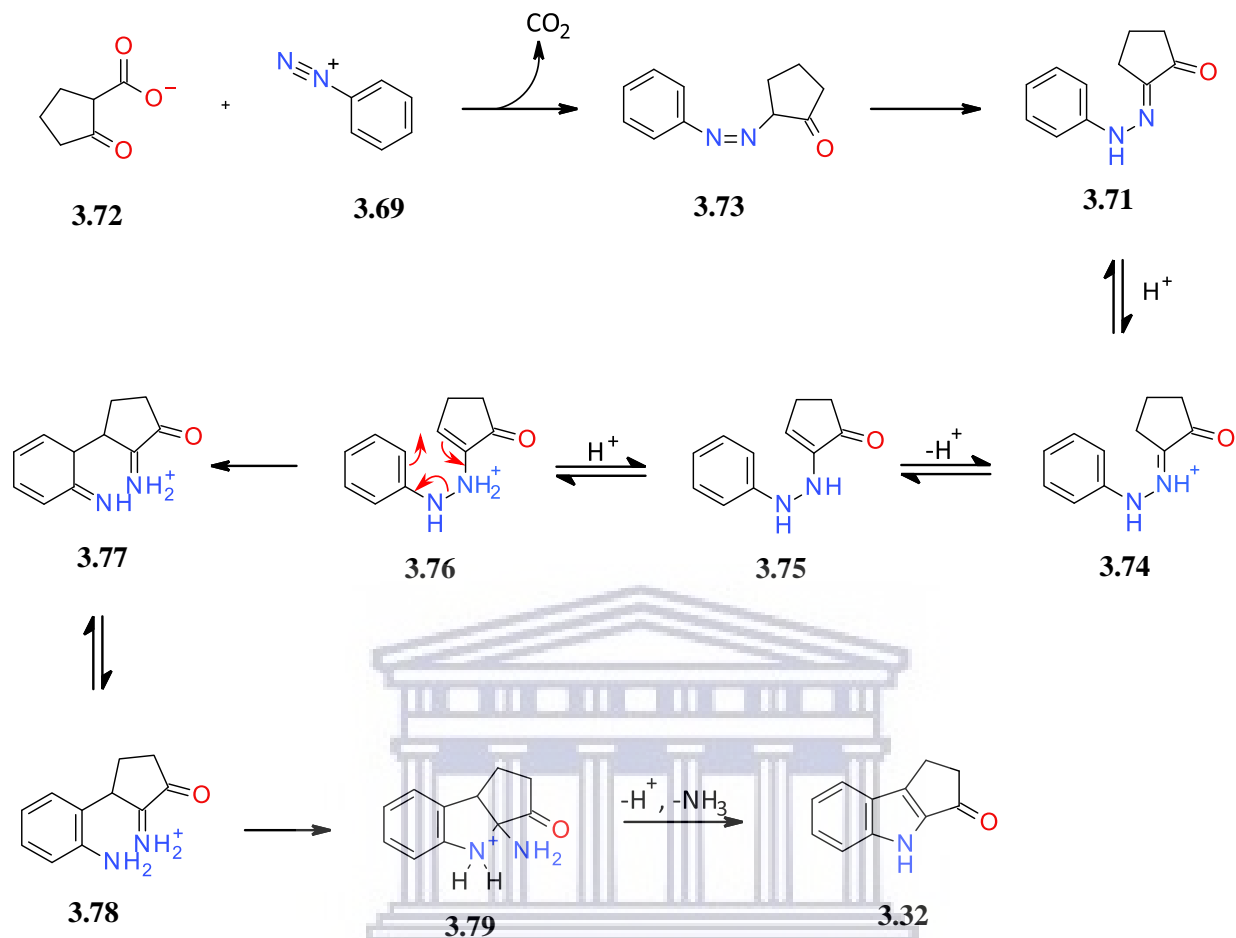
3.2 Results and discussion

The synthesis of the cycloalka[*b*]indoles from phenylhydrazones is one of the foremost methods in fusing cycloalkanes to the [*b*] side of indole derivatives. Our approach utilized the Japp–Klingemann condensation of diazonium salts (**3.69**) with the 2-oxocycloalkanecarboxylic acid (**3.70**) to obtain the corresponding cycloalkanone phenylhydrazones (**3.71**). This is followed by Fischer indole cyclization, under acidic conditions, to afford the cycloalka[*b*]indoles (**3.32**) (Scheme 3.14) (Gataullin, 2009; Hillier et al., 2005).



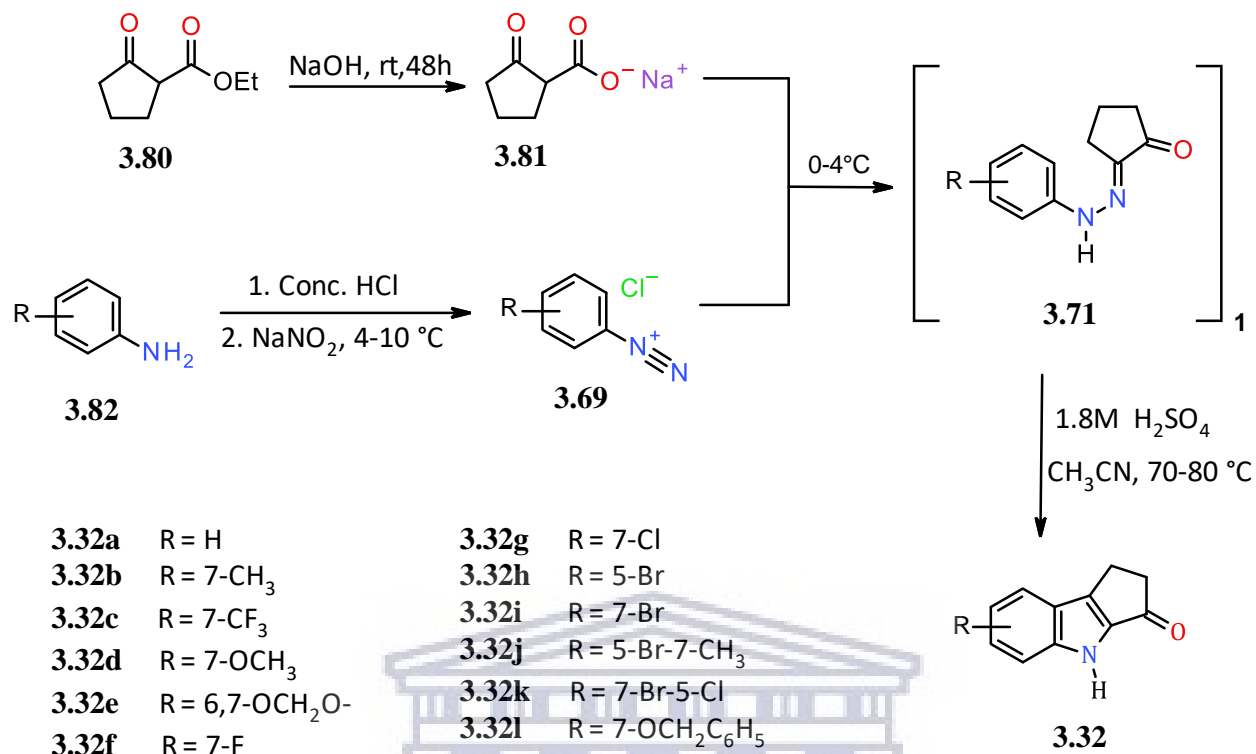
Scheme 3.14 Japp-Klingemann/Fischer synthesis of cycloalka[*b*]indoles.

The general mechanism of this reaction sequence is shown in Scheme 3.15. In the Japp–Klingemann reaction, the enolate of the β -keto-acid **3.72** attacks the diazonium salt *via* nucleophilic addition to generate an azo compound **3.73**. Decarboxylation and rearrangement of **3.73** produces the hydrazone **3.71** suitable for Fischer indolization. On heating under acidic conditions, the hydrazone **3.71** tautomerizes to the enamine **3.76** which undergoes a [3,3]-sigmatropic rearrangement producing imine **3.71**. The latter converts to a cyclic aminal which undergoes loss of ammonia to form an indole **3.32**.



Scheme 3.15 General mechanism of the Japp-Klingemann/Fischer synthesis of cycloalka[*b*]indoles.

The synthesis of indoles **3.32(a-l)** (Scheme 3.16) started with the hydrolysis of commercially available ethyl-2-oxocyclopentanecarboxylate (**3.80**) under mild basic conditions. The carboxylate salt **3.81** was then reacted with the diazonium salts of substituted anilines **3.69(a-l)** at 0-4 °C to give phenylhydrazones **3.71(a-l)** in moderate to high yields (45-98 %). Subsequent cyclization of the crude phenylhydrazones was carried out using 1.8 M H₂SO₄ to afford the cyclopenta[*b*]indoles **3.32(a-l)** in 18-65 % yield.



Scheme 3.16 Synthesis of cyclopenta[*b*]indole derivatives.

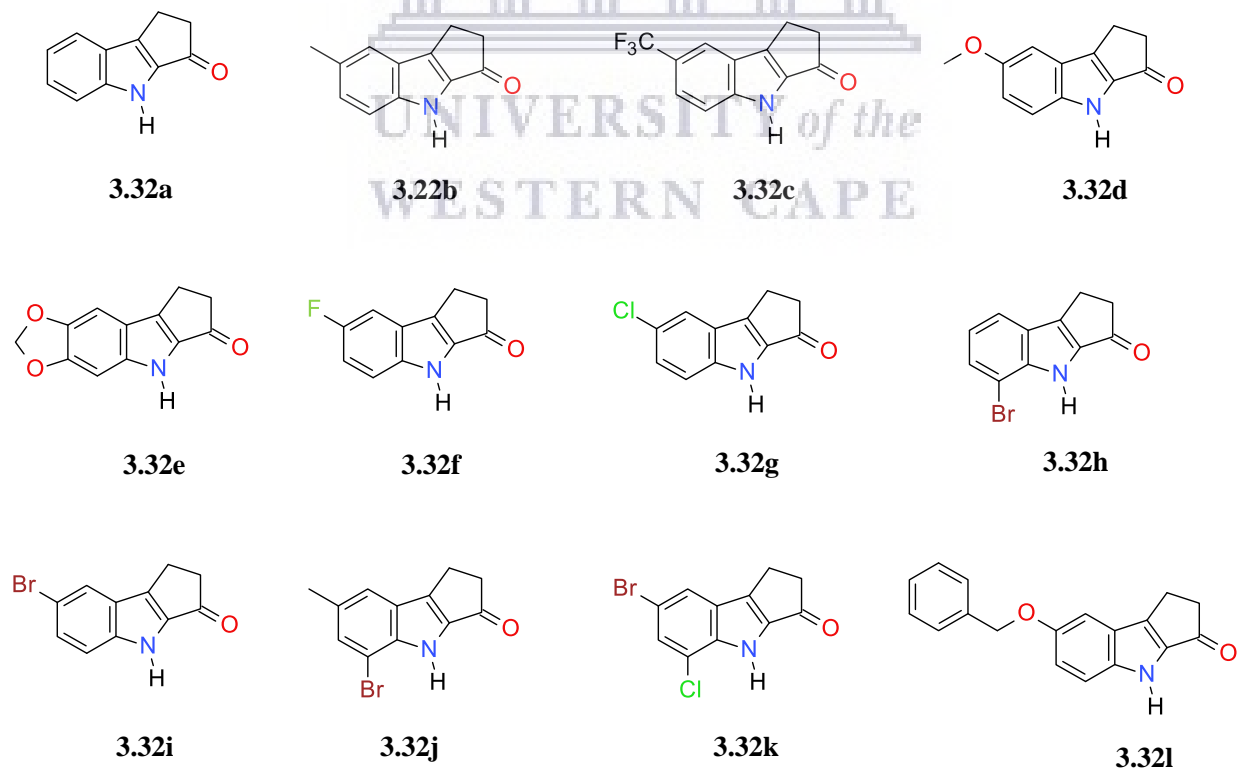
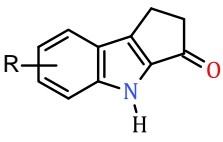


Figure 3.3 Summary of compounds synthesized.

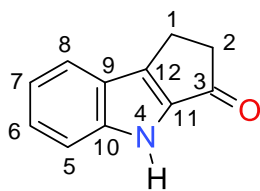
Generally, the yields were moderate (42-65 %) except for compound **3.32d** (18 %) with a low yield that was attributed to its poor stability under the reaction conditions (Table 3.1). This agrees with Hillier and co-workers' report (Hillier et al., 2005) that the methoxy-substituted substrate is less stable due to decomposition during the reaction. These compounds (Figure 3.3) were all obtained as solids and their structures were confirmed using NMR, HRMS and IR spectroscopy.

Table 3.1 Physical properties of the synthesized compounds **3.32(a-l)**.

				
Compounds	R	Appearance	Melting Point (°C)	Yield (%)
3.32a	H	Grey powder	249-253	65
3.32b	7- CH ₃	Dark brown powder	241-243	50
3.32c	7- CF ₃	Black powder	211-213	51
3.32d	7- OCH ₃	Black powder	259-261	18
3.324	6,7-OCH ₂ O-	Black powder	>310	55
3.32f	7-F	Brown powder	255-258	49
3.32g	7-Cl	Brick red powder	276-279	58
3.32h	5-Br	Black powder	185-188	52
3.32i	7-Br	Dark brown powder	254-257	51
3.32j	5-Br,7-CH ₃	Brown powder	202-203	51
3.32k	7-Br,5-Cl	Green powder	226-229	59
3.32l	7-OCH ₂ C ₆ H ₅	Black powder	207-210	42

3.2.1 Spectroscopic analysis of the compounds 3.32a

The structures of synthesized compounds were confirmed by NMR, IR and mass spectrometric analysis. In this section, the spectroscopic characteristics of compound **3.32a** was discussed herein as a representative example for the series.



3.32a

Compound **3.32a** was obtained as a grey powder that displayed a protonated molecular ion peak at m/z 172.0772, acquired from high resolution electrospray ionization mass spectrometry (HR-ESIMS), and affirmed the molecular formula of $C_{11}H_9NO$. The 1H NMR spectrum (Figure 3.4) displayed signals at δ_H 11.59 (br s, NH) together with four aromatic methine signals at δ_H 7.70 (d, 1H, $J = 8.0$ Hz), 7.44 (d, 1H, $J = 8.0$ Hz), 7.33 (t, 1H, $J = 8.1$ Hz), 7.11 (t, 1H, $J = 7.5$ Hz) and two methylene signals at 3.01 (br m, 2H) and 2.87 (br m, 2H).

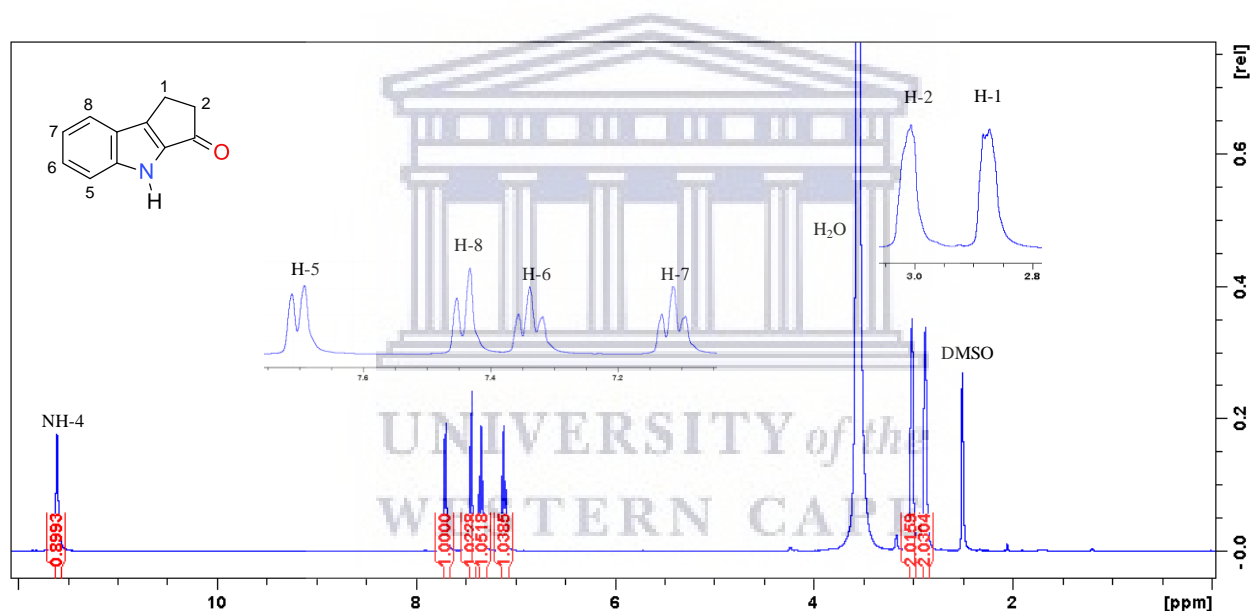


Figure 3.4 1H NMR spectrum of compound **3.32a** (400 MHz, $DMSO-d_6$).

The ^{13}C NMR spectrum (Figure 3.5) confirmed the presence of eleven carbons of which eight were aromatic and two sp^3 methylene signals. A signal at δ_C 194.1 in the ^{13}C NMR spectrum and an infra-red band at 1655 cm^{-1} confirmed the presence of an unsaturated ketone. The DEPT 135 spectrum (Figure 3.6) also confirmed the four aromatic sp^2 methines (C-5, C-6, C-7 & C-8) as positive signals while the two sp^3 methylene (C-1 & C-2) signals yielded negative.

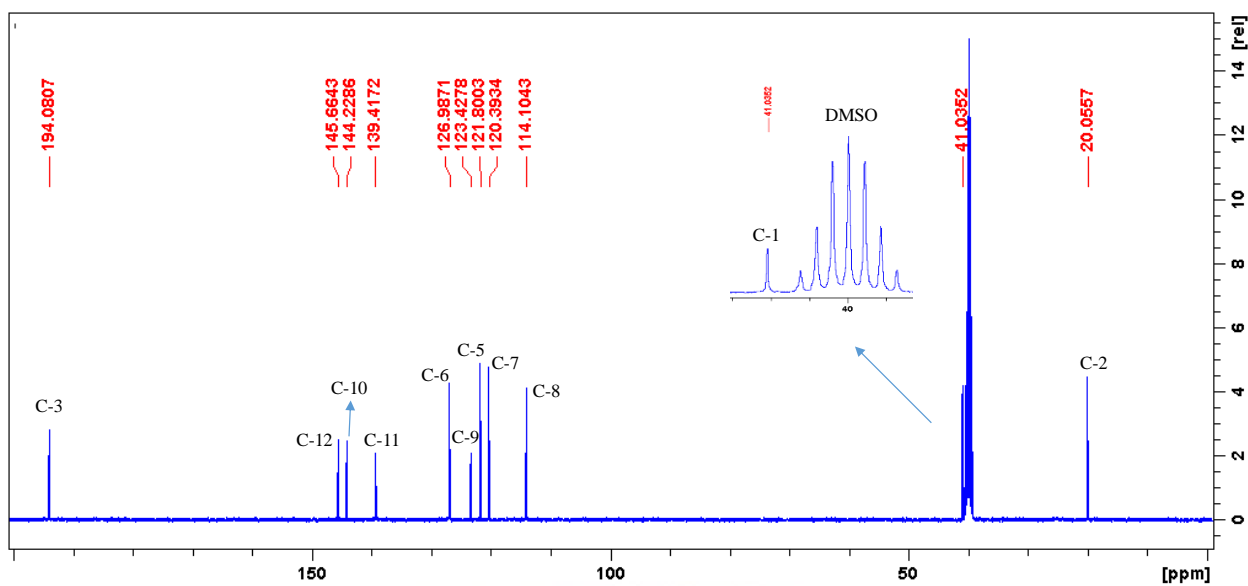


Figure 3.5 ^{13}C NMR spectrum of compound **3.32a** (100 MHz, DMSO- d_6).

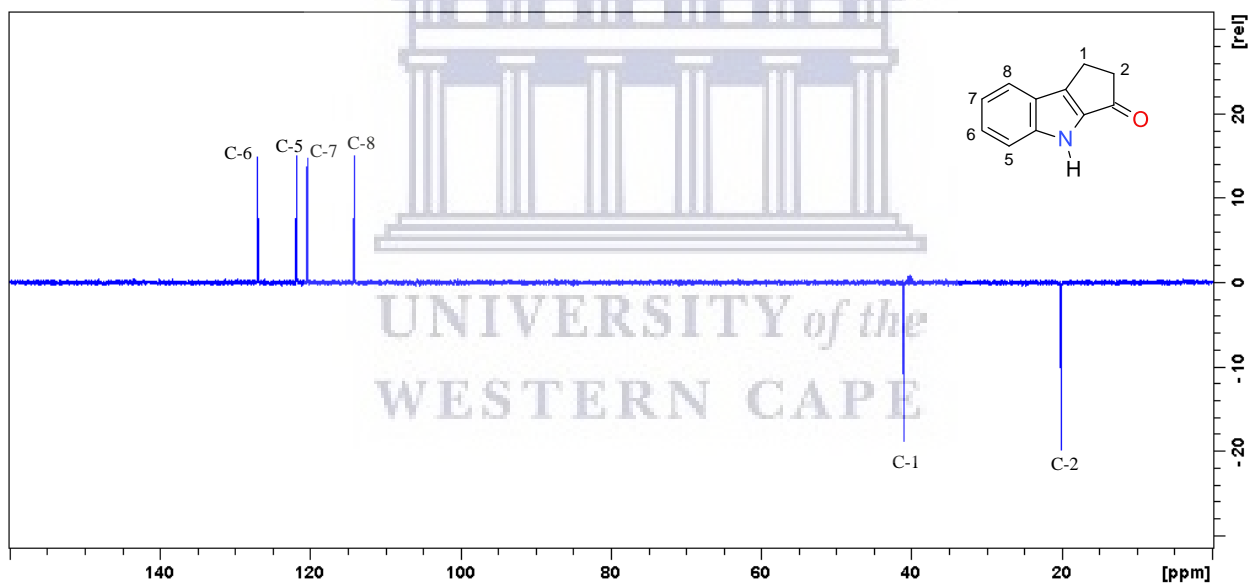


Figure 3.6 DEPT-135 NMR spectrum of compound **3.32a**.

Detailed analysis of 2D NMR data (Figures 3.7, 3.8 and 3.9, and Table 3.2) confirmed the structure of **3.32a** and allowed the complete assignment of all carbons and protons in its structure.

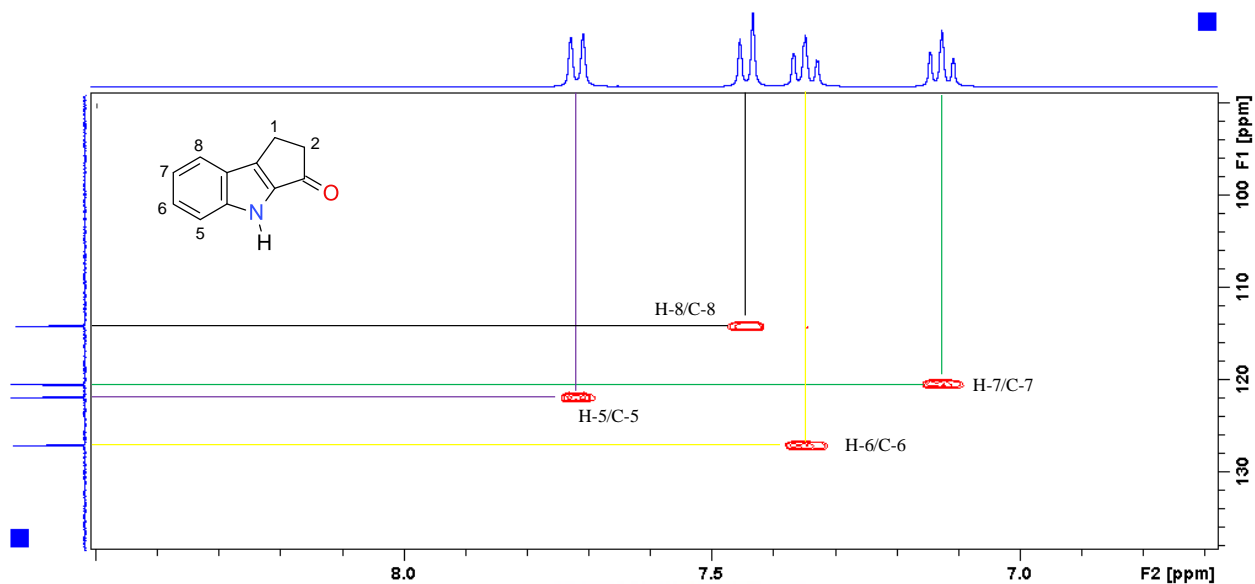


Figure 3.7 A section of the HSQC spectrum of **3.32a** showing the correlations of the aromatic protons to the corresponding carbon atoms.

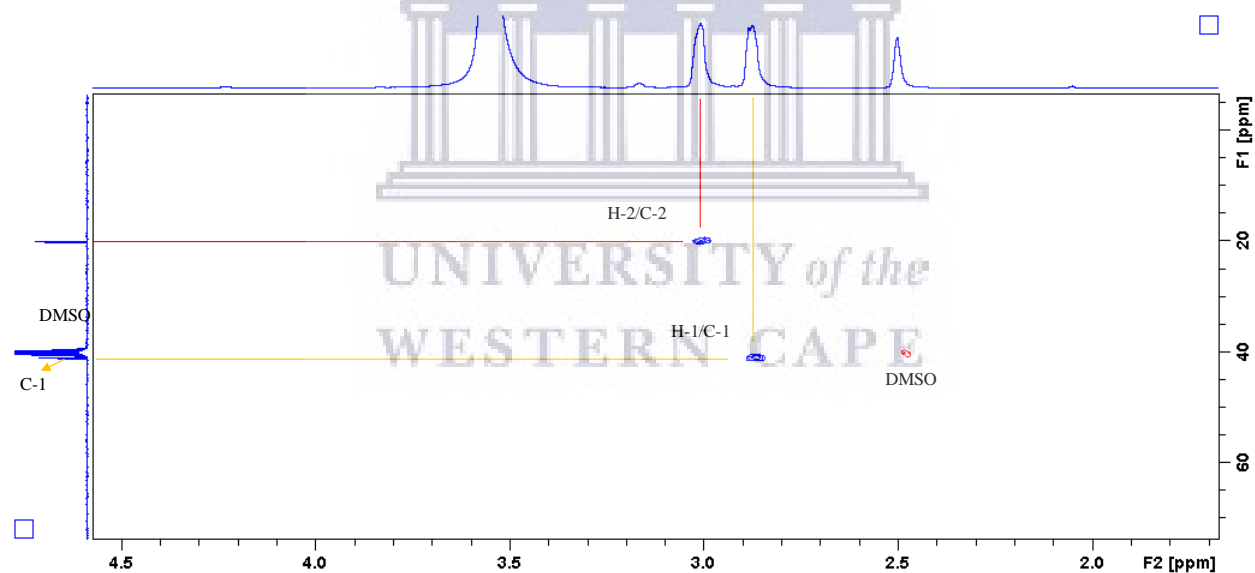


Figure 3.8 A section of HSQC spectrum of **3.32a** showing the methylene protons correlations to the corresponding carbon atoms.

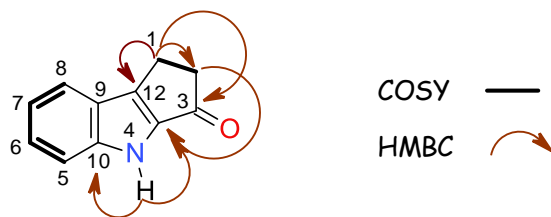


Figure 3.9 COSY and HMBC correlations of compound **3.32a**.

The COSY NMR data displayed correlations from protons resonating at δ_{H} 7.70 (H-5) to 7.11 (H-7) and δ_{H} 7.33 (H-6) to 7.44 (H-8). From the HMBC spectrum, the proton resonance at δ_{H} 2.87 (H₂-1) correlated with signals resonating at δ_{C} 20.1 (C-2), 194.1 (C-3) and 145.7 (C-12). Similarly, δ_{H} 3.03 (H₂-2) correlated with δ_{C} 145.7 (C-12) (Figure 3.10). Likewise, NH-4 proton resonating at δ_{H} 11.60 correlated with δ_{C} 144.2 (C-10) and 139.4 (C-11).

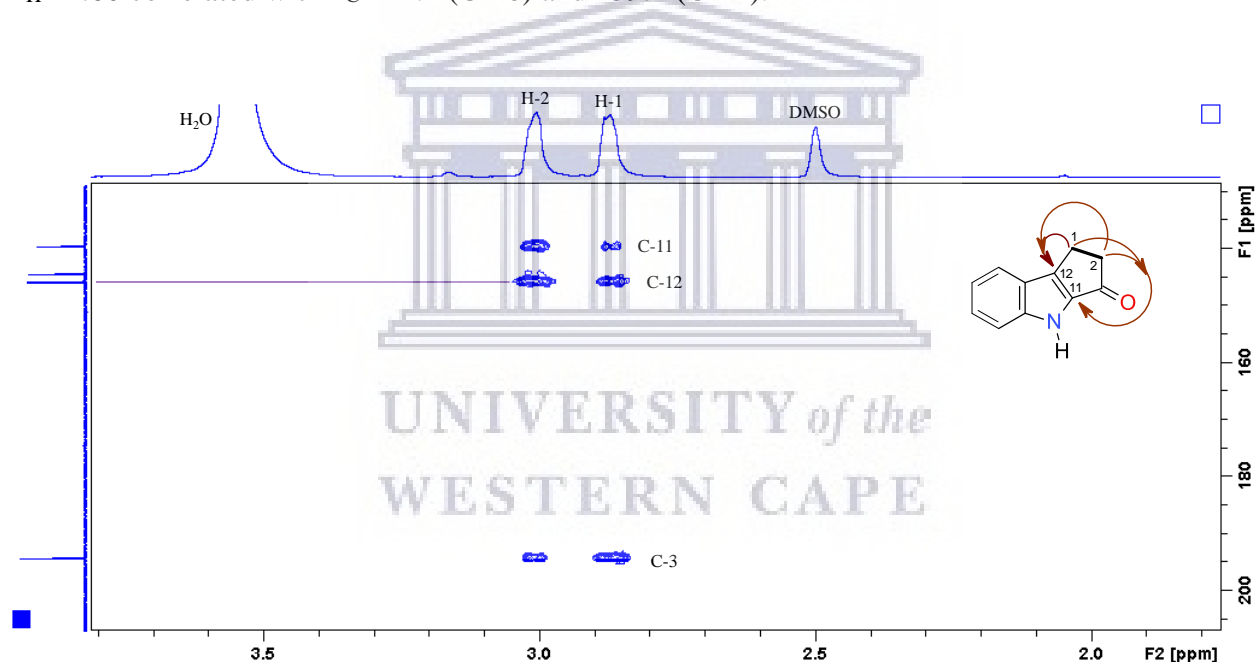
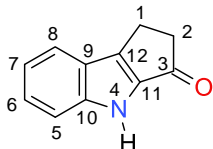


Figure 3.10 A section of the HMBC spectrum showing correlations from the methylene protons to the unsaturated ketone and confirming attachment to the cyclopentanone to the indole ring with correlations from C-1 and C-2 to C-11 and C-12.

Table 3.2 NMR data for compound **3.32a** (400 MHz for ^1H and 100 MHz for ^{13}C , DMSO- d_6).



Position	δ_{C}	δ_{H} (mult., J , Hz)	COSY	HMBC
1	41.0	2.87 (m, 2H)	H-2	C-2, C-3, C-11, C-12
2	20.1	3.01(m, 2H)	H-1	C-1, C-3, C-11, C-12
3	194.1	-		
NH-4	-	11.60 (br s, 1H)	H-5	C-9, C-10, C-11, C-12
5	121.8	7.70 (d, $J = 8.0$, 1H)	N-H, H-7	C-6, C-7, C-9, C-10
6	127.0	7.33 (t, $J = 8.1$, 1H)	H-8	C-5, C-7, C-10
7	120.4	7.11 (t, $J = 7.5$, 1H)	H-5	C-6, C-8, C-9
8	114.1	7.44 (d, $J = 8.0$, 1H)	H-6	C-7, C-9
9	123.4	-		
10	144.2	-		
11	139.4	-		
12	145.7	-		

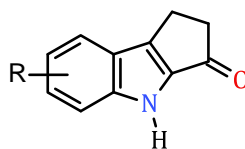
Generally, the characteristic NMR features discussed and presented in Table 3.2 were common to all synthesized compounds. The ^1H NMR chemical shifts for the NH protons were observed between δ_{H} 12.12 to 11.47 as broad singlets. The methylene protons of the sp^3 hybridized C-1 and C-2 were observed within the range δ_{H} 3.11 and 2.77 as multiplets. Although it was expected that they would be seen as triplets, however, that was not the case due to complex splitting between these diastereotopic protons. The aromatic protons resonated between δ_{H} 8.18 and 6.87, however, the multiplicity varied depending on the position of substitution. Compounds **3.32b**, **3.32d**, **3.32g** and **3.32i** with position-7 substitution displayed similar multiplicity except **3.32c** which had a pair of singlets but upon integration summed up to three (3) aromatic protons as expected. On the other hand, compound **3.32f** displayed a pair of doublets and triplet of doublets, this is due to the coupling of fluorine at position-7 with the other aromatic protons. Compounds **3.32e**, **3.32j**, and **3.32k** with two aromatic substitutions also showed similar multiplicity while compound **3.32l** displayed overlapping signals within the aromatic region.

The ^{13}C NMR spectra of the cyclopenta[*b*]indoles followed the same trend, the ketone (C-3) signals ranged between of δ_{C} 194.3 – 192.3. sp^3 hybridized carbons at C-1 and C-2 resonated within δ_{C} 41.0 – 40.9 and 21.5 – 19.98 respectively. Among the cyclopenta[*b*]indoles synthesized only compound **3.32a** is known. The ^1H and ^{13}C NMR data reported (Cui et al., 2004) were identical to those obtained in this study and no additional spectroscopic information was available from the literature. Therefore, this study presents the first 2D NMR data for compound **3.32a**.

3.2.2 *In vitro* antiproliferative study

The antiproliferative activity of the synthesized compounds was evaluated against the triple-negative breast cancer cell line, HCC70 (Table 3.3). Although no particular trend with respect to electron-donating/withdrawing groups was observed, the following observations can be made. The most active compounds were **3.32e** and **3.32k** with IC_{50} of 6.9 and 12.3 μM , respectively. A 7-bromo or chloro substituent showed moderate activity while the fluoro group at the same position shows poor activity. For the series of 7-substituted cyclopenta[*b*]indoles, the following sequence was observed: $-\text{Cl} > \text{CF}_3 > \text{Br/MeO} > \text{H/F/CH}_3$. A 5-bromo substituent was the least active but a 7-bromo, 5-chloro substitution showed good activity. Although the 7-methoxy group showed only moderate activity the 6,7-methylenedioxy substituents also showed good activity. A further series of compounds with multiple halogen or methoxy substituents or a combination of these may be useful in clarifying structure-activity relationships for this class of cyclopenta[*b*]ind-3ones.

Table 3.3 Antiproliferative activity of compounds **3.32(a-l)**^a against HCC70 cells.

			
Entry	R	IC ₅₀ μM	SEM
3.32a	H	147.7	232.27*
3.32b	7- CH ₃	163.9	13.09
3.32c	7- CF ₃	44.6	2.73
3.32d	7- OCH ₃	64.6	1.15
3.32e	6,7-OCH ₂ O-	12.3	1.16
3.32f	7-F	162.3	10.81
3.32g	7-Cl	28.6	1.39
3.32h	5-Br	208.2	5.37
3.32i	7-Br	64.5	1.27
3.32j	5-Br,7-CH ₃	175.5	1.36
3.32k	7-Br,5-Cl	6.9	1.30
3.32l	7-OCH ₂ C ₆ H ₅	NT	

^a NT: not tested. SEM: standard error of mean The poor solubility of **3.32a** is probably responsible for the poor reproducibility of its biological activity.

3.2.3 *In silico* predictions of the physicochemical and drug-likeness of the synthesized compounds

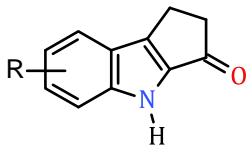
Many drugs fail clinical trials due to poor pharmacokinetic properties or side effects (Cheng et al., 2012). Thus, it is necessary to adopt a rapid approach to evaluate the absorption, distribution, metabolism, excretion, and toxicity (ADMET) properties of potential therapeutic compounds (Cheng et al., 2012). The *in silico* ADME tools are not a replacement for the experimental assessment but they offer good probability of identifying compounds with acceptable pharmacokinetic properties (Lombardo et al, 2017). Hence, it provides perspective into the pharmacokinetics and drug-likeness properties of drug candidates. It also saves time and costs associated with experimental studies (Van De Waterbeemd & Gifford, 2003). Lipinski developed rules important for the absorption, distribution, metabolism, and excretion (ADME) and drug-likeness of chemical compounds (Lipinski et al., 1997). The Lipinski's rules state that a drug would

likely be suitable for oral administration if it fulfills these requirements; not more than 5 hydrogen bond donors; not more than 10 hydrogen bond acceptors (n-ON); molecular weight of not more than 500 gmol⁻¹; the partition coefficient between n-octanol and water is not greater than 5 and number of violations greater than 1 could be problematic for the bioavailability (Lipinski et al., 1997). The topological surface area (TPSA) measures the ability of a compound to form hydrogen bonding and it is a good predictor of intestinal absorption, bioavailability, Caco-2 permeability and blood-brain barrier penetration (Ertl et al., 2000). The number of rotatable bonds evaluates the molecular flexibility and it is also a predictor for oral bioavailability and absorption (Veber et al., 2002).

A web-based prediction tool; Molinspiration, which has been reported in literature for theoretical predictions (Ammar et al., 2018; Laskar et al., 2018; Wang et al., 2018) was used to predict the ADME properties of the synthesized compounds (Table 3.4). The predictions were obtained online from the Molinspiration Cheminformatics server (<http://www.molinspiration.com/cgi-bin/properties>) version 2018.10. The analyses were based on the following descriptors; Logarithm of partition coefficient between n-octanol and water (miLogP), topological polar surface area (TPSA), number of hydrogen bond acceptors (n-ON), number of hydrogen bond donors (n-OHND), number of rotatable bonds (n-ROTB), and molecular volume (MV).

The results presented in Table 3.4 showed that the compounds were within the required limit for the descriptors with no violation of the Lipinski rules, thus indicates that these compounds have a high theoretical bioavailability according to the Lipinski “rule-of-five” (Lipinski et al., 1997). TPSA values were all below the designated limit of 160 Å suggesting that they will be readily absorbed (Ertl et al., 2000, Verma, 2012). Among the compounds tested against HCC70 cells, the most active compound **3.32k** (R = 7-Br,5-Cl) recorded the highest miLogP value of 3.55. It suggests that this compound is lipophilic and could readily penetrate the cells.

Table 3.4 *In silico* physicochemical properties and drug-likeness of the synthesized compounds **3.32(a-l)**^a.

									
Compounds	R	miLogP ^b	TPSA ^c	MW ^d	n-HBA ^e	n-HBD ^f	n-violations ^g	n-ROTB ^h	MV ⁱ
3.32a	H	2.16	32.86	171.2	2	1	0	0	154.77
3.32b	7- CH ₃	2.58	32.86	185.23	2	1	0	0	171.33
3.32c	7- CF ₃	3.03	32.86	239.2	2	1	0	1	186.06
3.32d	7- OCH ₃	2.19	42.1	201.22	3	1	0	1	180.31
3.32e	6,7-OCH ₂ O-	2.03	51.33	215.21	4	1	0	0	178.7
3.32f	7-F	1.33	32.86	189.19	2	1	0	0	159.7
3.32g	7-Cl	2.81	32.86	205.64	2	1	0	0	168.3
3.32h	5-Br	2.92	32.86	250.09	2	1	0	0	172.65
3.32i	7-Br	2.95	32.86	250.09	2	1	0	0	172.65
3.32j	5-Br,7-CH ₃	3.32	32.86	264.12	2	1	0	0	189.21
3.32k	7-Br,5-Cl	3.55	32.86	284.54	2	1	0	0	186.19
3.32l	7-OCH ₂ C ₆ H ₅	3.79	42.1	277.32	3	1	0	3	251.96

^a The parameters were determined using Molinspiration cheminformatics software. ^b The logarithm of the partition coefficient between n-octanol and water (miLogP ≤ 5). ^c Topological polar surface area (TPSA < 160 Å²). ^d Molecular weight (MW < 500). ^e The number of hydrogen bond acceptors (n-HBA ≤ 10). ^f The number of hydrogen bond donors (n-HBD ≤ 5). ^g The number of violations (n-violations ≤ 1). ^h The number of rotatable bonds (n-ROTB). ⁱ Molecular volume (MV).

3.3 Conclusion

A series of cyclopenta[*b*]indoles were successfully synthesized *via* the Japp-Klingemann reaction and Fischer indole cyclization. All compounds were obtained as solids in moderate yields except **3.32d** (R = OCH₃) that recorded a low yield due to decomposition during synthesis. The structures were confirmed by NMR, IR and mass spectrometry, and cell proliferation inhibition property of the compounds was examined against HCC70 cells. The bioassay results showed no clear pattern in activity regarding the effect of electron withdrawing or donating substituent on the scaffold. Although, the double-halogenated derivative **3.32k** (R = 4-Br, 2-Cl) exhibited the best activity with an IC₅₀ of 6.9 μM.

3.4 Experimental

3.4.1 General experimental details

Unless otherwise specified, all chemicals were obtained commercially and used without further purification. All reactions were monitored by thin-layer chromatography on Silica gel 60 F₂₅₄ aluminium sheets purchased from Merck KGaA. The visualization was achieved using UV light (254 nm and 365 nm) or iodine vapour. Purification was achieved by column chromatography with silica gel 60 (0.040-0.063 mm, Merck KGaA). Solvents were obtained from Crest chemicals (South Africa) and redistilled before use.

NMR data were recorded on a Bruker Avance 400 MHz spectrometer with deuterated chloroform (CDCl₃) or dimethyl sulphoxide (DMSO-d₆) as solvent. Chemical shifts were referenced to residual signal of solvent (CHCl₃ δ_H 7.26, δ_C 77.00 DMSO-d₆ δ_H 2.50, δ_C 39.43) and reported in parts per million (ppm). The following abbreviations were used to describe the multiplicity of the respective signals: s (singlet), br s (broad singlet), d (doublet), dd (doublet of doublets), t (triplet), td (triplet of doublets) and m (multiplet). The high resolution mass spectra were obtained using a Waters UPLCMS hyphenated with a Waters Synapt G2 QTOF instrument at the University of Pretoria mass spectral facility. IR spectra were recorded using a Perkin Elmer Spectrum 400 FT-IR/FT-NIR spectrometer. Melting points were determined on a Stuart SMP-10 melting point apparatus using the glass capillary method.

3.4.2 General Japp-Klingemann procedure

Sodium carboxylate preparation

Ethyl 2-oxocyclopentanecarboxylate (10 mmol) was weighed into a round-bottom flask, 1.0 M NaOH (13.6 mL) was added and stirred at ambient temperature for 48 h. The unreacted starting material was removed from the resulting mixture by extracting with EtOAc (2 x 3 mL) and the aqueous phase containing the sodium carboxylate was returned to the round-bottom flask. This solution was cooled to 0 °C, neutralized with 13.6 mL of 1 M HCl dropwise, and kept at this temperature for 45 min.

Diazonium salt preparation

Concentrated hydrochloric acid (40.8 mmol, 4 mL of 32% HCl) was added to a mixture of aniline (10 mmol) and water (6 mL) in a round-bottom flask. The resulting slurry was mixed with a glass rod and then cooled to 0 °C. A solution of NaNO₂ (10 mmol in 7 mL of water) was added dropwise such that the internal temperature of 10 °C was not exceeded. The reaction mixture was allowed to stand for 30 min. Where necessary, the diazonium salt solution was filtered to remove the insoluble precipitate before the Japp-Klingemann reaction.

Japp-klingemann reaction

The sodium carboxylate solution at 0 °C was added dropwise into the diazonium solution while stirring with a glass rod. The resulting slurry was allowed to stand overnight at <10 °C, filtered and the resulting crude hydrazone was dried in the fumehood.

General Fischer cyclization protocol

The crude hydrazone (5 mmol) was weighed into a three-neck flask equipped with a stirrer, a condenser and a thermometer and acetonitrile (12.5 mL) and 1.8 M H₂SO₄ (8.5 mL) were added. The resulting mixture was heated under reflux (75 °C) for 5 h, the reaction was judged complete by TLC. At the end of the reaction, water (25 mL) was added and the resultant slurry stirred at ambient temperature for 1 h and then filtered. The precipitate obtained was washed with

acetonitrile/water (1:3, 25 mL), water (3 x 25 mL) and dried to give the final cyclopenta[*b*]indole product.

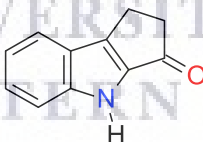
3.4.3 Synthesis of 4-benzyloxy aniline (3.32l)

A mixture of 4-acetamidophenol (19 mmol), benzylbromide (21 mmol), potassium carbonate (24 mmol) and acetone (50 mL) was heated under reflux for 6 h. The suspension was filtered, washed with EtOH and then concentrated under reduced pressure to obtain a white crystalline solid.

To benxyloxyacetanilide (3 mmol) in a round-bottom flask was added NaOH (150 mmol), EtOH (120 mL), water (28 mL) and heated to reflux for 7 h. The mixture was allowed to cool before drying by rotary evaporation. Water (100 mL) was added to the residue and the aqueous solution was extracted with CHCl₃ (100 mL). The organic phase was then washed with water (2 x 100 mL) and concentrated under reduced pressure. The crude product was purified by column chromatography with solvent mixture of EtOAc/hexane (2:3) as the mobile phase to afford a light brown solid.

3.4.4 Compounds

2,4-dihydro-1H-cyclopenta[*b*]indol-3-one (3.32a)



Yield: 65 % as grey powder. Mp 249-253 °C

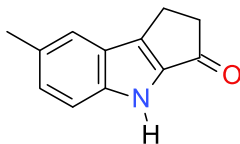
¹H NMR (400 MHz, DMSO-*d*₆) δ_H 11.60 (br s, N-H), 7.70 (d, *J* = 8.0 Hz, 1H), 7.44 (d, *J* = 8.0 Hz, 1H), 7.33 (t, *J* = 8.1 Hz, 1H), 7.11 (t, *J* = 7.5 Hz, 1H), 3.04 – 2.98 (m, 2H), 2.89 – 2.84 (m, 2H)

¹³C NMR (100 MHz, DMSO-*d*₆) δ_C 194.1, 145.7, 144.2, 139.4, 127.0, 123.4, 121.8, 120.4, 114.1, 41.0, 20.1

HRESIMS: *m/z*: [M + H]⁺ calculated for C₁₁H₁₀NO 172.0763 found 172.0772

FT-IR (ATR, cm⁻¹): 3182, 1654

7-methyl-2,4-dihydro-1H-cyclopenta[*b*]indol-3-one (3.32b)



Yield: 50 % as dark brown powder. Mp 241–243 °C

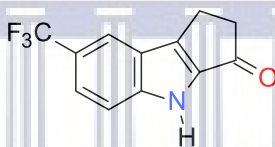
¹H NMR (400 MHz, DMSO-*d*₆) δ 11.49 (br s, N-H), 7.48 (s, 1H), 7.32 (d, *J* = 8.6 Hz, 1H), 7.17 (dd, *J* = 8.6, 1.5 Hz, 1H), 3.01 – 2.97 (m, 2H), 2.89 – 2.84 (m, 2H), 2.38 (s, 3H)

¹³C NMR (100 MHz, DMSO-*d*₆) δ 193.9, 145.1, 142.7, 139.4, 129.1, 128.8, 123.6, 121.0, 113.8, 41.0, 21.5, 20.0

HRESIMS: (*m/z*) [M + H]⁺ calculated for C₁₂H₁₂NO 186.0920; found 186.0927

FT-IR (ATR, cm⁻¹): 3189, 1655

7-(trifluoromethyl)-2,4-dihydro-1H-cyclopenta[*b*]indol-3-one (3.32c)



Yield: 51 % as black powder. Mp 211-213 °C

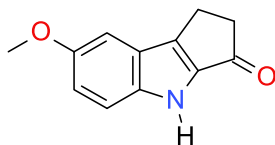
¹H NMR (400 MHz, DMSO-*d*₆) δ 12.13 (br s, N-H), 8.17 (s, 1H), 7.62 (s, 2H), 3.11 – 3.05 (m, 2H), 2.96 – 2.89 (m, 2H).

¹³C NMR (100 MHz, DMSO-*d*₆) δ 194.5, 146.2, 145.3, 141.3, 126.94, 122.9, 122.6, 121.3, 119.9, 115.1, 41.0, 20.1.

HRESIMS: (*m/z*) [M + H]⁺ calculated for C₁₂H₉F₃NO 240.0637; found 240.0525

FT-IR (ATR, cm⁻¹): 3187, 1675

7-methoxy-2,4-dihydro-1H-cyclopenta[*b*]indol-3-one (3.32d)



Yield: 18 % as black powder. Mp 259-261 °C

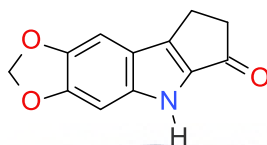
¹H NMR (400 MHz, DMSO-d₆) δ 11.47 (br s, N-H), 7.45 (s, 1H), 7.32 (d, *J* = 9.0 Hz, 1H), 7.17 (dd, *J* = 9.1, 1.41 Hz, 1H), 3.78 (s, 3H), 3.02 – 2.97 (m, 2H), 2.89 – 2.84 (m, 2H)

¹³C NMR (100 MHz, DMSO-d₆) δ 194.0, 154.1, 145.0, 139.7, 139.5, 123.5, 118.3, 115.0, 102.0, 55.8, 41.0, 20.0

HRESIMS: (*m/z*) [M + H]⁺ calculated for C₁₂H₁₂NO₂ 202.0869; found 202.0888

FT-IR (ATR, cm⁻¹): 3136, 1691

6,7-dioxolo-2,4-dihydro-1H-cyclopenta[*b*]indol-3-one (3.32e)



Yield: 55 % as black powder. Mp >310 °C

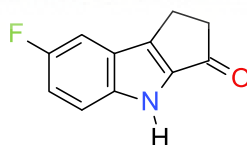
¹H NMR (400 MHz, DMSO-d₆) δ 11.48 (br s, N-H), 7.12 (s, 1H), 6.86 (s, 1H), 6.02 (s, 2H), 2.96 – 2.90 (m, 2H), 2.83 – 2.77 (m, 2H)

¹³C NMR (100 MHz, DMSO-d₆) δ 192.3, 148.6, 145.8, 143.7, 140.6, 138.2, 117.3, 101.5, 99.2, 93.6, 40.9, 20.0

HRESIMS: (*m/z*) [M + H]⁺ calculated for C₁₂H₁₀NO₃ 216.0661; found 216.0649

FT-IR (ATR, cm⁻¹): 3196, 1639

7-fluoro-2,4-dihydro-1H-cyclopenta[*b*]indol-3-one (3.32f)



Yield: 49 % as brown powder. Mp 255-258 °C

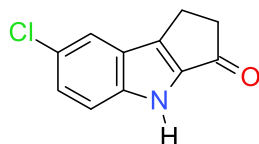
¹H NMR (400 MHz, DMSO-d₆) δ 11.74 (br s, N-H), 7.51 (dd, *J* = 9.5, 2.6 Hz, 1H), 7.44 (dd, *J* = 9.1, 4.6 Hz, 1H), 7.21 (td, *J* = 9.2, 2.7 Hz, 1H), 3.03 – 2.98 (m, 2H), 2.91 – 2.86 (m, 2H)

¹³C NMR = (100 MHz, DMSO-d₆) δ 194.3, 158.5, 156.2, 145.1, 141.0, 123.3, 115.7, 115.4, 106.3, 41.0, 20.0

HRESIMS: (*m/z*) [M + H]⁺ calculated for C₁₁H₉FNO 190.0669; found 190.0645

FT-IR (ATR, cm⁻¹): 3221, 1655

7-chloro-2,4-dihydro-1H-cyclopenta[*b*]indol-3-one (3.32g)



Yield: 58 % as brick red powder. Mp 276-279 °C

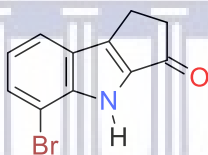
¹H NMR (400 MHz, DMSO-*d*₆) δ 11.84 (br s, N-H), 7.80 (d, *J* = 1.9 Hz, 1H), 7.44 (d, *J* = 8.8 Hz, 1H), 7.33 (dd, *J* = 8.8, 2.1 Hz, 1H), 3.03 – 2.98 (m, 2H), 2.91 – 2.86 (m, 2H)

¹³C NMR (100 MHz, DMSO-*d*₆) δ 194.3, 144.7, 142.5, 140.7, 126.9, 124.9, 124.3, 121.1, 115.8, 41.0, 20.0

HRESIMS: (*m/z*) [M + H]⁺ calculated for C₁₁H₉ClN 206.0374; found 206.0371

FT-IR (ATR, cm⁻¹): 3195, 1661

5-bromo-2,4-dihydro-1H-cyclopenta[*b*]indol-3-one (3.32h)



Yield: 52 % as black powder. Mp 185-188 °C

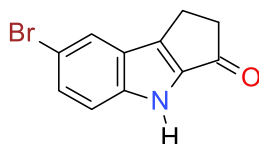
¹H NMR (400 MHz, DMSO-*d*₆) δ 11.90 (br s, N-H), 7.75 (d, *J* = 8.0 Hz, 1H), 7.57 (d, *J* = 7.6, 1H), 7.07 (t, *J* = 7.8 Hz, 1H), 3.05 – 3.01 (m, 2H), 2.94 – 2.89 (m, 2H)

¹³C NMR (100 MHz, DMSO-*d*₆) δ 194.1, 146.5, 142.4, 140.2, 129.5, 125.1, 121.7, 121.3, 106.1, 41.1, 20.1

HRESIMS: (*m/z*) [M + H]⁺ calculated for C₁₁H₉BrNO 251.9848; found 251.9840

FT-IR (ATR, cm⁻¹): 3236, 1675

7-bromo-2,4-dihydro-1H-cyclopenta[*b*]indol-3-one (3.32i)



Yield: 51 % as dark brown powder. Mp 254-257 °C

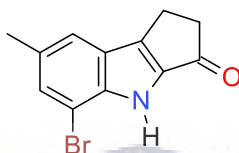
¹H NMR (400 MHz, DMSO-d₆) δ 11.85 (br s, N-H), 7.95 (d, *J* = 1.7 Hz, 1H), 7.46 – 7.38 (m, 2H), 3.04 – 2.98 (m, 2H), 2.92 – 2.87 (m, 2H)

¹³C NMR (100 MHz, DMSO-d₆) δ 194.3, 144.6, 142.7, 140.5, 129.4, 125.0, 124.2, 116.2, 112.8, 41.0, 20.0

HRESIMS: (*m/z*) [M + H]⁺ calculated for C₁₁H₉BrNO 251.9848; found 251.9840

FT-IR (ATR, cm⁻¹): 3195, 1659

5-bromo-7-methyl-2,4-dihydro-1H-cyclopenta[*b*]indol-3-one (3.32j)



Yield: 51 % as brown powder. Mp 202-203 °C

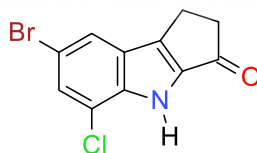
¹H NMR (400 MHz, DMSO-d₆) δ 11.75 (br s, N-H), 7.51 (s, 1H), 7.42 (d, *J* = 1.0 Hz, 1H), 3.02 – 2.96 (m, 2H), 2.92 – 2.86 (m, 2H), 2.38 (s, 3H)

¹³C NMR (100 MHz, DMSO-d₆) δ 194.0, 145.9, 140.8, 140.3, 131.0, 130.9, 125.1, 120.6, 105.7, 41.0, 21.0, 20.0

HRESIMS: (*m/z*) [M + H]⁺ calculated for C₁₂H₁₁BrNO 264.0024; found 264.0024

FT-IR (ATR, cm⁻¹): 3228, 1674

7-bromo-5-chloro-2,4-dihydro-1H-cyclopenta[*b*]indol-3-one (3.32k)



Yield: 59 % as green powder. Mp 226-229 °C

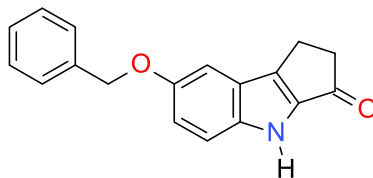
¹H NMR (400 MHz, DMSO-d₆) δ 12.27 (br s, N-H), 7.97 (d, *J* = 1.5 Hz, 1H), 7.62 (d, *J* = 1.7 Hz, 1H), 3.04 – 2.98 (m, 2H), 2.94 – 2.88 (m, 2H)

¹³C NMR (100 MHz, DMSO-d₆) δ 194.3, 145.4, 141.3, 139.8, 128.0, 126.2, 123.4, 119.2, 112.2, 41.1, 20.1

HRESIMS: (*m/z*) [M + H]⁺ calculated for C₁₁H₈BrClNO 285.9458; found 285.9464

FT-IR (ATR, cm⁻¹): 3196, 1690

7-benzyloxy-2,4-dihydro-1H-cyclopenta[*b*]indol-3-one (3.32l)



Yield: 42 % as black powder. Mp 207-210 °C

¹H NMR (400 MHz, DMSO-*d*₆) δ 11.49 (br s, N-H), 7.48 (d, *J* = 7.6 Hz, 2H), 7.42 – 7.31 (m, 4H), 7.29 (d, *J* = 2.5 Hz, 1H), 7.08 (dd, *J* = 9.1, 2.5 Hz, 1H), 5.11 (s, 2H), 3.02 – 2.96 (m, 2H), 2.89 – 2.83 (m, 2H)

¹³C NMR (100 MHz, DMSO-*d*₆) δ 193.9, 153.2, 144.9, 139.8, 139.6, 137.8, 128.9, 128.2, 128.1, 123.5, 118.7, 115.0, 103.6, 70.2, 41.0, 20.1

HRESIMS: (*m/z*) [M + H]⁺ calculated for C₁₈H₁₆NO₂ 278.1182; found 278.1190

FT-IR (ATR, cm⁻¹): 3210, 1667

3.4.5 Biological assay

3.4.5.1 Cell culture

The HCC70 (ATCC CRL-2315) cell line was cultured in RPMI-1640 containing 10% (v/v) FBS, 1 mM L-glutamine, 1% (v/v) PSA and 0.2% (v/v) sodium bicarbonate maintained at 37°C in 9% CO₂.

3.4.5.2 Antiproliferative assay

The cells were seeded at 5000 cells/well in a 96 well tissue culture plate and allowed to adhere overnight at 37 °C in a humidified 9% CO₂ incubator. The cells were treated with the compounds with dose dependent concentrations ranging from 0.4-250 μM, a 1% (v/v) DMSO vehicle control or paclitaxel (positive control). This was followed by an incubation of 96 h at 37 °C in a humidified 9% CO₂ incubator. After treatment, the resazurin assay was used in determining the viable cells using 0.54 mM resazurin solution. 20 μL of resazurin solution was added to each well and incubated for 2-4 h. The fluorescence of the blue to vivid pink dye was measured using a Spectromax spectrophotometer at an excitation wavelength of 560 nm and emission wavelength of 590 nm. The experiment was carried out in triplicate and the data were analyzed using GraphPad

Prism Inc, (USA). The half maximal inhibitory concentration (IC_{50} values) were calculated by 4 parameters non-linear regression, the regressions were constrained by control values and the IC_{50} s presented are relative.



References

Ammar, Y. A., El-Sharief, A. M. S., Belal, A., Abbas, S. Y., Mohamed, Y. A., Mehany, A. B., & Ragab, A. (2018). Design, synthesis, antiproliferative activity, molecular docking and cell cycle analysis of some novel (morpholinosulfonyl) isatins with potential EGFR inhibitory activity. *European Journal of Medicinal Chemistry*, 156, 918-932.

Balskus, E. P., & Walsh, C. T. (2008). Investigating the initial steps in the biosynthesis of cyanobacterial sunscreen scytonemin. *Journal of the American Chemical Society*, 130(46), 15260–15261.

Balskus, E. P., & Walsh, C. T. (2009). Supporting information an Enzymatic cyclopentyl [*b*] indole formation Involved in scytonemin biosynthesis. *Biological Chemistry*, 14648–14649.

Berger, L., & Corraz, A. J. (1977). Cyclopenta [*b*] indole-2-carboxylic acids and derivatives thereof. U.S. Patent No. 4,009,181.

Buzard, D. J., Kim, S. H., Lopez, L., Kawasaki, A., Zhu, X., Moody, J., Thoresen, L., Calderon, I., Ullman, B., Han, S., Jones, R. M. (2014). Discovery of APD334: Design of a clinical stage functional antagonist of the sphingosine-1-phosphate-1 receptor. *ACS Medicinal Chemistry Letters*, 5(12), 1313–1317.

Chadha, N., & Silakari, O. (2017). Indoles as therapeutics of interest in medicinal chemistry: Bird's eye view. *European Journal of Medicinal Chemistry*, 134, 159–184.

Chen, H., Bai, J., Fang, Z. F., Yu, S. S., Ma, S. G., Xu, S., Li, Y., Qu, J., Ren, J.H., Li, L., Si, Y.K., & Chen, X. G. (2011). Indole alkaloids and quassinoids from the stems of *brucea mollis*. *Journal of Natural Products*, 74(11), 2438–2445.

Cheng, F., Li, W., Zhou, Y., Shen, J., Wu, Z., Liu, G., Lee P.W., & Tang, Y. (2012). admetSAR: A comprehensive source and free tool for assessment of chemical ADMET properties. *Journal of Chemical Information and Modeling*, 52, 3099-3105.

Cui, D. M., Zhang, C., Kawamura, M., & Shimada, S. (2004). Synthesis of 1-indanones by intramolecular Friedel-Crafts reaction of 3-arylpropionic acids catalyzed by Tb(OTf)₃. *Tetrahedron Letters*, 45(8), 1741–1745.

Dethe, D. H., & Kumar B, V. (2015). Concise asymmetric total synthesis of bruceolline J. *Organic Chemistry Frontiers*, 2(5), 548–551.

Dhiman, S., & Ramasastry, S. S. V. (2015). Synthesis of polysubstituted cyclopenta [*b*] indoles *via* relay gold (i)/Brønsted acid catalysis. *Chemical Communications*, 51(3), 557-560.

Ekebergh, A., Lingblom, C., Sandin, P., Wenneras, C., & Martensson, J. (2015). Exploring a cascade Heck-Suzuki reaction based route to kinase inhibitors using design of experiments. *Organic and Biomolecular Chemistry*, 13(11), 3382–3392.

Ertl, P., Rohde, B., & Selzer, P. (2000). Fast calculation of molecular polar surface area as a sum of fragment-based contributions and its application to the prediction of drug transport properties. *Journal of Medicinal Chemistry*, 43(20), 3714-3717.

Ferreira, E. M., & Stoltz, B. M. (2003). Catalytic C–H bond functionalization with palladium (II): aerobic oxidative annulations of indoles. *Journal of the American Chemical Society*, 125(32), 9578-9579.

Gataullin, R. R. (2009). Synthesis of compounds containing a cycloalka[*b*]indole fragment. *Russian Journal of Organic Chemistry*, 45(3), 321–354.

Gerwick, W. H., Sorrels, C. M., & Proteau, P. J. (2009). Organization, Evolution, and Expression Analysis of the Biosynthetic Gene Cluster for Scytonemin, a Cyanobacterial UV-Absorbing Pigment. *Applied and Environmental Microbiology*, 75(14), 4861–4869.

Harrison, C. A., Leineweber, R., Moody, C. J., & Williams, J. M. (1995). Cyclopenta [*b*] indoles. Part 1. Synthesis of cyclopenta [*b*] indoles by formal [3+ 2] addition of indolylmethyl cations to alkenes. *Journal of the Chemical Society, Perkin Transactions 1*, (9), 1127-1130.

Hillier, M. C., Marcoux, J. F., Zhao, D., Grabowski, E. J. J., McKeown, A. E., & Tillyer, R. D. (2005). Stereoselective formation of carbon-carbon bonds *via* SN₂- displacement: Synthesis of substituted cycloalkyl[*b*]indoles. *Journal of Organic Chemistry*, 70(21), 8385–8394.

Kobayashi, A., Kajiyama, S. I., Inawaka, K., Kanzaki, H., & Kawazu, K. (1994). Nostodione A, a novel mitotic spindle poison from a blue-green alga *Nostoc commune*. *Zeitschrift für Naturforschung C*, 49(7-8), 464-470.

Kriechbaumer, V., Weigang, L., Fießelmann, A., Letzel, T., Frey, M., Gierl, A., & Glawischnig, E. (2008). Characterisation of the tryptophan synthase alpha subunit in maize. *BMC Plant Biology*, 8(1), 44.

Kung, P. J., Tao, Y. C., Hsu, H. C., Chen, W. L., Lin, T. H., Janreddy, D., Yao, C.F., Chang, K.H., Lin, J.Y., Su, M.T., Wu, C.H., & Hsieh-Li, H. M. (2014). Indole and synthetic derivative activate chaperone expression to reduce polyQ aggregation in SCA17 neuronal cell and slice culture models. *Drug Design, Development and Therapy*, 8, 1929–1939.

Laskar, S., Sánchez-Sánchez, L., Flores, S. M., López-Muñoz, H., Escobar-Sánchez, M. L., López-Ortiz, M., Hernández-Rodríguez, M., & Regla, I. (2018). Identification of (1S, 4S)-2, 5-diazabicyclo [2.2. 1] heptane-dithiocarbamate-nitrostyrene hybrid as potent antiproliferative and apoptotic inducing agent against cervical cancer cell lines. *European Journal of Medicinal Chemistry*, 146, 621-635.

Lipinski, C. A., Lombardo, F., Dominy, B. W., & Feeney, P. J. (1997). Experimental and computational approaches to estimate solubility and permeability in drug discovery and development settings. *Advanced drug delivery reviews*, 23(1-3), 3-25.

Lombardo, F., Desai, P. V., Arimoto, R., Desino, K. E., Fischer, H., Keefer, C. E., Petersson, C., Winiwarter, S., & Broccatelli, F. (2017). In Silico Absorption, Distribution, Metabolism, Excretion, and Pharmacokinetics (ADME-PK): Utility and best practices. An industry perspective from the international consortium for innovation through quality in pharmaceutical development: Miniperspective. *Journal of Medicinal Chemistry*, 60(22), 9097-9113.

Molinspiration Cheminformatics, Bratislava, Slovak Republic
<http://www.molinspiration.com/cgi-bin/properties> (accessed December 30, 2019).

Palmieri, A., & Petrini, M. (2007). Simplified synthesis of 3-(1-arylsulfonylalkyl) indoles and their reaction with reformatsky reagents. *Journal of Organic Chemistry*, 72(5), 1863–1866.

Santos, M. S., Fernandes, D. C., Rodrigues, M. T., Regiani, T., Andricopulo, A. D., Ruiz, A. L. T., Vendramini-Costa, D.B., de Carvalho, J.E., Eberlin, M.N., & Coelho, F. (2016). Diastereoselective synthesis of biologically active cyclopenta[b]indoles. *Journal of Organic Chemistry*, 81(15), 6626–6639.

Scarpi, D., Petrovic, M., Fiser, B., Gómez-Bengoia, E., & Occhiato, E. G. (2016). Construction of cyclopenta[*b*]indol-1-ones by a tandem gold (I)-catalyzed rearrangement/Nazarov reaction and application to the synthesis of Bruceolline H. *Organic Letters*, 18(15), 3922-3925.

Soule, T., Palmer, K., Gao, Q., Potrafka, R. M., Stout, V., & Garcia-Pichel, F. (2009). A comparative genomics approach to understanding the biosynthesis of the sunscreen scytonemin in cyanobacteria. *BMC Genomics*, 10(1), 336.

Tunbridge, G. A., Oram, J., & Caggiano, L. (2013). Design, synthesis and antiproliferative activity of indole analogues of indanocine. *Medicinal Chemistry Communications*, 4(11), 1452–1456.

Van De Waterbeemd, H., & Gifford, E. (2003). ADMET in silico modelling: towards prediction paradise?. *Nature Reviews Drug Discovery*, 2(3), 192-204.

Veber, D. F., Johnson, S. R., Cheng, H. Y., Smith, B. R., Ward, K. W., & Kopple, K. D. (2002). Molecular properties that influence the oral bioavailability of drug candidates. *Journal of Medicinal Chemistry*, 45(12), 2615-2623.

Verma, A. (2012). Lead finding from *Phyllanthus debelis* with hepatoprotective potentials. *Asian Pacific Journal of Tropical Biomedicine*, 2(3), 1735-1737.

Wang, G., Peng, Z., Peng, S., Qiu, J., Li, Y., & Lan, Y. (2018). (E)-N-Aryl-2-oxo-2-(3, 4, 5-trimethoxyphenyl) acetohydrazonoyl cyanides as tubulin polymerization inhibitors: Structure-based bioisosterism design, synthesis, biological evaluation, molecular docking and in silico ADME prediction. *Bioorganic & Medicinal Chemistry Letters*, 28(20), 3350-3355.

Wang, Z., Xu, X., Gu, Z., Feng, W., Qian, H., Li, Z., ... & Kwon, O. (2016). Nazarov cyclization of 1, 4-pentadien-3-ols: preparation of cyclopenta [*b*] indoles and spiro [indene-1, 4'-quinoline] s. *Chemical Communications*, 52(13), 2811-2814.

Wu, C. Y., Yu, Y. N., & Xu, M. H. (2017). Construction of Chiral Tricyclic Indoles through a Rhodium-Catalyzed Asymmetric Arylation Protocol. *Organic Letters*, 19(2), 384-387.

Zi, W., Wu, H., & Toste, F. D. (2015). Gold (I)-catalyzed dearomative Rautenstrauch rearrangement: enantioselective access to cyclopenta [*b*] indoles. *Journal of the American Chemical Society*, 137(9), 3225-3228.

Chapter 4

Synthesis and antiproliferative activity of arylidene cyclopenta[*b*]indol-3-one derivatives



UNIVERSITY *of the*
WESTERN CAPE

4.1 Introduction

Following the synthesis and antiproliferative screening of the cyclopenta[*b*]indol-3-one derivatives reported in chapter 3, we were interested in improving their biological activities by investigating their arylidene derivatives. Using indanocine as lead structure, Tunbridge et al. (2013) reported the synthesis, antimitotic and antiproliferative activity of cyclopenta[*b*]indol-3-one arylidene derivatives (Figure 4.1).

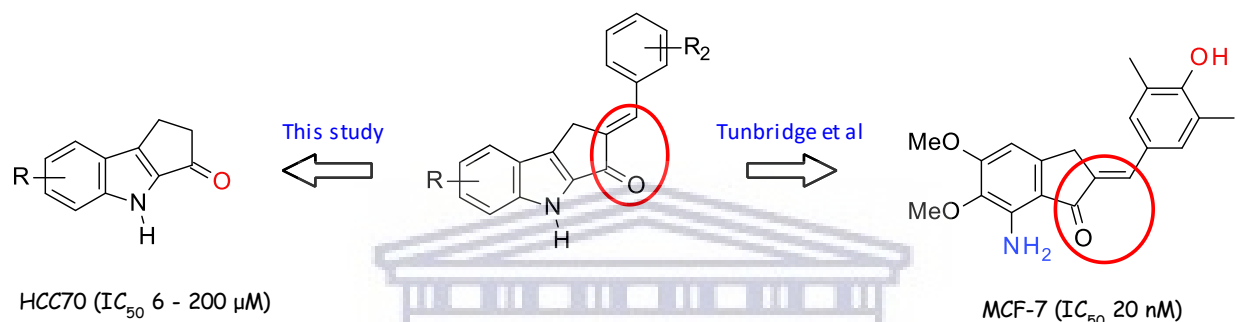


Figure 4.1 Development of indole derivatives of indanocine as potential anticancer agents.

Indanocine is a synthetic tubulin polymerization inhibitor that has demonstrated strong antiproliferative effects against many cancer cells. This activity is due to its ability to induce apoptosis in these cells and other multidrug-resistant tumours (Leoni et al., 2000). Studies also revealed that indanocine binds and interact at the colchicine binding site of the tubulin (Leoni et al., 2000; Das et al., 2009). Furthermore, computational techniques also displayed the interaction of indanocine with other human $\alpha\beta$ tubulin isotopes (Kumbhar et al., 2018). In this chapter, we briefly review cytotoxic arylidene indanone and related chalcone compounds before discussing the synthesis and antiproliferative activity of a series of cyclopenta[*b*]indole arylidene analogues. In addition, molecular docking studies were used to investigate the potential interaction of these compounds with tubulin.

4.1.1 Cytotoxic compounds containing the arylidene indanone/chalcone-core

Arylidene/benzylidene indanone analogues have not been reported as natural products, however, chalcones and arylidene indanones share structural similarity with the presence of an α,β -unsaturated ketone moiety in their structures. This feature is rigid in arylidene indanone but is

described as a “three-carbon α,β unsaturated ketone bridge” in chalcones (Menezes, 2017) (Figure 4.2).

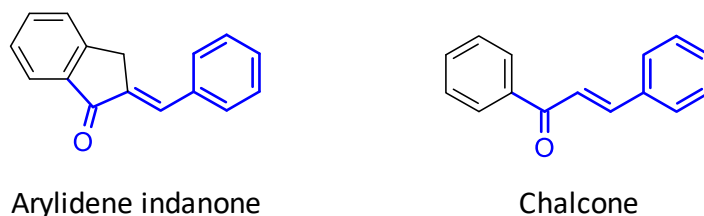


Figure 4.2 α,β -unsaturated ketone moiety in arylidene indanones and chalcone.

Chalcones are widely found in nature and have been reported to possess a variety of biological activities (Mahapatra et al., 2015). Veluchalcones A and B (**4.1** and **4.2**) were isolated from the stem of *Dalbergia velutina*, a leguminous plant from Thailand and these compounds exhibited IC_{50} values of 13.67 μ M and 10.12 μ M against KB cells, and 11.84 μ M and 13.29 μ M against HeLa - S3 cells, respectively (Kaennakam et al., 2019). Gao and co-workers evaluated the cytotoxic properties of three chalcones **4.3**, **4.4** and **4.5**, isolated from *Desmodium oxyphyllum*. They displayed IC_{50} values ranging from 3.6 – 10 μ M against five different cancer cell lines (Gao et al., 2015). Compounds **4.6** and **4.7** isolated from the bark of *Cryptocarya costata* showed IC_{50} values of 5.7 and 11.1 μ M, respectively, against murine leukaemia P-388 cells (Usman et al., 2006). Unique chalcones **4.8** and **4.9** containing epoxy- and methylenedioxy groups, respectively, were isolated from *Litsea rubescens* and *Litsea pedunculata* and exhibited potent cytotoxicity against myeloid leukaemia (HL-60) and epidermoid carcinoma (A431) cell lines (Li et al., 2011).

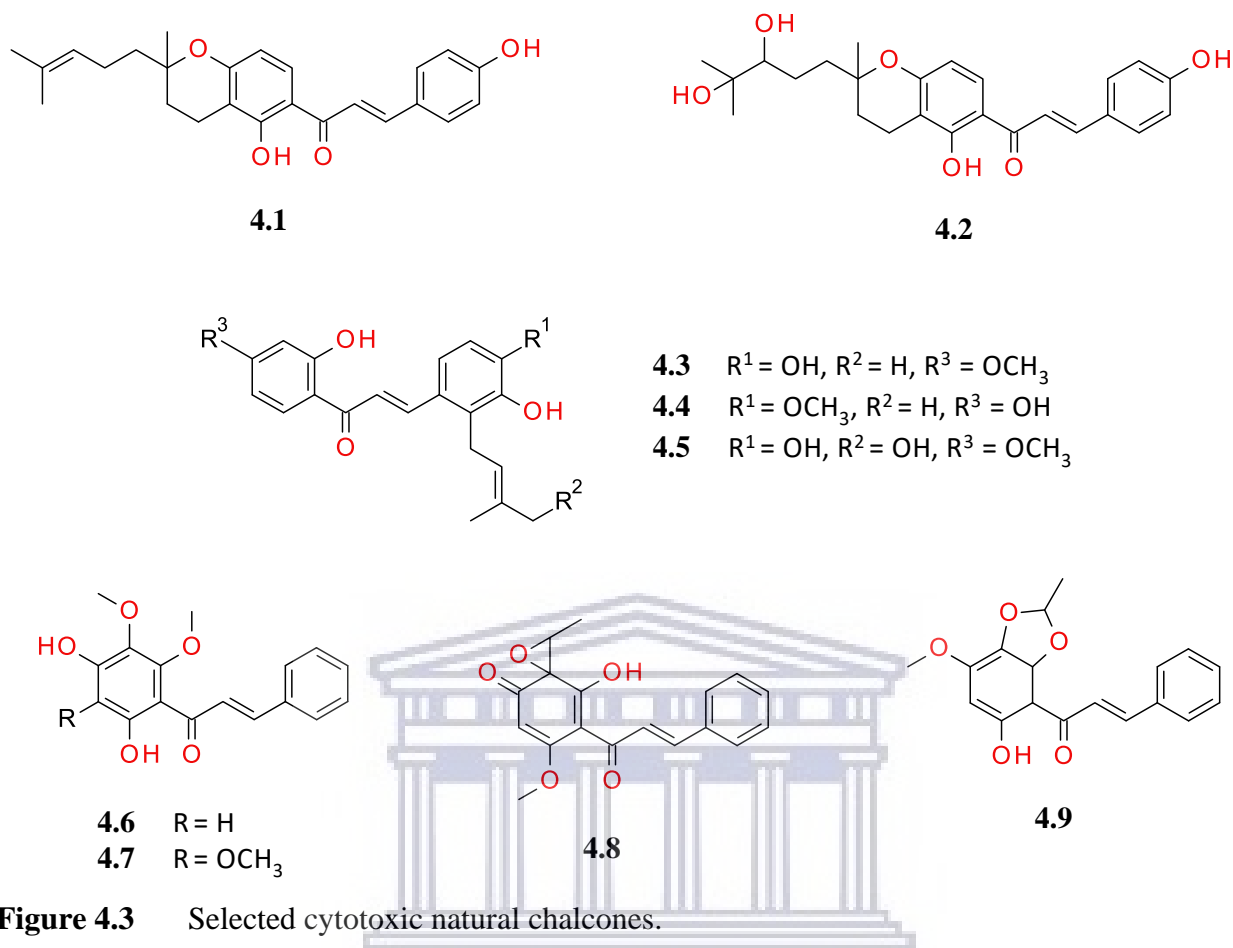


Figure 4.3 Selected cytotoxic natural chalcones.

Researchers have explored the synthesis and structure-activity relationships of many chalcone derivatives due to their attractive chemistry and exciting pharmacological potential (Mahapatra et al., 2015). The simple chalcone **4.10** is a synthetic analogue of the natural product xanthohumol that was reported to display high cytotoxicity with an IC_{50} value of $1.4 \mu\text{M}$ against HeLa cells; which was about 29 fold more active than the natural polyphenol chalcone (Zhang et al., 2015). Sometimes, the chalcone system is fused or linked to other heterocyclic moieties. Among these are anthraquinone-chalcones such as compound **4.11** demonstrated to have significant cytotoxicity against HeLa, LS174 and A549 with IC_{50} values 1.82, 1.76 and $6.11 \mu\text{M}$, respectively (Kolundžija et al., 2014). Indolyl-chalcone compounds **4.12** and **4.13** exhibited selective and excellent anticancer activity with IC_{50} values of 30 and 90 nM, respectively, against human pancreatic cancer (PaCa-2) cell lines (Kumar et al., 2010). Compound **4.14** is a synthetic derivative of artemisinin and displayed potent *in vitro* activity with an IC_{50} of $0.3 \mu\text{M}$ which was equivalent to the IC_{50} value obtained from the control drug, doxorubicin (Gaur et al., 2016). Compound **4.15**, consisting

of an indole moiety also demonstrated substantial cytotoxicity ranging between IC_{50} values of 0.22 - 1.80 μM against ten different human cancer cell lines (Wang et al., 2014).

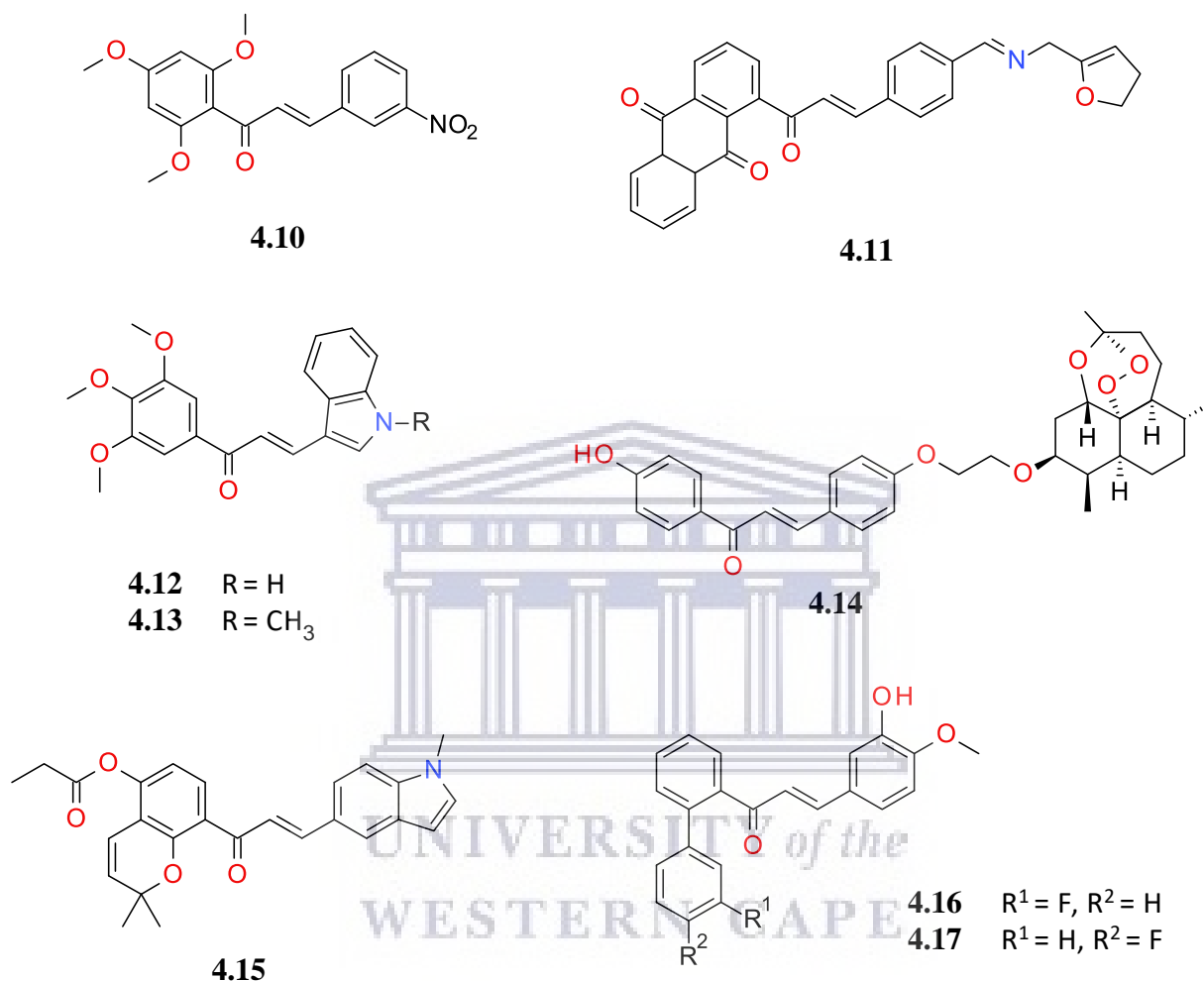


Figure 4.4 Synthetic cytotoxic chalcones.

Zhu and co-workers designed and synthesized a series of ortho-aryl chalcones and some of these compounds displayed potent cytotoxicity with IC_{50} values in the nanomolar range against many drug-resistant cancer cell lines. Compounds **4.16** and **4.17** exhibited the lowest IC_{50} values of 2 and 7 nM respectively against the drug-resistant MCF-7/DOX cell line. These values were a significant improvement over taxol, vincristine, doxorubicin and colchicine with IC_{50} values ranging from 1.5 – 4.3 μM (Zhu et al., 2014).

In the same way, there are some synthetic and cytotoxic arylidene/benzylidene indanones (Figure 4.5) reported in the literature such as compound **4.18**, which demonstrated antiproliferative activity against five cancer cell lines with GI₅₀ values ranging from 0.172 – 0.57 μM (Hu et al., 2015). Compound **4.19** displayed antiproliferative effect against NCI-H 460 and A549 cells with GI₅₀ of 0.28 μM and 0.77 μM respectively (Rajagopalan et al., 2016). The modification of gallic acid into a series of indanones followed by conversion to its benzylidene indanone derivatives (e.g. compound **4.20**) led to potently active compounds with an IC₅₀ of 10 nM against MCF-7 cells and tubulin polymerization inhibition (Prakasham et al., 2012; Negi, et al., 2014).

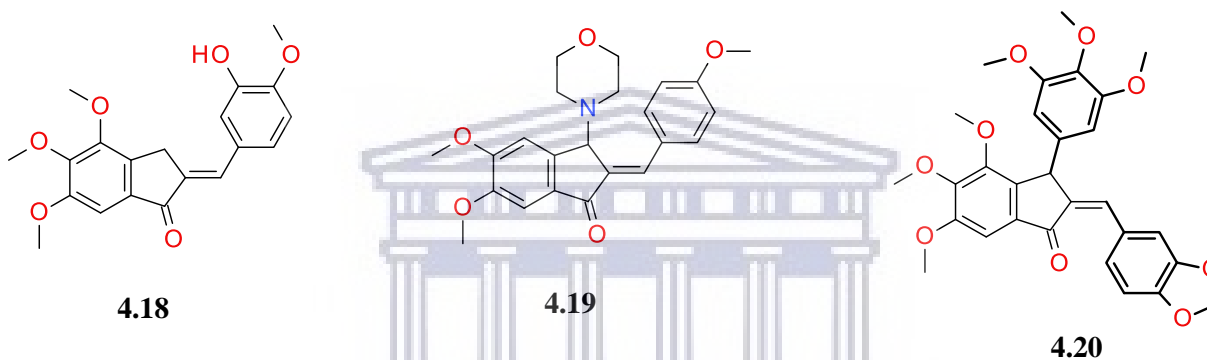
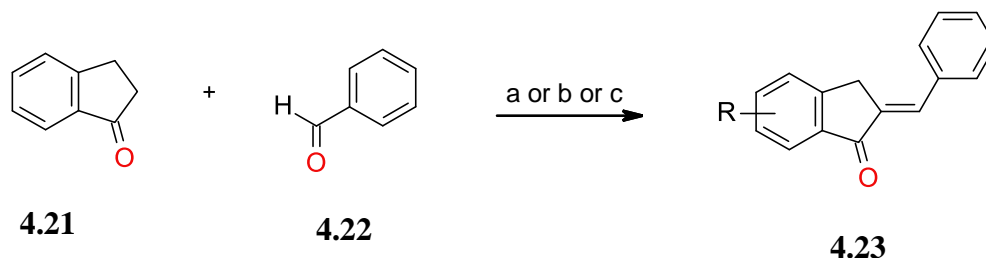


Figure 4.5 Synthetic and cytotoxic arylidene/benzylidene indanones.

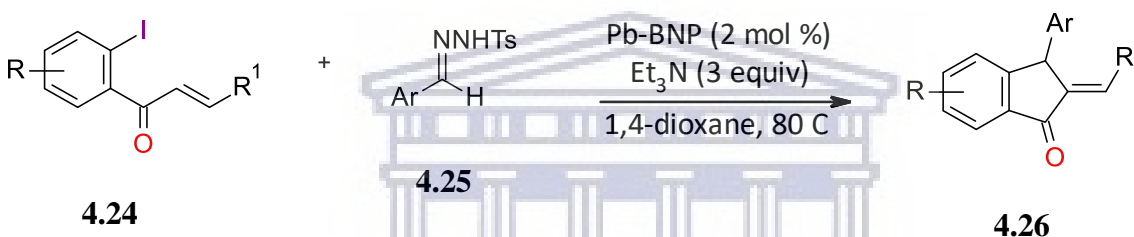
4.1.2 Synthesis of arylidene/benzylidene derivatives

In the synthesis of this type of α,β -unsaturated ketones, the aldol condensation is the most widely used reaction. The reaction is a common method used in the formation of a carbon-carbon bond from the condensation of an enolate with an aldehyde or ketone (Palomo et al., 2002). Aside from the popular acid or base-catalyzed aldol condensation (Scheme 4.1a or b) (Nel et al., 2016), TiCl₃(SO₃CF₃) catalyzed aldol condensation of indanone with aromatic aldehydes (Scheme 4.1c) has also been reported (Iranpoor et al., 1999). In addition, palladium-nanoparticle catalyzed domino reactions have been employed to generate the benzylidene indanone skeleton (Scheme 4.2) (Saha et al., 2018).



Reaction conditions:
 (a) methanol/32% HCl (1:1.5), reflux.
 (b) KOH, methanol, rt.
 (c) $\text{TiCl}_3(\text{SO}_3\text{CF}_3)$

Scheme 4.1 Aldol condensation of indanone with aromatic aldehydes.



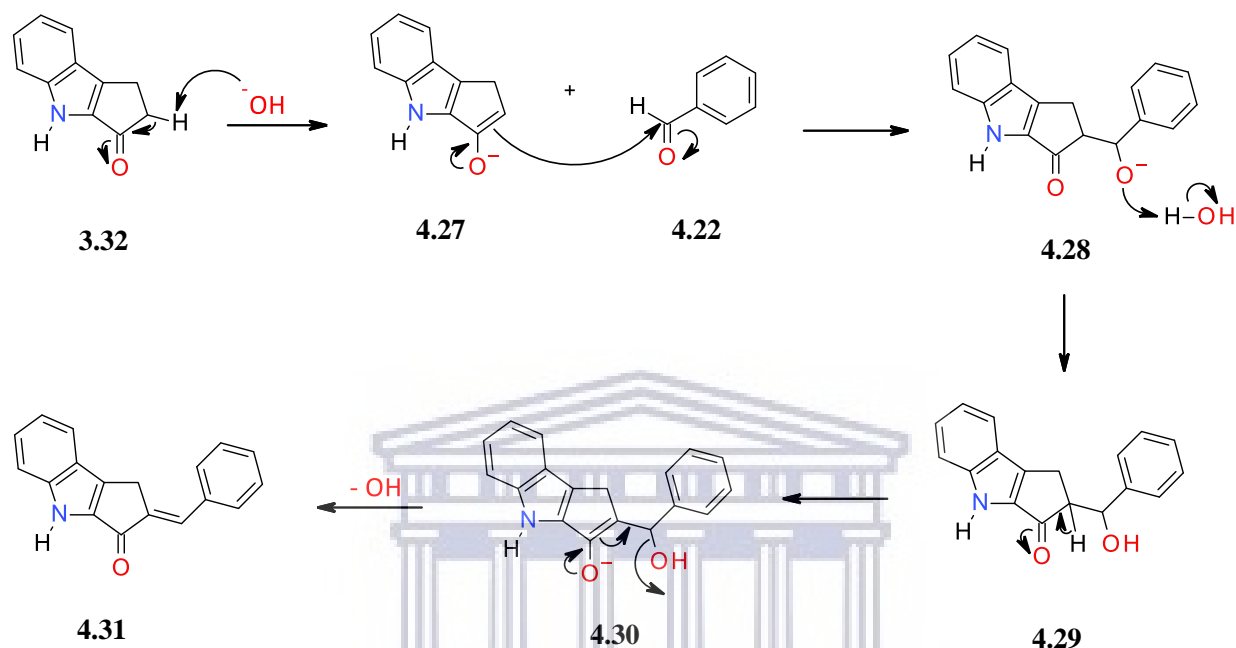
Scheme 4.2 Palladium-nanoparticle catalyzed domino reaction (Saha et al., 2018).

4.1.3 Synthetic approach to arylidene cyclopenta[*b*]indol-3-one derivatives – this study

The short review above provides some evidence that expanding the indanone system to its benzylidene indanone derivatives may lead to an improvement in cytotoxic activity from micromolar to low nanomolar IC_{50} values concentrations (Prakasham et al., 2012).

One of the guiding principles in designing new arylidene derivatives from cyclopenta[*b*]indoles in this study was to improve on the solubility of the compounds. Hence, 3-pyridinecarboxaldehyde **4.26c** was selected as it afforded a series of basic products that were converted to their corresponding pyridinium hydrochloride. The 3,4,5-trimethoxybenzaldehyde **4.26b** was selected to increase affinity for tubulin and mimic trimethoxyphenyl moiety in combretastatin A-4 **2.3**, and the unsubstituted benzaldehyde **4.26a** was included to provide a comparison with the other two aldehydes. In the synthesis of this group of compounds, the straightforward Claisen-Schmidt reaction was employed using alcoholic sodium hydroxide. The general mechanism of this reaction is presented in Scheme 4.3. The enolate ion **4.27** is formed through the removal of an α -hydrogen

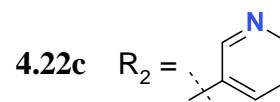
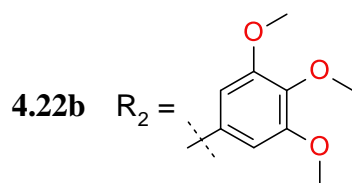
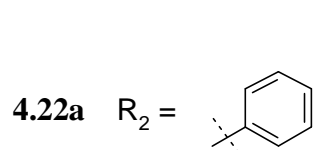
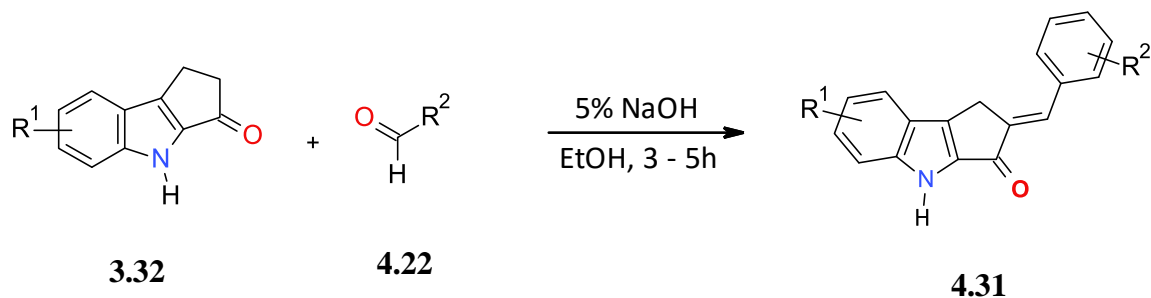
from **3.32** by the hydroxide ion, followed by reaction of the enolate ion **4.27** with benzaldehyde **4.22** to generate the alkoxide ion **4.28**. The intermediate **4.29** forms an enolate again **4.30** and the removal of hydroxyl gives the final product **4.31**.



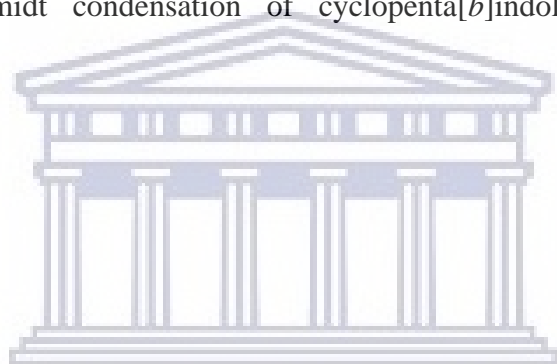
Scheme 4.3 General mechanism of Claisen-Schmidt synthesis of the arylidene cyclopenta[*b*]indol-3-one derivatives.

4.2 Results and discussion

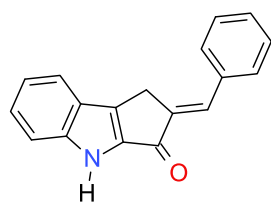
The arylidene cyclopenta[*b*]indol-3-one derivatives were prepared by Claisen-Schmidt condensation of the ketone and benzaldehyde using alcoholic sodium hydroxide solution at ambient temperature (Scheme 4.4). However, compound **3.32e** required elevated temperature (60 – 65 °C) to proceed. The products were all obtained by precipitation and were further purified by recrystallization, where necessary. The pyridinium chloride salts of selected members of the **4.33** series were prepared by reacting the base in dichloromethane with concentrated HCl. In general, the aldol products (Figure 4.6, 4.7 and 4.8) were obtained in moderate to high yields and were characterized by NMR, HRMS and IR spectroscopy. Compounds **4.33f**, **4.33g**, **4.33h**, **4.33i**, **4.33j** and **4.33k** displayed poor solubility in DMSO which made ^{13}C NMR characterization difficult, therefore the ^1H and ^{13}C NMR data of their hydrochloride salts was reported.



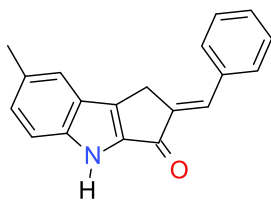
Scheme 4.4 Claisen-Schmidt condensation of cyclopenta[*b*]indol-3-one with substituted aromatic aldehydes.



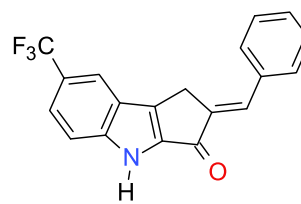
UNIVERSITY of the
WESTERN CAPE



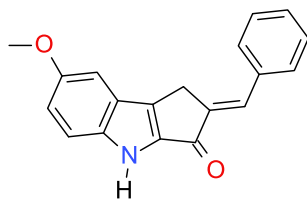
4.31a



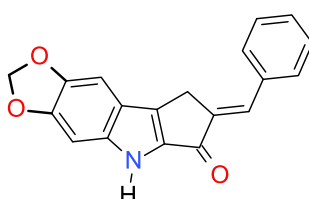
4.31b



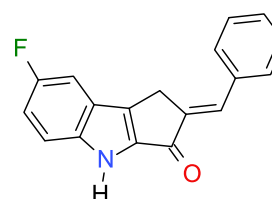
4.31c



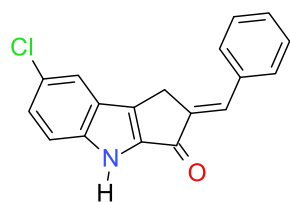
4.31d



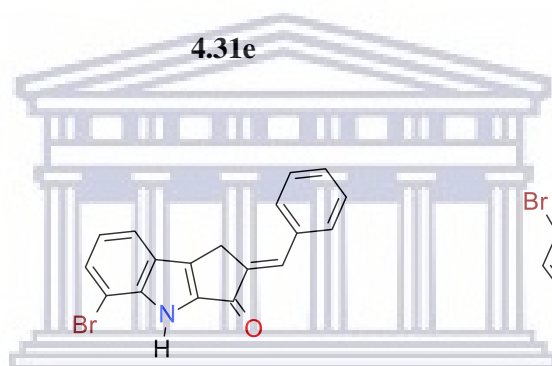
4.31e



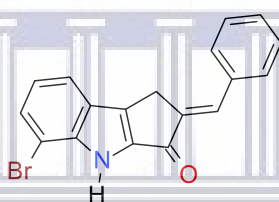
4.31f



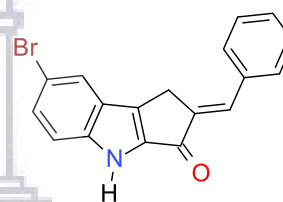
4.31g



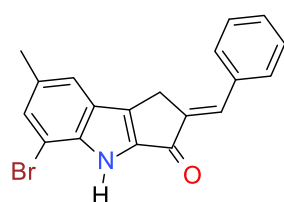
UNIVERSITY of the
WESTERN CAPE



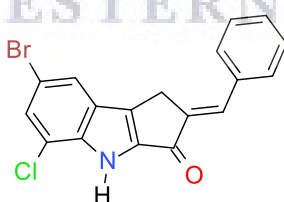
4.31h



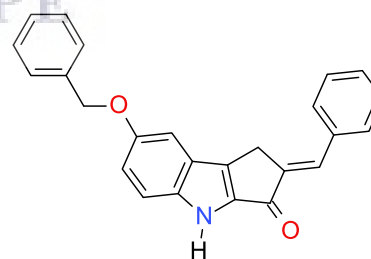
4.31i



4.31j

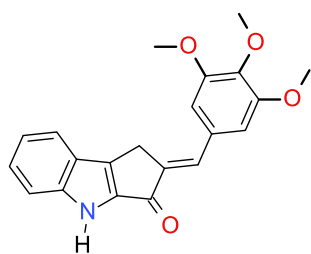


4.31k

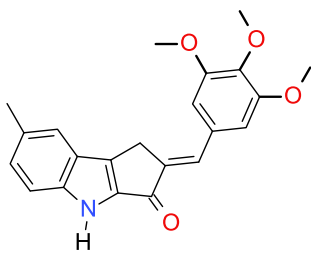


4.31l

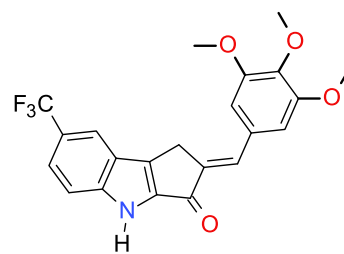
Figure 4.6 Summary of compounds synthesized (phenyl substituted **4.31** series).



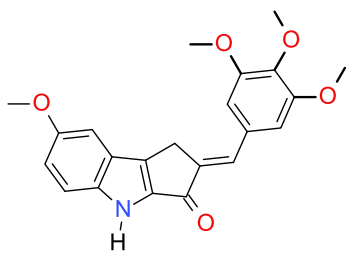
4.32a



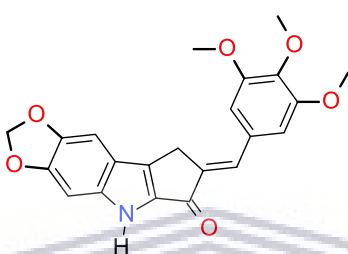
4.32b



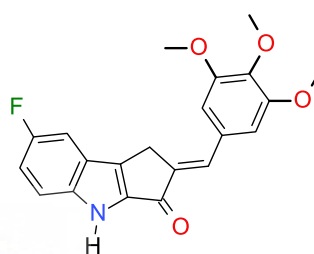
4.32c



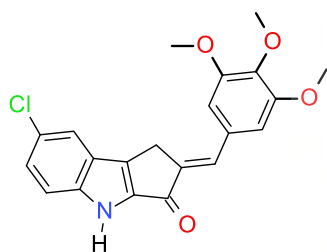
4.32d



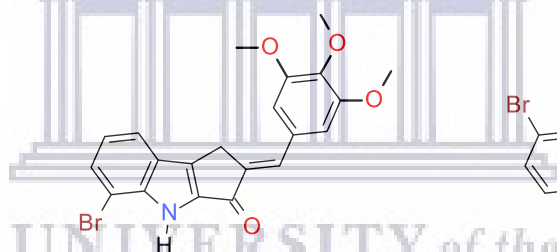
4.32e



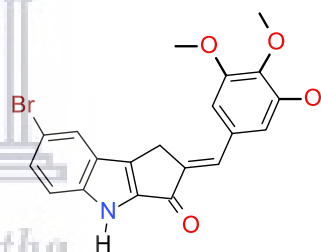
4.32f



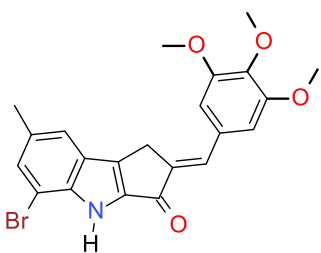
4.32g



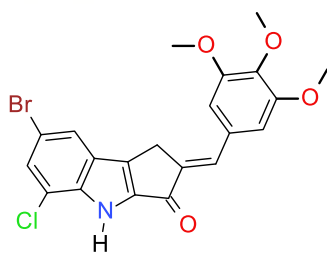
4.32h



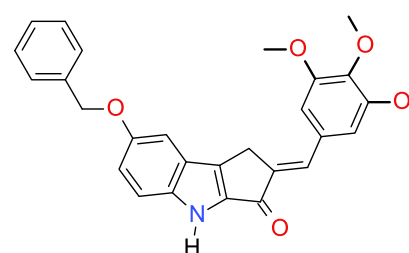
4.32i



4.32j

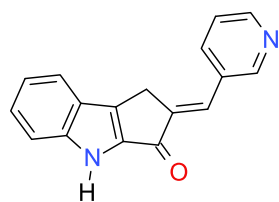


4.32k

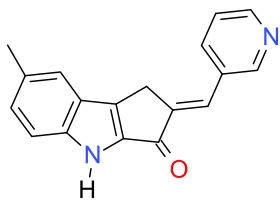


4.32l

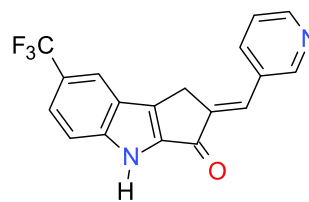
Figure 4.7 Summary of compounds synthesized (3,4,5-trimethoxyphenyl substituted 4.32 series).



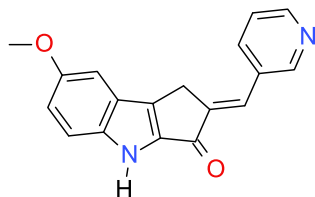
4.33a



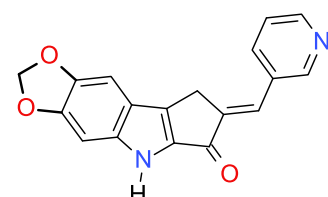
4.33b



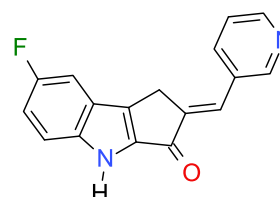
4.33c



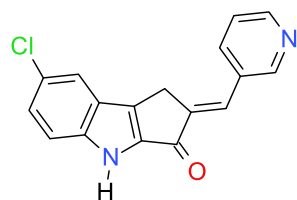
4.33d



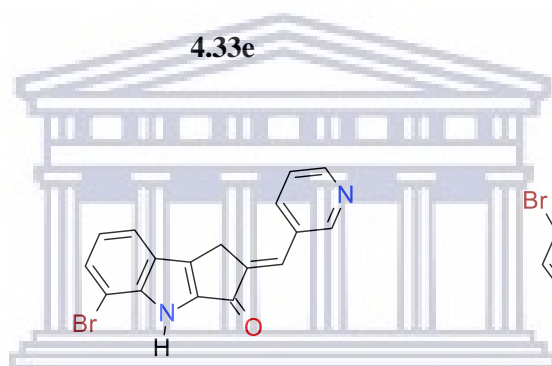
4.33e



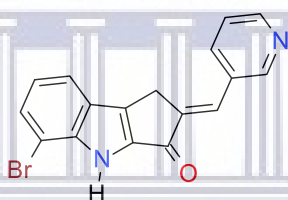
4.33f



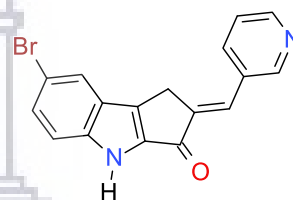
4.33g



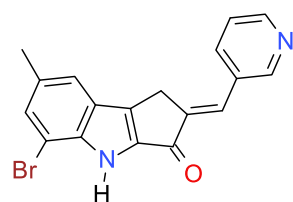
UNIVERSITY of the
WESTERN CAPE



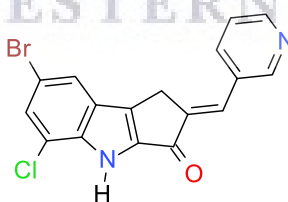
4.33h



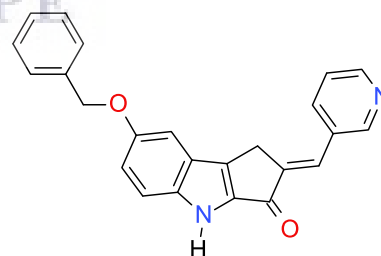
4.33i



4.33j



4.33k



4.33l

Figure 4.8 Summary of compounds synthesized (pyridyl substituted **4.33** series).

4.2.1 Physical properties of arylidene cyclopenta[*b*]indol-3-ones

All the compounds appeared as amorphous powder of different colours. The 3-pyridinecarboxaldehyde substituted series **4.33(a-l)** appeared to have the highest melting points while the 3,4,5-trimethoxybenzaldehyde substituted group showed the lowest melting points (Table 4.1).

Table 4.1 Physical properties of arylidene cyclopenta[*b*]indol-3-one derivatives.

Compounds	R	Appearance	Melting point (°C)	Yield (%)
4.31a	H	Light yellow powder	284-286	83
4.31b	7- CH ₃	Brown powder	287-290	90
4.31c	7- CF ₃	Black powder	290-295	81
4.31d	7- OCH ₃	Dark green powder	249-253	75
4.31e	6,7-OCH ₂ O-	Dark green powder	285-289	67
4.31f	7-F	Greenish-yellow powder	282-286	97
4.31g	7-Cl	Dark grey powder	288-292	99
4.31h	5-Br	Dark brown powder	247-249	89
4.31i	7-Br	Brownish green powder	282-286	86
4.31j	5-Br,7-CH ₃	Dark grey powder	275-278	93
4.31k	7-Br,5-Cl	Brown powder	207-211	93
4.31l	7-OCH ₂ C ₆ H ₅	Brown powder	218-225	89
4.32a	H	Light yellow powder	256-258	71
4.32b	7- CH ₃	Brown powder	253-255	95
4.32c	7- CF ₃	Black powder	272-276	98
4.32d	7- OCH ₃	Yellowish green powder	249-252	66
4.32e	6,7-OCH ₂ O-	Dark green powder	269-271	50
4.32f	7-F	Greenish-yellow powder	265-267	99
4.32g	7-Cl	Brownish green powder	274-277	87

4.32h	5-Br	Greenish brown powder	241-243	89
4.32i	7-Br	Brownish green powder	278-282	85
4.32j	5-Br,7-CH ₃	Brownish green powder	259-263	97
4.32k	7-Br,5-Cl	Green powder	188-193	85
4.32l	7-OCH ₂ C ₆ H ₅	Greenish-yellow powder	238-242	71
4.33a	H	Yellow powder	282-286	85
4.33b	7- CH ₃	Light yellow powder	262-265	80
4.33c	7- CF ₃	Black powder	>310	94
4.33d	7- OCH ₃	Dark grey powder	255-258	50
4.33e	6,7-OCH ₂ O-	Dark green powder	>310	47
4.33f	7-F	Greenish-yellow powder	305-308	76
4.33g	7-Cl	Dark grey powder	307-310	90
4.33h	5-Br	Dark brown powder	>310	87
4.33i	7-Br	Black powder	300-305	78
4.33j	5-Br,7-CH ₃	Brownish grey powder	305-308	84
4.33k	7-Br,5-Cl	Dark yellow powder	>310	82
4.33l	7-OCH ₂ C ₆ H ₅	Dark green powder	255-259	64

4.2.2 Spectroscopic analysis of synthesized compounds 4.31d, 4.32d, and 4.33d

The structures of all synthesized compounds were confirmed by NMR and mass spectrometric analysis. This section presents a concise description of the spectroscopic features of compounds **4.31d**, **4.32d**, and **4.33d** as the representative examples for the series. Compound **4.31d** was obtained as a dark green amorphous powder. Its high resolution electrospray ionization mass spectrum (HR-ESIMS) displayed a protonated molecular ion peak at m/z 290.1203 corresponding to a molecular formula of C₁₉H₁₆NO₂. Its ¹H NMR spectrum (Figure 4.9) showed the expected signals, i.e.: an NH signal at δ_H 11.77, followed by the aromatic protons 7.77 (d, 2H, $J = 7.5$ Hz), 7.50 (t, 2H, $J = 7.6$ Hz), 7.44 (m, 1H), 7.37 (m, 2H), 7.26 (d, 1H, $J = 2.3$ Hz), 7.03 (dd, 1H, $J = 9.0, 2.5$ Hz) and then the methylene and methoxy protons 4.03 (s, 2H) and 3.80 (s, 3H) respectively were observed as singlets.

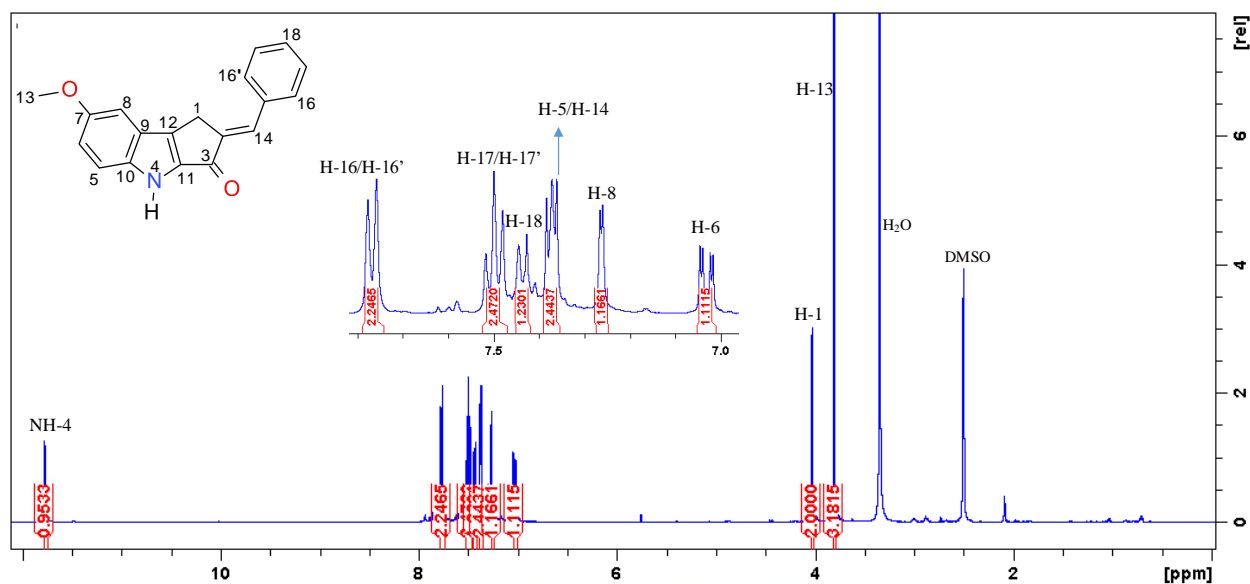


Figure 4.9 ^1H NMR spectrum of compound **4.31d** (400 MHz, DMSO-d_6).

Although the ^{13}C NMR spectrum (Figure 4.10) spectrum revealed seventeen resonances, the molecular formula accounted for the expected nineteen carbon resonances. This is an indication of the same chemical environment for C-16/C-16' and C-17/C-17', similarly these resonances also exhibited higher peak intensity. The unsaturated ketone was confirmed at δ_{C} 182.1 in the ^{13}C NMR spectrum and infrared band at 1664 cm^{-1} .

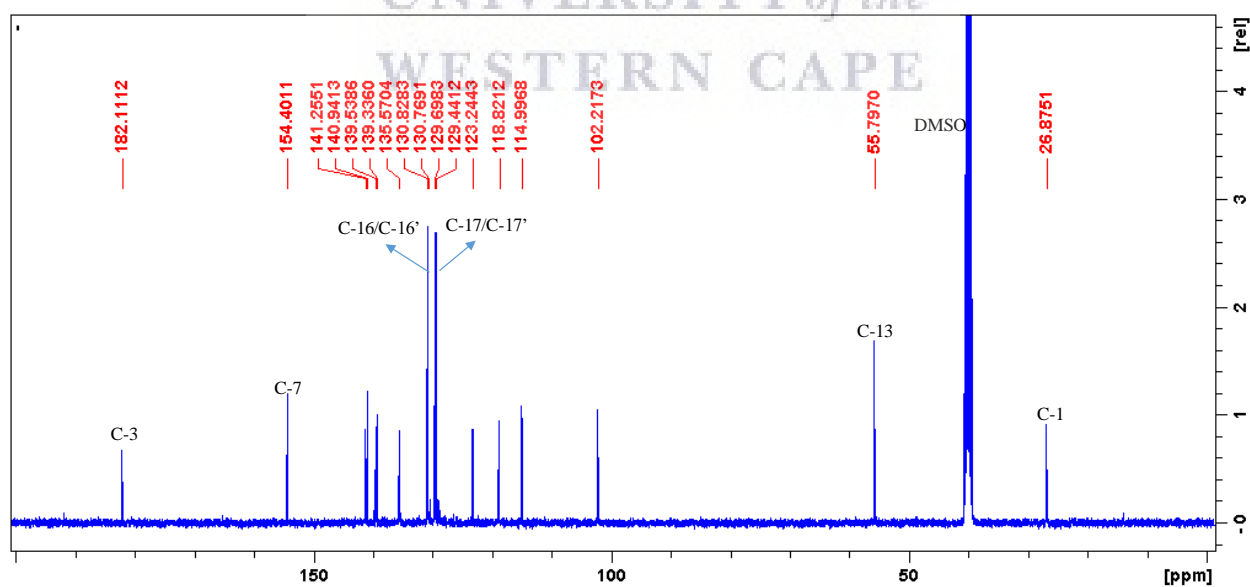


Figure 4.10 ^{13}C NMR spectrum of compound **4.31d** (100 MHz, DMSO-d_6).

The DEPT 135 spectrum (Figure 4.11) confirmed the aromatic sp^2 methines and sp^3 methyl (C-13) resonance as positive while the sp^3 methylene (C-1) was negative.

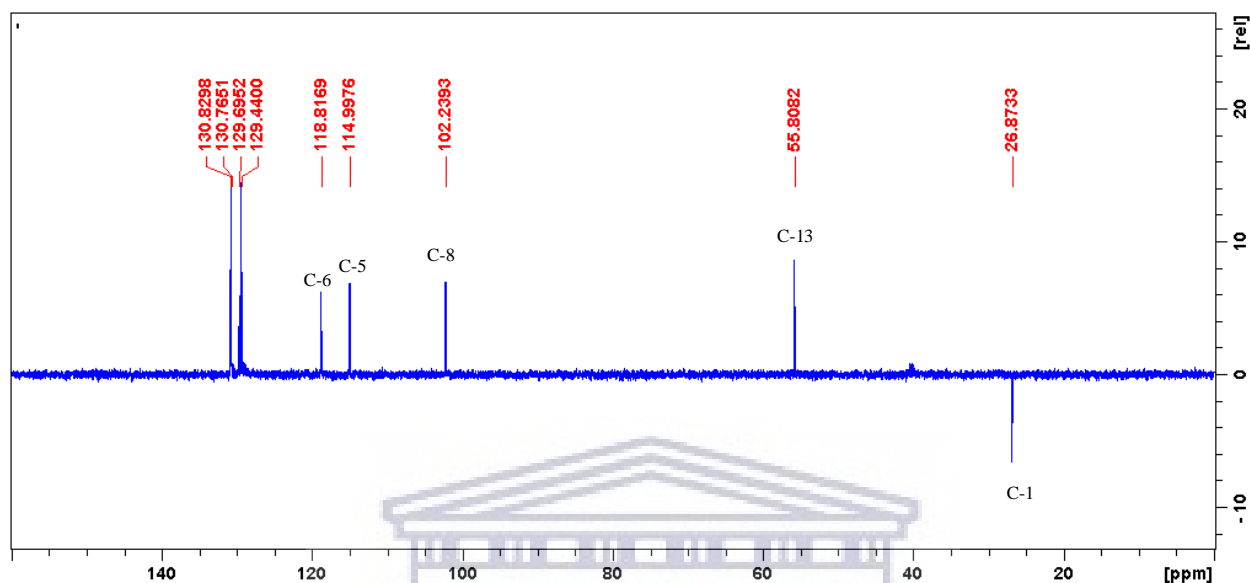


Figure 4.11 DEPT-135 NMR spectrum of compound **4.31d**.

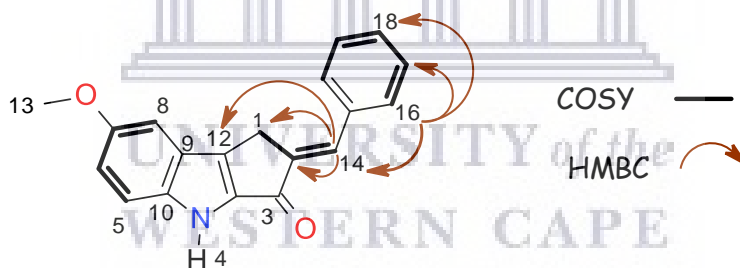


Figure 4.12 COSY and HMBC correlations for compound **4.31d**.

The COSY data showed correlations (Figure 4.12) from the proton resonance at δ_H 7.03 (H-6) to 7.37 (H-5) and 7.26 (H-8); δ_H 4.03 (H₂-1) to 7.37 (H-14), and from δ_H 7.77 (H-16) to 7.50 (H-17) and 7.44 (H-18). In addition, HMBC spectrum revealed correlations (Figure 4.12) from the proton resonance at δ_H 7.37 (H-14) to δ_C 26.9 (C-1), 141.3 (C-2) and 140.9 (C-12), while from the proton signal at δ_H 7.77 (H-16) is coupled to δ_C 130.8 (C-14), 129.4 (C-17) and 129.7 (C-18) (Table 4.2).

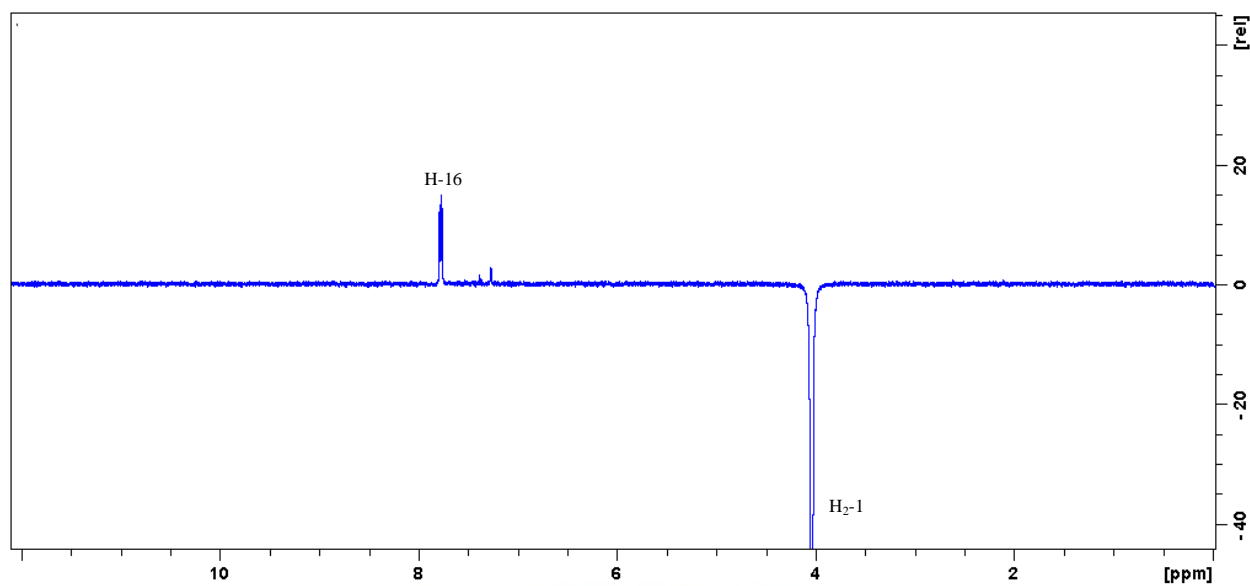


Figure 4.13 1D selective NOESY NMR spectrum of compound **4.31d**.

The 1D selective NOESY NMR spectrum (Figure 4.13) showed an NOE correlation between δ_{H} 4.03 (H₂-1) and 7.77 (H-16) and no correlation to H-14, thus confirming the geometry of the double bond to be *E*.

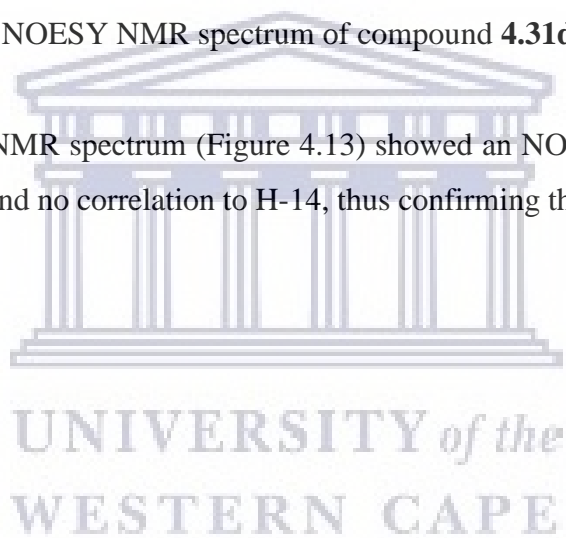


Table 4.2 NMR data for compound **4.31d** (400 MHz for ^1H and 100 MHz for ^{13}C , DMSO- d_6).

Position	δ_{C}	δ_{H} (mult., J , Hz)	COSY	HMBC
1	26.9	4.03 (s, 2H)	H-14	C-2, C-3, C-9, C-14, C-16
2	141.3			
3	182.1			
NH-4	-	11.77 (s)		C-10, C-11, C-12
5	115.0	7.37 (m, 2H)	H-6	C-8, C-10, C-7
6	118.8	7.03 (dd, $J = 9.0, 2.5, 1\text{H}$)	H-5, H-8	C-7, C-8, C-9
7	154.4			
8	102.2	7.26 (d, $J = 2.3, 1\text{H}$)	H-6	C-6, C-7, C-9
9	139.5			
10	123.2			
11	139.3			
12	140.9			
13	55.8	3.80 (s, 3H)		C-7
14	130.8	7.37 (m, 2H)	H-1	C-1, C-3, C-12
15	135.6			
16	130.8	7.77 (d, $J = 7.5, 2\text{H}$)	H-17, H-18	C-18, C-17, C-14
17	129.4	7.50 (t, $J = 7.6, 2\text{H}$)	H-16	C-18, C-16, C-14
18	129.7	7.44 (m, 1H)	H-16	C-16

Compound **4.32d** was obtained as a greenish yellow amorphous powder. Its protonated molecular ion peak obtained from HR-ESIMS was found at m/z 380.1532 corresponding to a molecular formula $\text{C}_{22}\text{H}_{22}\text{NO}_5$. The ^1H NMR spectrum (Figure 4.14) exhibited the expected signals including, i.e.: an NH signal δ_{H} 11.75, succeeded by the aromatic protons δ_{H} 7.37 (d, 1H, $J = 9.0$ Hz), 7.34 (s, 1H), 7.26 (d, 1H, $J = 2.4$ Hz), 7.07 (s, 2H), 7.02 (dd, 1H, $J = 9.0, 2.5$ Hz), the

methylene protons 4.05 (s, 2H) and then the methoxy protons 3.90 (s, 6H), 3.81 (s, 3H) and 3.73 (s, 3H).

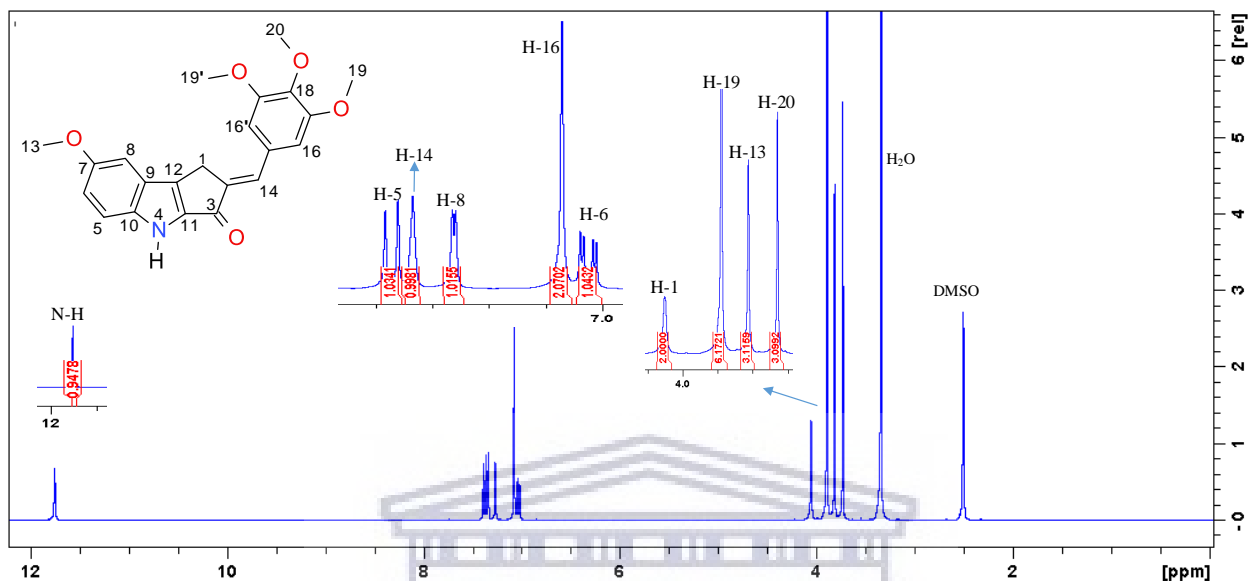


Figure 4.14 ^1H NMR spectrum of compound **4.32d** (400 MHz, DMSO-d_6).

The unsaturated ketone resonance was observed at δ_{C} 182.2 and its corresponding infrared stretch was observed at 1652 cm^{-1} . The ^{13}C NMR spectrum exhibited nineteen resonances and the same chemical environment was observed for C-16/C-16', C17/C-17' and C-19/C-19' (Figure 4.15).

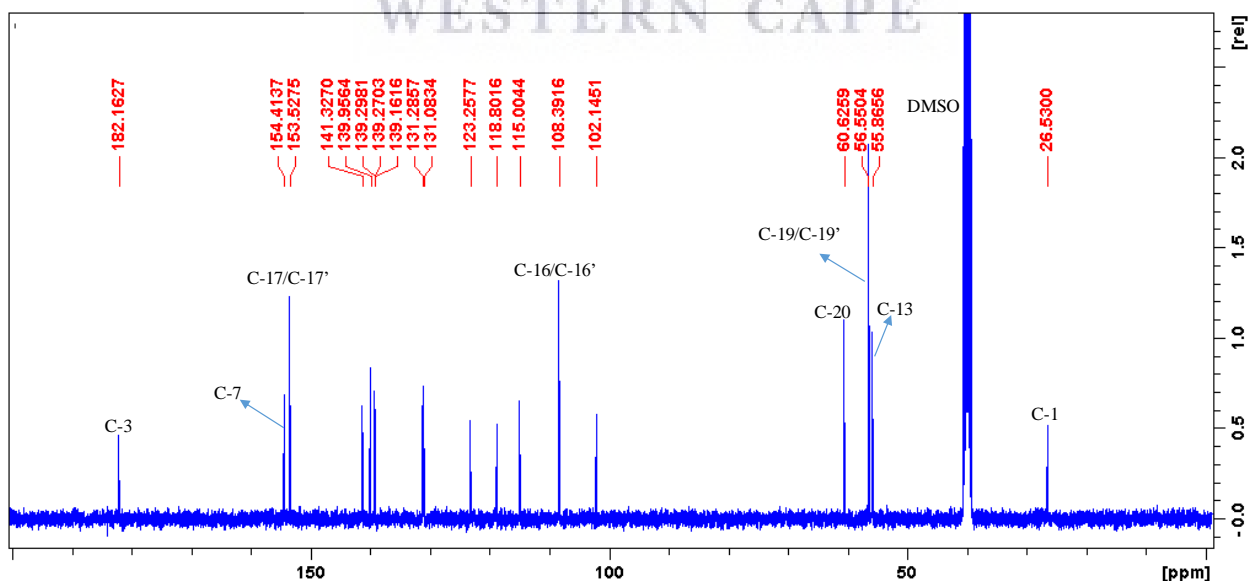


Figure 4.15 ^{13}C NMR spectrum of compound **4.32d** (100 MHz, DMSO-d_6).

As expected the NMR DEPT 135 spectrum confirmed signal δ_C 26.5 (C-1) as negative, while the rest of the proton signals positive (Figure 4.16).

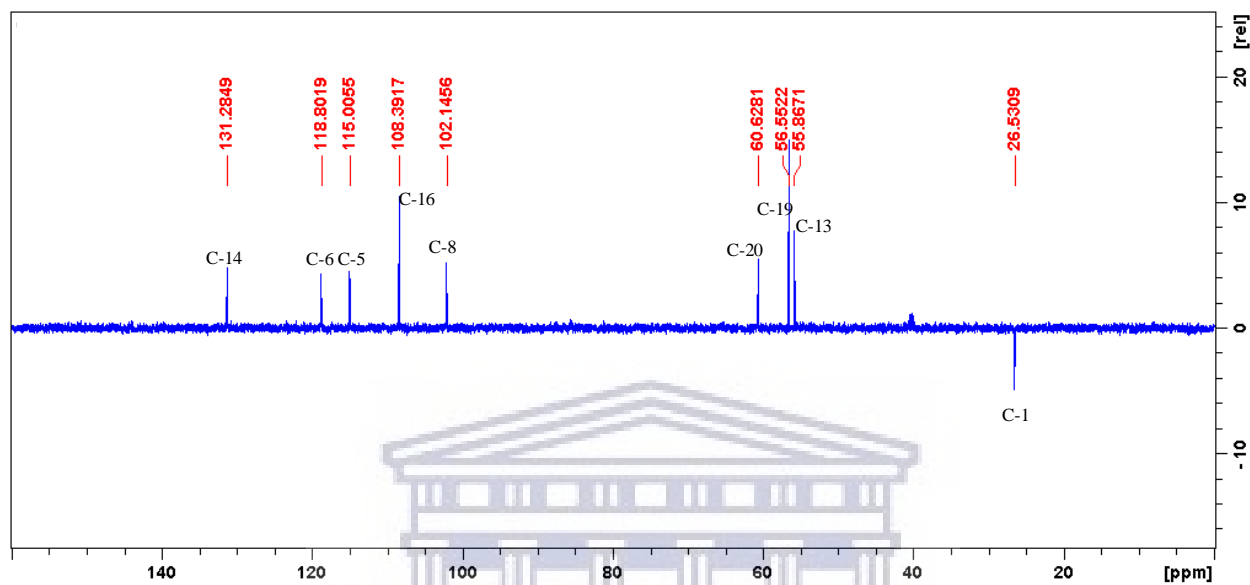


Figure 4.16 DEPT-135 NMR spectrum of compound 4.32d.

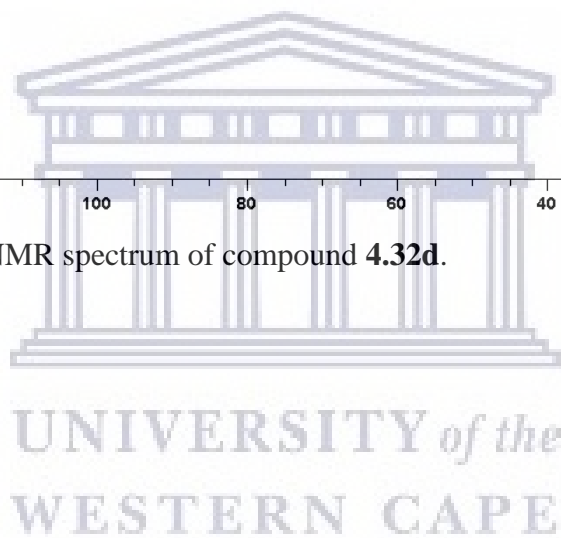
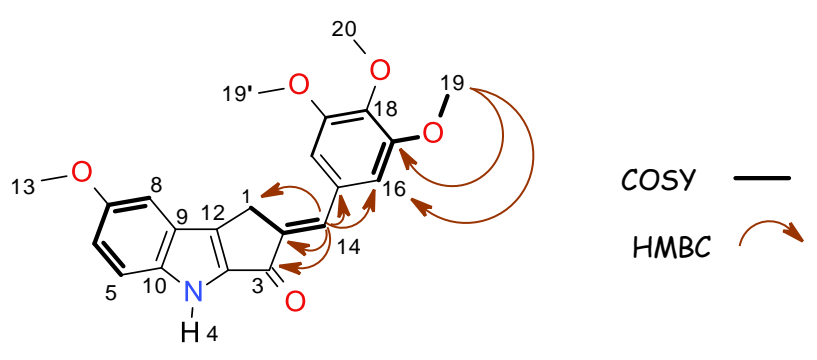


Table 4.3 NMR data for compound **4.32d** (400 MHz for ^1H and 100 MHz for ^{13}C , DMSO- d_6).



Position	δ_{C}	δ_{H} (mult., J , Hz)	COSY	HMBC
1	26.5	4.05 (s, 2H)	H-14	C-2, C-3, C-12, C-14
2	140.0			
3	182.2			
NH-4		11.75 (s)		C-10, C-11, C-12
5	115.0	7.37 (d, $J = 9.0$, 1H)	H-6	C-7, C-10
6	118.8	7.02 (dd, $J = 9.0, 2.5$, 1H)	H-5, H-8	C-7, C-8, C-9
7	154.4			
8	102.1	7.26 (d, $J = 2.4$, 1H)	H-6	C-6, C-7, C-9
9	139.3			
10	123.3			
11	139.3			
12	141.3			
13	55.9	3.81 (s, 3H)		C-7
14	131.3	7.34 (s, 1H)	H-1	C-1, C-2, C-3, C-15, C-16
15	131.1			
16	108.4	7.07 (s, 2H)	H-19	C-15, C-17, C-18
17	153.5			
18	139.2			
19	56.6	3.90 (s, 6H)	H-16	C-16, C-17
20	60.6	3.73 (s, 3H)		C-18

Compound **4.33d** was obtained as a dark grey amorphous powder. Its HR-ESIMS displayed a protonated molecular ion peak at m/z 291.1107 corresponding to a molecular formula $\text{C}_{18}\text{H}_{15}\text{N}_2\text{O}_2$.

Its ^1H NMR spectrum displayed the following signals (Figure 4.17); NH signal δ_{H} 11.80, followed by the aromatic protons 8.93 (d, 1H, $J = 1.6$ Hz), 8.59 (dd, 1H, $J = 4.8, 1.1$ Hz), 8.17 (dt, 1H, $J = 8.0, 1.7$ Hz), 7.52 (dd, 1H, $J = 8.1, 4.8$ Hz), 7.38 (m, 2H), 7.24 (d, 1H, $J = 2.3$ Hz), 7.04 (dd, 1H, $J = 9.0, 2.5$ Hz) and then methylene and methoxy protons were observed as singlets at 4.05 (s, 2H) and 3.80 (s, 3H) respectively.

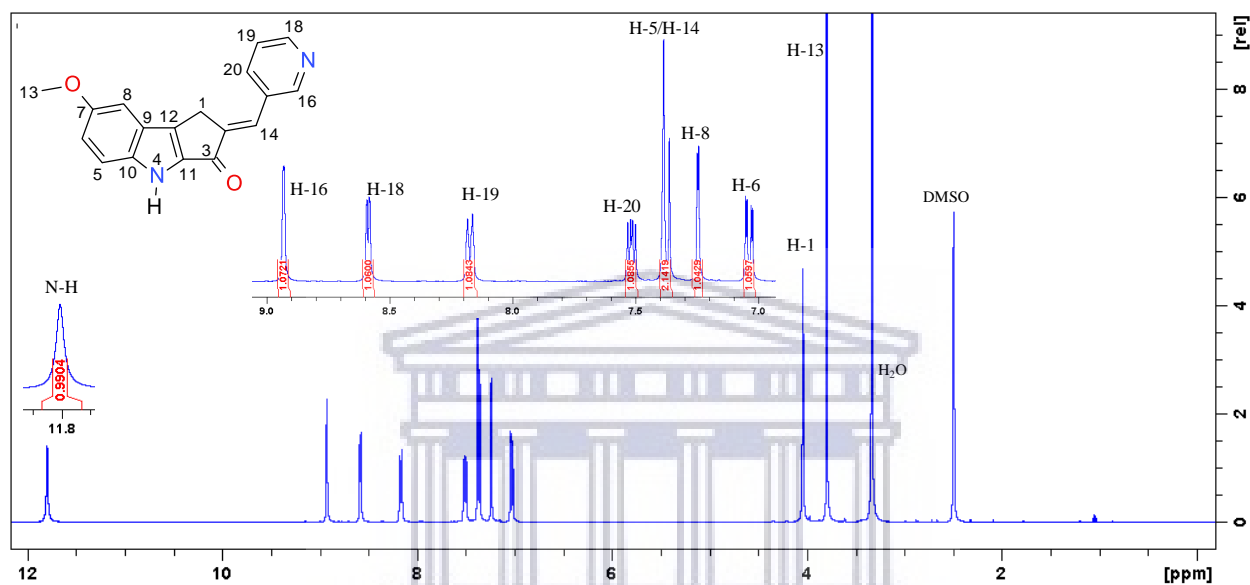


Figure 4.17 ^1H NMR spectrum of compound **4.33d** (400 MHz, DMSO-d_6).

The ^{13}C NMR spectrum (Figure 4.18) also confirmed the characteristic unsaturated ketone resonance carbon signal at δ_{C} 181.6 and infra-red absorption band at 1685 cm^{-1} .

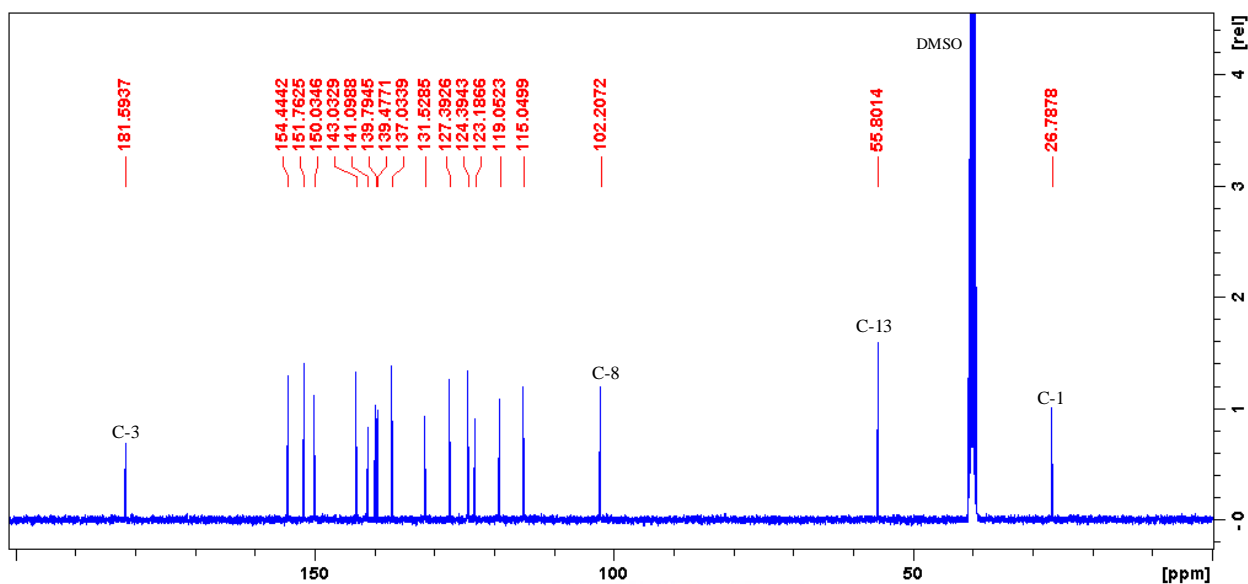


Figure 4.18 ^{13}C NMR spectrum of compound **4.33d** (100 MHz, DMSO-d_6).

The DEPT NMR spectrum (Figure 4.19) showed a carbon resonance at δ_{C} 26.8 (C-1) as the only negative signal (CH_2) and the rest were positive signals as expected.

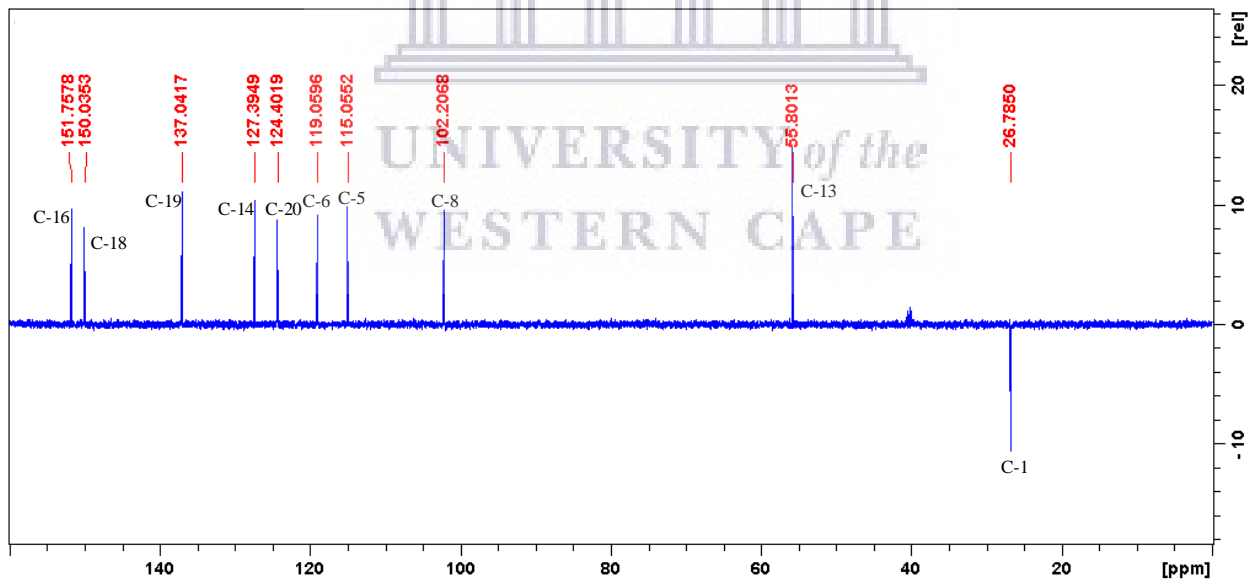


Figure 4.19 DEPT-135 NMR spectrum of compound **4.33d**.

The 2D NMR data presented in Table 4.4 supported the structure assignment of compound **4.33d**. Similar to **4.31d** and **4.32d**, the 1D selective NOESY spectrum of **4.33d** (Figure 4.20) also affirmed the geometry of the double bond as *E*.

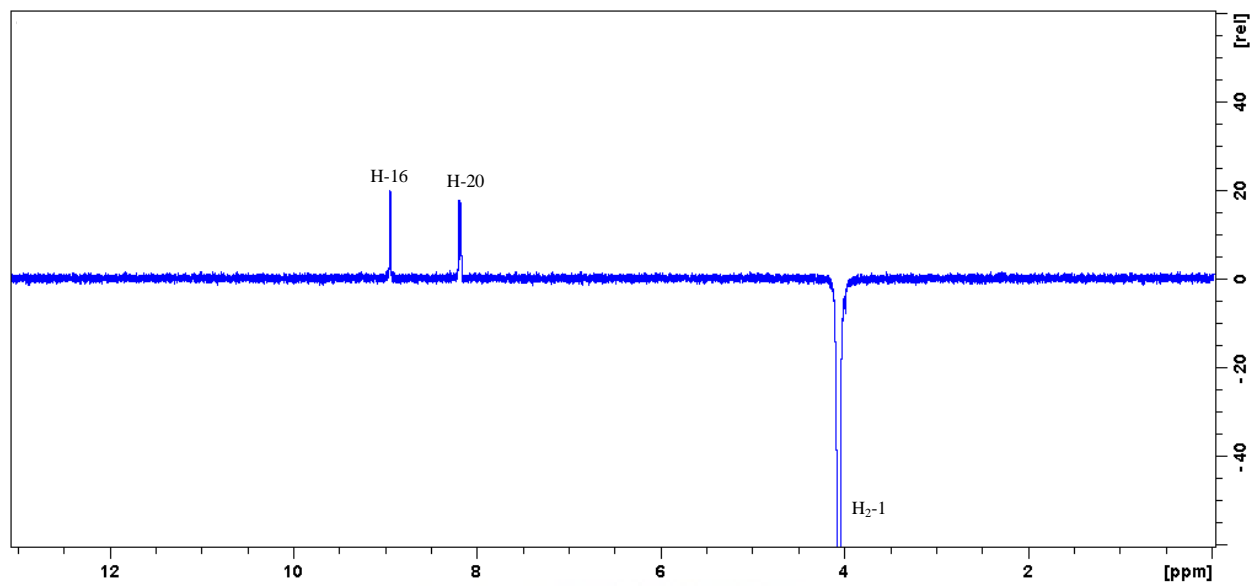


Figure 4.20 1D selective NOESY NMR spectrum of compound 4.33d

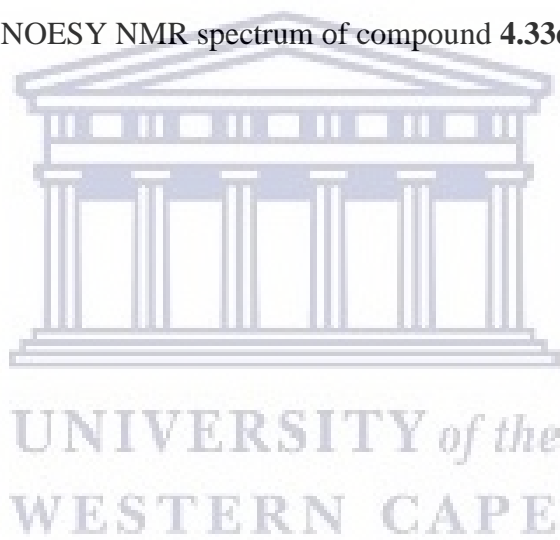
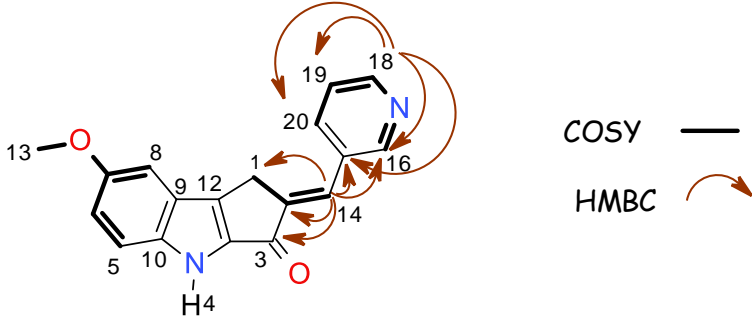


Table 4.4 NMR data for compound **4.33d** (400 MHz for ^1H and 100 MHz for ^{13}C , DMSO- d_6).



Position	δ_{C}	δ_{H} (mult., J , Hz)	COSY	HMBC
1	26.8	4.05 (s, 2H)	H-14	C-2, C-3, C-9, C-11, C-14
2	143.0			
3	181.6			
NH-4		11.80 (s)		
5	115.0	7.38 (m, 2H)	H-6	C-7, C-8, C-9, C-10
6	119.1	7.04 (dd, $J = 9.0, 2.5$, 1H)	H-5, H-8	C-7, C-8, C-9, C-10
7	154.4			
8	102.2	7.24 (d, $J = 2.3$, 1H)	H-6, H-13	C-5, C-6, C-7, C-9
9	139.5			
10	123.2			
11	139.8			
12	141.1			
13	55.8	3.80 (s, 3H)	H-8	C-7
14	127.4	7.38 (m, 2H)	H-1	C-1, C-2, C-3, C-11, C-15, C-16,
15	131.5			
16	151.8	8.93 (d, $J = 1.6$, 1H)	H-19, H-20	C-14, C-15, C-18, C-19, C-20
18	150.0	8.59 (dd, $J = 4.8, 1.1$, 1H)	H-19, H-20	C-15, C-16, C-19, C-20
19	137.0	8.17 (dt, $J = 8.0, 1.7$, 1H)	H-16, H-18, H-20	C-14, C-16, C-18
20	124.4	7.52 (dd, $J = 8.1, 4.8$, 1H)	H-16, H-18, H-19	C-15, C-16, C-18, C-19

Predominantly, the representative NMR features earlier discussed were consistent with each of the corresponding series **4.31a-l**, **4.32a-l** and **4.33a-l**. In the same way, the N-H signal was generally observed as broad singlet or singlet and resonated within the range of δ_{H} 12.53 - 11.75. However,

N-H signals were not observed for compounds **4.31g** (R = 7-Cl), **4.33c** (R = 7-CF₃) and **4.33g** (R = 7-Cl) but the pyridinium chloride salt of **4.33g** showed all the expected resonances. The CH₂-1 methylene protons were all observed as singlets and resonated within the range of δ_{H} 4.13 – 3.94. In addition, the ¹H-NMR data of phenyl substituted series **4.31a-l** and pyridyl substituted series **4.33a-l** series displayed overlapping resonances for H-5 doublet and H-14 singlet (Figure 4.21), this is due to the high number of aromatic protons for the series of compounds. On the other hand, clearly defined resonances were observed for the **4.32a-l** series due to fewer aromatic protons.

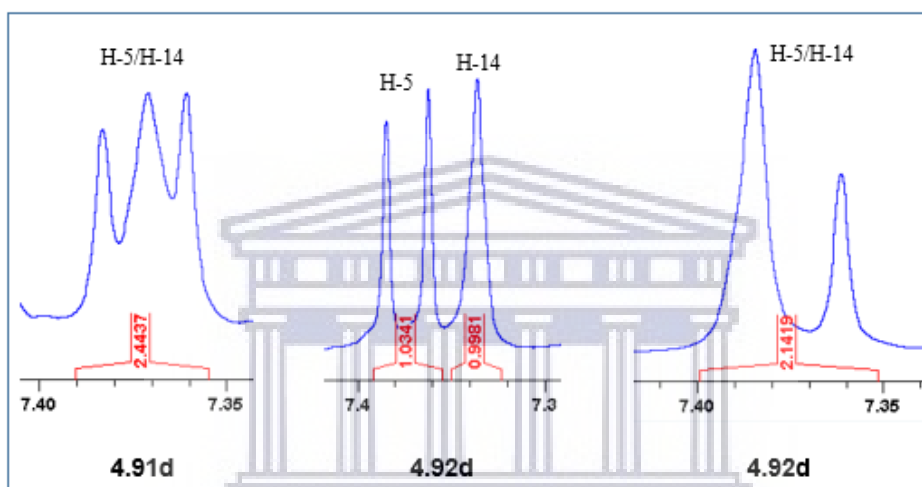


Figure 4.21 A section of ¹H NMR spectra of **4.31d**, **4.32d** and **4.33d** showing H-5 and H-14.

The ¹³C NMR spectra of the aryldene cyclopenta[*b*]indol-3-one derivatives displayed the same trends: the ketone (C-3) signals resonated within a range of δ_{C} 182.7 – 180.0 whereas the ketone (C-3) of the cyclopenta[*b*]indoles (chapter 3) resonated within the range of δ_{C} 194.3 – 192.3, the resonance shift is due to the α , β -unsaturation of the aryldene cyclopenta[*b*]indol-3-one series. Tables of NMR data of the selected compounds for discussion showed COSY and HMBC data confirming the proper assignment of resonances.

Compounds **4.33(f-k)** from the pyridyl substituted series were sparingly soluble in DMSO-d₆, therefore the NMR data were recorded for their hydrochloride salts.

4.2.3 Biological evaluation

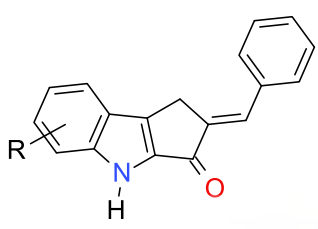
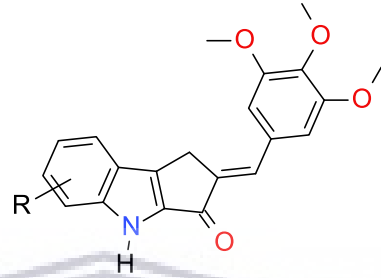
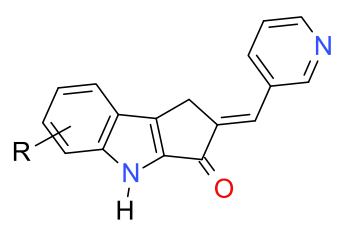
4.2.3.1 *In vitro* antiproliferative studies

To begin with, an initial single point concentration (25 μM) screening of the synthesized compounds was conducted to evaluate the antiproliferative profile against HCC70 cancer cells (Table 4.5). The most active compounds were selected for further antiproliferative evaluation and ten compounds selected exhibited cell viability of less than 33% at a concentration of 25 μM .

The ten selected compounds (**4.31k**, **4.32c**, **4.32i**, **4.32j**, **4.32k**, **4.33a**, **4.33b**, **4.33c**, **4.33d** and **4.33k**) were tested against HeLa, MDA-MB231, HCC70 cancer cell lines, and MCF-12A “normal” cells. The IC_{50} values obtained are summarized in Table 4.6. Surprisingly, most compounds showed only moderate activity, suggesting that single point assay (Table 4.5) is not the best way to identify compounds for further study (Turner & Charlton, 2005; Murray & Wigglesworth, 2016). Furthermore, the single point concentration cell viability screening results did not show clear correlations with the IC_{50} values obtained. It was assumed that stability of the compounds or changes in testing conditions could be responsible for this discrepancy since the assays were not conducted on the same day.

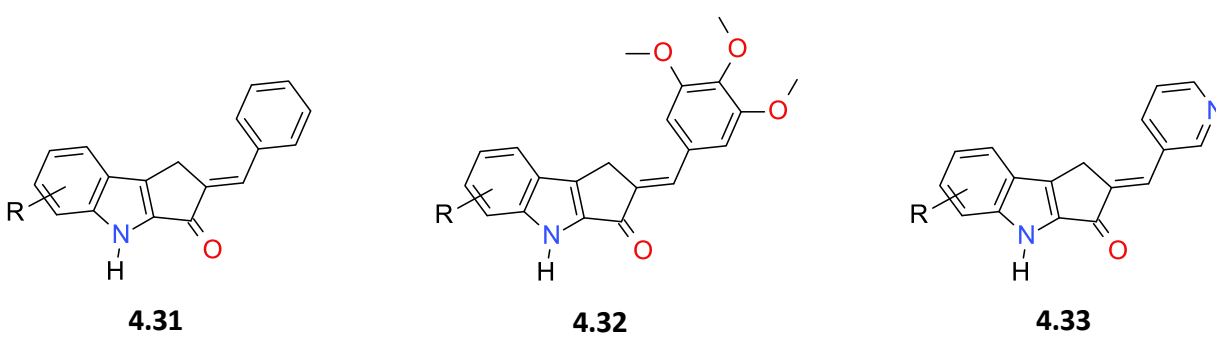
Compound **4.32k** (R = 7-Br,5-Cl) showed moderate activity against the three cancer cell lines, however, it lacked selectivity as it was also toxic to normal cells (MCF-12A). On the other hand, compounds **4.32i** (R = 7-Br), **4.33b** (R = 7-CH₃) and **4.33d** (R = 7-OCH₃) displayed weak but selective antiproliferative properties (Table 4.6). Compound **4.33a** (R = H) exhibited the best antiproliferative activity with an IC_{50} value of 10.2 μM against HCC70 cells and it was completely non-toxic to MCF-12A normal cells which is an indication of a very good selectivity for HCC70 cancer cells (Figure 4.22; Table 4.6). Tunbridge and co-workers suggested that the indole analogues may be sensitive to specific cancer cells and compounds showing more structural resemblance to indanocine were more active (Tunbridge et al., 2013). Some of the synthesized compounds were sparingly soluble in DMSO, thus the biological data acquired may not be a fair indication of their biological activity.

Table 4.5 Percentage cell viability relative to DMSO at 25 μM of synthesized compounds against HCC70 cancer cells.

R	 4.31		 4.32		 4.33	
	Compounds	% Viability at 25 (μM) ^a	Compounds	% Viability at 25 (μM) ^a	Compounds	% Viability at 25 (μM) ^a
H	4.31a	39.3 \pm 2.52	4.32a	46.6 \pm 1.61	4.33a	23.9 \pm 0.36
7- CH ₃	4.31b	75.0 \pm 1.87	4.32b	26.7 \pm 0.65	4.33b	22.2 \pm 0.46
7- CF ₃	4.31c	45.3 \pm 1.11	4.32c	32.8 \pm 0.25	4.33c	22.7 \pm 1.16
7- OCH ₃	4.31d	25.7 \pm 3.28	4.32d	32.1 \pm 1.20	4.33d	22.9 \pm 2.71
6,7-OCH ₂ O-	4.31e	38.2 \pm 0.63	4.32e	68.1 \pm 3.91	4.33e	44.2 \pm 1.62
7-F	4.31f	97.3 \pm 2.58	4.32f	64.2 \pm 5.47	4.33f	34.7 \pm 1.70
7-Cl	4.31g	74.8 \pm 0.39	4.32g	37.6 \pm 2.08	4.33g	32.5 \pm 0.49
5-Br	4.31h	33.3 \pm 0.58	4.32h	36.4 \pm 1.72	4.33h	30.2 \pm 1.37
7-Br	4.31i	37.4 \pm 1.13	4.32i	20.6 \pm 0.79	4.33i	54.1 \pm 2.45
5-Br,7-CH ₃	4.31j	91.4 \pm 3.68	4.32j	21.6 \pm 0.46	4.33j	86.8 \pm 0.96
7-Br,5-Cl	4.31k	18.7 \pm 0.22	4.32k	8.8 \pm 0.51	4.33k	28.64 \pm 0.25
7-OCH ₂ C ₆ H ₅	4.31l	71.1 \pm 1.08	4.32l	102.5 \pm 1.49	4.33l	56.8 \pm 1.01

^a Cell viability relative to DMSO (%) \pm standard error against HCC70 cells. The compounds with the best activities were highlighted.

Table 4.6 Antiproliferative activities of the selected compounds against three cancer cell lines and normal human cell line.

						
Compounds	R	HCC70 ^a	IC ₅₀ (μM) ^b			
			HeLa	MDA-MB-231	HCC70	MCF-12A
4.31k	7-Br,5-Cl	18.7 ± 0.22	NT	59.7 ± 1.37	NT	65.6 ± 1.27
4.32c	7- CF ₃	32.8 ± 0.25	56.6 ± 1.09	63.1 ± 1.44	72.7 ± 6.82	42.1 ± 1.05
4.32i	7-Br	20.6 ± 0.79	64.4 ± 1.15	NT	NT	NT
4.32j	5-Br,7-CH ₃	21.6 ± 0.46	60.9 ± 1.30	NT	NT	63.5 ± 1.90
4.32k	7-Br,5-Cl	8.8 ± 0.51	47.9 ± 1.03	47.0 ± 1.02	49.3 ± 1.06	12.9 ± 1.03
4.33a	H	23.9 ± 0.36	NT	NT	10.2 ± 1.22	NT
4.33b	7- CH ₃	22.2 ± 0.46	62.0 ± 1.11	NT	NT	NT
4.33c	7- CF ₃	22.7 ± 1.16	63.7 ± 1.14	55.3 ± 1.05	74.1 ± 6.86	72.7 ± 3.98
4.33d	7- OCH ₃	22.9 ± 2.71	NT	NT	71.4 ± 2.50	NT
4.33k	7-Br,5-Cl	28.6 ± 0.25	NT	NT	NT	NT
Paclitaxel (nM)			72.2 ± 1.11	2.2 ± 1.06	3.4 ± 1.01	6.0 ± 1.16

^a Percentage cell viability at 25 μM (from Table 4.5).

^b IC₅₀ values were indicated as mean ± standard error. Each data represents three different experiments performed in triplicate and IC₅₀ values greater than 250 μM were recorded as non-toxic (NT).

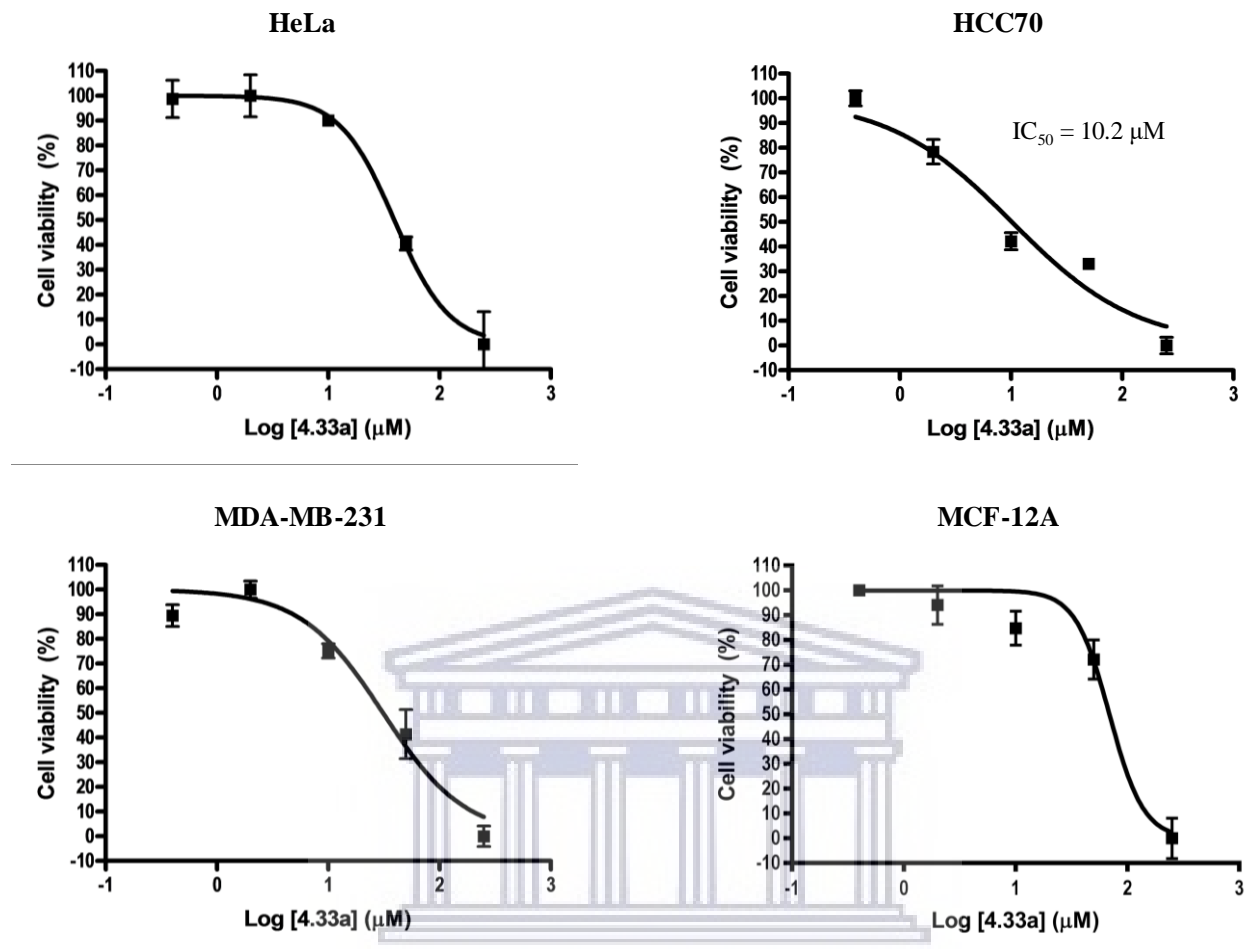


Figure 4.22 Non-linear regression curves for the antiproliferative activity of compound **4.33a** against the cell lines. IC_{50} values greater than 250 μM were recorded as non-toxic.

4.2.3.2 Molecular docking studies

Since indanocine and indolocine derivatives (Tunbridge et al, 2013) were shown to potently interact with microtubules, we used molecular docking studies to further investigate the potential of the cyclopenta[*b*]indol-3-one derivatives synthesized here as antimicrotubule inhibitors. Molecular Operating Environment (MOE) software version 2016.08 was used to evaluate the binding affinity and interactions with the Tubulin-Colchicine domain. The crystal structure of tubulin (PDB ID: 1SA0) (Ravelli et al, 2004) retrieved online from the RCSB Protein Data Bank (<https://www.rcsb.org/structure/1SA0>). The docking results generated were visualized directly on the MOE software and the docking pose with the best interactions were selected for each of the ligands. The docking results are presented in Table 4.7 showing the docking energies, $\pi - H$

interactions with amino acid residue and distance. Colchicine, combretastatin A-4 and indanocine were selected as standards to make binding interaction comparisons with the compounds. The negative docking energies obtained indicate good binding affinity for the active site. On average, the 3,4,5-trimethoxyphenyl (TMP) **4.32** series showed the best binding affinity with an average binding energy of -7.439 Kcal/mol, followed by the pyridyl **4.33** series; -6.521 Kcal/mol and then the unsubstituted phenyl **4.31** series; -6.466 Kcal/mol. The strong affinity exhibited by the TMP **4.32** series aligned with literature findings of good binding affinity and interactions of TMP based tubulin inhibitors with the colchicine binding site (Li et al., 2018). Compound **4.32i** (R = 7-OCH₂C₆H₅) showed the best affinity for the receptor with a binding energy -8.524 Kcal/mol which is more favorable than the standards; indanocine (-7.137 Kcal/mol), combretastatin A4 (-7.586 Kcal/mol) and colchicine (-8.028Kcal/mol). The TMP **4.32** series also showed similar orientation with colchicine and were surrounded by almost identical amino acid residues.

Table 4.7 The binding energies and intermolecular interactions of the compounds.

Compounds	R	Binding energy (Kcal/mol)	Amino acid residue in interaction	Distance (Å)	Bonding type
4.31a	H	-5.972	Ala B316 Lys B254	4.05 4.41	π - H π - H
4.31b	7- CH ₃	-6.160	Ala B316	4.51	π - H
4.31c	7- CF ₃	-6.846	Cys B241 Asn B258	4.14 3.54	π - H π - H
4.31d	7- OCH ₃	-6.316	Lys B254	3.50	π - H
4.31e	6,7-OCH ₂ O-	-6.408	Thr A179	3.12	H-bonding
4.31f	7-F	-6.099	Leu B248 Ala B316	4.53 4.21	π - H π - H
4.33			Cys B242	3.84	π - H

4.31g	7-Cl	-6.466	Lys B254	3.59	π - H
4.31h	5-Br	-6.319	Lys B254	3.74	π - H
4.31i	7-Br	-6.367	Lys B254	3.94	π - H
4.31j	5-Br,7-CH ₃	-6.676	Lys B252	3.83	π - H
4.31k	7-Br,5-Cl	-6.695	Asn B258	3.61	π - H
4.31l	7-OCH ₂ C ₆ H ₅	-7.270	Leu B255	4.51	π - H
			Ala B317	3.25	H-bonding
			Leu B248	3.74	π - H
			Lys B254	4.57	π - H
4.32a	H	-7.431	Ala A180	4.21	π - H
4.32b	7- CH ₃	-6.871	Leu B248	3.59	π - H
4.32c	7- CF ₃	-7.257	Leu B248	3.70	π - H
4.32d	7- OCH ₃	-7.345	Leu B248	4.37	π - H
4.32e	6,7-OCH ₂ O-	-7.805	Lys B254	3.82	π - H
			Leu B248	3.67	π - H
4.32f	7-F	-7.146	Ala B352	4.09	π - H
4.32g	7-Cl	-7.615	Ala B316	4.19	π - H
4.32h	5-Br	-6.711	Leu B248	4.21	π - H
4.32i	7-Br	-7.756	Ala B354	4.44	π - H
			Ala E354	4.44	π - H
4.32j	5-Br,7-CH ₃	-7.719	Leu B248	4.44	π - H
			Leu E248	4.44	π - H
4.32k	7-Br,5-Cl	-7.088	Leu B248	4.61	π - H
4.32l	7-OCH ₂ C ₆ H ₅	-8.524	Lys B352	3.57	π - H
			Ala B250	3.16	H - Bonding
4.33a	H	-6.537	Tyr A224	3.64	π - π
			Tyr B224	3.47	π - π
			Cys A12	4.01	π - H
			Cys B12	4.01	π - H
4.33b	7- CH ₃	-6.289	Tyr A239	4.42	π - H
			Tyr B239	4.42	π - H
			Ala A316	4.41	π - H
4.33c	7- CF ₃	-6.631	Leu B248	3.78	π - H
4.33d	7- OCH ₃	-6.846	Ala A180	4.23	π - H
			Ala D180	4.23	π - H
			Ala B316	3.94	π - H
			Ala E316	3.96	π - H

4.33e	6,7-OCH ₂ O-	-6.311	Ala B316	4.21	π - H
			Leu B255	4.52	π - H
4.33f	7-F	-6.023	Leu B255	3.54	π - H
			Cys B241	3.28	H - bonding
4.33g	7-Cl	-6.204	Cys B241	3.87	π - H
4.33h	5-Br	-6.533	Ala B16	4.07	π - H
			Lys B352	3.62	π - H
			Ala A180	3.37	H - bonding
			Val A181	3.35	H - bonding
4.33i	7-Br	-6.496	Cys B241	4.12	π - H
			Lys B352	4.08	π - H
			Asn B258	3.52	π - H
4.33j		-6.623	Lys B254	3.81	π - H
4.33k	7-Br,5-Cl	-6.126	Lys B254	3.72	π - H
4.33l	7-OCH ₂ C ₆ H ₅	-7.638	Cys B241	4.17	π - H
			Ser A178	4.35	π - H
			Ala B317	3.02	H - bonding
			Thr A239	3.50	H - bonding
Colchicine	-	-8.028	Leu B248	4.12	π - H
			Leu E248	4.12	π - H
			Lys B254	4.39	π - H
			Asn A101	3.33	H - bonding
			Asn D101	3.10	H - bonding
Combretastatin A-4	-	-7.586	Leu B248	3.88	π - H
			Leu E248	3.87	π - H
Indanocine	-	-7.137	Tyr A224	4.05	π - π
			Tyr B224	3.91	π - π
			Asn A206	3.66	H - bonding
			Asn B206	3.98	H - bonding

Colchicine and combretastatin A-4 showed π - H stacking interactions with Leu B248 and Leu E248 through their TMP moiety (Figure 4.23; Figure 4.24). In addition, colchicine also showed π - H stacking interaction with Lys B254 and hydrogen bonding interactions with Asn A101 and Asn D101 residues (Figure 4.23). Although indanocine did not interact with these amino acid residues, it displayed π - π stacking interactions Tyr A224 and Tyr B224 residues, and hydrogen bonding interactions with Asn A206 and Asn B206 residues (Figure 4.25). Among the

unsubstituted phenyl **4.31** series, 7 compounds from this group shared the same interaction with colchicine; compounds **4.31a** (R = H), **4.31d** (R = 7-OCH₃), **4.31g** (R = 7-Cl), **4.31h** (R = 5-Br), and **4.31i** (R = 7-Br), showed a $\pi - H$ stacking interactions with Lys B254 residue, compound **4.31e** (R = 6,7-OCH₂O-), exhibited a $\pi - H$ stacking interacted with Leu B248 residue and compound **4.31l** (R = 7-OCH₂C₆H₅), displayed $\pi - H$ stacking interactions with both Leu B248 and Lys B254 residues. In the TMP **4.32** series, 7 compounds showed the same interaction with colchicine and combretastatin A-4; compounds **4.32b** (R = 7-CH₃), **4.32c** (R = 7-CF₃), **4.32d** (R = 7-OCH₃), **4.32h** (R = 5-Br), and **4.32k** (R = 7-Br,5-Cl) showed a $\pi - H$ stacking interactions with Leu B248 residue, compound **4.32e** (R = 6,7-OCH₂O-), interacted with Leu B248 and Lys B254 residues while compound **4.32j** (R = 5-Br,7-CH₃) interacted with Leu B248 and Leu E248 residues. Whereas only 4 compounds from the pyridyl **4.33** series shared interaction with the reference compounds. Compound **4.33c** (R = 7-CF₃), interacted with Leu B248, this interaction was also common to colchicine and combretastatin A-4, while compounds **4.33j** (R = 5-Br,7-CH₃) and **4.33k** (R = 7-Br,5-Cl) interacted with Lys B254 which was seen in colchicine.

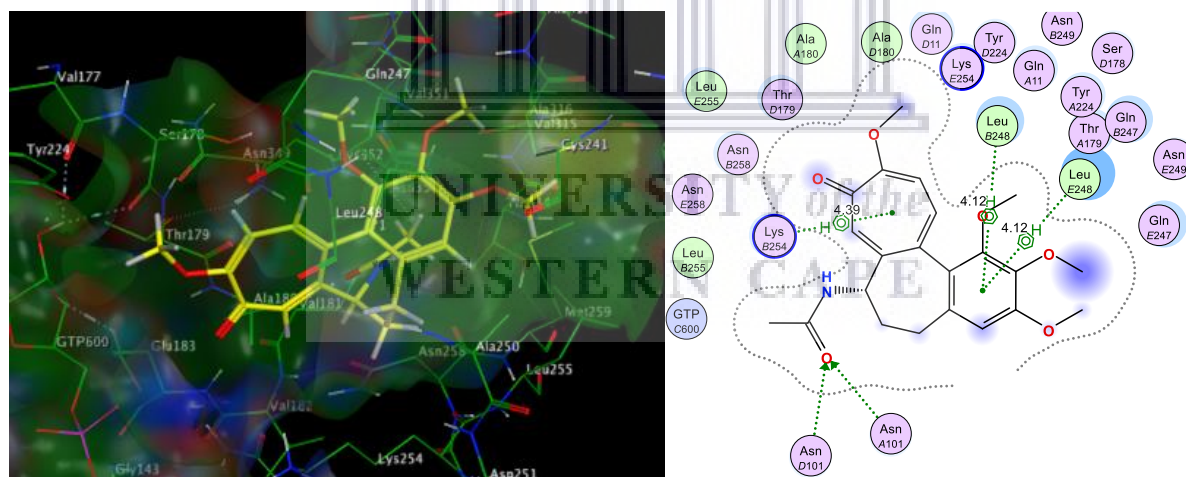


Figure 4.23 Tubulin-Colchicine active site (left) and 2D interaction map showing the binding interactions of colchicine with the ligand coloured in yellow.

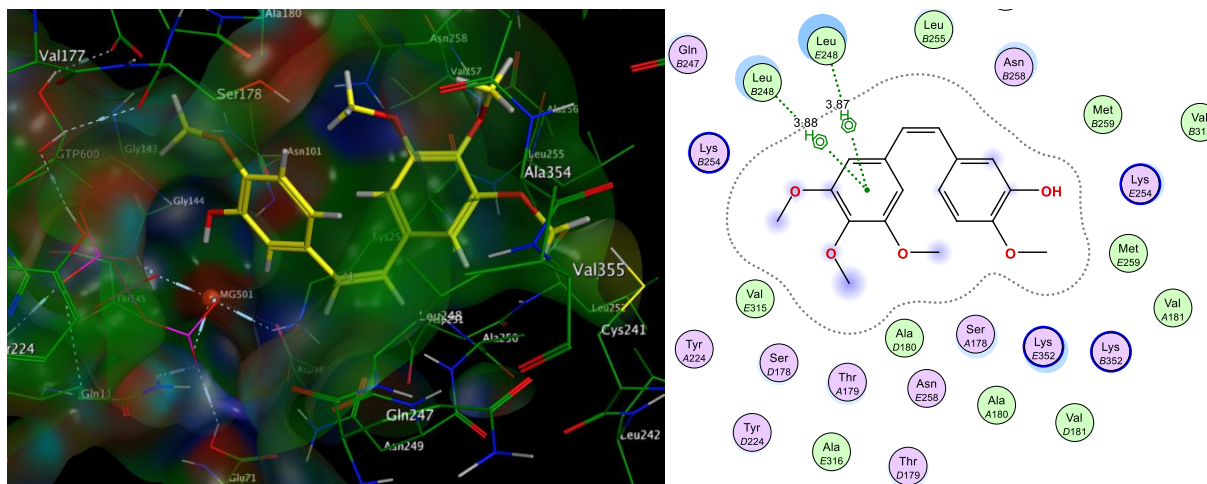


Figure 4.24 Tubulin-Colchicine active site (left) and 2D interaction map showing the binding interactions of combretastatin A-4 (bottom) with the ligand coloured in yellow.

Comparing the interactions displayed by these three groups of compounds, the phenyl **4.31** series seems to favour interaction with Lys B254 similar to colchicine and the TMP **4.32** series tends to favour interaction with Leu B248 in the same way as colchicine (Figure 4.23) and combretastatin A-4 (Figure 4.24). Interestingly, the most active compound **4.33a** (R = H) from the pyridyl **4.33** series exhibit significant $\pi - \pi$ stacking interactions with Tyr A224 and Tyr B224 residues which were the same interactions displayed by indanocine shown in Figure 4.25. This suggests that the $\pi - \pi$ stacking interactions with Tyr A224 and Tyr B224 residues could be important for the tubulin polymerization activity of the indanocine analogues. It is important to note this assumption is based on computational predictions and further biological studies would be required to establish this fact.

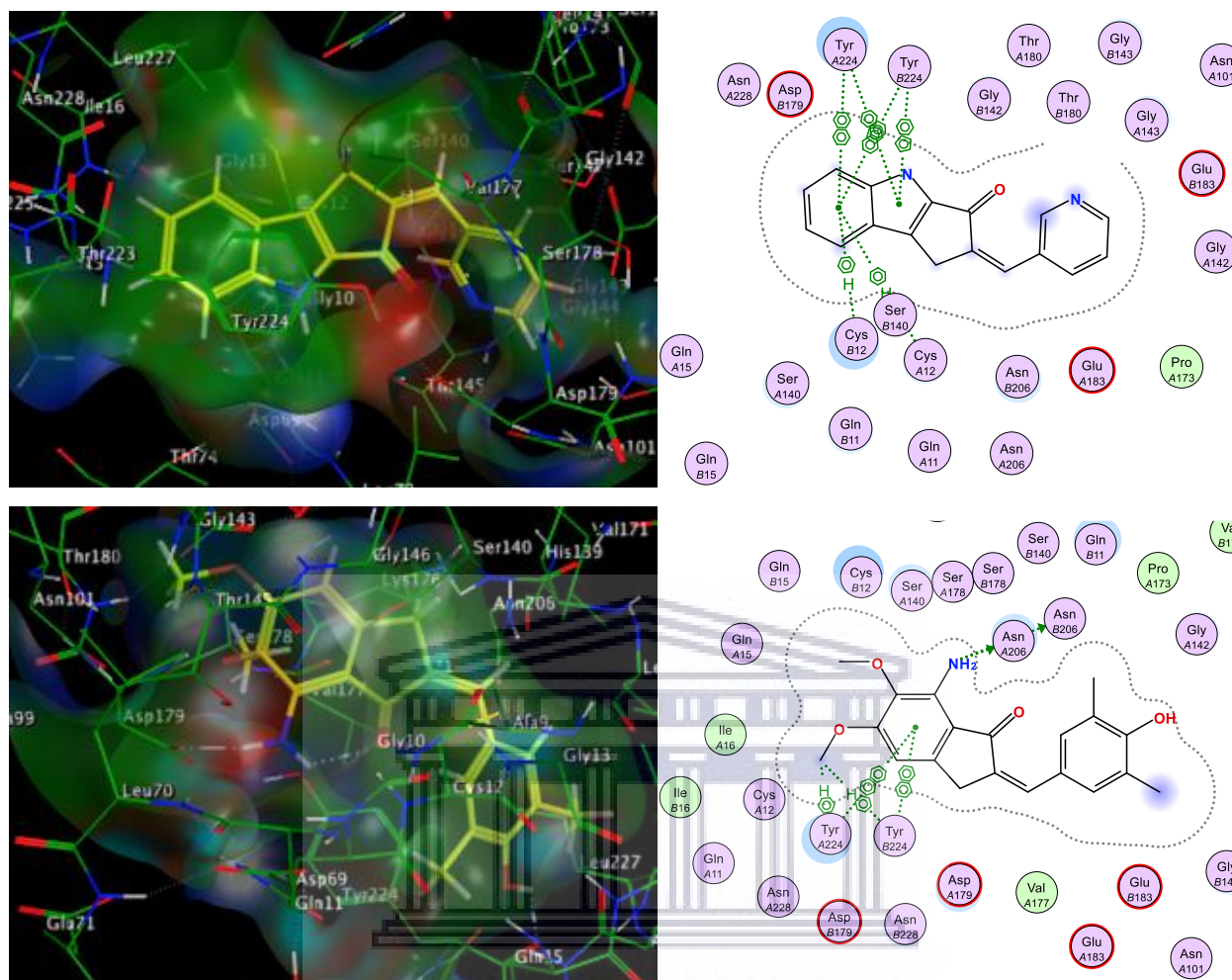


Figure 4.25 Tubulin-Colchicine active site (left) and 2D interaction map showing the binding interactions of **4.33a** (top) and **Indanocine** (bottom) with the ligand coloured in yellow.

In general, the synthesized compounds showed docking orientation similar to the reference compound and they displayed at least a hydrogen bonding, $\pi - H$ or $\pi - \pi$ stacking interaction with one amino acid residue. They also docked well into the colchicine binding site of tubulin and displayed good binding energies, however, the docking studies did not explain the general trend in the antiproliferative activities of the selected compounds against three cancer cell lines.

4.2.3.3 *In silico* predictions of the physicochemical and drug-likeness of the synthesized compounds.

The predicted molecular properties of the synthesized compounds (Table 4.8) were obtained online from the Molinspiration Cheminformatics server (<http://www.molinspiration.com/cgi->

[bin/properties](#)). In the evaluation of the logarithm of the partition coefficient between n-octanol and water (miLogP), the values obtained for the compounds were within the required limit (miLogP \leq 5). This means that the compounds are predicted to exhibit satisfactory oral bioavailability, although **4.31c** (R = 7- CF₃), **4.31j** (R = 5-Br,7-CH₃), **4.31k** (R = 7-Br,5-Cl), **4.31l** (R = 7-OCH₂C₆H₅), **4.32k** (R = 7-Br,5-Cl), and **4.32l** (R = 7-OCH₂C₆H₅) exceeded the limit. The phenyl **4.31** series and TMP **4.32** series appeared to be more lipophilic which is significant for drug absorption. They displayed values within the acceptable range except for the compounds mentioned above that exceeded the limit. The pyridyl **4.33** series were less lipophilic compared to the other two groups and compound **4.33f** (R = 7-F) was predicted to be the most hydrophilic with a miLogP value of 1.93. Our most active compound **4.33f** (R = H) appeared to maintain a balance between lipophilicity and hydrophilicity, it displayed a miLogP value of 2.76. The topological polar surface area (TPSA) of the compounds were within the required range of less than 160 Å which implies that the requirements for drug transport properties are satisfactory (Ertl et al., 2000, Verma, 2012). In general, the compounds did not exceed the set limit of not more than one violation thus complied with Lipinski's rule, this means that all the compounds could exhibit good oral bioavailability for absorption (Lipinski et al., 1997).

Table 4.8 *In silico* physicochemical of aryldene cyclopenta[b]indol-3-ones^a.

Compounds	R	miLogP ^b	TPSA (Å) ^c	MW ^d	n-HBA ^e	n-HBD ^f	n-violations ^g	n-ROTB ^h	MV ⁱ
4.31a	H	4.18	32.86	259.31	2	1	0	1	236.79
4.31b	7- CH ₃	4.60	32.86	273.33	2	1	0	1	253.35
4.31c	7- CF ₃	5.05	32.86	327.31	2	1	1	2	268.09
4.31d	7- OCH ₃	4.21	42.10	289.33	3	1	0	2	262.34
4.31e	6,7- OCH ₂ O-	4.04	51.33	303.32	4	1	0	1	260.72

4.31f	7-F	3.35	32.86	277.30	2	1	0	1	241.72
4.31g	7-Cl	4.83	32.86	293.75	2	1	0	1	250.33
4.31h	5-Br	4.94	32.86	338.20	2	1	0	1	254.68
4.31i	7-Br	4.96	32.86	338.20	2	1	0	1	254.68
4.31j	5-Br,7- CH ₃	5.34	32.86	352.23	2	1	1	1	271.24
4.31k	7-Br,5-Cl	5.57	32.86	372.65	2	1	1	1	268.21
4.31l	7- OCH ₂ C ₆ H ₅	5.81	42.10	365.43	3	1	1	4	333.99
4.32a	H	3.81	60.56	349.39	5	1	0	4	313.43
4.32b	7- CH ₃	4.24	60.56	363.41	5	1	0	4	329.99
4.32c	7- CF ₃	4.68	60.56	417.38	5	1	0	5	344.72
4.32d	7- OCH ₃	3.84	69.80	379.41	6	1	0	5	338.97
4.32e	6,7- OCH ₂ O-	3.68	79.03	393.39	7	1	0	4	337.36
4.32f	7-F	2.98	60.56	367.38	5	1	0	4	318.36
4.32g	7-Cl	4.46	60.56	383.83	5	1	0	4	326.96
4.32h	5-Br	4.57	60.56	428.28	5	1	0	4	331.31
4.32i	7-Br	4.60	60.56	428.28	5	1	0	4	331.31
4.32j	5-Br,7- CH ₃	4.97	60.56	442.31	5	1	0	4	347.87
4.32k	7-Br,5-Cl	5.20	60.56	462.73	5	1	1	4	344.85
4.32l	7- OCH ₂ C ₆ H ₅	5.44	69.80	455.51	6	1	1	7	410.62
4.33a	H	2.76	45.75	260.30	3	1	0	1	232.63
4.33b	7- CH ₃	3.19	45.75	274.32	3	1	0	1	249.19
4.33c	7- CF ₃	3.63	45.75	328.29	3	1	0	2	263.93
4.33d	7- OCH ₃	2.80	54.99	290.32	4	1	0	2	258.18
4.33e	6,7- OCH ₂ O-	2.63	64.22	304.31	5	1	0	1	256.56
4.33f	7-F	1.93	45.75	278.29	3	1	0	1	237.56
4.33g	7-Cl	3.42	45.75	294.74	3	1	0	1	246.17
4.33h	5-Br	3.52	45.75	339.19	3	1	0	1	250.52
4.33i	7-Br	3.55	45.75	339.19	3	1	0	1	250.52
4.33j	5-Br,7- CH ₃	3.92	45.75	353.22	3	1	0	1	267.08
4.33k	7-Br,5-Cl	4.15	45.75	373.64	3	1	0	1	264.06

4.33l	7- OCH ₂ C ₆ H ₅	4.39	54.99	366.42	4	1	0	4	329.83
--------------	--	------	-------	--------	---	---	---	---	--------

^a The parameters were determined using Molinspiration cheminformatics software. ^b The logarithm of the partition coefficient between n-octanol and water (miLogP \leq 5). ^c Topological polar surface area (TPSA $<$ 160 Å). ^d Molecular weight (MW $<$ 500). ^e The number of hydrogen bond acceptors (n-HBA \leq 10), ^f The number of hydrogen bond donors (n-HBD \leq 5). ^g The number of violations (n-violations \leq 1). ^h The number of rotatable bonds (n-ROTB). ⁱ Molecular volume (MV).

4.3 Conclusion

A series of arylidene cyclopenta[*b*]indol-3-one derivatives were synthesized *via* aldol condensation of cyclopenta[*b*]indoles with aromatic aldehydes. Ten compounds were selected for IC₅₀ determination against three cancer cell lines after a single concentration screening had been performed. Compound **4.32k** (R = 7-Br, 5-Cl) exhibited moderate antiproliferative activities against the cancer cell lines but did not discriminate against the normal cells. In contrast, compound **4.33a** (R = H) displayed the most potent and selective antiproliferative activity against HCC70 cells and was non-toxic to normal breast cells. In addition, docking studies revealed that all the compounds exhibited good affinity for the tubulin-colchicine binding site. Furthermore, the significant docking interactions displayed by compound **4.33a** (R = H) aligned with that of their analogous parent compound and a known inhibitor; indanocine. Thus providing a basis for further investigation into the arylidene cyclopenta[*b*]indol-3-one as tubulin polymerization inhibitors.

4.4 General experimental details

4.4.1 Materials

See section 3.4.1

4.4.2 General procedure for the Claisen-Schmidt reaction

Cyclopent(b)indol-3-one (1 mmol) was stirred in EtOH (5 mL) for 5 min at 0 °C followed by addition of substituted aromatic aldehydes (1.2 mmol) and stirred for another 5 min. The reaction was removed from the ice bath and 5% NaOH aq. (5 mL) was added dropwise and the reaction mixture was stirred for 3 – 5 h at ambient temperature. The reaction was monitored by TLC for

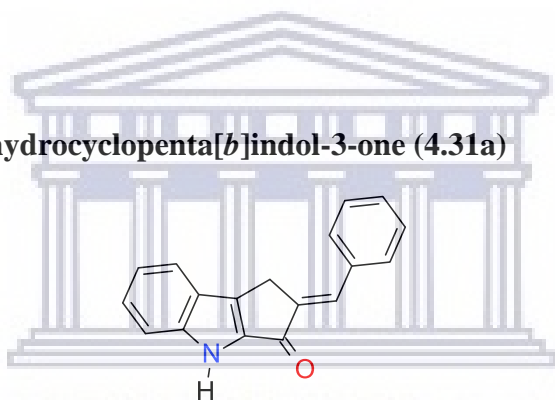
the disappearance of starting materials. When the reaction was complete the mixture was cooled at 0 °C for 30 min and the precipitate was collected and washed successively with water (2 x 10 mL) and cold MeOH (10 mL) followed by air drying overnight in the fume hood. Compounds **4.31k** (R =7-Br,5-Cl), **4.32k** (R =7-Br,5-Cl) and **4.33k** (R =7-Br,5-Cl) were further purified by column chromatography using a mixture of EtOAc and hexane as mobile phase.

4.4.3 Pyridinium chloride salt formation

Compound **4.33** (0.1 mmol) in vial was dissolved in DCM (1 mL) and 32% HCl (0.1 mL) was added and the mixture stirred for 2 h at ambient temperature. The solid mass was filtered and washed with DCM (3 mL) and allowed to dry in a fumehood.

4.4.4 Compounds

(2E)-2-benzylidene-1,4-dihydrocyclopenta[*b*]indol-3-one (**4.31a**)



Yield: 83% as light yellow powder; Mp 284-286 °C

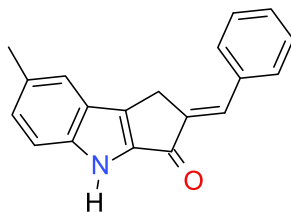
¹H NMR (400 MHz, DMSO-*d*₆) δ 11.92 (br s, N-H), 7.82 – 7.75 (m, 3H), 7.54 – 7.34 (m, 6H), 7.17 (t, *J* = 7.5 Hz, 1H), 4.05 (s, 2H)

¹³C NMR (100 MHz, DMSO-*d*₆) δ 182.3, 144.0, 140.9, 140.8, 140.3, 135.5, 131.0, 130.8, 129.7, 129.5, 127.4, 123.1, 122.2, 120.8, 114.1, 26.8

HRESIMS: *m/z*: [M + H]⁺ calculated for C₁₈H₁₄NO 260.1076: found 260.1060

FT-IR (ATR, cm⁻¹): 3166, 1673

(2E)-2-benzylidene-7-methyl-1,4-dihydrocyclopenta[*b*]indol-3-one (4.31b)



Yield: 90% as brown powder; Mp 287-290 °C

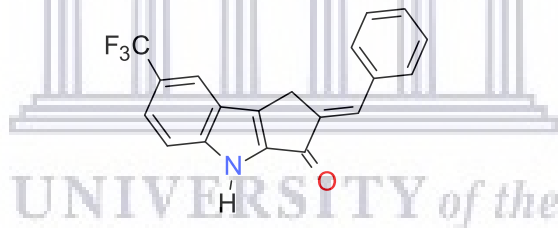
¹H NMR (400 MHz, DMSO-*d*₆) δ 11.79 (s, N-H), 7.77 (d, *J* = 6.6 Hz, 2H), 7.54 – 7.34 (m, 6H), 7.21 (d, *J* = 8.4 Hz, 1H), 4.02 (s, 2H), 2.42 (s, 3H)

¹³C NMR (100 MHz, DMSO-*d*₆) δ 142.5, 141.0, 140.9, 139.7, 135.6, 130.8, 130.8, 129.7, 129.6, 129.5, 129.3, 123.3, 121.4, 113.9, 26.7, 21.5

HRESIMS: *m/z*: [M + H]⁺ calculated for C₁₉H₁₆NO 274.1233: found 274.1143

FT-IR (ATR, cm⁻¹): 3204, 1667

(2E)-2-benzylidene-7-(trifluoromethyl)-1,4-dihydrocyclopenta[*b*]indol-3-one (4.31c)



Yield: 81% as black powder; Mp 290-295 °C

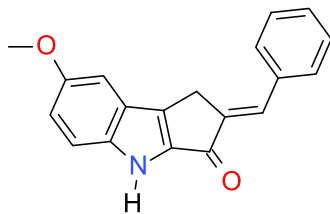
¹H NMR (400 MHz, DMSO-*d*₆) δ 12.38 (br s, N-H), 8.26 (s, 1H), 7.78 (d, *J* = 7.4 Hz, 2H), 7.67 – 7.63 (m, 2H), 7.51 (t, *J* = 7.6 Hz, 2H), 7.47 – 7.42 (m, 2H), 4.11 (s, 2H)

¹³C NMR (100 MHz, DMSO-*d*₆) δ 182.6, 145.0, 142.7, 140.7, 140.3, 135.3, 131.8, 130.9, 130.0, 129.5, 126.9, 126.4, 123.1, 122.3, 120.2, 115.2, 26.9

HRESIMS: *m/z*: [M + H]⁺ calculated for C₁₉H₁₃F₃NO 328.0950: found 328.0959

FT-IR (ATR, cm⁻¹): 3134, 1678

(2E)-2-benzylidene-7-methoxy-1,4-dihydrocyclopenta[*b*]indol-3-one (4.31d)



Yield: 75% as dark green powder; Mp 249-253 °C

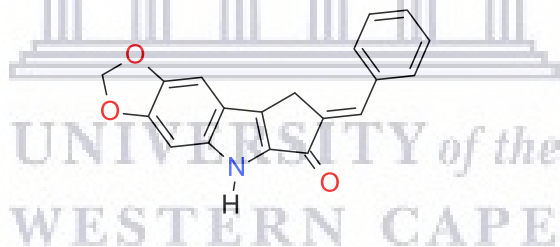
¹H NMR (400 MHz, DMSO-*d*₆) δ 11.77 (s, N-H), 7.77 (d, *J* = 7.5 Hz, 2H), 7.50 (t, *J* = 7.4 Hz, 2H), 7.45 – 7.41 (m, 1H), 7.39 – 7.35 (m, 2H), 7.26 (d, *J* = 2.3 Hz, 1H), 7.03 (dd, *J* = 9.0, 2.5 Hz, 1H), 4.03 (s, 2H), 3.80 (s, 3H)

¹³C NMR (100 MHz, DMSO-*d*₆) δ 182.1, 154.4, 141.3, 140.9, 139.5, 139.3, 135.6, 130.8, 130.8, 129.7, 129.4, 123.2, 118.8, 115.0, 102.2, 55.8, 26.9

HRESIMS: *m/z*: [M + H]⁺ calculated for C₁₉H₁₆NO₂ 290.1182; found 290.1203

FT-IR (ATR, cm⁻¹): 3173, 1664

(2E)-2-benzylidene-6,7-dioxolo-1,4-dihydrocyclopenta[*b*]indol-3-one (4.31e)



Yield: 67% as dark green powder; Mp 285-289 °C

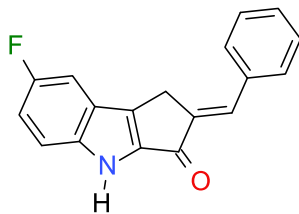
¹H NMR (400 MHz, DMSO-*d*₆) δ 11.79 (br s, N-H), 7.73(d, *J* = 7.3 Hz, 2H), 7.49 (t, *J* = 7.7 Hz, 2H), 7.41 (t, *J* = 7.4 Hz, 1H), 7.31 (s, 1H), 7.19 (s, 1H), 6.91 (s, 1H), 6.05 (s, 2H), 3.94 (s, 2H)

¹³C NMR (100 MHz, DMSO-*d*₆) δ 180.6, 149.1, 144.0, 141.2, 140.6, 140.4, 139.9, 135.7, 130.6, 130.1, 129.5, 129.4, 117.1, 101.7, 99.3, 93.6, 26.8

HRESIMS: *m/z*: [M + H]⁺ calculated for C₁₉H₁₄NO₃ 304.0974; found 304.0942

FT-IR (ATR, cm⁻¹): 2904, 1666

(2E)-2-benzylidene-7-fluoro-1,4-dihydrocyclopenta[*b*]indol-3-one (4.31f)



Yield: 97% as greenish yellow powder; Mp 282-286 °C

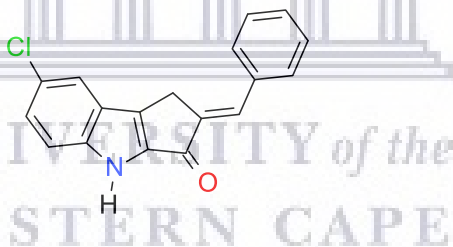
¹H NMR (400 MHz, DMSO-*d*₆) δ 12.03 (br s, N-H), 7.76 (d, *J* = 7.6 Hz, 2H), 7.58 (dd, *J* = 9.4, 2.5 Hz, 1H), 7.53 – 7.47 (m, 3H), 7.46 – 7.43 (m, 1H), 7.40(s, 1H), 7.25 (td, *J* = 9.2, 2.6 Hz, 1H), 4.03 (s, 2H)

¹³C NMR (100 MHz, DMSO-*d*₆) δ 182.5, 158.8, 156.4, 142.4, 140.6, 140.5, 139.7, 139.6, 135.4, 131.5, 129.9, 123.1 116.2, 115.5, 106.6, 26.8

HRESIMS: *m/z*: [M + H]⁺ calculated for C₁₈H₁₃FNO 278.0982: found 278.0971

FT-IR (ATR, cm⁻¹): 3187, 1669

(2E)-2-benzylidene-7-chloro-1,4-dihydrocyclopenta[*b*]indol-3-one (4.31g)



Yield: 99% as dark grey powder; Mp 288-292 °C

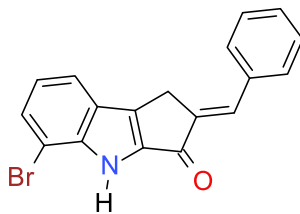
¹H NMR (400 MHz, DMSO-*d*₆) δ 7.86 (d, *J* = 1.8 Hz, 1H), 7.76 (d, *J* = 7.4 Hz, 2H), 7.54 – 7.43 (m, 4H), 7.40 (s, 1H), 7.36 (dd, *J* = 8.6, 2.0 Hz, 1H), 4.04 (s, 2H)

¹³C NMR (100 MHz, DMSO-*d*₆) δ 182.5, 142.3, 142.2, 140.4, 139.3, 135.4, 131.6, 130.8, 129.9, 129.5, 127.2, 125.2, 124.0, 121.3, 115.8, 26.8

HRESIMS: *m/z*: [M + H]⁺ calculated for C₁₈H₁₃ClNO 294.0687: found 294.0697

FT-IR (ATR, cm⁻¹): 3194, 1669

(2E)-2-benzylidene-5-bromo-1,4-dihydrocyclopenta[*b*]indol-3-one (4.31h)



Yield: 89% as dark brown powder; Mp 247-249 °C

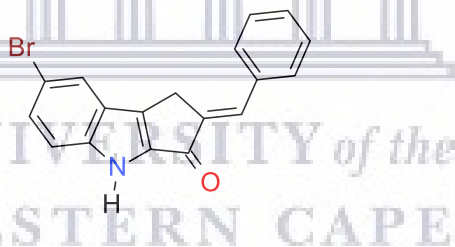
¹H NMR (400 MHz, DMSO-*d*₆) δ 12.21 (br s, N-H), 7.83 (d, *J* = 8.2 Hz, 1H), 7.78 (d, *J* = 7.3 Hz, 2H) 7.61 (d, *J* = 7.7 Hz, 1H), 7.51 (t, *J* = 7.7 Hz, 2H), 7.46 – 7.40 (m, 2H), 7.12 (t, *J* = 7.8 Hz, 1H), 4.07 (s, 2H)

¹³C NMR (100 MHz, DMSO-*d*₆) δ 182.4, 142.2, 141.7, 141.0, 140.3, 135.4, 131.6, 130.9, 129.9, 129.8, 129.5, 124.8, 122.1, 121.6, 106.3, 26.9

HRESIMS: *m/z*: [M + H]⁺ calculated for C₁₈H₁₃BrNO 340.0161: found 340.0157

FT-IR (ATR, cm⁻¹): 3203, 1677

(2E)-2-benzylidene-7-bromo-1,4-dihydrocyclopenta[*b*]indol-3-one (4.31i)



Yield: 86% as brownish green powder; Mp 282-286 °C

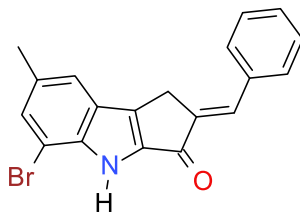
¹H NMR (400 MHz, DMSO-*d*₆) δ 12.10 (br s, N-H), 8.02 (d, *J* = 1.6 Hz, 1H), 7.76 (d, *J* = 7.8 Hz, 2H), 7.53 – 7.48 (m, 2H), 7.47 – 7.39 (m, 4H), 4.04 (s, 2H)

¹³C NMR (100 MHz, DMSO-*d*₆) δ 182.5, 142.4, 141.9, 140.4, 139.2, 135.4, 131.6, 130.8, 129.9, 129.7, 129.5, 124.7, 124.5, 116.2, 113.1, 26.8

HRESIMS: *m/z*: [M + H]⁺ calculated for C₁₈H₁₃BrNO 340.0161: found 340.0157

FT-IR (ATR, cm⁻¹): 3190, 1678

(2E)-2-benzylidene-5-bromo-7-methyl-1,4-dihydrocyclopenta[*b*]indol-3-one (4.31j)



Yield: 93% as dark grey powder; Mp 275-278 °C

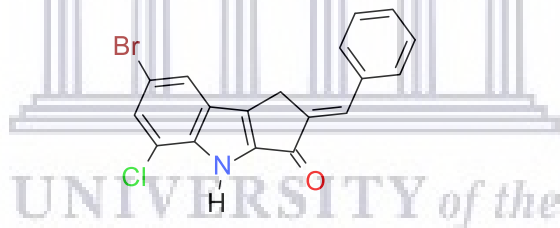
¹H NMR (400 MHz, DMSO-*d*₆) δ 11.96 (br s, N-H), 7.76 (d, *J* = 7.40 Hz, 2H), 7.58 (s, 1H), 7.51 (t, *J* = 7.8 Hz, 2H), 7.46 – 7.38 (m, 3H) 4.03 (s, 2H), 2.41 (s, 3H)

¹³C NMR (100 MHz, DMSO-*d*₆) δ 182.4, 142.9, 140.5, 140.3, 135.5, 131.4, 131.2, 130.8, 130.4, 129.8, 129.5, 129.3, 129.1, 124.9, 120.9, 26.8, 21.1

HRESIMS: *m/z*: [M + H]⁺ calculated for C₁₉H₁₅BrNO 352.0338: found 352.0333

FT-IR (ATR, cm⁻¹): 3186, 1680

(2E)-2-benzylidene-7-bromo-5-chloro-1,4-dihydrocyclopenta[*b*]indol-3-one (4.31k)



Yield: 93% as brown powder; Mp 207-211 °C

¹H NMR (400 MHz, DMSO-*d*₆) δ 12.57 (br s, N-H), 8.04 (d, *J* = 1.7 Hz, 1H), 7.77 (d, *J* = 7.3 Hz, 2H), 7.66 (d, *J* = 1.7 Hz, 1H), 7.52 (t, *J* = 7.6 Hz, 2H), 7.46 – 7.42 (m, 2H), 4.05 (s, 2H)

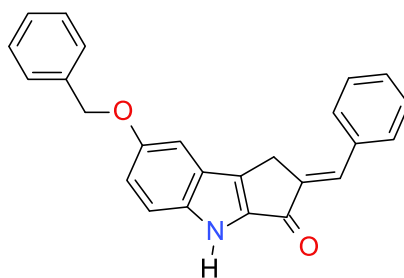
¹³C NMR (100 MHz, DMSO-*d*₆) δ 182.7, 142.8, 140.2, 139.7, 135.4, 132.1, 131.0, 130.8, 129.7, 129.5, 129.0, 128.3, 123.6, 119.6, 112.6, 26.7

¹³C chemical shifts were extracted from HSQC and HMBC NMR spectra due to weak ¹³C NMR.

HRESIMS: *m/z*: [M + H]⁺ calculated for C₁₈H₁₂ClBrNO 375.9742: found 375.2463

FT-IR (ATR, cm⁻¹): 3177, 1698

(2E)-2-benzylidene-7-benzyloxy-1,4-dihydrocyclopenta[*b*]indol-3-one (4.311).



Yield: 89% as brown powder; Mp 218-225 °C

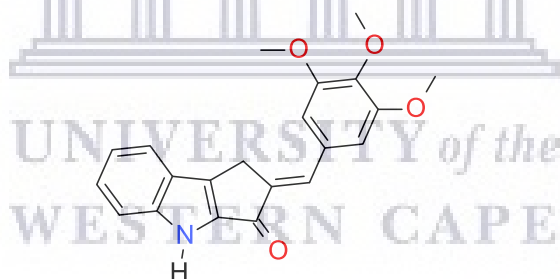
¹H NMR (400 MHz, DMSO-*d*₆) δ 11.80 (s, N-H), 7.77 (d, *J* = 7.5 Hz, 2H), 7.53 – 7.31 (m, 11H), 7.12 (dd, *J* = 8.9, 2.3 Hz, 1H) 5.14 (s, 2H), 4.02 (s, 2H)

¹³C NMR (100 MHz, DMSO-*d*₆) δ 182.1, 153.4, 142.9, 141.4, 140.9, 139.5, 137.8, 135.6, 130.9, 130.8, 130.4, 129.7, 129.4, 128.9, 128.1, 123.2, 119.3, 103.8, 70.1, 55.4, 26.9

HRESIMS: *m/z*: [M + H]⁺ calculated for C₂₅H₂₀NO₂ 366.1495: found 366.1463

FT-IR (ATR, cm⁻¹): 3162, 1677

(2E)-2-[(3,4,5-trimethoxyphenyl)methylene]-1,4-dihydrocyclopenta[*b*]indol-3-one (4.32a)



Yield: 71% as light yellow powder; Mp 256-258 °C

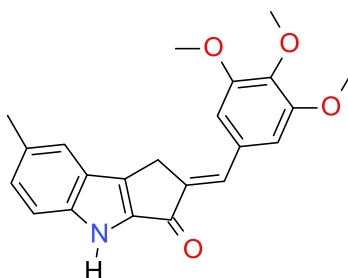
¹H NMR (400 MHz, DMSO-*d*₆) δ 11.90 (s, N-H), 7.82 (d, *J* = 8.0 Hz, 1H), 7.47 (d, *J* = 8.4 Hz, 1H), 7.40 – 7.34 (m, 2H), 7.16 (t, *J* = 7.5 Hz, 1H), 7.08 (s, 2H), 4.09 (s, 2H), 3.89 (s, 6H), 3.73 (s, 3H)

¹³C NMR (100 MHz, DMSO-*d*₆) δ 182.3, 153.5, 143.9, 141.0, 140.0, 139.8, 139.2, 131.4, 131.0, 127.3, 123.1, 122.2, 120.7, 114.1, 108.4, 60.6, 56.5, 26.5

HRESIMS: *m/z*: [M + H]⁺ calculated for C₂₁H₂₀NO₄ 350.1393: found 350.1425

FT-IR (ATR, cm⁻¹): 3163, 1659

(2E)-7-methyl-2-[(3,4,5-trimethoxyphenyl)methylene]-1,4-dihydrocyclopenta[*b*]indol-3-one (4.32b)



Yield: 95% as brown powder; Mp 253-255 °C

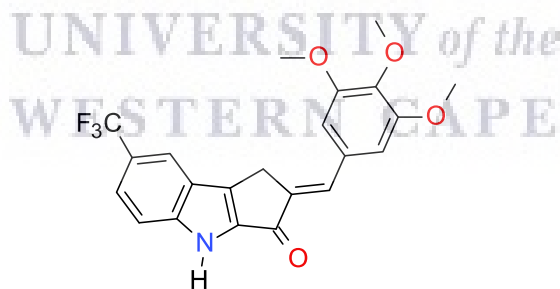
¹H NMR (400 MHz, DMSO-*d*₆) δ 11.75 (s, N-H), 7.59 (s, 1H), 7.38 – 7.32 (m, 2H), 7.20 (dd, *J* = 8.6, 1.4 Hz, 1H), 7.07 (s, 2H), 4.05 (s, 2H), 3.88 (s, 6H), 3.73 (s, 3H), 2.41 (s, 3H)

¹³C NMR (100 MHz, DMSO-*d*₆) δ 182.2, 153.5, 142.4, 141.1, 139.9, 139.5, 139.1, 131.2, 131.1, 129.5, 129.2, 123.3, 121.4, 113.8, 108.3, 60.6, 56.5, 26.5, 21.4

HRESIMS: *m/z*: [M + H]⁺ calculated for C₂₂H₂₂NO₄ 364.1550: found 364.1512

FT-IR (ATR, cm⁻¹): 3183, 1669

(2E)-7-(trifluoromethyl)-2-[(3,4,5-trimethoxyphenyl)methylene]-1,4-dihydrocyclopenta[*b*]indol-3-one (4.32c)



Yield: 98% as black powder; Mp 272-276 °C

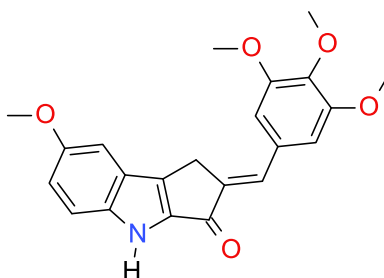
¹H NMR (400 MHz, DMSO-*d*₆) δ 12.37 (br s, N-H), 8.30 (s, 1H), 7.69 – 7.64 (m, 2H), 7.39 (s, 1H), 7.10 (s, 2H), 4.13 (s, 2H), 3.90 (s, 6H), 3.74 (s, 3H)

¹³C NMR (100 MHz, DMSO-*d*₆) δ 182.7, 153.5, 145.0, 142.8, 140.5, 139.3, 132.2, 130.8, 127.0, 124.3, 123.0, 122.4, 121.3, 120.2, 115.2, 108.5, 60.6, 56.5, 26.7

HRESIMS: *m/z*: [M + H]⁺ calculated for C₂₂H₁₉F₃NO₄ 418.1267: found 418.1233

FT-IR (ATR, cm⁻¹): 3131, 1675

(2E)-7-methoxy-2-[(3,4,5-trimethoxyphenyl)methylene]-1,4-dihydrocyclopenta[*b*]indol-3-one (4.32d)



Yield: 66% as greenish yellow powder; Mp 249-252 °C

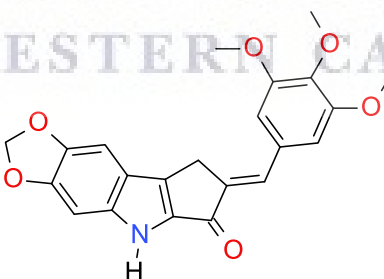
¹H NMR (400 MHz, DMSO-*d*₆) δ 11.75 (s, N-H), 7.37 (d, *J* = 9.0 Hz, 1H), 7.34 (s, 1H), 7.26 (d, *J* = 2.4 Hz, 1H), 7.07 (s, 2H), 7.02 (dd, *J* = 9.0, 2.5 Hz, 1H), 4.05 (s, 2H), 3.90 (s, 6H), 3.81 (s, 3H), 3.73 (s, 3H)

¹³C NMR (100 MHz, DMSO-*d*₆) δ 182.2, 154.4, 153.5, 141.3, 140.0, 139.3, 139.3, 139.2, 131.3, 131.1, 123.3, 118.8, 115.0, 108.4, 102.1, 60.6, 56.6, 55.9, 26.5

HRESIMS: *m/z*: [M + H]⁺ calculated for C₂₂H₂₂NO₅ 380.1499: found 380.1532

FT-IR (ATR, cm⁻¹): 3172, 1652

(2E)-6,7--dioxolo-2-[(3,4,5-trimethoxyphenyl)methylene]-1,4-dihydrocyclopenta[*b*]indol-3-one (4.32e)



Yield: 50% as dark green powder; Mp 269-271 °C

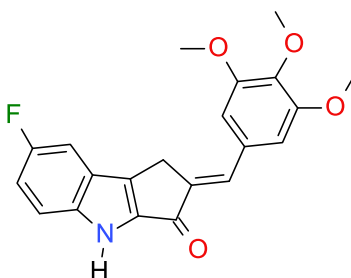
¹H NMR (400 MHz, DMSO-*d*₆) δ 11.76 (br s, N-H), 7.74 (s, 1H), 7.22 (s, 1H), 7.03 (s, 2H), 6.92 (s, 1H), 6.06 (s, 2H), 3.98 (s, 2H), 3.88 (s, 6H), 3.72 (s, 3H)

¹³C NMR (100 MHz, DMSO-*d*₆) δ 180.6, 153.5, 149.1, 144.0, 140.3, 139.0, 135.7, 131.2, 130.6, 130.5, 129.4, 117.1, 108.2, 101.7, 99.3, 93.6, 60.6, 56.5, 26.5

HRESIMS: *m/z*: [M + H]⁺ calculated for C₂₂H₂₀NO₆ 394.1291: found 394.1166

FT-IR (ATR, cm⁻¹): 3155, 1664

(2E)-7-fluoro-2-[(3,4,5-trimethoxyphenyl)methylene]-1,4-dihydrocyclopenta[*b*]indol-3-one
(4.32f)



Yield: 99% as greenish yellow powder; Mp 265-267 °C

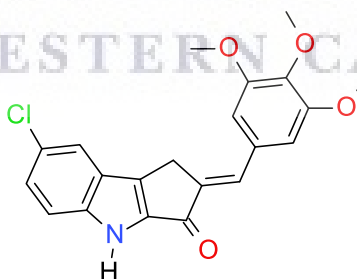
¹H NMR (400 MHz, DMSO-*d*₆) δ 12.02 (br s, N-H), 7.60 (dd, *J* = 9.5, 2.51 Hz, 1H), 7.48 (dd, *J* = 9.0, 4.5 Hz, 1H), 7.36 (s, 1H), 7.28 – 7.20 (m, 1H), 7.07 (s, 2H), 4.06 (s, 2H), 3.89 (s, 6H), 3.73 (s, 3H)

¹³C NMR (100 MHz, DMSO-*d*₆) δ 182.5, 158.7, 156.4, 153.5, 142.5, 140.6, 139.6, 139.3, 131.8, 123.1, 115.8, 115.4, 108.5, 107.2, 106.6, 60.6, 56.5, 26.5

HRESIMS: *m/z*: [M + H]⁺ calculated for C₂₁H₁₉FNO₄ 368.1299: found 368.1300

FT-IR (ATR, cm⁻¹): 3172, 1677

(2E)-7-chloro-2-[(3,4,5-trimethoxyphenyl)methylene]-1,4-dihydrocyclopenta[*b*]indol-3-one
(4.32g)



Yield: 87% as brownish green powder; Mp 274-277 °C

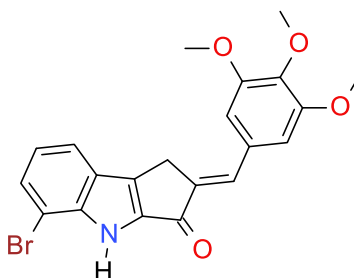
¹H NMR (400 MHz, DMSO-*d*₆) δ 12.10 (s, N-H), 7.92 (s, 1H), 7.49 (d, *J* = 8.8 Hz, 1H), 7.40 – 7.34 (m, 2H), 7.07 (s, 2H), 4.07 (s, 2H), 3.89 (s, 6H), 3.73 (s, 3H)

¹³C NMR (100 MHz, DMSO-*d*₆) δ 182.5, 153.5, 142.2, 142.2, 139.5, 139.3, 139.1, 132.0, 130.9, 127.1, 125.2, 124.0, 121.3, 115.8, 108.5, 60.6, 56.5, 26.6

HRESIMS: *m/z*: [M + H]⁺ calculated for C₂₁H₁₉ClNO₄ 384.1004: found 384.0983

FT-IR (ATR, cm⁻¹): 3168, 1671

(2E)-5-bromo-2-[(3,4,5-trimethoxyphenyl)methylene]-1,4-dihydrocyclopenta[*b*]indol-3-one
(4.32h)



Yield: 89% as greenish brown powder; Mp 241-243 °C

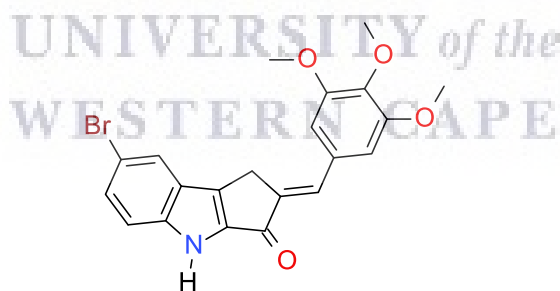
¹H NMR (400 MHz, DMSO-*d*₆) δ 12.17 (s, N-H), 7.85 (d, *J* = 8.0 Hz, 1H), 7.61 (d, *J* = 7.53 Hz, 1H), 7.39 (s, 1H), 7.14 – 7.07 (m, 3H), 4.10 (s, 2H), 3.89 (s, 6H), 3.73 (s, 3H)

¹³C NMR (100 MHz, DMSO-*d*₆) δ 182.4, 153.5, 142.1, 141.7, 140.8, 139.4, 139.3, 132.1, 130.9, 129.7, 124.8, 122.0, 121.6, 108.5, 106.2, 60.6, 56.5, 26.5

HRESIMS: *m/z*: [M + H]⁺ calculated for C₂₁H₁₉BrNO₄ 430.0478: found 430.0515

FT-IR (ATR, cm⁻¹): 3187, 1685

(2E)-7-bromo-2-[(3,4,5-trimethoxyphenyl)methylene]-1,4-dihydrocyclopenta[*b*]indol-3-one
(4.32i)



Yield: 85% as brownish green powder; Mp 278-282 °C

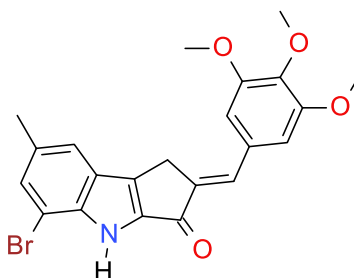
¹H NMR (400 MHz, DMSO-*d*₆) δ 12.11 (s, N-H), 8.09 (d, *J* = 1.4 Hz, 1H), 7.51 – 7.43 (m, 2H), 7.37 (s, 1H), 7.09 (s, 2H), 4.07 (s, 2H), 3.90 (s, 6H), 3.74 (s, 3H)

¹³C NMR (100 MHz, DMSO-*d*₆) δ 182.5, 153.5, 142.4, 142.0, 139.5, 139.3, 139.0, 132.0, 130.9, 129.6, 124.7, 124.5, 116.2, 113.1, 108.5, 60.6, 56.5, 26.6

HRESIMS: *m/z*: [M + H]⁺ calculated for C₂₁H₁₉BrNO₄ 430.0478: found 430.0515

FT-IR (ATR, cm⁻¹): 3186, 1670

(2E)-5-bromo-7-methyl-2-[(3,4,5-trimethoxyphenyl)methylene]-1,4-dihydrocyclopenta[*b*]indol-3-one (4.32j)



Yield: 97% as brownish green powder; Mp 259-263 °C

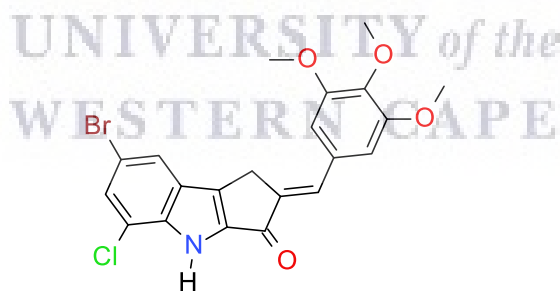
¹H NMR (400 MHz, DMSO-*d*₆) δ 12.02 (s, N-H), 7.62 (s, 1H), 7.45 (s, 1H), 7.37 (s, 1H), 7.07 (s, 2H), 4.05 (s, 2H), 3.89 (s, 6H), 3.73 (s, 3H), 2.41 (s, 3H)

¹³C NMR (100 MHz, DMSO-*d*₆) δ 182.3, 153.5, 141.8, 140.6, 140.2, 139.4, 139.2, 131.9, 131.4, 131.2, 130.9, 124.8, 120.9, 108.4, 105.8, 60.6, 56.5, 26.5, 21.0

HRESIMS: *m/z*: [M + H]⁺ calculated for C₂₂H₂₁BrNO₄ 442.0654: found 442.0647

FT-IR (ATR, cm⁻¹): 3192, 1665

(2E)-7-bromo-5-chloro-2-[(3,4,5-trimethoxyphenyl)methylene]-1,4-dihydrocyclopenta[*b*]indol-3-one (4.32k)



Yield: 85% as green powder; Mp 188-193 °C

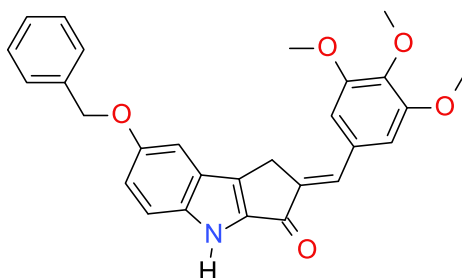
¹H NMR (400 MHz, DMSO-*d*₆) 12.54 (br s, N-H), 8.09 (d, *J* = 1.6 Hz, 1H), 7.64 (d, 1H) 7.39 (s, *J* = 1.6 Hz, 1H), 7.08 (s, 2H), 4.07 (s, 2H), 3.89 (s, 6H), 3.73 (s, 3H)

¹³C NMR (100 MHz, DMSO-*d*₆) δ 182.5, 153.5, 142.8, 139.7, 139.5, 139.4, 139.2, 132.5, 130.8, 128.1, 126, 123.6, 119.4, 112.5, 108.5, 60.6, 56.5, 26.6

HRESIMS: *m/z*: [M + H]⁺ calculated for C₂₁H₁₈ClBrNO₄ 462.0108: found 462.0465

FT-IR (ATR, cm⁻¹): 3210, 1690

(2E)-7-benzyloxy-2-[(3,4,5-trimethoxyphenyl)methylene]-1,4-dihydrocyclopenta[*b*]indol-3-one (4.32l)



Yield: 71% as greenish yellow powder; Mp 238-242 °C

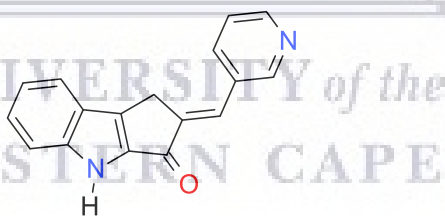
¹H NMR (400 MHz, DMSO-*d*₆) δ 11.78 (br s, N-H), 7.52 – 7.47 (m, 2H), 7.44 – 7.33 (m, 6H), 7.11 (dd, *J* = 9.0, 2.5 Hz, 1H), 7.07 (s, 2H), 5.14 (s, 2H), 4.05 (s, 2H), 3.90 (s, 6H), 3.73 (s, 3H).

¹³C NMR (100 MHz, DMSO-*d*₆) δ 26.5, 56.5, 60.6, 70.2, 103.8, 107.2, 108.4, 115.0, 119.2, 123.3, 128.2, 128.9, 131.1, 131.3, 137.8, 139.3, 139.5, 139.9, 141.4, 153.5, 153.8, 182.2

HRESIMS: *m/z*: [M + H]⁺ calculated for C₂₈H₂₆NO₅ 456.1812: found 456.1668

FT-IR (ATR, cm⁻¹): 3187, 1670

(2E)-2-(3-pyridylmethylene)-1,4-dihydrocyclopenta[*b*]indol-3-one (4.33a)



Yield: 85% as yellow powder; Mp 282-286 °C

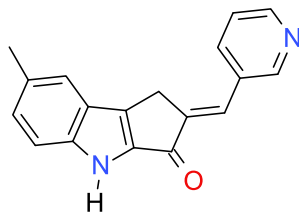
¹H NMR (400 MHz, DMSO-*d*₆) δ 11.94 (br s, N-H), 8.94 (d, *J* = 1.7 Hz, 1H), 8.59 (dd, *J* = 4.8, 1.3 Hz, 1H), 8.19 (dt, *J* = 8.0, 1.8 Hz, 1H), 7.78 (d, *J* = 8.1 Hz, 1H), 7.52 (dd, *J* = 8.0, 4.7 Hz, 1H), 7.47 (d, *J* = 8.4 Hz, 1H), 7.43 – 7.35 (m, 2H), 7.16 (t, *J* = 7.5 Hz, 1H), 4.08 (s, 2H)

¹³C NMR (100 MHz, DMSO-*d*₆) δ 181.8, 151.8, 150.1, 144.1, 142.9, 140.8, 140.6, 137.1, 131.5, 127.6, 127.6, 124.4, 123.0, 122.2, 120.9, 114.2, 26.7

HRESIMS: *m/z*: [M + H]⁺ calculated for C₁₇H₁₃N₂O 261.1029: found 261.1215

FT-IR (ATR, cm⁻¹): 3115, 1682

(2E)-7-methyl-2-(3-pyridylmethylene)-1,4-dihydrocyclopenta[*b*]indol-3-one (4.33b)



Yield: 80% as light yellow powder; Mp 262-265 °C

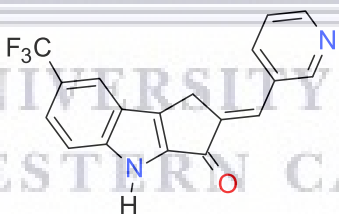
¹H NMR (400 MHz, DMSO-*d*₆) δ 11.81 (br s, N-H), 8.93 (d, *J* = 1.6 Hz, 1H), 8.59 (dd, *J* = 4.9, 1.3 Hz, 1H), 8.17 (dt, *J* = 8.1, 1.7 Hz, 1H), 7.56 – 7.49 (m, 2H), 7.41 – 7.34 (m, 2H), 7.22 (dd, *J* = 8.4, 1.0 Hz, 1H), 4.04 (s, 2H), 2.40 (s, 3H).

¹³C NMR (100 MHz, DMSO-*d*₆) δ 181.7, 151.7, 150.0, 143.0, 142.6, 140.9, 140.0, 137.1, 131.5, 129.6, 129.5, 127.4, 124.4, 123.2, 121.4, 113.9, 26.7, 21.5

HRESIMS: *m/z*: [M + H]⁺ calculated for C₁₈H₁₅N₂O 275.1186; found 275.1184

FT-IR (ATR, cm⁻¹): 3042, 1682

(2E)-2-(3-pyridylmethylene)-7-(trifluoromethyl)-1,4-dihydrocyclopenta[*b*]indol-3-one (4.33c)



Yield: 94% as black powder; Mp >310 °C

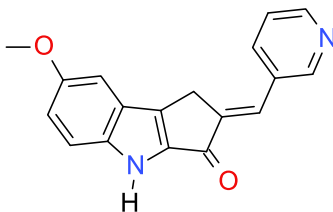
¹H NMR (400 MHz, DMSO-*d*₆) δ 8.94 (d, *J* = 1.2 Hz, 1H), 8.60 (dd, *J* = 4.8, 1.0 Hz, 1H), 8.23 (s, 1H), 8.16 (dt, *J* = 8.0, 1.6 Hz, 1H), 7.68 – 7.60 (m, 2H), 7.53 (dd, *J* = 8.1, 4.9 Hz, 1H), 7.43 (s, 1H), 4.12 (s, 2H)

¹³C NMR (100 MHz, DMSO-*d*₆) δ 182.1, 151.8, 150.3, 145.1, 142.6, 142.3, 141.0, 137.2, 131.3, 128.4, 126.9, 124.4, 123.3, 122.2, 121.7, 120.2, 115.2, 26.8

HRESIMS: *m/z*: [M + H]⁺ calculated for C₁₈H₁₂F₃N₂O 329.0903; found 329.1095

FT-IR (ATR, cm⁻¹): 3120, 1685

(2E)-7-methoxy-2-(3-pyridylmethylene)-1,4-dihydrocyclopenta[*b*]indol-3-one (4.33d)



Yield: 50% as dark grey powder; Mp 255-258 °C

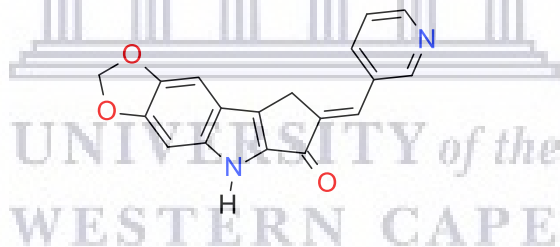
¹H NMR (400 MHz, DMSO-*d*₆) δ 11.80 (s, N-H), 8.93 (d, *J* = 1.6 Hz, 1H), 8.59 (dd, *J* = 4.8, 1.1 Hz, 1H), 8.17 (dt, *J* = 8.0, 1.7 Hz, 1H), 7.52 (dd, *J* = 8.1, 4.8 Hz, 1H), 7.40 – 7.35 (m, 2H), 7.24 (d, *J* = 2.3 Hz, 1H), 7.04 (dd, *J* = 9.0, 2.5 Hz, 1H), 4.05 (s, 2H), 3.80 (s, 3H)

¹³C NMR (100 MHz, DMSO-*d*₆) δ 181.6, 154.4, 151.8, 150.0, 143.0, 141.1, 139.8, 139.5, 137.0, 131.5, 127.4, 124.4, 123.2, 119.1, 115.0, 102.2, 55.8, 26.8

HRESIMS: *m/z*: [M + H]⁺ calculated for C₁₈H₁₅N₂O₂ 291.1135: found 291.1107

FT-IR (ATR, cm⁻¹): 3047, 1685

(2E)-6,7--dioxolo-2-(3-pyridylmethylene)-1,4-dihydrocyclopenta[*b*]indol-3-one (4.33e)



Yield: 47% as dark green powder; Mp >310 °C

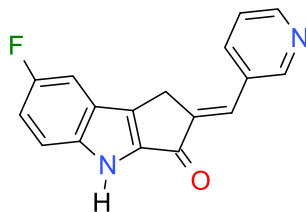
¹H NMR (400 MHz, DMSO-*d*₆) δ 11.83 (s, N-H), 8.90 (d, *J* = 1.6 Hz, 1H), 8.57 (dd, *J* = 4.8, 1.2 Hz, 1H), 8.13 (dt, *J* = 8.08, 1.68 Hz, 1H), 7.53 – 7.47 (m, 1H), 7.32 (s, 1H), 7.18 (s, 1H), 6.91 (s, 1H), 6.06 (s, 2H), 3.97 (s, 2H)

¹³C NMR (100 MHz, DMSO-*d*₆) δ 180.0, 151.6, 149.8, 149.3, 144.1, 143.3, 140.8, 140.7, 139.8, 136.9, 131.6, 129.4, 126.6, 124.4, 117.0, 101.7, 99.3, 26.7

HRESIMS: *m/z*: [M + H]⁺ calculated for C₁₈H₁₃N₂O₃ 305.0927: found 305.0862

FT-IR (ATR, cm⁻¹): 3162, 1667

(2E)-7-fluoro-2-(3-pyridylmethylene)-1,4-dihydrocyclopenta[*b*]indol-3-one (4.33f)



Yield: 76% as greenish yellow powder; Mp 305-308 °C

The ¹H and ¹³C NMR data were recorded for the hydrochloride salt of 4.33f

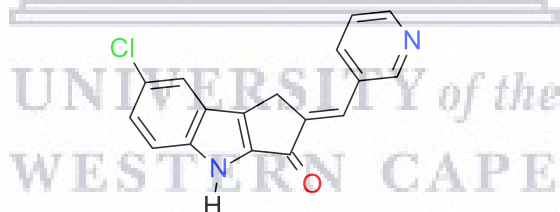
¹H NMR (400 MHz, DMSO-*d*₆) δ 12.18 (s, N-H), 9.19 (s, 1H), 8.86 (d, *J* = 5.3 Hz, 1H), 8.76 (d, *J* = 8.2 Hz, 1H), 8.05 (dd, *J* = 8.4, 5.5 Hz, 1H), 7.56 – 7.47 (m, 3H), 7.26 (td, *J* = 9.3, 2.5 Hz, 1H), 4.09 (s, 2H)

¹³C NMR (100 MHz, DMSO-*d*₆) δ 181.3, 158.8, 156.5, 145.4, 144.6, 142.9, 141.9, 141.0, 140.4, 134.2, 127.2, 125.3, 122.8, 116.8, 115.7, 106.6, 26.5

HRESIMS: *m/z*: [M + H]⁺ calculated for C₁₇H₁₂FN₂O 279.0935: found 279.0960

FT-IR (ATR, cm⁻¹): 3060, 1678

(2E)-7-chloro-2-(3-pyridylmethylene)-1,4-dihydrocyclopenta[*b*]indol-3-one (4.33g)



Yield: 90% as dark grey powder; Mp 307-310 °C

The ¹H and ¹³C NMR data were recorded for the hydrochloride salt of 4.33g

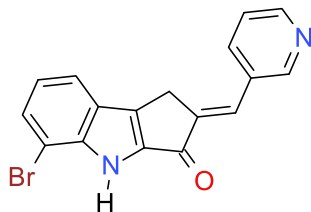
¹H NMR (400 MHz, DMSO-*d*₆) δ 12.30 (s, N-H), 9.19 (s, 1H), 8.86 (d, *J* = 5.4 Hz, 1H), 8.74 (d, *J* = 8.3 Hz, 1H), 8.05 (dd, *J* = 8.6, 5.5 Hz, 1H), 7.84 (d, *J* = 1.5 Hz, 1H), 7.54 – 7.47 (m, 2H), 7.38 (dd, *J* = 8.8, 2.0 Hz, 1H), 4.11 (s, 2H)

¹³C NMR (100 MHz, DMSO-*d*₆) δ 181.4, 145.2, 144.8, 144.0, 143.2, 142.5, 141.7, 139.9, 134.1, 127.8, 127.1, 125.5, 123.7, 121.3, 116.0, 26.5

HRESIMS: *m/z*: [M + H]⁺ calculated for C₁₇H₁₂ClN₂O 295.0640: found 295.0593

FT-IR (ATR, cm⁻¹): 3044, 1683

(2E)-5-bromo-2-(3-pyridylmethylene)-1,4-dihydrocyclopenta[b]indol-3-one (4.33h)



Yield: 87% as dark brown powder; Mp >310 °C

The ¹H and ¹³C NMR data were recorded for the hydrochloride salt of 4.33h

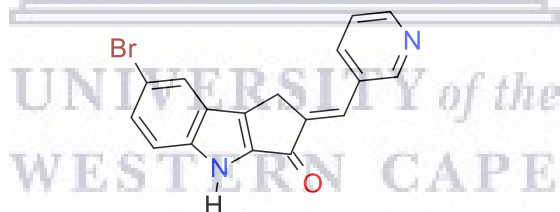
¹H NMR (400 MHz, DMSO-d₆) δ 12.29 (s, N-H), 9.17 (s, 1H), 8.83 (d, *J* = 5.2 Hz, 1H), 8.70 (d, *J* = 8.2 Hz, 1H), 7.98 (dd, *J* = 8.0, 5.4 Hz, 1H), 7.82 (d, *J* = 7.9 Hz, 1H), 7.64 (d, *J* = 7.6 Hz, 1H), 7.53 (s, 1H), 7.14 (t, *J* = 7.9 Hz, 1H), 4.16 (s, 2H)

¹³C NMR (100 MHz, DMSO-d₆) δ 181.4, 145.8, 144.8, 144.2, 143.2, 142.4, 141.7, 141.3, 133.8, 130.3, 126.8, 125.9, 124.6, 122.4, 121.7, 106.4, 26.6

HRESIMS: *m/z*: [M + H]⁺ calculated for C₁₇H₁₂BrN₂O 339.0134; found 339.0176

FT-IR (ATR, cm⁻¹): 3071, 1694

(2E)-7-bromo-2-(3-pyridylmethylene)-1,4-dihydrocyclopenta[b]indol-3-one (4.33i).



Yield: 78% as black powder; Mp 300-305 °C

The ¹H and ¹³C NMR data were recorded for the hydrochloride salt of 4.33i

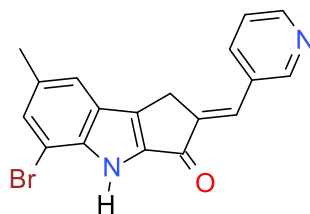
¹H NMR (400 MHz, DMSO-d₆) δ 12.28 (s, N-H), 9.17 (s, 1H), 8.84 (d, *J* = 4.3 Hz, 1H), 8.71 (d, *J* = 6.9 Hz, 1H), 8.06 – 7.96 (m, 2H), 7.55 – 7.42 (m, 3H), 4.11 (s, 2H)

¹³C NMR (100 MHz, DMSO-d₆) δ 181.4, 145.3, 145.1, 143.8, 143.5, 142.7, 141.5, 139.8, 133.9, 130.2, 126.9, 125.7, 124.5, 116.4, 113.4, 26.5

HRESIMS: *m/z*: [M + H]⁺ calculated for C₁₇H₁₂BrN₂O 339.0134; found 339.0176

FT-IR (ATR, cm⁻¹): 3040, 1685

(2E)-5-bromo-7-methyl-2-(3-pyridylmethylene)-1,4-dihydrocyclopenta[*b*]indol-3-one (4.33j)



Yield: 84% as brownish grey powder; Mp 305-308 °C

The ¹H NMR data was recorded for the hydrochloride salt of 4.33j

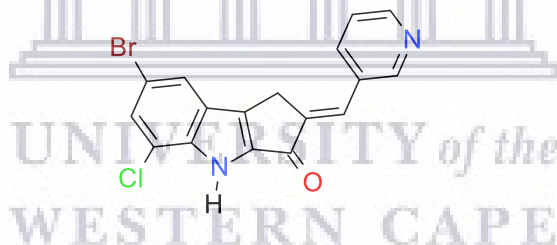
¹H NMR (400 MHz, DMSO-*d*₆) δ 12.13 (s, N-H), 9.14 (s, 1H), 8.81 (s, 1H), 8.54 (d, *J* = 8.1 Hz, 1H), 7.85 (s, 1H), 7.58 (s, 1H), 7.51 (s, 2H), 4.11 (s, 2H), 2.42 (s, 3H)

We were unable to record the ¹³C chemical shifts due to weak ¹³C, HSQC and HMBC NMR that resulted from poor solubility in NMR solvents.

HRESIMS: *m/z*: [M + H]⁺ calculated for C₁₈H₁₄BrN₂O 355.0270: found 355.0230

FT-IR (ATR, cm⁻¹): 2895, 1695

(2E)-7-bromo-5-chloro-2-(3-pyridylmethylene)-1,4-dihydrocyclopenta[*b*]indol-3-one (4.33k)



Yield: 82% as dark yellow powder. Mp >310 °C.

The ¹H NMR data was recorded for the hydrochloride salt of 4.33k

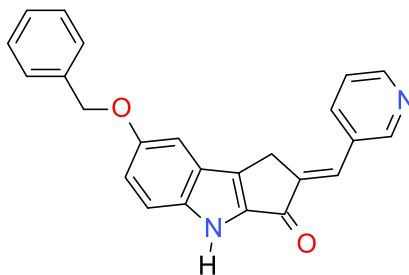
¹H NMR (400 MHz, DMSO-*d*₆) δ 12.68 (s, N-H), 9.18 (s, 1H), 8.89 – 8.84 (m, 1H), 8.76 – 8.72 (m, 1H), 8.07 – 8.02 (m, 2H), 7.71 (d, *J* = 1.7 Hz, 1H), 7.57 (s, 1H), 4.15 (s, 2H)

We were unable to record the ¹³C chemical shifts due to weak ¹³C, HSQC and HMBC NMR that resulted from poor solubility in NMR solvents.

HRESIMS: *m/z*: [M + H]⁺ calculated for C₁₇H₁₁ClBrN₂O 374.9724: found 374.9755

FT-IR (ATR, cm⁻¹): 2951, 1686

(2E)-7-benzyloxy-2-(3-pyridylmethylene)-1,4-dihydrocyclopenta[*b*]indol-3-one (4.33I).



Yield: 64% as dark green powder; Mp 255-259 °C

¹H NMR (400 MHz, DMSO-*d*₆) δ 11.85 (br s, N-H), 8.94 (d, *J* = 1.7 Hz, 1H), 8.59 (dd, *J* = 4.9, 1.3 Hz, 1H), 8.17 (d, *J* = 8.1 Hz, 1H), 7.55 – 7.45 (m, 5H), 7.44 – 7.30 (m, 4H), 7.13 (dd, *J* = 9.0, 2.4 Hz, 1H), 5.14 (s, 2H), 4.05 (s, 2H)

¹³C NMR (100 MHz, DMSO-*d*₆) δ 181.6, 153.5, 151.8, 150.0, 143.0, 141.2, 139.8, 137.8, 137.1, 131.5, 128.9, 128.2, 128.1, 127.5, 124.4, 123.2, 119.5, 115.1, 103.8, 70.1, 49.1, 26.8

HRESIMS: *m/z*: [M + H]⁺ calculated for C₂₄H₁₉N₂O₂ 367.1448: found 367.1400

FT-IR (ATR, cm⁻¹): 3174, 1665

4.4.5 Biological assay

4.4.5.1 Cell cultures

HeLa (ATCC CCL-2) and MDA-MB-231 (ATCC HTB-26) cell lines were cultured in Dulbecco's Modified Eagle Medium (DMEM) containing 10% (v/v) foetal bovine serum (FBS), 1 mM L-glutamine, 100 U/mL penicillin, 100 µg/mL streptomycin and 12.5 µg/mL amphotericin (1% [v/v] PSA). The HCC70 (ATCC CRL-2315) cell line was cultured in RPMI-1640 containing 10% (v/v) FBS, 1 mM L-glutamine, 1% (v/v) PSA and 0.2% (v/v) sodium bicarbonate. The MCF-12A (ATCC CRL-10782) cell line was maintained in DMEM/F-12 (Ham) (1:1), 10% (v/v) FBS, 1% (v/v) PSA, 20 ng/ml human epidermal growth factor, 0.3 U insulin, 100 ng/ml cholera toxin and 500 ng/ml hydrocortisone. All cell lines were maintained at 37°C in 9% CO₂.

4.4.5.2 Antiproliferative assay

See section 3.4.5.2

4.4.6 Molecular docking

A computer-assisted docking was conducted using the tubulin crystal structure (PDB ID: 1SA0) (Ravelli et al, 2004) retrieved online from the RCSB Protein Data Bank (<https://www.rcsb.org/structure/1SA0>). Docking simulations were conducted using Molecular Operating Environment (MOE) software version 2015.10. Prior to docking of the test compounds, the receptor protein was checked for missing atoms, hydrogen and partial charges. These were added by protonating 3D application in MOE, pH was adjusted to 7.4 while other parameters were kept at default. The co-crystallized ligand 2-mercapto-n-[1,2,3,10-tetramethoxy-9-oxo-5,6,7,9-tetrahydro-benzo[a]heptalen-7-yl]acetamide was identified in the protein receptor (PDB ID: 1SA0) and redocked with refinement set to induced fit. This was done to determine the accuracy of the docking protocol, the best-ranked RMSD value was 1.14 Å from the position of the co-crystallized ligand was selected. Generally, RMSD values smaller than 2.0 Å indicates that the docking protocol is capable of accurately predicting the binding orientation of the co-crystallized ligand. Hence, the protocols were considered suitable for the docking of inhibitors into the active site model of tubulin. Ligands (compounds) were constructed using BIOVIA Draw 2017 R2 academic version software, saved as “molfile”. The ligands were imported to the MOE database and energy minimized using the MMFF94 force field and set up to run in induced fit refinement.

UNIVERSITY of the
WESTERN CAPE

References

Das, L., Gupta, S., Dasgupta, D., Poddar, A., Janik, M. E., & Bhattacharyya, B. (2009). Binding of indanocine to the colchicine site on tubulin promotes fluorescence, and its binding parameters resemble those of the colchicine analogue AC. *Biochemistry*, 48(7), 1628-1635.

Ertl, P., Rohde, B., & Selzer, P. (2000). Fast calculation of molecular polar surface area as a sum of fragment-based contributions and its application to the prediction of drug transport properties. *Journal of Medicinal Chemistry*, 43(20), 3714-3717.

Gao, X. M., Wang, H., Li, Y. K., Ji, B. K., Xia, C. F., Yang, J. X., Zhou, M., Ye, Y. Q., & Hu, Q. F. (2015). Cytotoxic chalcones from *Desmodium oxyphyllum*. *Journal of the Brazilian Chemical Society*, 26(4), 736-740.

Gaur, R., Pathania, A. S., Malik, F. A., Bhakuni, R. S., & Verma, R. K. (2016). Synthesis of a series of novel dihydroartemisinin monomers and dimers containing chalcone as a linker and their anticancer activity. *European Journal of Medicinal Chemistry*, 122, 232-246.

Hu, J., Yan, J., Chen, J., Pang, Y., Huang, L., & Li, X. (2015). Synthesis, biological evaluation and mechanism study of a class of benzylideneindanone derivatives as novel anticancer agents. *Medicinal Chemistry Communications*, 6(7), 1318-1327.

Iranpoor, N., Zeynizadeh, B., & Aghapour, A. (1999). Aldol condensation of cycloalkanones with aromatic aldehydes catalysed with $TiCl_3$ (SO_3CF_3). *Journal of Chemical Research*, 23(9), 554-555.

Kaennakam, S., Sukandar, E. R., Rassamee, K., Siripong, P., & Tip-pyang, S. (2019). Cytotoxic chalcones and isoflavones from the stems of *Dalbergia velutina*. *Phytochemistry Letters*, 31, 187-191.

Kolundžija, B., Marković, V., Stanojković, T., Joksović, L., Matić, I., Todorović, N., Nikolić, M., & Joksović, M. D. (2014). Novel anthraquinone based chalcone analogues containing an imine fragment: synthesis, cytotoxicity and anti-angiogenic activity. *Bioorganic & Medicinal Chemistry Letters*, 24(1), 65-71.

Kumar, D., Kumar, N. M., Akamatsu, K., Kusaka, E., Harada, H., & Ito, T. (2010). Synthesis and biological evaluation of indolyl chalcones as antitumor agents. *Bioorganic & Medicinal Chemistry Letters*, 20(13), 3916-3919.

Kumbhar, B. V., Panda, D., & Kunwar, A. (2018). Interaction of microtubule depolymerizing agent indanocine with different human $\alpha\beta$ tubulin isotypes. *PLOS One*, 13(3).

Leoni, L. M., Hamel, E., Genini, D., Shih, H., Carrera, C. J., Cottam, H. B., & Carson, D. A. (2000). Indanocine, a microtubule-binding indanone and a selective inducer of apoptosis in multidrug-resistant cancer cells. *Journal of the National Cancer Institute*, 92(3), 217-224.

Li, L., Jiang, S., Li, X., Liu, Y., Su, J., & Chen, J. (2018). Recent advances in trimethoxyphenyl (TMP) based tubulin inhibitors targeting the colchicine binding site. *European Journal of Medicinal Chemistry*, 151, 482-494.

Li, L., Zhao, X. T., Luo, Y. P., Zhao, J. F., Yang, X. D., & Zhang, H. B. (2011). Novel cytotoxic chalcones from *Litsea rubescens* and *Litsea pedunculata*. *Bioorganic & Medicinal Chemistry Letters*, 21(24), 7431-7433.

Lipinski, C. A., Lombardo, F., Dominy, B. W., & Feeney, P. J. (1997). Experimental and computational approaches to estimate solubility and permeability in drug discovery and development settings. *Advanced Drug Delivery Reviews*, 23(1-3), 3-25.

Mahapatra, D. K., Bharti, S. K., & Asati, V. (2015). Anti-cancer chalcones: Structural and molecular target perspectives. *European Journal of Medicinal Chemistry*, 98, 69-114.

Menezes, J. C. (2017). Arylidene indanone scaffold: medicinal chemistry and structure–activity relationship view. *RSC Advances*, 7(15), 9357-9372.

Molecular Operating Environment (MOE), 2016.08; Chemical Computing Group Inc., 1010 Sherbrooke St. West, Suite #910, Montreal, QC, Canada, H3A 2R7, 2016

Molinspiration Cheminformatics, Bratislava, Slovak Republic
<http://www.molinspiration.com/cgi-bin/properties> (accessed December 30, 2019).

Murray, D., & Wigglesworth, M. (2017). Chapter 1: HTS Methods: Assay design and optimization, in high throughput screening methods: evolution and refinement. The Royal Society of Chemistry: London, 1–15.

Negi, A. S., Prakasham, A. P., Saxena, A. K., Luqman, S., Chanda, D., Kaur, T., & Gupta, A. (2014). Benzylidene indanones and processes for preparation and use thereof. U.S. Patent No. 8,633,242.

Nel, M. S., Petzer, A., Petzer, J. P., & Legoabe, L. J. (2016). 2-Benzylidene-1-indanone derivatives as inhibitors of monoamine oxidase. *Bioorganic & Medicinal Chemistry Letters*, 26(19), 4599-4605.

Palomo, C., Oiarbide, M., & García, J. M. (2002). The aldol addition reaction: an old transformation at constant rebirth. *Chemistry—A European Journal*, 8(1), 36-44.

Prakasham, A. P., Saxena, A. K., Luqman, S., Chanda, D., Kaur, T., Gupta, A., Yadav, D.K., Chanotiya, C.S., Shanker, K., Khan, F., & Negi, A. S. (2012). Synthesis and anticancer activity of 2-benzylidene indanones through inhibiting tubulin polymerization. *Bioorganic & Medicinal Chemistry*, 20(9), 3049-3057.

Rajagopalan, P., Alahmari, K. A., Elbessoumy, A. A., Balasubramaniam, M., Suresh, R., Shariff, M. E. A., & Chandramoorthy, H. C. (2016). Biological evaluation of 2-arylidene-4, 7-dimethyl indan-1-one (FXY-1): a novel Akt inhibitor with potent activity in lung cancer. *Cancer Chemotherapy and Pharmacology*, 77(2), 393-404.

Ravelli, R. B., Gigant, B., Curmi, P. A., Jourdain, I., Lachkar, S., Sobel, A., & Knossow, M. (2004). Insight into tubulin regulation from a complex with colchicine and a stathmin-like domain. *Nature*, 428(6979), 198-202.

Saha, R., Arunprasath, D., & Sekar, G. (2018). Phosphine-free and reusable palladium nanoparticles-catalyzed domino strategy: synthesis of indanone derivatives. *The Journal of Organic Chemistry*, 83(8), 4692-4702.

Tunbridge, G. A., Oram, J., & Caggiano, L. (2013). Design, synthesis and antiproliferative activity of indole analogues of indanocine. *Medicinal Chemistry Communications*, 4(11), 1452–1456.

Turner, R. J., & Charlton, S. J. (2005). Assessing the minimum number of data points required for accurate IC50 determination. *Assay and Drug Development Technologies*, 3(5), 525-531.

Usman, H., Hakim, E. H., Harlim, T., Jalaluddin, M. N., Syah, Y. M., Achmad, S. A., & Takayama, H. (2006). Cytotoxic chalcones and flavanones from the tree bark of *Cryptocarya costata*. *Zeitschrift für Naturforschung C*, 61(3-4), 184-188.

Wang, G., Li, C., He, L., Lei, K., Wang, F., Pu, Y., ... & Sang, Y. (2014). Design, synthesis and biological evaluation of a series of pyrano chalcone derivatives containing indole moiety as novel anti-tubulin agents. *Bioorganic & Medicinal Chemistry*, 22(7), 2060-2079.

Zhang, B., Duan, D., Ge, C., Yao, J., Liu, Y., Li, X., & Fang, J. (2015). Synthesis of xanthohumol analogues and discovery of potent thioredoxin reductase inhibitor as potential anticancer agent. *Journal of Medicinal Chemistry*, 58(4), 1795-1805.

Zhu, C., Zuo, Y., Wang, R., Liang, B., Yue, X., Wen, G., ... & Bu, X. (2014). Discovery of potent cytotoxic ortho-aryl chalcones as new scaffold targeting tubulin and mitosis with affinity-based fluorescence. *Journal of Medicinal Chemistry*, 57(15), 6364-6382.



Chapter 5

Synthesis and antiproliferative activity of prenylated diketopiperazine, barbituric acid and purine derivatives as analogues of sargaquinoic acid and potential Hsp90 inhibitors

UNIVERSITY of the
WESTERN CAPE

5.1 Introduction

Natural products have been significant in the discovery of chemotherapeutic agents, not only have they served as drugs but also as leads in the development of more effective semi-synthetic or synthetic anticancer drugs (Newman et al., 2000, Das & Satyalakshmi, 2012). Usually, structural optimization of natural leads is achieved from the knowledge of the structure-activity relationships obtained through the synthesis of improved derivatives or analogues (Das & Satyalakshmi, 2012). Hsp90 became a promising target for anticancer drug development following the discovery of binding interactions of geldanamycin and novobiocin to the Hsp90 complex (Whitesell et al., 1994; Marcu et al., 2000a; Marcu et al., 2000b). Despite the fact that these compounds were not suitable for clinical use (Supko et al., 1995; Burlison et al., 2006), their novel mechanism of action created a new avenue for researchers to explore. In addition, they continue to inspire the design and synthesis of anticancer drug candidates that have the potential for clinical evaluation.

Sargaquinoic acid (SQA) is a tetraprenylated toluquinone natural product, originally isolated from a brown seaweed *Sargassum serratifolium* by Kusumi and colleagues (1979). Subsequently, it has been reported in other *Sargassum* species including *S. thunbergii* (Seo et al., 2004) and *S. sagamianum* (Choi, et al., 2007). Also, SQA has been isolated from terrestrial plants used in herbal remedies such as fruits of *Iryanthera juruensis* (Silva et al., 2001) and seeds of *Pycnanthus angolensis* (Simon et al., 2008). Organic extracts from organisms producing SQA and derivatives have also been reported to show a range of biological activities (Oh et al., 2016; Lim et al., 2019). SQA as a single entity has demonstrated neuroprotection (Tsang & Kamei, 2004), and potent butyrylcholinesterase inhibition of 26 nM with good selectivity, thus making it a promising drug candidate for Alzheimer's disease (Choi, et al., 2007). SQA is also well known for its antioxidant properties (Ham et al., 2010), and several reports have shown its anti-inflammatory properties (Kang et al., 2013; Joung et al., 2015; Gwon et al., 2015; Oh et al., 2016). Furthermore, SQA displayed weak cytotoxicity and induced apoptosis in human keratinocyte cells (Hur et al., 2008) and was also reported to exhibit some antitumour activity (Reddy & Urban, 2009).

During the screening of the South African marine algae for bioactive compounds, Afolayan and colleagues (2008) isolated SQA along with other compounds from an endemic South African seaweed *Sargassum heterophyllum*. This compound was reported to exhibit weak antiplasmodial activity (Afolayan et al., 2008). De la Mare and colleagues (2012) showed that SQA exhibited weak cytotoxicity against MDA-MB-231 and MCF-7 cells, and the mechanism of action against

MDA-MB-231 cells was demonstrated to be through the induction of apoptosis. This process was further confirmed by assessment of the degree of expression of the anti-apoptotic protein Bcl-2 and a reduction in the amount of this regulatory protein was recorded (de la Mare et al., 2012).

5.1.1 Interaction of sargaquinoic acid with Hsp90

Moyo (2013) explored the interaction of SQA with Hsp90 and showed that its modulation patterns are more related to novobiocin and that it could disrupt the Hsp90-Hop interaction. A dose-dependent reduction in the amount of Hsp90 associating with Hop is observed for SQA in a way similar to novobiocin. On the other hand, geldanamycin did not affect Hsp90-Hop interaction as the level of Hsp90 remains constant despite increasing the concentrations of geldanamycin (Figure 5.1) (Moyo, 2013).

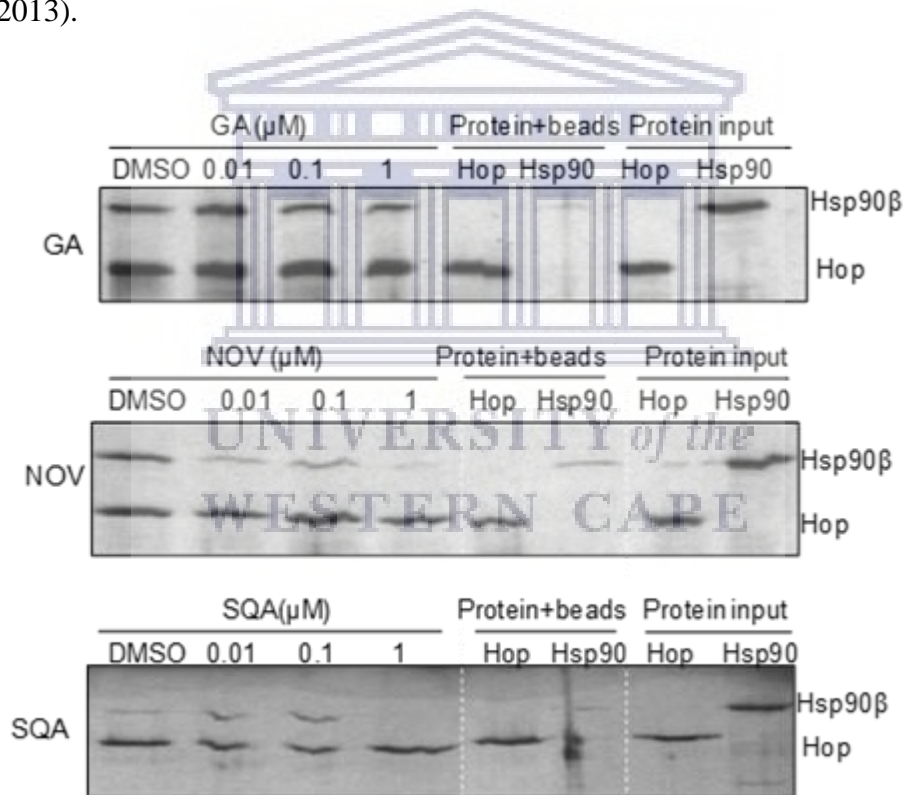


Figure 5.1 Data showing the results of a pull-down assay testing the interaction between Hsp90 and Hop (Moyo, 2013).

5.1.2 Aim of this study

Sargaquinoic acid did not display significant cytotoxic properties, however, the overview above revealed its ability to inhibit the function of Hsp90 and thus provided a reason to explore its synthetic analogues. It was anticipated that diketopiperazine, barbituric acid and theophylline scaffolds will offer a new dimension towards potentially improving the antiproliferative properties of SQA analogues while maintaining their interaction with Hsp90.

Hence, the aim of this study is to design and synthesize a series of SQA analogues based on the three scaffolds and to evaluate their antiproliferative activities and ability to inhibit the function of Hsp90.

5.2 Results and discussion

5.2.1 Rationale for the synthesis of diketopiperazine, barbituric acid and theophylline derivatives

In medicinal chemistry, the quinone scaffold is very common in nature with a range of biological activities (El-Najjar et al., 2011). However, it has also been identified as a pan-assay interference compound (PAINS) (Bisson et al., 2016) due to its ability to act as a Michael acceptors and its redox activity (Bolton & Dunlap, 2017). These mechanisms may lead to cellular damage due to the alkylation of important biomolecules or production reactive oxygen species (Bolton & Dunlap, 2017).

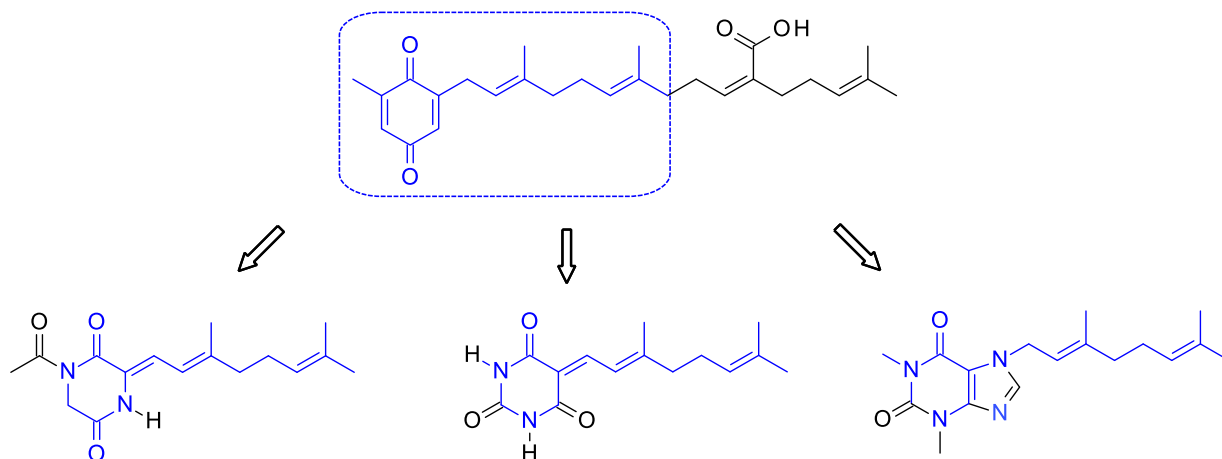


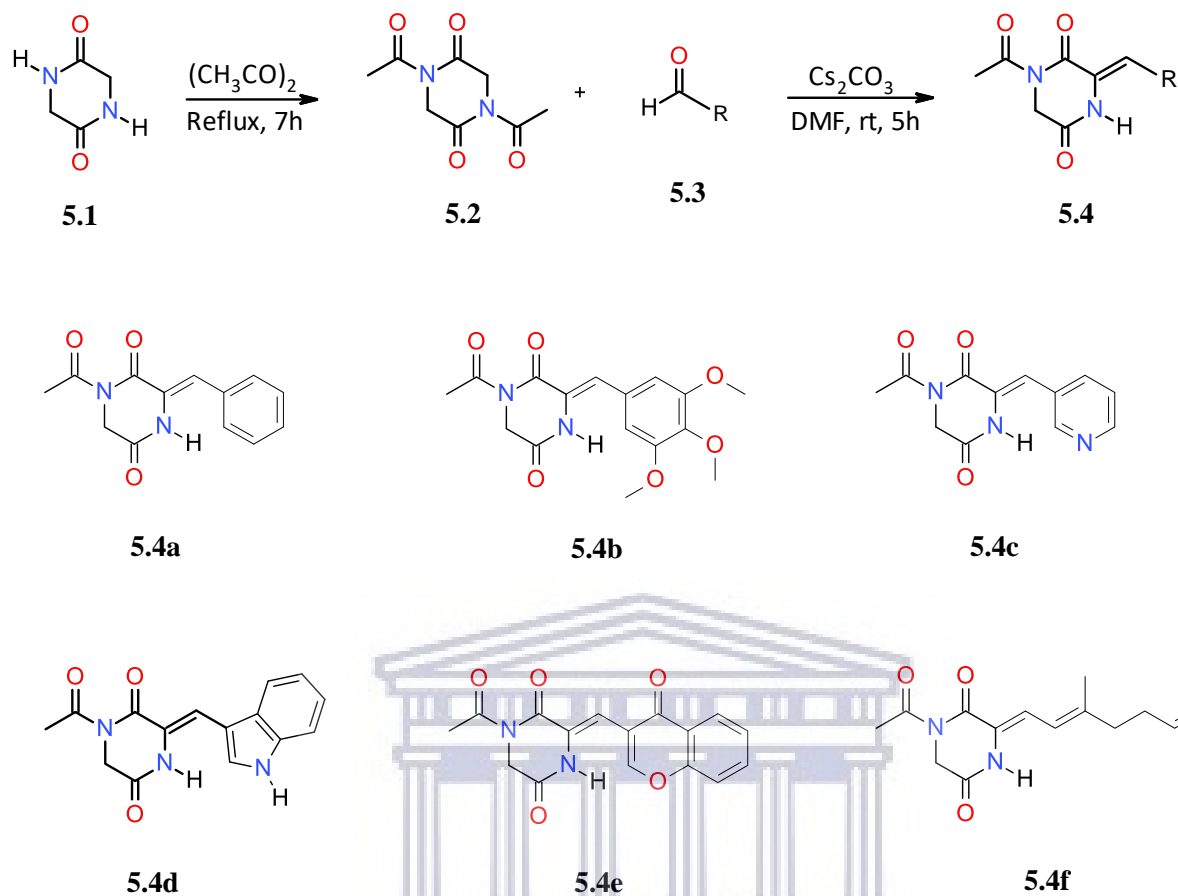
Figure 5.2 The design of sargaquinoic acid analogues.

Therefore, we considered replacing the quinone moiety in SQA with diketopiperazine, barbiturate and theophylline scaffolds as isosteres of the quinone group (Figure 5.2) while shortening the prenyl chain. Shortening the chain was considered because it is more accessible compared to SQA that contains a carboxyl group on its chain. In addition, the prenyl chain present in novobiocin (**2.32**) and its derivative DHN2 (**2.35**) is necessary for the activity (Burlison et al., 2006). We also investigated replacing the prenyl side chains with selected aromatic moieties to examine their biological activities.

5.2.2 Synthesis of diketopiperazine, barbituric acid and theophylline analogues

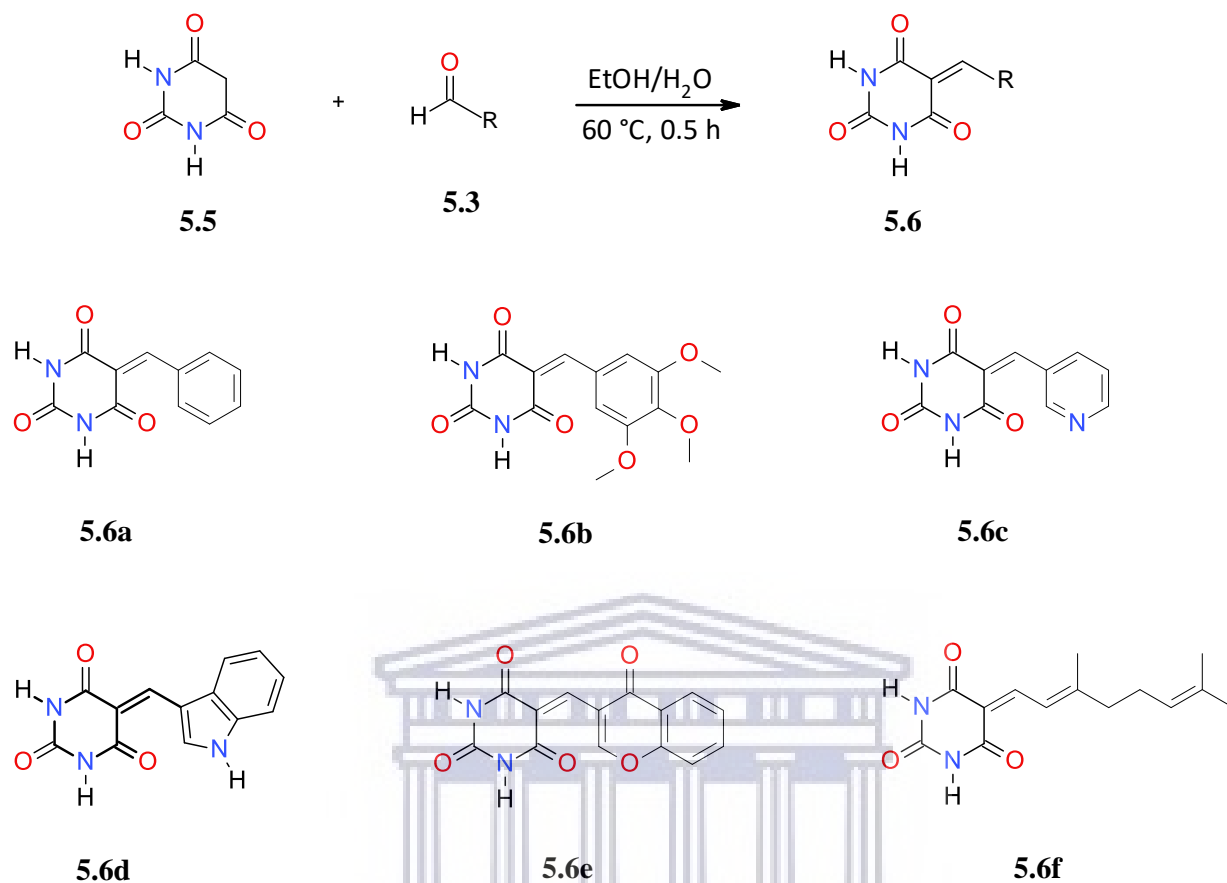
The synthesis of the diketopiperazine derivatives (Scheme 5.1) started with acetylation of the commercially available glycine anhydride (**5.1**) with acetic anhydride under reflux to obtain 1,4-diacetylpiperazine-2,5-dione (**5.2**) in excellent yield (Sasikumar et al., 2016). This was followed by condensation of substituted aldehydes **5.3(a-f)** with **5.2** at ambient temperature, under basic conditions to afford the products **5.4(a-f)** (Liao et al., 2014). The mechanism of reaction is a standard aldol condensation but with a loss of an acetyl group, this general mechanism has been discussed in chapter 4. The compounds were obtained in yields ranging from 66-97 % except for **5.4e** and **5.4f** with 18 and 37% yield respectively.

UNIVERSITY of the
WESTERN CAPE



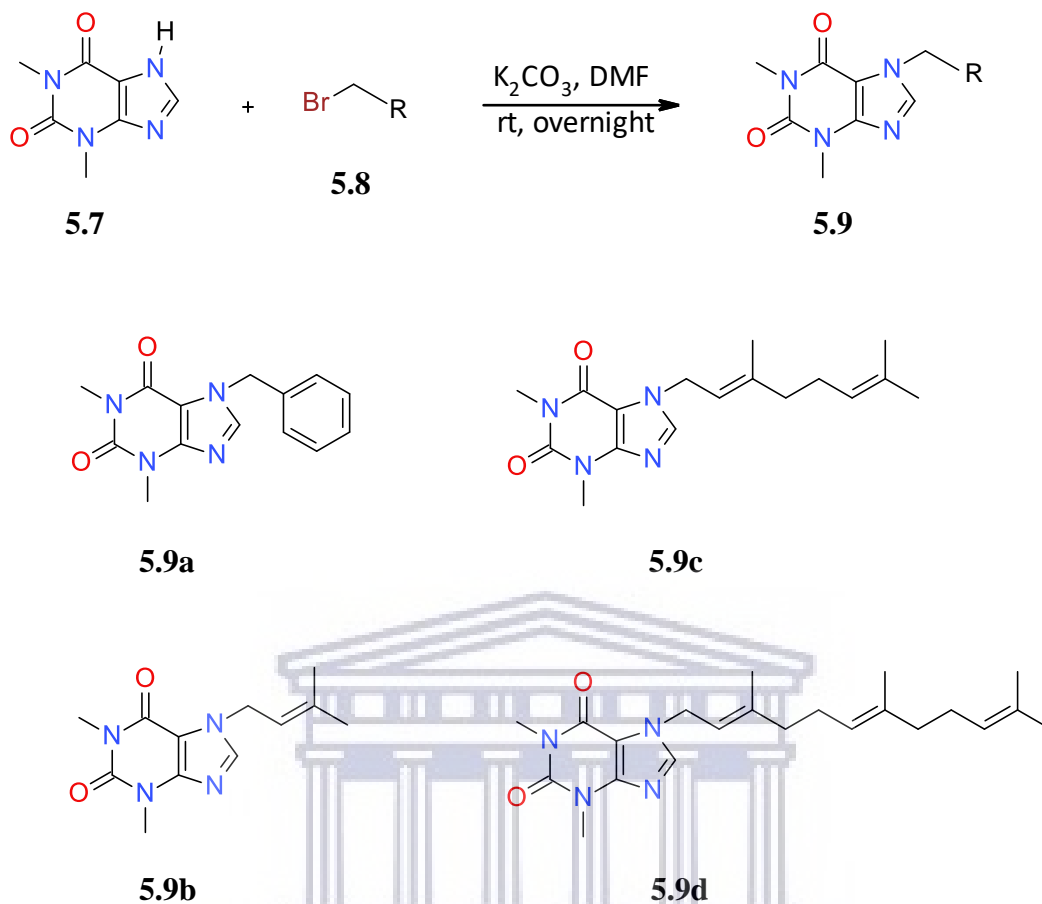
Scheme 5.1 Synthesis of 1-acetyl-3-arylidene-piperazine-2,5-dione derivatives.

The condensation of barbituric acid with substituted aldehydes (Scheme 5.2) was also achieved in a one-step reaction (Vieira et al., 2011) with yields between 87 and 99%.



Scheme 5.2 Synthesis of barbituric acid derivatives *via* Knoevenagel condensation.

The synthesis of theophylline derivatives was achieved by a nucleophilic substitution reaction of allyl halides with theophylline in the presence of K_2CO_3 in dry DMF (Scheme 5.3) (Bertrand et al., 2014). The products were obtained by precipitation in moderate (5.9b and 5.9d) to excellent (5.9a and 5.9c) yields. Where necessary, compounds were purified by column chromatography using EtOAc/ hexane as mobile phase.

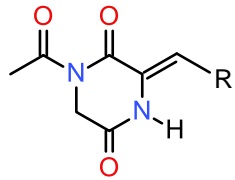
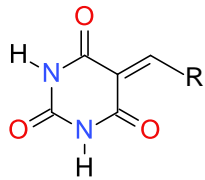
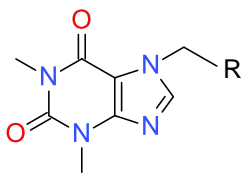


Scheme 5.3 Synthesis of prenylated theophylline derivatives.

5.2.3 Physical properties of the synthesized SQA analogues

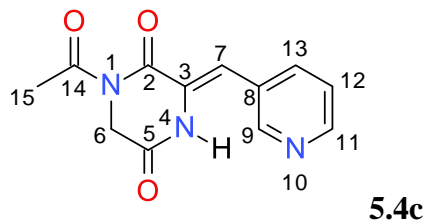
In the assessment of the physical properties of the synthesized compounds (Table 5.1), no particular trend was expected in the melting points for the diketopiperazine derivatives **5.4(a-f)** and the barbiturates **5.6(a-f)**. Although the barbiturates showed a higher melting point compared to the diketopiperazine derivatives. In contrast, the theophylline series **5.9(a-d)** demonstrated a consistent increase in melting points with an increase in the length of the prenyl chain. Compound **5.9d** displayed the lowest melting point range of 48-50 °C, thus accounts for its waxy property at ambient temperature (25 °C).

Table 5.1 Physical properties of the synthesized compounds.

Compounds	R	Appearance	Melting Point (°C)	Yield (%)
<div style="display: flex; justify-content: space-around; align-items: center;"> <div style="text-align: center;">  <p>5.4</p> </div> <div style="text-align: center;">  <p>5.6</p> </div> <div style="text-align: center;">  <p>5.9</p> </div> </div>				
5.4a	C ₆ H ₅	Light yellow powder	195-198	97
5.4b	C ₆ H ₂ (OCH ₃) ₃	Yellow powder	144-148	66
5.4c	C ₅ H ₄ N	Light yellow powder	193-196	71
5.4d	C ₈ H ₆ N	Yellow powder	246-250	69
5.4e	C ₉ H ₅ O ₂	Dark yellow powder	204-207	18
5.4f	C ₉ H ₁₅	Light yellow powder	127-131	37
5.6a	C ₆ H ₅	White powder	263-266	92
5.6b	C ₆ H ₂ (OCH ₃) ₃	Yellow powder	274-276	99
5.6c	C ₅ H ₄ N	Off white powder	282-286	87
5.6d	C ₈ H ₆ N	Yellow powder	>310	42
5.6e	C ₉ H ₅ O ₂	Light yellow powder	278-281	88
5.6f	C ₉ H ₁₅	Light yellow powder	164-168	90
5.9a	C ₆ H ₅	Fine white needles	159-160	95
5.9b	C ₄ H ₇	white crystalline solid	131-133	55
5.9c	C ₉ H ₁₅	Off white crystalline solid	92-96	98
5.9d	C ₁₄ H ₂₄	Light yellow waxy solid	48-50	60

5.2.4 Spectroscopic analysis of the compounds

The synthesized compounds were all characterized by NMR, IR and mass spectrometric analysis. A representative compound from each of these series was selected for a short spectroscopic discussion.



Compound **5.4c** was obtained as a light yellow powder and a protonated HR-ESIMS ion peak was recorded at m/z 246.0901 consistent with a molecular formula of $C_{12}H_{12}N_3O_3$. The 1H NMR spectrum (Figure 5.3) displayed eight distinct signals, at δ_H 10.6 (s, N-H), 3-pyridyl protons at δ_H 8.7 (d, 1H, $J = 2.0$ Hz), 8.5 (dd, 1H, $J = 4.8, 1.4$ Hz), 8.0 (dt, 1H, $J = 8.0, 1.6$ Hz), 7.4 (dd, 1H, $J = 7.9, 4.8$ Hz), a methine at δ_H 6.9 (s, 1H), methylene at δ_H 4.4 (s, 2H) and a methyl at δ_H 2.5 (s, 3H).

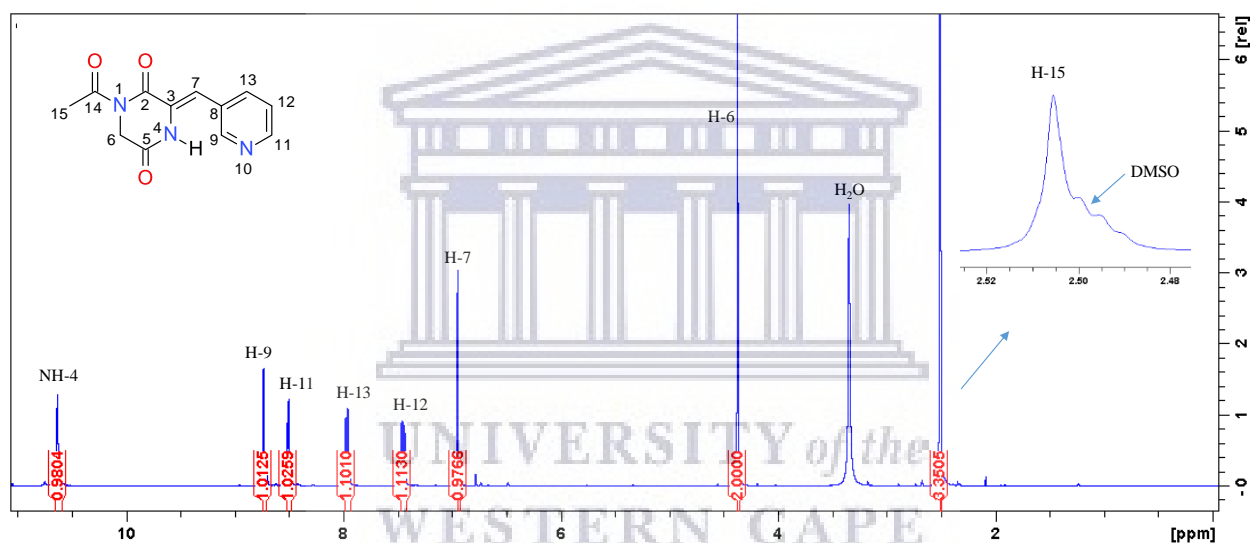


Figure 5.3 1H NMR spectrum of compound **5.4c** (400 MHz, $DMSO-d_6$).

The ^{13}C NMR spectrum (Figure 5.4) showed the expected twelve carbon signals, including signals at δ_C 172.3 (C-14), 164.7 (C-2) and 161.7 (C-5) due to the carbonyl resonances. The presence of the carbonyl group was confirmed by the presence of the infra-red band at 1688 cm^{-1} . The sp^3 methylene and methyl signals resonated at δ_C 46.2 (C-5) and 27.2 (C-15) respectively, while the remaining seven carbons signals were within the aromatic region.

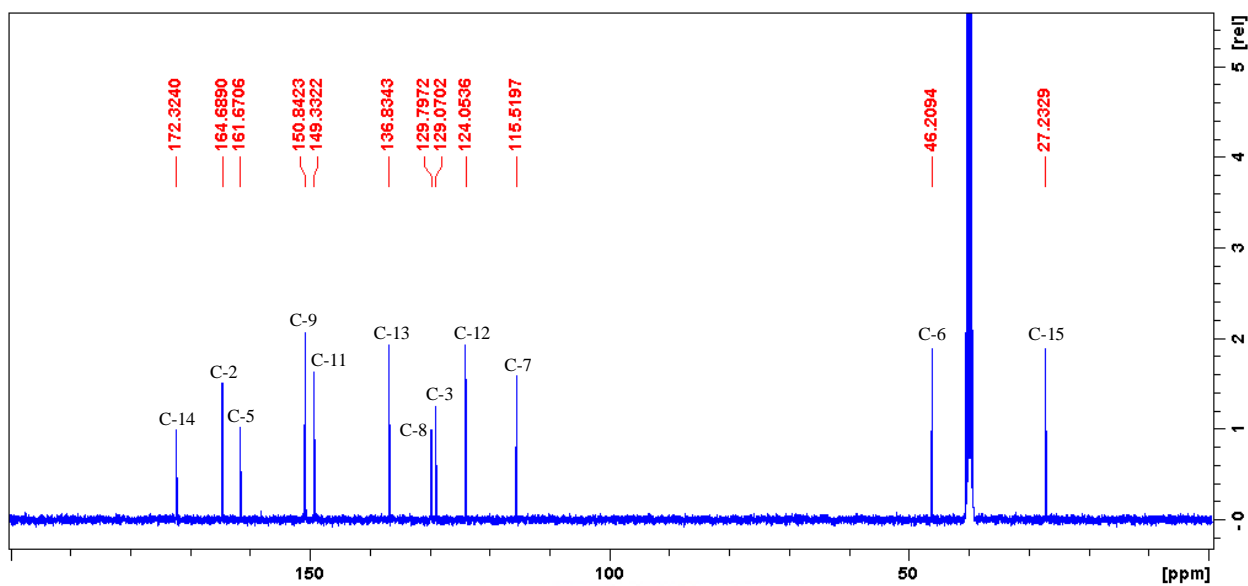


Figure 5.4 ^{13}C NMR spectrum of compound **5.4c** (100 MHz, DMSO-d_6).

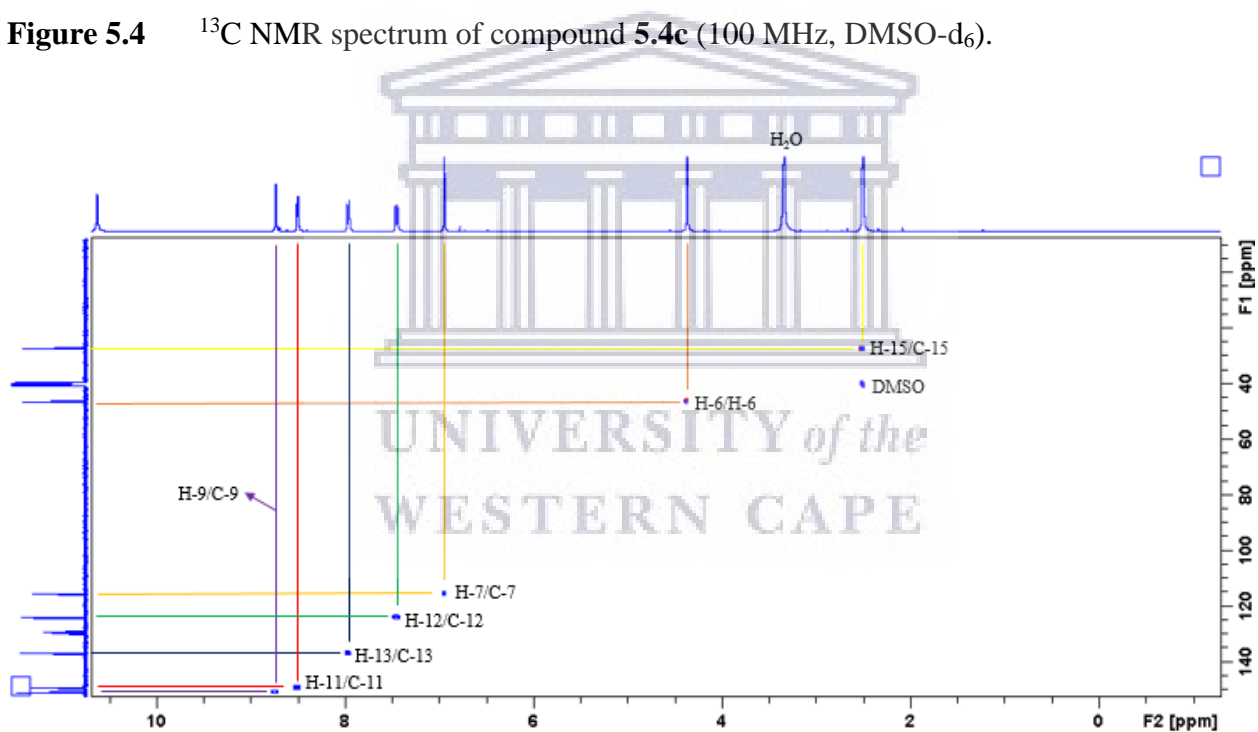


Figure 5.5 HSQC NMR spectrum of compound **5.4c** (400 MHz, DMSO-d_6).

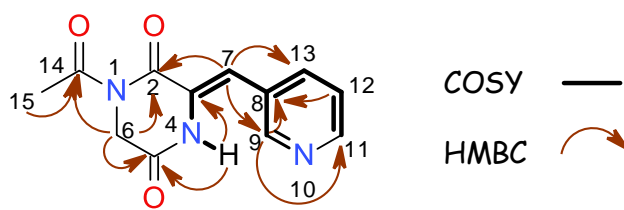


Figure 5.6 COSY and HMBC correlations of compound **5.4c**.

In the COSY spectrum, H-12 resonating at δ_H 7.45 shows correlations to H-11 and H-13 at δ_H 8.50 and 7.97 respectively (Figure 5.6). Similarly, H-13 at δ_H 7.97 displayed correlations to H-9 and H-11 at δ_H 8.73 and 8.50 respectively. COSY correlations were also observed between H-7 at δ_H 6.94 and NH-4 at δ_H 10.63. The HMBC correlations from H₂-6 at δ_H 4.37 to carbon resonances at δ_C 172.3, 164.7 and 161.7 confirmed the position of the carbonyl groups. The assignment of these functionalities were achieved with these proton correlations to carbon; H-15 at δ_H 2.51 to C-14 at δ_C 172.3, H-7 at δ_H 6.94 to C-2 at δ_C 164.7 and NH-4 at δ_H 10.63 to C-5 at δ_C 161.7. The HBMC correlation from protons H-9 and H-12 resonating at δ_H 8.73 and 7.45 respectively confirmed the assignment of the quaternary carbon C-8 at δ_C 129.8. Although a weak HMBC correlation was observed from NH-4 at δ_H 10.63 to C-3 at δ_C 129.1, this assignment was justified as it was the only unassigned resonance (Table 5.2).

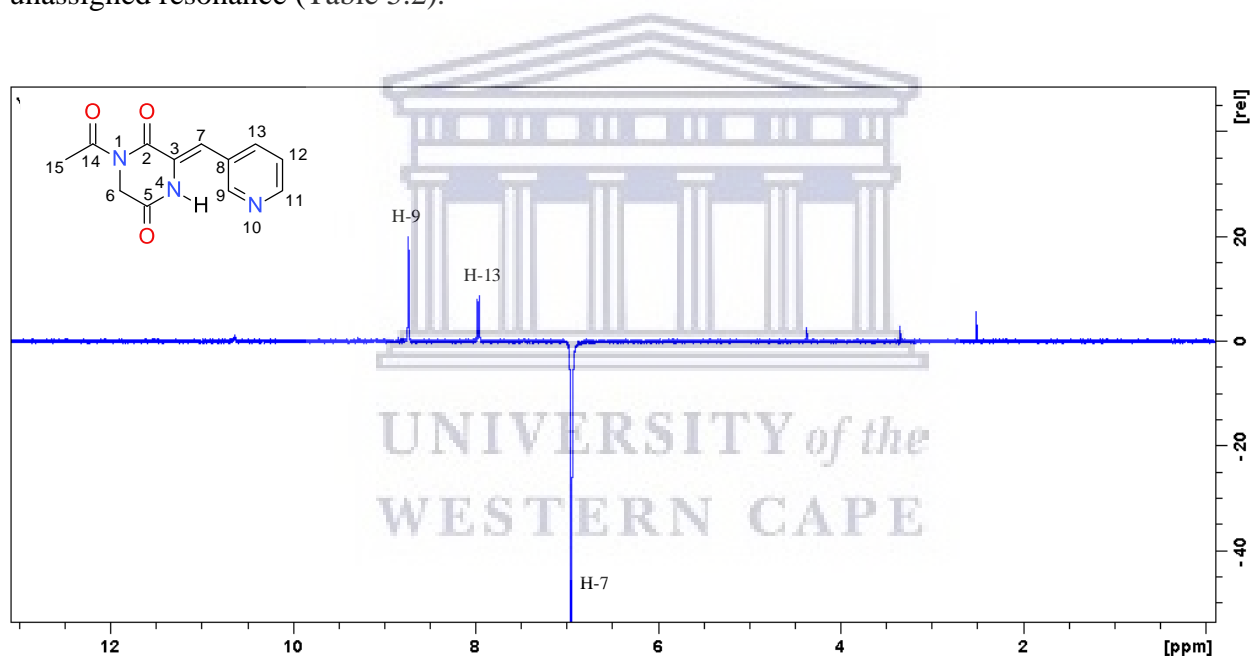
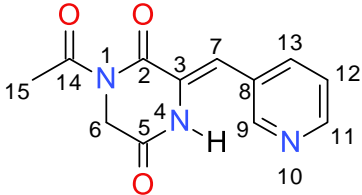


Figure 5.7 1D selective NOESY NMR spectrum of compound **5.4c**.

The 1D selective NOESY NMR spectrum presented in Figure 5.7 established NOE correlations from H-7 to H-9 and H-13 confirming their closeness in space. Correlation to NH-4 was not visible and therefore confirms that this compound has a *Z* geometry.

Table 5.2 NMR data for compound **5.4c** (400 MHz for ^1H and 100 MHz for ^{13}C , DMSO- d_6).


Position	δ_{C}	δ_{H} (mult., J , Hz)	COSY	HMBC
N-1	-	-	-	-
2	164.7	-	-	-
3	129.1	-	-	-
NH-4	-	10.63 (s, 1H)	H-7	C-3, C-5, C-6
5	161.7	-	-	-
6	46.2	4.37 (s, 2H)	-	C-14, C-5, C-2
7	115.5	6.94 (s, 1H)	NH-4	C-2, C-9, C-13
8	129.8	-	-	-
9	150.8	8.73 (d, $J = 2.0$, 1H)	-	C-11, C-13, C-8, C-7
N-10	-	-	-	-
11	149.3	8.50 (dd, $J = 4.8, 1.4$, 1H)	-	C-9, C-12, C-13
12	124.1	7.45 (dd, $J = 7.9, 4.8$, 1H)	H-11, H-13	C-11, C-8
13	136.8	7.97 (dt, $J = 8.0, 1.6$, 1H)	H-9, H-11	C-9, C-11, C-7
14	172.3	-	-	-
15	27.2	2.51 (s, 2H)	-	C-14

The characteristic ^1H NMR chemical shifts and carbon resonances were consistent for the 1-acetyl-3-ethylidene-piperazine-2,5-dione of this series of compounds. Even though different deuterated solvents were used, the proton chemical shift for H-15 ranged within $\delta_{\text{H}} 2.73 - 2.50$, (H-6) $\delta_{\text{H}} 4.51 - 4.44$ and NH-4 $\delta_{\text{H}} 12.08 - 8.00$ while the functionalities were the three most downfield signals in the ^{13}C -NMR spectrum. Also, these features were in agreement with the infra-red data within the range of $1695 - 1674 \text{ cm}^{-1}$ while the NH ranges between $3291 - 2916 \text{ cm}^{-1}$.

Compound **5.6e** was obtained as a light yellow powder and the HR-ESIMS data showed a protonated molecular ion peak at m/z 285.0476 $[\text{M} + \text{H}]^+$ and established a molecular formula of $\text{C}_{14}\text{H}_9\text{N}_2\text{O}_5$ (calculated for 285.0512). The ^1H NMR spectrum (Figure 5.8) showed the two distinctive amine signals at $\delta_{\text{H}} 11.46$ (s, NH-1) and 11.36 (s, NH-3), (IR band at 3371 cm^{-1}). This

was followed by the deshielded methine at δ_{H} 9.72 (d, 1H, $J = 0.9$) H-17, an olefinic signal at δ_{H} 8.43 (s, 1H) H-7 and finally are the four aromatic signals at δ_{H} 8.14 (dd, 1H, $J = 8.0, 1.5$) H-11, 7.89 (td, 1H, $J = 7.9, 1.7$) H-13, 7.76 (d, 1H, $J = 8.3$) H-14, 7.58 (td, 1H, $J = 7.6, 1.0$) H-12 displaying clear multiplicities.

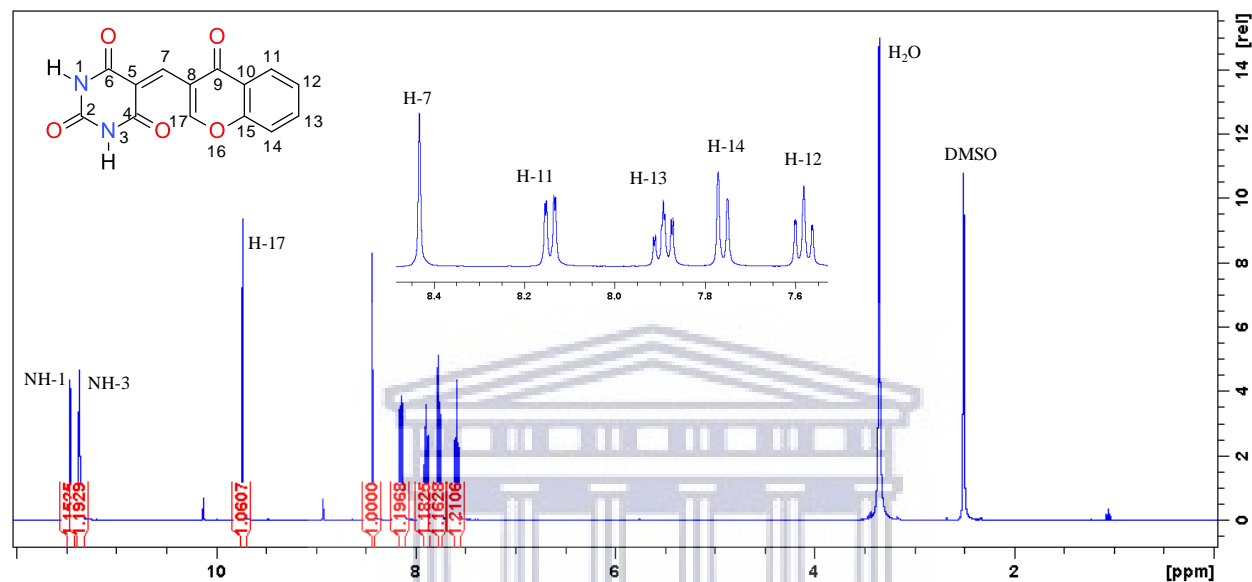


Figure 5.8 ¹H NMR spectrum of compound 5.6e (400 MHz, DMSO-d₆).

As expected the ¹³C NMR spectrum (Figure 5.9) revealed the four functionalities resonating downfield at δ_{C} 175.2 (C-9), 163.6 (C-6), 163.4 (C-4) and 162.8 (C-2) and infra-red band at 1684 cm^{-1} confirmed these functionalities. Although the unsaturated C-7 and C-17 at δ_{C} 144.8 and 150.6 respectively are both carrying an olefinic proton, C-17 recorded a higher resonance due to the electronegative effect of oxygen (O-16) directly bonded it.

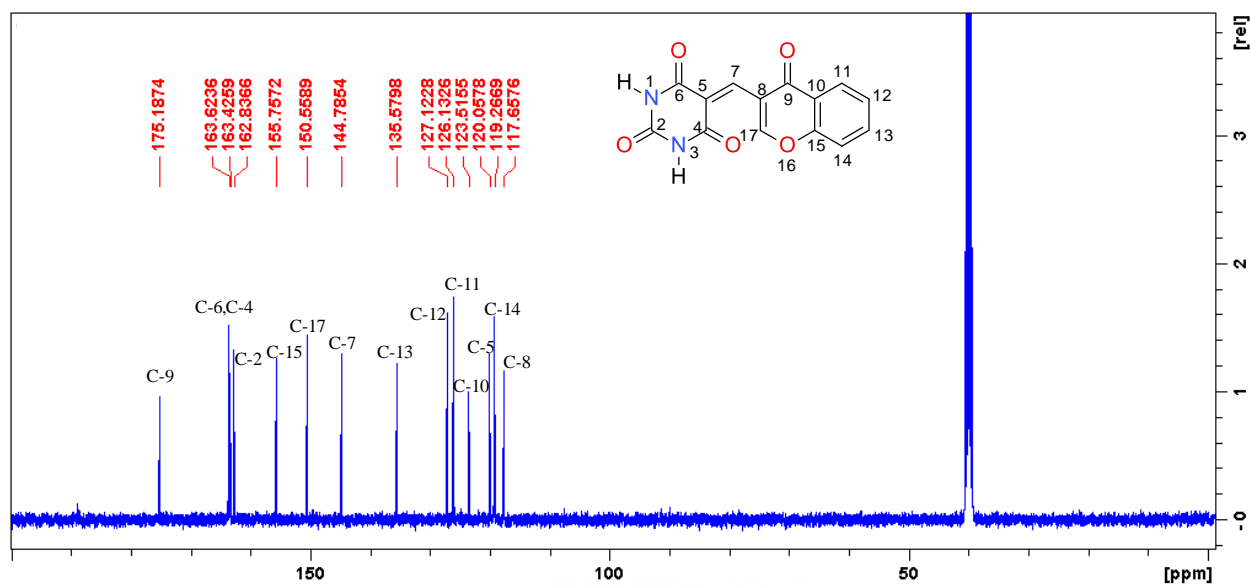


Figure 5.9 ^{13}C NMR spectrum of compound **5.6e** (100 MHz, DMSO-d_6).

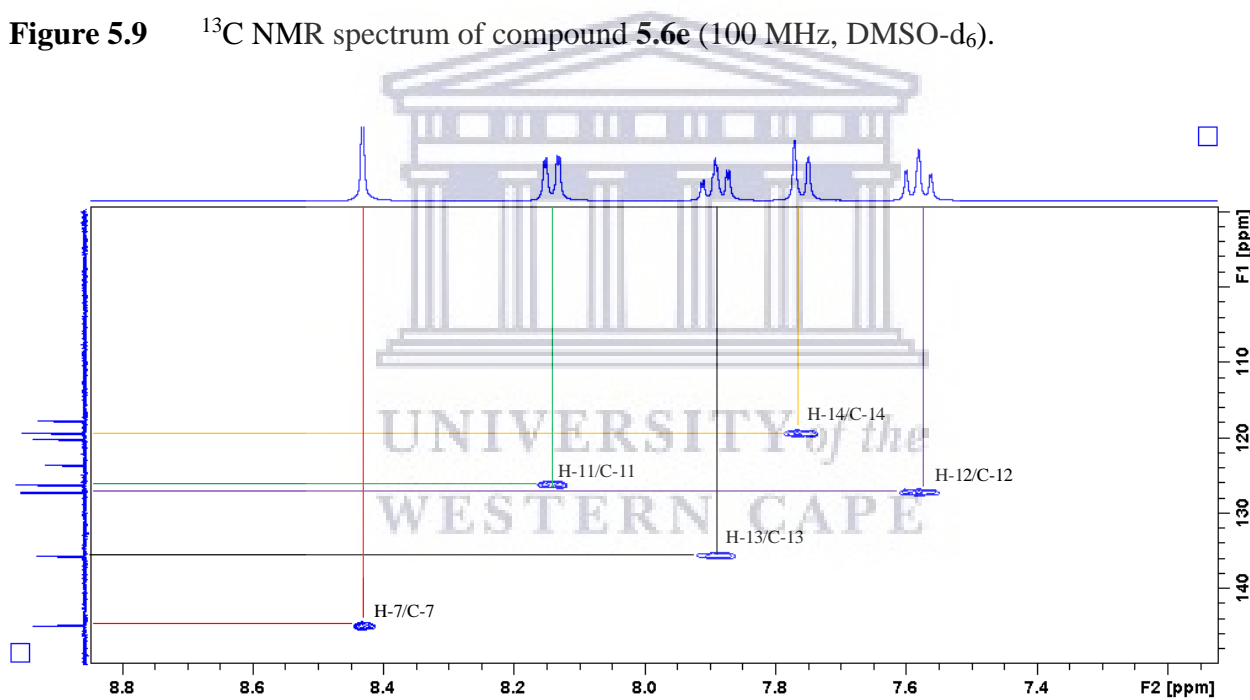


Figure 5.10 HSQC NMR spectrum of compound **5.6e** (400 MHz, DMSO-d_6) showing the aromatic region.

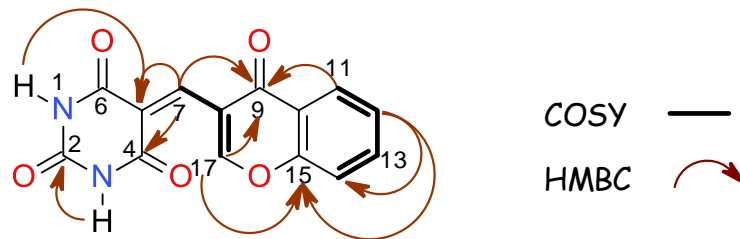


Figure 5.11 COSY and HMBC correlations of compound **5.6e**.

In the COSY data, $^1\text{H} - ^1\text{H}$ correlations were established between the aromatic signals at δ_{H} 7.58 (td, $J = 7.6, 1.0$, H-12), 8.14 (dd, $J = 8.0, 1.5$, H-11), 7.89 (td, $J = 7.9, 1.7$, H-13) and 7.76 (d, $J = 8.3$, H-14) (Figure 5.11). COSY correlation was also observed between H-7 and H-17 signals at δ_{H} 8.43 (s) and 9.72 (d, $J = 0.9$) respectively. HMBC correlations from proton signals at H-7, H-11 and H-17 confirmed the assignment C-9 resonating at δ_{C} 175.2, while the other functionalities at δ_{C} 163.4 (C-4) and 162.8 (C-2) were confirmed by correlations from H-7 and NH-3 respectively (Table 5.3).

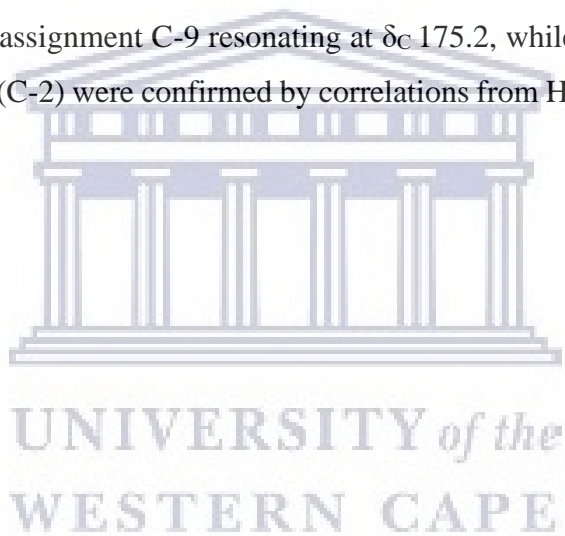
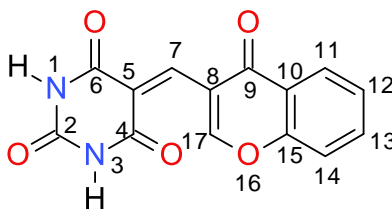
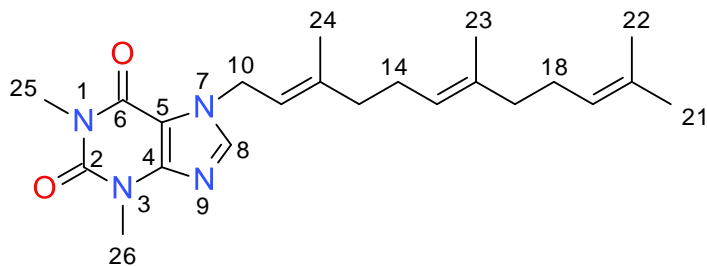


Table 5.3 NMR data for compound **5.6e** (400 MHz for ^1H and 100 MHz for ^{13}C , DMSO- d_6).


Position	δ_{C}	δ_{H} (mult., J , Hz)	COSY	HMBC
NH-1	-	11.46 (s, 1H)	-	C-5
2	162.8	-	-	-
NH-1	-	11.36 (s, 1H)	-	C-2, C-5
4	163.4	-	-	-
5	120.1	-	-	-
6	163.6	-	-	-
7	144.8	8.43 (s, 1H)	H-17	C-4, C-5, C-8, C-9
8	117.7	-	-	-
9	175.2	-	-	-
10	123.5	-	-	-
11	126.1	8.14 (dd, $J = 8.0, 1.5$, 1H)	H-12	C-9, C-13, C-15
12	127.1	7.58 (td, $J = 7.6, 1.0$, 1H)	H-11, H-13, H-14	C-10, C-11, C-13, C-14, C-15
13	135.6	7.89 (td, $J = 7.9, 1.7$, 1H)	H-11	11, 15
14	119.3	7.76 (d, $J = 8.3$, 1H)	H-13	C-9, C-10, C-12, C-15
15	155.8	-	-	-
O-16	-	-	-	-
17	150.6	9.72 (d, $J = 0.85$, 1H)	H-7	C-7, C-8, C-9, C-15,

In general, the characteristic features of the barbiturates **5.6(a-f)** were consistent. The proton signals for NH-1 and NH-3 ranged between δ_{H} 11.40 – 11.09 while the carbonyl resonances were within δ_{C} 167.1 – 150.8. These were consistent with the infra-red data which were 3371 – 3207 cm^{-1} for the amine and 1752 – 1718 cm^{-1} for the carbonyl functionalities. Although the NH signals were not visible in the ^1H NMR data for compound **5.8c**, the HR-ESIMS data displayed a protonated molecular ion peak m/z of 218.0536, calculated for $\text{C}_{10}\text{H}_8\text{N}_3\text{O}_3$, thus confirmed the compound.



5.9d

Compound **5.9d** was obtained as a light yellow waxy solid. HR-ESIMS presented a protonated molecular ion peak at m/z 385.2635 $[M+H]^+$ which is in agreement with a molecular formula of $C_{22}H_{33}N_4O_2$ (calculated for 385.2606). The 1H NMR spectrum (Figure 5.12) exhibited the characteristic olefinic, methylene and methyl resonances of a prenyl system. The most downfield signal at δ_H 7.52 (s, H-8) is due to the deshielding effect of nitrogen groups at positions 7 and 9, followed by olefinic proton at δ_H 5.42 (t, H-11). The remaining two olefinic protons H-15 and H-19 appeared to overlap and resonated at δ_H 5.05. The methylene; H₂-13, H₂-14, H₂-17 and H₂-18 appeared in a cluster upfield while H₂-10 at δ_H 4.91(d) was more downfield field due to electronegative effect of N-7. Also prominent are the 1,3-dimethyl signals at δ_H 3.56 (s, H₃-26) and δ_H 3.39 (s, H₃-25) while H₃-24 and H₃-23 resonated at δ_H 1.77(s) and 1.66(s) respectively. The two-terminal methyl signals of the prenyl chain (H₃-21 and H₃-22) appeared as a single at δ_H 1.56 and integrated to approximately six protons but the intensity of this peak is about the same level as H₃-25 and H₃-26 which was expected to almost double.

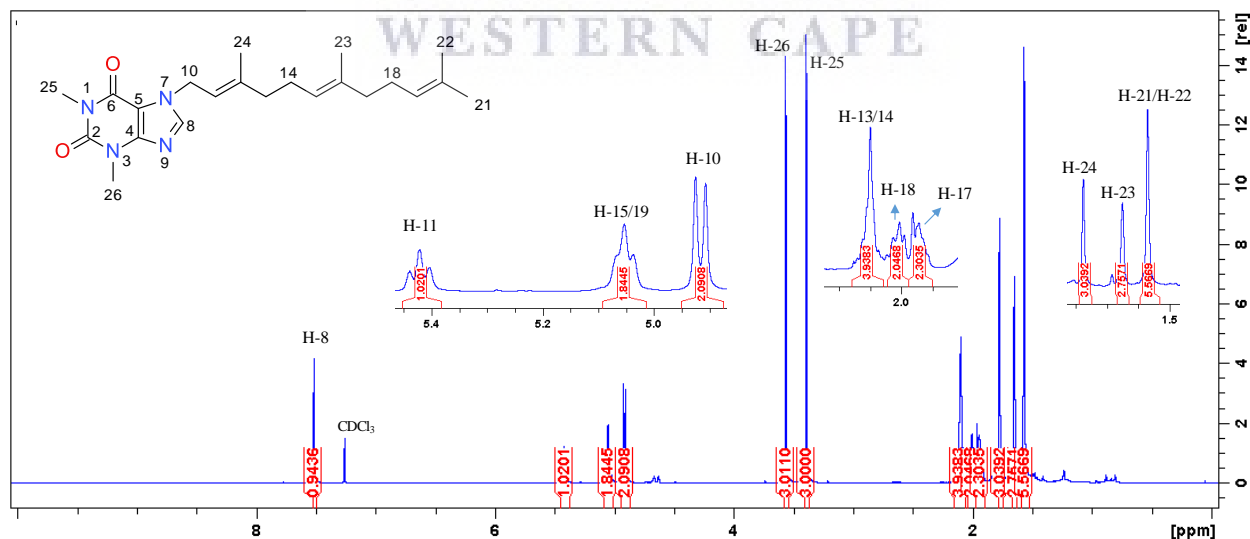


Figure 5.12 1H NMR spectrum of compound **5.9d** (400 MHz, $CDCl_3$).

The ^{13}C NMR spectrum (Figure 5.13) presented all the anticipated signals, the two functionalities were visible at δ_{C} 155.3 (C-6) and 151.7 (C-2). In confirmation of that is the Infra-red band at 1695 cm^{-1} . The methyl and methylene sp^3 hybridized carbon moieties were all evident upfield ranging between δ_{C} 45.0 – 16.0 while the sp^2 hybridized carbons were all downfield.

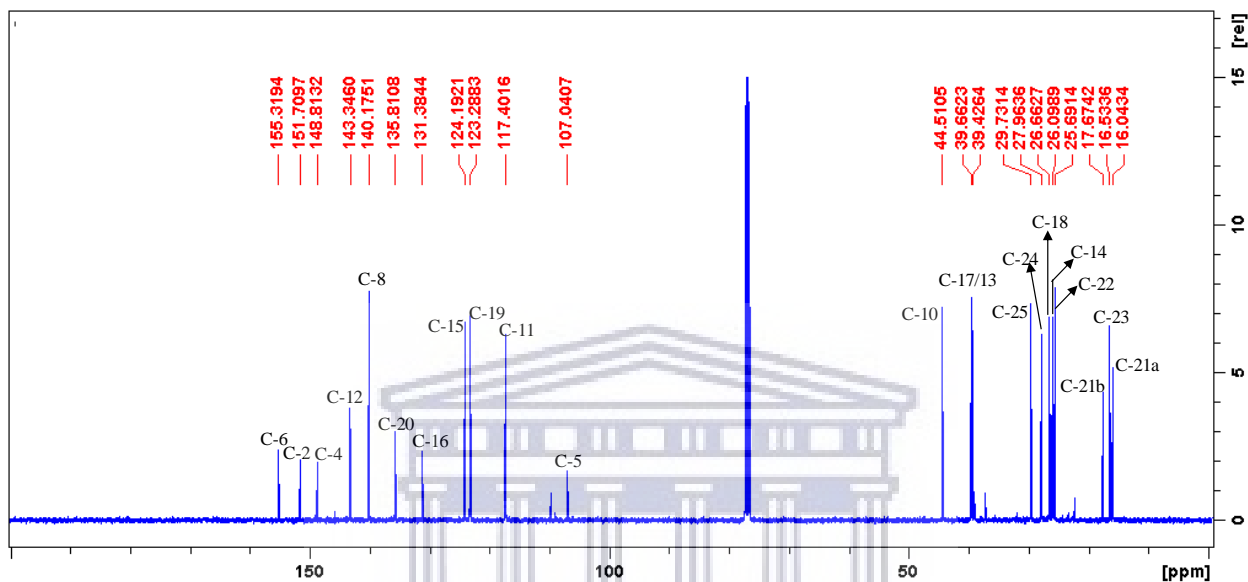


Figure 5.13 ^{13}C NMR spectrum of compound **5.9d** (100 MHz, CDCl_3).

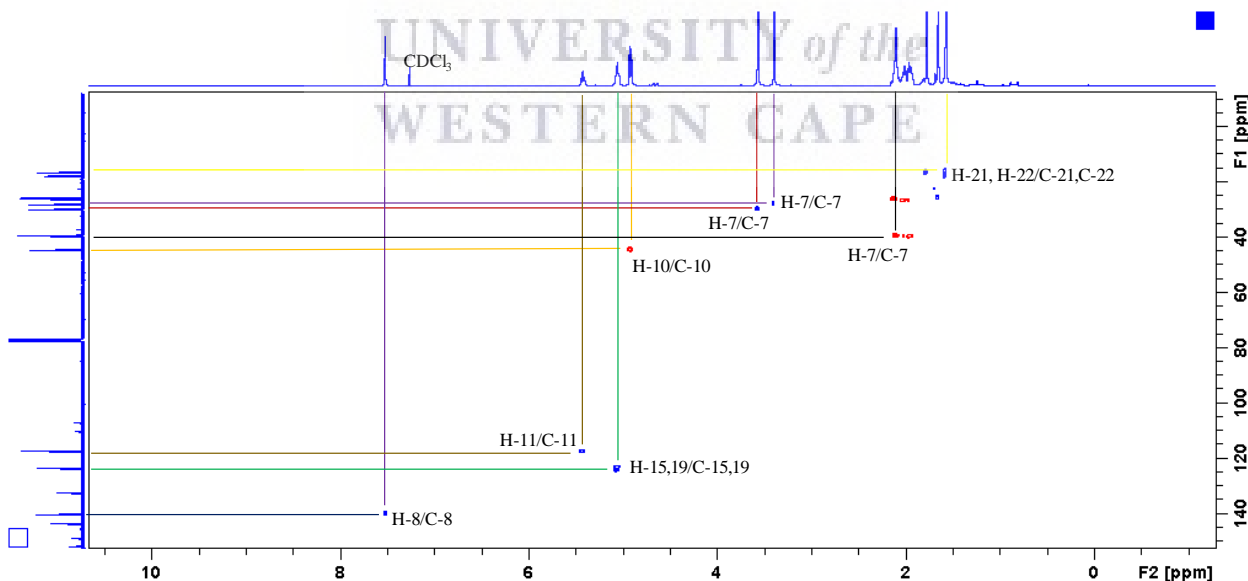


Figure 5.14 HSQC NMR spectrum of compound **5.9d** (400 MHz, CDCl_3) showing some of the $^1\text{H} - ^{13}\text{C}$ correlations.

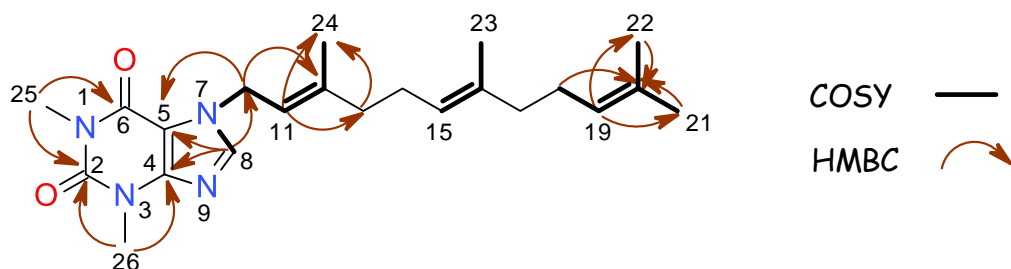


Figure 5.15 COSY and HMBC correlations of compound **5.9d**.

The COSY NMR experiment showed correlations between H₂-10 at δ_{H} 4.91 (d, $J = 7.2$) to protons resonating at δ_{H} 7.52 (s, H-8), 5.42 (t, $J = 7.2$, H-11) and 1.77 (s, H₃-24). The overlapping signals at δ_{H} (5.05, m) assigned H-15 and H-19 correlated to protons at δ_{H} 1.65 (s, H₃-23) and δ_{H} 1.56 (s, H₃-21, and H₃-22). The HMBC correlations from H-8 at δ_{H} 7.52 to C-10 at δ_{C} 44.5 and H-10 at δ_{H} to C-5 at δ_{C} 107.0 confirmed the attachment of the prenyl chain to the purine ring. HMBC correlation from H₃-25 at δ_{H} 3.39 confirmed the assignment of the C-6 carbonyl group at δ_{C} 155.3, while H₃-26 at δ_{H} 3.56 confirmed the second carbonyl group C-2 at δ_{C} 151.7.

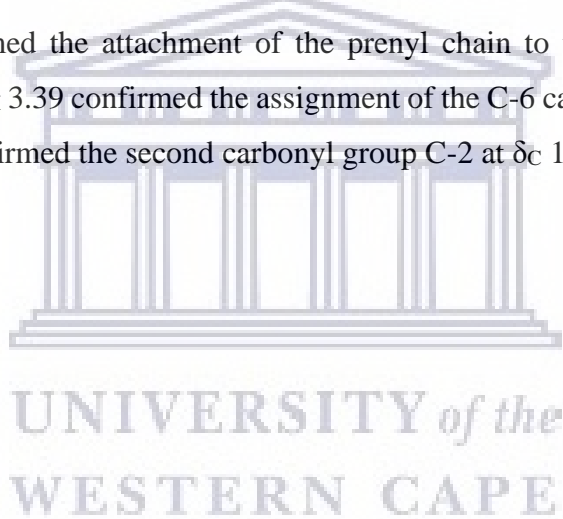


Table 5.4 NMR data for compound **5.9d** (400 MHz for ^1H and 100 MHz for ^{13}C , CDCl_3).

Position	δ_{C}	δ_{H} (mult., J , Hz)	COSY	HMBC
N-1	-	-	-	-
2	151.7	-	-	-
N-3	-	-	-	-
4	148.8	-	-	-
5	107.0	-	-	-
6	155.3	-	-	-
N-7	-	-	-	-
8	140.2	7.52 (s, 1H)	H-10	C-4, C-5, C-6, C-10
N-9	-	-	-	-
10	44.5	4.91 (d, $J = 7.2$, 2H)	H-8, H-11, H-24	C-5, C-8, C-11, C-12
11	117.4	5.42 (t, $J = 7.2$, 1H)	H-10, H-24	C-10, C-13, C-24
12	143.3	-	-	-
13	39.4	2.11 (m, 2H)	-	C-11, C-12, C-14, C-24
14	26.1	2.11 (m, 2H)	-	C-13, C-15, C-17
15	124.2	5.05 (m, 1H)	H-23	C-14, C-17
16	131.4	-	-	-
17	39.7	1.94 (m, 2H)	-	C-15, C-18, C-20
18	26.7	2.01 (m, 2H)	H-23	C-15, C-16, C-17, C-20
19	123.3	5.05 (m, 1H)	H-21, H-22	C-20, C-21
20	135.8	-	-	-
21	16.0	1.56 (s, 3H)	-	C-19, C-20
22	17.7	1.56 (s, 3H)	-	C-19, C-20
23	25.7	1.66 (s, 3H)	H-15, H-18	C-15, C-16, C-17
24	16.5	1.77 (s, 3H)	H-10	C-11, C-12, C-13
25	28.0	3.39 (s, 3H)	-	C-2, C-6
26	29.7	3.56 (s, 3H)	-	C-2, C-4

Although the two-terminal methyl groups at positions 21 and 22 appeared to be in the same chemical environment from the proton data (Figure 5.12), the HSQC and HMBC data suggest otherwise. The HSQC data (Figure 5.14) displayed $^1\text{H} - ^{13}\text{C}$ correlations from δ_{H} 1.56 to δ_{C} 16.0 and 17.7. Similarly, HMBC correlations were observed from H-19 at δ_{H} 5.05 to these two carbon resonances (Table 5.4).

5.2.5 Biological evaluation

5.2.5.1 *In vitro* antiproliferative studies

The synthesized compounds were evaluated for activity against HCC70 breast cancer cells at a single point concentration of 25 μM . The theophylline series **5.9(a-d)** (Table 5.5) appeared to have the highest activity followed by the diketopiperazines series **5.4(a-f)**, although the best activity was recorded for geranyl diketopiperazine **5.4f**. Comparing the diketopiperazines **5.4(a-f)** and the barbiturates **5.6(a-f)** since both series had the same substitutions on their scaffold, benzylidene diketopiperazine **5.4a** and geranyl diketopiperazine **5.4f** displayed notably better activity over benzylidene barbituric acid **5.6a** and geranyl barbituric acid **5.6f** respectively.



Table 5.5 Percentage cell viability relative to DMSO at 25 μM of synthesized compounds against HCC70 cancer cells.

Compounds	R	% Viability at 25 (μM) ^a
5.4a	C ₆ H ₅	43.91 \pm 0.87
5.4b	C ₆ H ₂ (OCH ₃) ₃	90.55 \pm 4.87
5.4c	C ₅ H ₄ N	83.28 \pm 4.53
5.4d	C ₈ H ₆ N	98.66 \pm 1.34
5.4e	C ₉ H ₅ O ₂	97.70 \pm 2.41
5.4f	C ₉ H ₁₅	37.28 \pm 0.93
5.6a	C ₆ H ₅	93.47 \pm 6.84
5.6b	C ₆ H ₂ (OCH ₃) ₃	75.57 \pm 5.76
5.6c	C ₅ H ₄ N	96.79 \pm 4.09
5.6d	C ₈ H ₆ N	66.51 \pm 0.75
5.6e	C ₉ H ₅ O ₂	88.15 \pm 2.49
5.6f	C ₉ H ₁₅	72.94 \pm 1.30
5.9a	C ₆ H ₅	46.65 \pm 1.58
5.9b	C ₄ H ₇	81.87 \pm 4.27
5.9c	C ₉ H ₁₅	64.78 \pm 1.03
5.9d	C ₁₄ H ₂₄	43.82 \pm 1.94

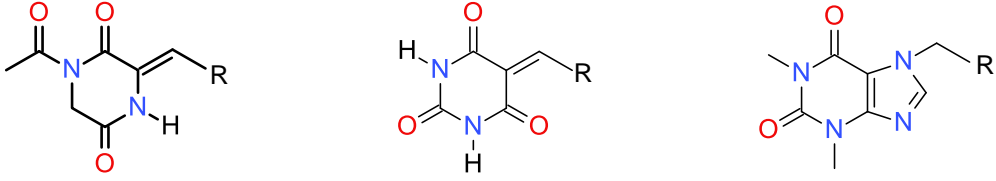
^a Cell viability relative to DMSO (%) \pm standard error against HCC70 cells. The compounds selected for further studies were highlighted.

To determine the IC₅₀ values, compounds **5.4f**, **5.6f**, **5.9a**, **5.9b**, **5.9c** and **5.9d** were selected for further biological evaluation. Even though geranyl barbituric acid **5.6f** was not the most active in its group, it was selected due to its geranyl side chain. The four purine derivatives were also selected to examine the trend in antiproliferative properties and the effect of increase in length of the prenyl side chain on this scaffold.

The activity of the selected compounds were further investigated against three cancer cell lines; HeLa, MDA-MB-231, HCC70 and MCF-12A normal cells (Table 5.6). In general, the compounds were non-toxic to normal mammary epithelial cells except purine geranyl **5.9d** that displayed weak antiproliferative activity. Compared to SQA and the positive control paclitaxel, these compounds exhibited some discrimination between normal cells and cancer cells. The prenylated compounds geranyl diketopiperazine **5.4f** manifested weak antiproliferative activity against the three cancer cells while geranyl barbituric acid **5.6f** displayed a weak antiproliferative activity against HCC70 cells only. The compounds selected from the diketopiperazine derivatives and barbiturates did not display improved antiproliferative activity over SQA. Although the prenyl purine **5.9b** was selective to HeLa cells, it only displayed weak antiproliferative activity with IC_{50} value of 75.1 μ M. On the other hand, geranyl purine **5.9c** was not just selective to HeLa cells but also showed good activity with an IC_{50} value of 6.6 μ M (Figure 5.16).

Geranyl purine **5.9d** exhibited the most potent activity against HeLa cells, exhibiting an IC_{50} value of 1.4 μ M and moderate against HCC70 cells (Figure 5.17). The theophylline derivatives compound **5.9c** and **5.9d** showed improvement over SQA in terms of antiproliferative activity and selectivity. In addition, compound **5.9a** was non-toxic to all the cell lines and it is the only selected compound without a prenyl chain. This suggests that the prenyl side chain has some effect on antiproliferative activity. Furthermore, an increase in antiproliferative activity was observed with an increase in the length of the prenyl chain. In support of this observation, it was also reported that the prenyl side chain of derrubone (**2.36**), a natural product natural Hsp90 inhibitor is also necessary for the activity (Hastings et al., 2008).

Table 5.6 IC₅₀ values of the selected compounds.

													
		5.4				5.6				5.9			
Compounds	R	IC ₅₀ (μM) ^a											
		HeLa	MDA-MB-231	HCC70	MCF-12A								
5.4f	C ₉ H ₁₅	70.4 ± 4.78	71.2 ± 2.81	80.5 ± 2.95	NT								
5.6f	C ₉ H ₁₅	NT	NT	72.8 ± 1.81	NT								
5.9a	C ₆ H ₅	NT	NT	NT	NT								
5.9b	C ₄ H ₇	75.1 ± 9.83	NT	NT	NT								
5.9c	C ₉ H ₁₅	6.6 ± 1.36	NT	NT	NT								
5.9d	C ₁₄ H ₂₄	1.4 ± 1.32	79.5 ± 89.74	42.1 ± 1.11	67.3 ± 2.24								
SQA	-	27.5 ± 2.14	14.7 ± 2.81	NT	32.8 ± 3.91								
Paclitaxel (nM)	-	72.2 ± 1.11	2.2 ± 1.06	3.4 ± 1.01	6.0 ± 1.16								

^a IC₅₀ values were indicated as mean ± standard error. Each data represents three different experiments performed in triplicate and IC₅₀ values greater than 250 μM were recorded as non-toxic (NT).

UNIVERSITY of the
WESTERN CAPE

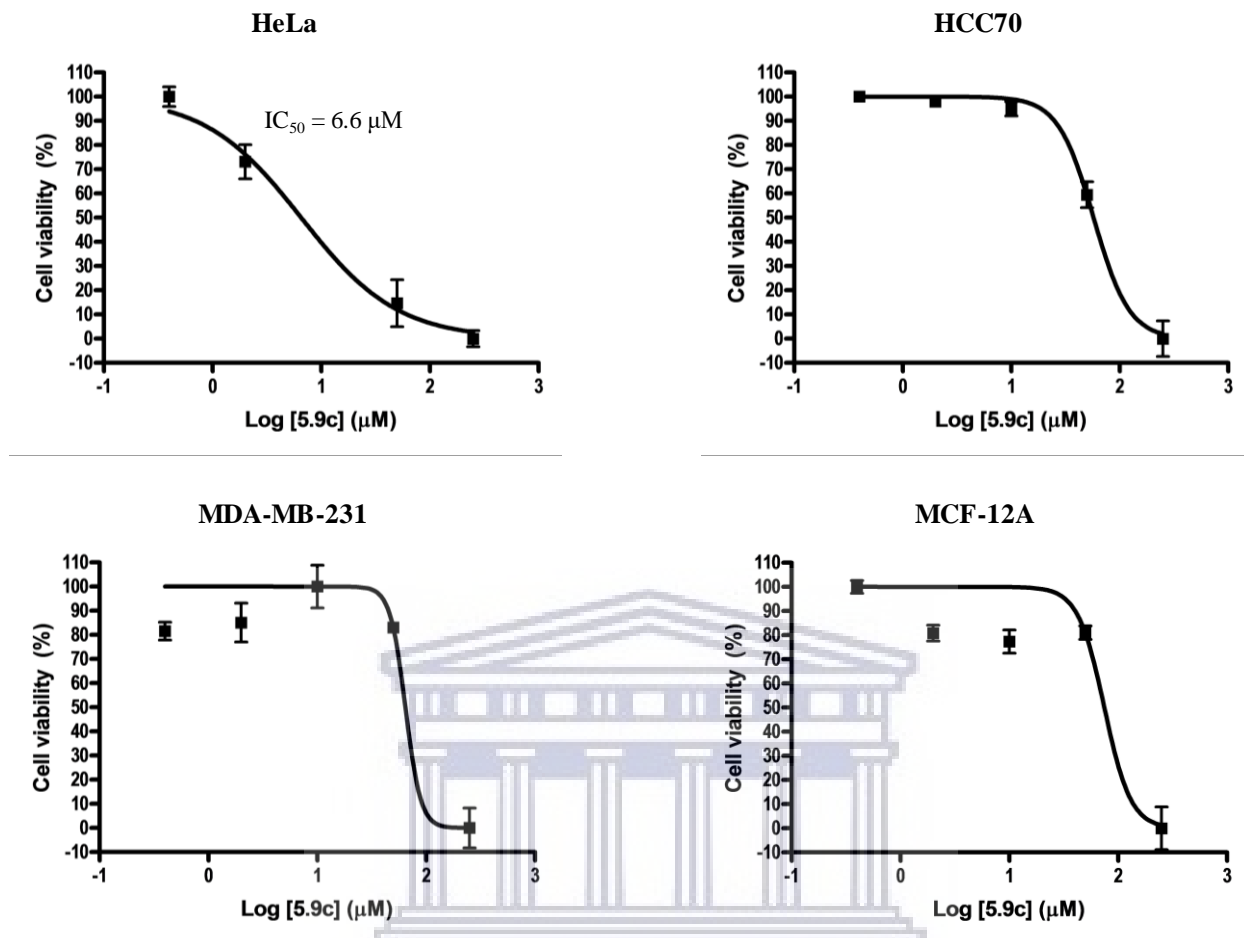


Figure 5.16 Non-linear regression curves for the antiproliferative activities of compound **5.9c** against the cell lines. IC₅₀ values greater than 250 μM were recorded as non-toxic.

UNIVERSITY of the
WESTERN CAPE

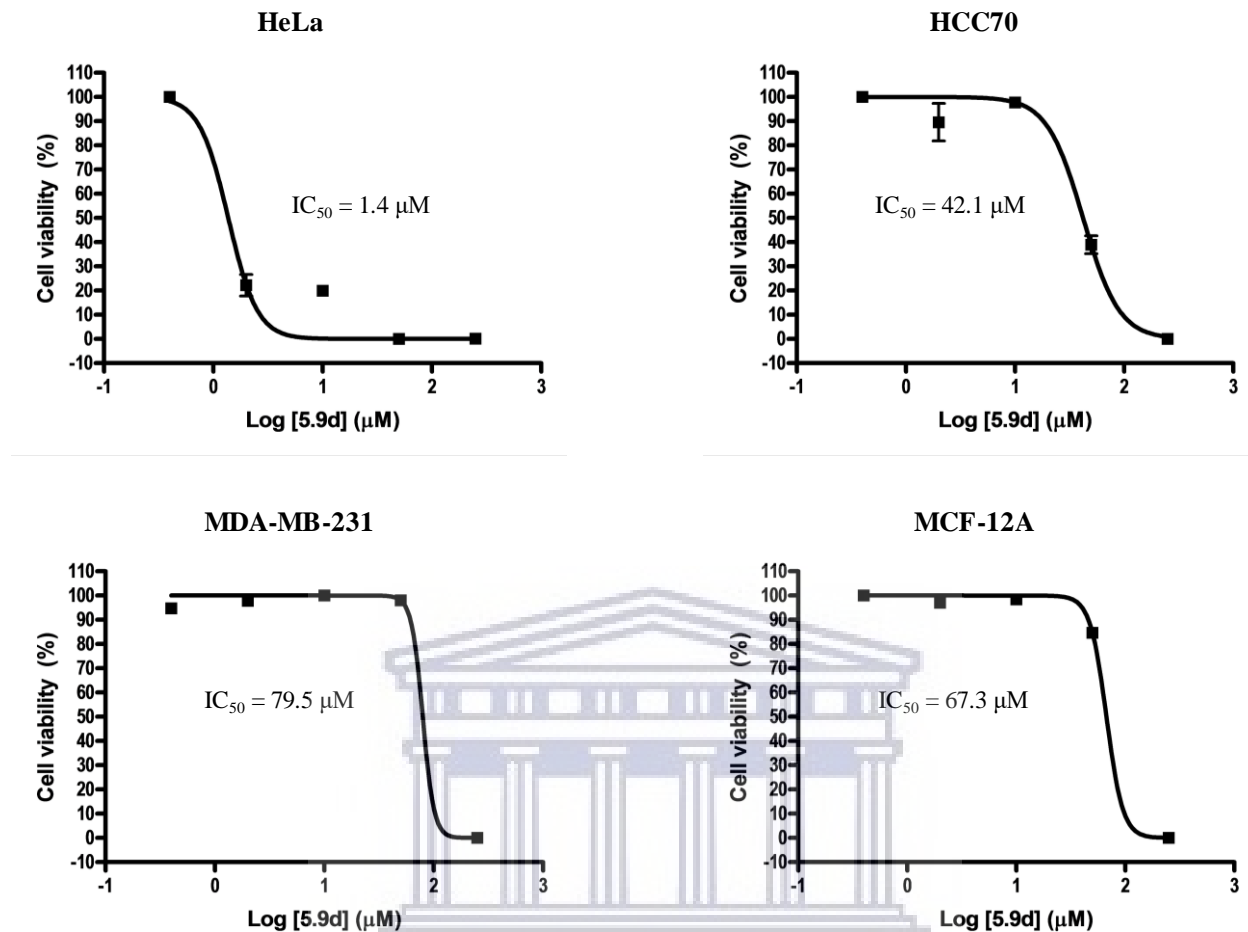


Figure 5.17 Non-linear regression curves for the antiproliferative activities of compound 5.9d against the cell lines.

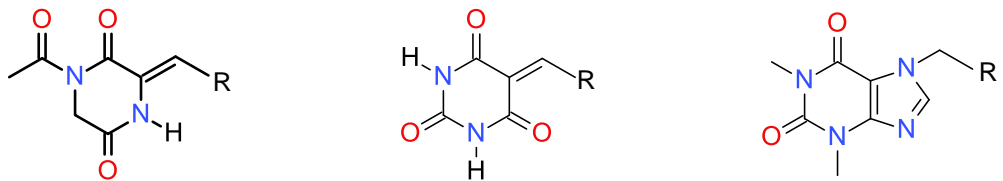
5.2.5.2 *In silico* predictions of the physicochemical and drug-likeness properties

The computed molecular properties of the synthesized compounds presented in Table 5.7 were obtained online from the Molinspiration Cheminformatics server (<http://www.molinspiration.com/cgi-bin/properties>). In the evaluation of the predicted parameters, compounds in both diketopiperazine 5.4 and barbituric acid 5.6 series recorded miLogP (octanol/water partition coefficient) values of <1 which is hydrophilic except for geranyl diketopiperazine 5.4f and geranyl barbituric acid 5.6f that recorded less hydrophilic values of 2.64 and 2.22 respectively. The purine series 5.9 exhibited an almost uniform increase in miLogP values with increase in prenyl chain length showing an increase in lipophilicity, this trend is also consistent with the IC₅₀ values recorded against HeLa cells as shown in Table 5.6. Although the

values were all within the required limit ($\text{miLogP} \leq 5$), a value of 5.37 was obtained for farnesyl purine **5.9d** which is slightly higher than the accepted limit of 5. Despite the logP limit violation displayed by **5.9d**, it was within the acceptable limit for the total number of violations not exceeding one according to Lipinski's rules of five. This is an indication of good oral bioavailability (Lipinski et al., 1997). Regarding the topological polar surface area (TPSA) and other parameters necessary for drug absorption, the values obtained showed that the compounds are within the recommended limit (Table 5.7) (Ertl et al., 2000, Verma, 2012).



Table 5.7 *In silico* physicochemical properties and drug-likeness of the synthesized compounds.

									
<div style="display: flex; justify-content: space-around;"> <div style="text-align: center;">5.4</div> <div style="text-align: center;">5.6</div> <div style="text-align: center;">5.9</div> </div>									
Compounds	R	miLogP	TPSA	MW	n-ON	n-OHNH	n-violations	n-ROTB	MV
5.4a	C ₆ H ₅	0.95	66.48	244.25	5	1	0	1	216.12
5.4b	C ₆ H ₂ (OCH ₃) ₃	0.58	94.18	334.33	8	1	0	4	292.75
5.4c	C ₅ H ₄ N	-0.46	79.37	245.24	6	1	0	1	211.96
5.4d	C ₈ H ₆ N	0.92	82.27	283.29	6	2	0	1	245.1
5.4e	C ₉ H ₅ O ₂	0.58	96.69	312.28	7	1	0	1	260.66
5.4f	C ₉ H ₁₅	2.64	66.48	290.36	5	1	0	4	282.83
5.6a	C ₆ H ₅	0.29	82.8	216.2	5	2	0	1	182.37
5.6b	C ₆ H ₂ (OCH ₃) ₃	-0.08	110.5	306.27	8	2	0	4	259.01
5.6c	C ₅ H ₄ N	-0.94	95.69	217.18	6	2	0	1	178.22
5.6d	C ₈ H ₆ N	0.44	98.59	255.23	6	3	0	1	211.35
5.6e	C ₉ H ₅ O ₂	0.1	113.01	284.23	7	2	0	1	226.92
5.6f	C ₉ H ₁₅	2.22	82.8	262.31	5	2	0	4	249.09
5.9a	C ₆ H ₅	1.66	61.84	270.29	6	0	0	2	239.28
5.9b	C ₄ H ₇	1.74	61.84	248.29	6	0	0	2	228.41
5.9c	C ₉ H ₁₅	3.58	61.84	316.4	6	0	0	5	305.99
5.9d	C ₁₄ H ₂₄	5.43	61.84	384.52	6	0	1	8	383.57

^a The parameters were determined using Molinspiration cheminformatics software. ^b The logarithm of the partition coefficient between n-octanol and water (miLogP ≤ 5). ^c Topological polar surface area (TPSA < 160 Å). ^d Molecular weight (MW < 500). ^e The number of hydrogen bond acceptors (n-HBA ≤ 10). ^f The number

of hydrogen bond donors (n-HBD ≤ 5). ^g The number of violations (n-violations ≤ 1). ^h The number of rotatable bonds (n-ROTB). ⁱ Molecular volume (MV).

5.2.5.3 Hsp90 docking studies

The molecular docking studies were conducted to investigate the binding affinities and interactions of the selected compounds with the N-terminal domain of Hsp90. These sargaquinoic acid analogues were designed to target the C-terminal domain, however, the crystal structure of the C-terminal domain is currently unavailable in literature because it has not been resolved. Hence, the N-terminal binding site was selected for this study. Hsp90 geldanamycin binding site co-crystallized with geldanamycin (PDB ID: 1YET) (Stebbins et al., 1997) selected for this study was obtained online from the RCSB Protein Data Bank (<https://www.rcsb.org/structure/1YET>). The docking simulations were performed using the Molecular Operating Environment (MOE) 2016.08 software. The receptor protein was prepared for docking by adding missing atoms and residues, and the co-crystallized ligand; geldanamycin was redocked into the active site to validate the method. The best-ranked RMSD value obtained was 0.48 Å from the position of the co-crystallized which was lower than the threshold value of 2 Å, thus confirming that the docking protocol was suitable for the predictions.

Table 5.8 The binding energies and intermolecular interactions of the compounds.

Compounds	R	Binding energy (Kcal/mol)	Amino acid residue involved in the interaction	Distance (Å)	Type of interaction
5.4f	C ₉ H ₁₅	-6.518	Thr A184 Thr B184 Met A98 Met A98	2.88 3.03 3.88 3.10	H - bonding H - bonding H - bonding H - bonding

			Asp A93	3.29	H - bonding
			Asn A51	3.03	H - bonding
5.6f	C ₉ H ₁₅	-6.307	Ser B52	3.29	H - bonding
			Thr B184	3.84	π - H stacking
			Asn A51	4.42	π - H stacking
			Asn B51	4.42	π - H stacking
5.9a	C ₆ H ₅	-6.324	Thr A184	3.84	π - H stacking
			Thr B184	3.24	π - H stacking
			Asn A51	3.51	H - bonding
			Asn B51	3.08	H - bonding
5.9b	C ₄ H ₇	-5.783	Met A98	4.07	π - H stacking
			Met B98	2.78	π - H stacking
			Thr B184	3.05	H - bonding
5.9c	C ₉ H ₁₅	-7.034	Asn A51	3.25	π - H stacking
			Asn B51	3.24	π - H stacking
			Thr A184	4.51	π - H stacking
5.9d	C ₁₄ H ₂₄	-7.831	Asn A51	3.05	π - H stacking
			Lys B58	2.42	H - bonding
			Thr B184	3.55	H - bonding
SQA	-	-7.745	Gly 135	4.07	π - H stacking
			Asn 51	3.07	H - bonding
DMAG	-	-8.597	Asp A54	3.10	H - bonding
			Asp B54	3.03	H - bonding
			Lys A58	2.95	H - bonding
			Lys B58	3.05	H - bonding
Geldanamycin	-	-8.008	Lys A112	3.09	H - bonding
			Lys B112	3.35	H - bonding
			Lys A58	2.84	H - bonding
			Lys B58	2.82	H - bonding
			Thr A184	2.78	H - bonding
			Thr B184	2.78	H - bonding

The docking results presented in Table 5.8 demonstrated that the test compounds do have affinity for Hsp90 with good negative binding energies. The most potent compound **5.9d** recorded the best binding energy of -7.831 Kcal/mol hence a better affinity compared to SQA that gave a value of -7.745 Kcal/mol. Although the established N-terminal binders geldanamycin and DMAG recorded

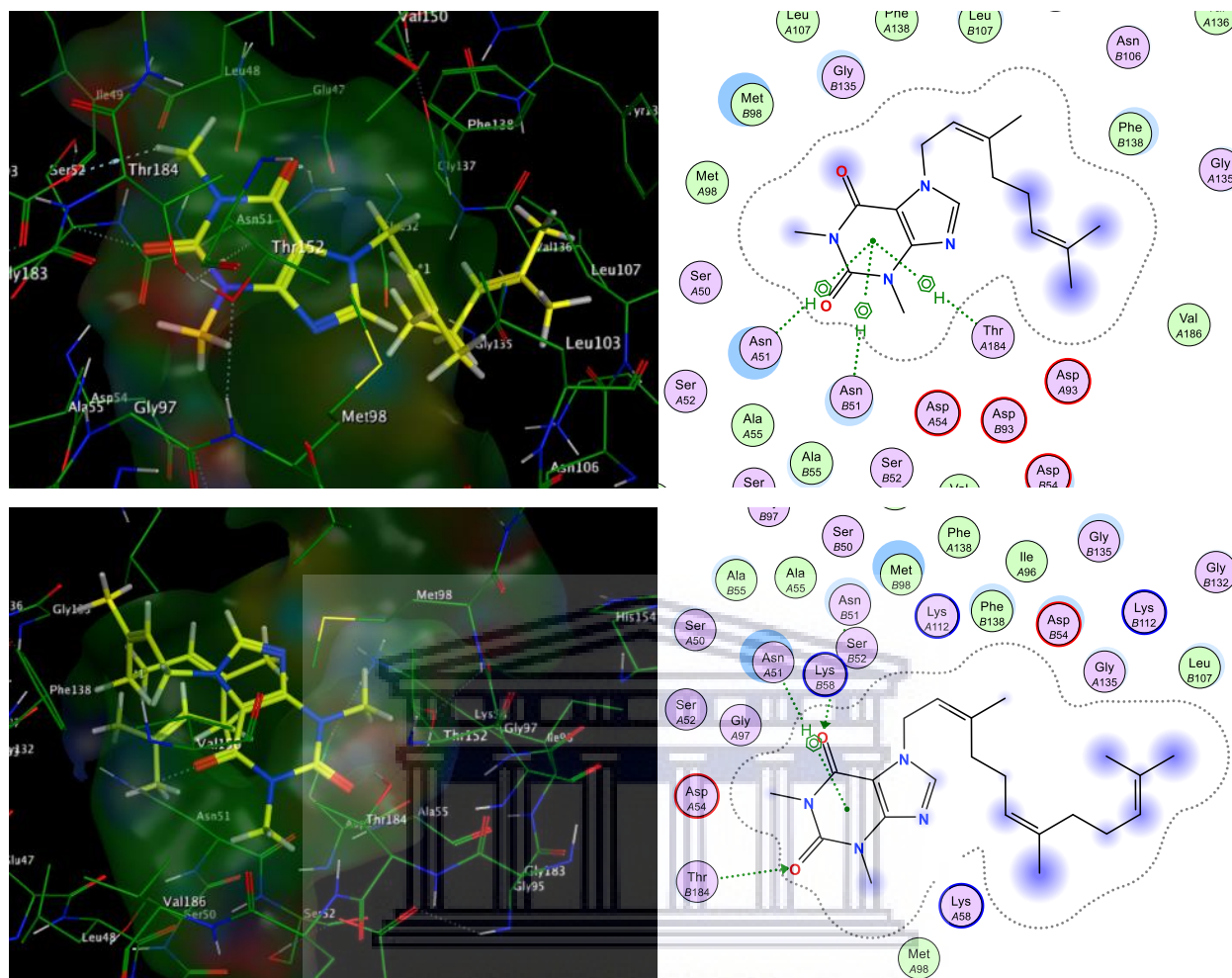


Figure 5.20 3D and 2D showing the binding interactions of **5.9c** (top) and **5.9d** (bottom) with Hsp90 geldanamycin-binding domain, the compounds are coloured yellow in the active site.

The molecular docking studies revealed that the test compounds bind and interact with Hsp90 but we could not ascertain whether these compounds would target the C-terminal domain of Hsp90. On this account, the Hsp90 inhibition assay was carried out to assess the degradation of client protein and expression level of Hsp70.

5.2.5.4 Hsp90 client protein degradation assay

Six compounds selected for IC_{50} value determination against the cancer cell lines were all subjected to Hsp90 client protein degradation assay. These compounds provided representation for the three scaffolds as well as a different degree of antiproliferative activity. This was done to establish a correlation between antiproliferative activity and Hsp90 inhibition through client

protein degradation. Comparisons were made among the test compounds, SQA and a known Hsp90 N-terminal domain inhibitor; 17-DMAG (2.26).

Hsp90 N-terminal inhibitors are characterized by overexpression of Hsp70 and this has been attributed to Hsp90 drug resistance, hence their failure as clinical anticancer drugs (McCollum et al., 2006). N-terminal inhibitors result in activation of the heat shock transcription factor 1 (HSF1) that induces pro-survival response and increased cellular levels of chaperone Hsp70 and Hsp27, as such cancer cells are protected from apoptosis (Neckers & Workman, 2012). Silencing the expression of Hsp70 was demonstrated to support proteasome-degradation of Hsp90 client proteins. Furthermore, G1 cell-cycle arrest, as well as extensive apoptosis, was reported in a few cancer cell lines (Powers et al., 2008). The molecular chaperone (Hsp90) occurs as several isoforms in humans, although Hsp90 α and Hsp90 β are widely studied. Hsp90 α is the stress-inducible isoform and functions completely different from Hsp90 β (Zuehlke et al., 2015). Interestingly, only compound **5.9d** almost completely abolished the expression of Hsp90 α (Figure 5.21). A clear expression of this isoform was observed and the level did not appear to have changed for the rest of the test compounds including the positive control 17-DMAG (2.26).

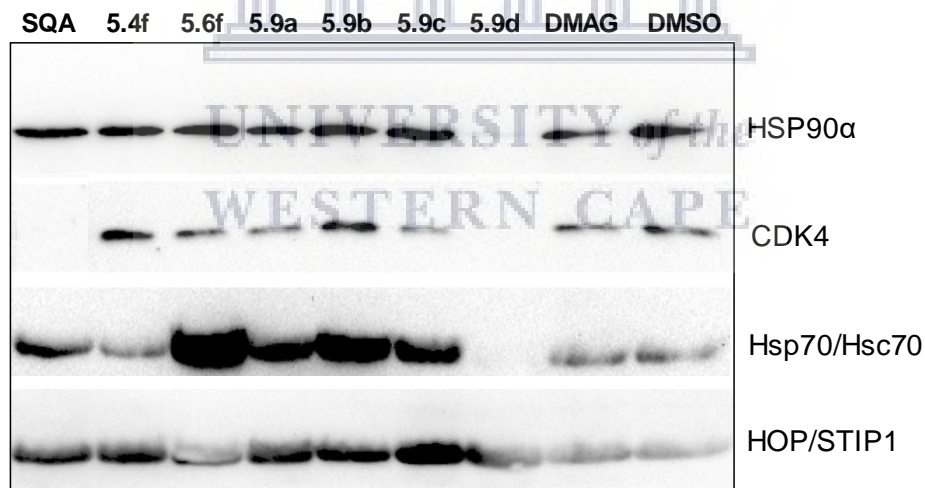


Figure 5.21 Western blot analyses showing bands for Hsp90 α , CDK4, Hsp70/Hsc70 and HOP/STIP1 upon treatment with the set of compounds.

CDK4 is one of the clients of Hsp90 and it is used as a marker of Hsp90 inhibition as it should decrease with Hsp90 inhibition. Likewise, Hsp70 is also used in this principle as its level should remain the same and no increment in its expression. Compound **5.9b** showed no reduction in the

level of CDK4 but a large increase in Hsp70 concentration. A minor loss of CDK4 was observed for compound **5.6f**, however, a significantly high concentration level of Hsp70 was displayed. Compounds **5.9a** and **5.9c** manifested inhibition activity similar to 17-DMAG with a loss in CDK4 and an increase in Hsp70 concentration. Compound **5.9d** exhibited the most promising activity with a complete loss in the expression level of CDK4 and Hsp70 concentration (Figure 5.21). The inhibition activities were obtained in this order; **5.9d** > **5.9c** > **5.9a** > **5.6f**, compounds **5.4f** and **5.9b** did not show a major response compared to 17-DMAG. This result suggests that there was no induction of the heat shock response leading to the overexpression of Hsp70. This is a great improvement over SQA which also showed loss of CDK4 but Hsp70 concentration remained the same. Compound **5.9d** exhibiting the most potent antiproliferative activity and Hsp90 inhibition established a correlation between these two concepts hence, suggest that the antiproliferative activity is due to Hsp90 inhibition. The induction of pro-survival heat shock response leading to resistance is a major shortcoming of the N-terminal domain inhibitors (Vaughan et al., 2010). On the contrary, the C-terminal domain inhibitors do not induce heat shock response but degradation of Hsp70 and Hsp90 has been reported for these molecules (Shelton et al., 2009). Thus, it can be inferred that compound **5.9d** is a binder of the Hsp90 C-terminus due to the characteristics manifested.

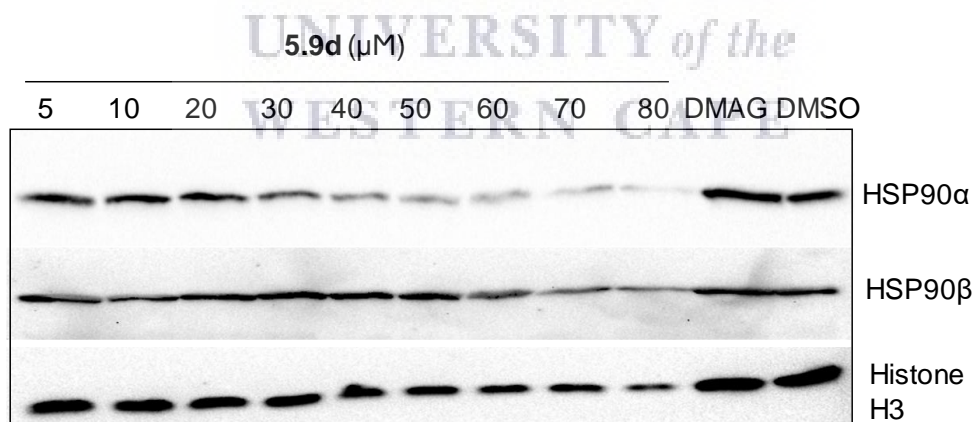


Figure 5.22 Western blot analysis of the dose-dependent inhibition of Hsp90α.

The significant reduction in expression of Hsp90α showed in Figure 5.21 prompted an investigation into a dose-dependent western blot analysis of compound **5.9d**. A dose-dependent reduction in the concentration of Hsp90α was displayed but not in Hsp90β levels in treated MDA-

MB-231 cell lysates (Figure 5.22). This suggests a higher affinity for the stress-inducible extracellular isoform Hsp90 α and a potentially unique mechanism of action.

5.3 Conclusion

A series of three different scaffolds were synthesized as analogues of a natural product; sargaquinoic acid (SQA). Based on the initial cell viability screening, six compounds were selected from these groups of compounds for IC₅₀ value determination against three different carcinoma cell lines. Compounds **5.9c** and **5.9d** manifested the most potent antiproliferative activity with an IC₅₀ value of 6.6 and 1.4 μ M respectively. This represents a significant improvement over SQA with a 4-fold and 20-fold increase in activity against HeLa cells respectively, as well as remarkable selectivity for cancer cells. Furthermore, western blot analyses revealed that compound **5.9d** inhibited the function of Hsp90 through the degradation of client protein and lack induction of heat shock response which has been detrimental to the N-terminal inhibitors. In addition, a selective dose-dependent reduction of Hsp90 α suggests compound **5.9d** to be very promising.

5.4 General experimental details

5.4.1 Materials

See section 3.4.1 for materials specification and characterization. Dimethylformamide (DMF) was obtained from Sigma Aldrich and dried over molecular sieves.

5.4.2 Synthesis of 1,4-diacetylpiperazine-2,5-dione (5.2)

To a two-neck round bottom flask equipped with a condenser was added glycine anhydride (26.31 mmol) and acetic anhydride (15 mL), heated and stirred under reflux for 7 h while using TLC to monitor the completion of the reaction. The solvent was removed by rotary evaporation to obtain a light brown solid, it was then purified by silica gel column chromatography with EtOAc/hexane (4:1) to afford a white crystalline solid.

5.4.3 General protocol for synthesis of (1-acetyl-3-arylidene-piperazine-2,5-dione) derivatives 5.4(a-f)

To a mixture of 1,4-diacetylpiperazine-2,5-dione (1.5mmol), substituted aldehyde (1.7mmol) and dry DMF (2mL) was added Cs₂CO₃ (1.5mmol), the reaction was stirred at ambient temperature for 5 h and product formation was monitored by TLC. After the reaction was judged complete, the product mixture was poured onto crushed ice and allowed to warm to ambient temperature. The precipitate was washed thoroughly with water and filtered, and dried overnight in the fumehood.

5.4.4 General procedure for the preparation of barbiturates 5.6(a-f)

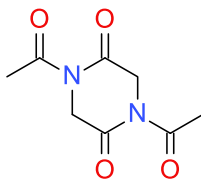
To barbituric acid (1mmol) in a poly top vial was added 5ml of water and heated to dissolution, a solution of 1.2mmol of aldehyde in 1mL of 95% EtOH was added. The reaction mixture was heated for a few minutes until precipitation was observed, it was then removed from heat and stirred at ambient temperature for 30 mins. The suspension was filtered, washed with water and MeOH.

5.4.5 General procedure for the synthesis of compound 5.9(a-d)

To a poly top vial was added dry DMF (3mL), theophylline (1mmol), K₂CO₃ (2 mmol), and allyl bromide (2mmol). The reaction mixture was stirred at ambient temperature for 12 h. Water (6mL) was added and the reaction mixture was cooled in ice for 2 h. The precipitate formed was filtered, washed with water (5mL) and dried to obtain the product.

5.4.6 Compounds

1,4-diacetylpiperazine-2,5-dione (5.2)

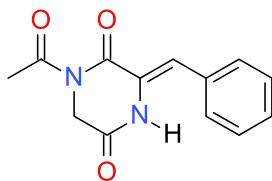


Yield: 97% as white solid. Mp 95-98 °C

¹H NMR (400 MHz, CDCl₃) δ 4.59 (s, 2H), 2.58 (s, 3H)

¹³C NMR (100 MHz, CDCl₃) δ 170.8, 165.9, 47.2, 26.8

(3Z)-1-acetyl-3-benzylidene-piperazine-2,5-dione (5.4a)



Yield: 97% as light yellow powder. Mp 195-199 °C

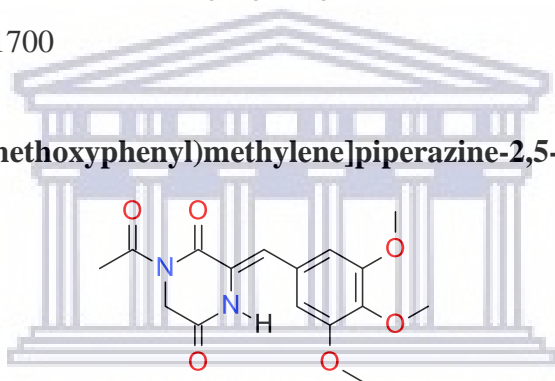
¹H NMR (400 MHz, CDCl₃) δ 8.00 (br s, N-H), 7.50 – 7.44 (m, 2H), 7.42 – 7.37 (m, 3H), 7.18 (s, 1H), 4.51 (s, 2H), 2.65 (s, 3H)

¹³C NMR (100 MHz, CDCl₃) δ 172.5, 162.7, 160.0, 132.5, 129.6, 129.4, 128.6, 128.4, 125.7, 120.0, 116.8, 46.1, 27.2

HRESIMS: *m/z*: [M + H]⁺ calculated for C₁₃H₁₃N₂O₃ 245.0927: found 245.0906

FT-IR (ATR, cm⁻¹): 3212, 1700

(3Z)-1-acetyl-3-[(3,4,5-trimethoxyphenyl)methylene]piperazine-2,5-dione (5.4b)



Yield: 66% as yellow powder. Mp 144-148 °C

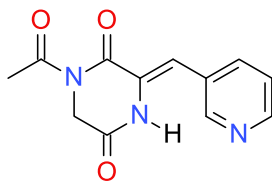
¹H NMR (400 MHz, CDCl₃) δ 8.09 (br s, N-H), 7.09 (s, 1H), 6.57 (s, 2H), 4.51 (s, 2H), 3.88 (s, 3H), 3.86 (s, 6H), 2.65 (s, 3H)

¹³C NMR (100 MHz, CDCl₃) δ 172.5, 162.7, 160.0, 154.0, 154.0, 139.0, 127.9, 125.4, 120.2, 117.0, 105.7, 105.6, 61.0, 56.3, 46.1, 27.2

HRESIMS: *m/z*: [M + H]⁺ calculated for C₁₆H₁₉N₂O₆ 335.1244: found 335.1279

FT-IR (ATR, cm⁻¹): 3291, 1696

(3Z)-1-acetyl-3-(3-pyridylmethylene)piperazine-2,5-dione (5.4c)



Yield: 71% as light yellow powder. Mp 193-196 °C

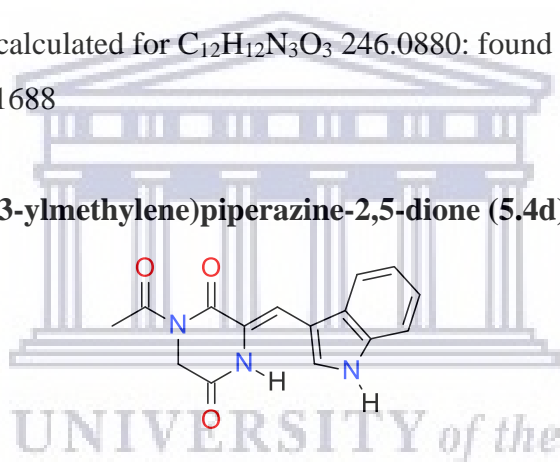
¹H NMR (400 MHz, DMSO-*d*₆) δ 10.63 (s, N-H), 8.73 (d, *J* = 2.0 Hz, 1H), 8.50 (dd, *J* = 4.8, 1.4 Hz, 1H), 7.97 (dt, *J* = 8.0, 1.6 Hz, 1H), 7.45 (dd, *J* = 7.9, 4.8 Hz, 1H), 6.94 (s, 1H), 4.37 (s, 2H), 2.51 (s, 3H)

¹³C NMR (100 MHz, DMSO-*d*₆) δ 172.3, 164.7, 161.7, 150.8, 149.3, 136.8, 129.8, 129.1, 124.1, 115.5, 46.2, 27.2

HRESIMS: *m/z*: [M + H]⁺ calculated for C₁₂H₁₂N₃O₃ 246.0880: found 246.0901

FT-IR (ATR, cm⁻¹): 3037, 1688

(3Z)-1-acetyl-3-(3H-indol-3-ylmethylene)piperazine-2,5-dione (5.4d)



Yield: 69% as yellow powder. Mp 246-250 °C

¹H NMR (400 MHz, DMSO-*d*₆) δ 10.01 (br s, N-H), 8.36 – 8.32 (m, 1H), 8.22 (s, 1H), 7.67 (d, *J* = 7.1 Hz, 1H), 7.42 – 7.38 (m, 1H), 7.36 – 7.31 (m, 1H), 6.86 (s, 1H), 4.06 (d, *J* = 1.8 Hz, 2H), 2.73 (s, 3H)

¹³C NMR (100 MHz, DMSO-*d*₆) δ 170.2, 165.2, 159.9, 135.0, 130.2, 127.5, 126.8, 125.8, 124.3, 119.2, 116.4, 113.6, 104.0, 45.3, 24.4

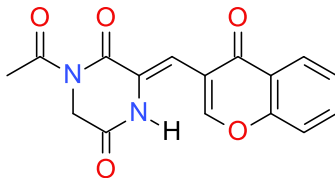
HRESIMS: *m/z*: [M + H]⁺ calculated for C₁₅H₁₄N₃O₃ 284.1036: found 284.1027

FT-IR (ATR, cm⁻¹): 3205, 1699

(3Z)-1-acetyl-3-[(4-oxochromen-3-yl)methylene]piperazine-2,5-dione (5.4e)

Following the general procedure (Section 5.4.3), the product mixture was extracted twice with EtOAc. The combined organic layers were washed with water and then saturated brine before

drying over Na₂SO₄ and further reduced to dryness under reduced pressure. The crude was further purified by column chromatography with EtOAc/hexane (1:1), and the titled product was obtained as a dark yellow powder. Yield: 18%; Mp 204-207 °C.



¹H NMR (400 MHz, CDCl₃) δ 12.08 (br s, N-H) 8.33 (dd, *J* = 8.1, 1.4 Hz, 1H), 8.19 (s, 1H), 7.78 (t, *J* = 7.77 Hz, 1H), 7.54 – 7.48 (m, 2H), 6.59 (s, 1H), 4.47 (s, 2H), 2.63 (s, 3H)

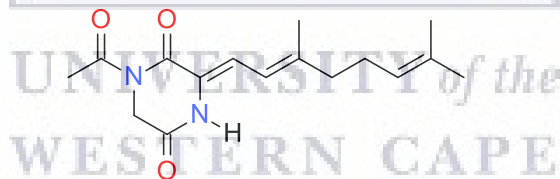
¹³C NMR (100 MHz, CDCl₃) δ 177.3, 172.7, 162.0, 160.4, 159.8, 155.6, 135.0, 128.1, 126.9, 126.5, 123.5, 120.5, 118.0, 110.0, 46.5, 27.3

HRESIMS: *m/z*: [M + H]⁺ calculated for C₁₆H₁₃N₂O₅ 313.0825: found 313.0798

FT-IR (ATR, cm⁻¹): 2922, 1678

(3Z)-1-acetyl-3-[(2E)-3,7-dimethylocta-2,6-dienylidene]piperazine-2,5-dione (5.4f)

The crude was purified by column chromatography with EtOAc/hexane (3:7), the titled product obtained was obtained as a light yellow powder. Yield: 37%; Mp 127-131 °C.



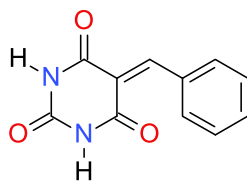
¹H NMR (400 MHz, CDCl₃) δ 9.03 (br s, N-H), 7.05 (dd, *J* = 12.4, 3.4 Hz, 1H), 6.15 (d, *J* = 12.5 Hz, 1H), 5.10 (br s, 1H), 4.44 (s, 2H), 2.61 (s, 3H), 2.26 – 2.11 (m, 4H), 1.94 (s, 3H), 1.69 (s, 3H), 1.62 (s, 3H)

¹³C NMR (100 MHz, CDCl₃) δ 172.6, 163.9, 160.7, 152.2, 132.6, 123.1, 122.3, 118.2, 116.5, 46.0, 40.8, 27.1, 26.4, 25.7, 25.1, 17.8

HRESIMS: *m/z*: [M + H]⁺ calculated for C₁₆H₂₃N₂O₃ 291.1710: found 291.1703

FT-IR (ATR, cm⁻¹): 2916, 1706

5-benzylidenehexahydropyrimidine-2,4,6-trione (5.6a)



Yield: 92% as white powder. Mp 263-266 °C.

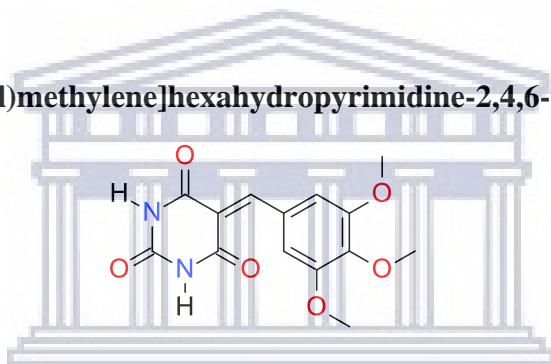
¹H NMR (400 MHz, DMSO-*d*₆) δ 11.40 (s, N-H), 11.24 (s, N-H), 8.28 (s, 1H), 8.07 (d, *J* = 7.3 Hz, 2H), 7.53 (t, *J* = 7.4 Hz, 1H), 7.47 (t, *J* = 7.7 Hz, 2H)

¹³C NMR (100 MHz, DMSO-*d*₆) δ 163.9, 162.1, 155.1, 150.7, 133.6, 133.1, 132.7, 128.5, 119.6.

HRESIMS: *m/z*: [M + H]⁺ calculated for C₁₁H₈N₂O₃ 217.0614; found 217.0605

FT-IR (ATR, cm⁻¹): 3208, 1738

5-[(3,4,5-trimethoxyphenyl)methylene]hexahydropyrimidine-2,4,6-trione (5.6b)



Yield: 99% as yellow powder. Mp 274-276 °C

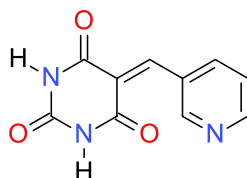
¹H NMR (400 MHz, DMSO-*d*₆) δ 11.36 (s, N-H), 11.23 (s, N-H), 8.26 (s, 1H), 7.84(s, 2H), 3.82 (s, 6H), 3.79(s, 3H)

¹³C NMR (100 MHz, DMSO-*d*₆) δ 164.2, 162.6, 155.6, 152.4, 150.6, 142.4, 128.0, 117.8, 113.1, 60.8, 56.5

HRESIMS: *m/z*: [M + H]⁺ calculated for C₁₄H₁₅N₂O₆ 307.0931; found 307.0953

FT-IR (ATR, cm⁻¹): 3234, 1752

5-(3-pyridylmethylene)hexahydropyrimidine-2,4,6-trione (5.6c)



Yield: 87% as off white powder. Mp 282-286 °C

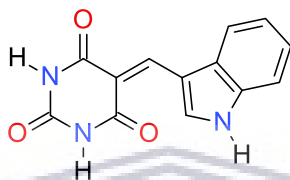
¹H NMR (400 MHz, DMSO-*d*₆) δ 8.65 (d, *J* = 5.5 Hz, 1H), 8.44 (s, 1H), 8.20 (d, *J* = 8.2 Hz, 1H), 7.9 (t, *J* = 7.1 Hz, 1H), 6.14 (s, 1H)

¹³C NMR (100 MHz, DMSO-*d*₆) δ 165.0, 151.1, 146.0, 145.0, 140.4, 139.2, 126.8, 123.6, 89.5, 55.4

HRESIMS: *m/z*: [M + H]⁺ calculated for C₁₀H₈N₃O₃ 218.0566: found 218.0536

FT-IR (ATR, cm⁻¹): 2989, 1704

5-(1H-indol-3-ylmethylene)hexahydropyrimidine-2,4,6-trione (5.6d)



Yield: 42% as yellow powder. Mp >300 °C

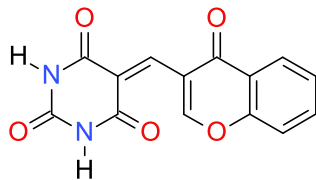
¹H NMR (400 MHz, DMSO-*d*₆) δ 12.73 (s, N-H), 11.12 (s, N-H), 11.03 (s, N-H), 9.51 (d, *J* = 3.4 Hz, 1H) 8.72 (s, 1H), 7.90 – 7.85 (m, 1H), 7.62 – 7.56 (m, 1H), 7.34 – 7.29 (m, 2H)

¹³C NMR (100 MHz, DMSO-*d*₆) δ 165.0 163.7 150.9, 144.2, 140.2 136.9, 129.6, 124.2, 123.2, 118.1, 113.6, 111.9, 109.1

HRESIMS: *m/z*: [M + H]⁺ calculated for C₁₃H₁₀N₃O₃ 256.0723: found 256.0709

FT-IR (ATR, cm⁻¹): 3277, 1718

1,3-diamino-5-[(4-oxochromen-3-yl)methylene]hexahydropyrimidine-2,4,6-trione (5.6e)



Yield: 88% as light yellow powder. Mp 278-281 °C

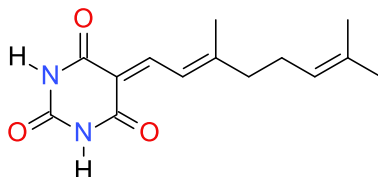
¹H NMR (400 MHz, DMSO-*d*₆) δ 11.46 (s, N-H), 11.36 (s, N-H), 9.72 (d, *J* = 0.9 Hz, 1H), 8.43 (s, 1H), 8.14 (dd, *J* = 8.0, 1.5 Hz, 1H), 7.89 (td, *J* = 7.9, 1.7 Hz, 1H), 7.76 (d, *J* = 8.3 Hz, 1H), 7.58 (td, *J* = 7.6, 1.0 Hz, 1H)

¹³C NMR (100 MHz, DMSO-*d*₆) δ 175.2, 163.6, 163.4, 162.8, 155.8, 150.6, 144.8, 135.6, 127.1, 126.1, 123.5, 120.1, 119.3, 117.7

HRESIMS: m/z : $[M + H]^+$ calculated for $C_{14}H_9N_2O_5$ 285.0512: found 285.0476

FT-IR (ATR, cm^{-1}): 3371, 1749

5-[(2E)-3,7-dimethylocta-2,6-dienylidene]hexahydropyrimidine-2,4,6-trione (5.6f)



Yield: 90% as light yellow powder. Mp 164-168 °C.

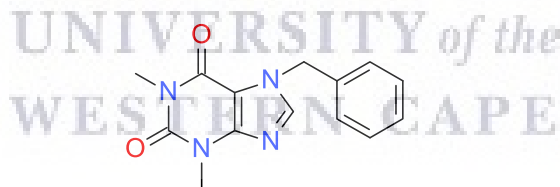
1H NMR (400 MHz, $DMSO-d_6$) δ 11.19 (s, N-H), 11.09 (s, N-H), 8.09 (dd, 20.40, 12.59 Hz, 1H), 7.62 (dd, 12.86, 3.57 Hz, 1H), 5.09 (m, 1H), 2.18 (m, 2H), 2.06 (m, 2H), 1.65 (s, 3H), 1.59 (s, 3H), 1.56 (s, 3H)

^{13}C NMR (100 MHz, $DMSO-d_6$) δ 167.1, 164.1, 150.8, 149.3, 133.2, 132.3, 123.5, 122.6 114.3, 41.6, 33.1, 26.3, 26.0, 18.2

HRESIMS: m/z : $[M + H]^+$ calculated for $C_{14}H_{19}N_2O_3$ 263.1397: found 263.1372

FT-IR (ATR, cm^{-1}): 3207, 1726

7-benzyl-1,3-dimethyl-purine-2,6-dione (5.9a)



Yield: 95% as fine white needles. Mp 159-160 °C

1H NMR (400 MHz, $CDCl_3$) δ 7.56 (s, 1H), 7.39 – 7.30 (m, 5H), 5.50 (s, 2H), 3.58 (s, 3H), 3.40 (s, 3H)

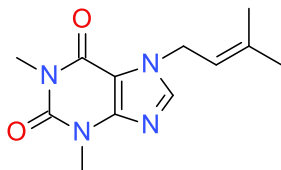
^{13}C NMR (100 MHz, $CDCl_3$) δ 155.3, 151.7, 148.9 140.9, 135.3, 129.1, 128.7, 128.0 107.0, 50.3, 29.8, 28.0

HRESIMS: m/z : $[M + H]^+$ calculated for $C_{14}H_{15}N_4O_2$ 271.1197: found 271.1190

FT-IR (ATR, cm^{-1}): 3105, 1701

1,3-dimethyl-7-(3-methylbut-2-enyl)purine-2,6-dione (5.9b)

The crude was purified by column chromatography with EtOAc/hexanes (1:1). The titled product obtained was obtained as a white crystalline solid. Yield: 55%, Mp 131-133 °C.



¹H NMR (400 MHz, CDCl₃) δ 7.52 (s, 1H) 5.42 (tt, *J* = 7.4, 1.4 Hz, 1H), 4.90 (d, *J* = 7.2 Hz, 2H), 3.57 (s, 3H), 3.40 (s, 3H), 1.78 (s, 6H)

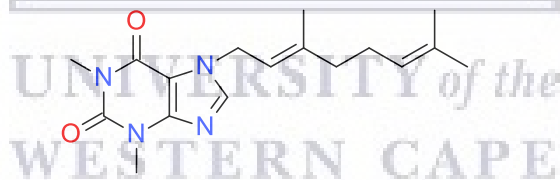
¹³C NMR (100 MHz, CDCl₃) δ 155.3, 151.7, 148.8, 140.2, 139.7, 117.7, 107.0, 44.6, 29.7, 28.0, 25.7, 18.1

HRESIMS: *m/z*: [M + H]⁺ calculated for C₁₂H₁₇N₄O₂ 249.1353: found 249.1312

FT-IR (ATR, cm⁻¹): 3120, 1702

7-[(2E)-3,7-dimethylocta-2,6-dienyl]-1,3-dimethyl-purine-2,6-dione (5.9c)

The crude was purified by column chromatography with EtOAc/hexanes (1:1). The titled product obtained was obtained as an off white crystalline solid Yield: 98%, Mp 92-96 °C.



¹H NMR (400 MHz, CDCl₃) δ 7.52 (s, 1H), 5.43 (t, *J* = 7.3 Hz, 1H), 5.07 – 5.00 (m, 1H), 4.92 (d, *J* = 7.3 Hz, 2H), 3.58 (s, 3H), 3.40 (s, 3H), 2.13 – 2.07 (m, 4H), 1.77 (s, 3H), 1.66 (s, 3H), 1.58 (s, 3H)

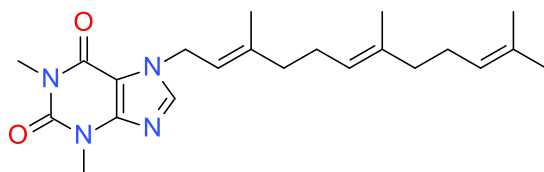
¹³C NMR (100 MHz, CDCl₃) δ 155.3, 151.7, 148.8, 143.4, 140.2, 132.2, 123.5, 117.4, 107.1, 44.5, 39.4, 29.8, 28.0, 26.1, 25.7, 17.7, 16.5

HRESIMS: *m/z*: [M + H]⁺ calculated C₁₇H₂₅N₄O₂ 317.1980: found 317.1902

FT-IR (ATR, cm⁻¹): 3099, 1696

1,3-dimethyl-7-[(2E,6E)-3,7,11-trimethyldodeca-2,6,10-trienyl]purine-2,6-dione (5.9d)

The crude was purified by column chromatography with EtOAc/hexanes (1:1). The titled product obtained was obtained as a light yellow liquid that solidified into a waxy solid. Yield: 60%, Mp 48-50 °C.



¹H NMR (400 MHz, CDCl₃) δ 7.52 (s, 1H), 5.42 (t, *J* = 7.2 Hz, 1H), 5.10 - 5.00 (m, 2H), 4.91 (d, *J* = 7.2 Hz, 2H), 3.56 (s, 3H), 3.39 (s, 3H), 2.16 – 2.06 (m, 4H), 2.05 – 1.98 (m, 2H), 1.98 - 1.90 (m, 2H), 1.77(s, 3H), 1.65 (s, 3H), 1.56 (s, 6H)

¹³C NMR (100 MHz, CDCl₃) δ 155.3, 151.7, 148.8, 143.3, 140.2, 135.8, 131.4, 124.2, 123.3, 117.4, 107.0, 44.5, 39.7, 39.4, 29.7, 28.0, 26.7, 26.1, 25.7, 17.7, 16.5, 16.0

HRESIMS: *m/z*: [M + H]⁺ calculated for C₂₂H₃₃N₄O₂ 385.2606: found 385.2635

FT-IR (ATR, cm⁻¹): 3097, 1695

5.4.7 Biological Assays

5.4.7.1 Cell cultures

See section 4.4.5.1

5.4.7.2 Antiproliferative assay

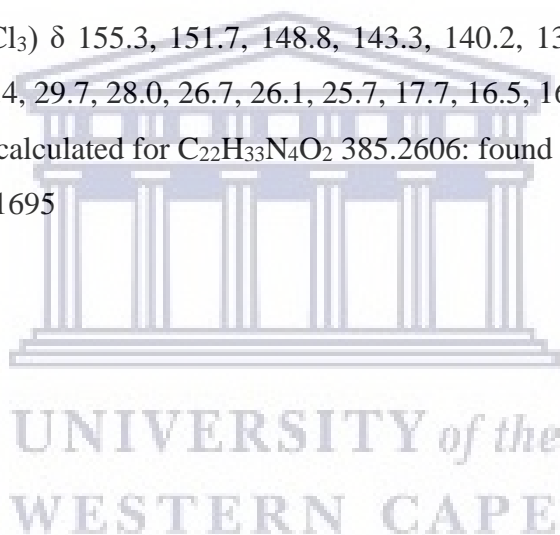
See section 3.4.5.2

5.4.7.3 Western blot assay

A general protocol used in Prof. Adrienne Edkin's lab was used as described by Hunter and colleagues (2014).

5.4.8 Molecular docking

See section 4.4.6



References

Afolayan, A. F., Bolton, J. J., Lategan, C. A., Smith, P. J., & Beukes, D. R. (2008). Fucoxanthin, tetraprenylated toluquinone and toluhydroquinone metabolites from *Sargassum heterophyllum* inhibit the *in vitro* growth of the malaria parasite *Plasmodium falciparum*. *Zeitschrift für Naturforschung C*, 63(11-12), 848-852.

Bertrand, B., Stefan, L., Pirrotta, M., Monchaud, D., Bodio, E., Richard, P., P., Le Gendre, P., Warmerdam, E., de Jager, M.H., Groothuis, G.M., & Picquet, M. (2014). Caffeine-based gold (I) N-heterocyclic carbenes as possible anticancer agents: synthesis and biological properties. *Inorganic Chemistry*, 53(4), 2296-2303.

Bisson, J., McAlpine, J. B., Friesen, J. B., Chen, S. N., Graham, J., & Pauli, G. F. (2016). Can invalid bioactives undermine natural product-based drug discovery?. *Journal of Medicinal Chemistry*, 59(5), 1671-1690.

Bolton, J. L., & Dunlap, T. (2017). Formation and biological targets of quinones: cytotoxic versus cytoprotective effects. *Chemical Research in Toxicology*, 30(1), 13-37.

Burlison, J. A., Neckers, L., Smith, A. B., Maxwell, A., & Blagg, B. S. (2006). Novobiocin: redesigning a DNA gyrase inhibitor for selective inhibition of hsp90. *Journal of the American Chemical Society*, 128(48), 15529-15536.

Choi, B. W., Ryu, G., Park, S. H., Kim, E. S., Shin, J., Roh, S. S., Shin, H.C., & Lee, B. H. (2007). Anticholinesterase activity of plastoquinones from *Sargassum sagamianum*: lead compounds for Alzheimer's disease therapy. *Phytotherapy Research: An International Journal Devoted to Pharmacological and Toxicological Evaluation of Natural Product Derivatives*, 21(5), 423-426.

Das, B., & Satyalakshmi, G. (2012). Natural products based anticancer agents. *Mini-Reviews in Organic Chemistry*, 9(2), 169-177.

de la Mare, J. A., Lawson, J. C., Chiwakata, M. T., Beukes, D. R., Edkins, A. L., & Blatch, G. L. (2012). Quinones and halogenated monoterpenes of algal origin show anti-proliferative effects against breast cancer cells *in vitro*. *Investigational New Drugs*, 30(6), 2187-2200.

El-Najjar, N., Gali-Muhtasib, H., Ketola, R. A., Vuorela, P., Urtti, A., & Vuorela, H. (2011). The chemical and biological activities of quinones: overview and implications in analytical detection. *Phytochemistry Reviews*, 10(3), 353-370.

Ertl, P., Rohde, B., & Selzer, P. (2000). Fast calculation of molecular polar surface area as a sum of fragment-based contributions and its application to the prediction of drug transport properties. *Journal of Medicinal Chemistry*, 43(20), 3714-3717.

Gwon, W. G., Lee, B., Joung, E. J., Choi, M. W., Yoon, N., Shin, T., Oh, C.W., & Kim, H. R. (2015). Sargaquinoic acid inhibits TNF- α -induced NF- κ B signaling, thereby contributing to decreased monocyte adhesion to human umbilical vein endothelial cells (HUVECs). *Journal of Agricultural and Food Chemistry*, 63(41), 9053-9061.

Ham, Y. M., Kim, K. N., Lee, W. J., Lee, N. H., & Hyun, C. G. (2010). Chemical constituents from *Sargassum micracanthum* and antioxidant activity. *International Journal of Pharmacology*, 6(2), 147-151.

Hastings, J. M., Hadden, M. K., & Blagg, B. S. (2008). Synthesis and evaluation of derrubone and select analogues. *The Journal of Organic Chemistry*, 73(2), 369-373.

Hunter, M. C., O'Hagan, K. L., Kenyon, A., Dhanani, K. C., Prinsloo, E., & Edkins, A. L. (2014). Hsp90 binds directly to fibronectin (FN) and inhibition reduces the extracellular fibronectin matrix in breast cancer cells. *PLoS One*, 9(1), 1-24.

Hur, S., Lee, H., Kim, Y., Lee, B. H., Shin, J., & Kim, T. Y. (2008). Sargaquinoic acid and sargachromenol, extracts of *Sargassum sagamianum*, induce apoptosis in HaCaT cells and mice skin: Its potentiation of UVB-induced apoptosis. *European Journal of Pharmacology*, 582(1-3), 1-11.

Joung, E. J., Lee, B., Gwon, W. G., Shin, T., Jung, B. M., Yoon, N. Y., Choi, J.S., Oh, C.W., & Kim, H. R. (2015). Sargaquinoic acid attenuates inflammatory responses by regulating NF- κ B and Nrf2 pathways in lipopolysaccharide-stimulated RAW 264.7 cells. *International Immunopharmacology*, 29(2), 693-700.

Kang, G. J., Han, S. C., Yoon, W. J., Koh, Y. S., Hyun, J. W., Kang, H. K., Youl Cho, J., & Yoo, E. S. (2013). Sargaquinoic acid isolated from *Sargassum siliquastrum* inhibits lipopolysaccharide-induced nitric oxide production in macrophages via modulation of nuclear

factor- κ B and c-Jun N-terminal kinase pathways. *Immunopharmacology and Immunotoxicology*, 35(1), 80-87.

Kusumi, T., Shibata, Y., Ishitsuka, M., Kinoshita, T., & Kakisawa, H. (1979). Structures of new plastoquinones from the brown alga *Sargassum serratifolium*. *Chemistry Letters*, 8(3), 277-278.

Liao, S., Qin, X., Li, D., Tu, Z., Li, J., Zhou, X., Wang, J., Yang, B., Lin, X., Liu, J., & Yang, X. (2014). Design and synthesis of novel soluble 2, 5-diketopiperazine derivatives as potential anticancer agents. *European Journal of Medicinal Chemistry*, 83, 236-244.

Lim, S., Choi, A. H., Kwon, M., Joung, E. J., Shin, T., Lee, S. G., Kim, N.G., & Kim, H. R. (2019). Evaluation of antioxidant activities of various solvent extract from *Sargassum serratifolium* and its major antioxidant components. *Food Chemistry*, 278, 178-184.

Lipinski, C. A., Lombardo, F., Dominy, B. W., & Feeney, P. J. (1997). Experimental and computational approaches to estimate solubility and permeability in drug discovery and development settings. *Advanced Drug Delivery Reviews*, 23(1-3), 3-25.

Marcu, M. G., Chadli, A., Bouhouche, I., Catelli, M., & Neckers, L. M. (2000a). The heat shock protein 90 antagonist novobiocin interacts with a previously unrecognized ATP-binding domain in the carboxyl terminus of the chaperone. *Journal of Biological Chemistry*, 275(47), 37181-37186.

Marcu, M. G., Schulte, T. W., & Neckers, L. (2000b). Novobiocin and related coumarins and depletion of heat shock protein 90-dependent signaling proteins. *Journal of the National Cancer Institute*, 92(3), 242-248.

McCollum, A. K., TenEyck, C. J., Sauer, B. M., Toft, D. O., & Erlichman, C. (2006). Up-regulation of heat shock protein 27 induces resistance to 17-allylamino-demethoxygeldanamycin through a glutathione-mediated mechanism. *Cancer Research*, 66(22), 10967-10975.

Molecular Operating Environment (MOE), 2016.08; Chemical Computing Group Inc., 1010 Sherbrooke St. West, Suite #910, Montreal, QC, Canada, H3A 2R7, 2016

Molinspiration Cheminformatics, Bratislava, Slovak Republic
<http://www.molinspiration.com/cgi-bin/properties> (accessed December 30, 2019).

Moyo, B. (2013). PhD thesis; The screening and characterisation of compounds for modulators of Heat shock protein (Hsp90) in a breast cancer cell model. Rhodes University, 73-76.

Neckers, L., & Workman, P. (2012). Hsp90 molecular chaperone inhibitors: are we there yet?. *Clinical Cancer Research*, 18(1), 64-76.

Newman, D. J., Cragg, G. M., & Snader, K. M. (2000). The influence of natural products upon drug discovery. *Natural Product Reports*, 17(3), 215-234.

Oh, S. J., Joung, E. J., Kwon, M. S., Lee, B., Utsuki, T., Oh, C. W., & Kim, H. R. (2016). Anti-inflammatory effect of ethanolic extract of *Sargassum serratifolium* in lipopolysaccharide-stimulated BV2 microglial cells. *Journal of Medicinal Food*, 19(11), 1023-1031.

Powers, M. V., Clarke, P. A., & Workman, P. (2008). Dual targeting of HSC70 and HSP72 inhibits HSP90 function and induces tumor-specific apoptosis. *Cancer Cell*, 14(3), 250-262.

Reddy, P., & Urban, S. (2009). Meroditerpenoids from the southern Australian marine brown alga *Sargassum fallax*. *Phytochemistry*, 70(2), 250-255.

Sasikumar, M., Bharath, D., Kumar, G. S., Chereddy, N. R., Chithiravel, S., Krishnamoorthy, K., & Rao, V. J. (2016). Role of acceptor strength on OFET properties of small molecular organic semiconducting materials with DAD architecture. *Synthetic Metals*, 220, 236-246.

Seo, Y., Lee, H. J., Park, K. E., Kim, Y. A., Ahn, J. W., Yoo, J. S., & Lee, B. J. (2004). Peroxynitrite-scavenging constituents from the brown alga *Sargassum thunbergii*. *Biotechnology and Bioprocess Engineering*, 9(3), 212-216.

Shelton, S. N., Shawgo, M. E., Matthews, S. B., Lu, Y., Donnelly, A. C., Szabla, K., Tanol, M., Vielhauer, G.A., Rajewski, R.A., Matts, R.L., & Blagg, B. S. (2009). KU135, a novel novobiocin-derived C-terminal inhibitor of the 90-kDa heat shock protein, exerts potent antiproliferative effects in human leukemic cells. *Molecular Pharmacology*, 76(6), 1314-1322.

Silva, D. H., Pereira, F. C., Zanoni, M. V., & Yoshida, M. (2001). Lipophyllic antioxidants from *Iryanthera juruensis* fruits. *Phytochemistry*, 57(3), 437-442.

Simon, J. E., Wang, M., Gbewonyo, K., Rafi, M. M., Acquaye, D. F., & Asianowa, Y. (2008). Antioxidant and anti-inflammatory activity of compounds and preparations from African nutmeg seeds. U.S. Patent No. 7,371,413.

Stebbins, C. E., Russo, A. A., Schneider, C., Rosen, N., Hartl, F. U., & Pavletich, N. P. (1997). Crystal structure of an Hsp90–geldanamycin complex: targeting of a protein chaperone by an antitumor agent. *Cell*, 89(2), 239-250.

Supko, J. G., Hickman, R. L., Grever, M. R., & Malspeis, L. (1995). Preclinical pharmacologic evaluation of geldanamycin as an antitumor agent. *Cancer Chemotherapy and Pharmacology*, 36(4), 305-315.

Tsang, C. K., & Kamei, Y. (2004). Sargaquinoic acid supports the survival of neuronal PC12D cells in a nerve growth factor-independent manner. *European Journal of Pharmacology*, 488(1-3), 11-18.

Vaughan, C. K., Neckers, L., & Piper, P. W. (2010). Understanding of the Hsp90 molecular chaperone reaches new heights. *Nature Structural & Molecular Biology*, 17(12), 1400-1404.

Verma, A. (2012). Lead finding from *Phyllanthus debelis* with hepatoprotective potentials. *Asian Pacific Journal of Tropical Biomedicine*, 2(3), S1735-S1737.

Vieira, A. A., Gomes, N. M., Matheus, M. E., Fernandes, P. D., & Figueroa-Villar, J. D. (2011). Synthesis and *in vivo* evaluation of 5-chloro-5-benzobarbiturates as new central nervous system depressants. *Journal of the Brazilian Chemical Society*, 22(2), 364-371.

Whitesell, L., Mimnaugh, E. G., De Costa, B., Myers, C. E., & Neckers, L. M. (1994). Inhibition of heat shock protein HSP90-pp60v-src heteroprotein complex formation by benzoquinone ansamycins: essential role for stress proteins in oncogenic transformation. *Proceedings of the National Academy of Sciences*, 91(18), 8324-8328

Zuehlke, A. D., Beebe, K., Neckers, L., & Prince, T. (2015). Regulation and function of the human HSP90AA1 gene. *Gene*, 570(1), 8-16.

Chapter 6

Conclusion



UNIVERSITY *of the*
WESTERN CAPE

6.1 General summary

The design and synthesis of natural product analogues or natural product-inspired small molecules in cancer chemotherapy remain relevant in the quest for improved anticancer drugs. With a continuous effort to improve the selectivity of anticancer drugs through the discrimination between cancerous and normal cells, this has increased focus on targeting certain features that are important to cancer for its malignancy. This research project aimed to design and synthesize new scaffolds as antiproliferative agents that could target mitosis and the function of heat shock protein 90 (Hsp90). Six objectives were set to achieve this goal and they were accomplished, overall, this research was successful.

In this thesis, we reported on the synthesis and antiproliferative activity of the cyclopenta[*b*]indoles (chapter 3). This cyclopenta[*b*]indole scaffold has been found in some natural products while the indole motif has been reported for a vast range of biological activity. The most active compound from the cyclopenta[*b*]indole series was **3.32k** (R = 7-Br,5-Cl) with an IC₅₀ value of 6.9 μM against HCC70 breast cancer cells.

Furthermore, we explored the synthesis and antiproliferative activity of the arylidene cyclopenta[*b*]indol-3-ones (chapter 4) *via* Claisen-Schmidt condensation of substituted aromatic aldehydes with the synthesized cyclopenta[*b*]indoles in chapter 3. The rationale behind this was intended to improve the antiproliferative activity, the affinity for tubulin and solubility by the formation of their hydrochloride salts. Molecular docking studies established that these compounds could bind and interact with the colchicine-tubulin domain but the good docking scores obtained did not correlate with the IC₅₀ values obtained. This implied that the single point cell viability screening employed did not provide the best screening assessment of the compounds selected for further studies. We suspect that changes in testing conditions or stability of the compounds could be responsible for this inconsistency.

The unsubstituted cyclopenta[*b*]indole **3.32a** (R = H) with an IC₅₀ value of 147.7 μM against HCC70 breast cancer cells reported in chapter 3 recorded higher improvement in activity for its aldol product; pyridyl substituted cyclopenta[*b*]indol-3-one **4.33a** (R = H) in chapter 4. It displayed the most potent and selective antiproliferative activity against HCC70 cells with an IC₅₀ value of

10.2 μM . In contrast, that was not the case for the 7-bromo-5-chloro substituted cyclopenta[*b*]indole **3.32k** (R = 7-Br,5-Cl), which was the most active compound in chapter 3 but the aldol products fell short at inhibiting proliferation against three (3) cancer cell lines. The phenyl substituted **4.31k** (R = 7-Br,5-Cl) and 3,4,5-trimethoxyphenyl substituted **4.32k** (R = 7-Br,5-Cl) cyclopenta[*b*]indol-3-ones only showed moderate to non-toxic activity across the three cancer cell lines while activity was lost completely for the pyridyl substituted cyclopenta[*b*]indol-3-ones **4.33k** (R = 7-Br,5-Cl), which is contrary to the docking results. Besides, solubility in dimethyl sulphoxide (DMSO) was still a problem for some of the compounds such as **4.33j**, **4.31k**, **4.32k** and **4.33k**. This could have impacted the biological results although it is only a possibility as it was not a general trend for all the compounds.

The design and synthesis of prenylated sargaquinoic acid analogues was reported in chapter 5. Sargaquinoic acid (SQA), isolated from brown algae was reported to inhibit the function of Hsp90. However, it was not very potent against MB-231-MB cells, at the same time it was also active against non-cancerous MCF-12A cells. Therefore, we set out to develop new scaffolds as antiproliferative agents and potential Hsp90 inhibitors. A series of diketopiperazine, barbituric acid and purine derivatives were synthesized as analogues of sargaquinoic acid. The geranyl purine **5.9c** and farnesyl purine **5.9d** showed the most potent cell proliferation inhibition activity against HeLa cells with an IC_{50} value of 6.6 and 1.4 μM respectively. A molecular docking study was carried out using the co-crystal N-terminal domain of Hsp90, this is because the co-crystal structure of the C-terminal domain has not been resolved. The results revealed that these compounds could bind and interact with the Hsp90 but it was impossible to assume that they would target the C-terminal end without additional investigation. Hence, a western blot analysis was performed and it showed the degradation of Hsp90 client protein CDK4 without inducing the expression of Hsp70. Overexpression of Hsp70 has been a major drawback for the N-terminal targeting Hsp90 inhibitors which has led to resistance. This implies that the farnesyl purine **5.9d** is targeting the C-terminal domain of Hsp90 and the dose-dependent degradation of Hsp90 of this compound suggest a unique mechanism of action worth investigating.

In conclusion, we developed a series of compounds targeting tubulin polymerization and documented a selective compound; **4.33a** with good antiproliferative activity. Also, a potent

sargaquinoic acid analogue; the farnesyl purine **5.9d** was also documented which showed a significant affinity for Hsp90 α and inhibited the function of Hsp90 without inducing the heat shock response.

6.2 Limitation of the study

Due to a large number of samples, it was not possible to determine IC₅₀ values for all the compounds against the three cancer cell lines and the normal cells reported, but a single point concentration testing was adopted in selection of compounds for further antiproliferative investigation.

The *in vitro* assessment of tubulin polymerization could have supported the molecular docking studies.

6.3 Recommendation for future study

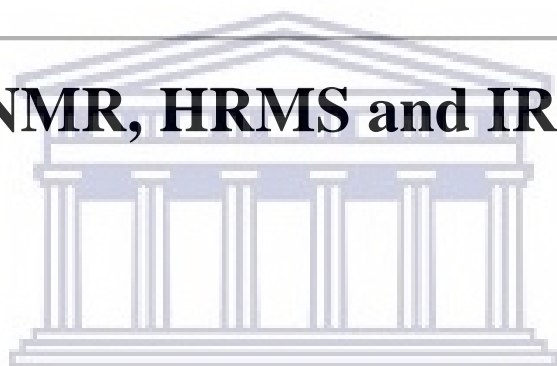
Although the aim and objectives of this study were achieved, it also provided a new perspective for future studies. A further modification of this arylidene cyclopenta[*b*]indol-3-ones can be explored which could also address the solubility problem with some of the compounds. This can be achieved *via* a one-pot Mannich reaction of the cyclopenta[*b*]indole **3.32**, aromatic aldehyde and an amine to form a β -aminoketone.

Some compounds reported in this study were non-toxic to both cancerous and normal cells, they also displayed good pharmacokinetic scores. These compounds could serve as leads in exploring other biological targets such as antimalarial or neurodegeneration.

In view of the dose-dependent inhibition of Hsp90 α which was anticipated to be a unique mechanism of action. Biotinylation of compound **5.9d** can be used to aid the identification of target protein responsible for the biological activity. This may be achieved by reacting this compound with a hydrazine-functionalized biotin to form a biotinylated product. Subsequently, protein interaction studies can be conducted to identify the target protein.

Supplementary data

NMR, HRMS and IR



UNIVERSITY *of the*
WESTERN CAPE

Chapter 3

Cyclopenta[*b*]indole derivatives 3.32(a-l)

Figure S3.1: COSY NMR spectrum of compound 3.32a

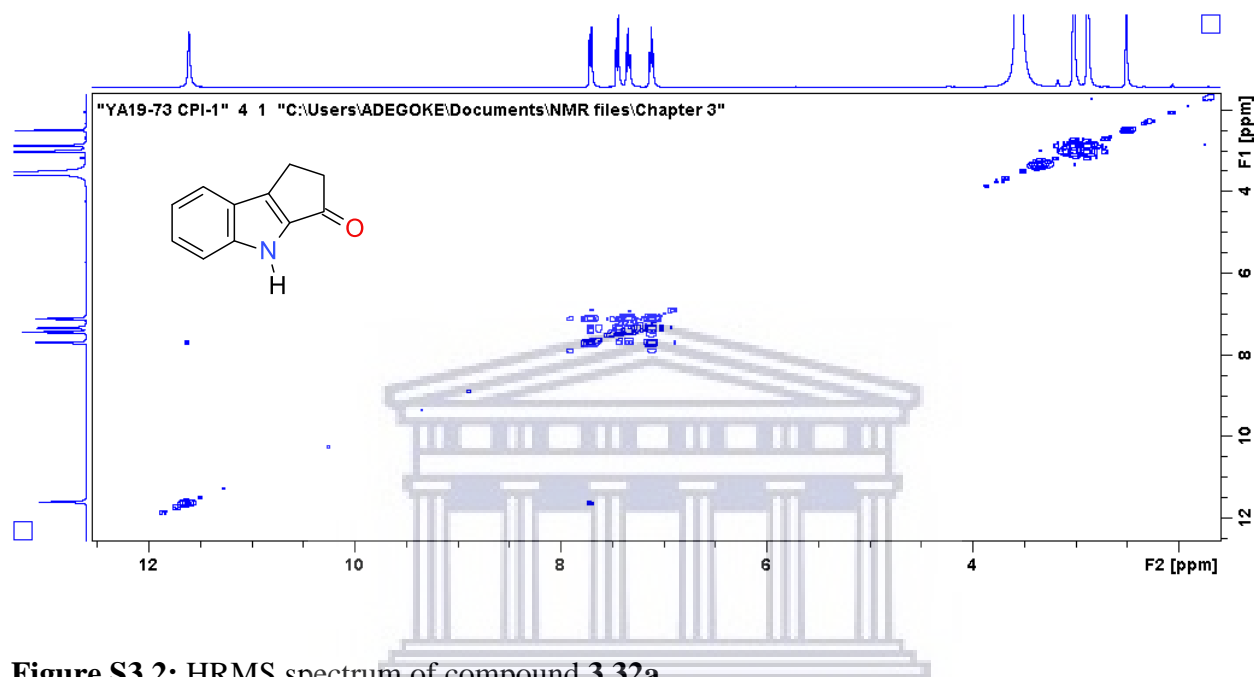


Figure S3.2: HRMS spectrum of compound 3.32a

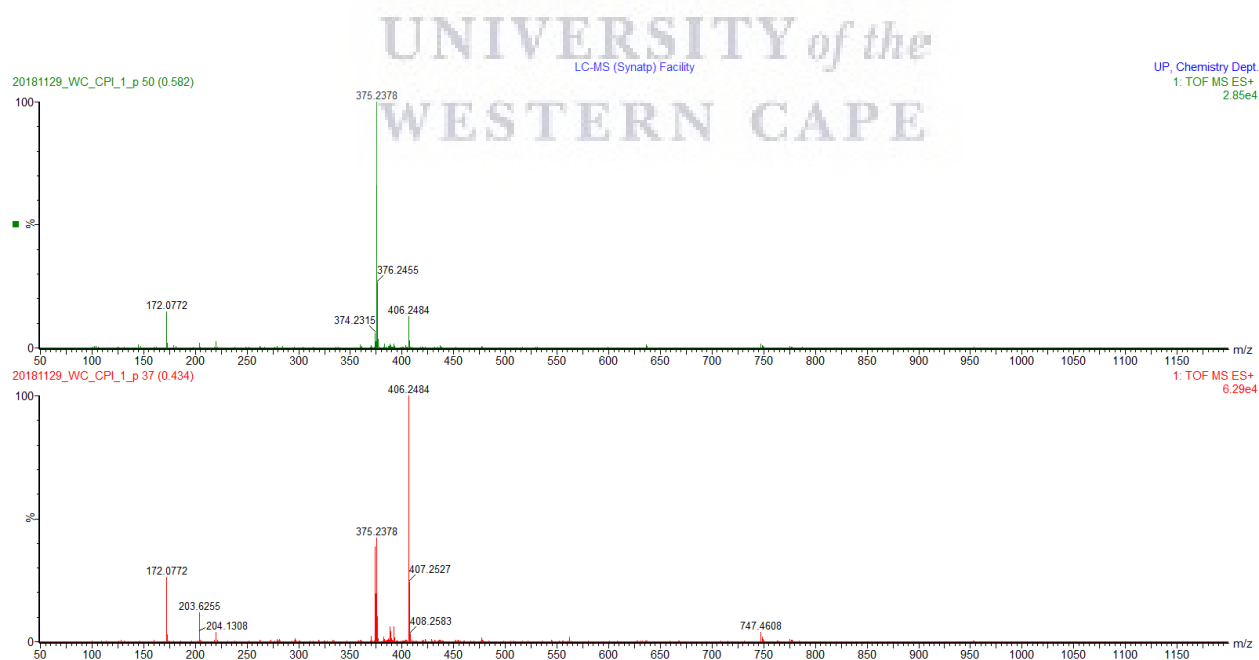
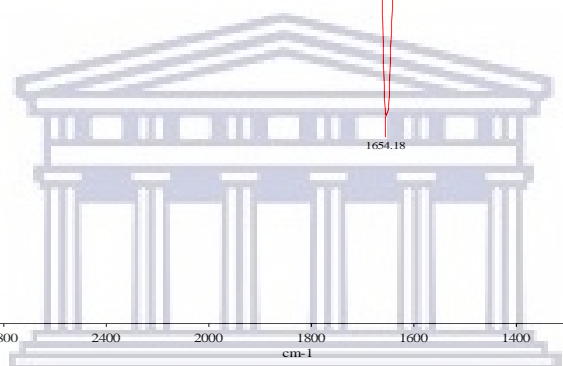
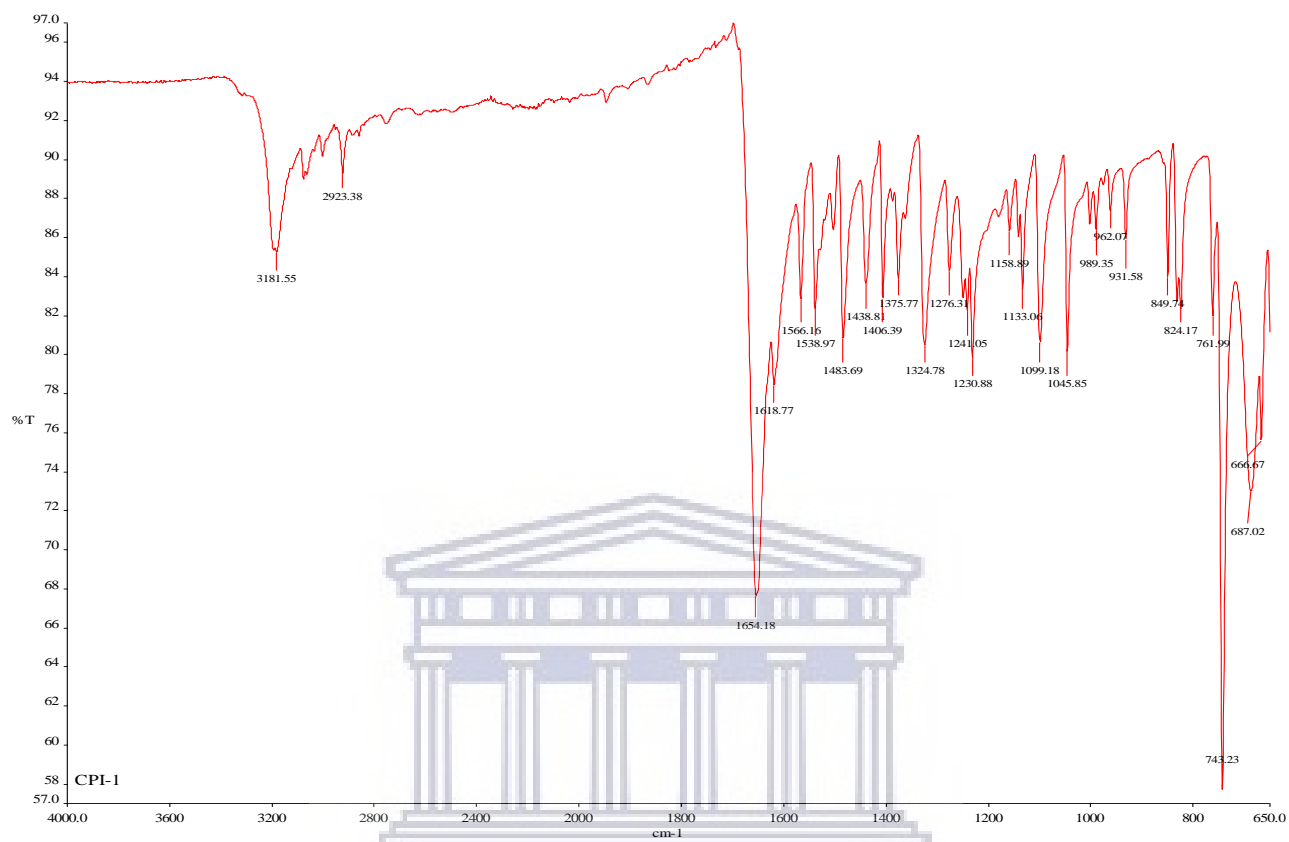


Figure S3.3: IR spectrum of compound **3.32a**



UNIVERSITY of the
WESTERN CAPE

Figure S3.4: ^1H NMR spectrum of compound **3.32b** (400 MHz, DMSO- d_6)

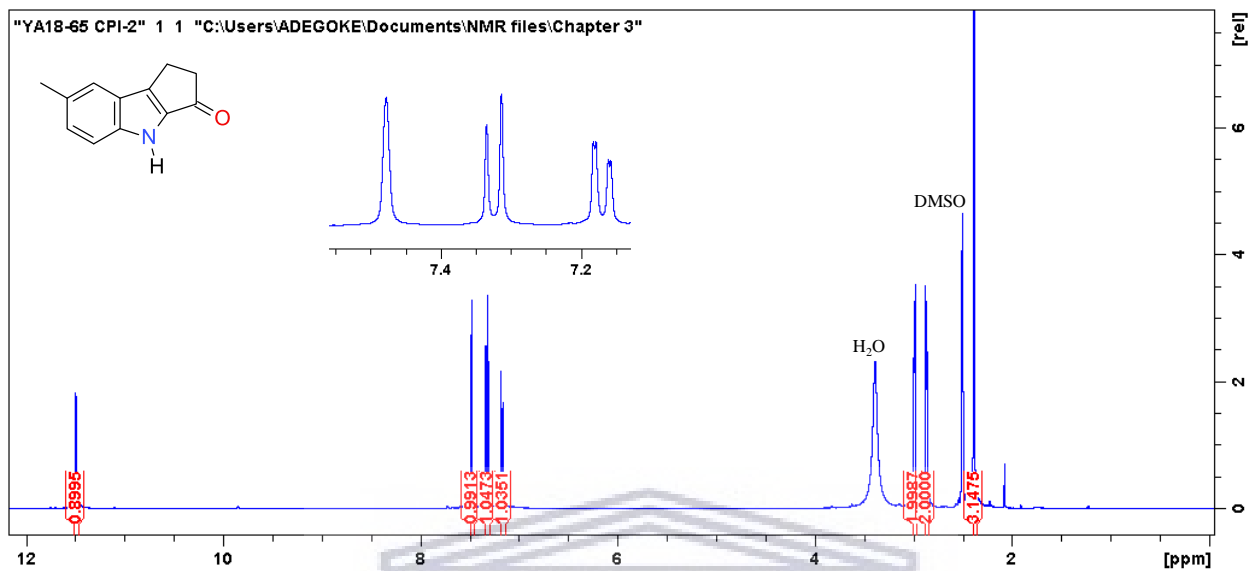


Figure S3.5: ^{13}C NMR spectrum of compound **3.32b** (100 MHz, DMSO- d_6)

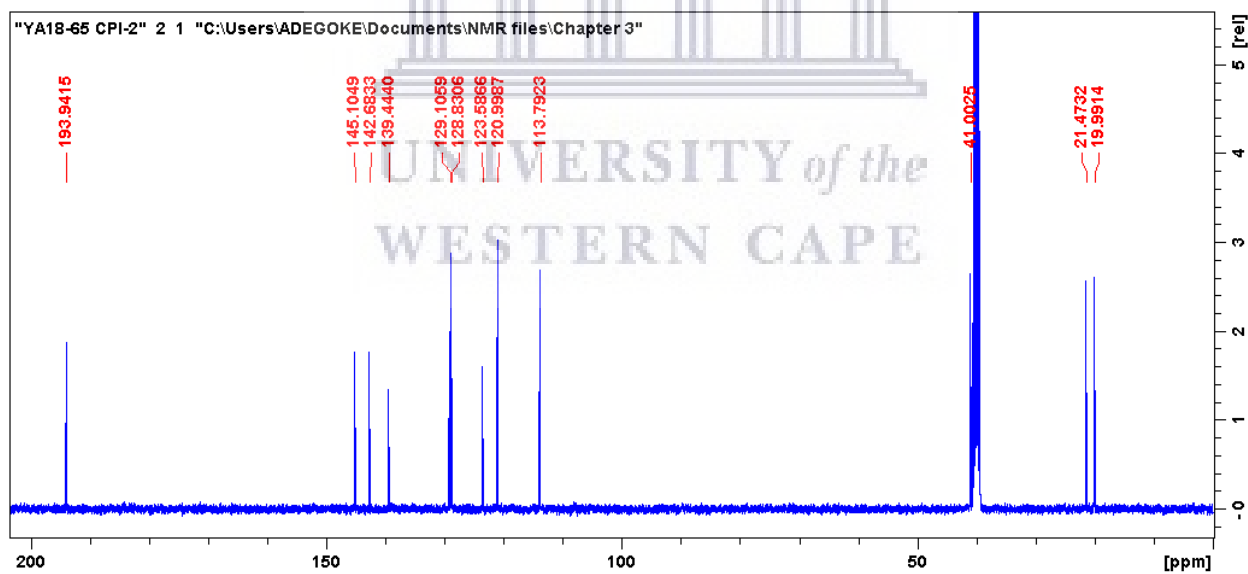


Figure S3.6: HRMS spectrum of compound 3.32b

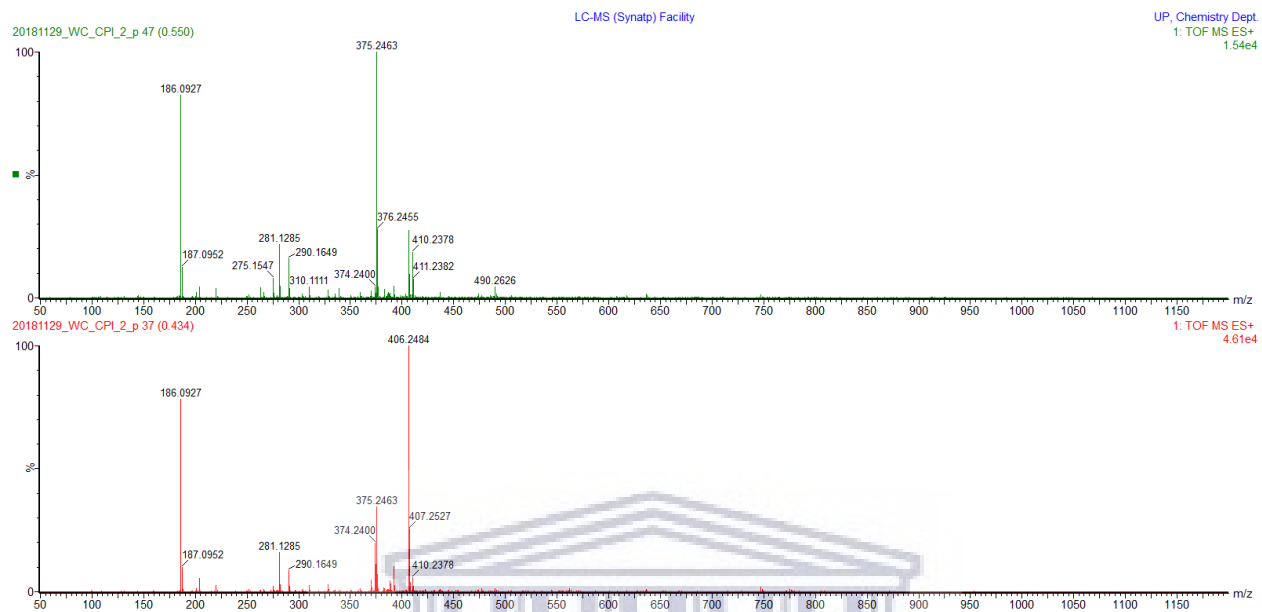


Figure S3.7: IR spectrum of compound 3.32b

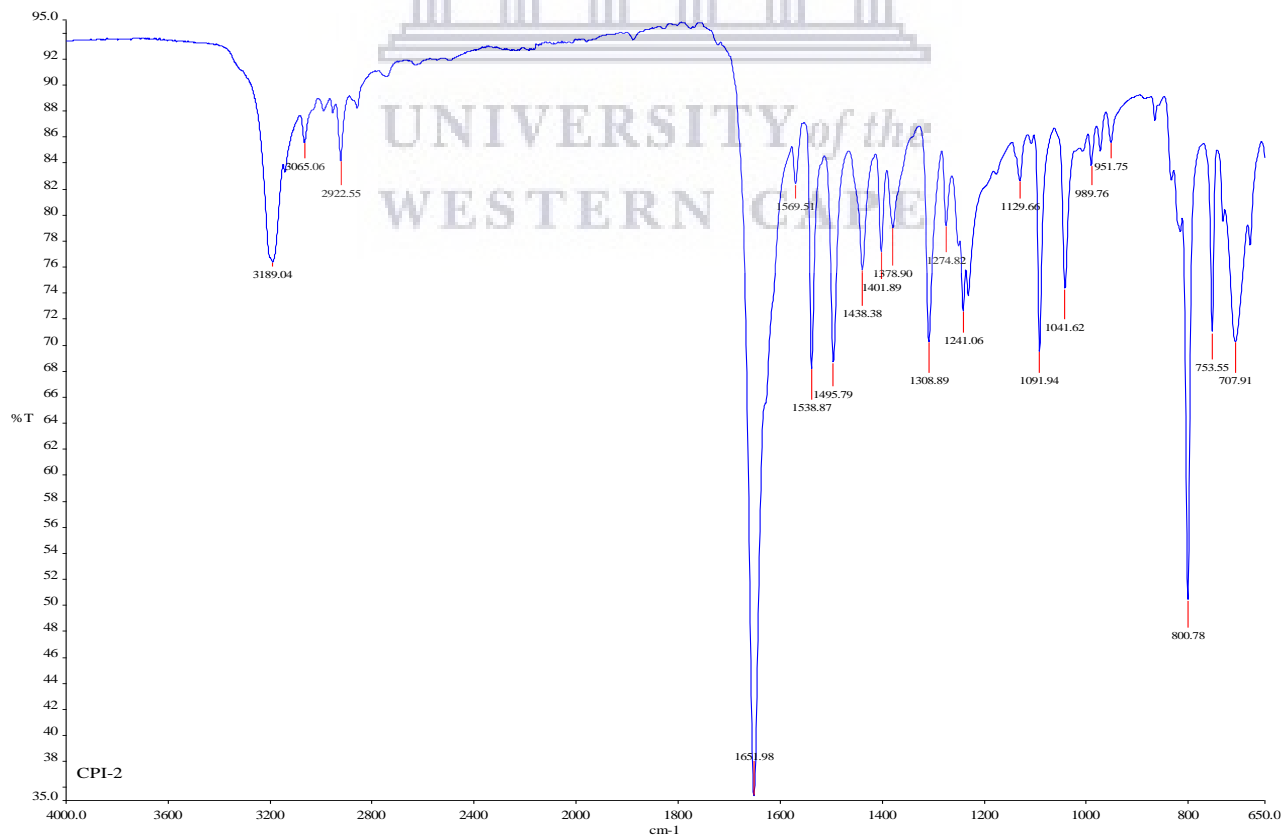


Figure S3.8: ^1H NMR spectrum of compound **3.32c** (400 MHz, DMSO-d_6)

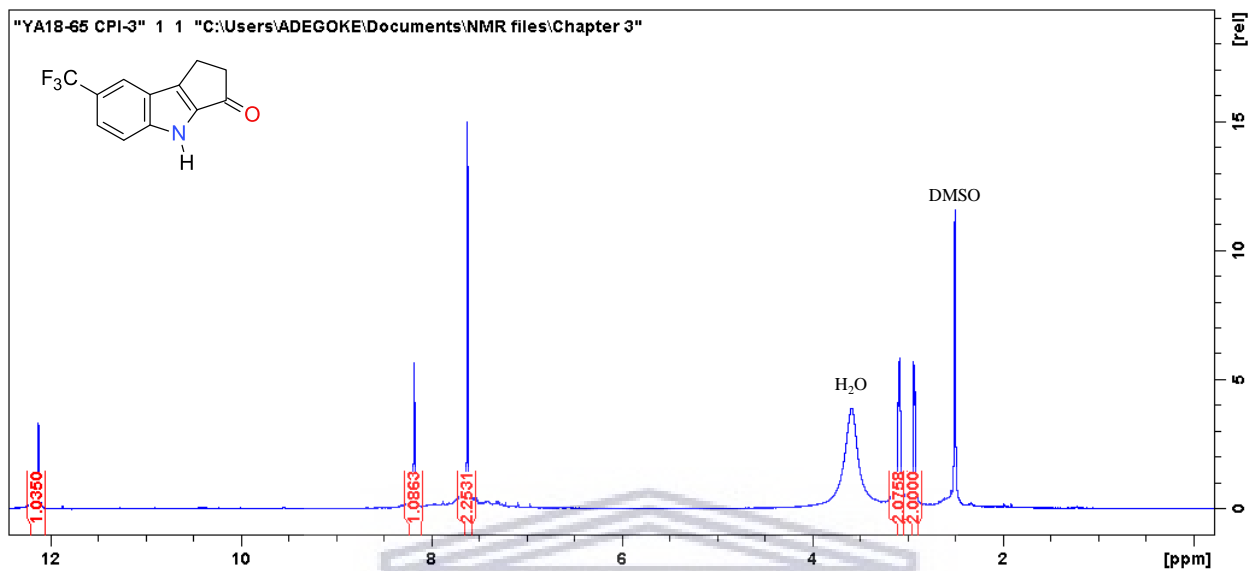


Figure S3.9: ^{13}C NMR spectrum of compound **3.32c** (100 MHz, DMSO-d_6)

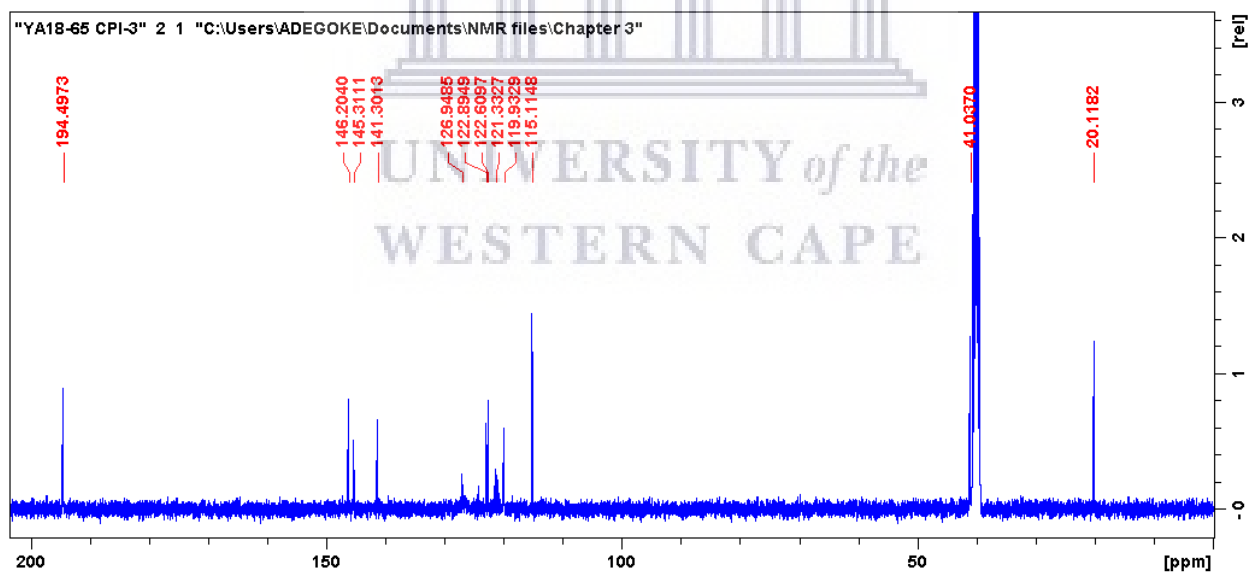


Figure S3.10: HRMS of compound **3.32c**

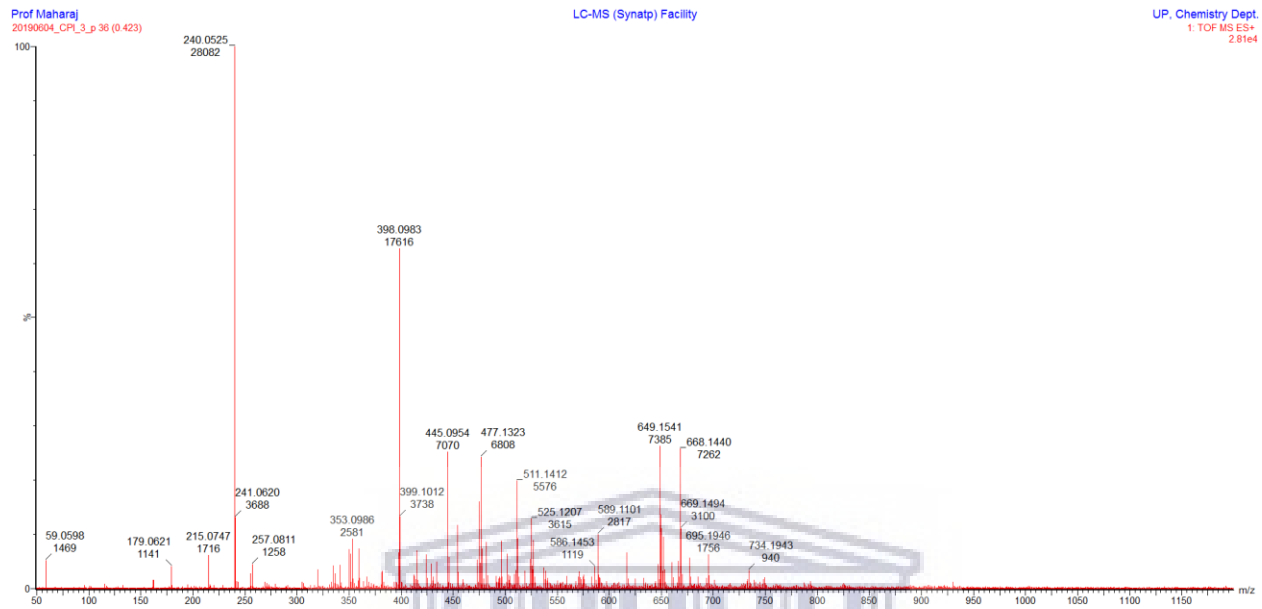


Figure S3.11: IR spectrum of compound **3.32c**

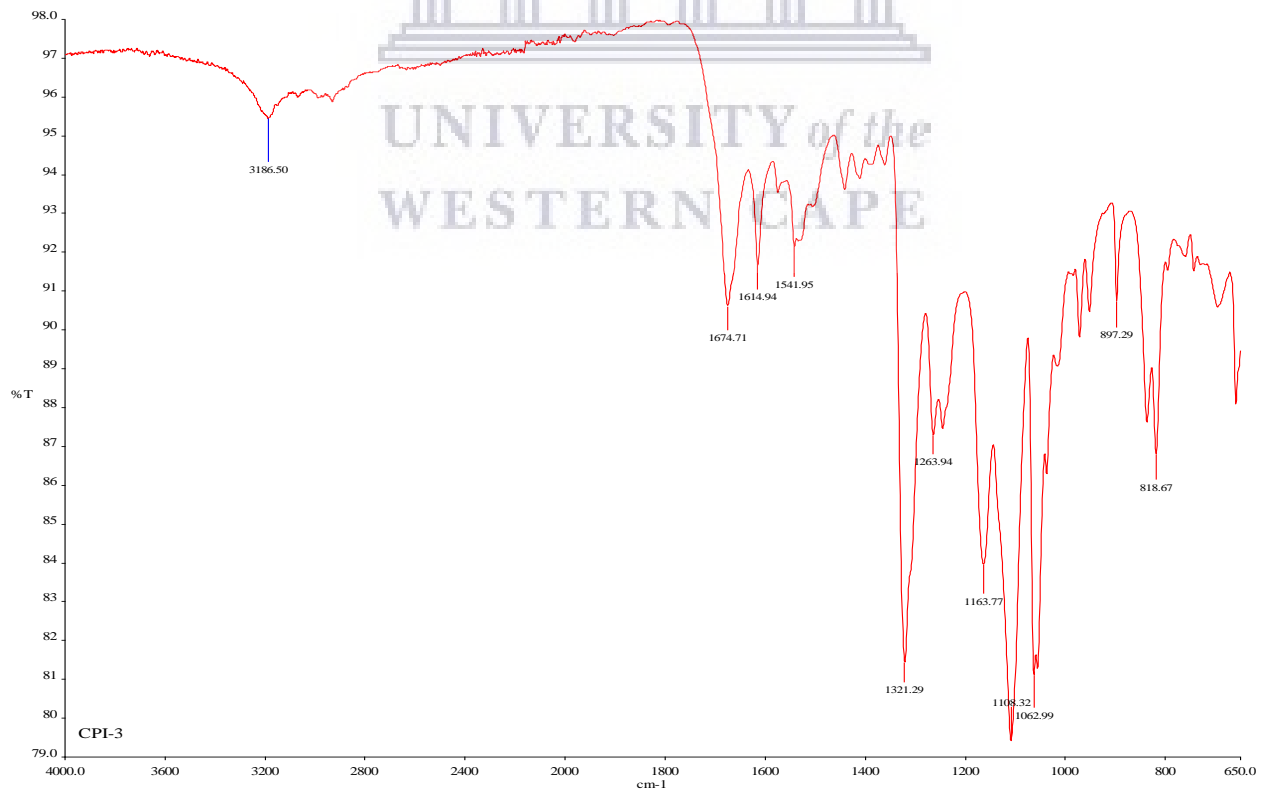


Figure S3.12: ^1H NMR spectrum of compound **3.32d** (400 MHz, DMSO- d_6)

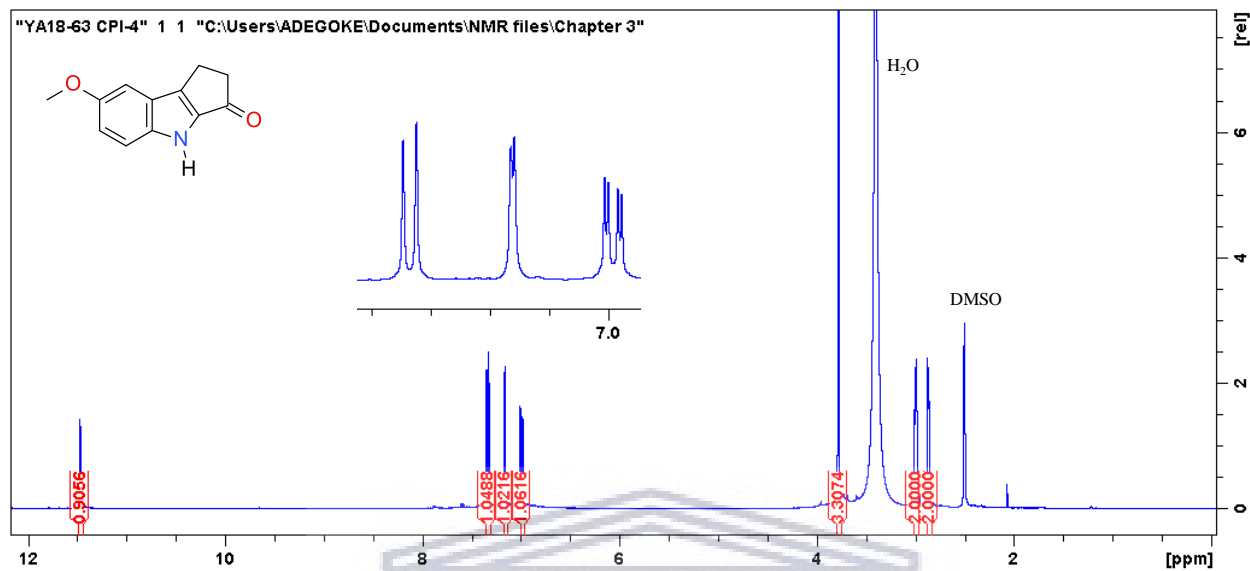


Figure S3.13: ^{13}C NMR spectrum of compound **3.32d** (100 MHz, DMSO- d_6)

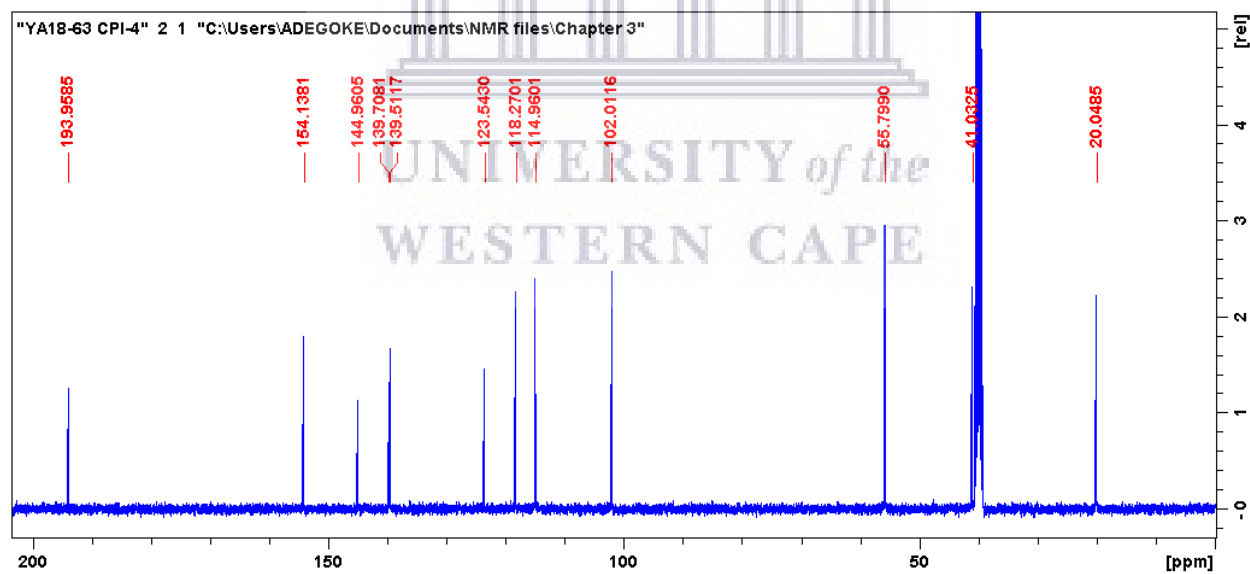


Figure S3.14: HRMS spectrum of compound **3.32d**

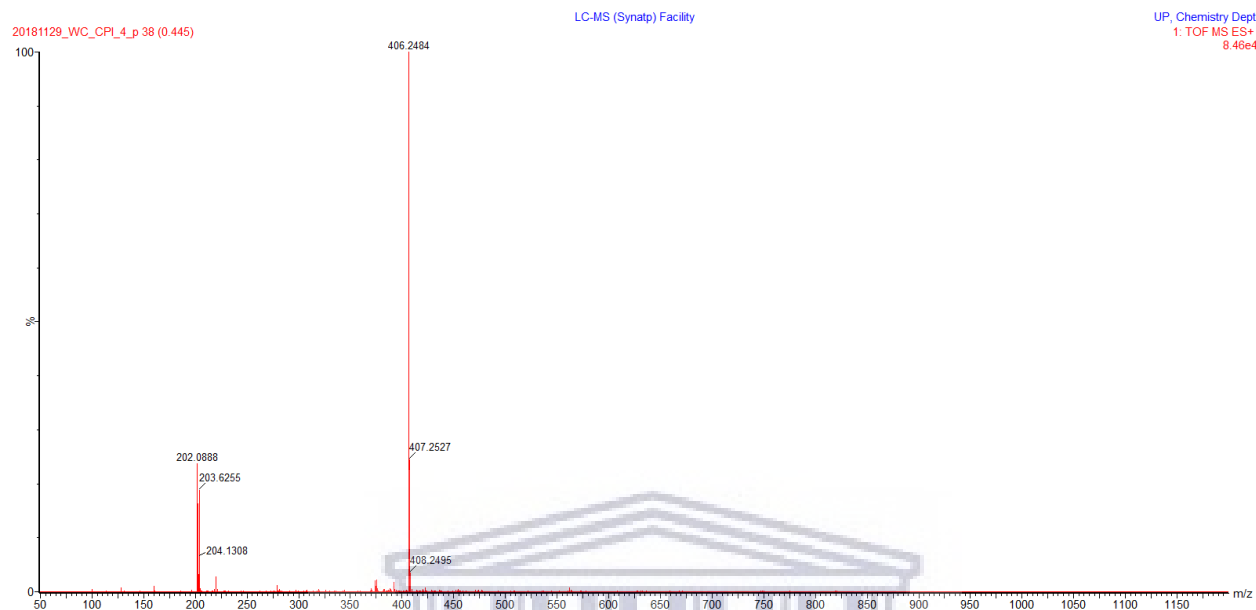


Figure S3.15: IR spectrum of compound **3.32d**

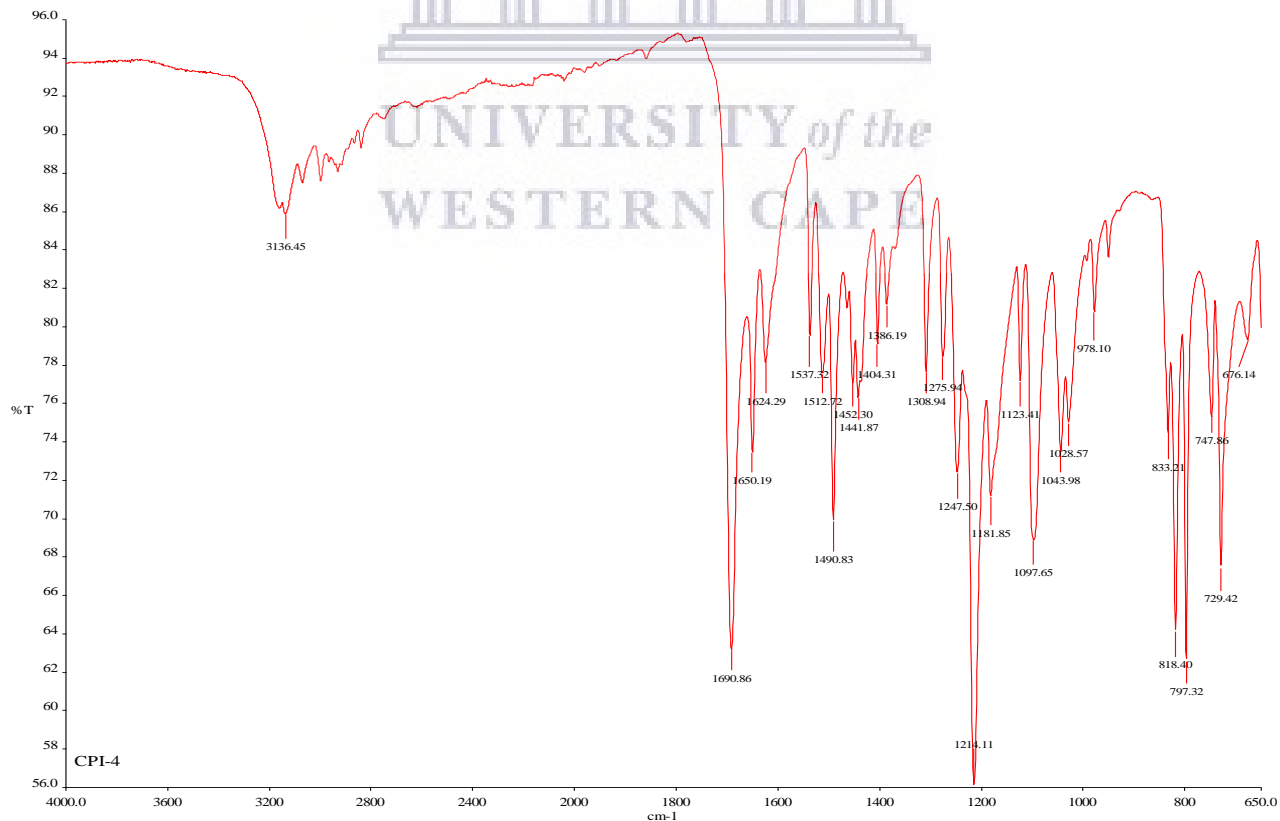


Figure S3.16: ^1H NMR spectrum of compound **3.32e** (400 MHz, DMSO-d_6)

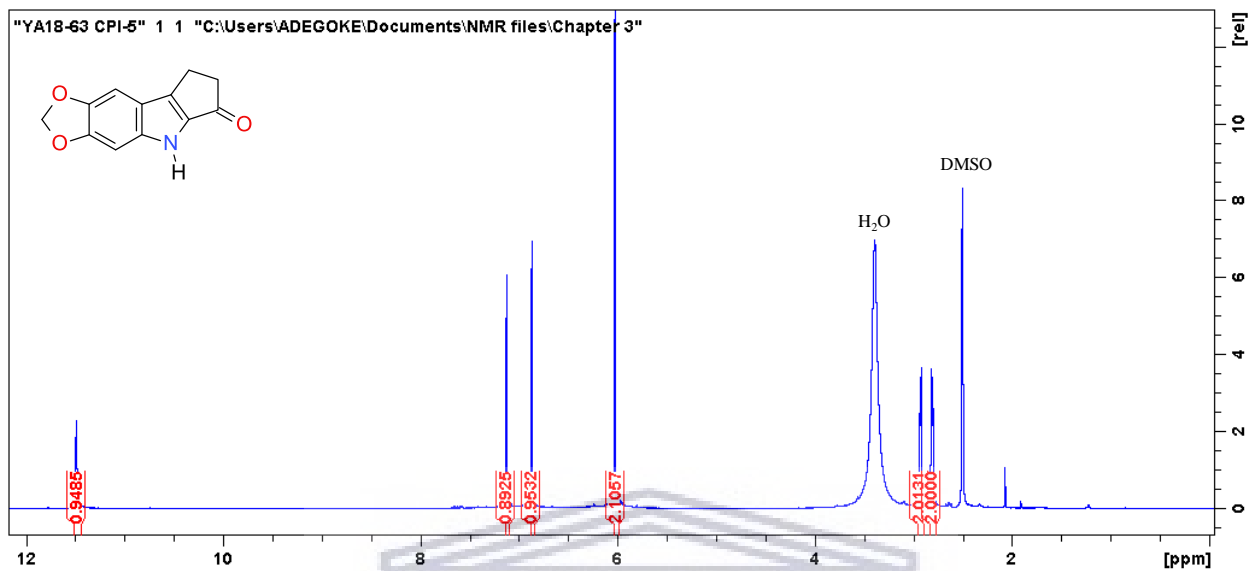


Figure S3.17: ^{13}C NMR spectrum of compound **3.32e** (100 MHz, DMSO-d_6)

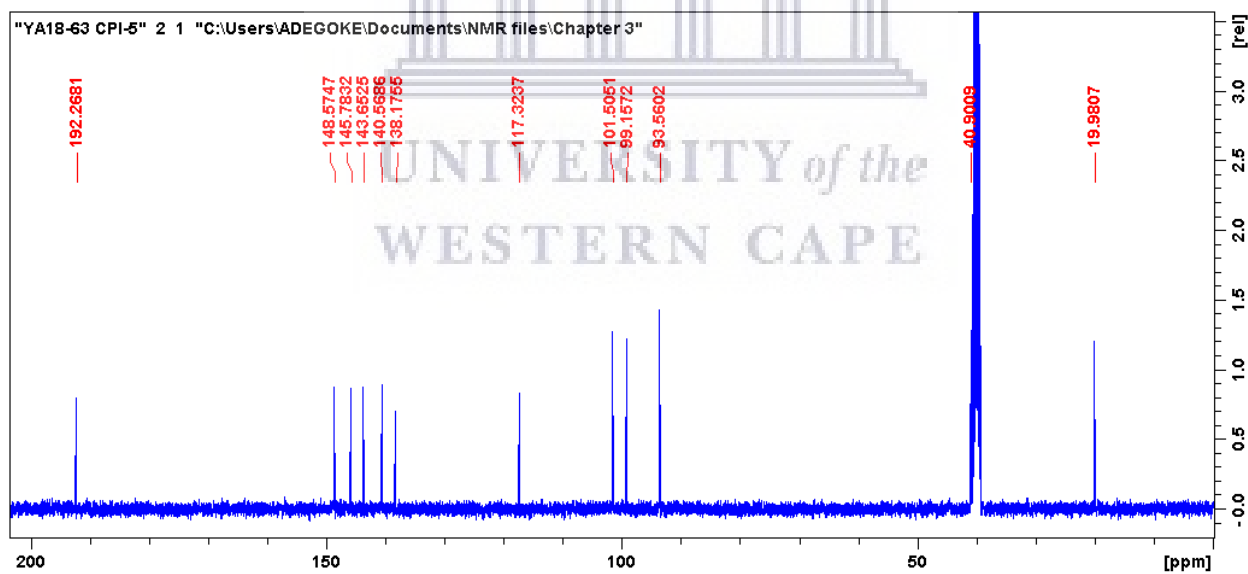


Figure S3.18: HRMS spectrum of compound **3.32e**

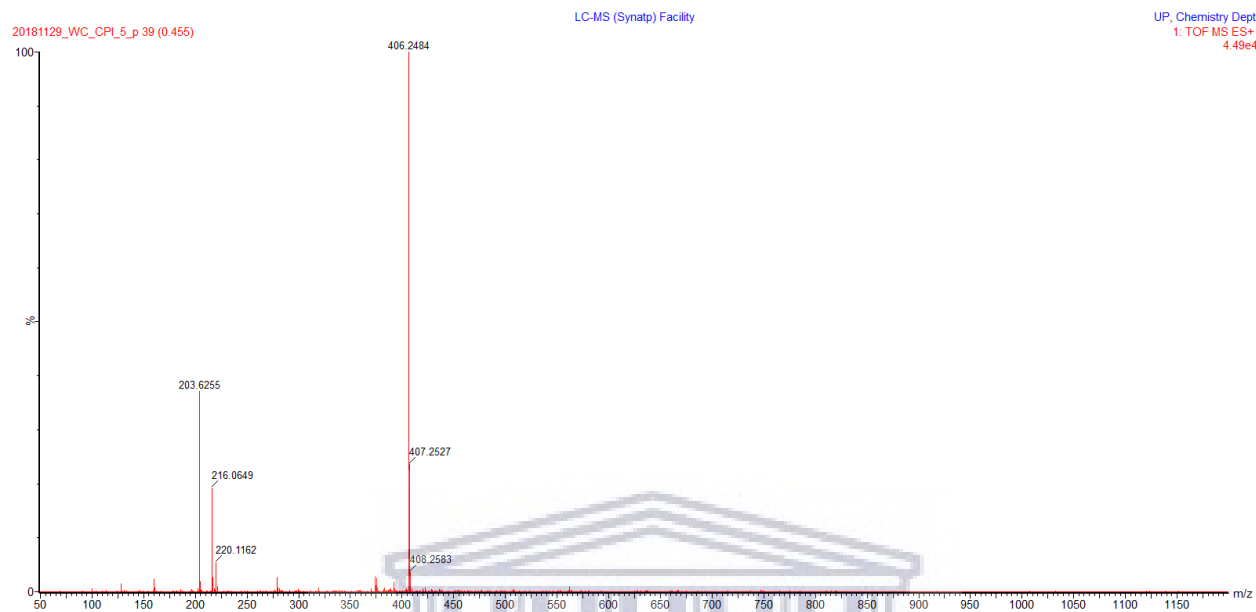


Figure S3.19: IR spectrum of compound **3.32e**

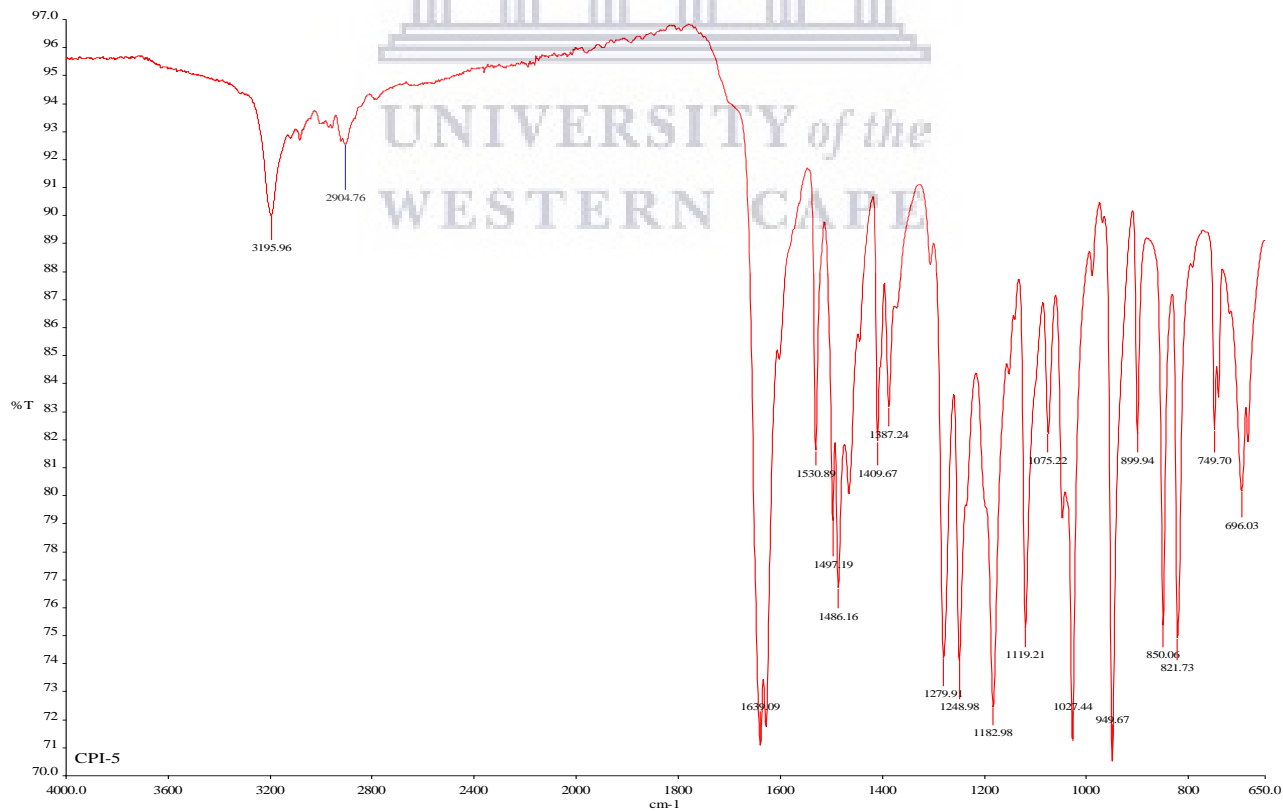


Figure S3.20: ^1H NMR spectrum of compound **3.32f** (400 MHz, DMSO- d_6)

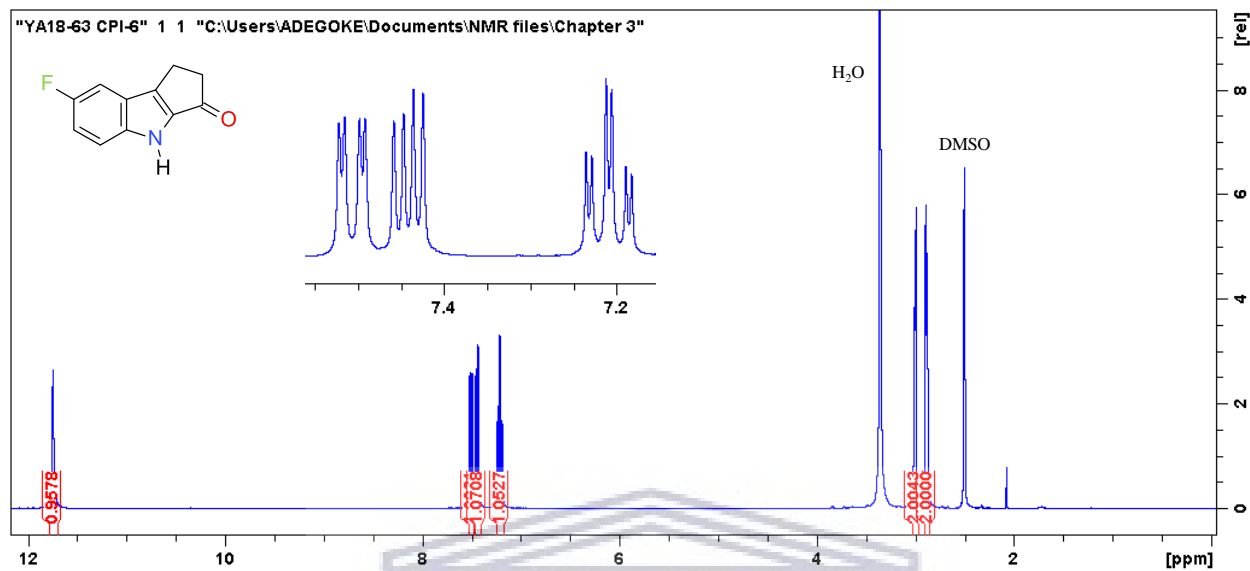


Figure S3.21: ^{13}C NMR spectrum of compound **3.32f** (100 MHz, DMSO- d_6)

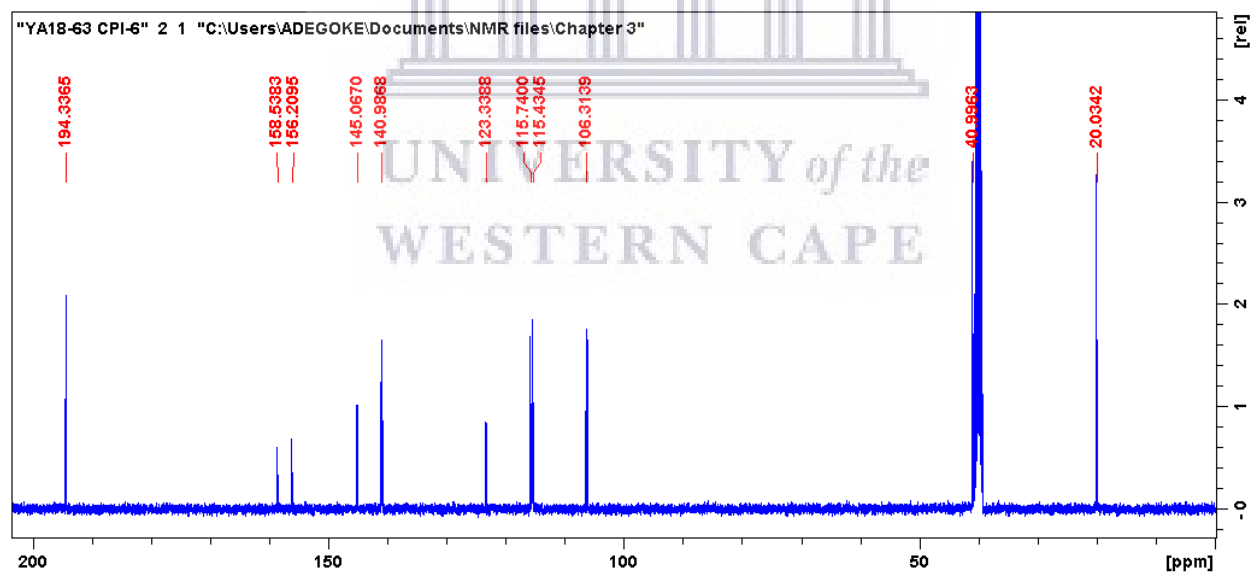


Figure S3.22: HRMS spectrum of compound **3.32f**

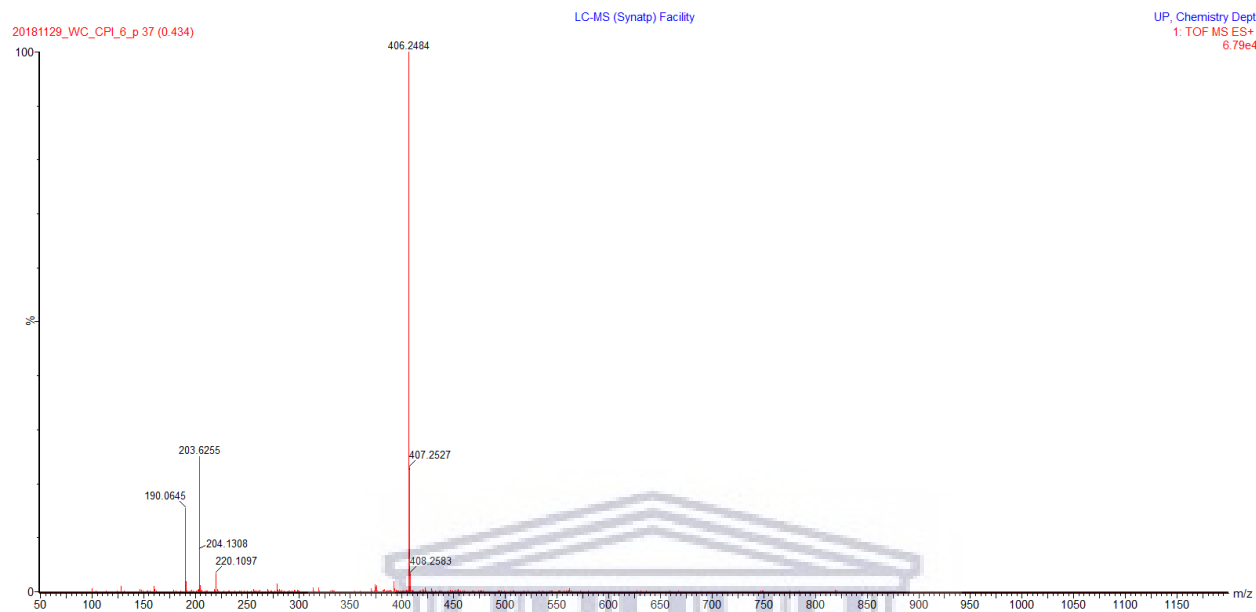


Figure S3.23: IR spectrum of compound **3.32f**

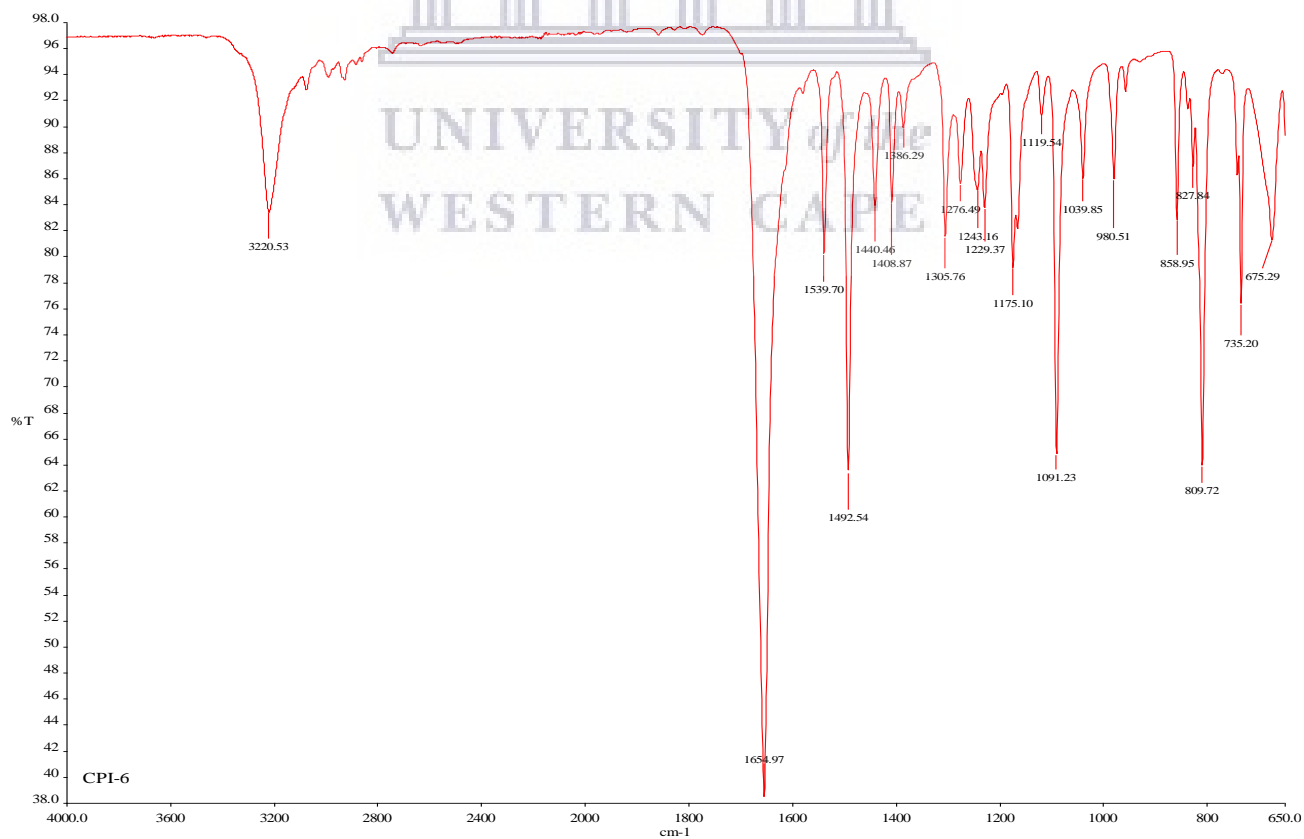


Figure S3.24: ^1H NMR spectrum of compound **3.32g** (400 MHz, DMSO- d_6)

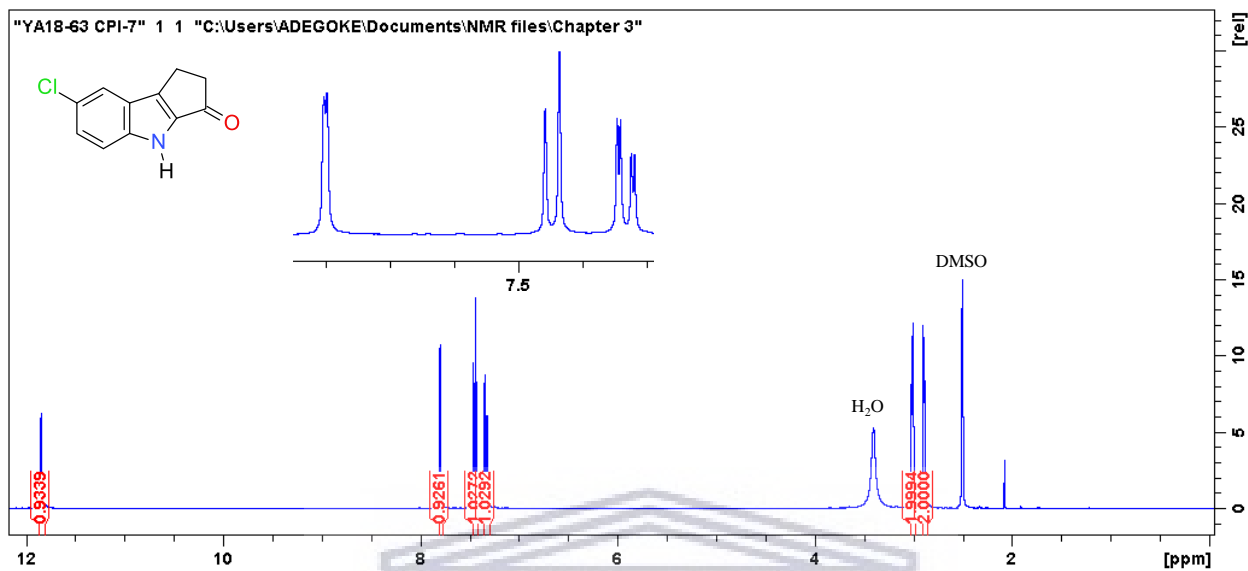


Figure S3.25: ^{13}C NMR spectrum of compound **3.32g** (100 MHz, DMSO- d_6)

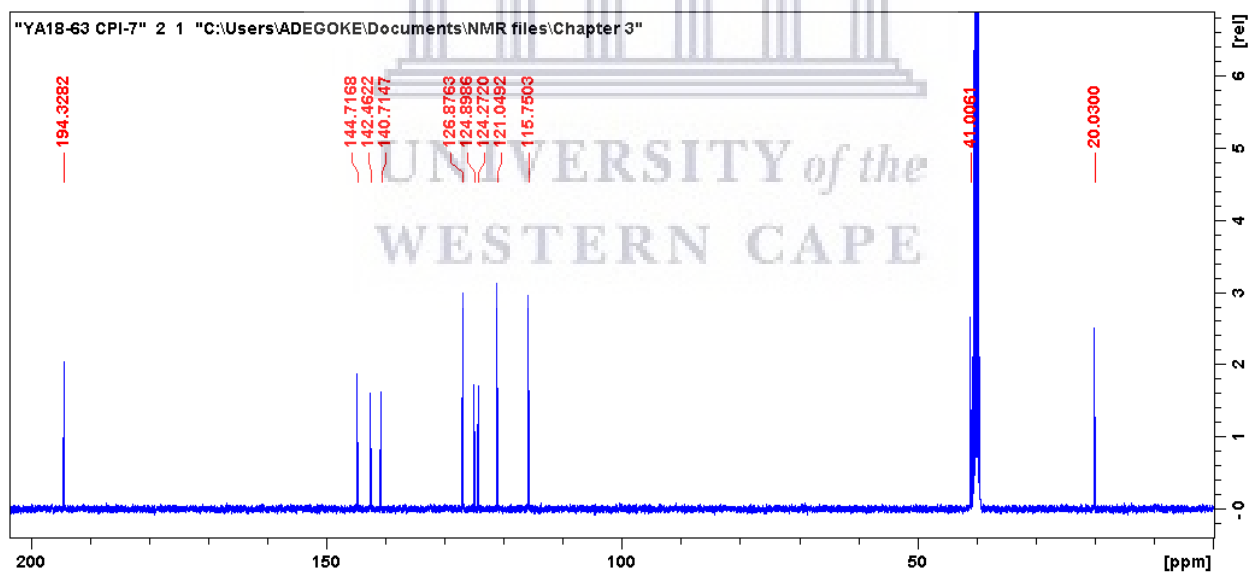


Figure S3.26: HRMS spectrum of compound **3.32g**

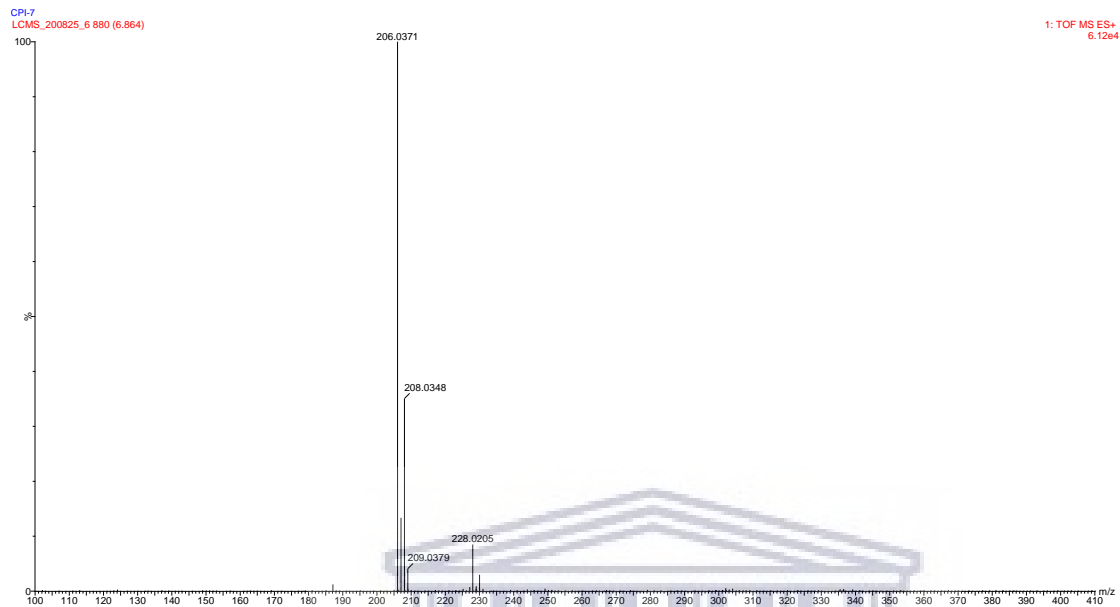


Figure S3.27: IR spectrum of compound **3.32g**

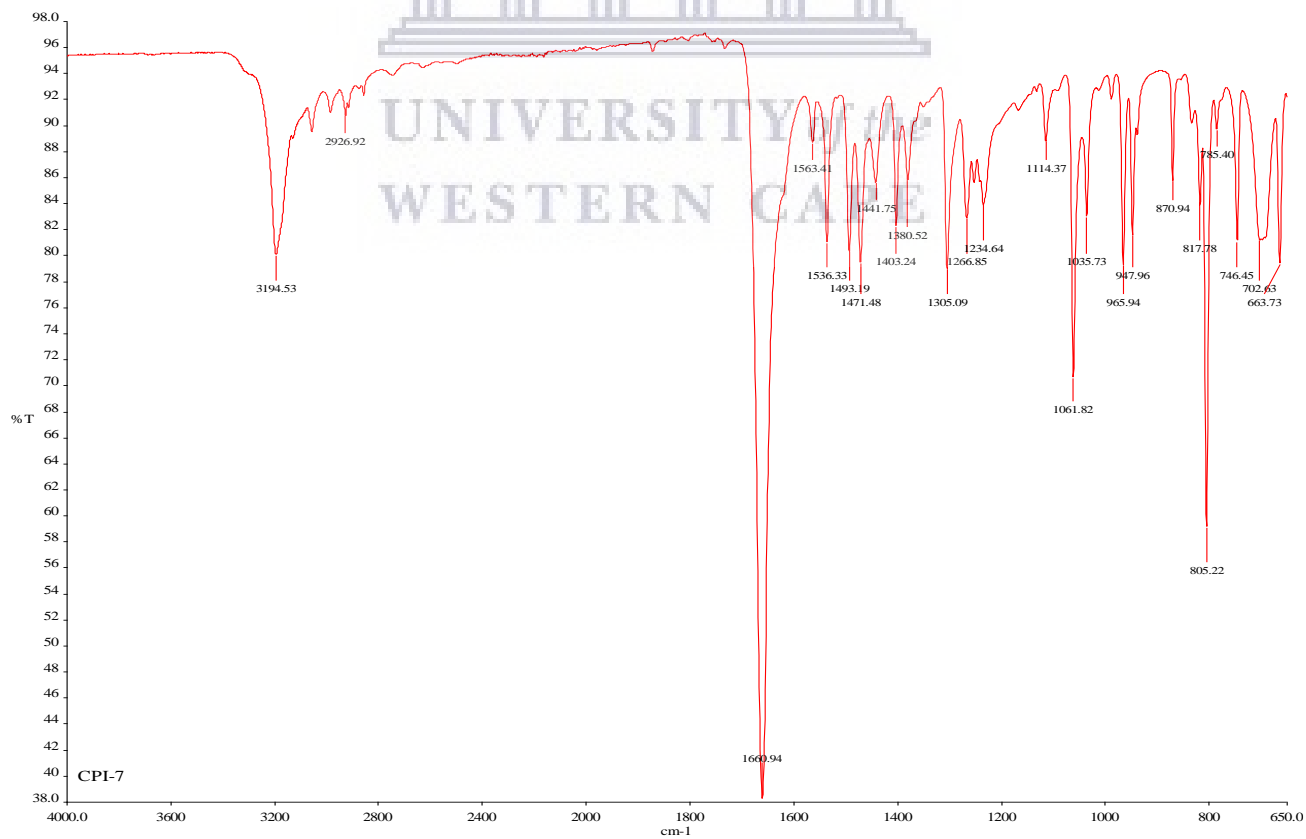


Figure S3.28: ^1H NMR spectrum of compound **3.32h** (400 MHz, DMSO-d_6)

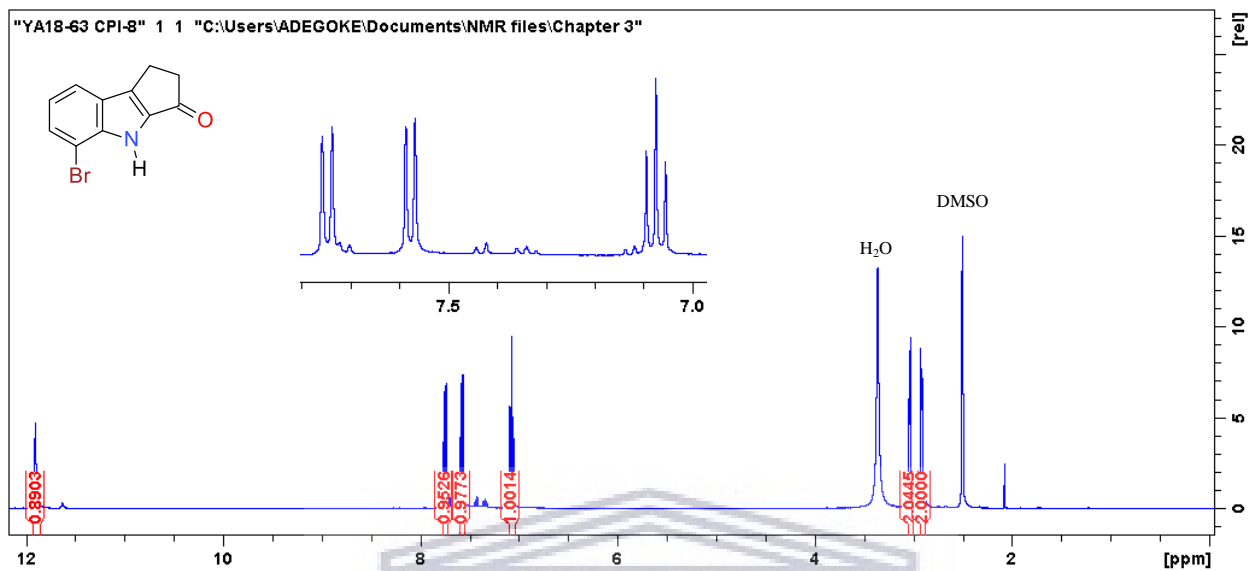


Figure S3.29: ^{13}C NMR spectrum of compound **3.32h** (100 MHz, DMSO-d_6)

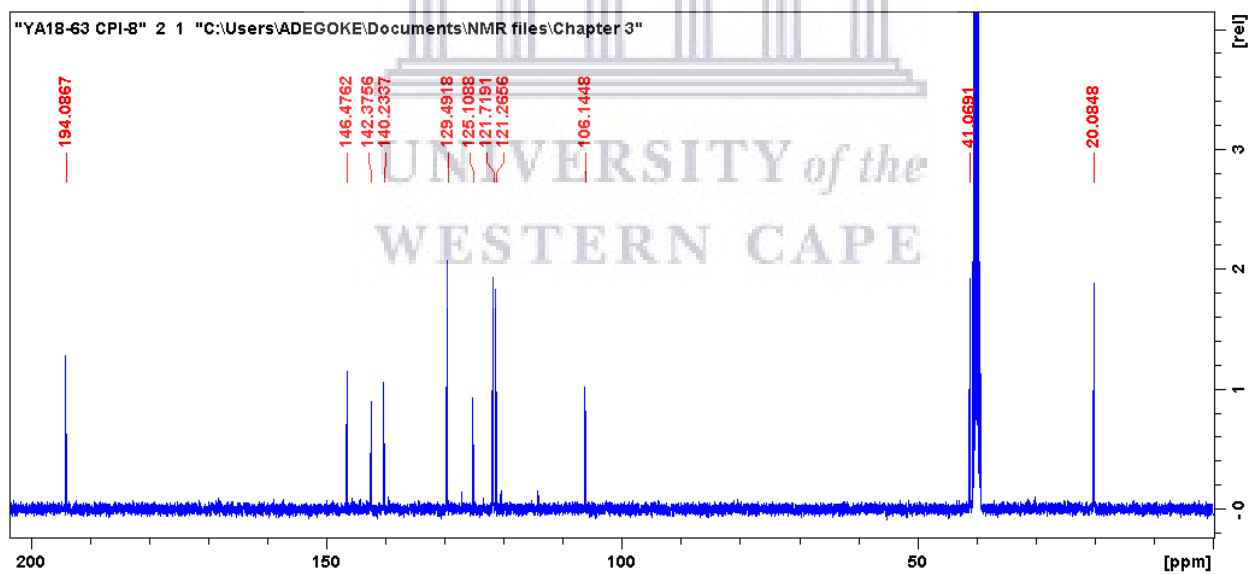


Figure S3.30: HRMS spectrum of compound **3.32h**

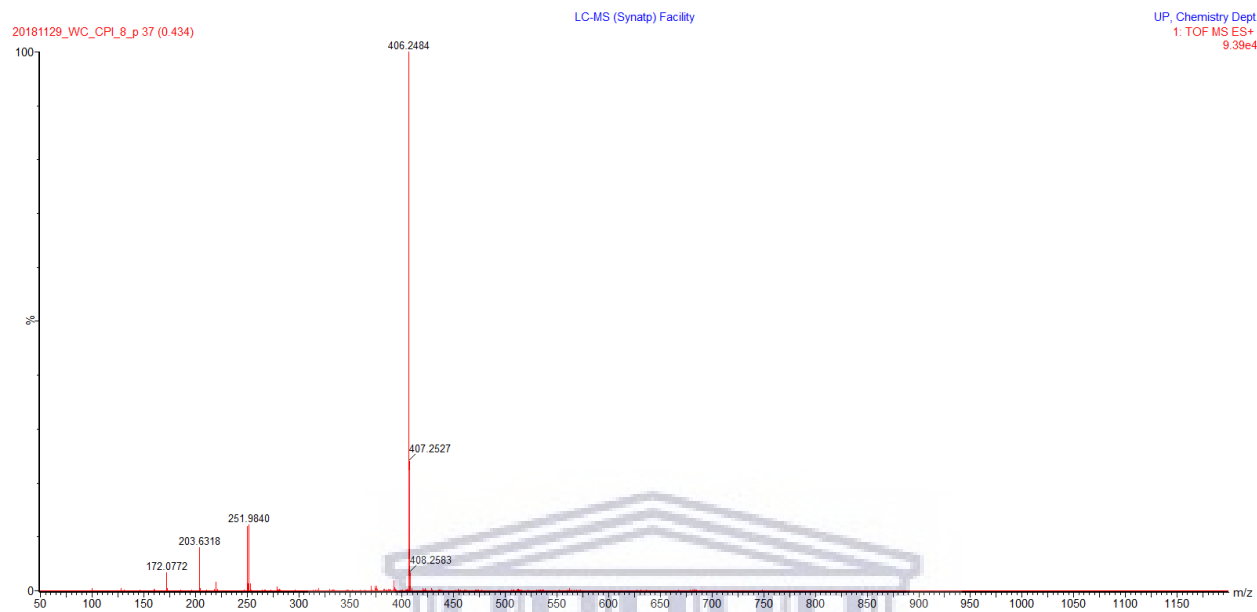


Figure S3.31: IR spectrum of compound **3.32h**

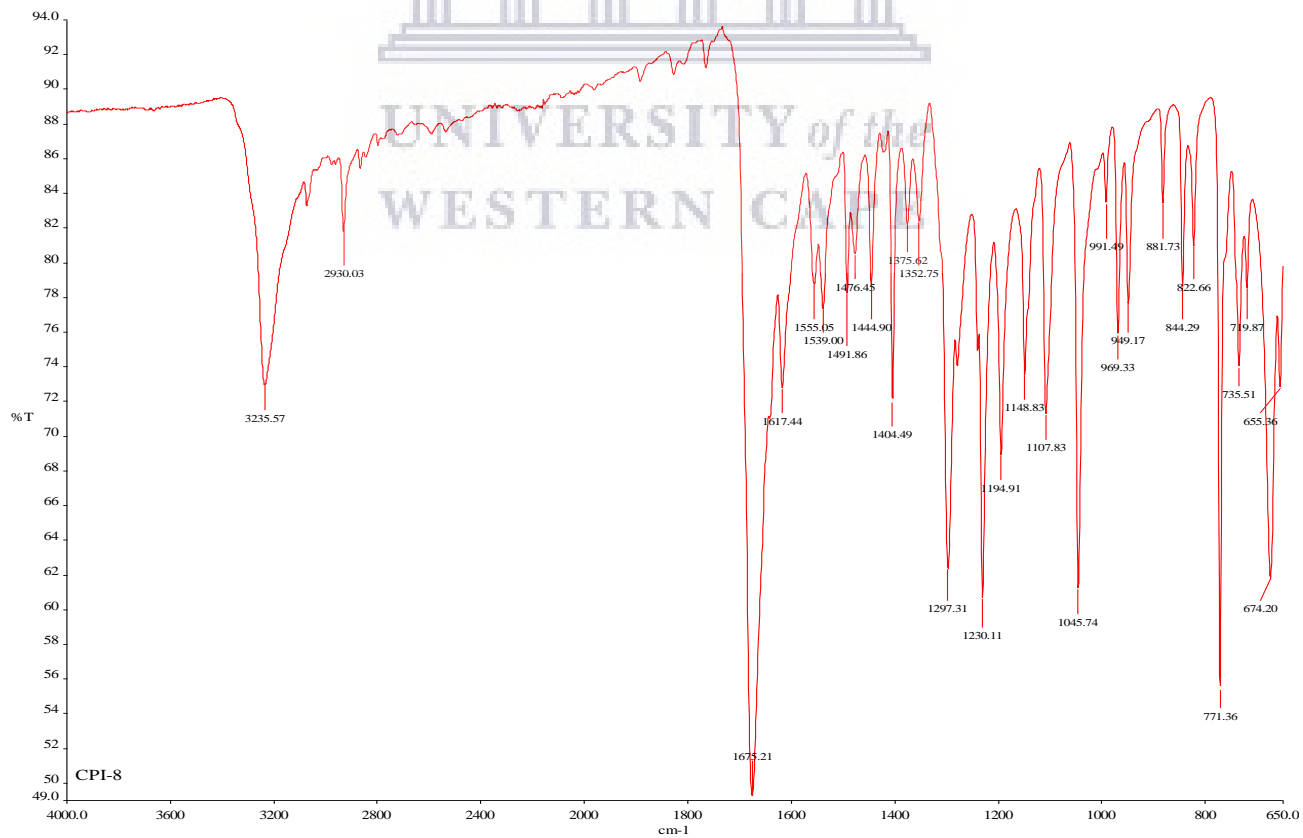


Figure S3.32: ^1H NMR spectrum of compound **3.32i** (400 MHz, DMSO-d_6)

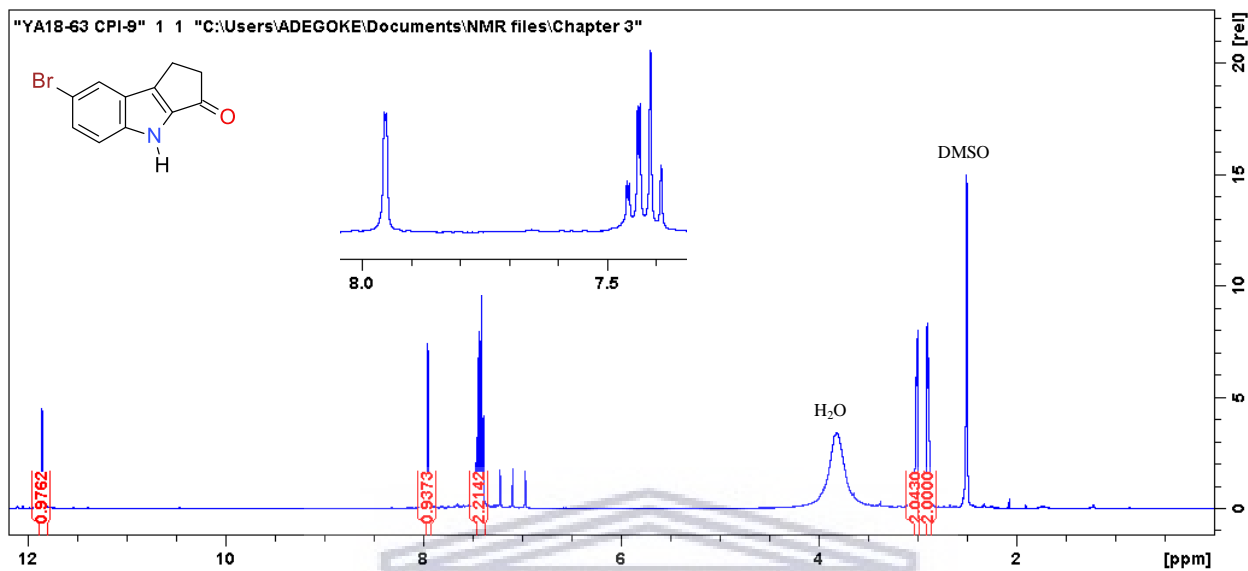


Figure S3.33: ^{13}C NMR spectrum of compound **3.32i** (100 MHz, DMSO-d_6)

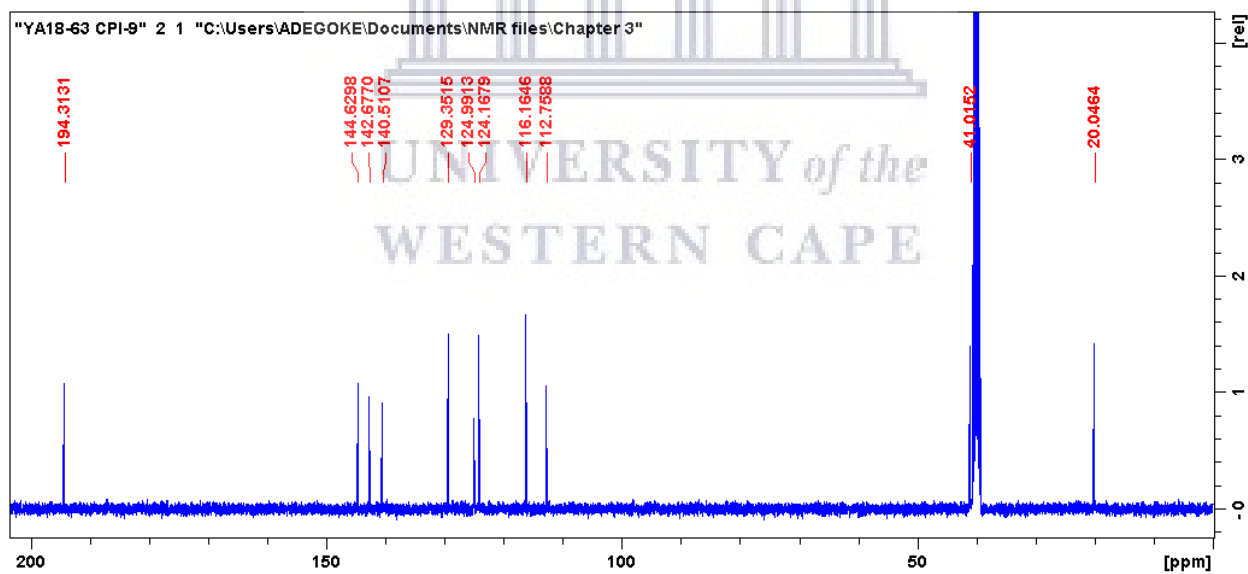


Figure S3.34: HRMS spectrum of compound **3.32i**

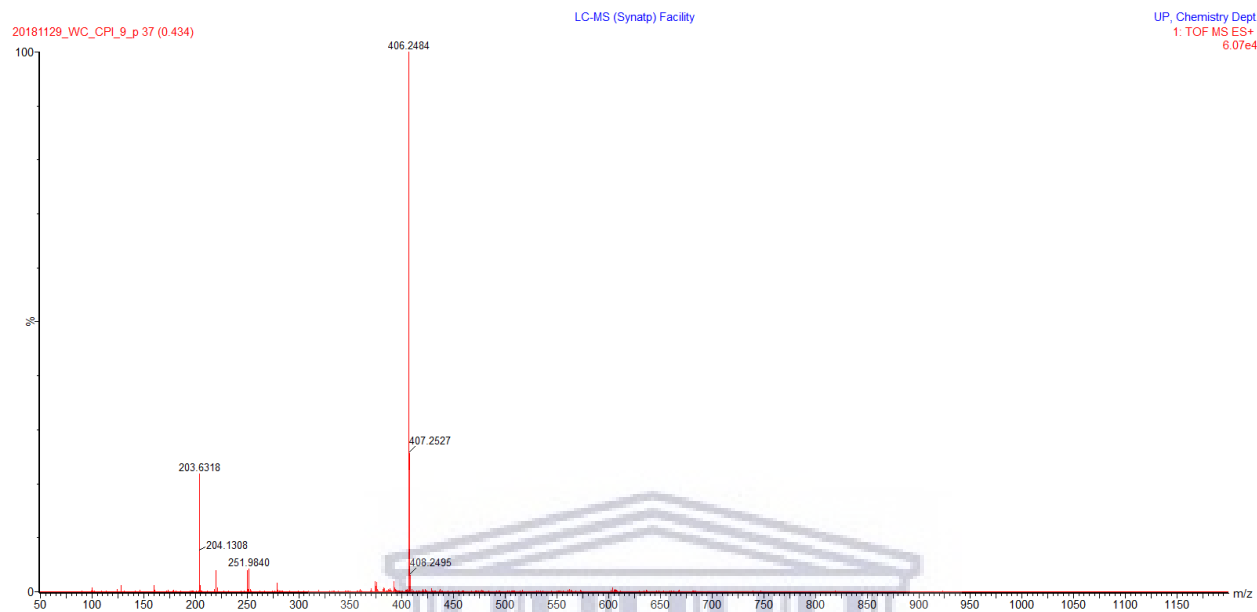


Figure S3.35: IR spectrum of compound **3.32i**

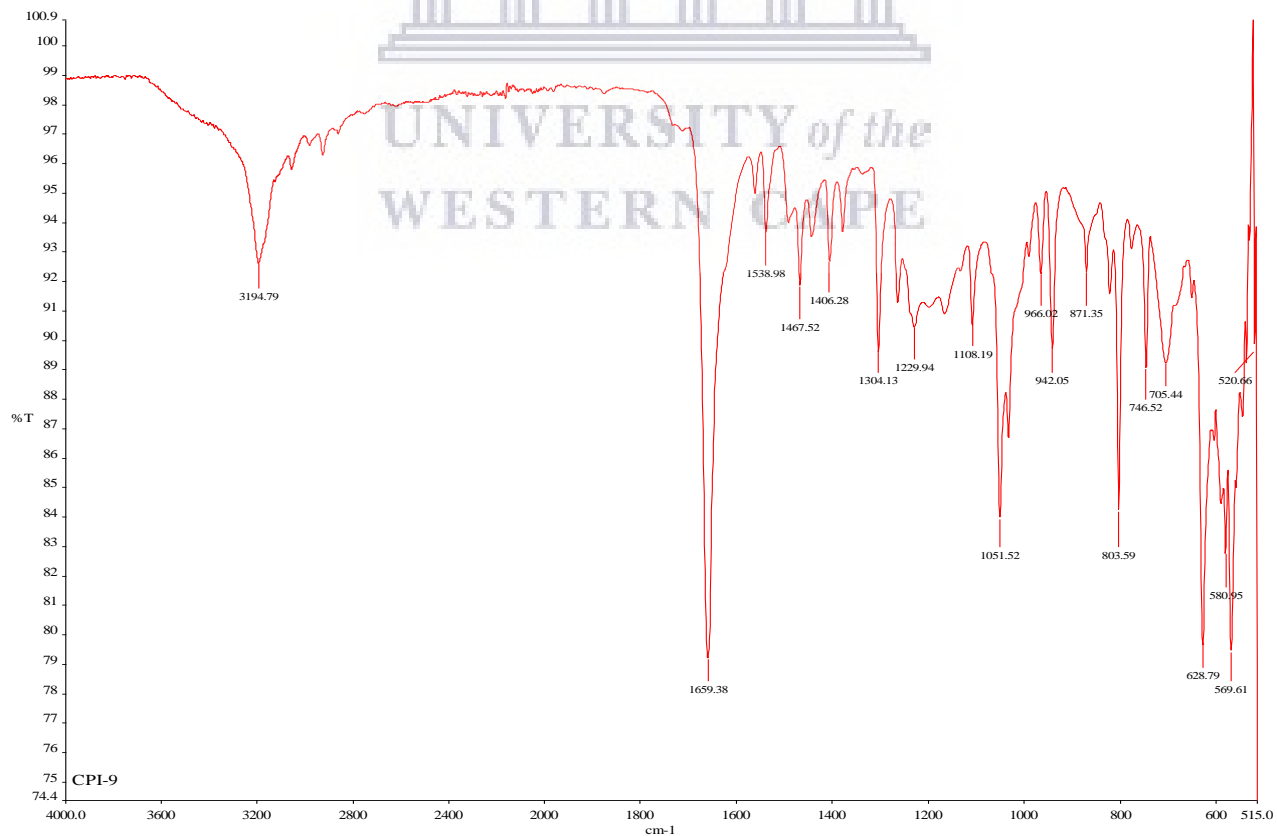


Figure S3.36: ^1H NMR spectrum of compound **3.32j** (400 MHz, DMSO-d_6)

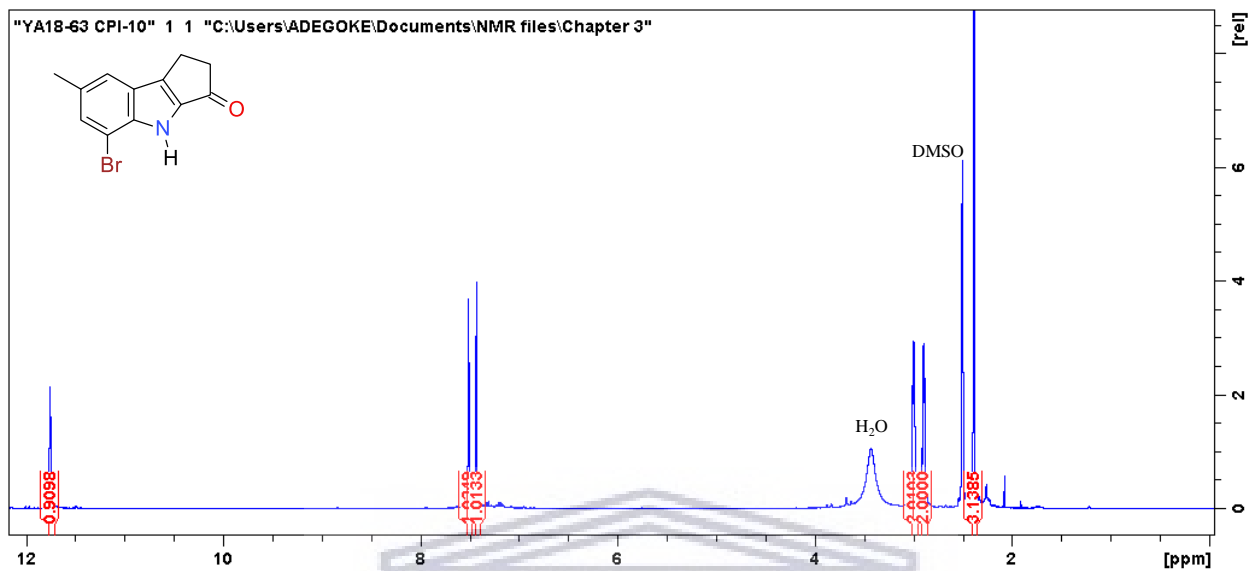


Figure S3.37: ^{13}C NMR spectrum of compound **3.32j** (100 MHz, DMSO-d_6)

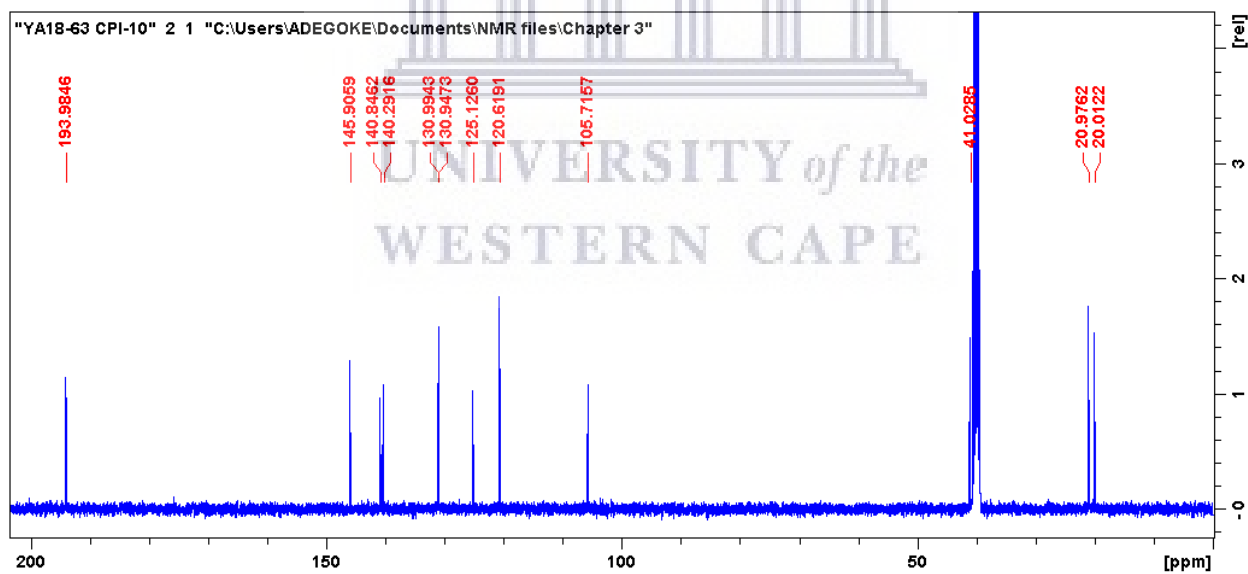


Figure S3.38: HRMS spectrum of compound **3.32j**

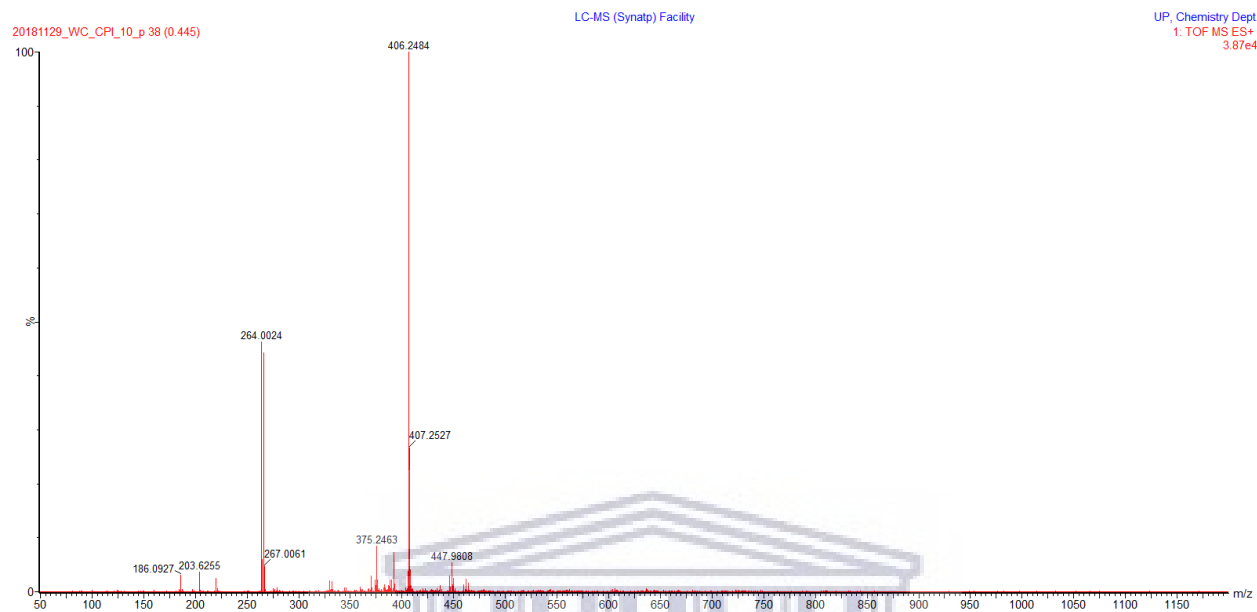


Figure S3.39: IR spectrum of compound **3.32j**

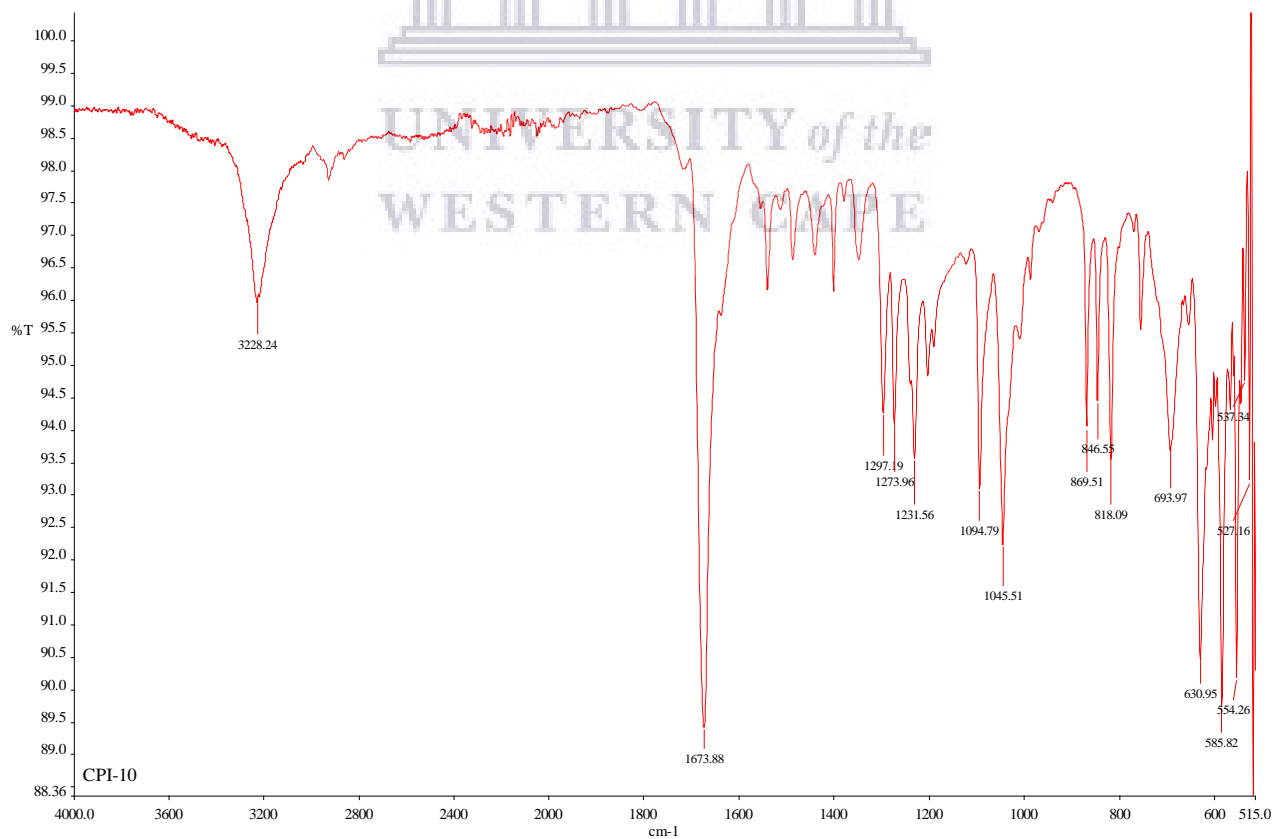


Figure S3.40: ^1H NMR spectrum of compound **3.32k** (400 MHz, DMSO- d_6)

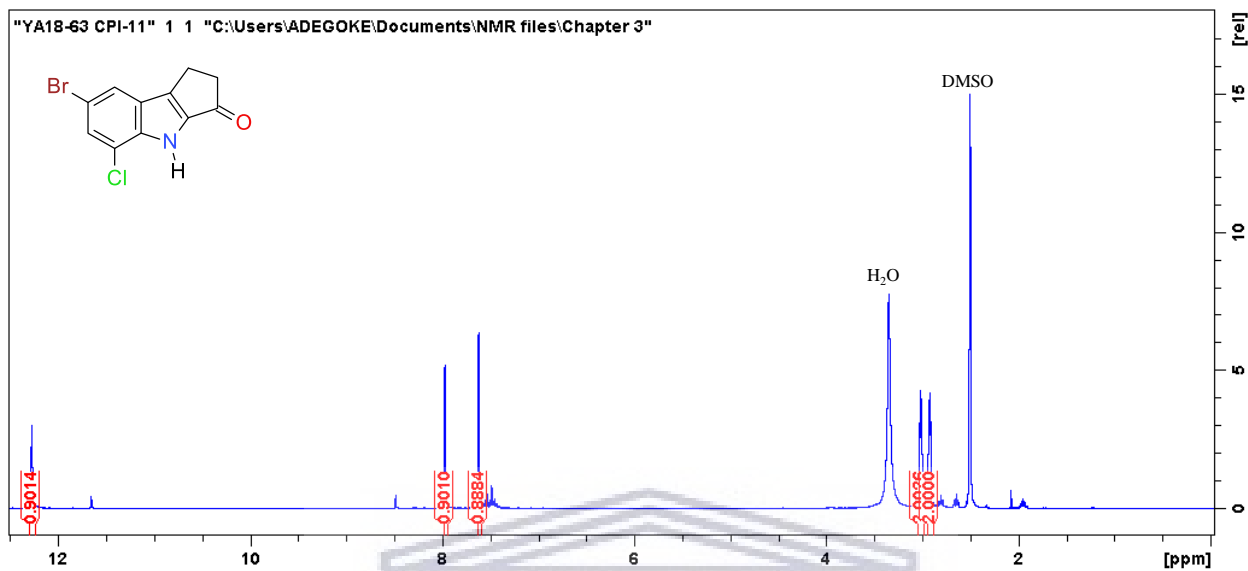


Figure S3.41: ^{13}C NMR spectrum of compound **3.32k** (100 MHz, DMSO- d_6)

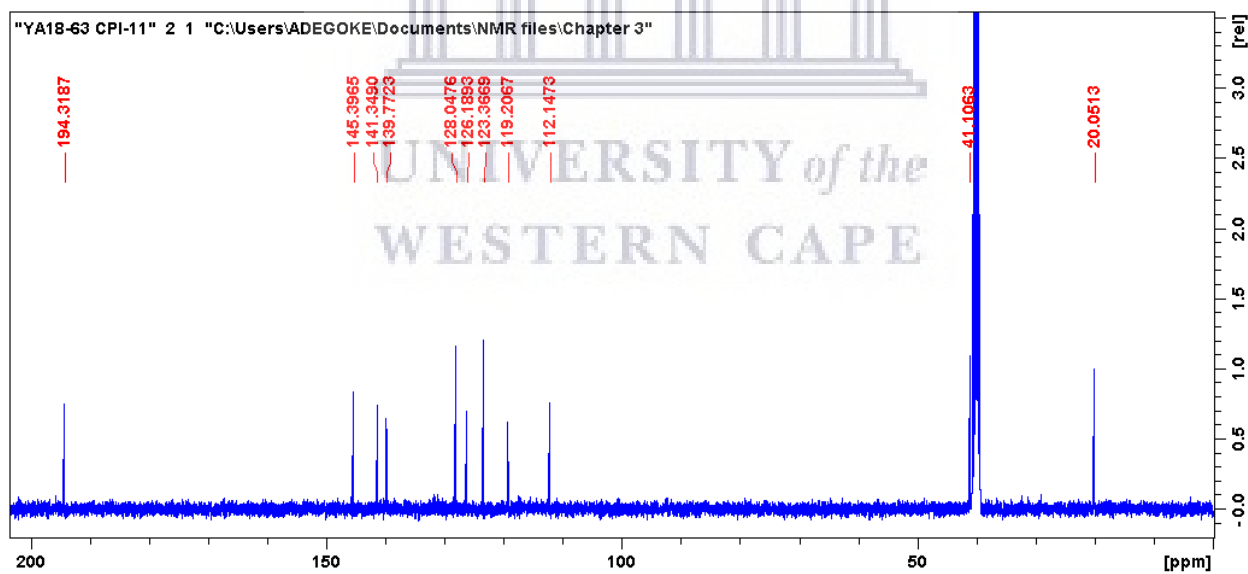


Figure S3.42: HRMS spectrum of compound **3.32k**

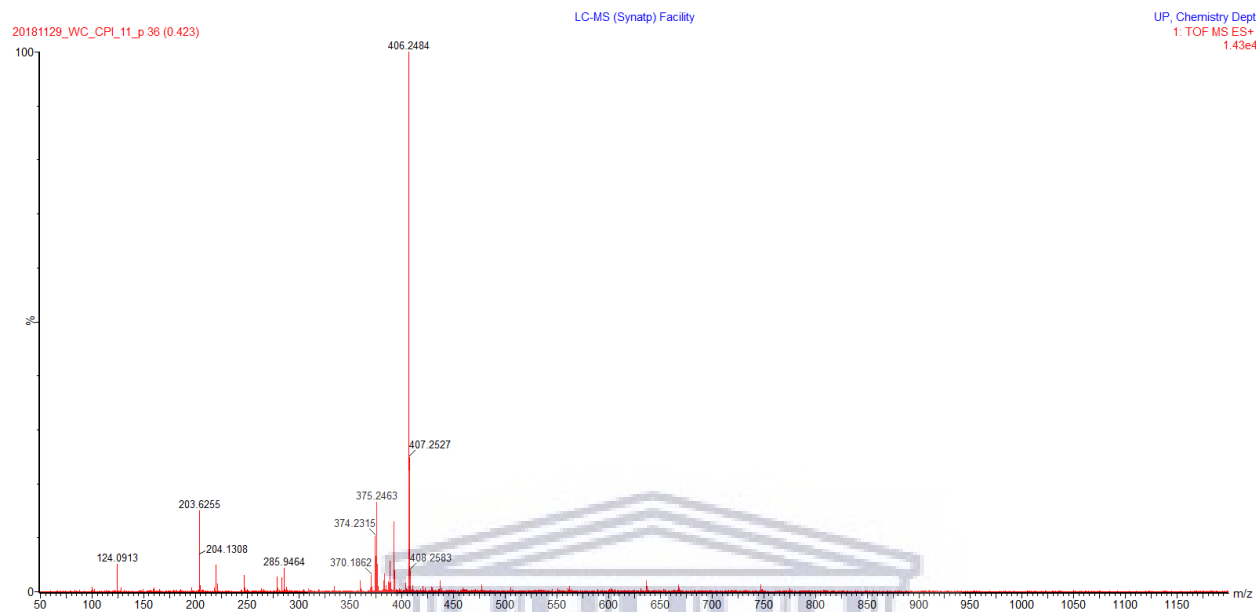


Figure S3.43: IR spectrum of compound **3.32k**

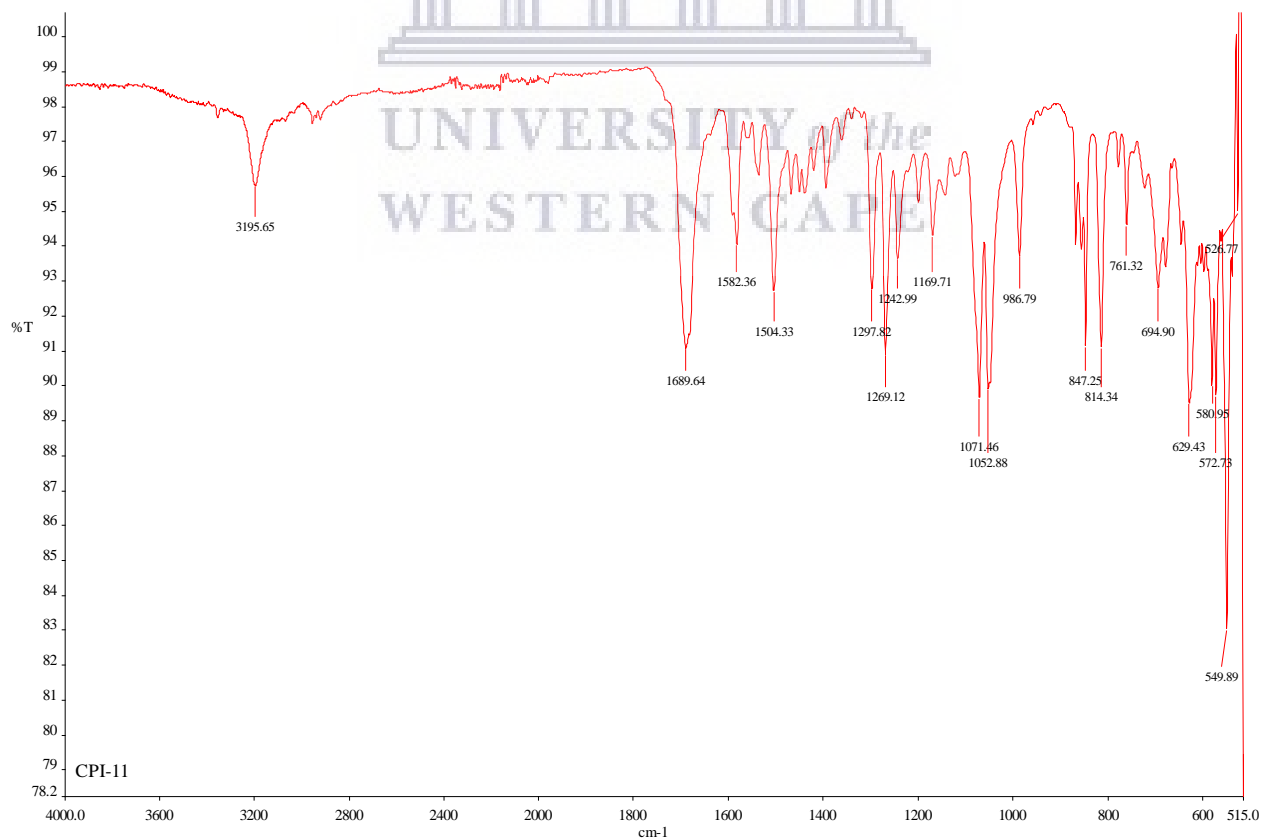


Figure S3.44: ^1H spectrum of compound **3.321** (400 MHz, DMSO-d_6)

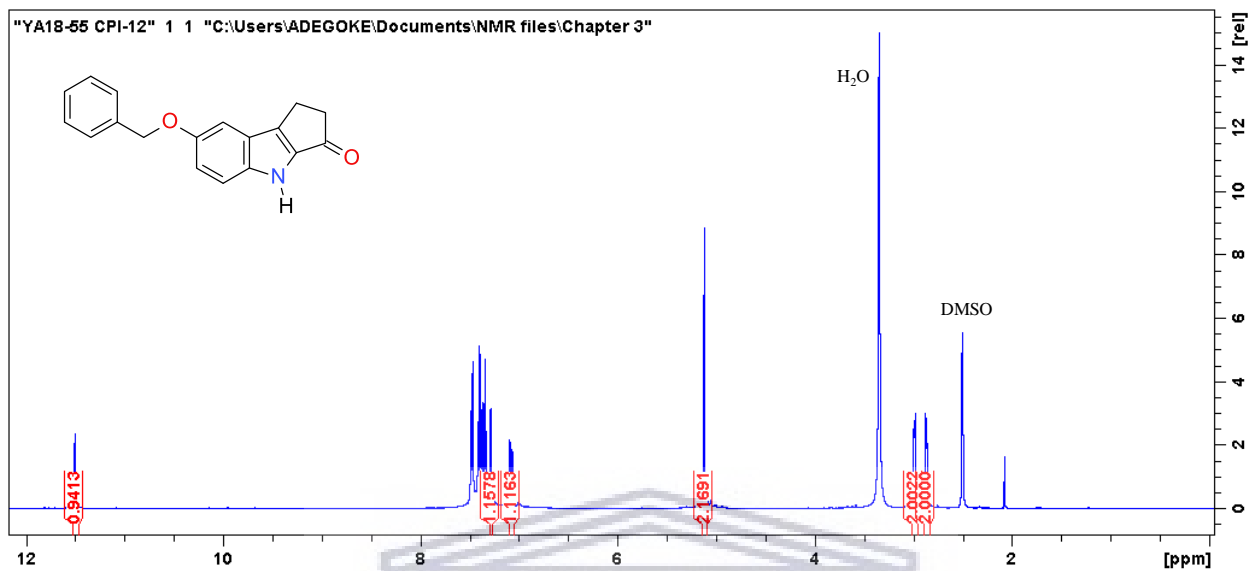


Figure S3.45: ^{13}C NMR spectrum of compound **3.321** (100 MHz, DMSO-d_6)

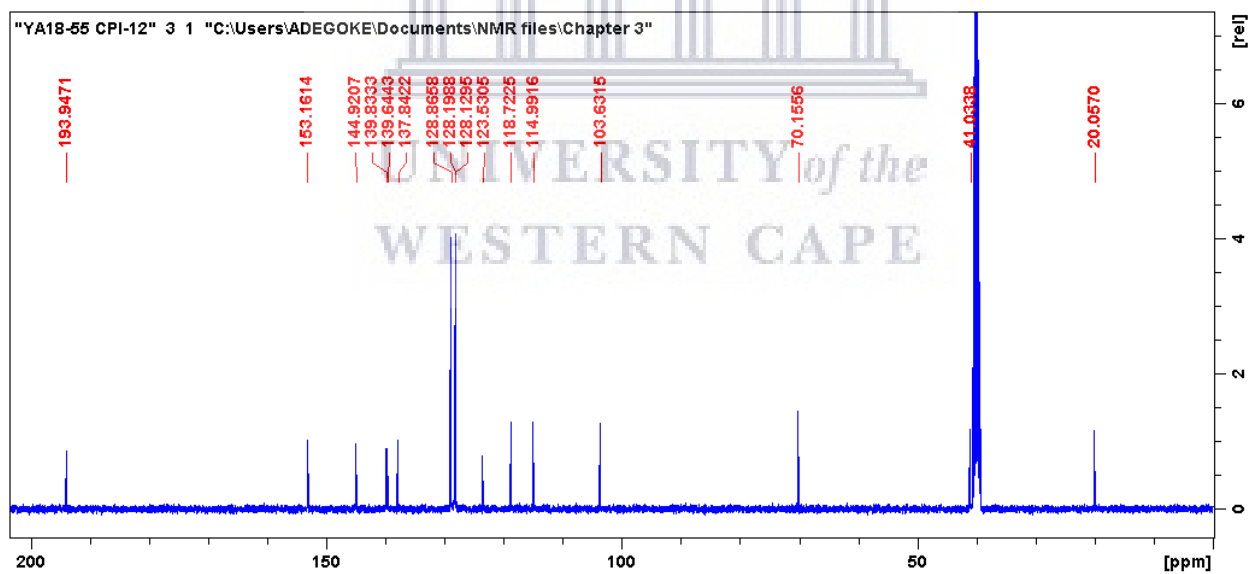


Figure S3.46: HRMS spectrum of compound **3.321**

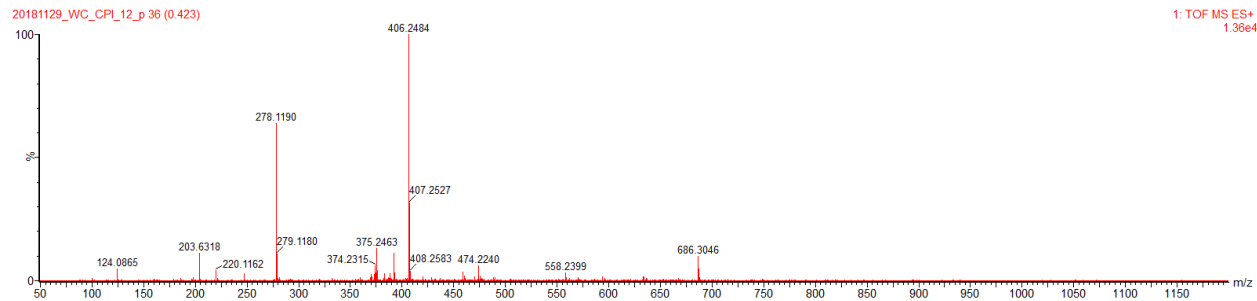
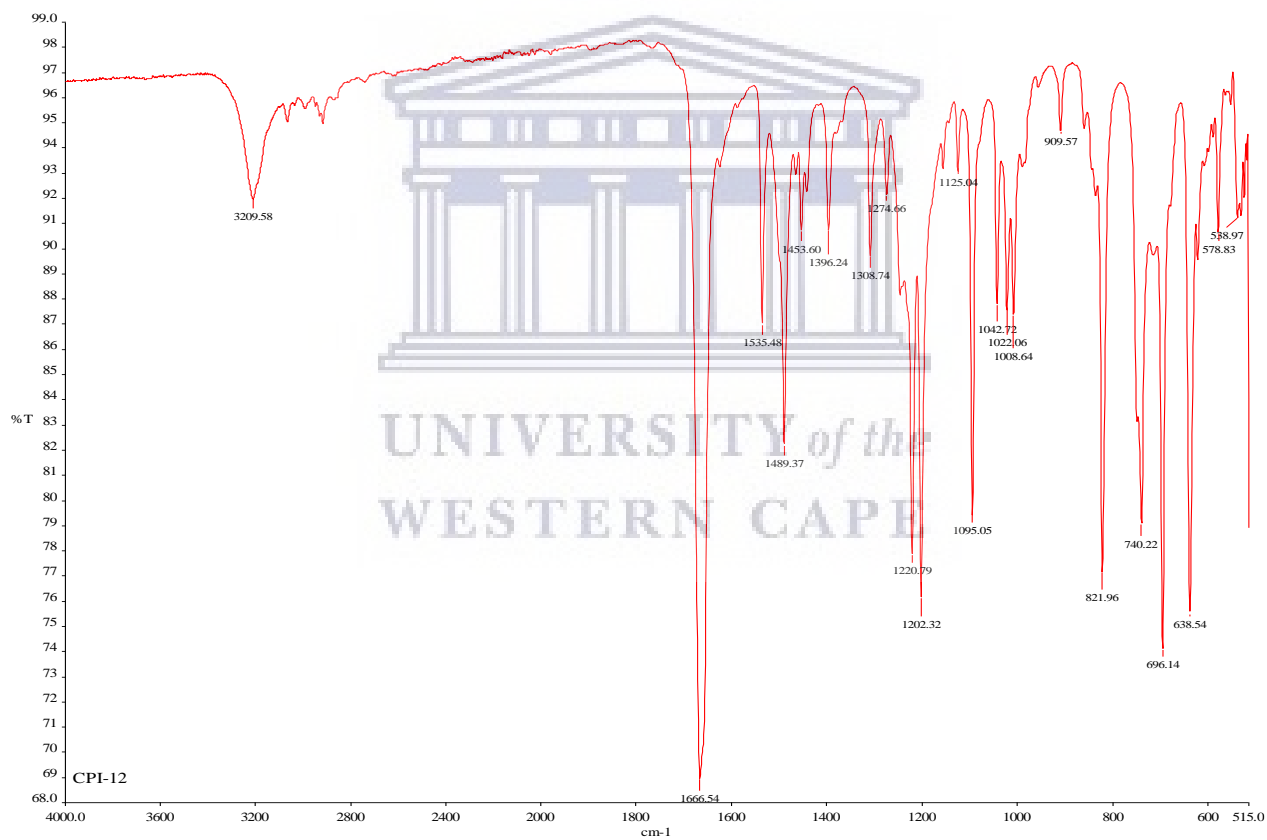


Figure S3.47: IR spectrum of compound **3.321**



Chapter 4

Phenyl substituted cyclopenta[*b*]indol-3-one series 4.31(a-l)

Figure S4.1: ^1H NMR spectrum of compound 4.31a (400 MHz, DMSO- d_6)

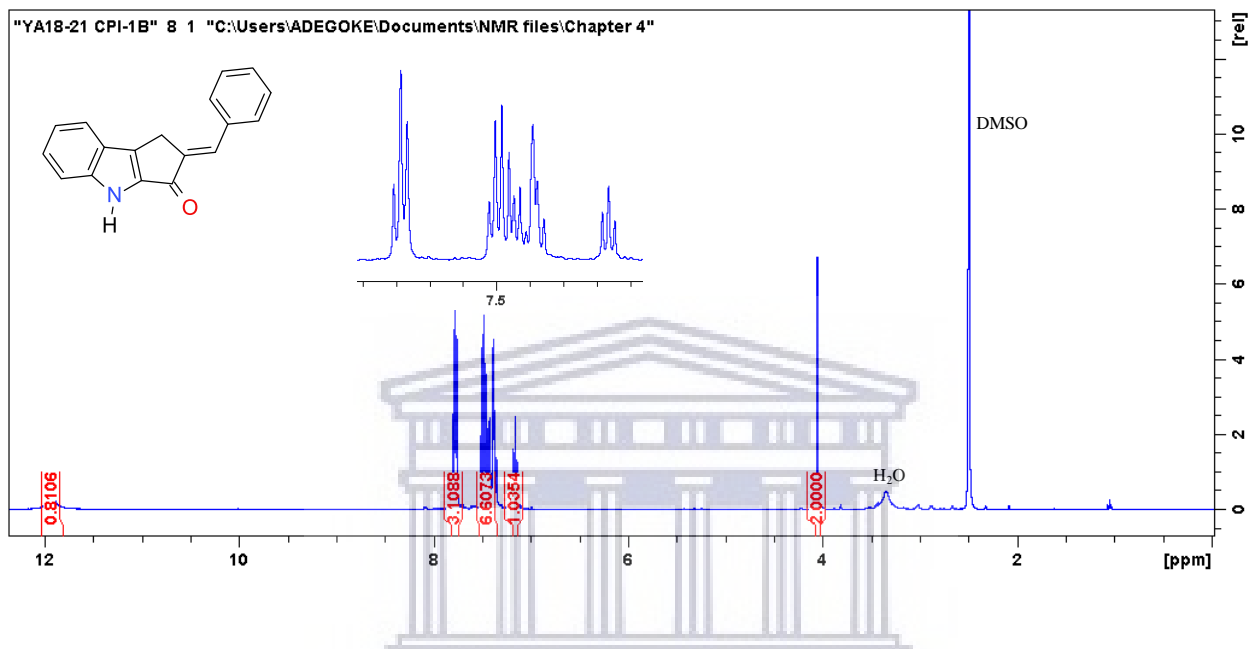


Figure S4.2: ^{13}C NMR spectrum of compound 4.31a (100 MHz, DMSO- d_6)

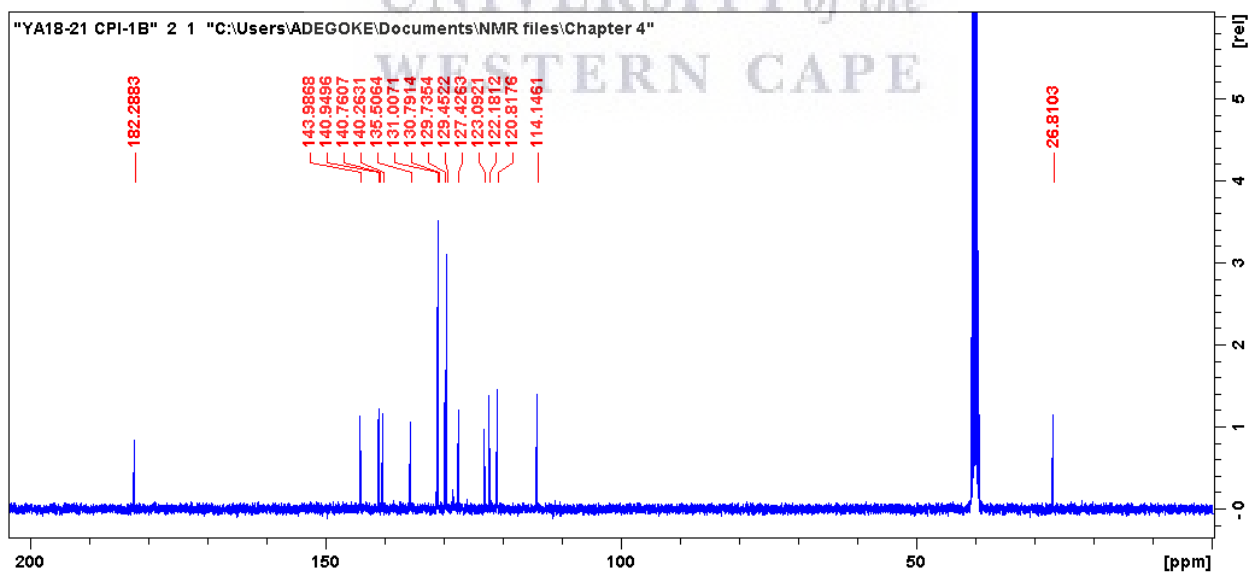


Figure S4.3: HRMS spectrum of compound **4.31a**

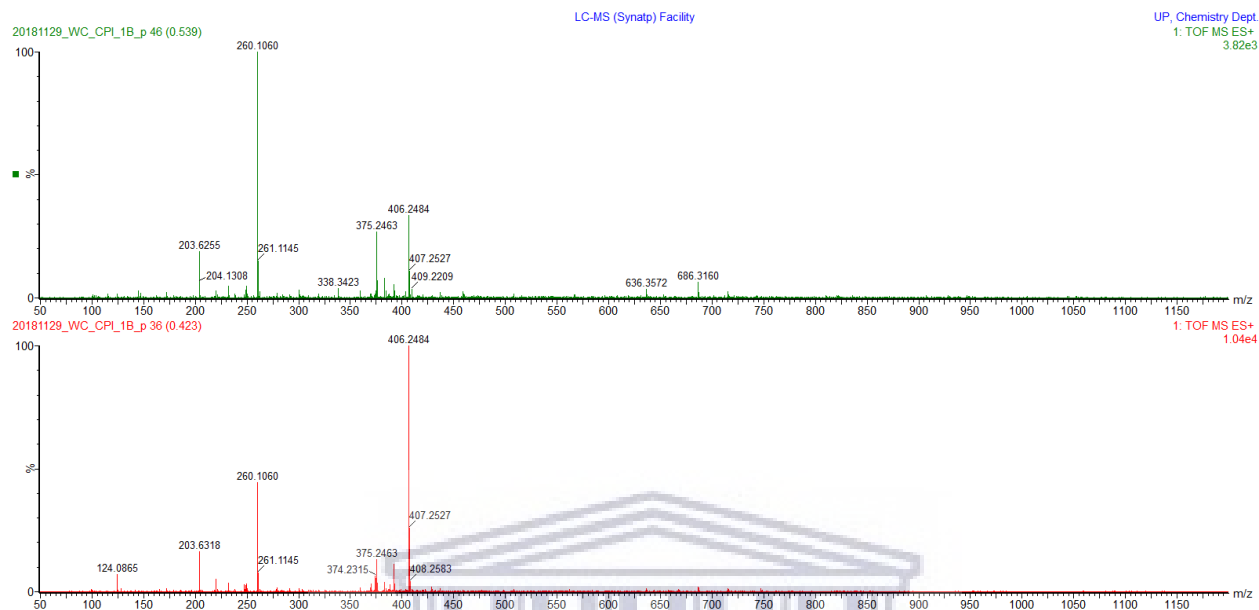


Figure S4.4: IR spectrum of compound **4.31a**

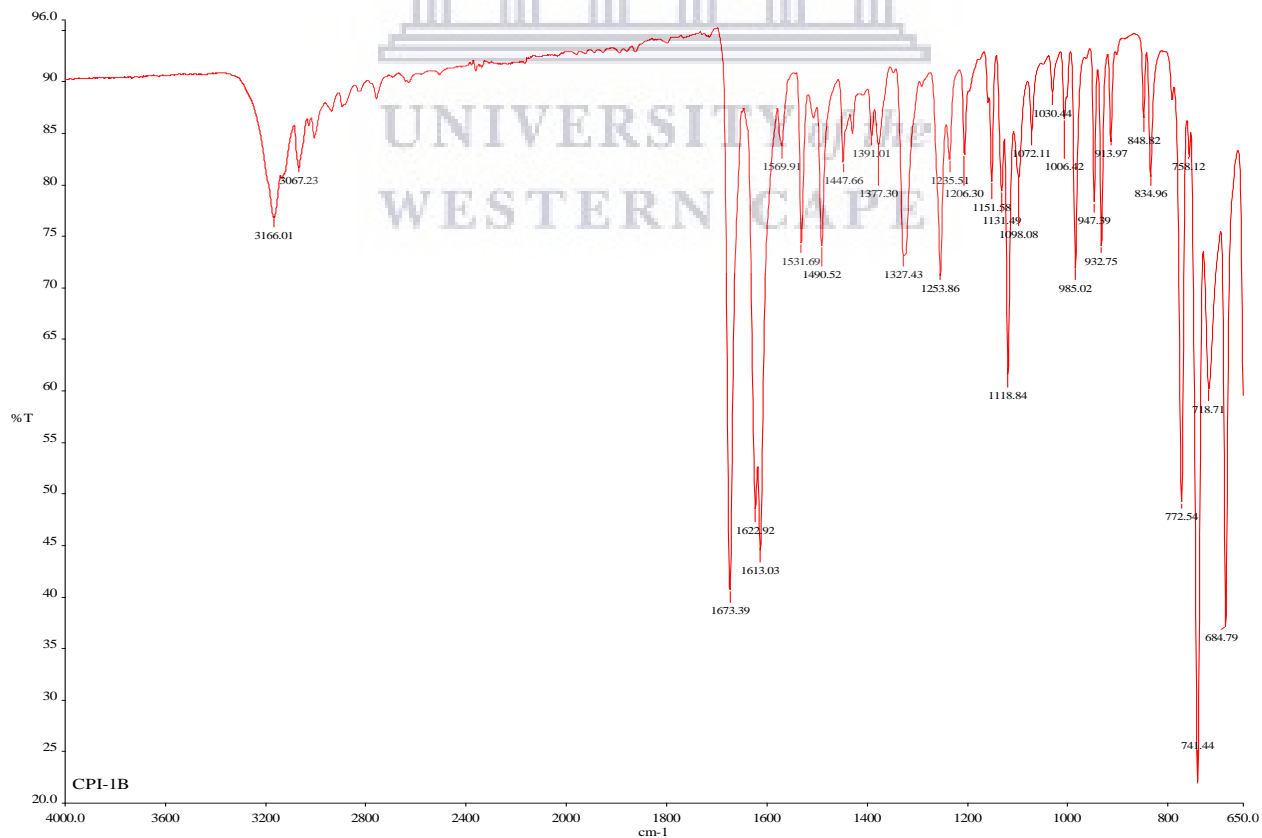


Figure S4.5: ^1H NMR spectrum of compound **4.31b** (400 MHz, DMSO- d_6)

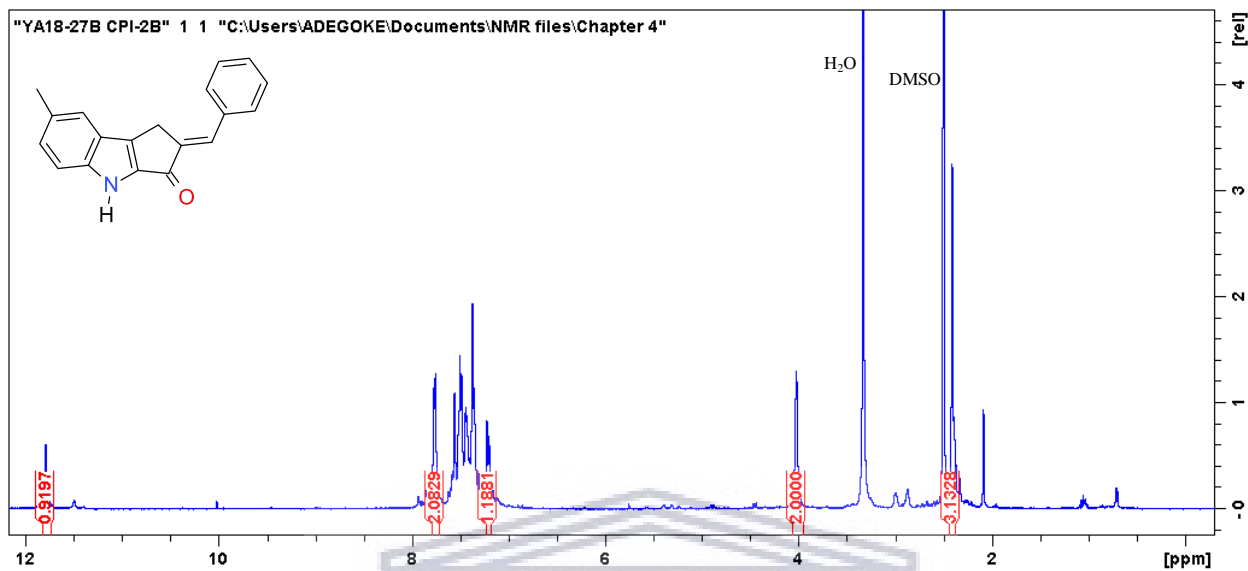


Figure S4.6: ^{13}C NMR spectrum of compound **4.31b** (100 MHz, DMSO- d_6)

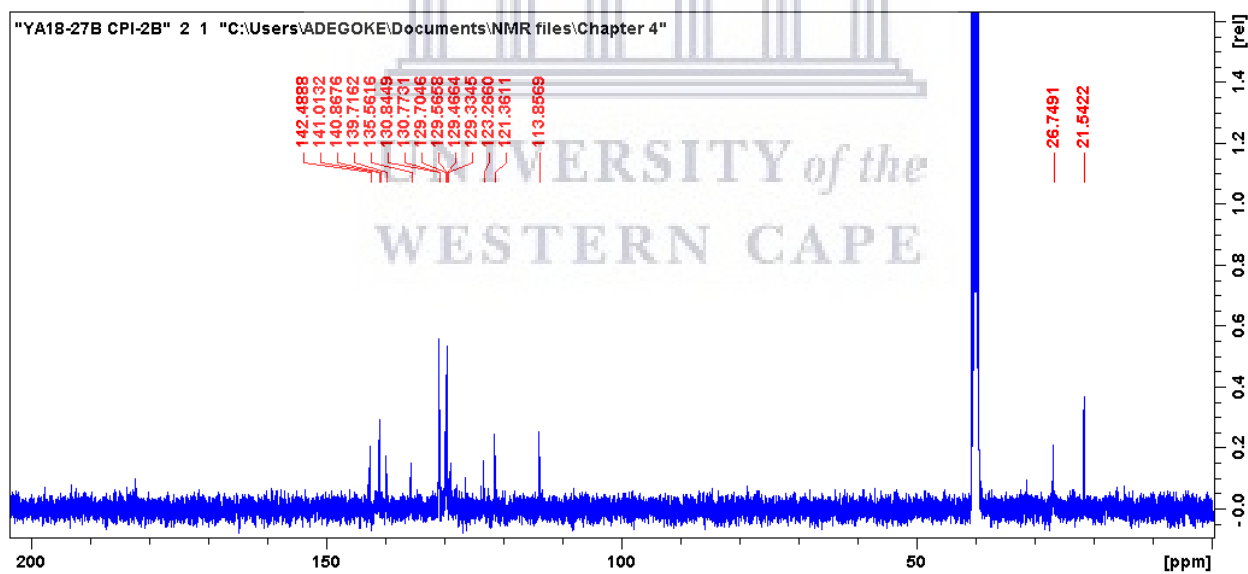


Figure S4.7: HRMS spectrum of compound **4.31b**

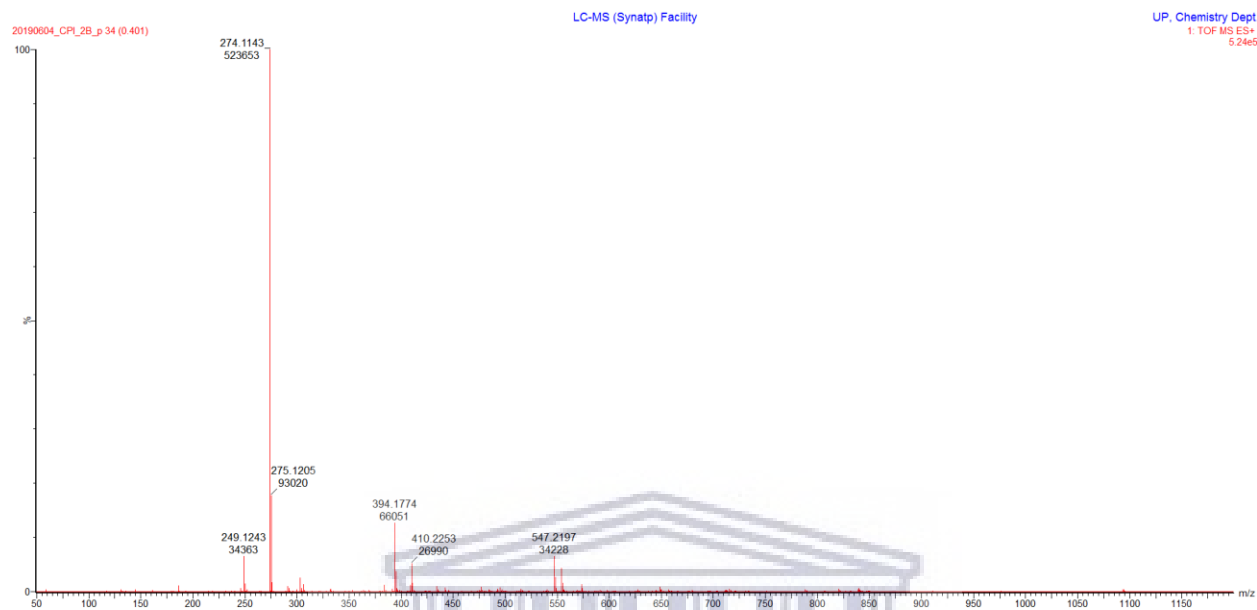


Figure S4.8: IR spectrum of compound **4.31b**

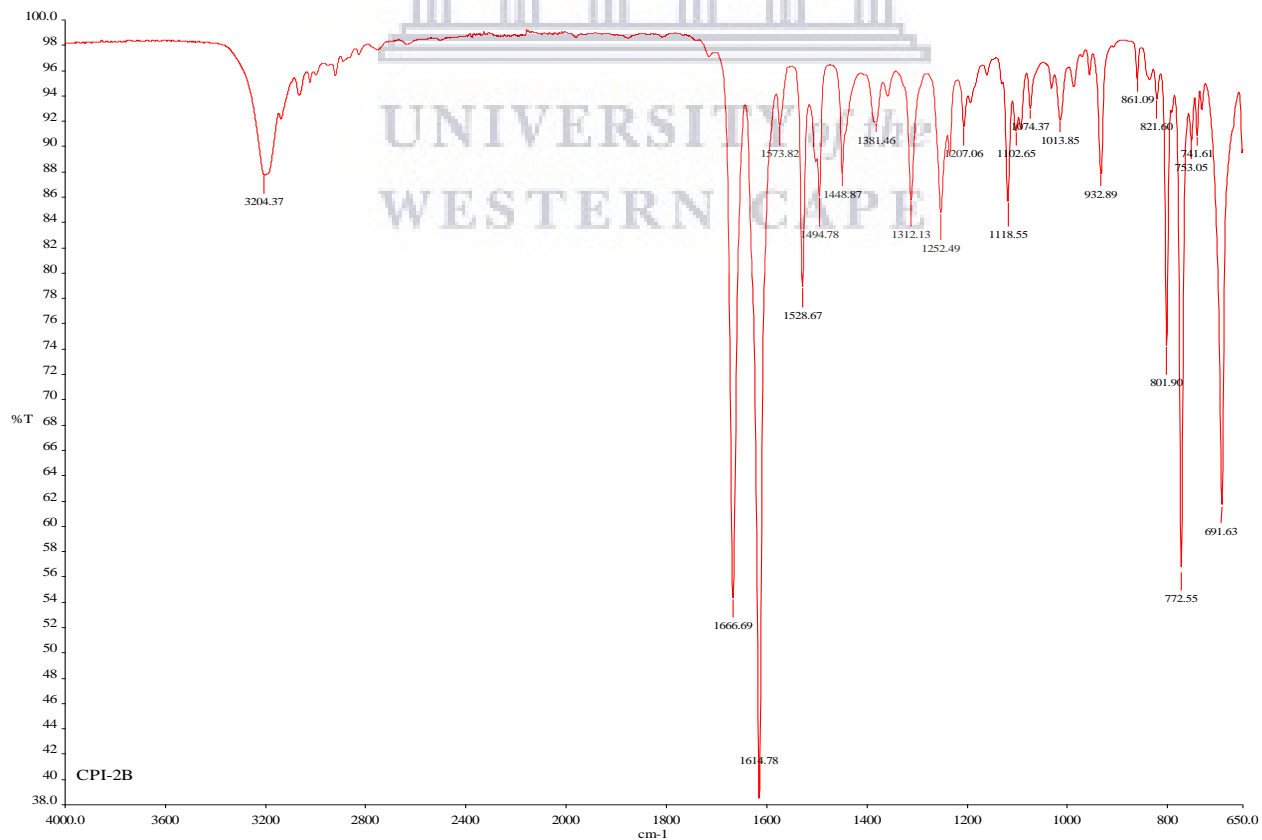


Figure S4.9: ^1H NMR spectrum of compound **4.31c** (400 MHz, DMSO-d_6)

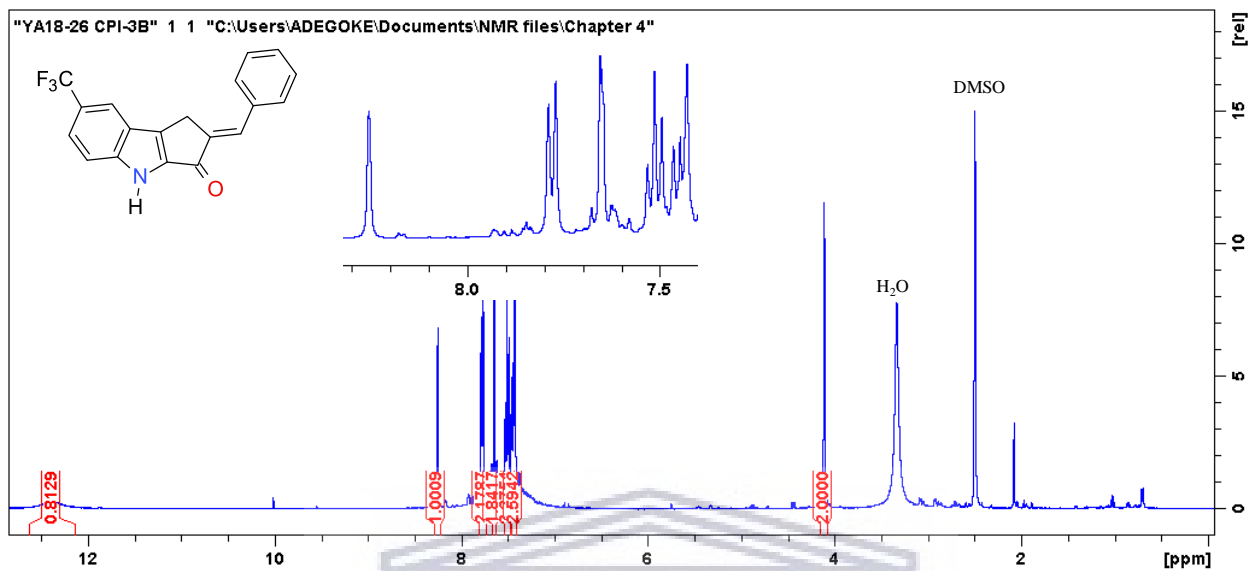


Figure S4.10: ^{13}C NMR spectrum of compound **4.31c** (100 MHz, DMSO-d_6)

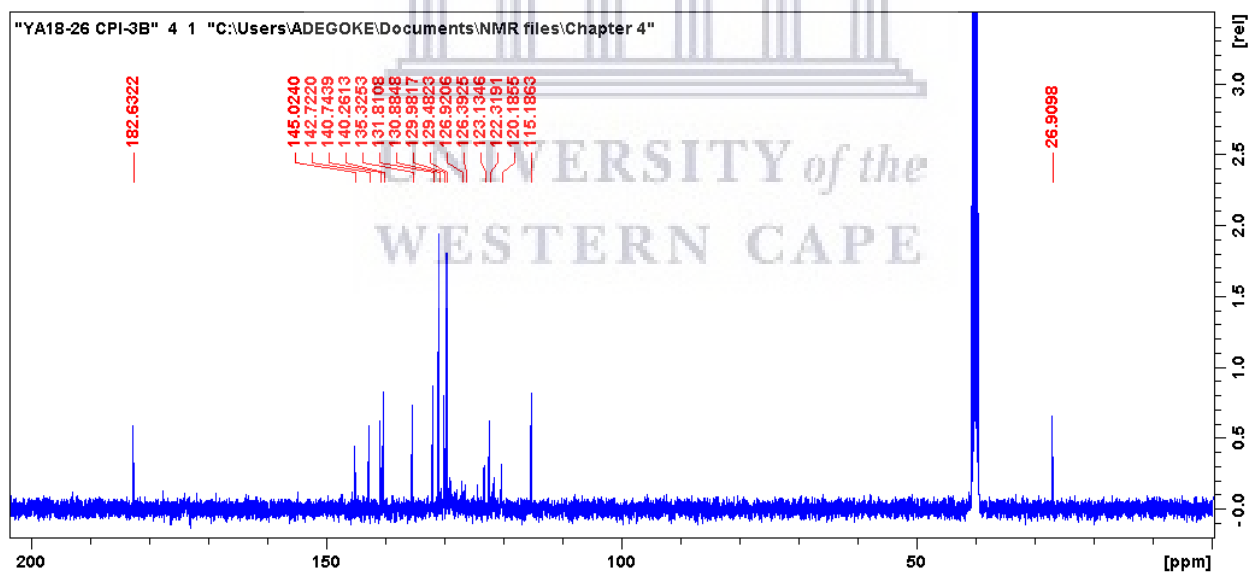


Figure S4.11: HRMS spectrum of compound **4.31c**

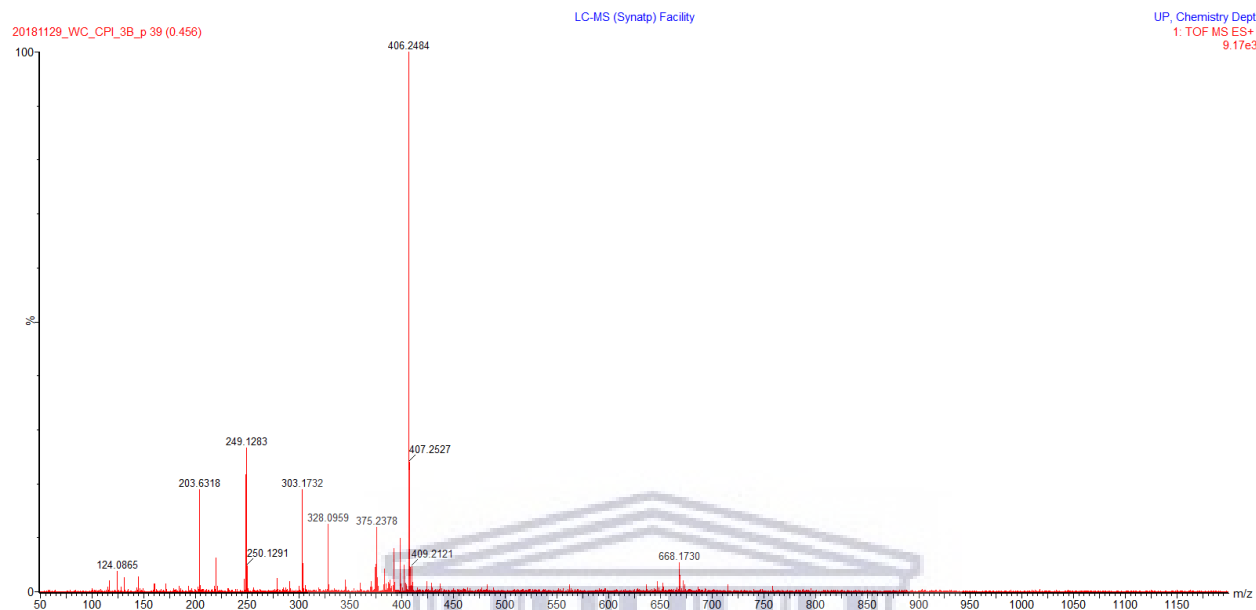


Figure S4.12: IR spectrum of compound **4.31c**

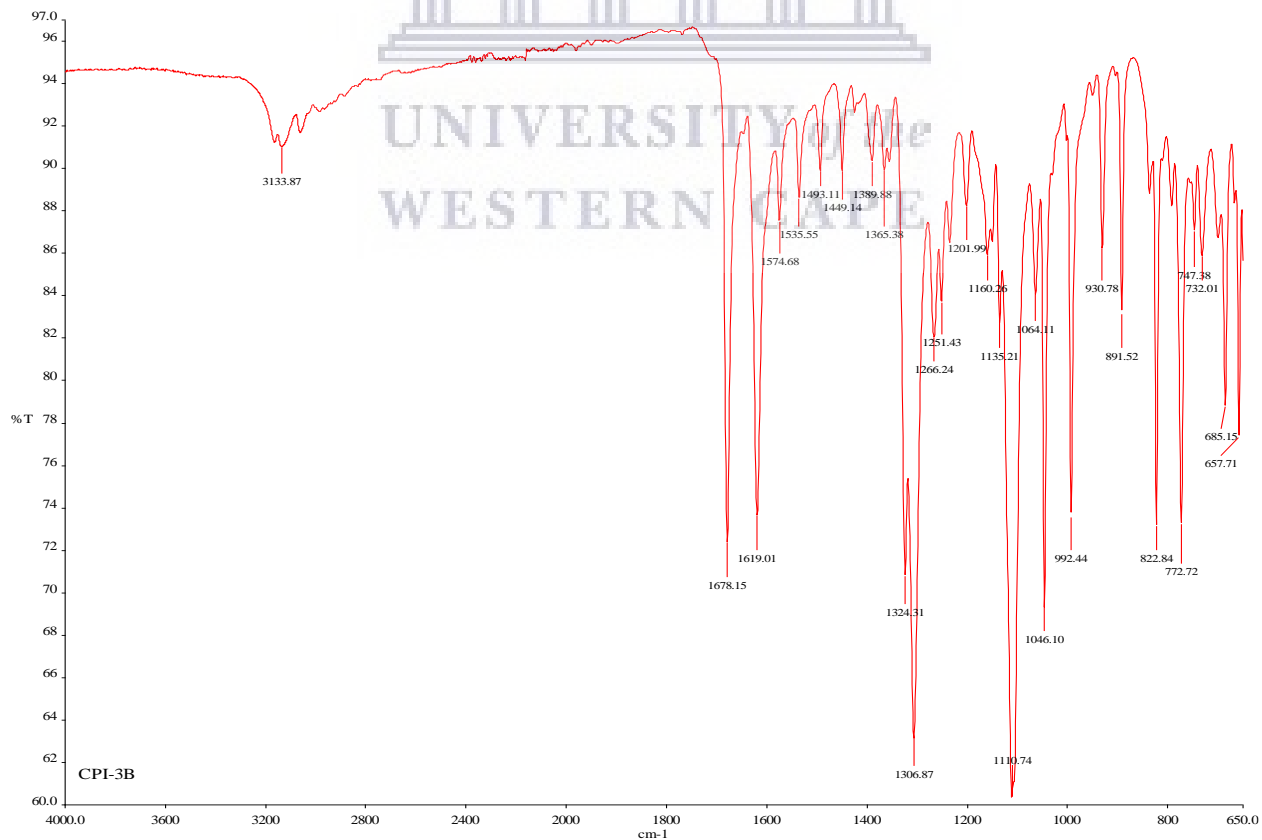


Figure S4.13: COSY NMR spectrum of compound **4.31d**

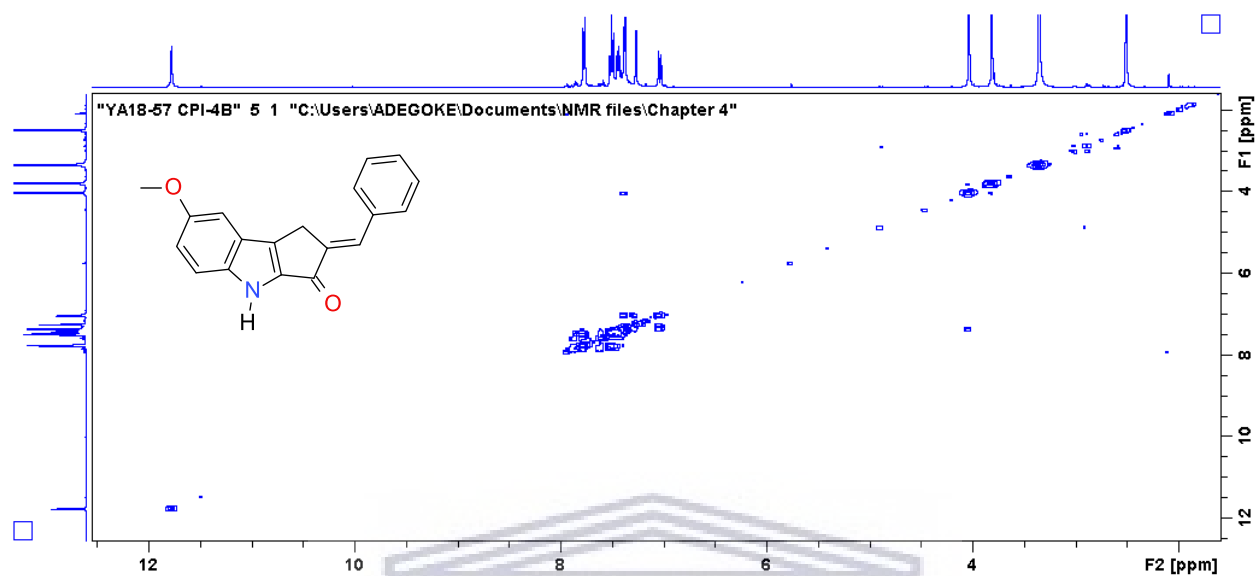


Figure S4.14: HSQC NMR spectrum of compound **4.31d**

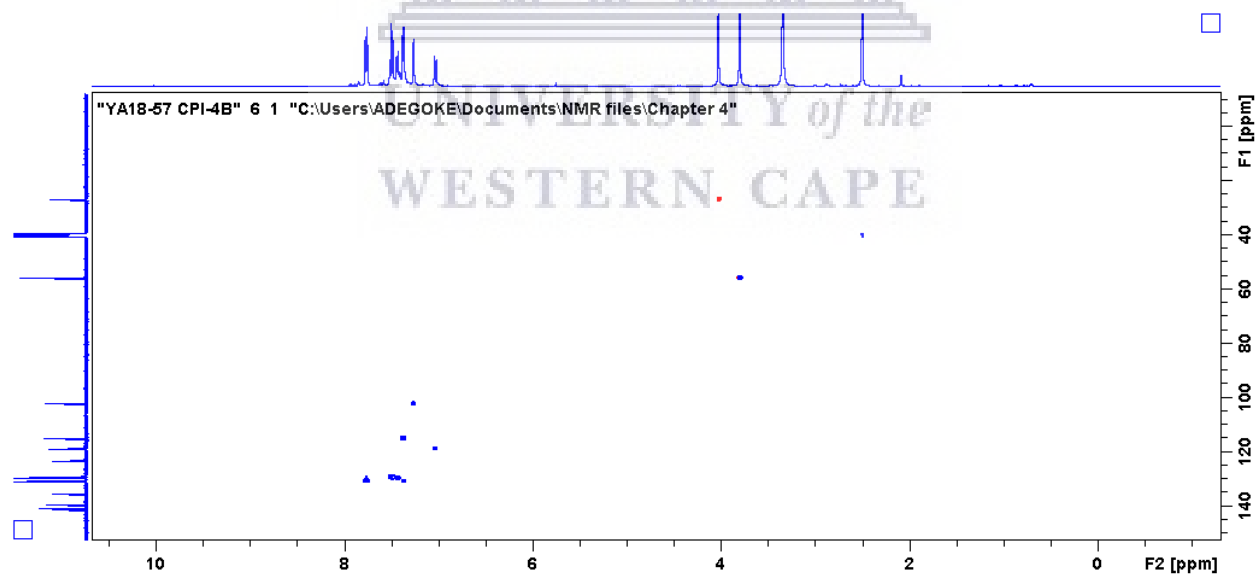


Figure S4.15: HMBC NMR spectrum of compound **4.31d**

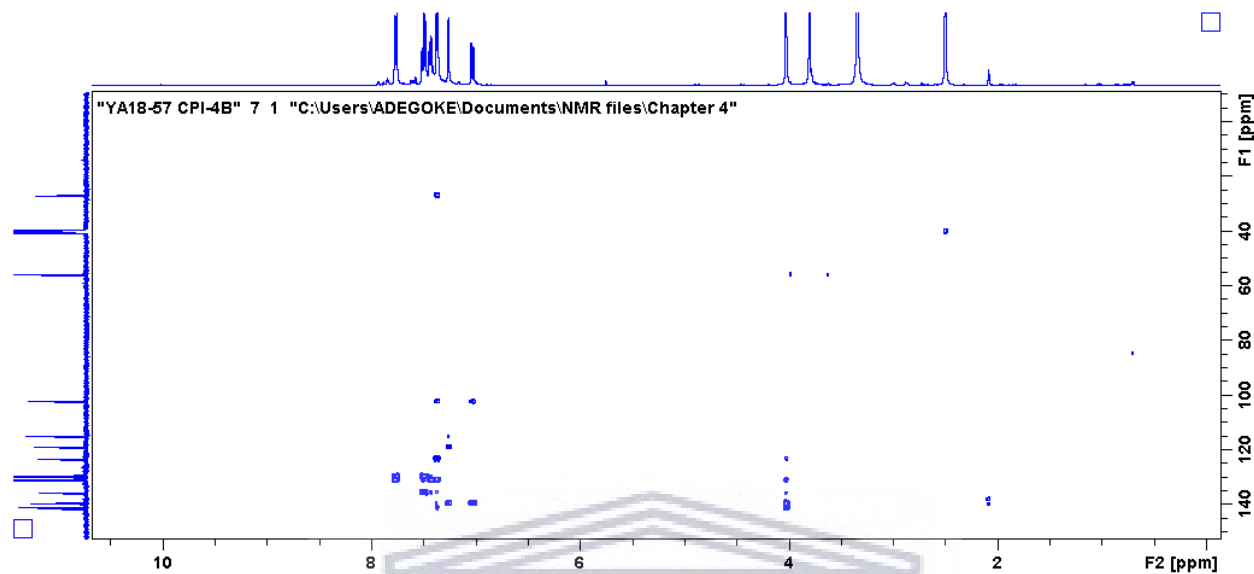


Figure S4.16: HRMS spectrum of compound **4.31d**

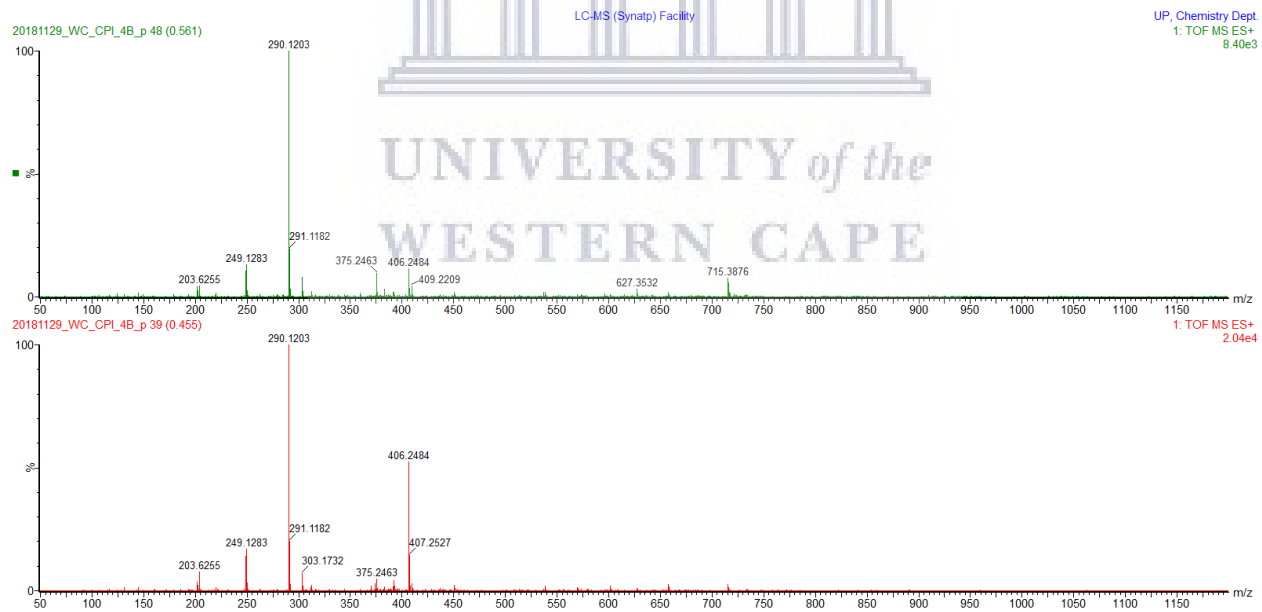
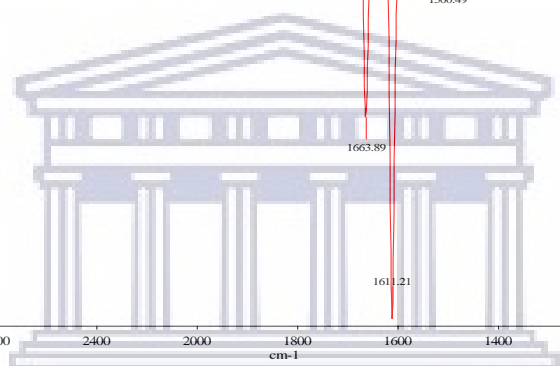
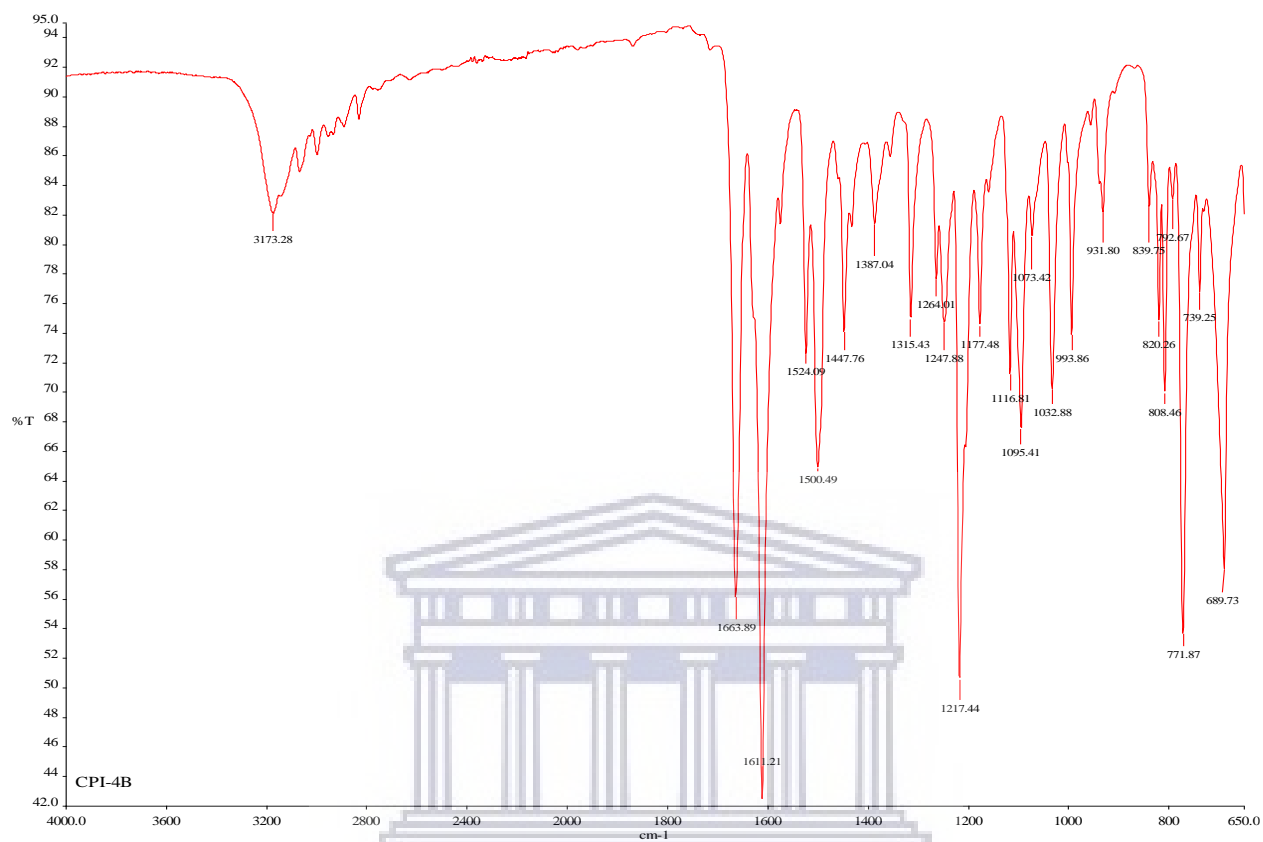


Figure S4.17: IR spectrum of compound **4.31d**



UNIVERSITY of the
WESTERN CAPE

Figure S4.18: ^1H NMR spectrum of compound **4.31e** (400 MHz, DMSO-d_6)

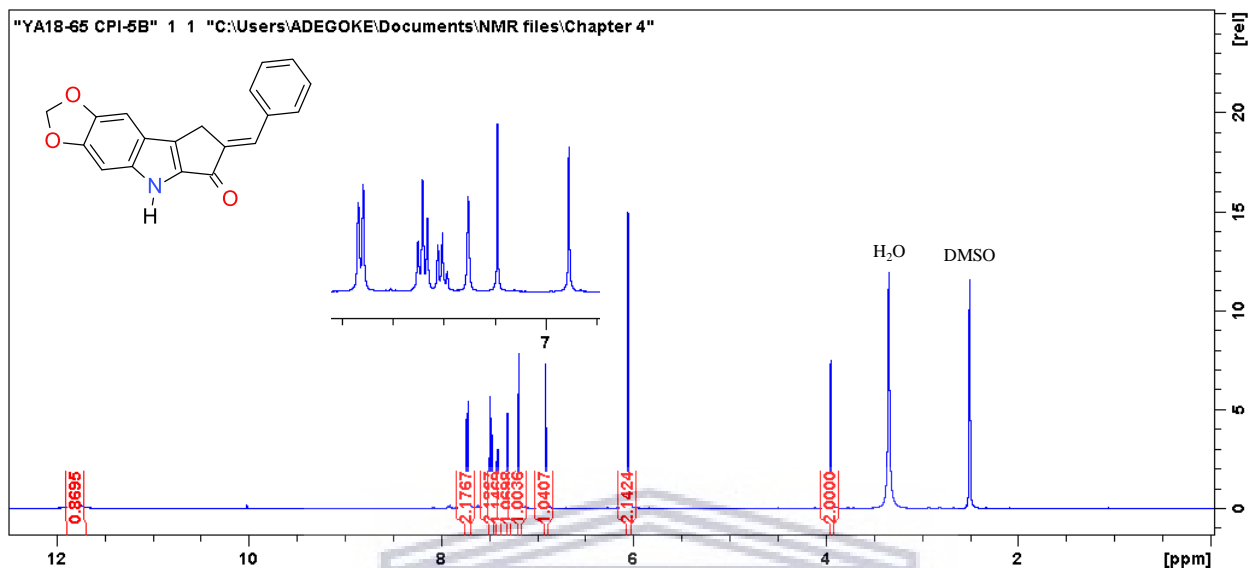


Figure S4.19: ^{13}C NMR spectrum of compound **4.31e** (100 MHz, DMSO-d_6)

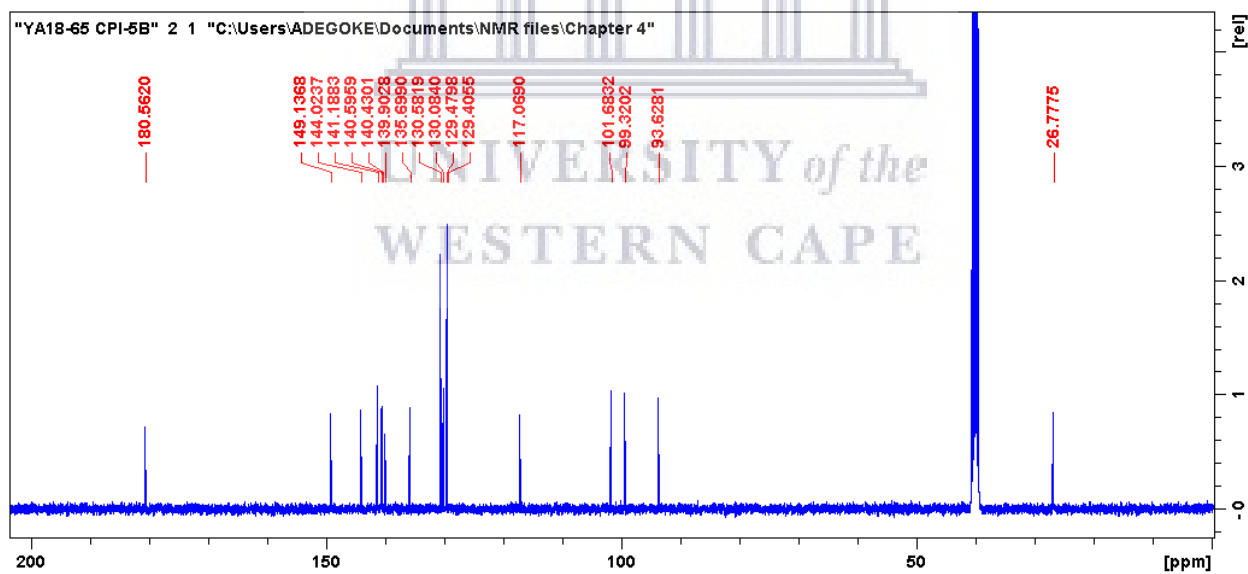


Figure S4.20: HRMS spectrum of compound **4.31e**

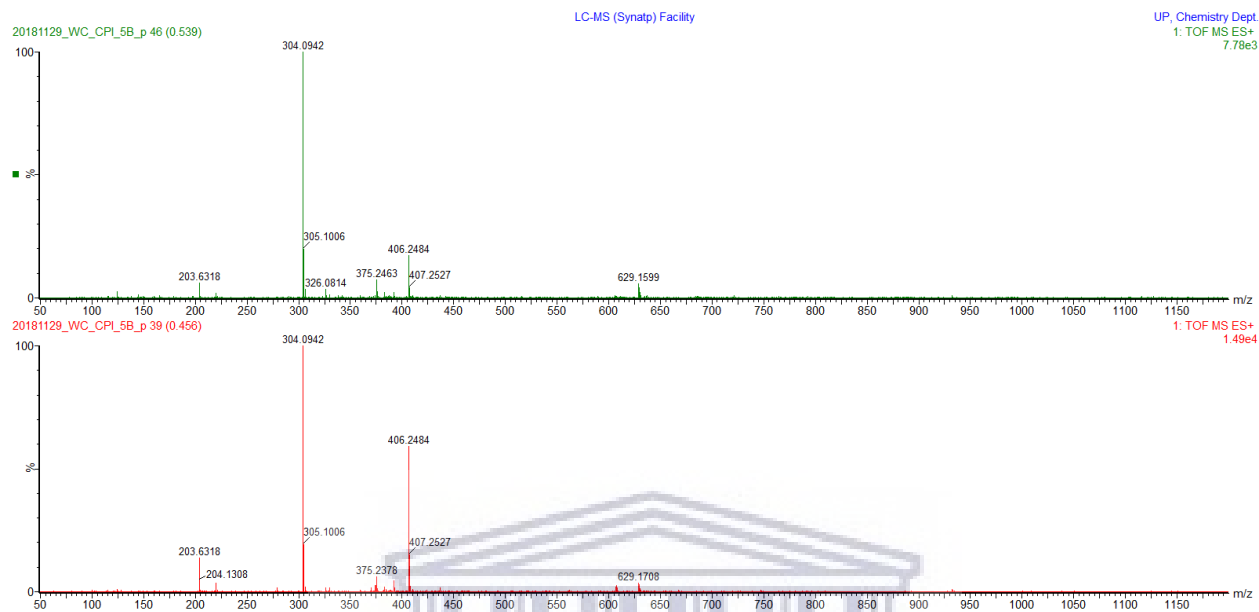


Figure S4.21: IR spectrum of compound **4.31e**

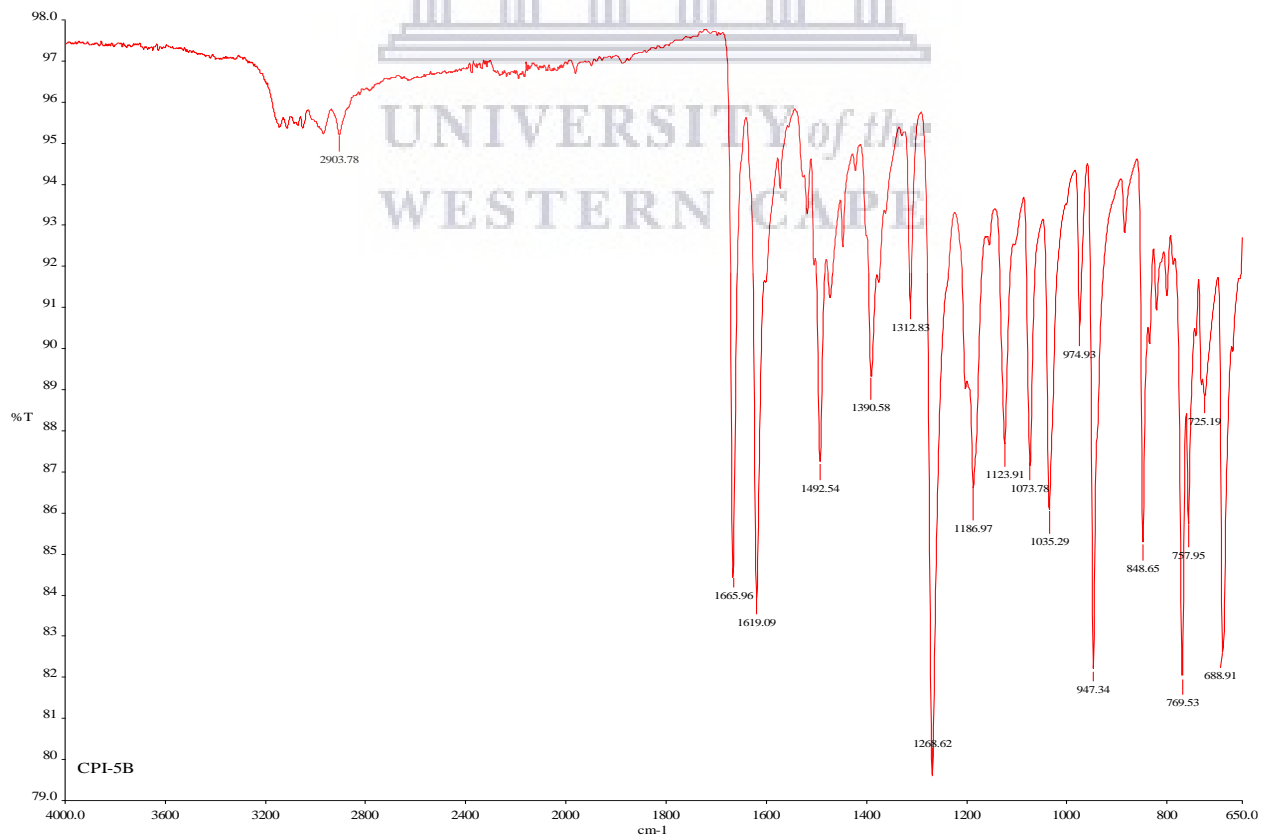


Figure S4.22: ^1H NMR spectrum of compound **4.31f** (400 MHz, DMSO- d_6)

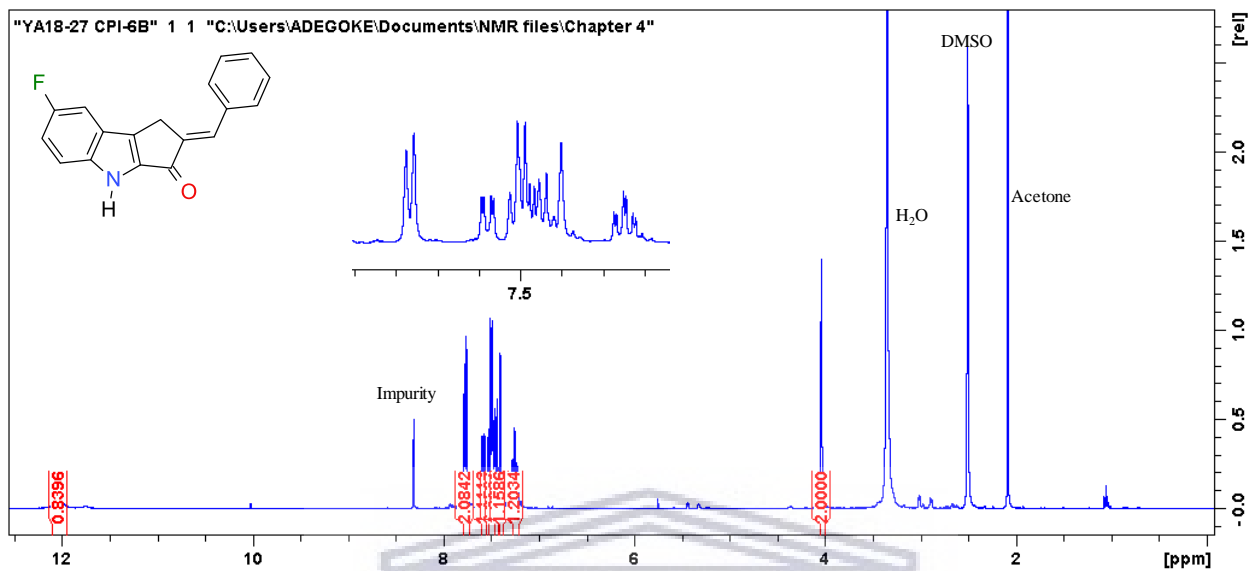


Figure S4.23: ^{13}C NMR spectrum of compound **4.31f** (100 MHz, DMSO- d_6)

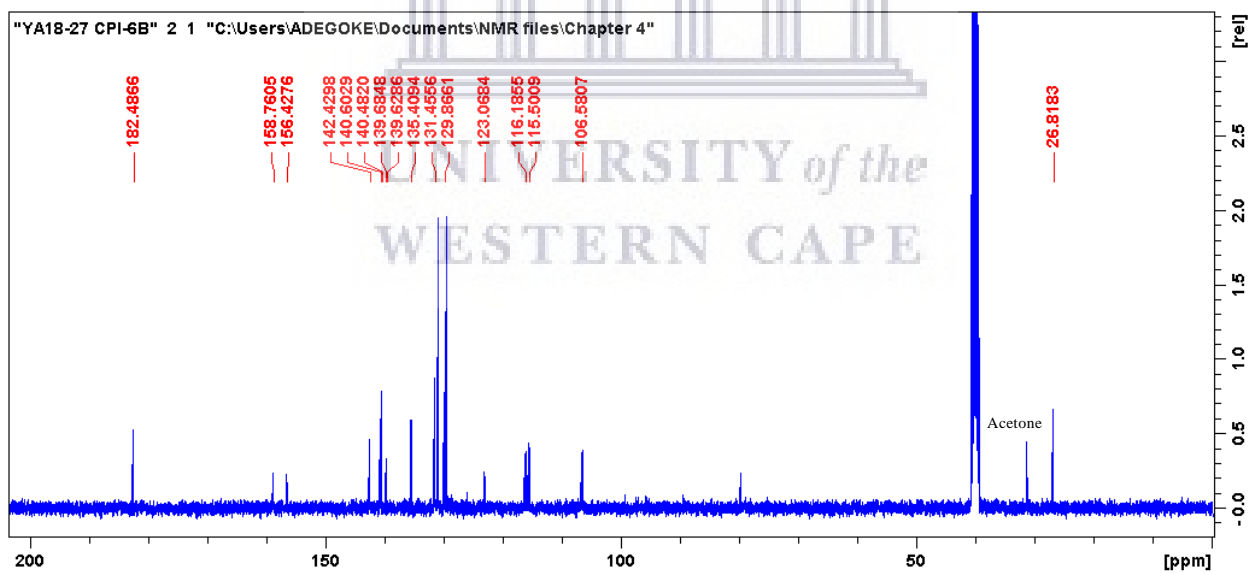


Figure S4.24: HRMS spectrum of compound **4.31f**

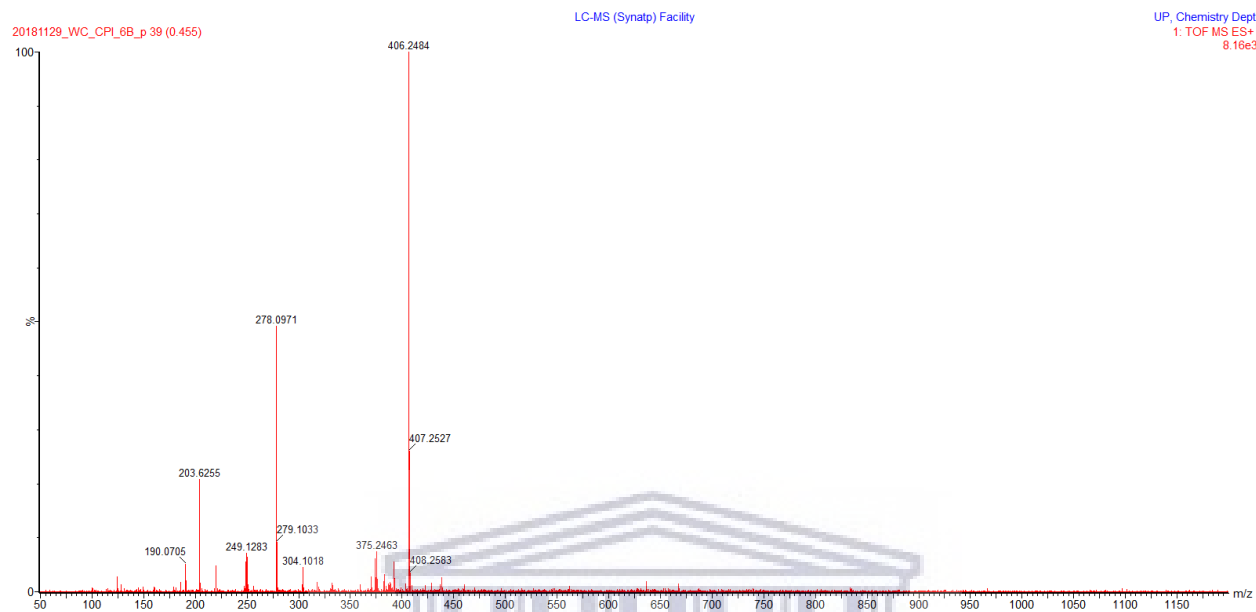


Figure S4.25: IR spectrum of compound **4.31f**

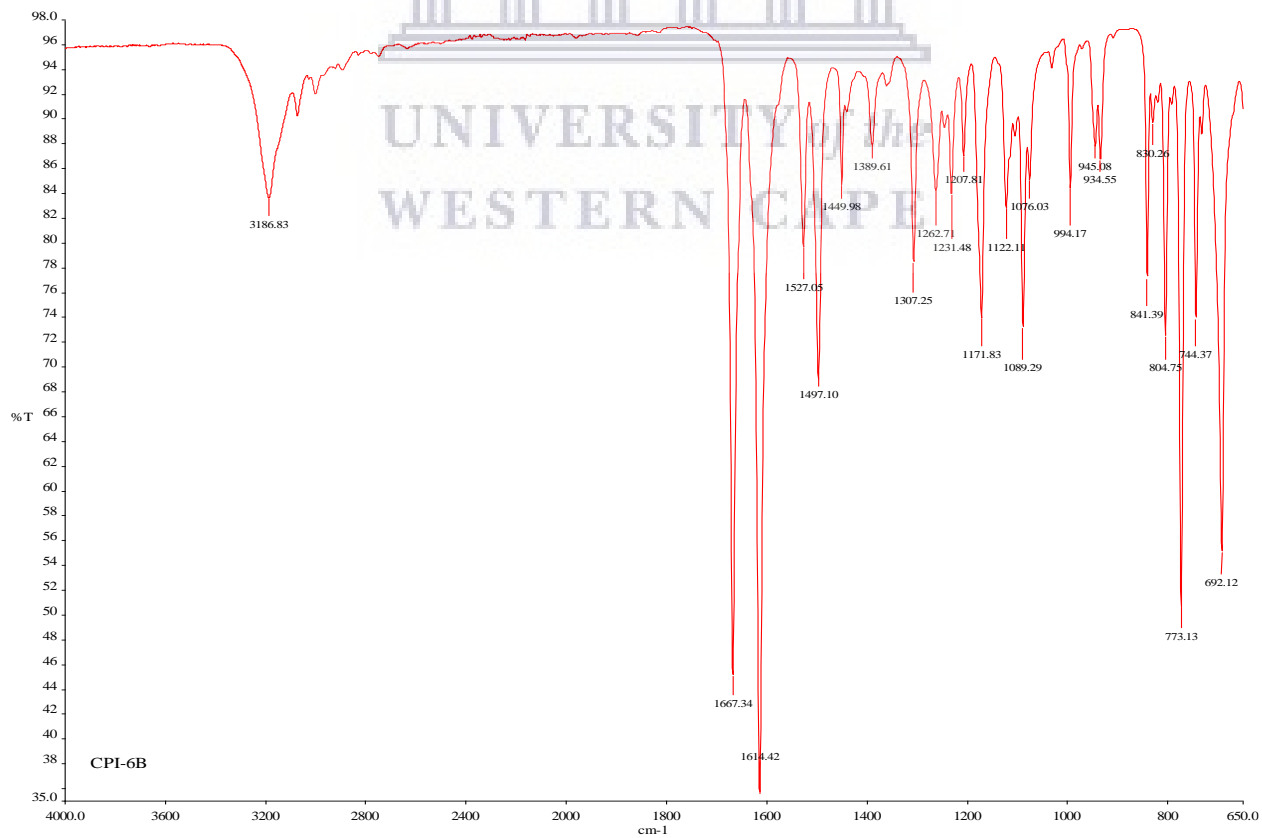


Figure S4.26: ^1H NMR spectrum of compound **4.31g** (400 MHz, DMSO- d_6)

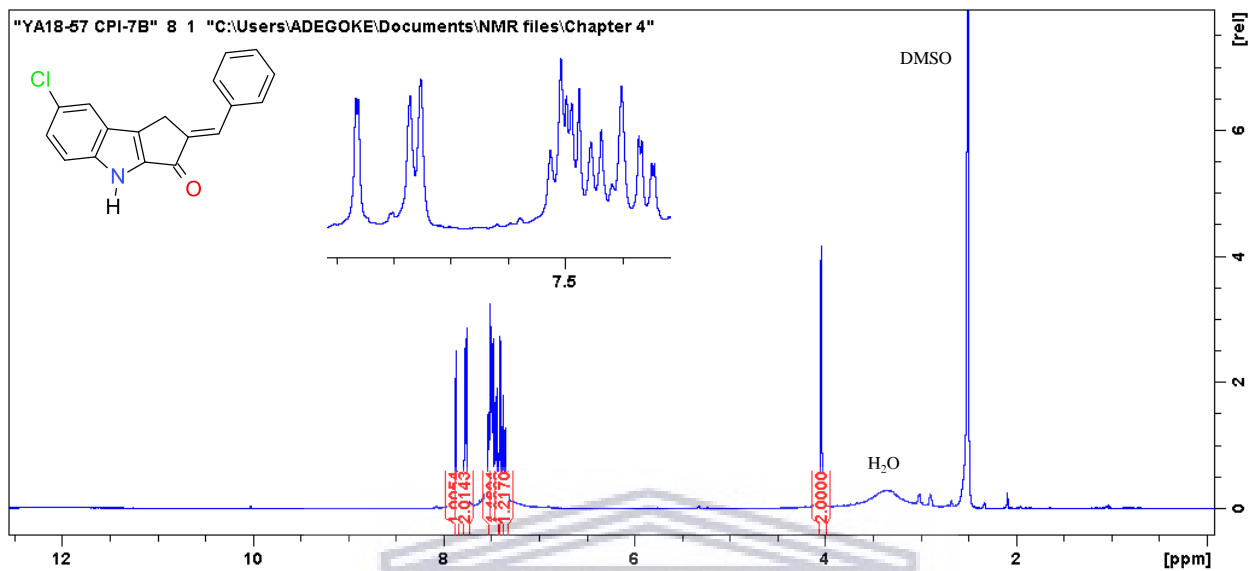


Figure S4.27: ^{13}C NMR spectrum of compound **4.31g** (100 MHz, DMSO- d_6)

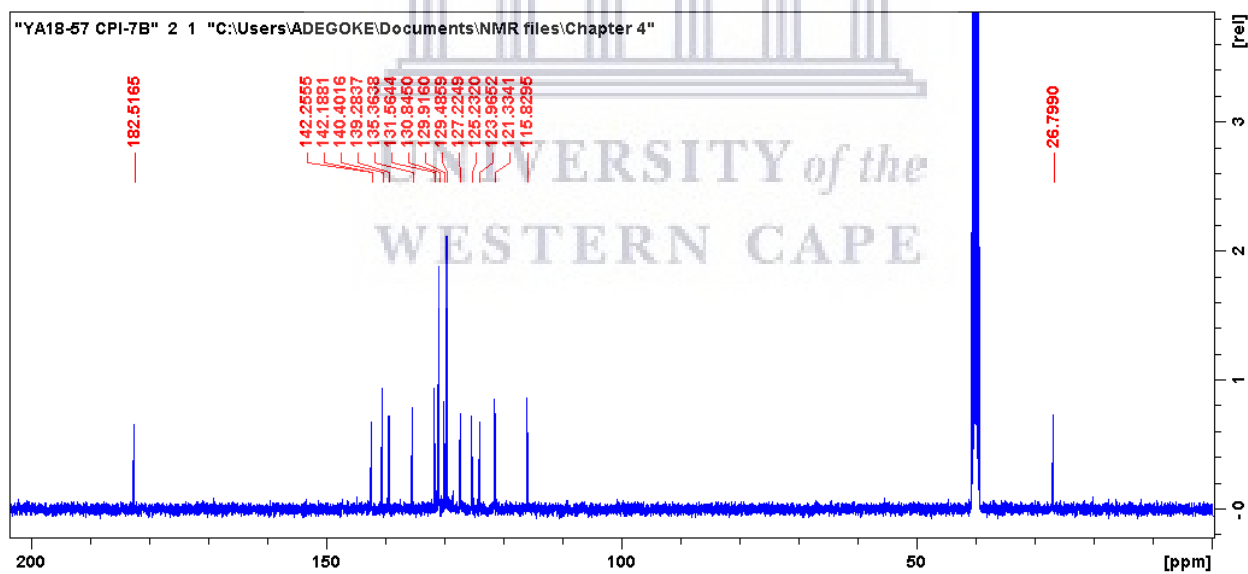


Figure S4.28: HRMS spectrum of compound **4.31g**

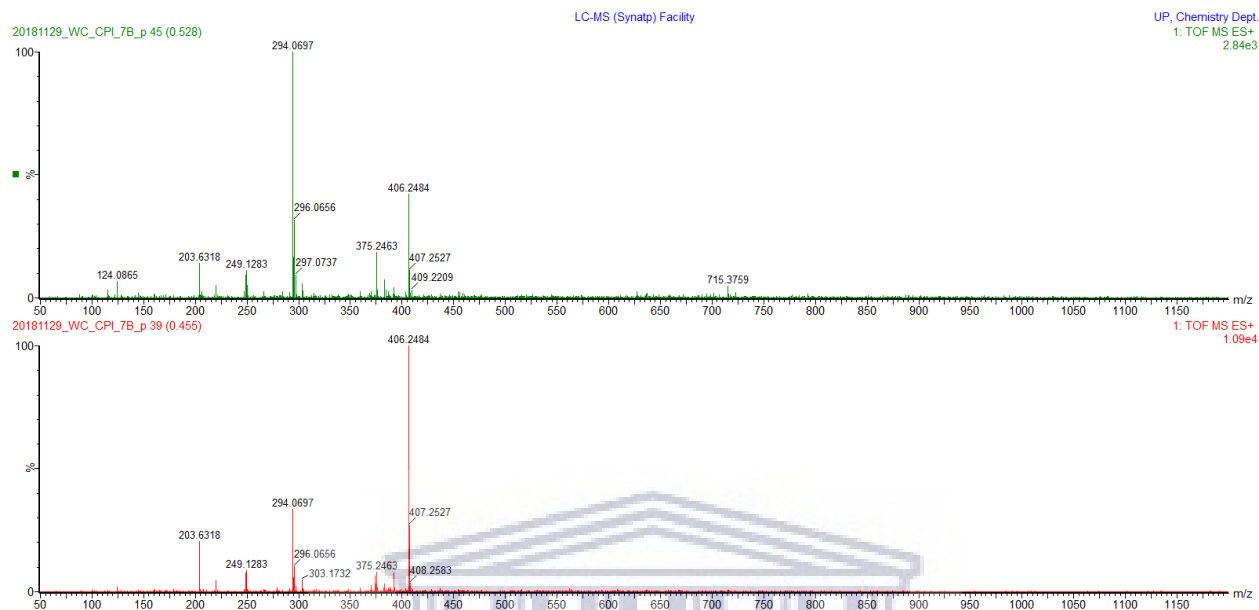


Figure S4.29: IR spectrum of compound **4.31g**

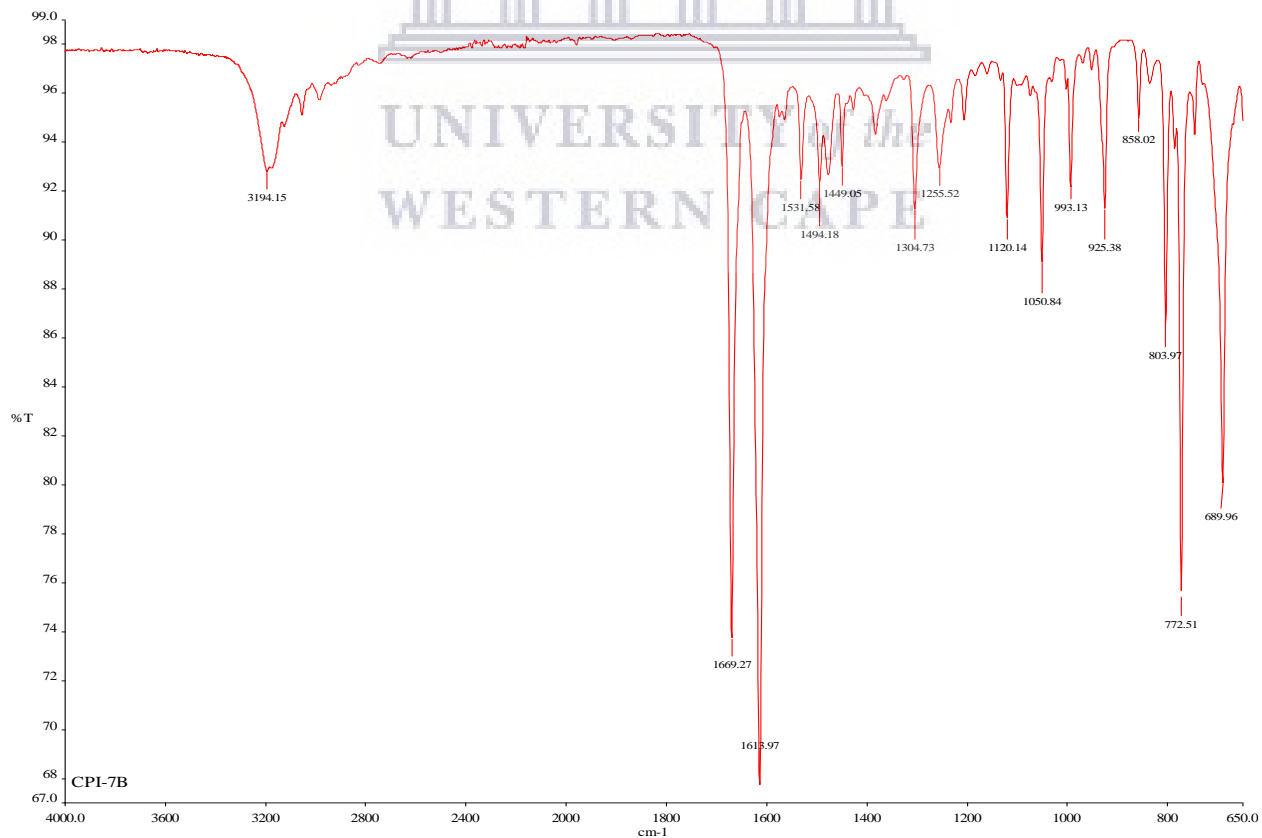


Figure S4.30: ^1H NMR spectrum of compound **4.31h** (400 MHz, DMSO- d_6)

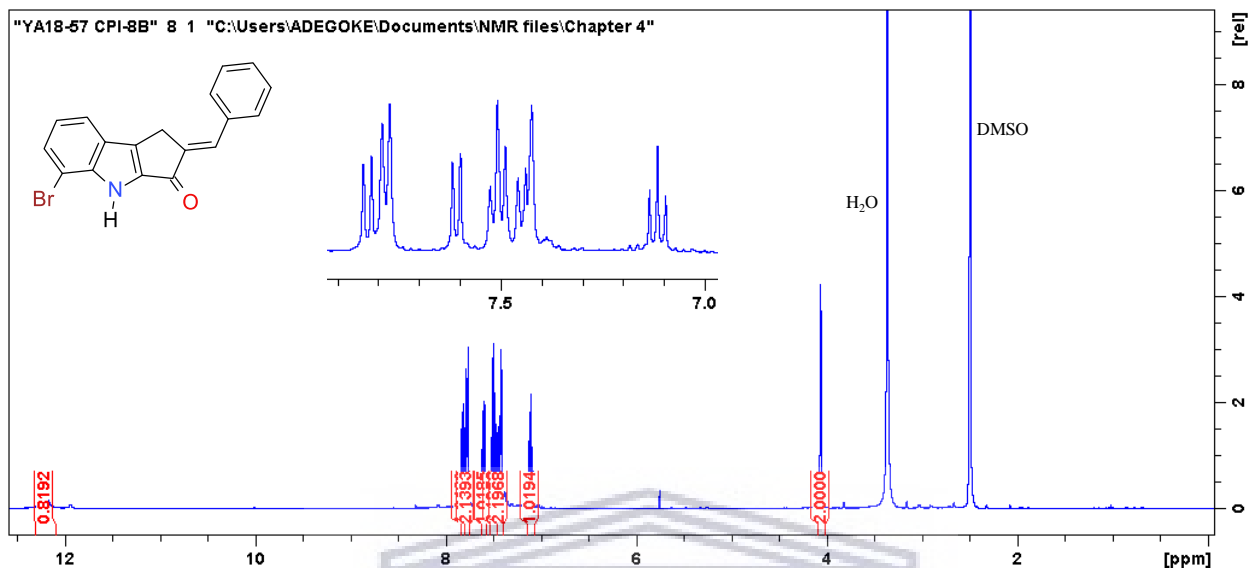


Figure S4.31: ^{13}C NMR spectrum of compound **4.31h** (100 MHz, DMSO- d_6)

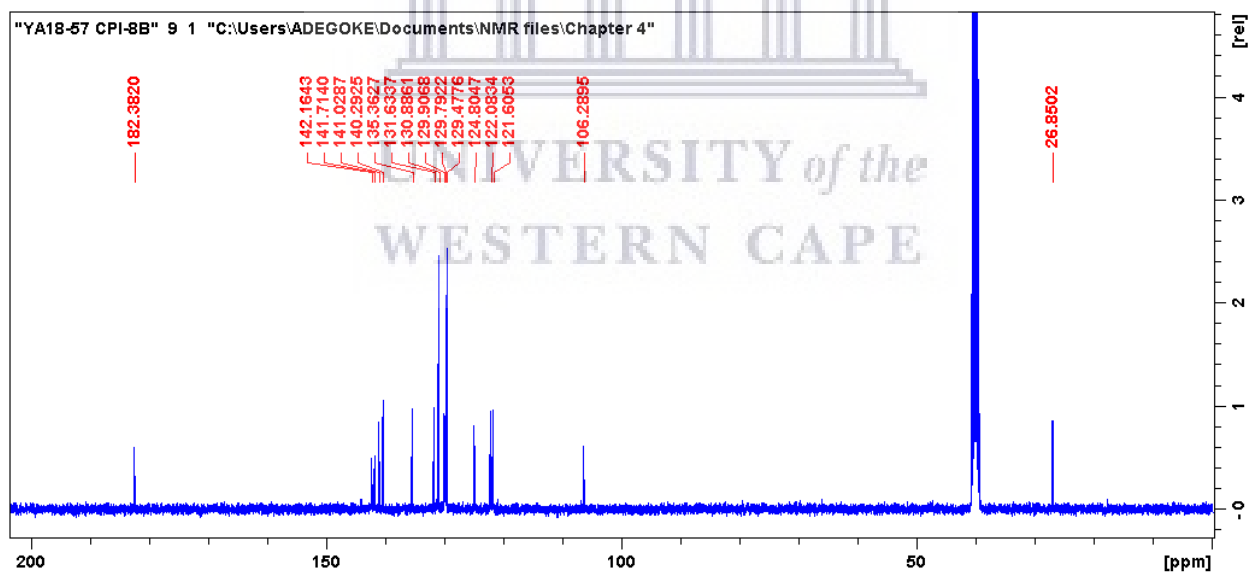


Figure S4.32: HRMS spectrum of compound **4.31h**

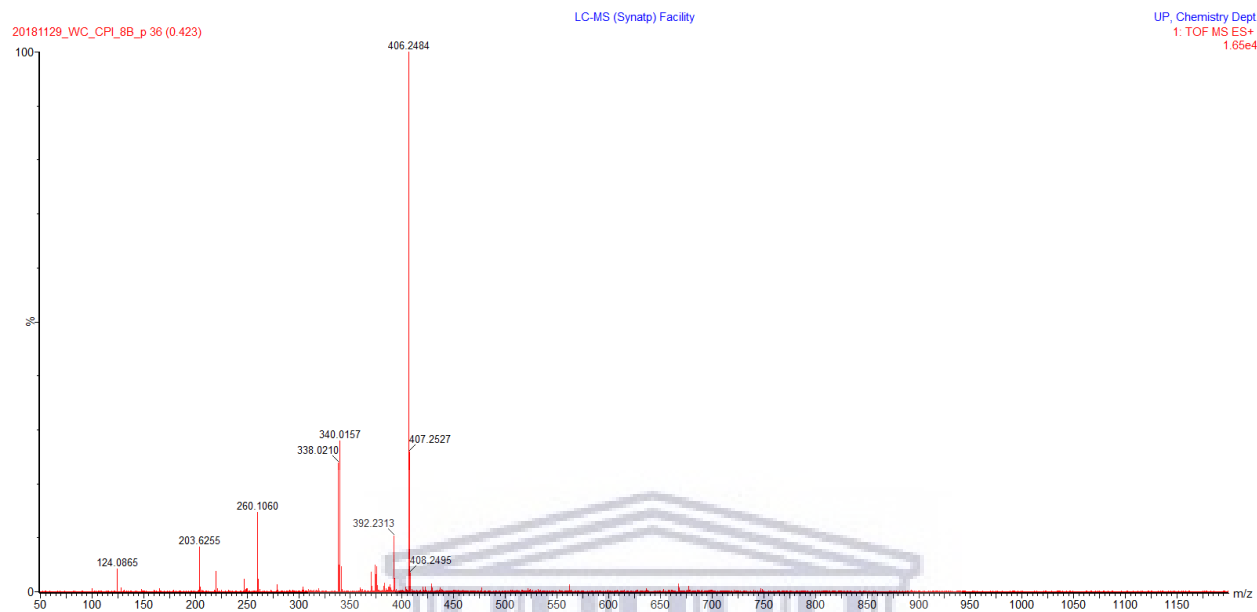


Figure S4.33: IR spectrum of compound **4.31h**

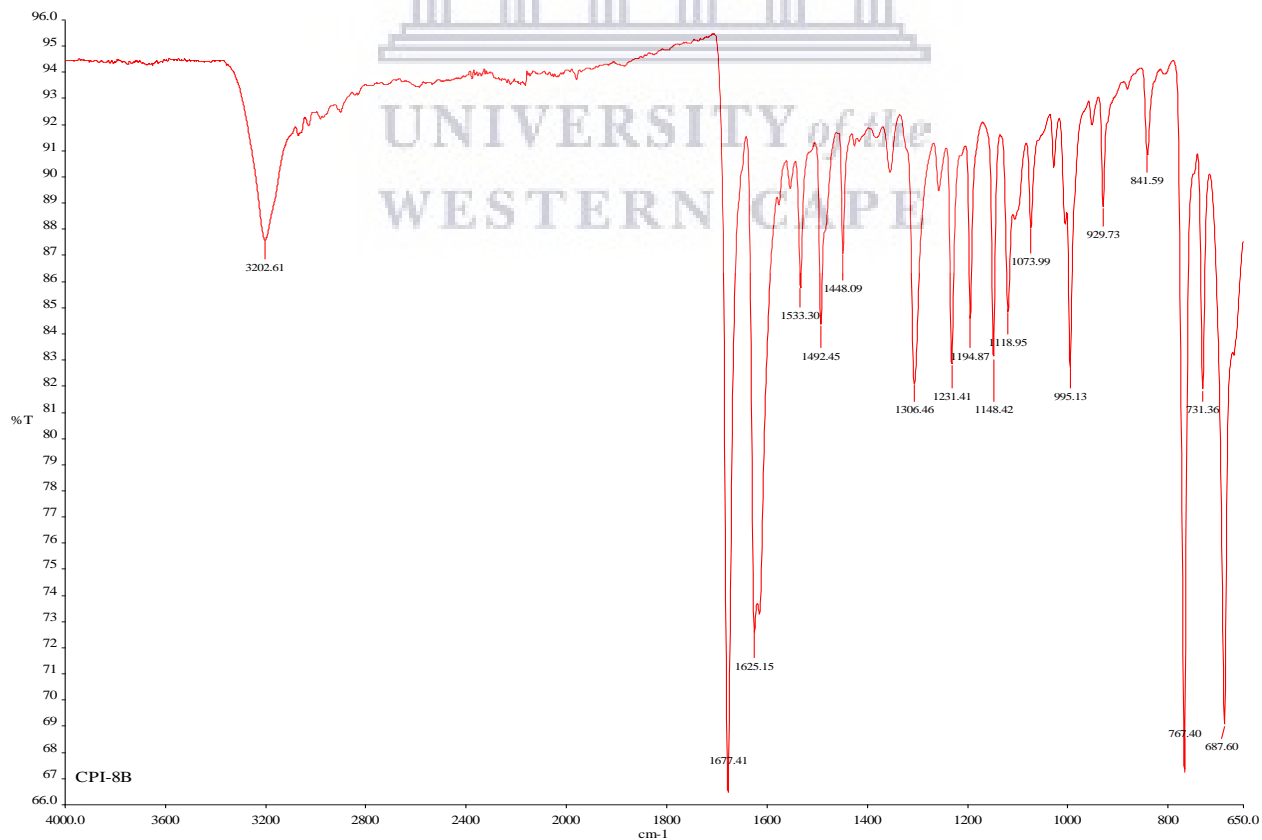


Figure S4.34: ^1H NMR spectrum of compound **4.31i** (400 MHz, DMSO- d_6)

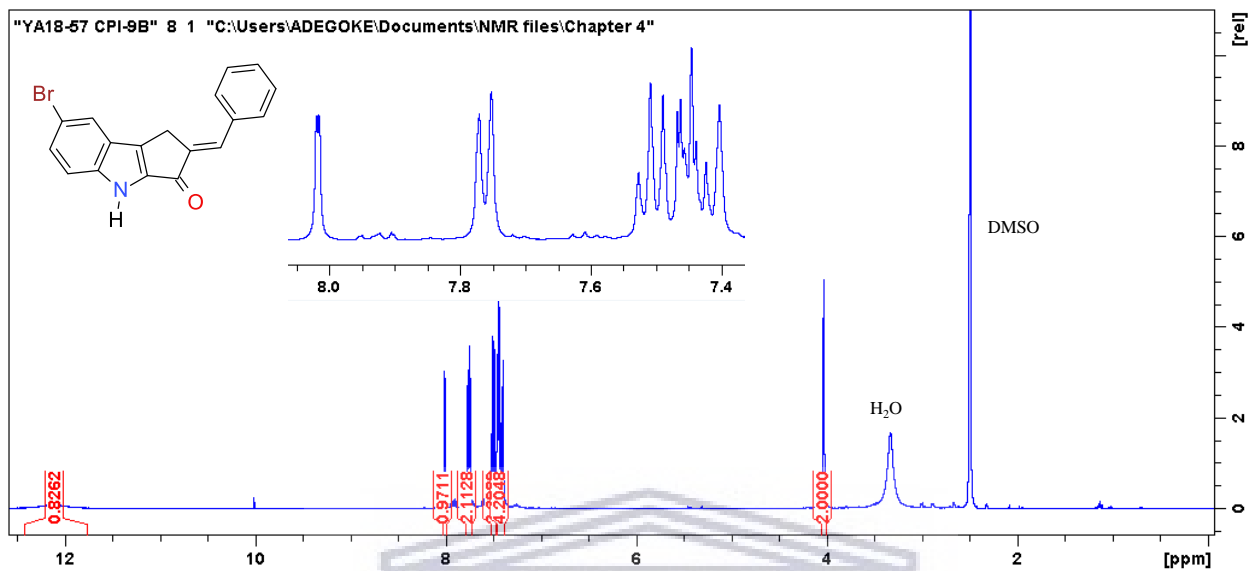


Figure S4.35: ^{13}C NMR spectrum of compound **4.31i** (100 MHz, DMSO- d_6)

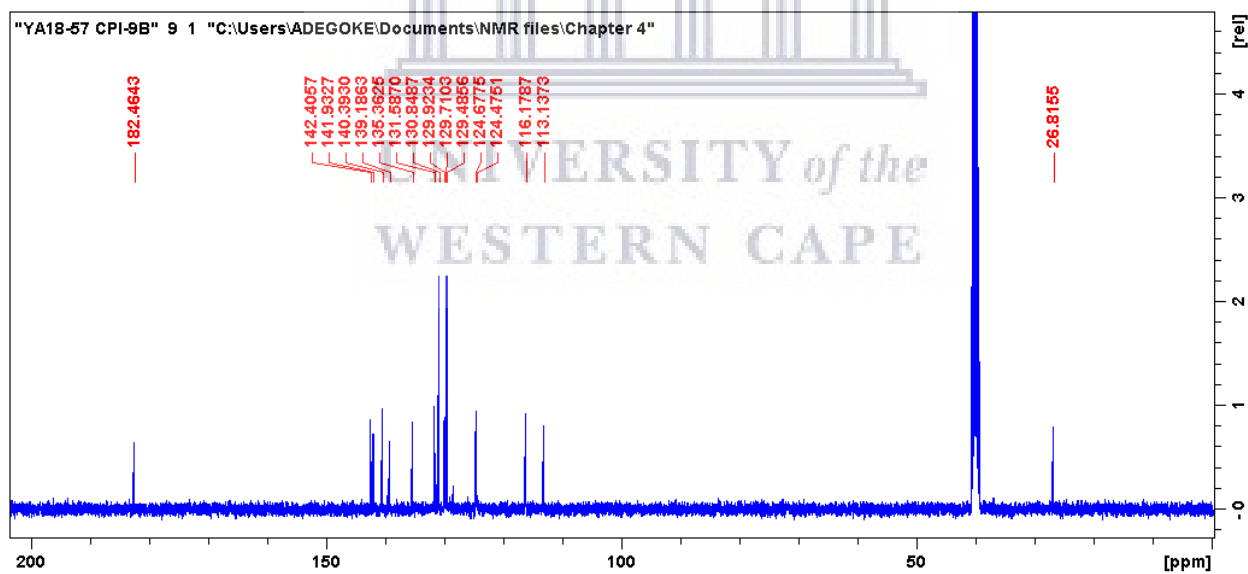


Figure S4.36: HRMS spectrum of compound **4.31i**

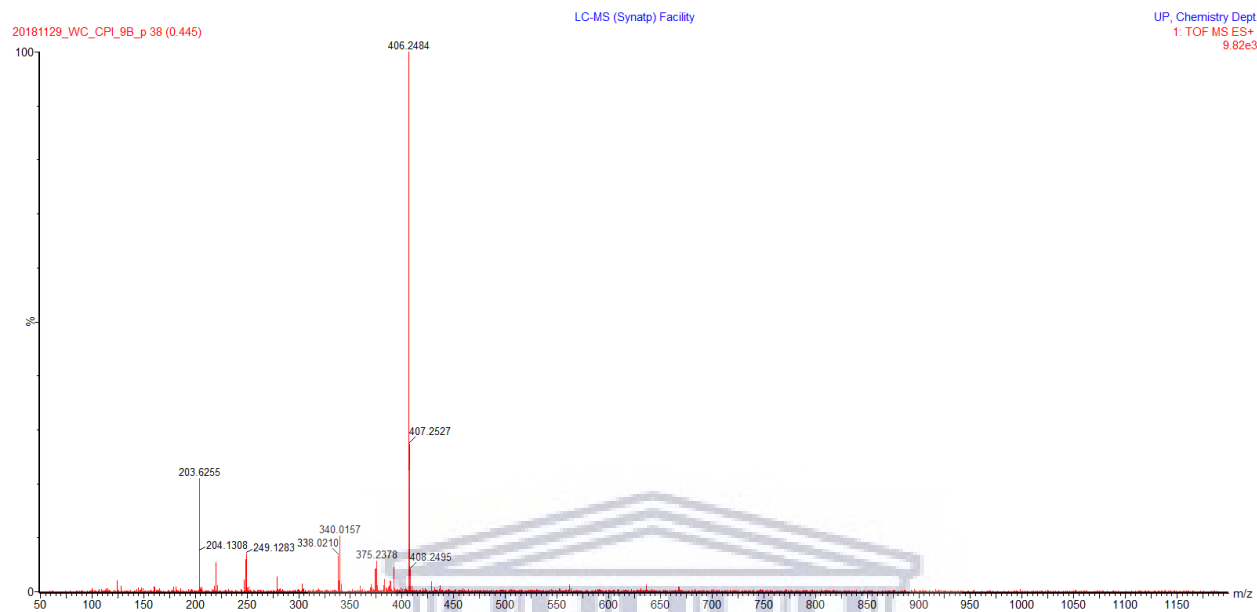


Figure S4.37: IR spectrum of compound **4.31i**

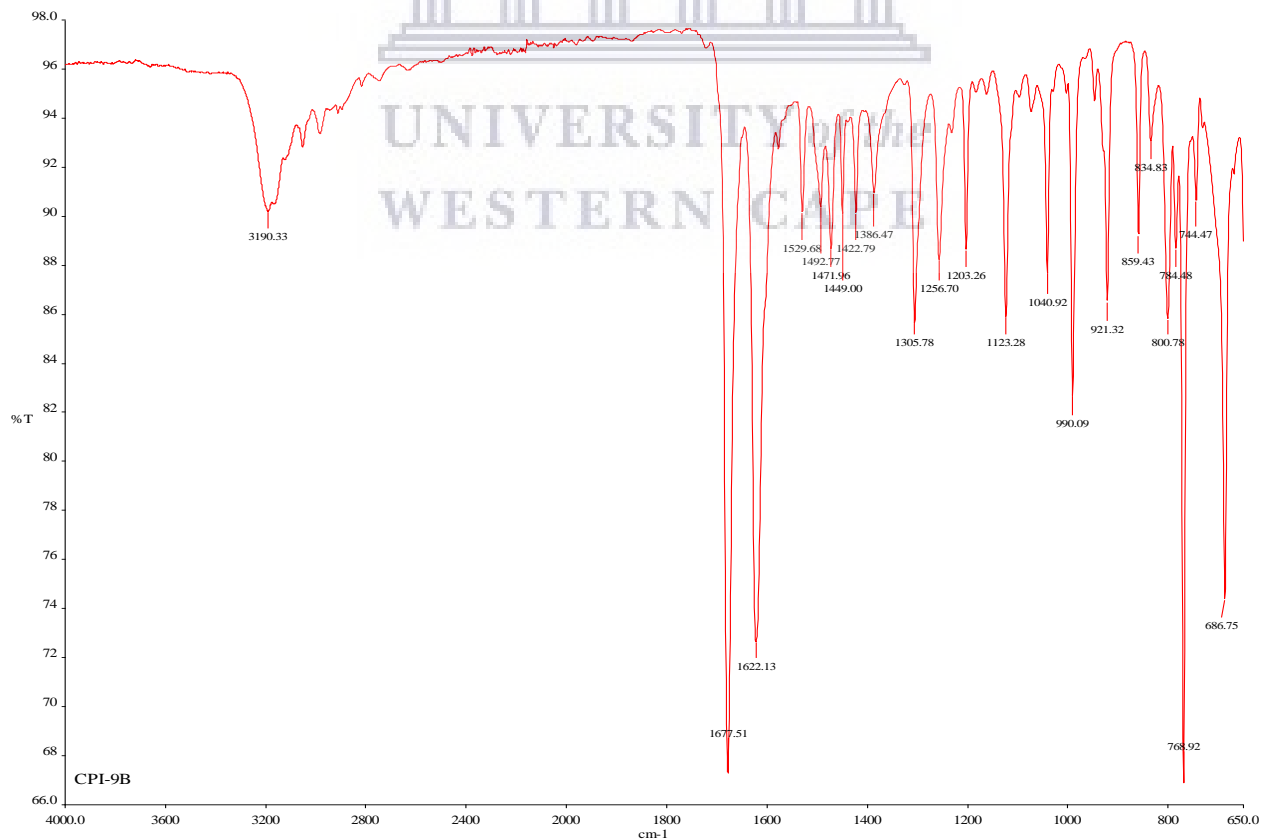


Figure S4.38: ^1H NMR spectrum of compound **4.31j** (400 MHz, DMSO-d_6)

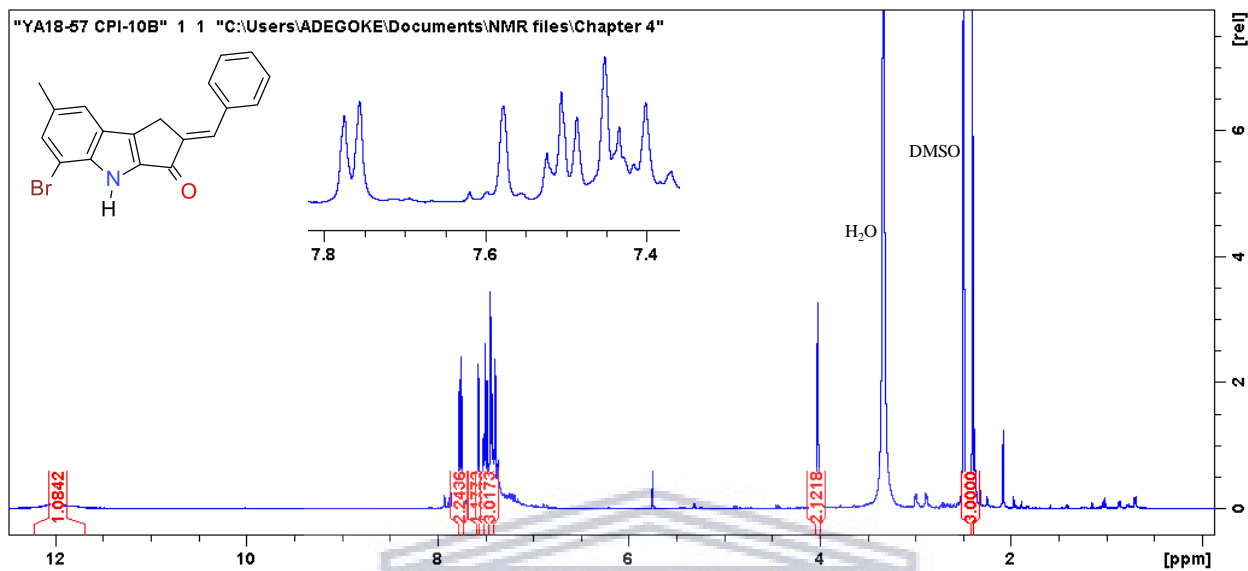


Figure S4.39: ^{13}C NMR spectrum of compound **4.31j** (100 MHz, DMSO-d_6)

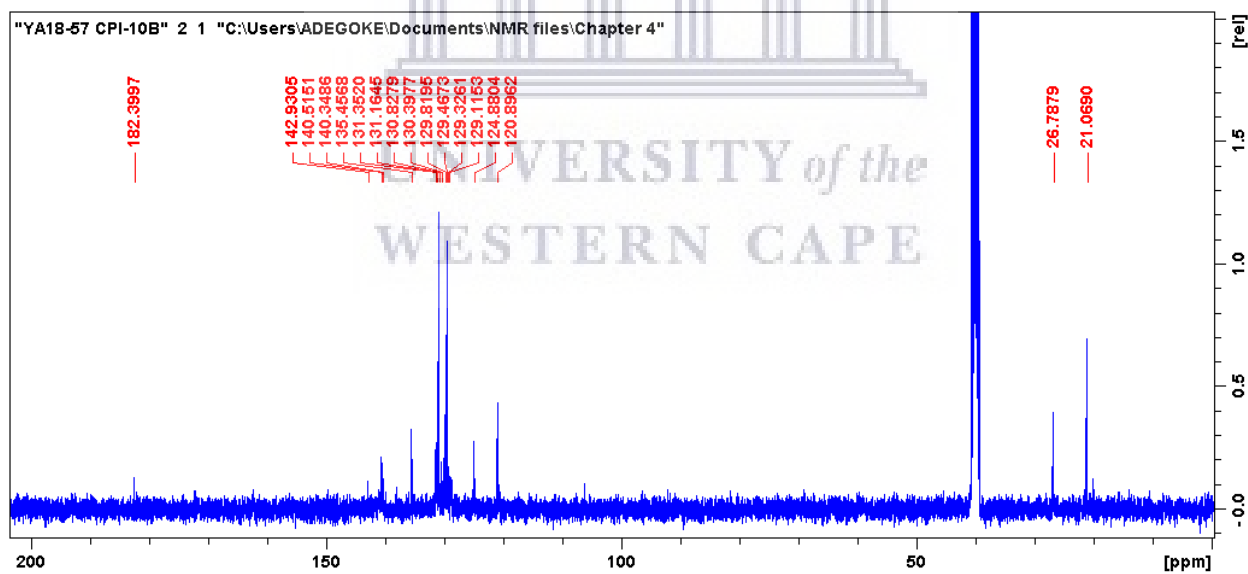


Figure S4.40: HRMS spectrum of compound **4.31j**

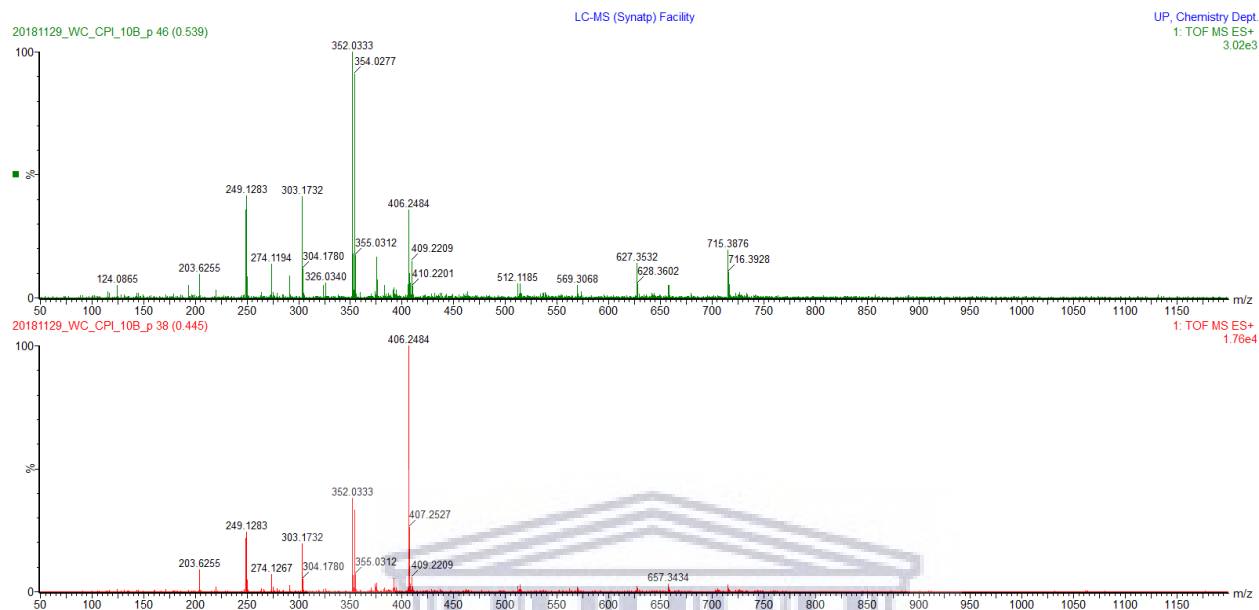


Figure S4.41: IR spectrum of compound **4.31j**

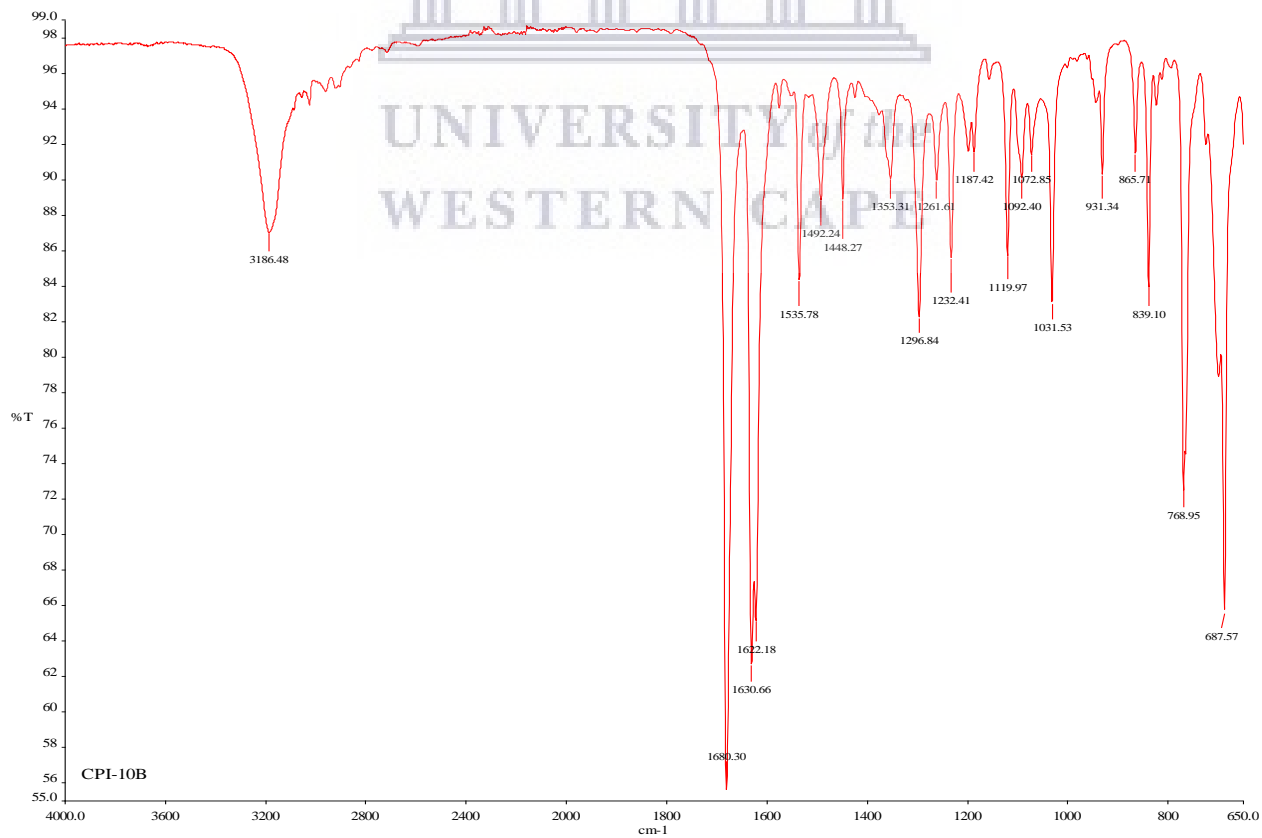


Figure S4.42: ^1H NMR spectrum of compound **4.31k** (400 MHz, DMSO- d_6)

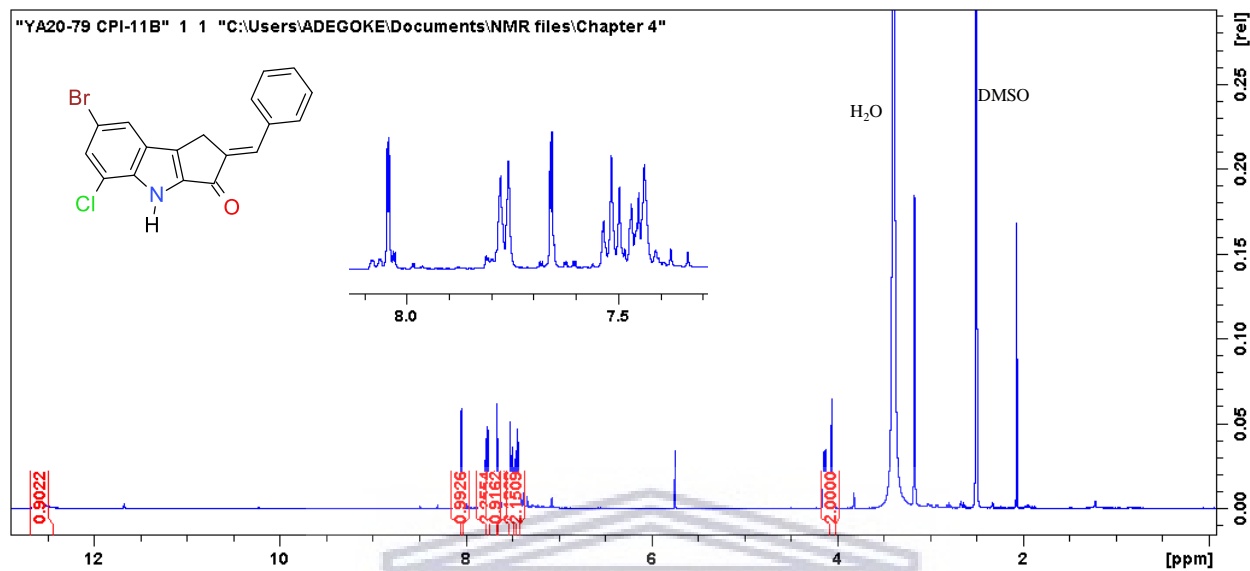


Figure S4.43: HSQC NMR spectrum of compound **4.31k**

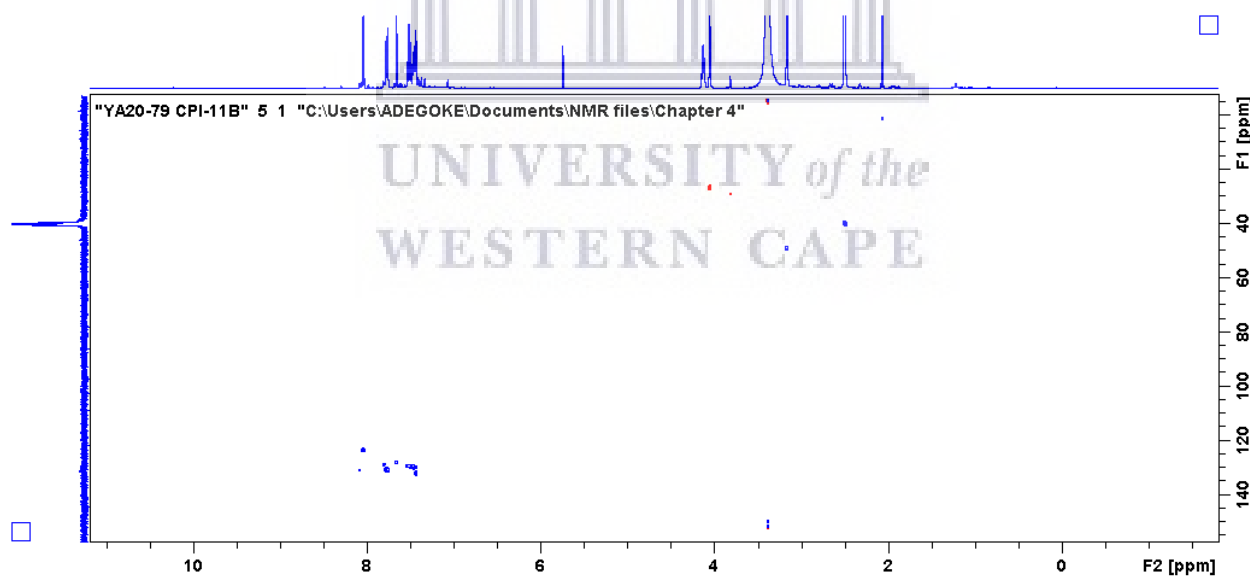


Figure S4.44: HMBC NMR spectrum of compound **4.31k**

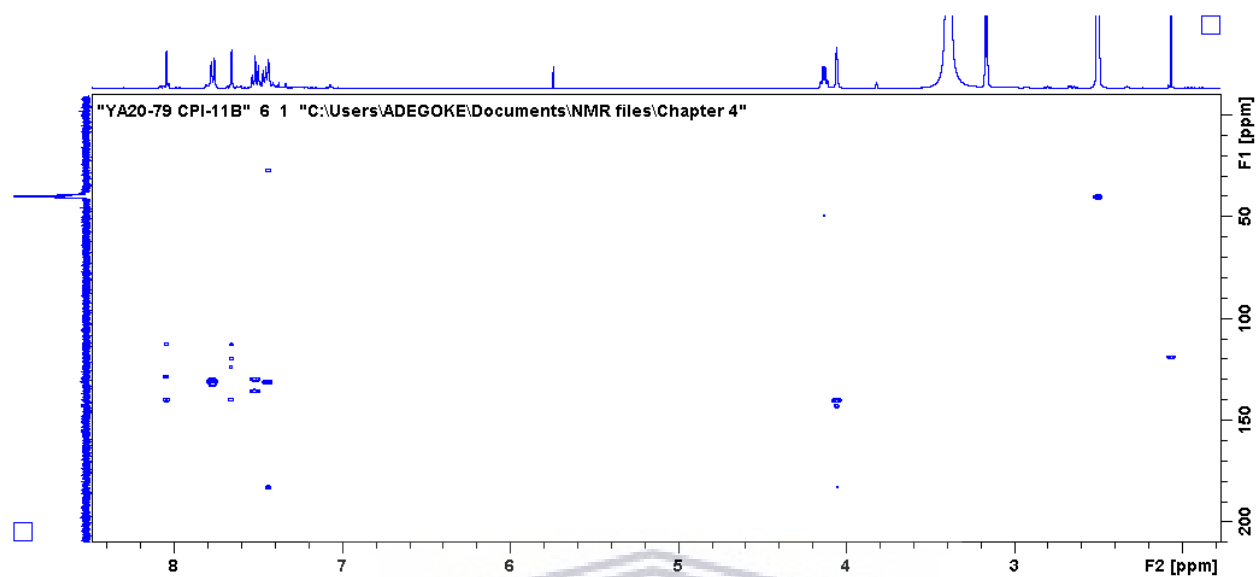


Figure S4.45: HRMS spectrum of compound **4.31k**

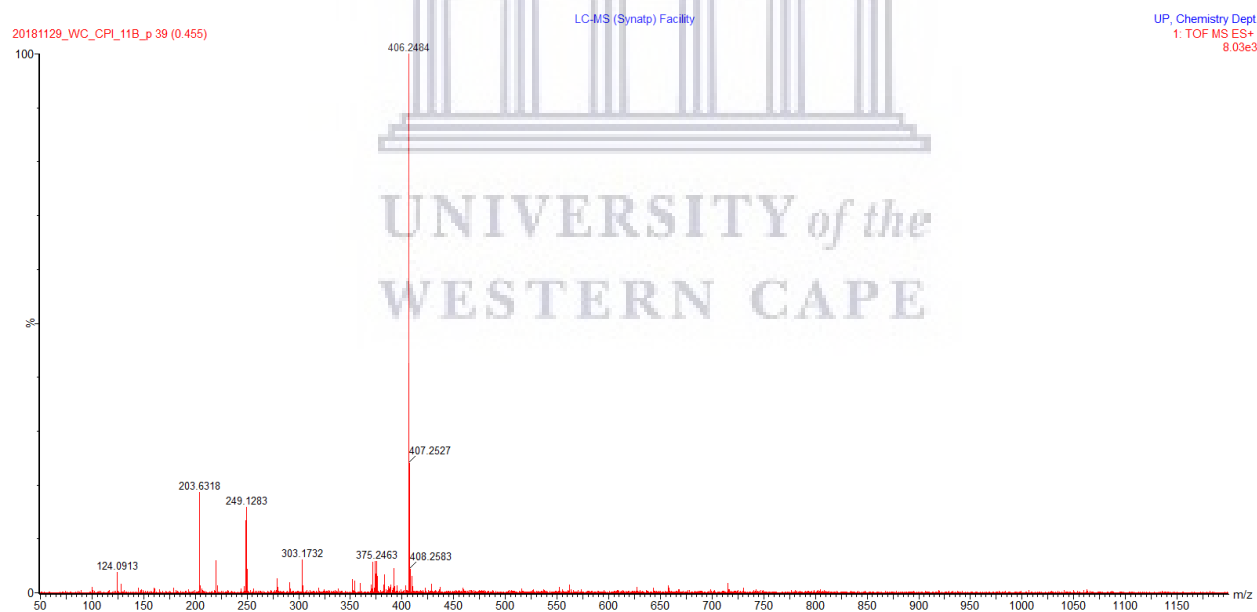
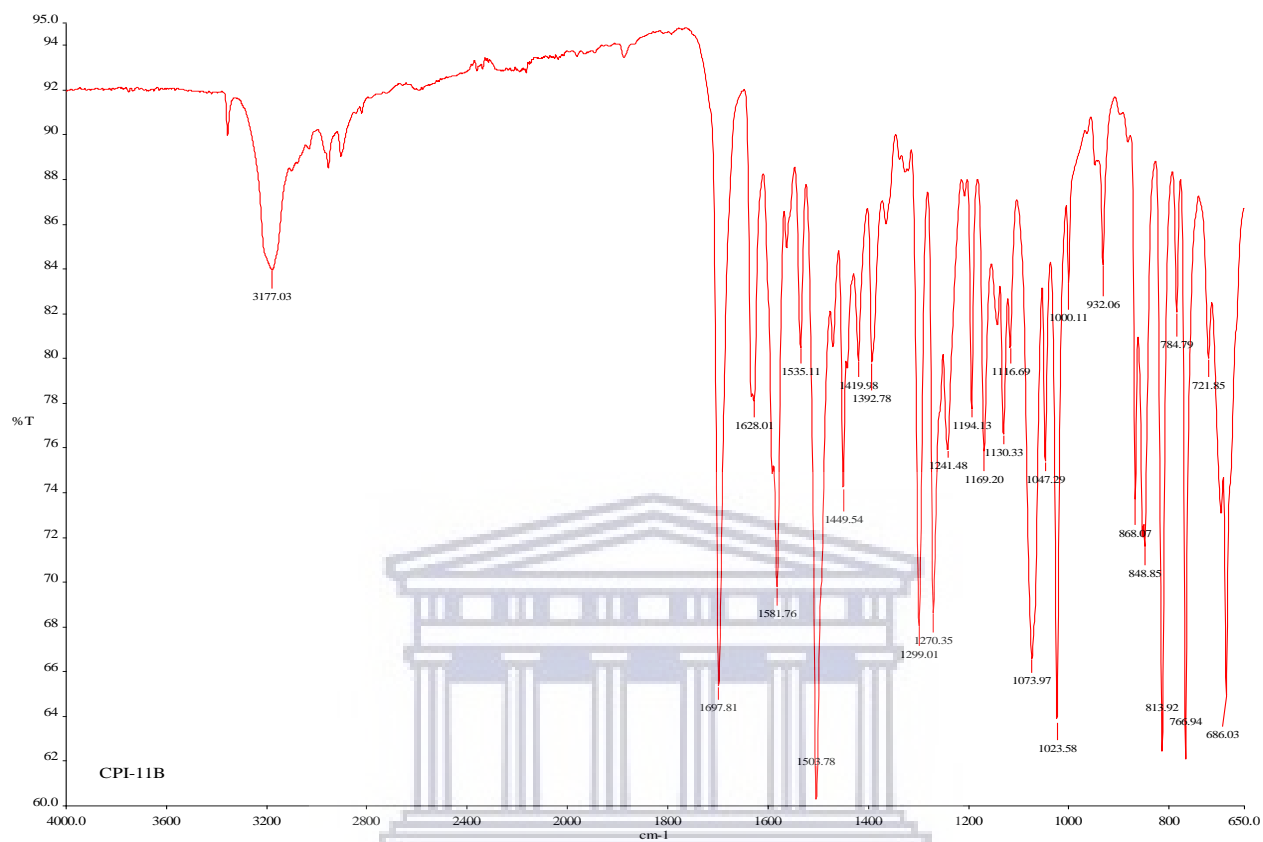


Figure S4.46: IR spectrum of compound **4.31k**



UNIVERSITY of the
WESTERN CAPE

Figure S4.47: ^1H NMR spectrum of compound **4.311** (400 MHz, DMSO- d_6)

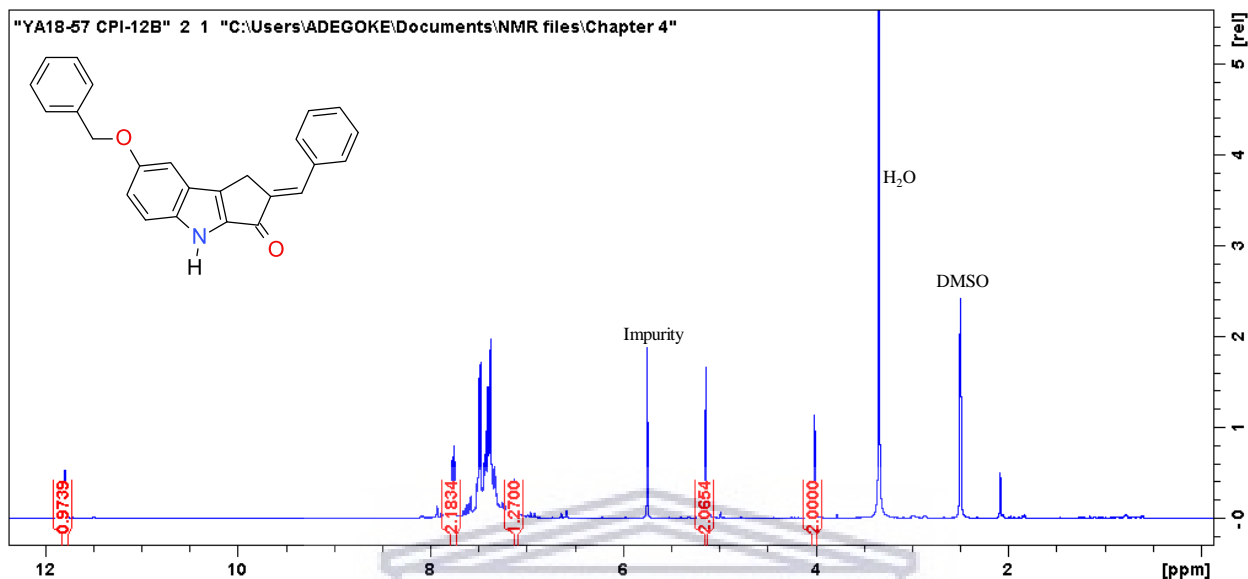


Figure S4.48: ^{13}C NMR spectrum of compound **4.311** (100 MHz, DMSO- d_6)

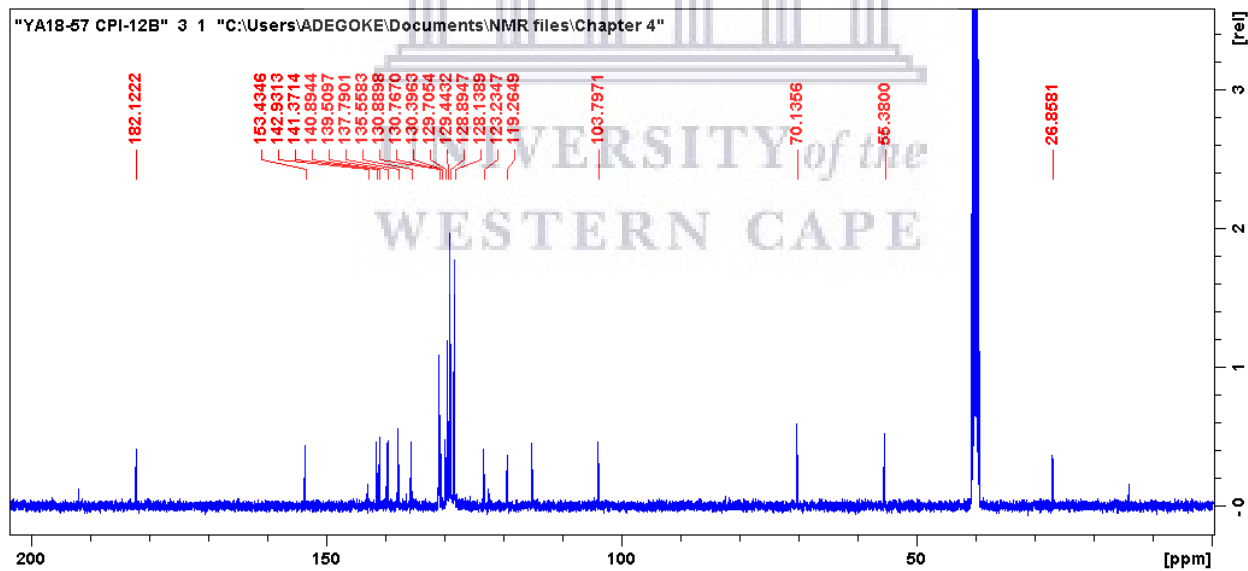


Figure S4.49: HRMS spectrum of compound **4.311**

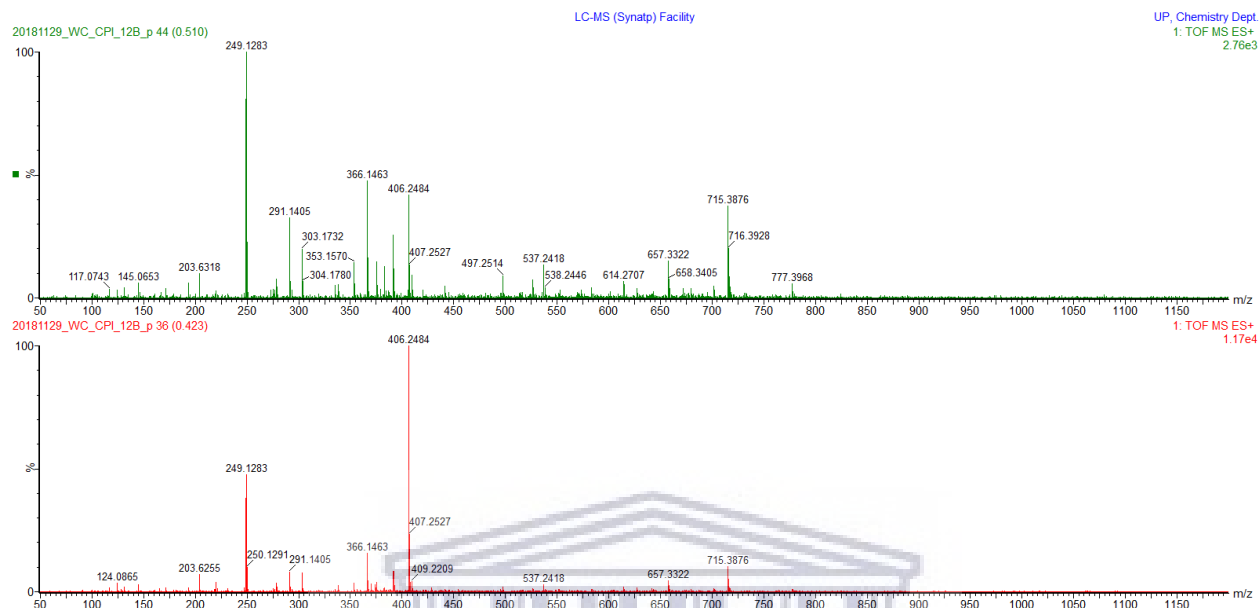
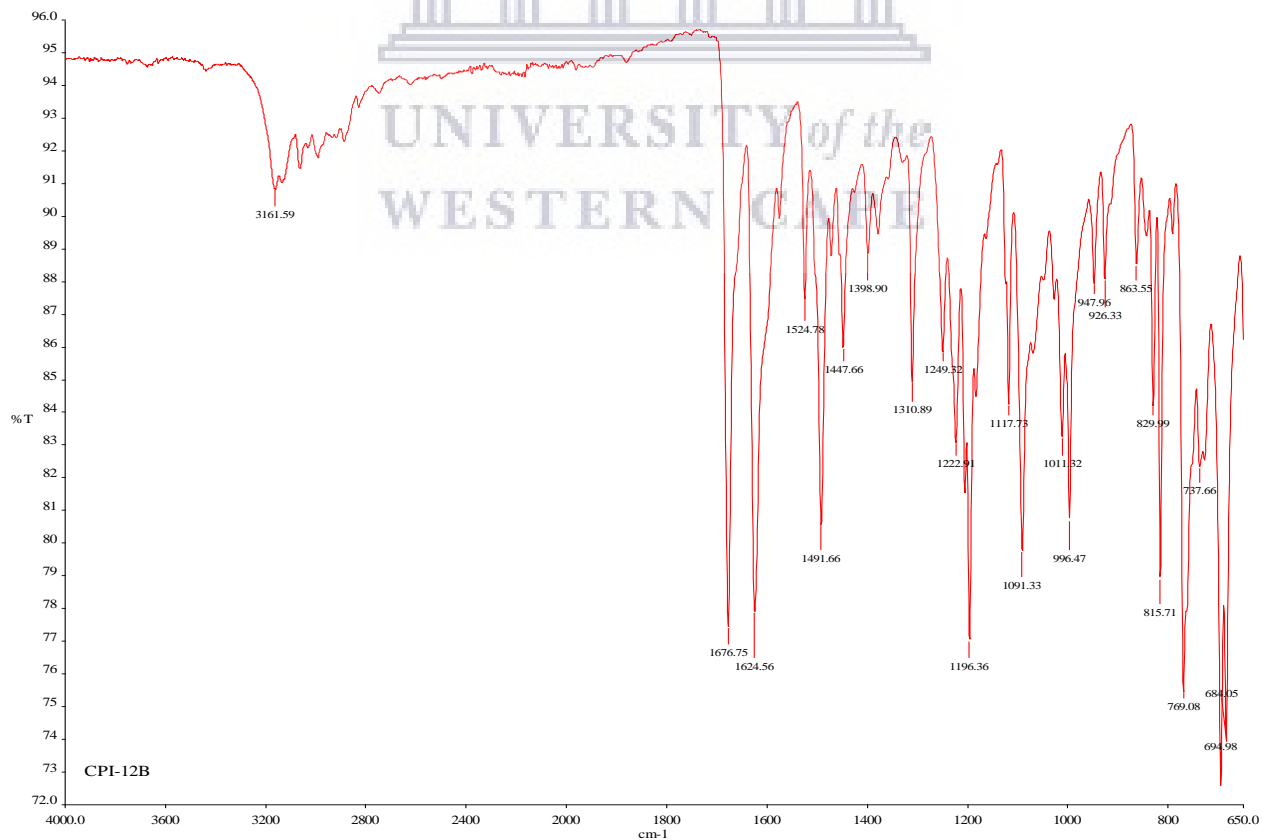


Figure S4.50: IR spectrum of compound **4.311**



3,4,5-trimethoxyphenyl substituted cyclopenta[*b*]indol-3-one series 4.32(a-l)

Figure S4.51: ¹H NMR spectrum of compound 4.32a (400 MHz, DMSO-d₆)

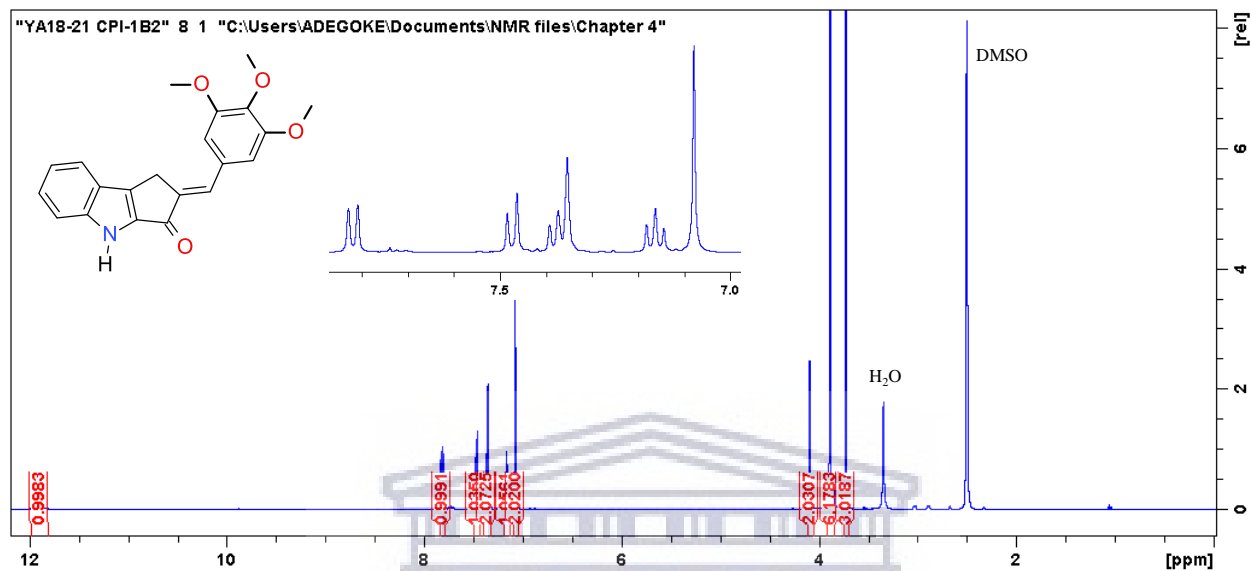


Figure S4.52: ¹³C NMR spectrum of compound 4.32a (100 MHz, DMSO-d₆)

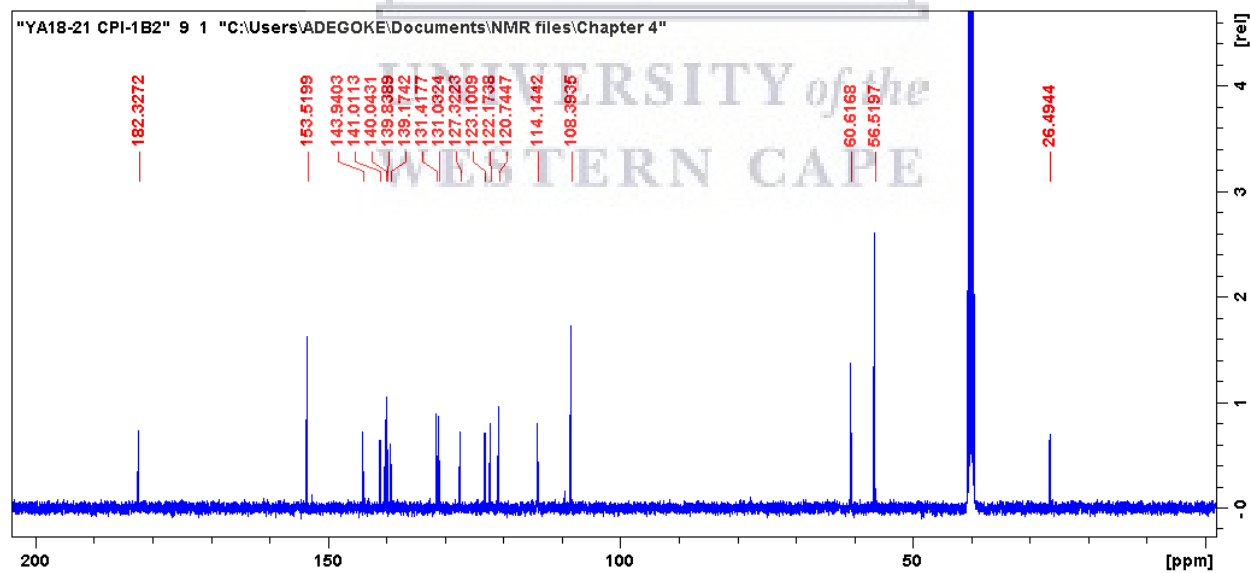


Figure S4.53: HRMS spectrum of compound **4.32a**

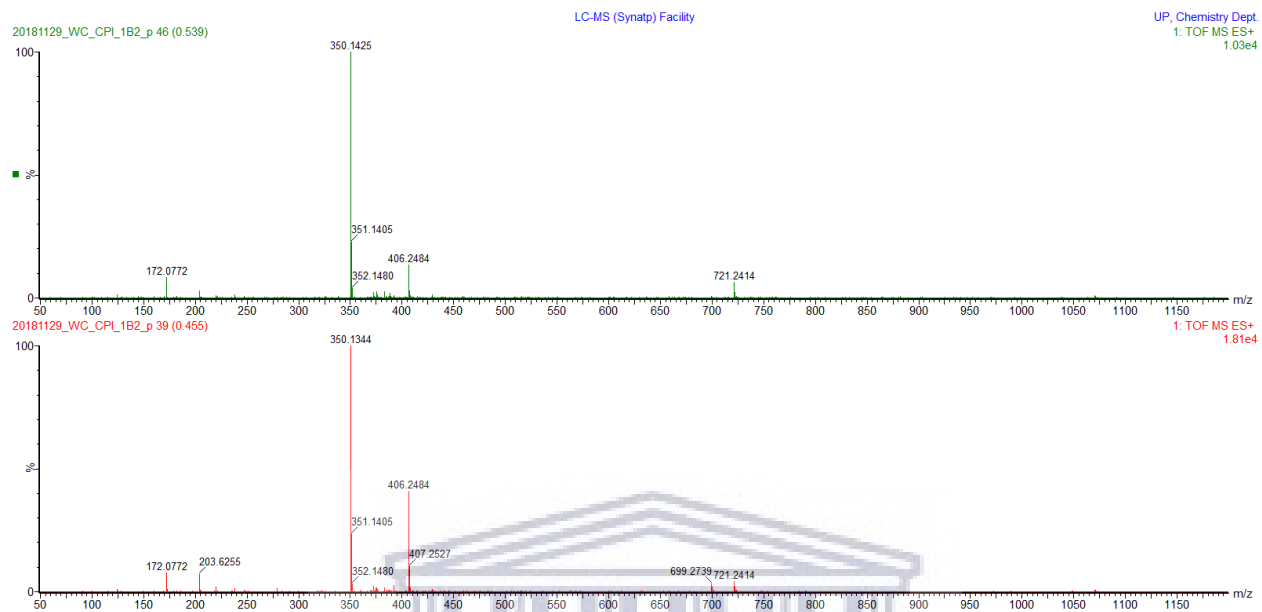


Figure S4.54: IR spectrum of compound **4.32a**

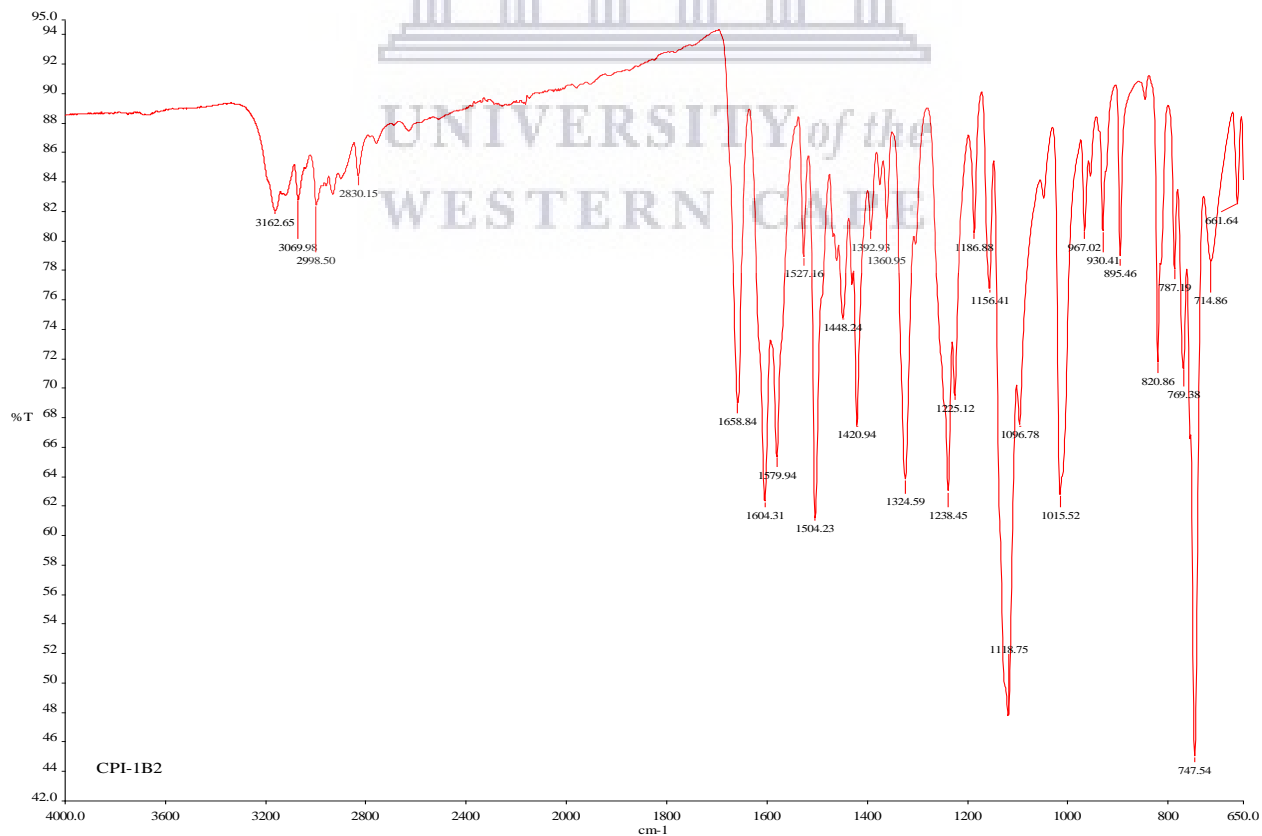


Figure S4.55: ^1H NMR spectrum of compound **4.32b** (400 MHz, DMSO- d_6)

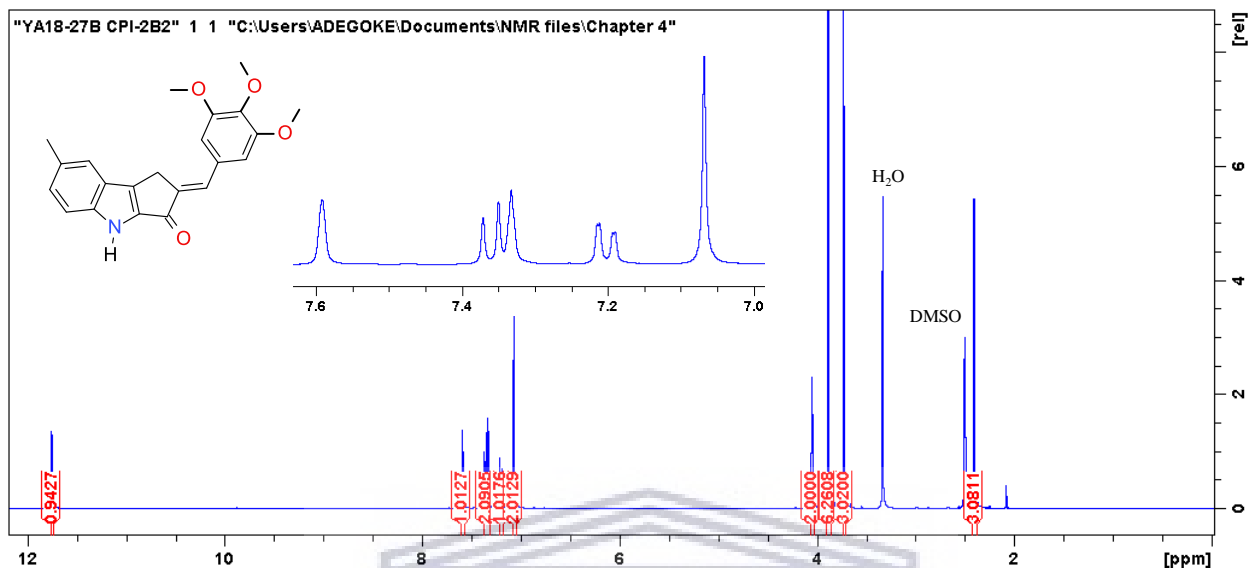


Figure S4.56: ^{13}C NMR spectrum of compound **4.32b** (100 MHz, DMSO- d_6)

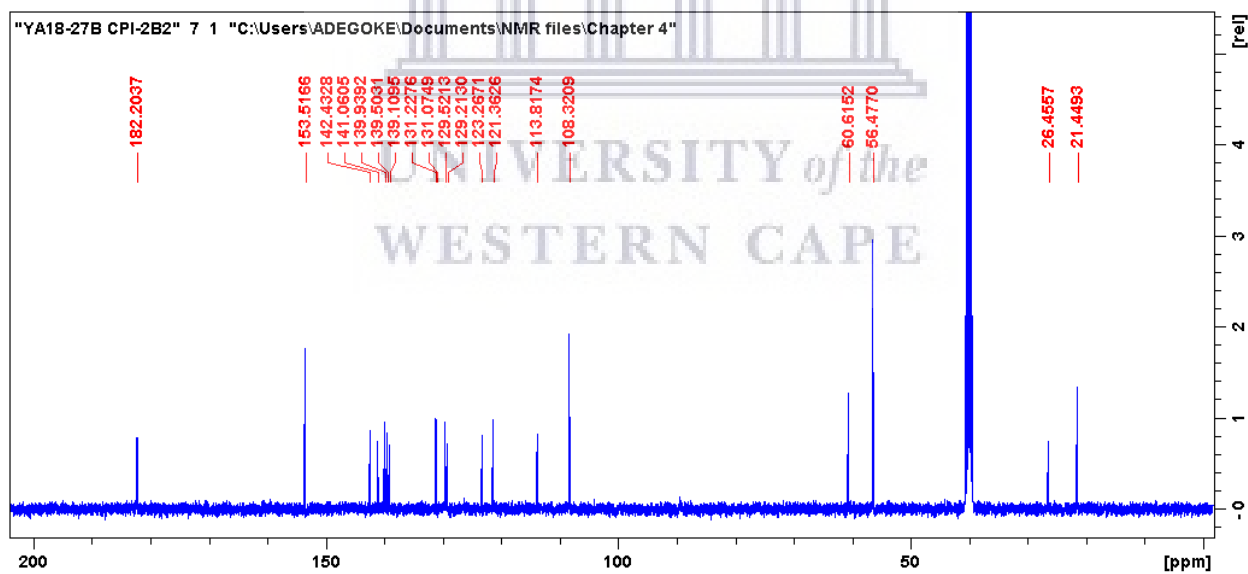


Figure S4.57: HRMS spectrum of compound 4.32b

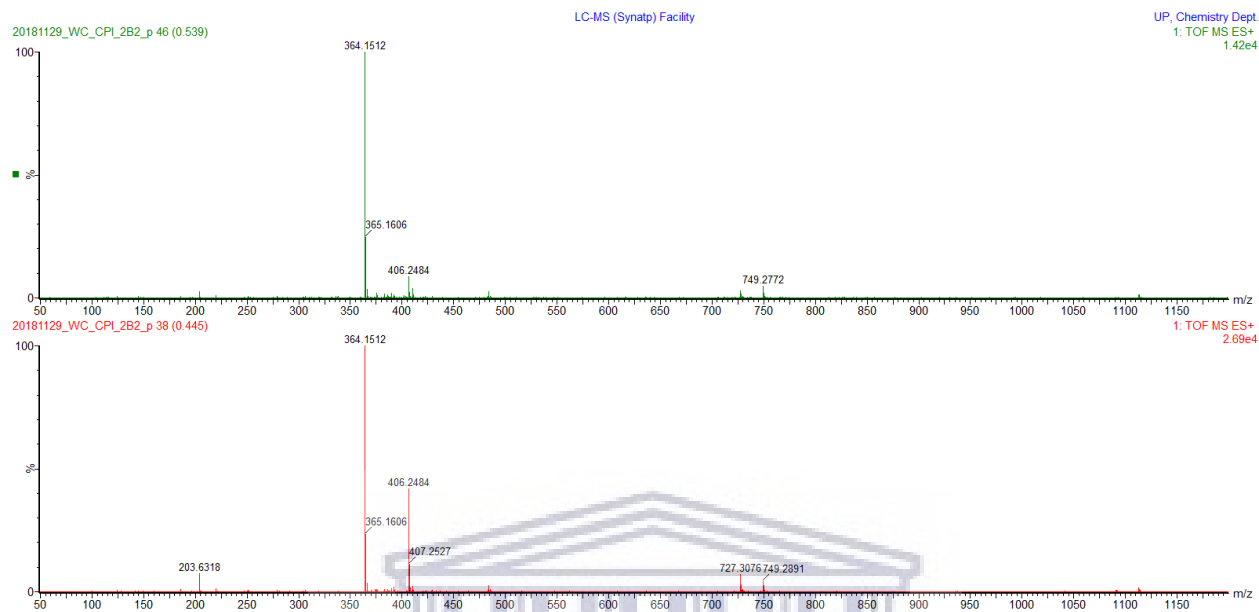


Figure S4.58: IR spectrum of compound 4.32b

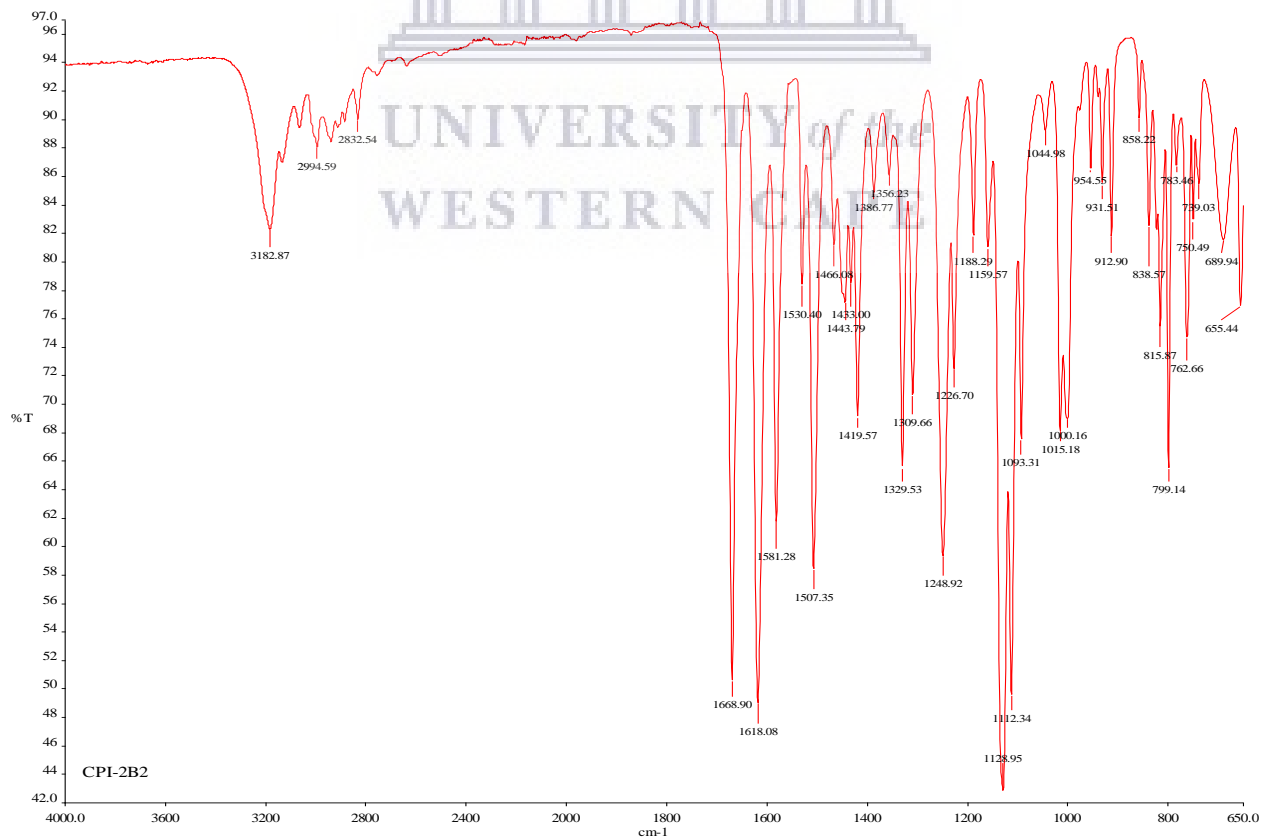


Figure S4.59: ^1H NMR spectrum of compound **4.32c** (400 MHz, DMSO-d_6)

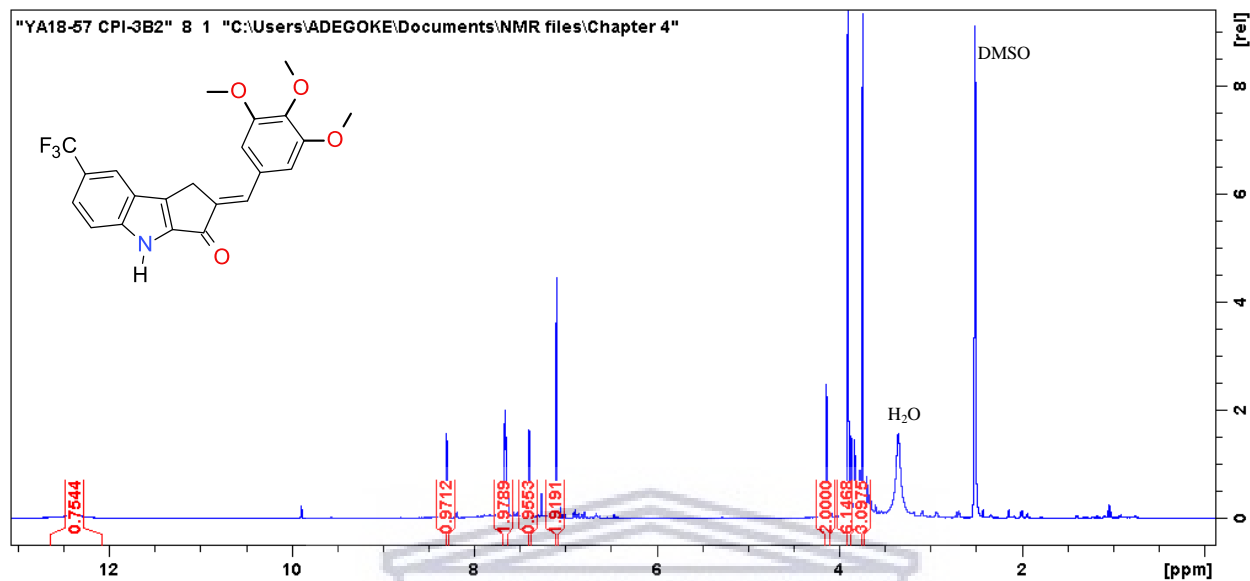


Figure S4.60: ^{13}C NMR spectrum of compound **4.32c** (100 MHz, DMSO-d_6)

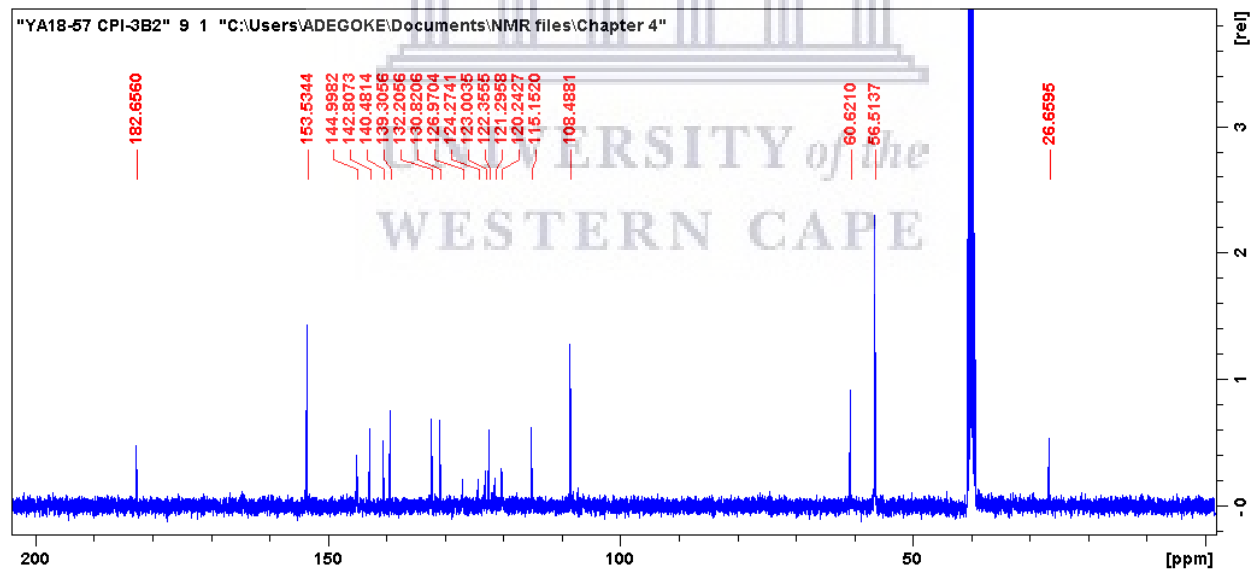


Figure S4.61: HRMS spectrum of compound **4.32c**

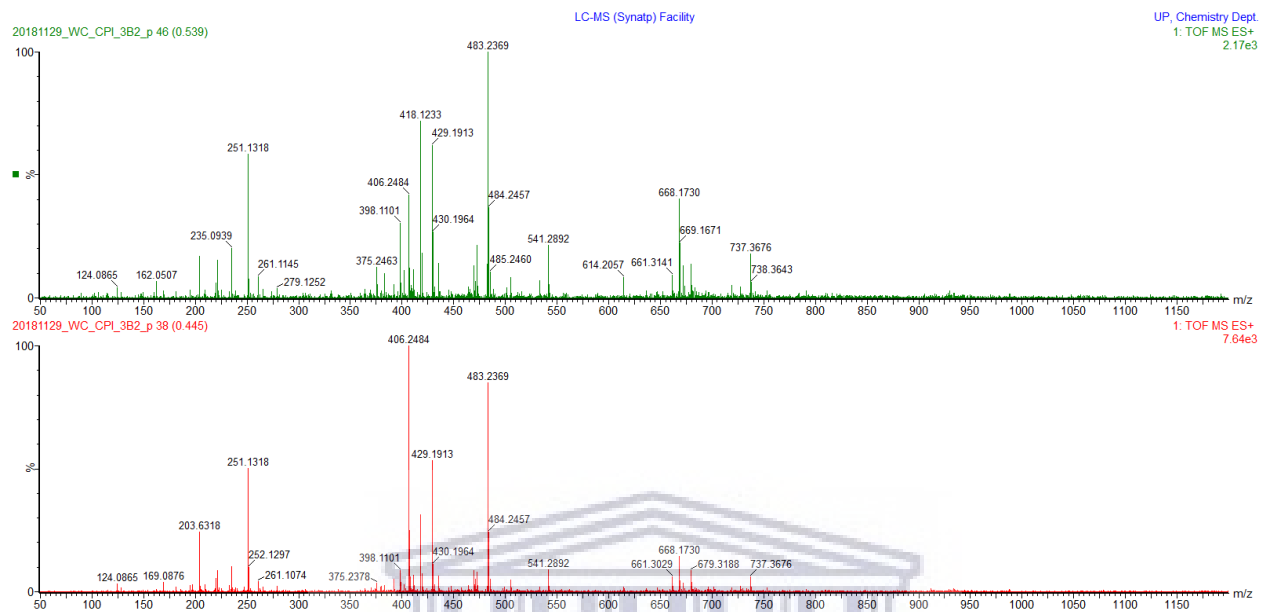


Figure S4.62: IR spectrum of compound **4.32c**

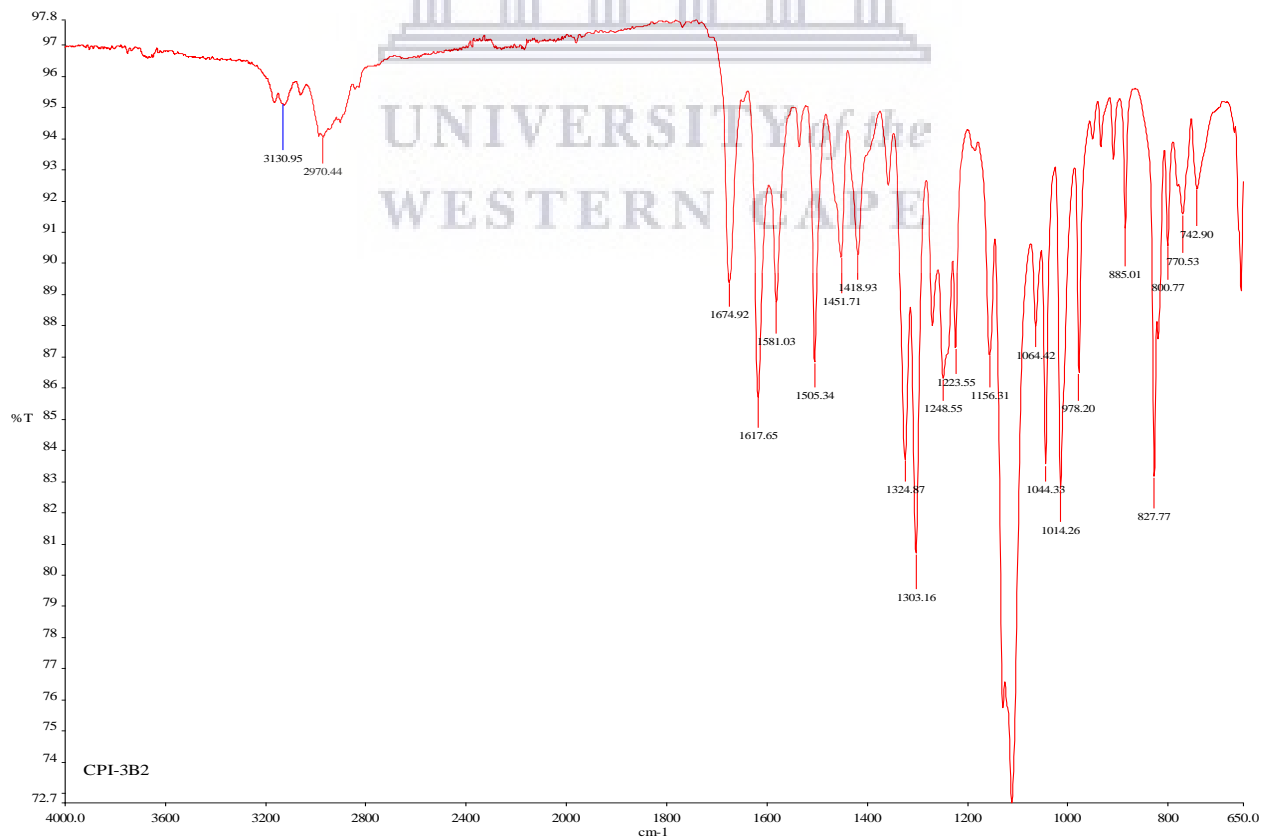


Figure S4.63: DEPT-135 NMR spectrum of compound **4.32d**

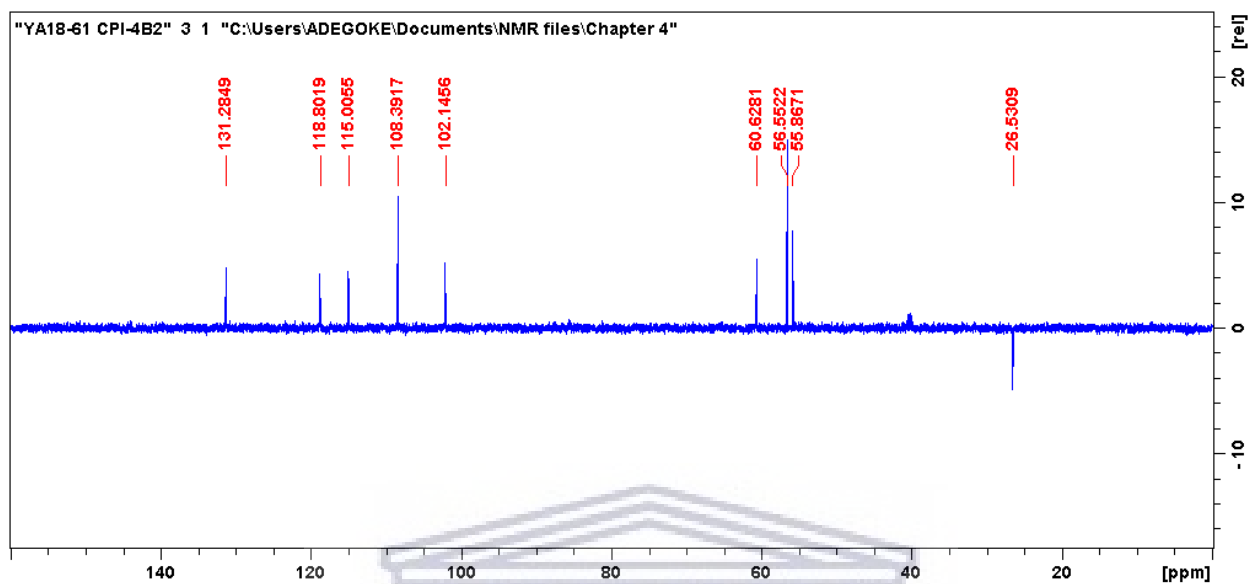


Figure S4.64: COSY NMR spectrum of compound **4.32d**

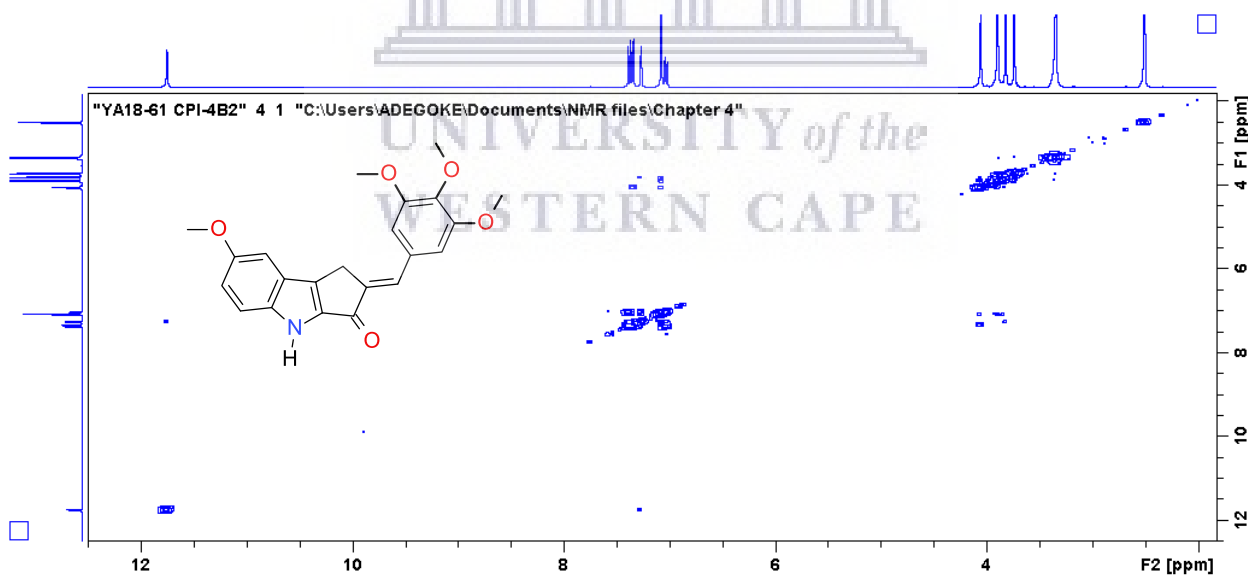


Figure S4.65: HSQC NMR spectrum of compound **4.32d**

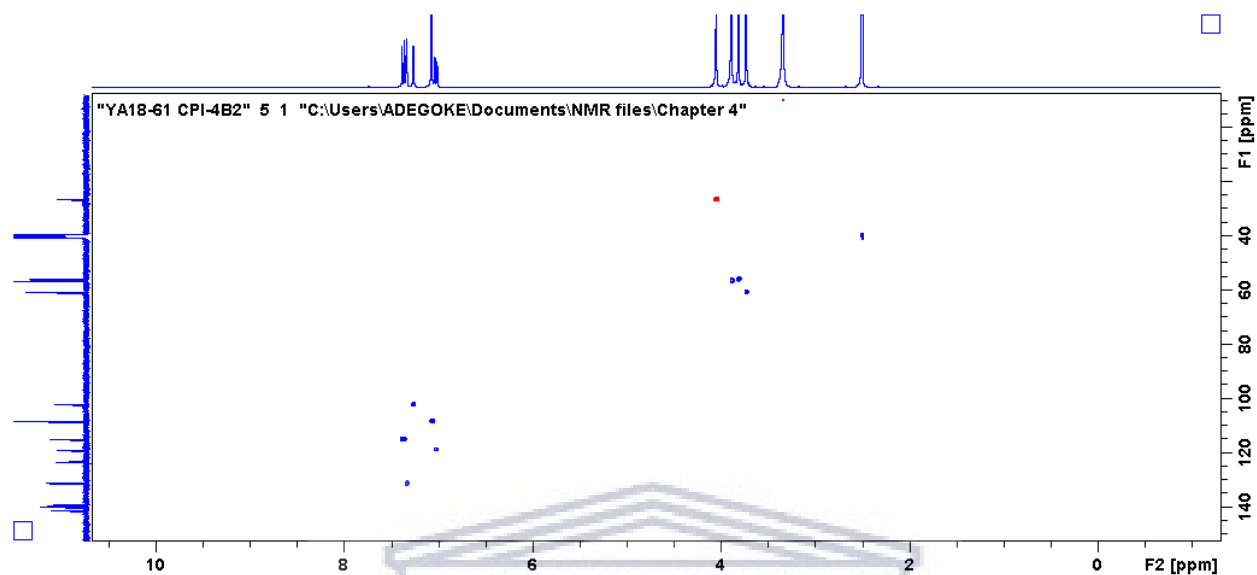


Figure S4.66: HMBC NMR spectrum of compound **4.32d**

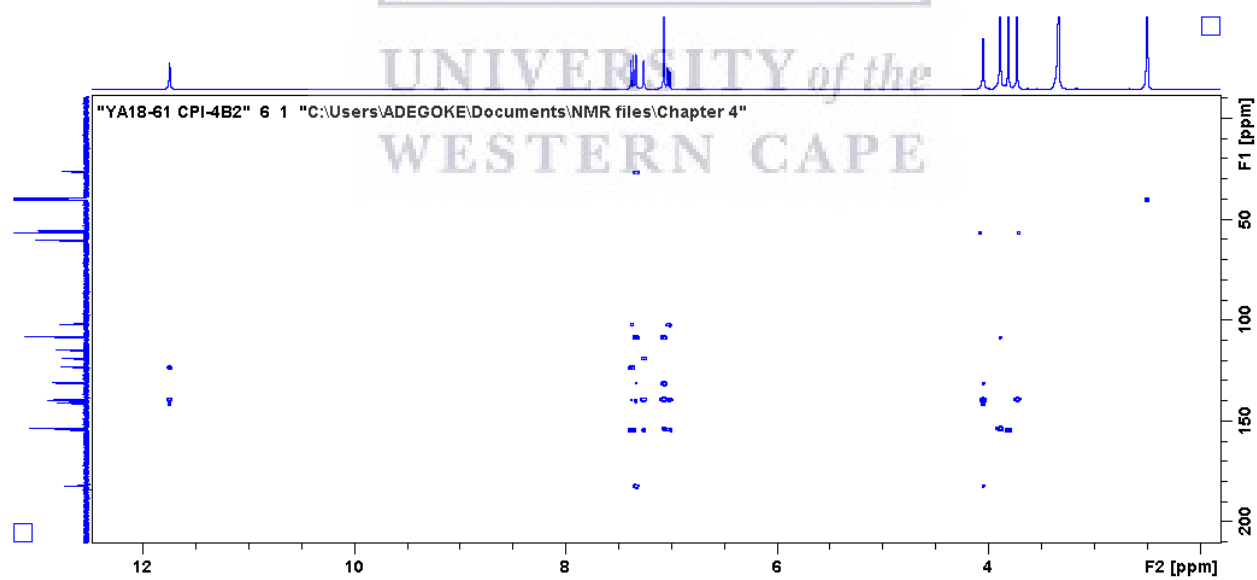


Figure S4.67: 1D selective NOESY NMR spectrum of compound **4.32d**

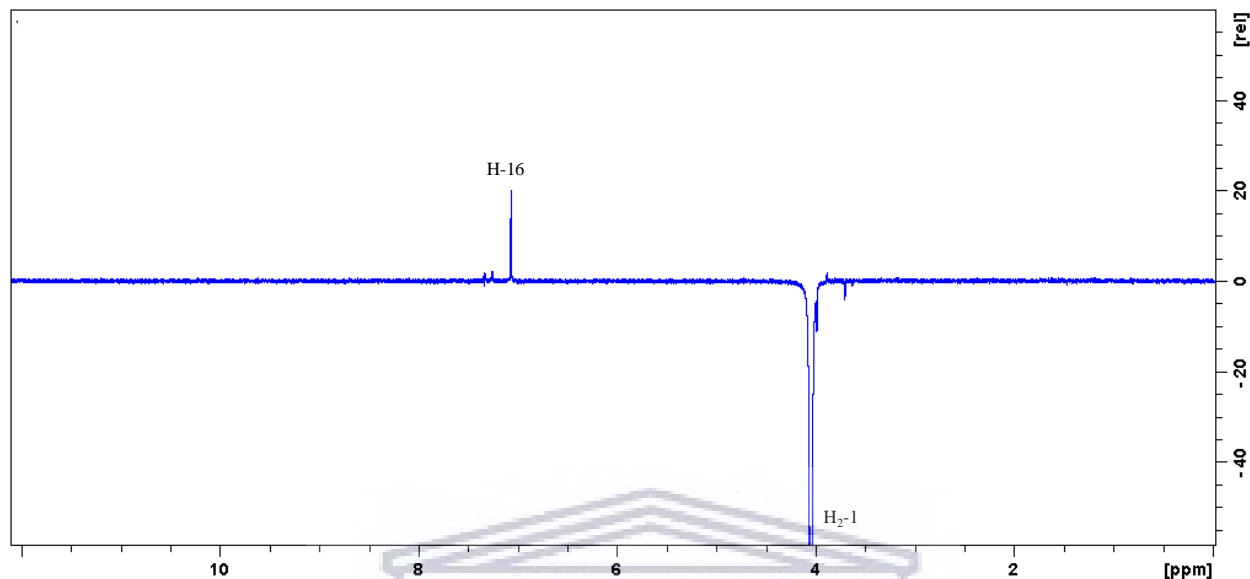


Figure S4.68 HRMS spectrum of compound **4.32d**

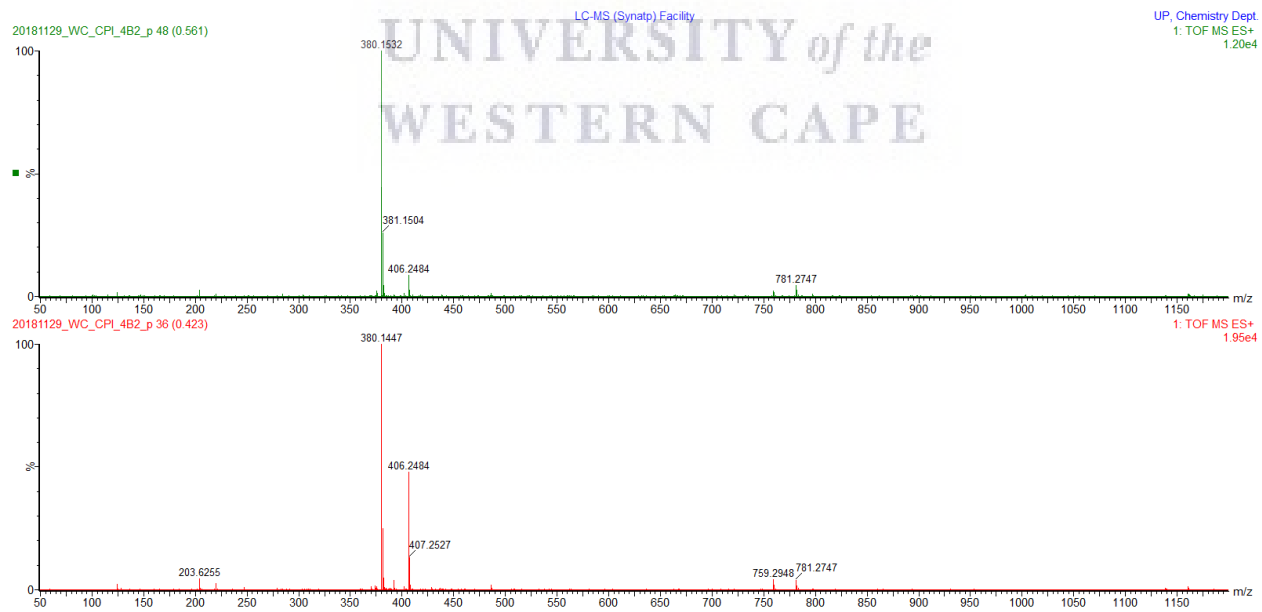


Figure S4.69: IR spectrum of compound **4.32d**

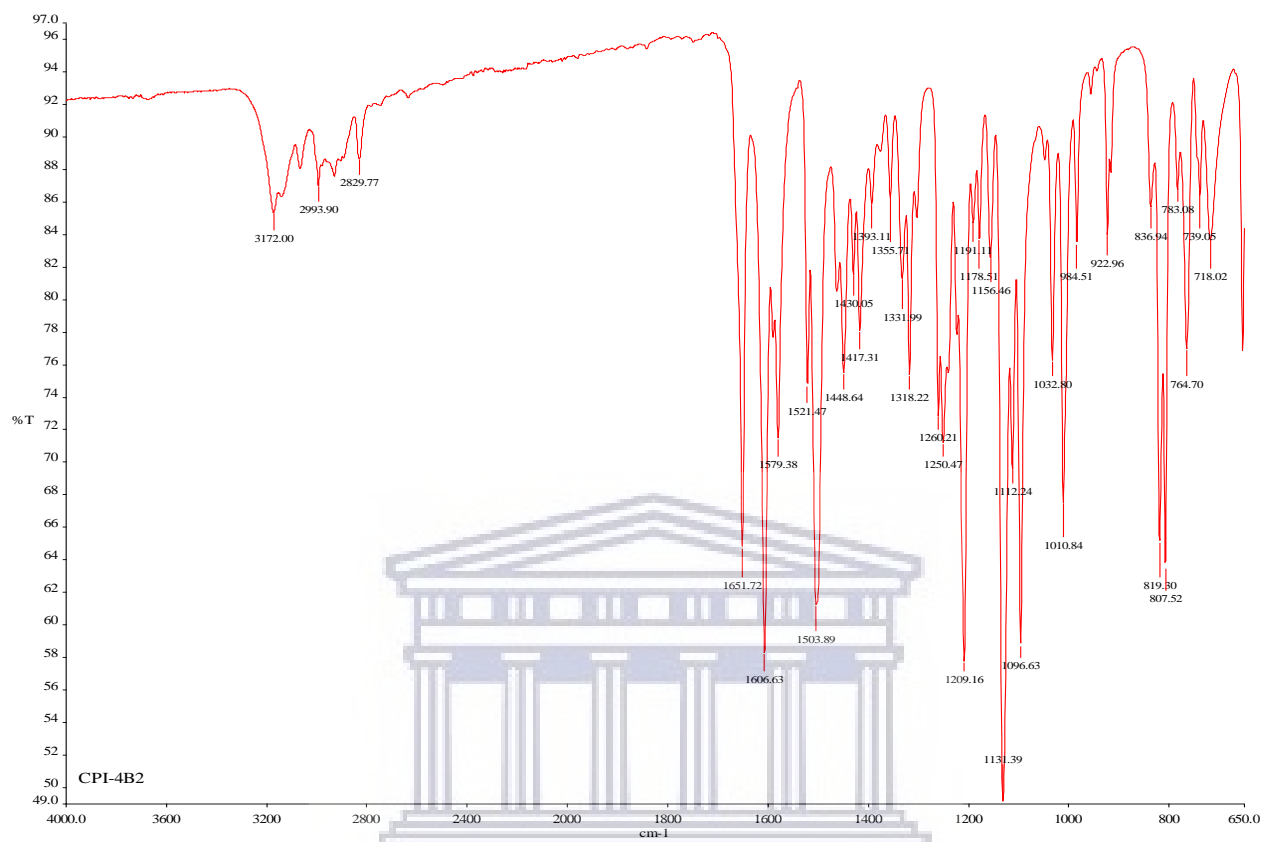


Figure S4.70: ^1H NMR spectrum of compound **4.32e** (400 MHz, DMSO-d_6)

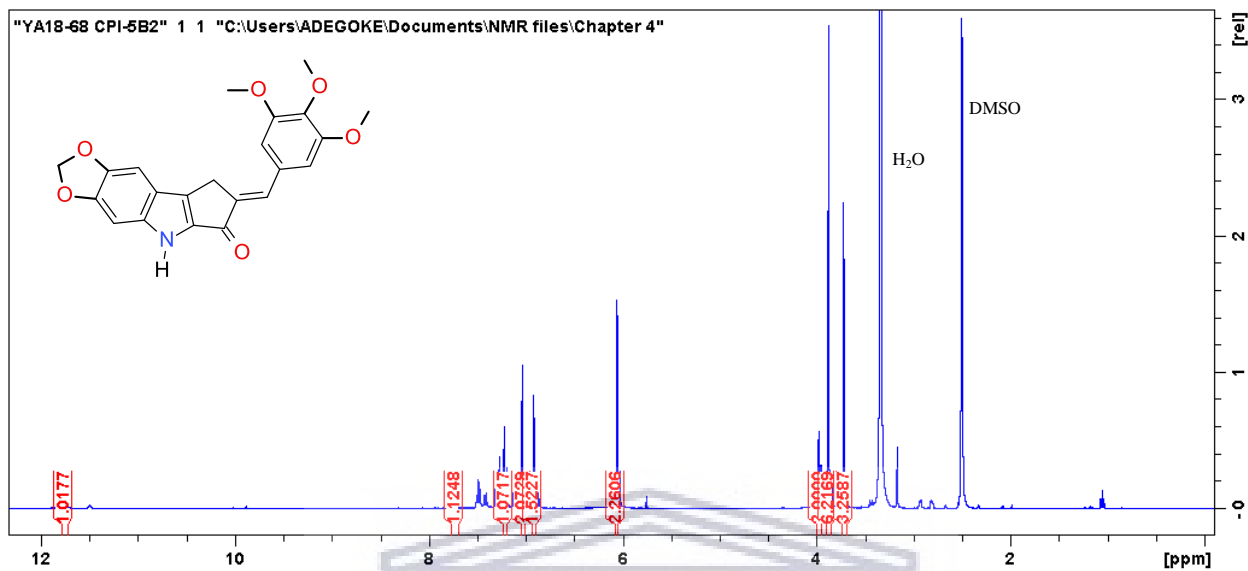


Figure S4.71: ^{13}C NMR spectrum of compound **4.32e** (100 MHz, DMSO-d_6)

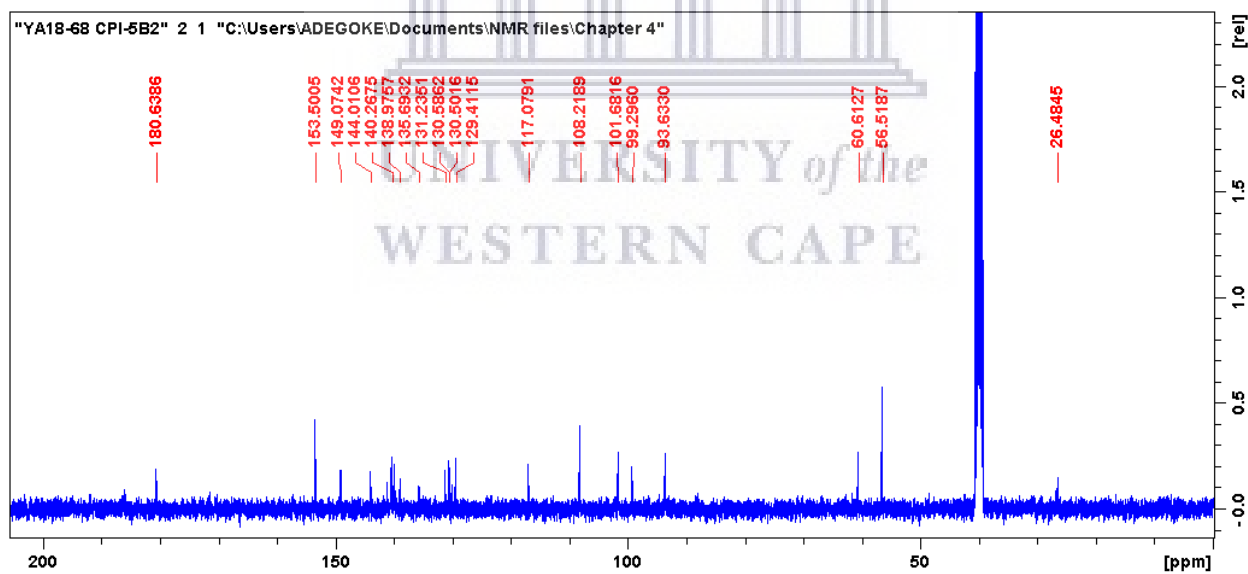


Figure S4.72: HRMS spectrum of compound **4.32e**

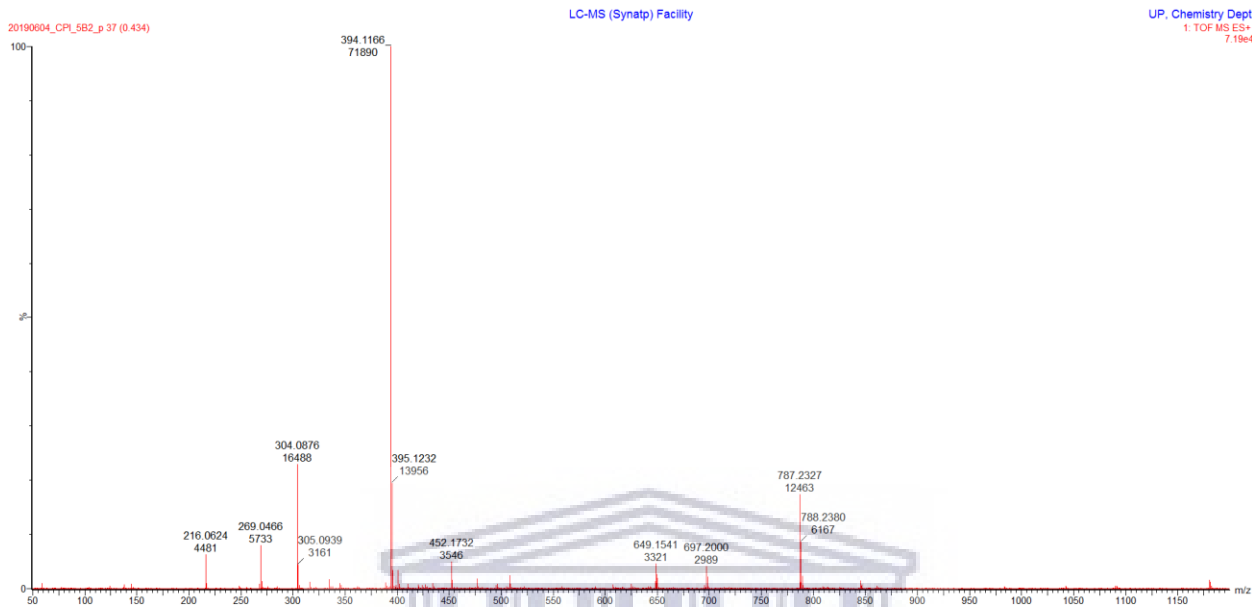


Figure S4.73: IR spectrum of compound **4.32e**

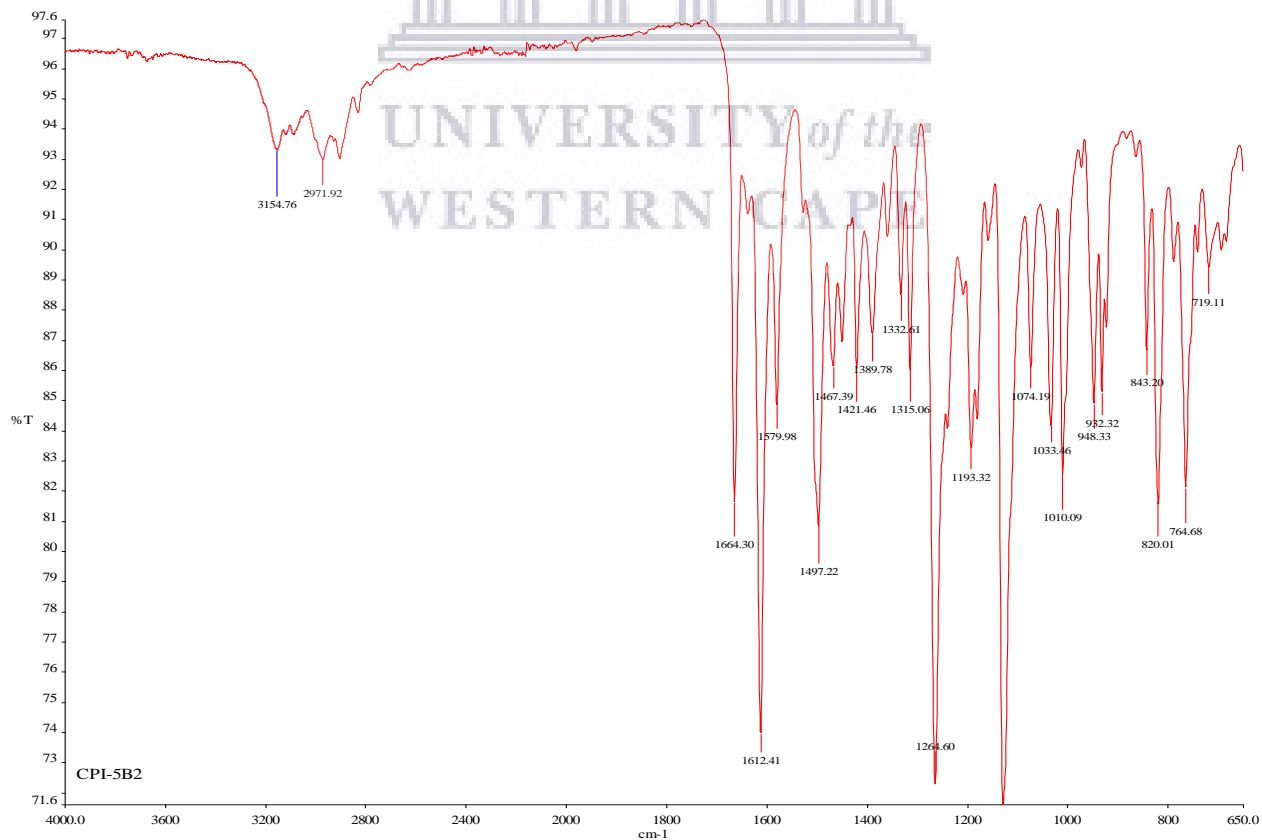


Figure S4.74: ^1H NMR spectrum of compound **4.32f** (400 MHz, DMSO- d_6)

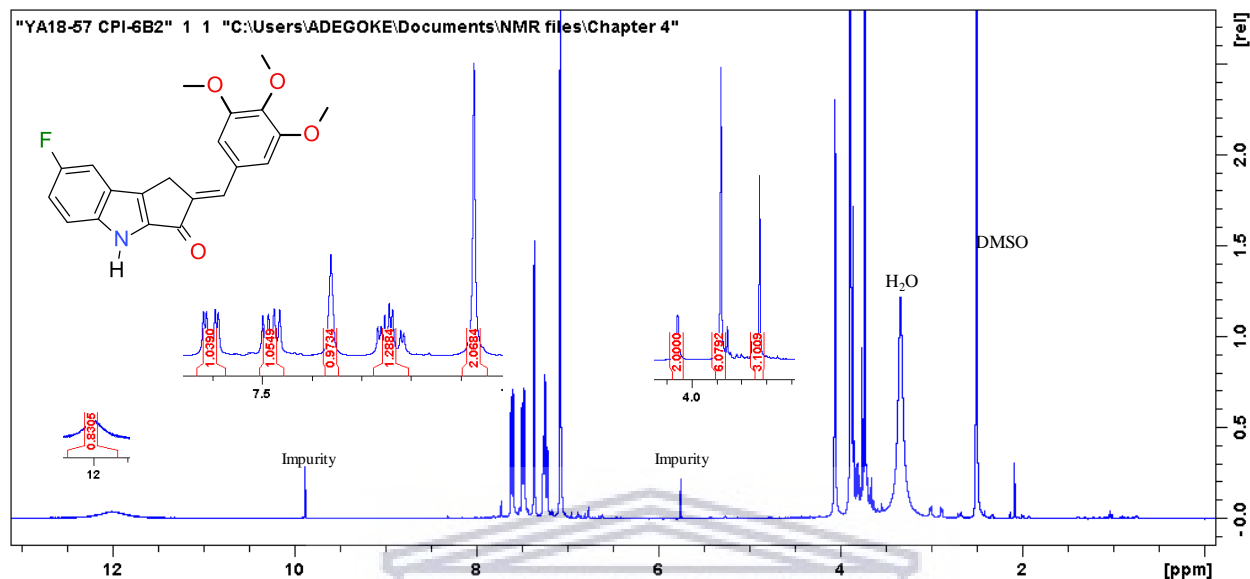


Figure S4.75: ^{13}C NMR spectrum of compound **4.32f** (100 MHz, DMSO- d_6)

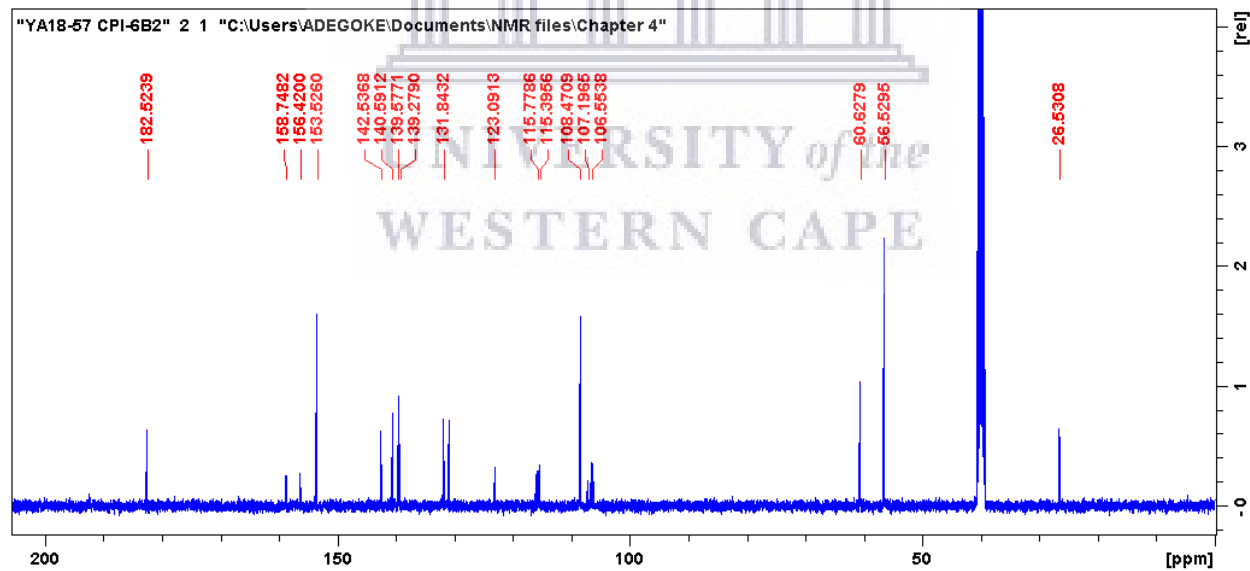


Figure S4.76: HRMS spectrum of compound **4.32f**

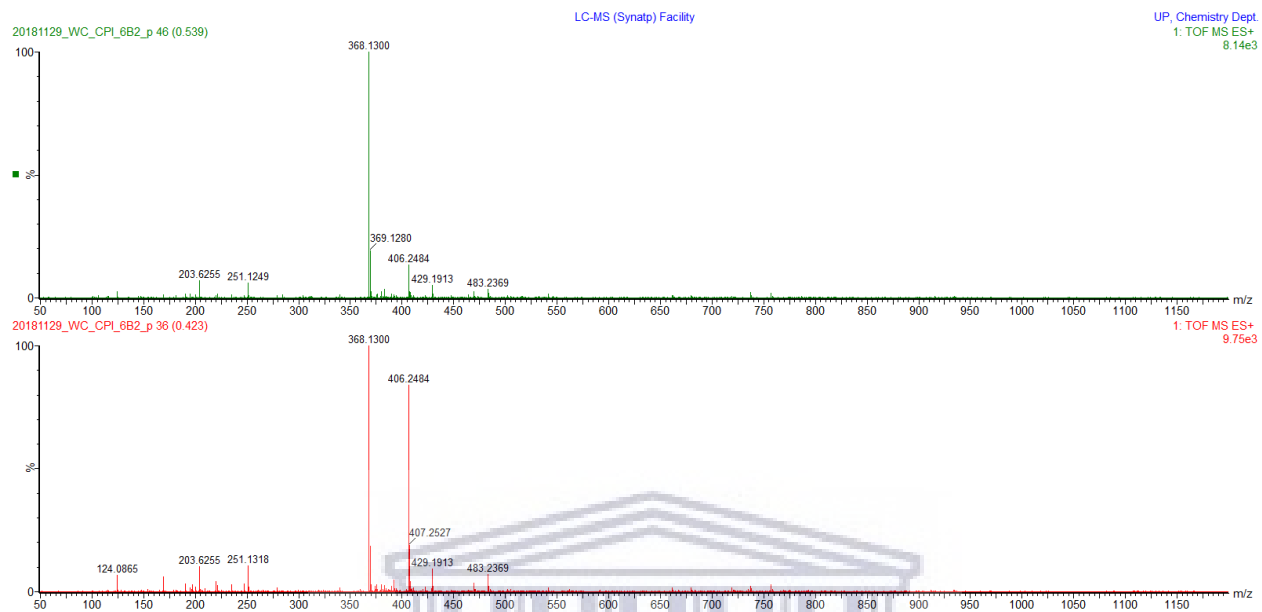


Figure S4.77: IR spectrum of compound **4.32f**

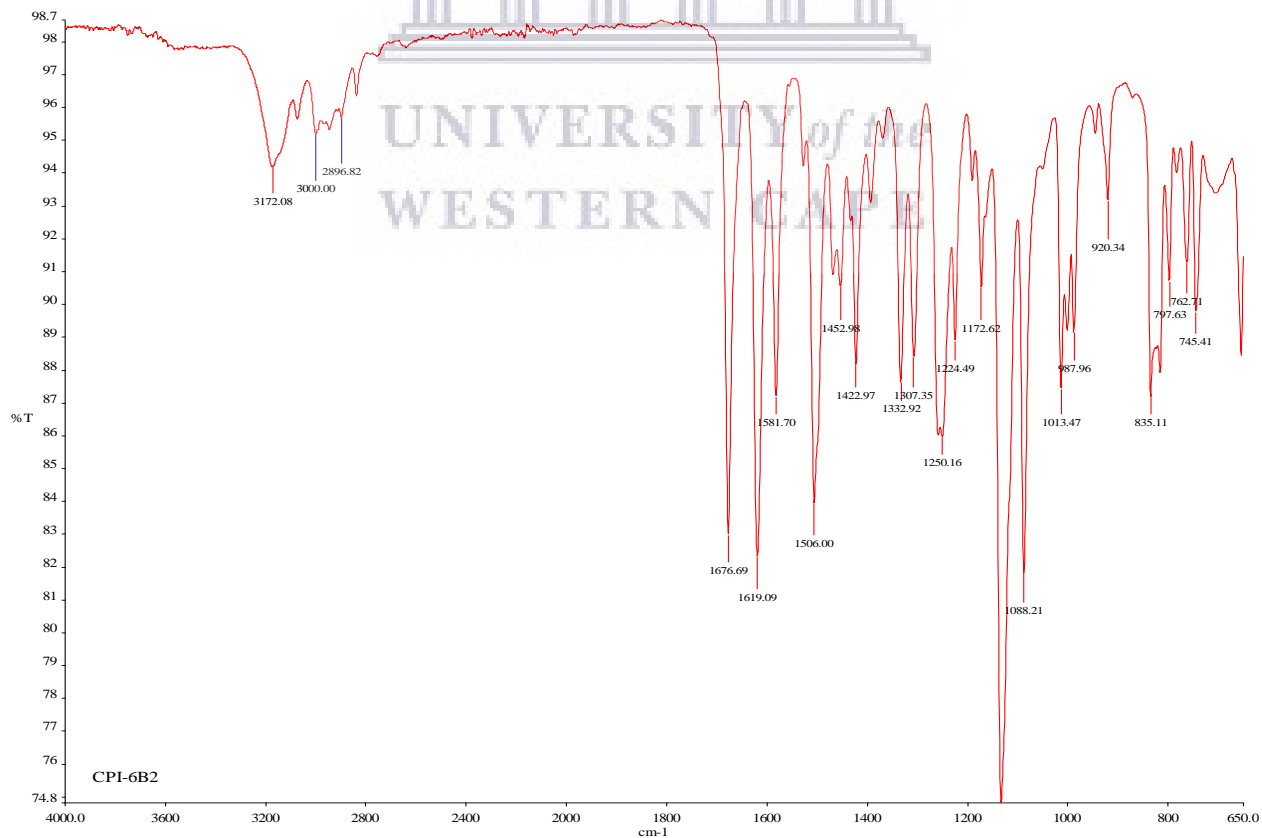


Figure S4.78: ^1H NMR spectrum of compound **4.32g** (400 MHz, DMSO- d_6)

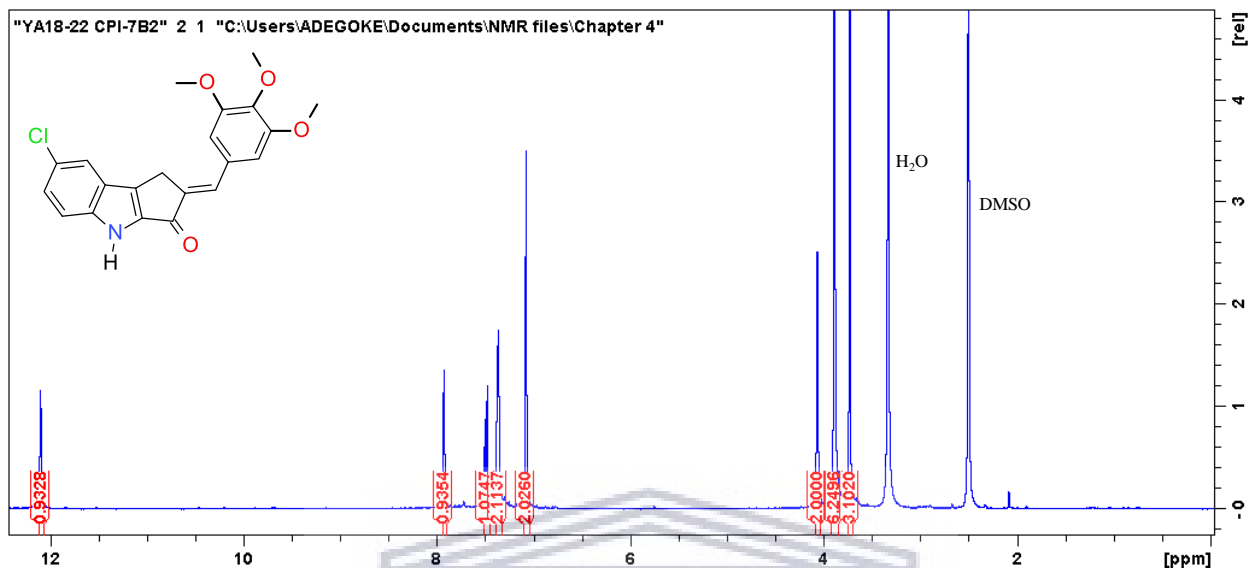


Figure S4.79: ^{13}C NMR spectrum of compound **4.32g** (100 MHz, DMSO- d_6)

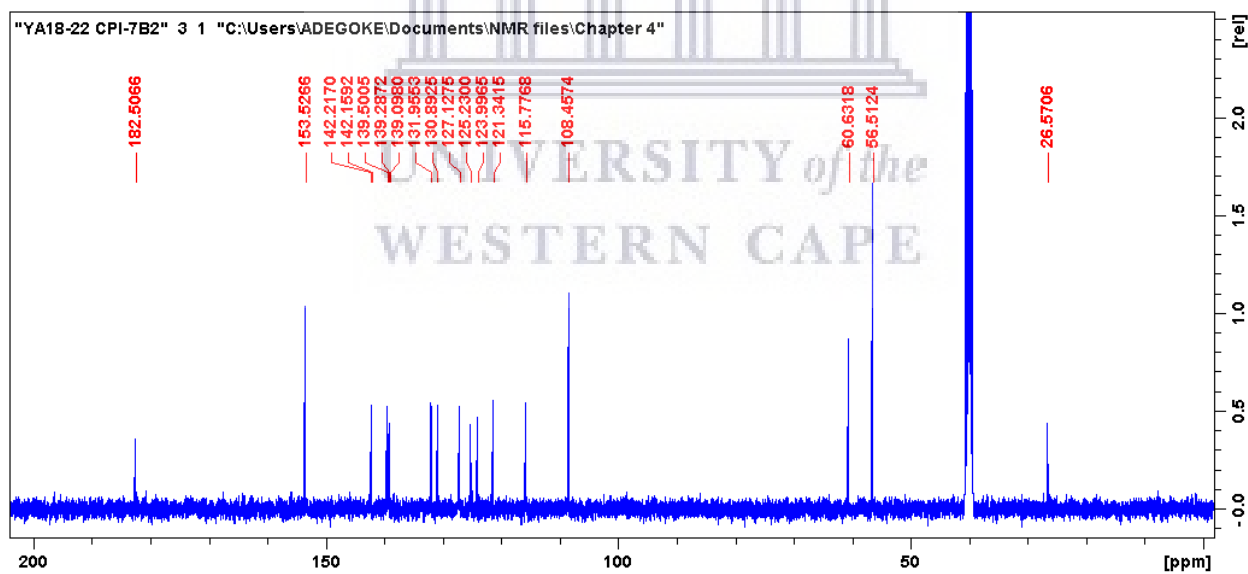


Figure S4.80: HRMS spectrum of compound **4.32g**

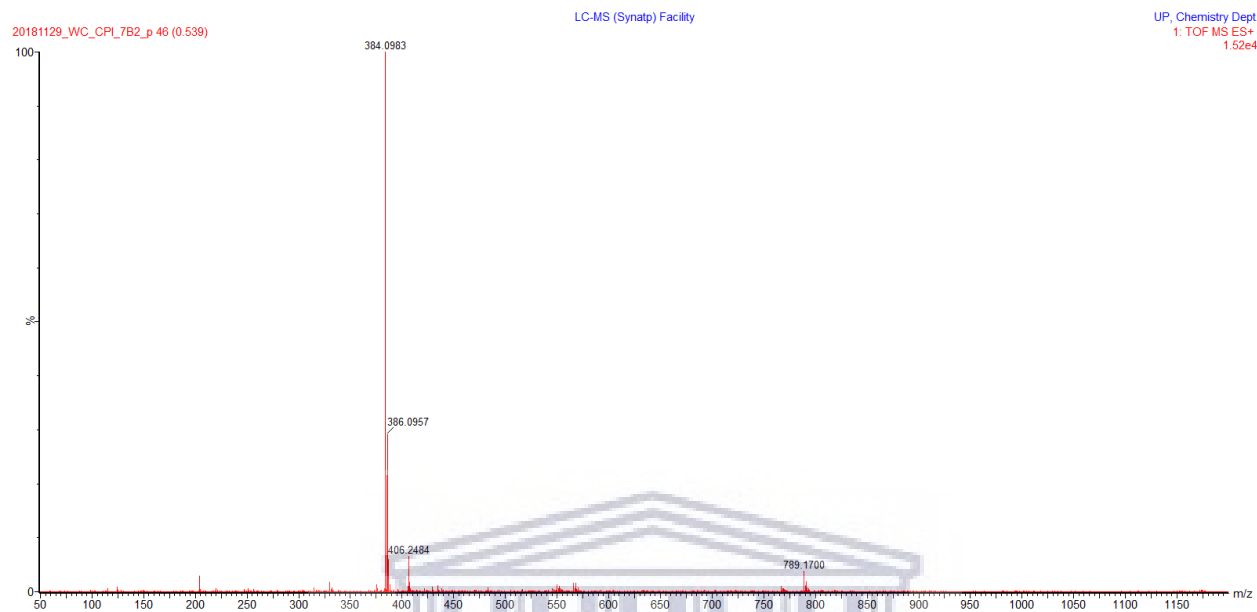


Figure S4.81: IR spectrum of compound **4.32g**

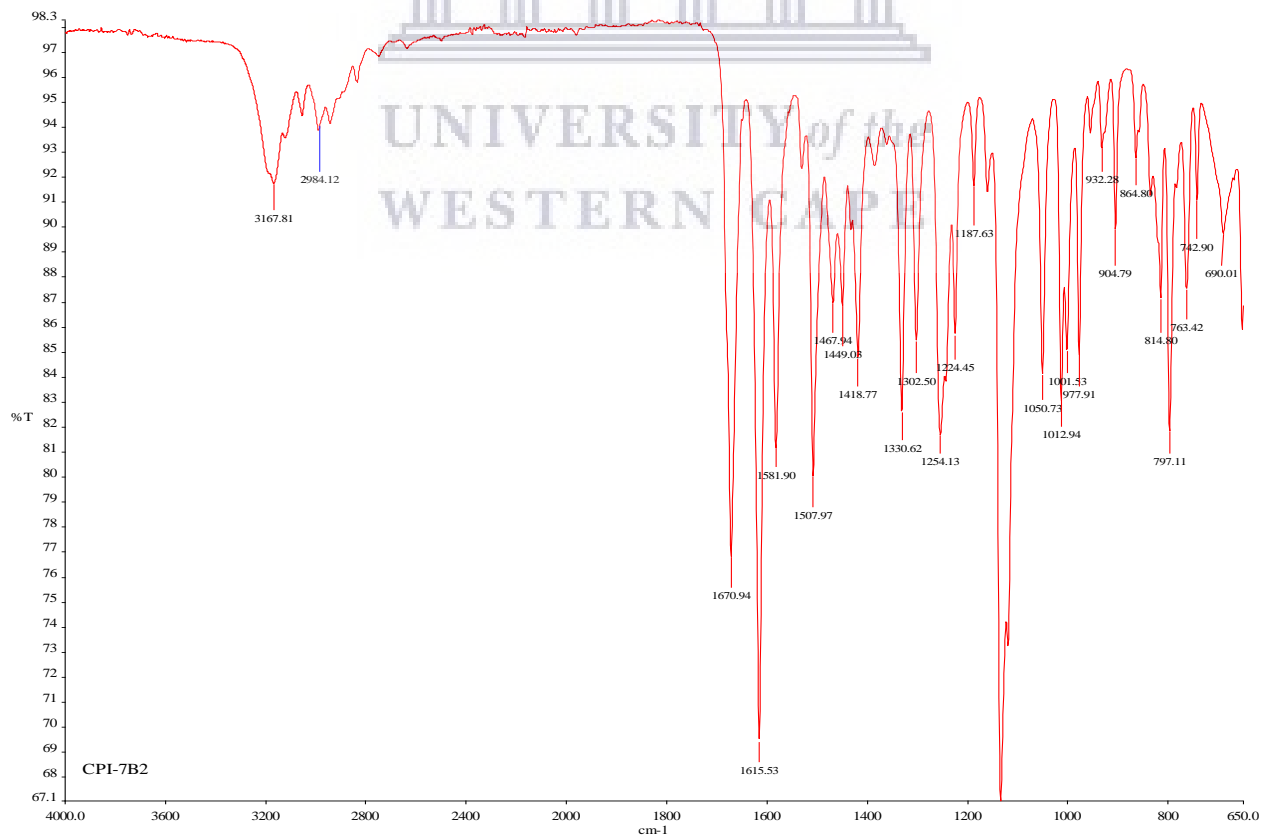


Figure S4.82: ^1H NMR spectrum of compound **4.32h** (400 MHz, DMSO-d_6)

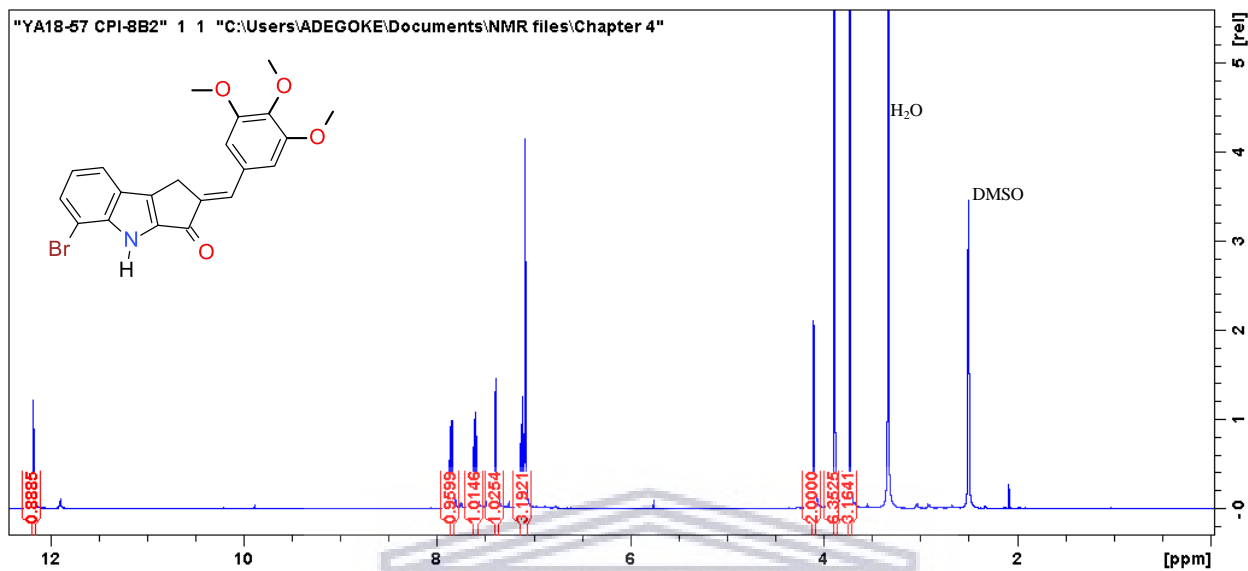


Figure S4.83: ^{13}C NMR spectrum of compound **4.32h** (100 MHz, DMSO-d_6)

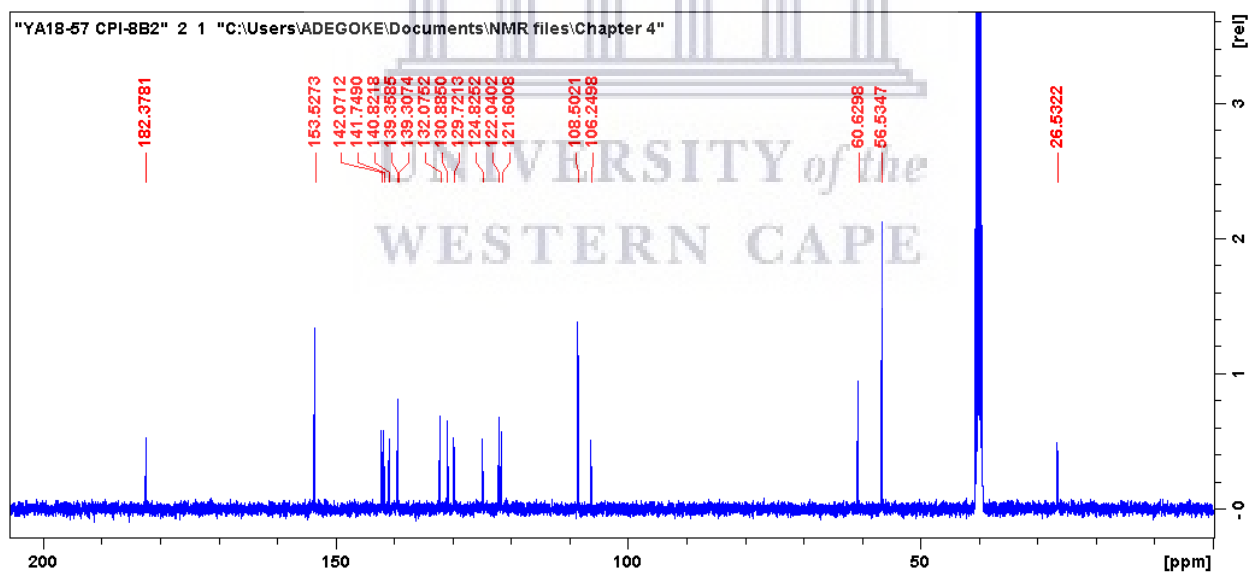


Figure S4.84: HRMS spectrum of compound **4.32h**

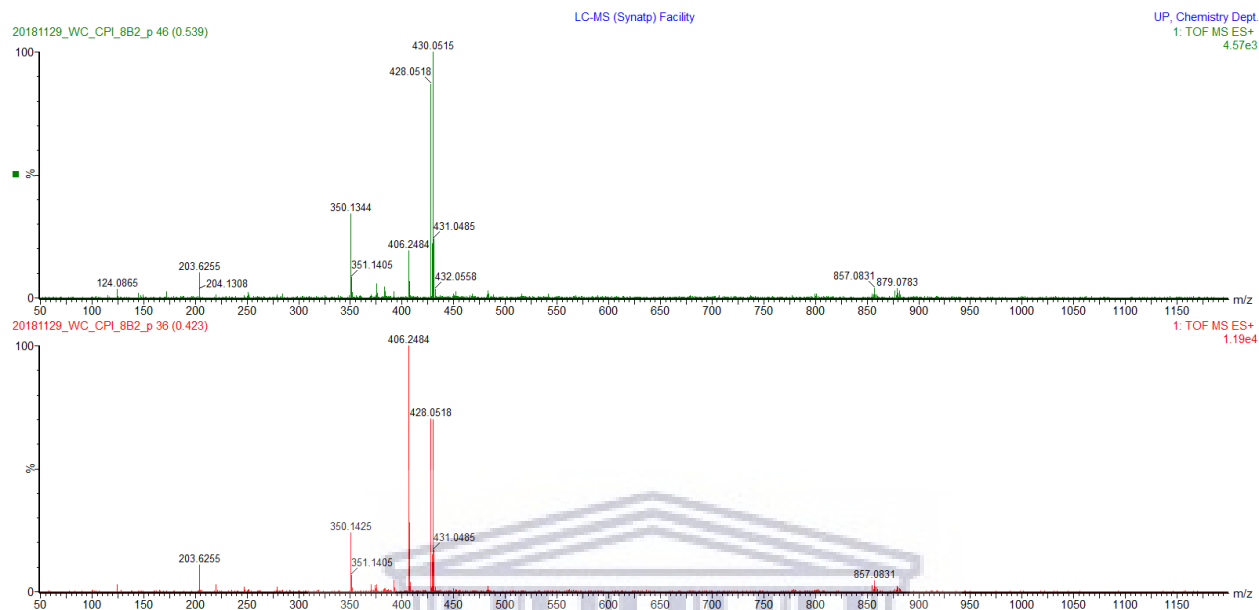


Figure S4.85: IR spectrum of compound **4.32h**

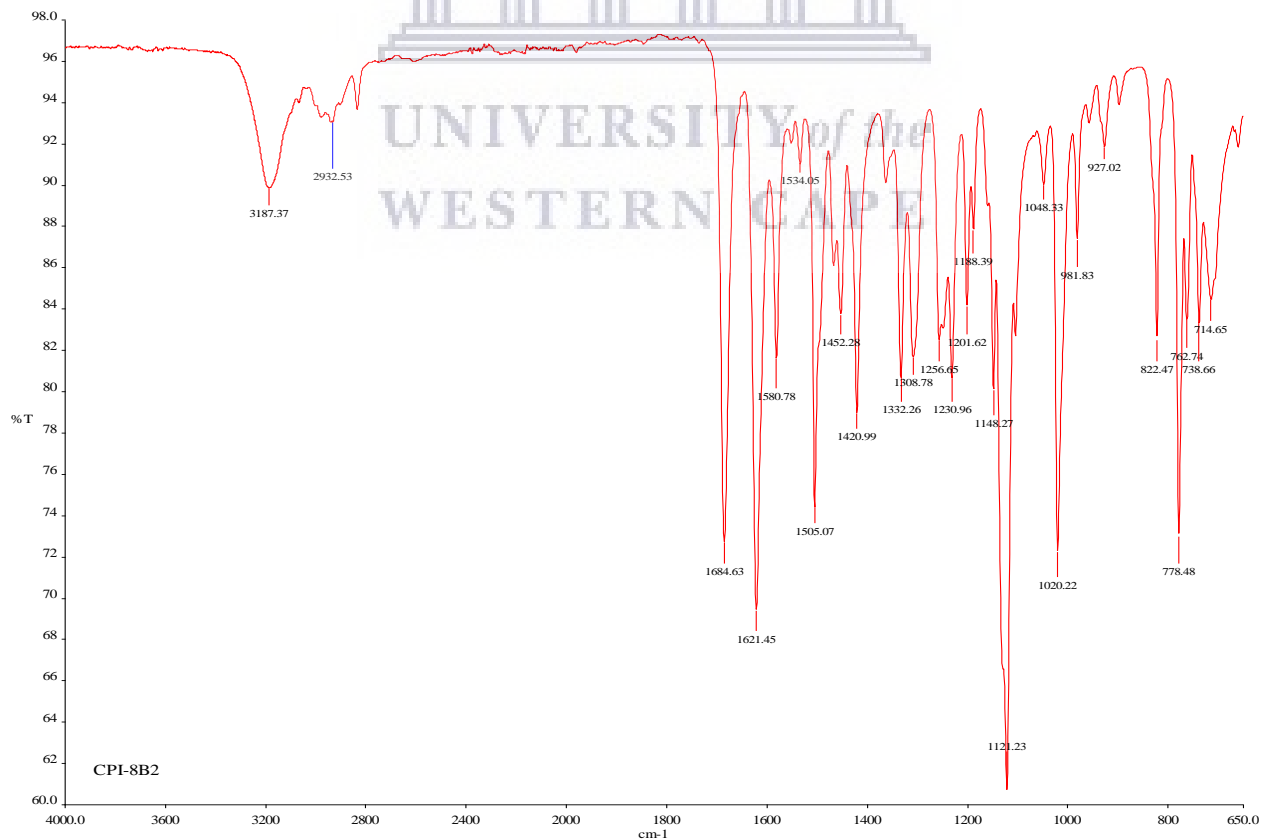


Figure S4.86: ^1H NMR spectrum of compound **4.32i** (400 MHz, DMSO-d_6)

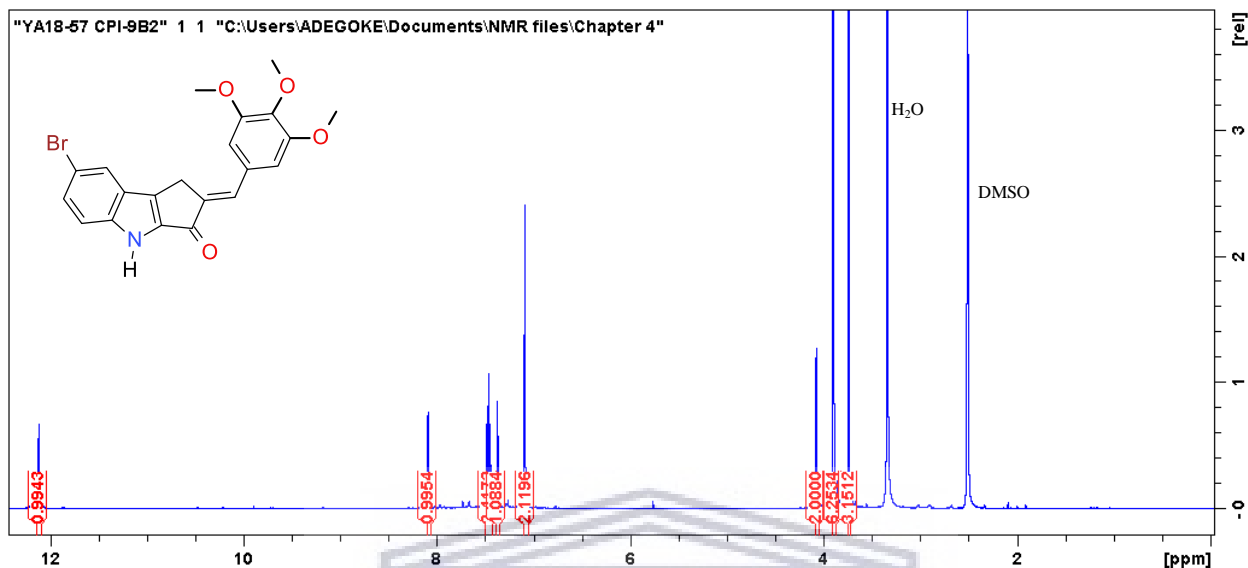


Figure S4.87: ^{13}C NMR spectrum of compound **4.32i** (100 MHz, DMSO-d_6)

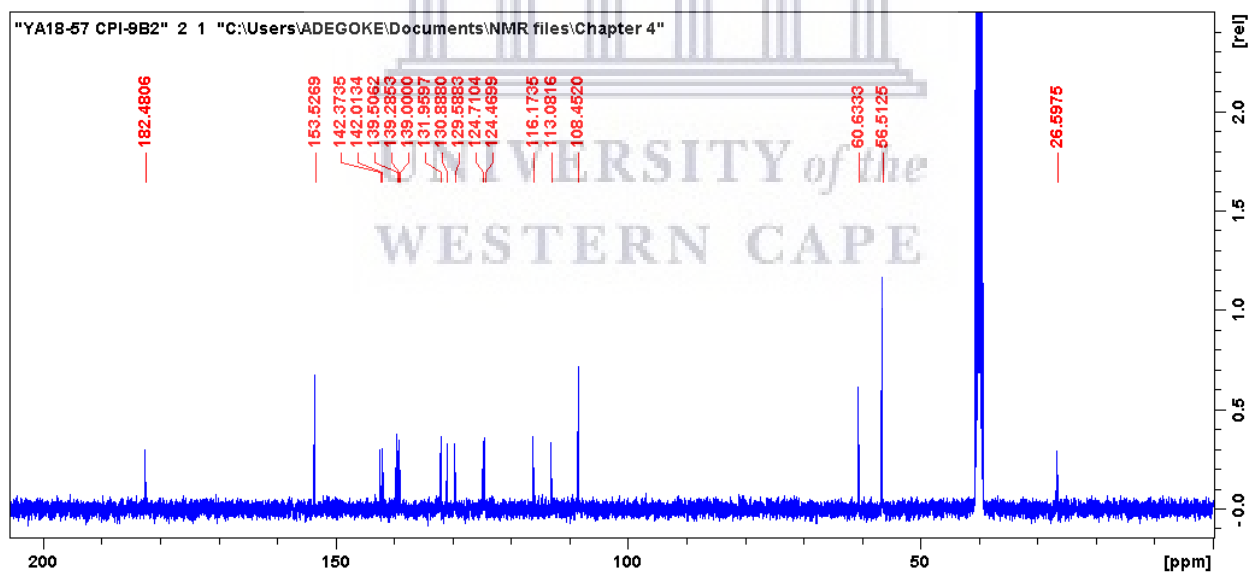


Figure S4.88: HRMS spectrum of compound **4.32i**

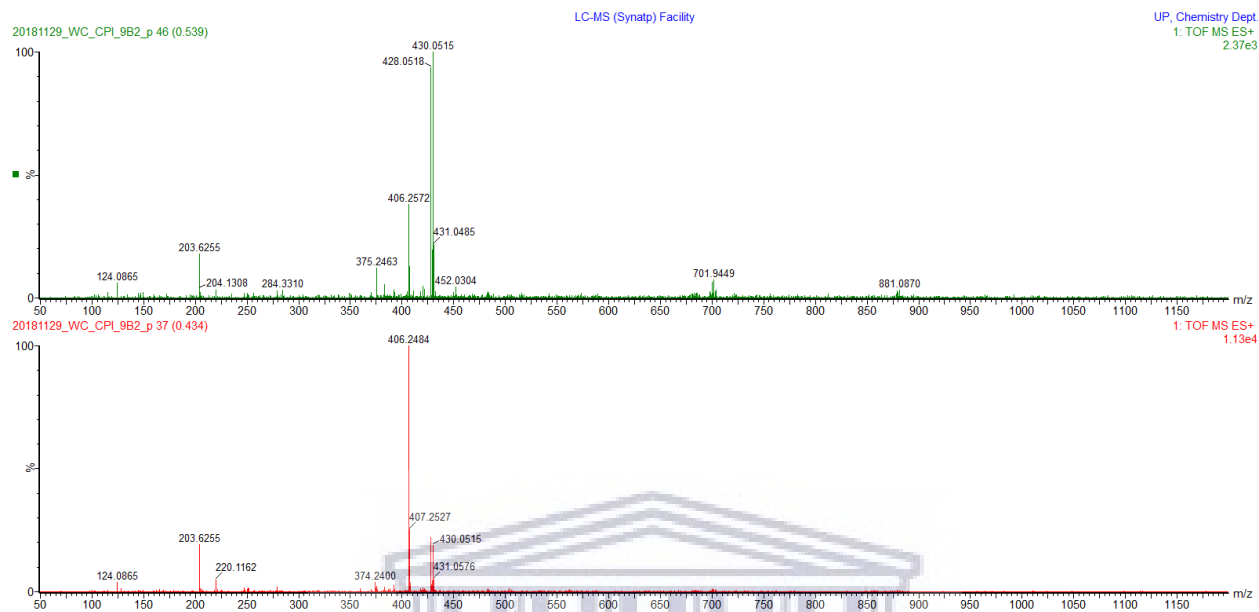


Figure S4.89: IR spectrum of compound **4.32i**

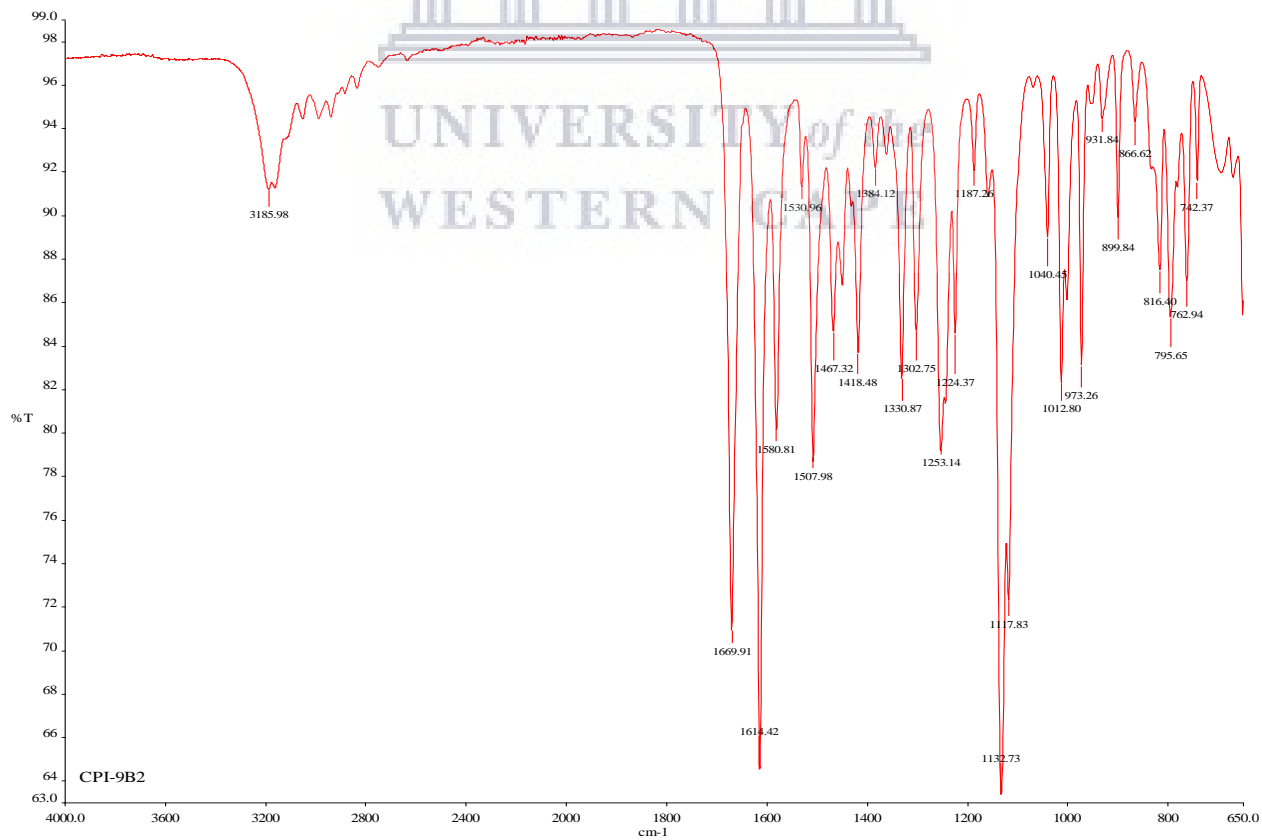


Figure S4.90: ^1H NMR spectrum of compound **4.32j** (400 MHz, DMSO-d_6)

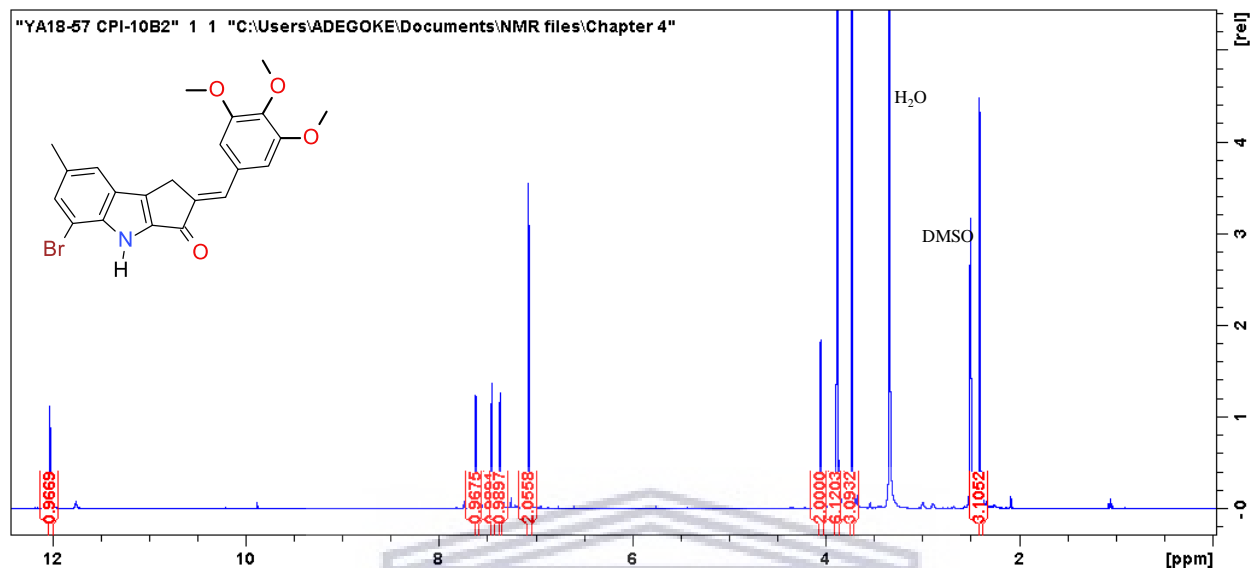


Figure S4.91: ^{13}C NMR spectrum of compound **4.32j** (100 MHz, DMSO-d_6)

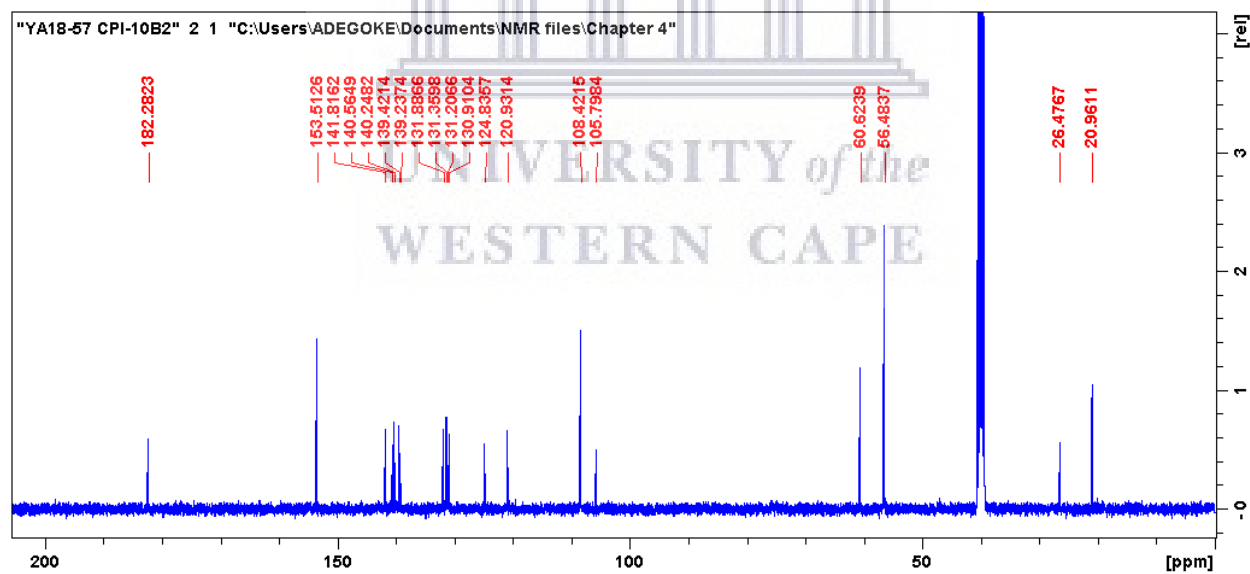


Figure S4.92: HRMS spectrum of compound **4.32j**

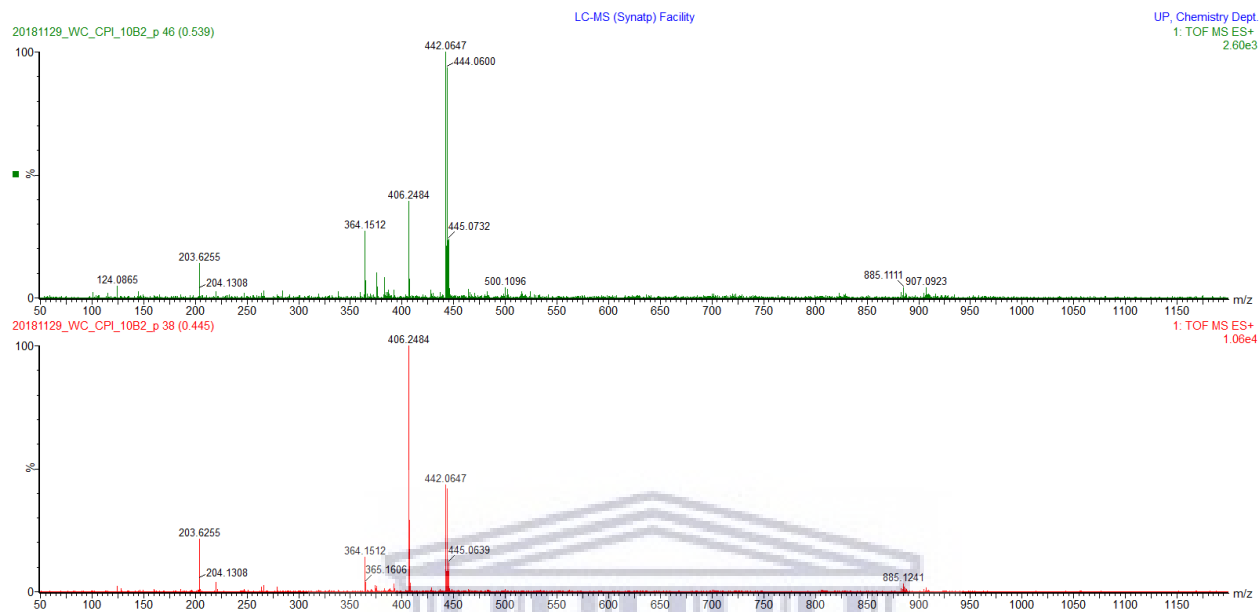


Figure S4.93: IR spectrum of compound **4.32j**

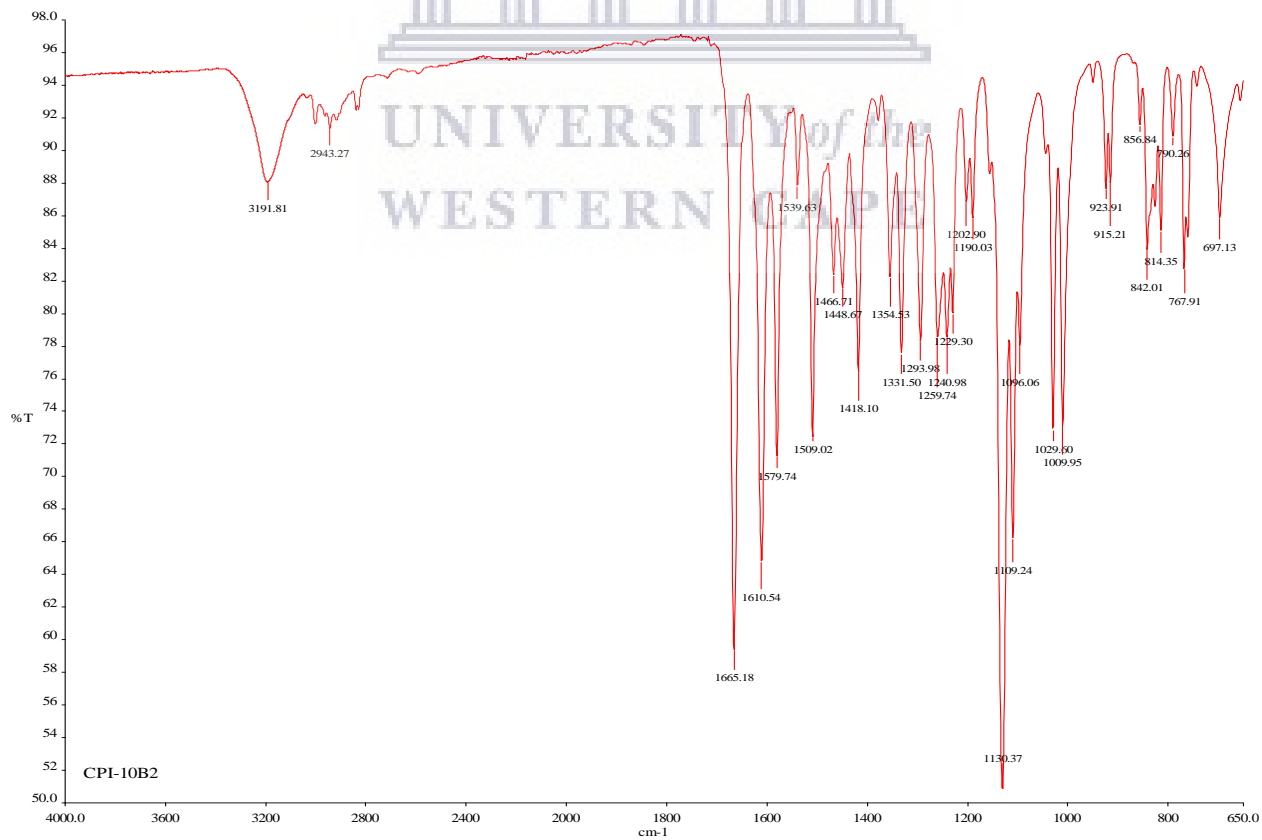


Figure S4.94: ^1H NMR spectrum of compound **4.32k** (400 MHz, DMSO-d_6)

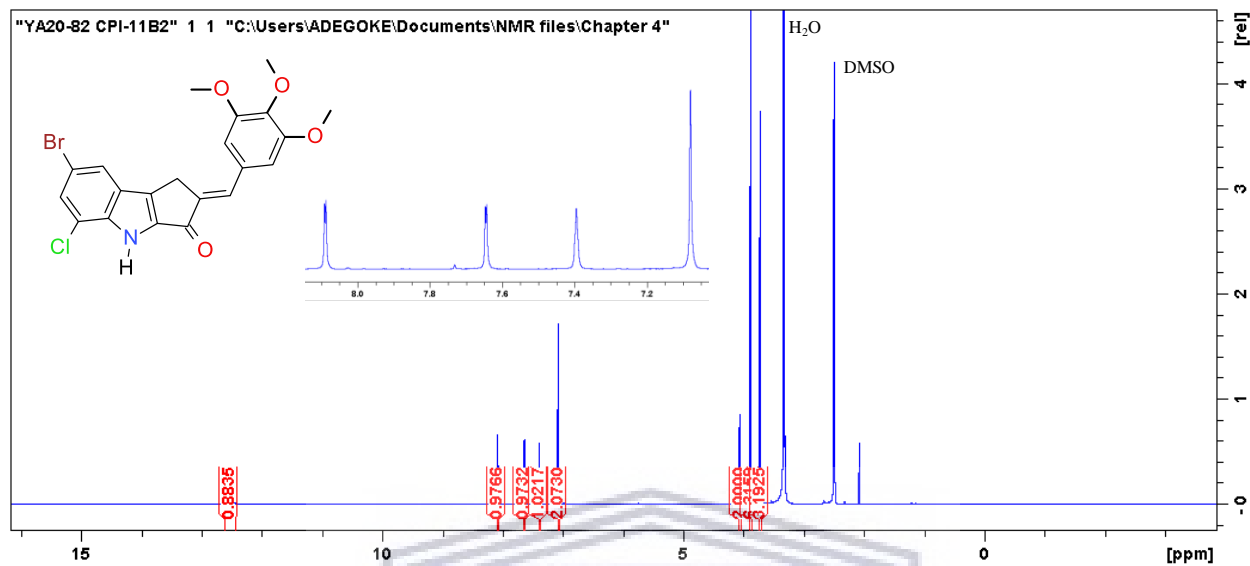


Figure S4.95: HSQC NMR spectrum of compound **4.32k**

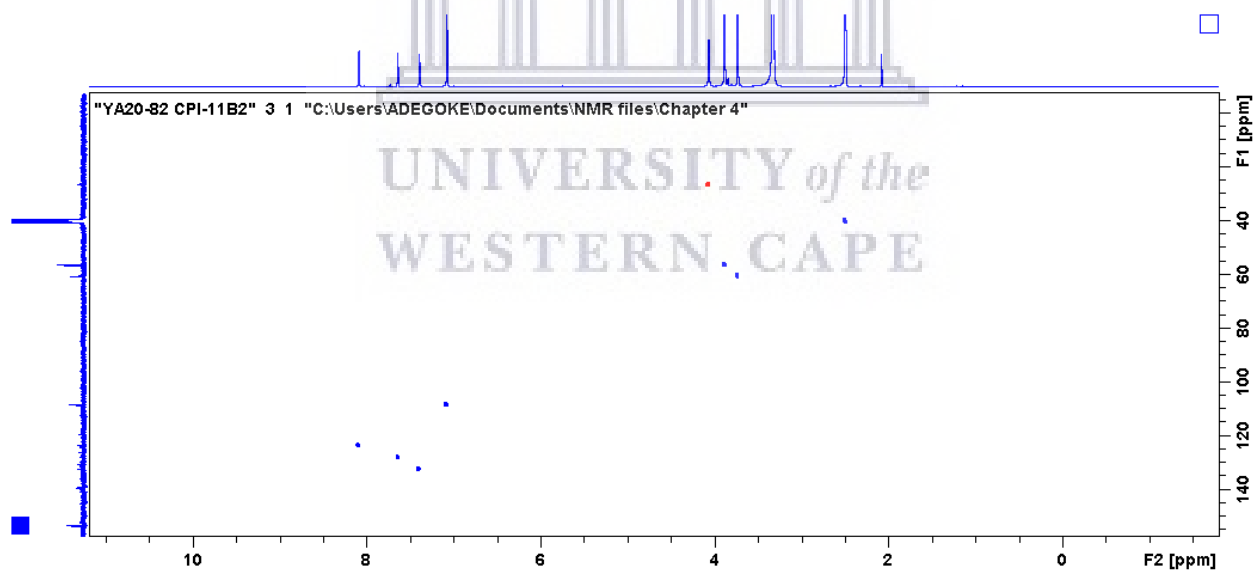


Figure S4.96: HMBC NMR spectrum of compound 4.32k

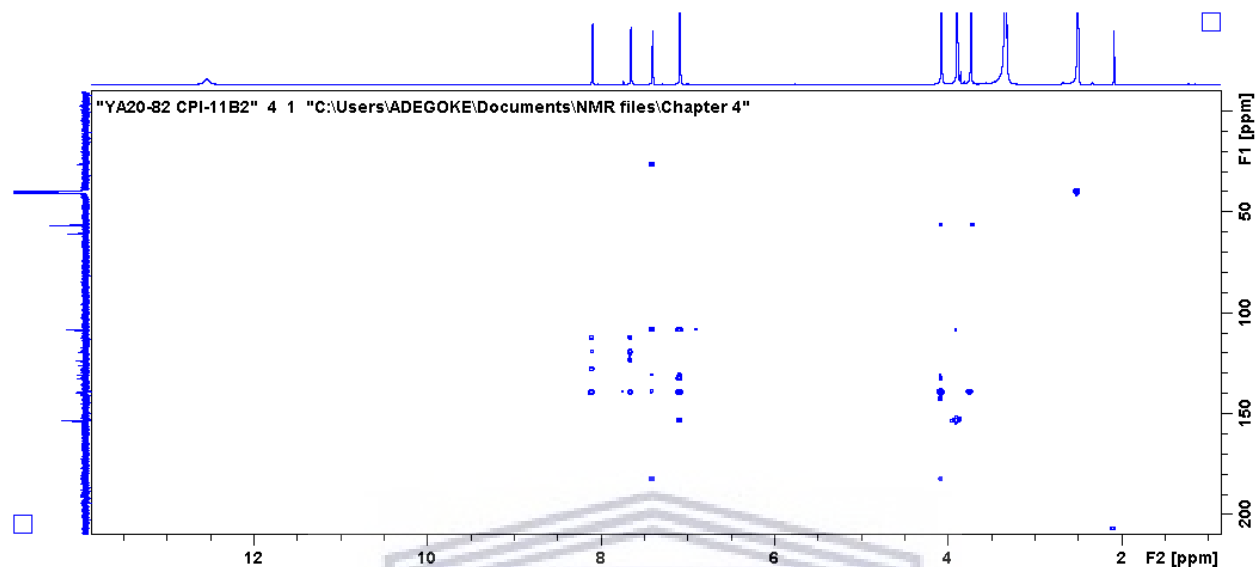


Figure S4.97: HRMS spectrum of compound 4.32k

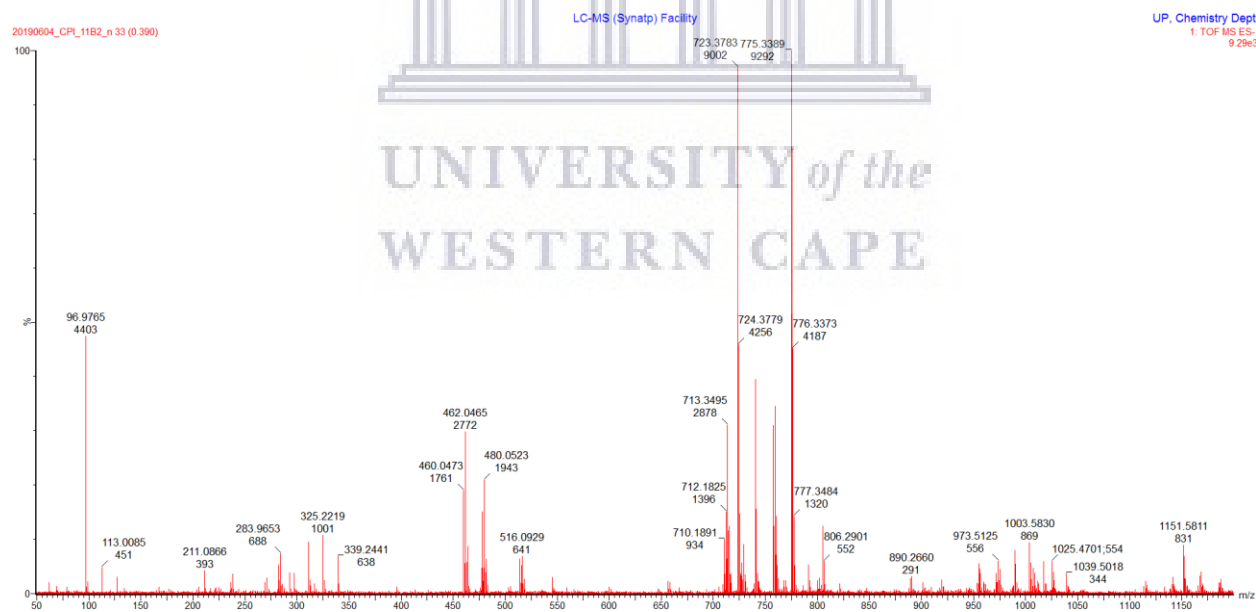
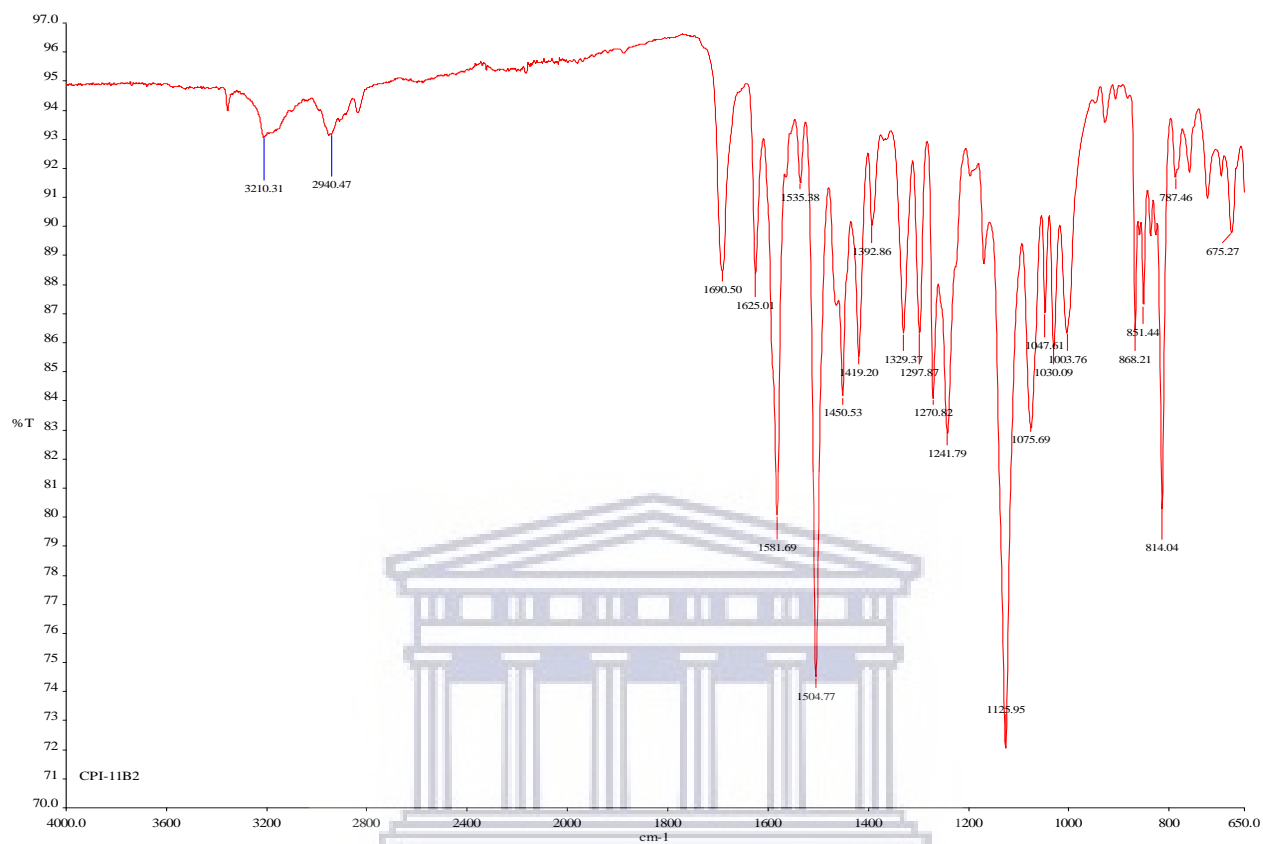


Figure S4.98: IR spectrum of compound **4.32k**



UNIVERSITY of the
WESTERN CAPE

Figure S4.99: ^1H NMR spectrum of compound **4.321** (400 MHz, DMSO- d_6)

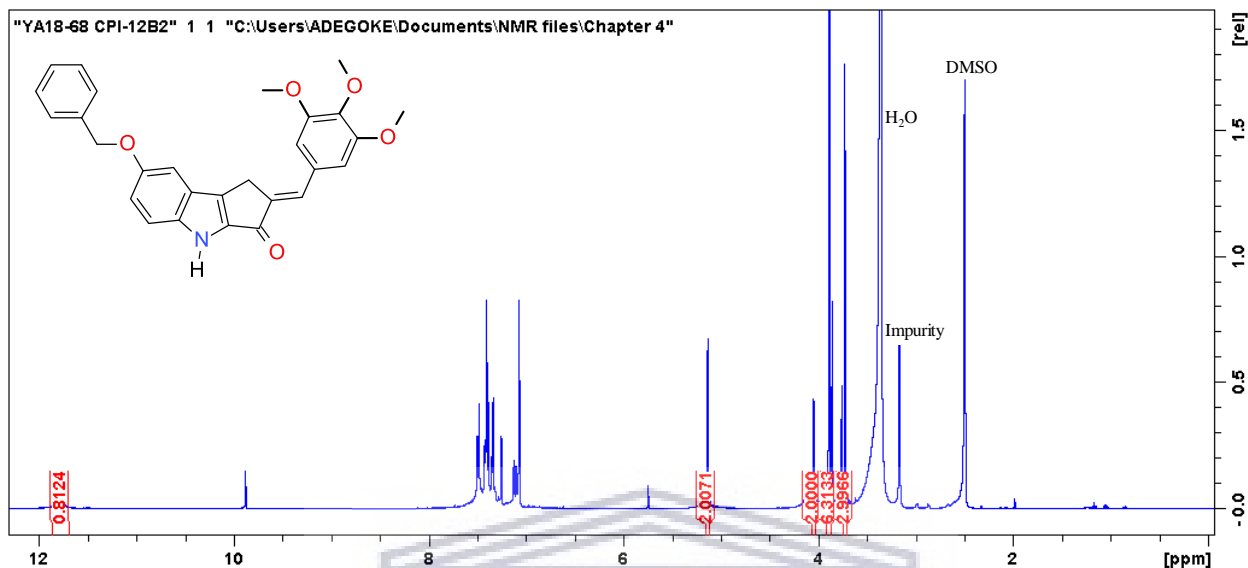


Figure S4.100: ^{13}C NMR spectrum of compound **4.321** (100 MHz, DMSO- d_6)

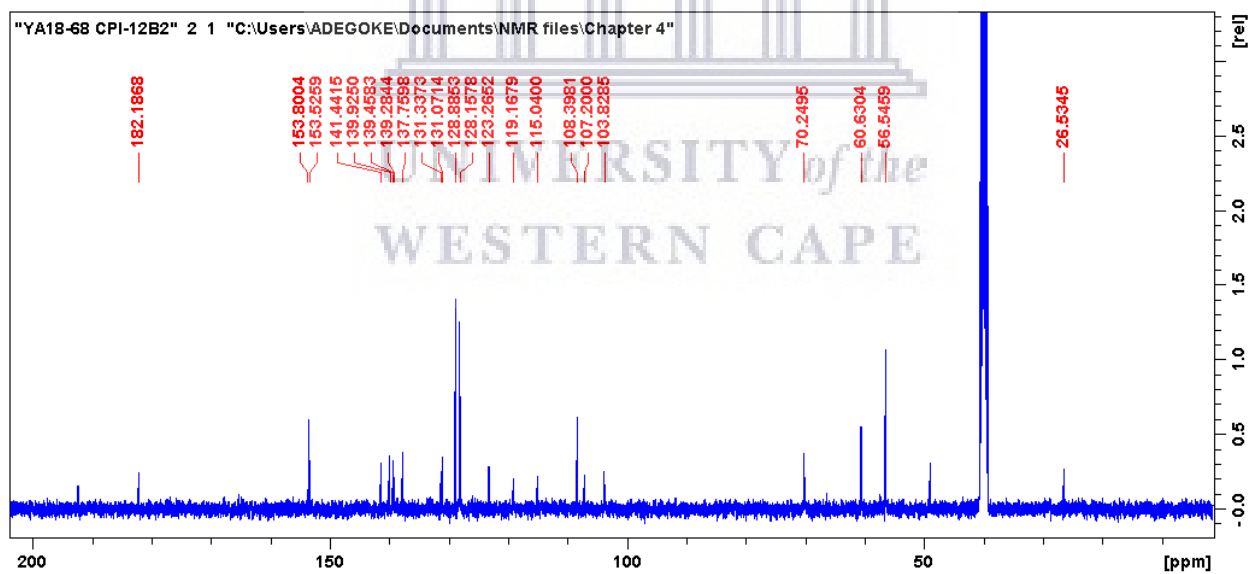


Figure S4.101: HRMS spectrum of compound 4.321

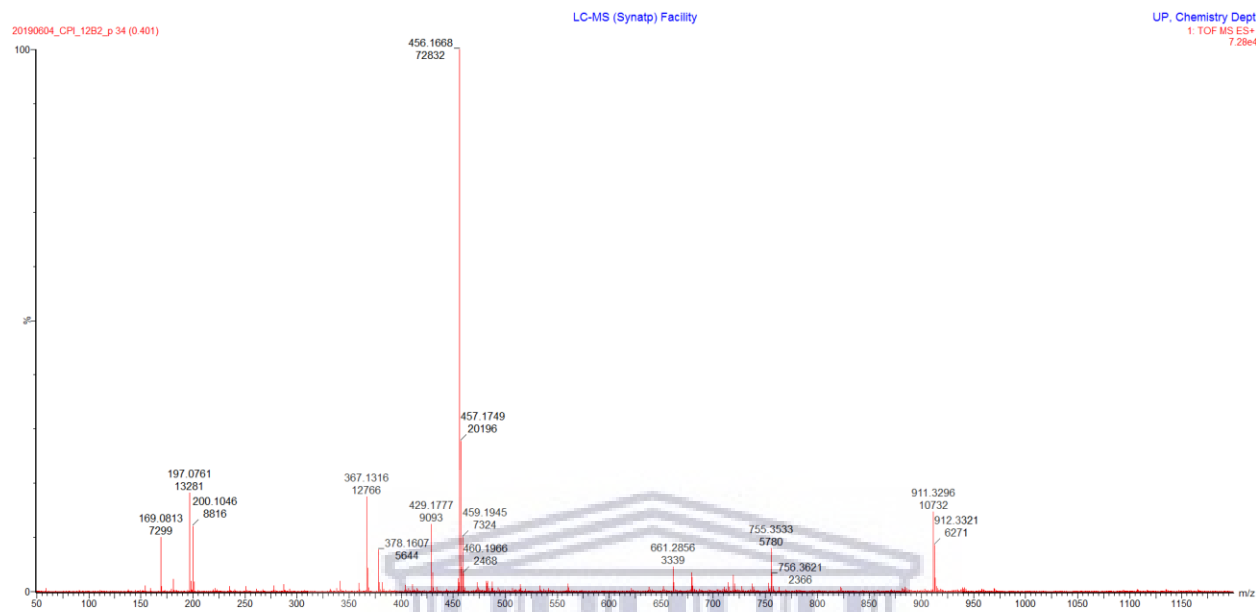
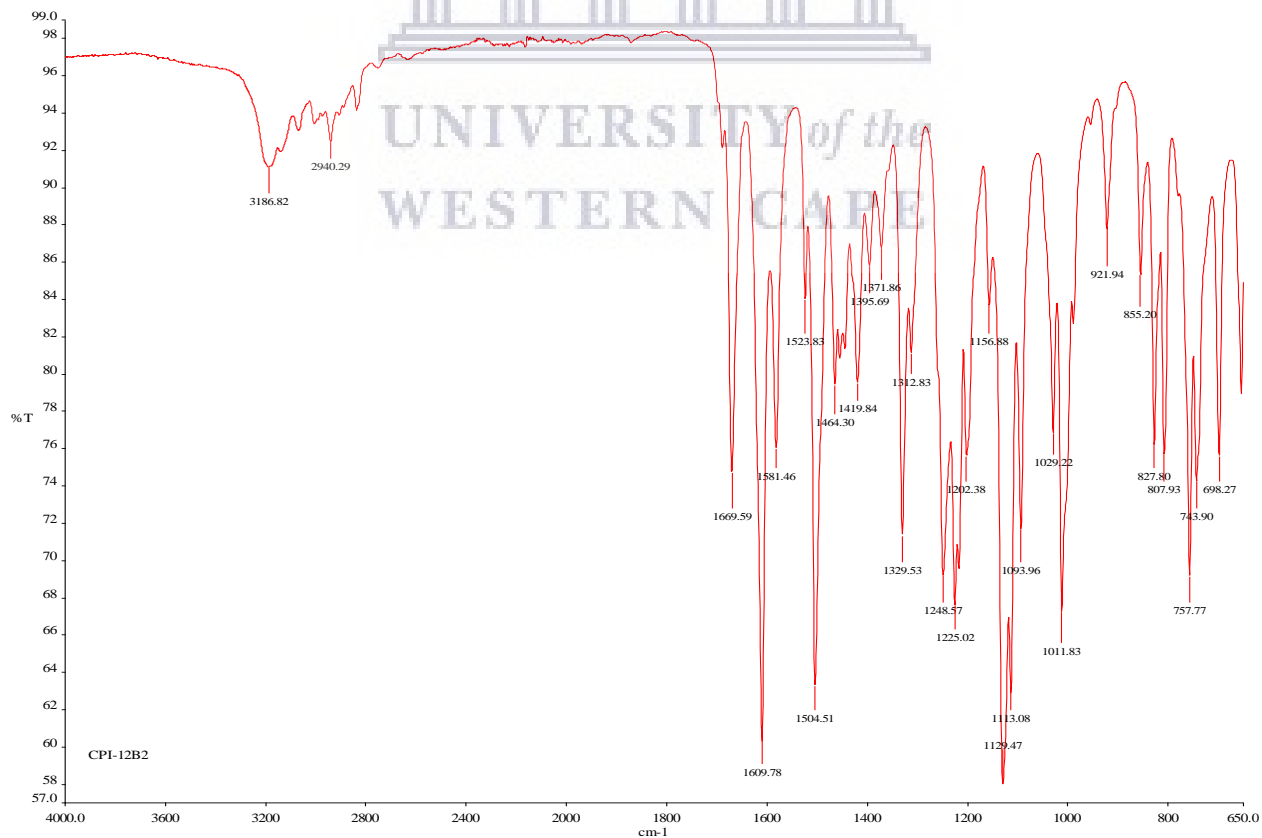


Figure S4.102: IR spectrum of compound 4.321



Pyridyl substituted cyclopenta[b]indol-3-one series 4.33(a-l)

Figure S4.103: ^1H NMR spectrum of compound 4.33a (400 MHz, DMSO-d_6)

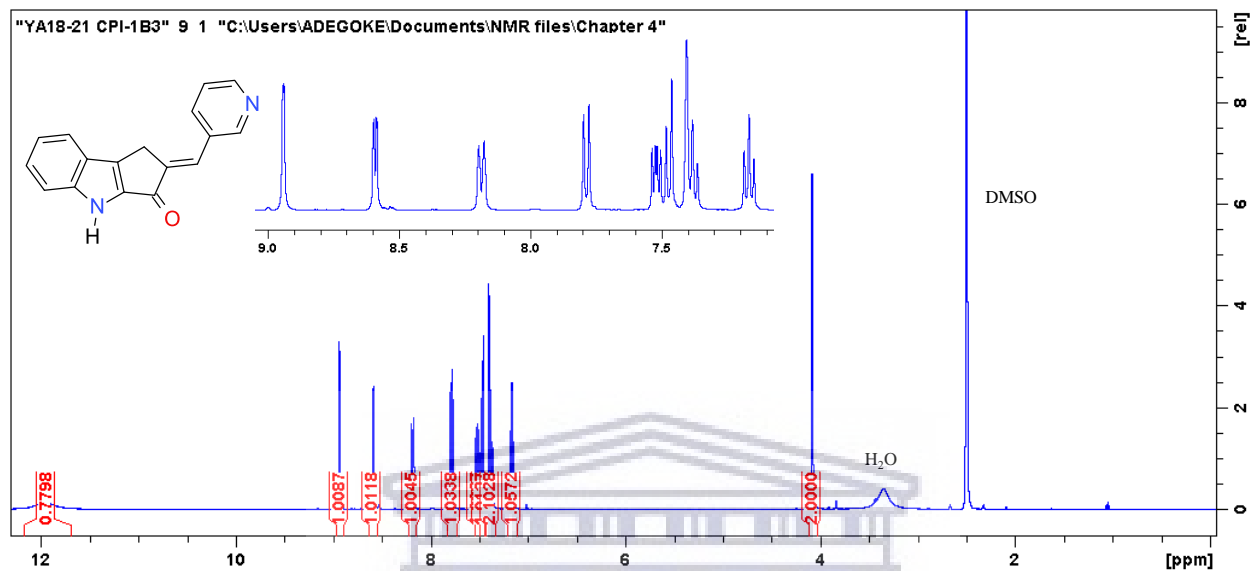


Figure S4.104: ^{13}C NMR spectrum of compound 4.33a (100 MHz, DMSO-d_6)

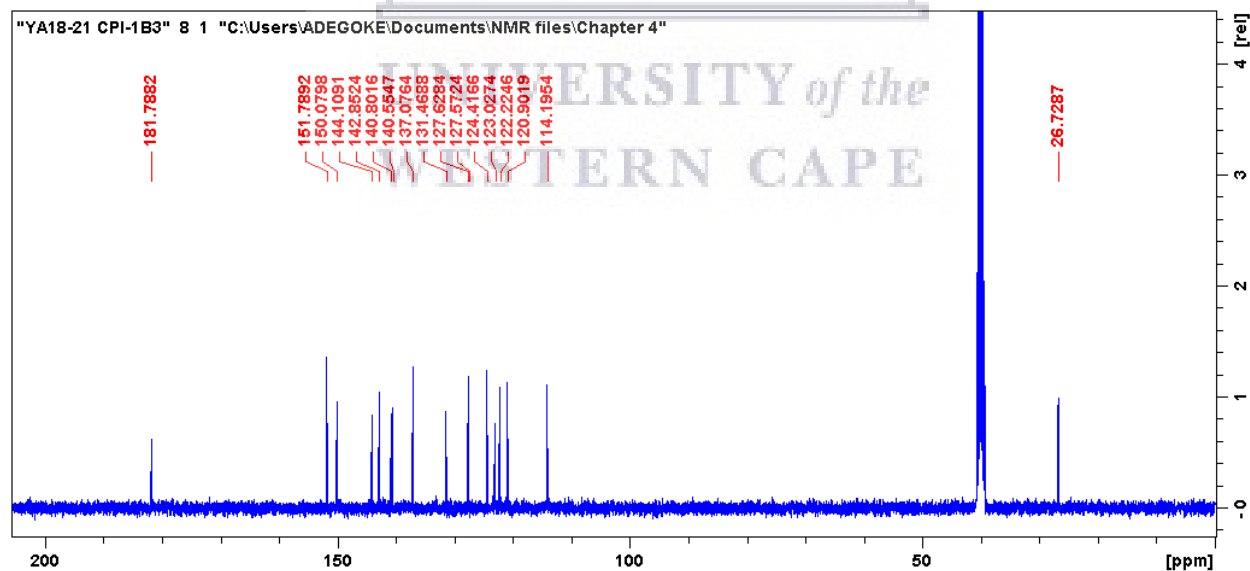


Figure S4.105: HRMS spectrum of compound 4.33a

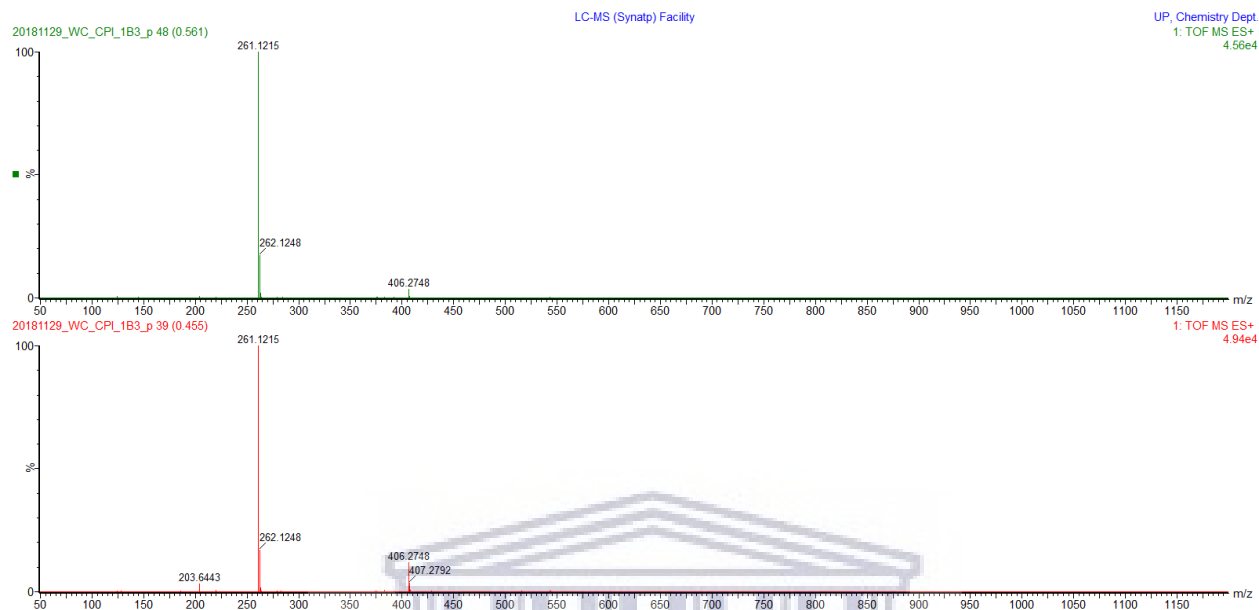


Figure S4.106: IR spectrum of compound 4.33a

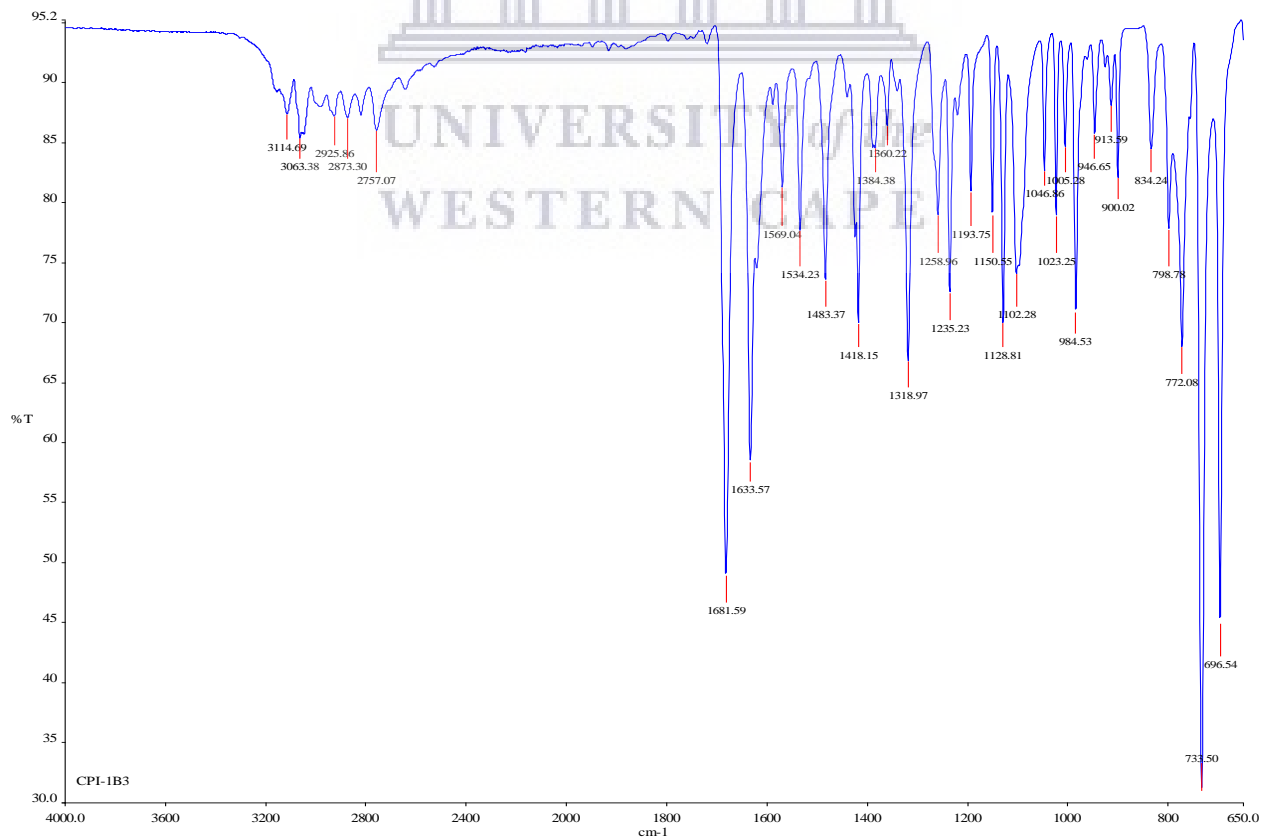


Figure S4.107: ^1H NMR spectrum of compound **4.33b** (400 MHz, DMSO-d_6)

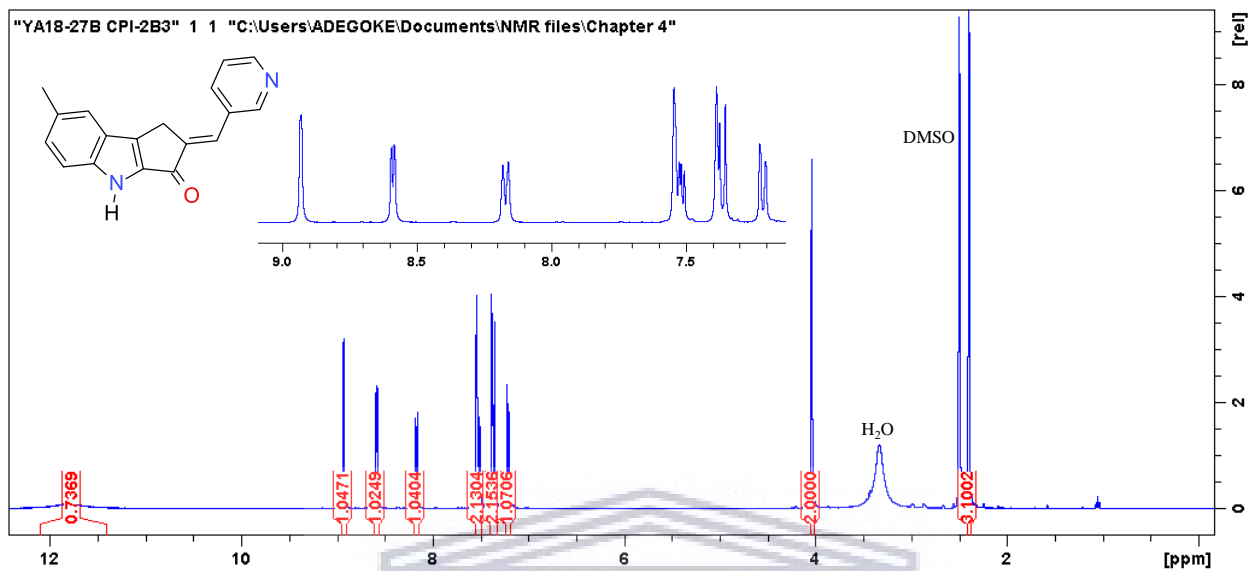


Figure S4.108: ^{13}C NMR spectrum of compound **4.33b** (100 MHz, DMSO-d_6)

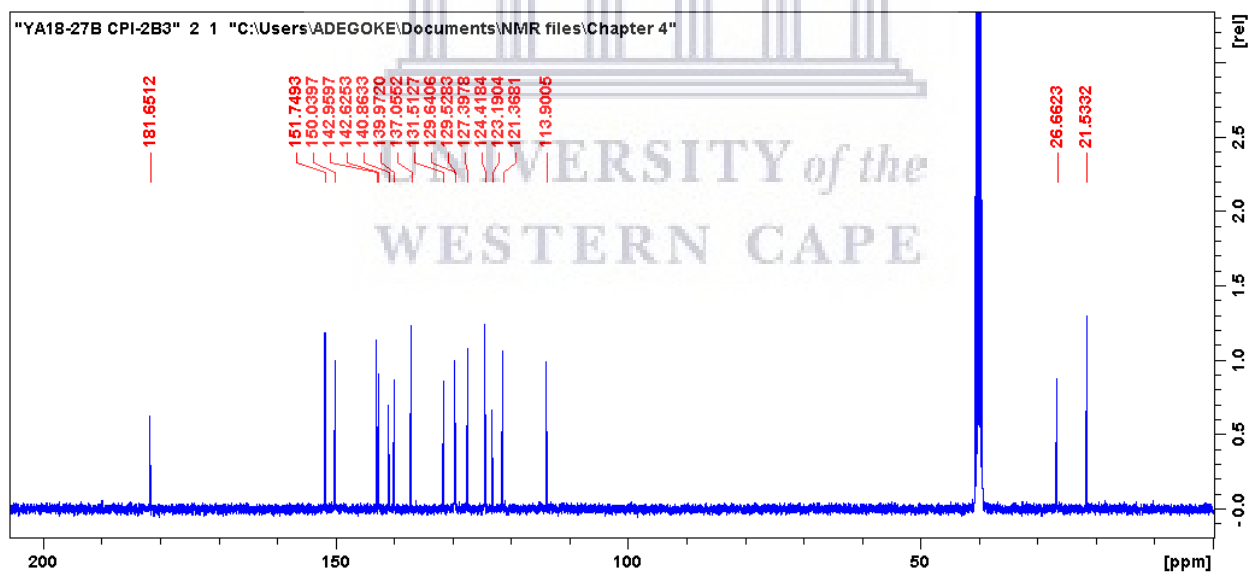


Figure S4.109: HRMS spectrum of compound **4.33b**

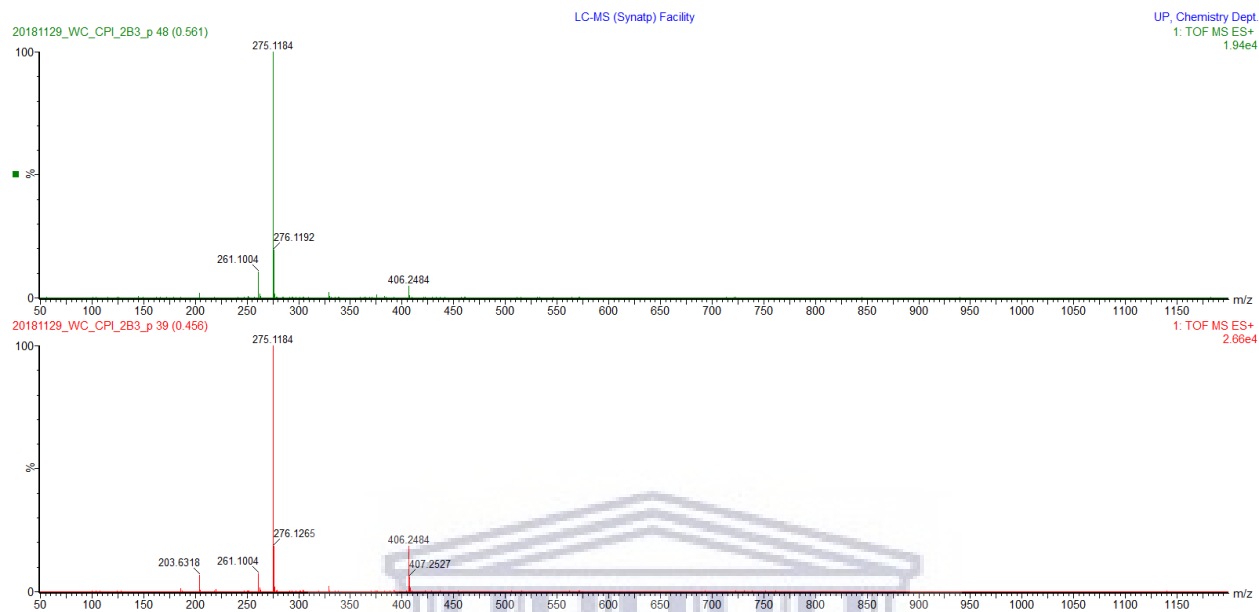


Figure S4.110: IR spectrum of compound **4.33b**

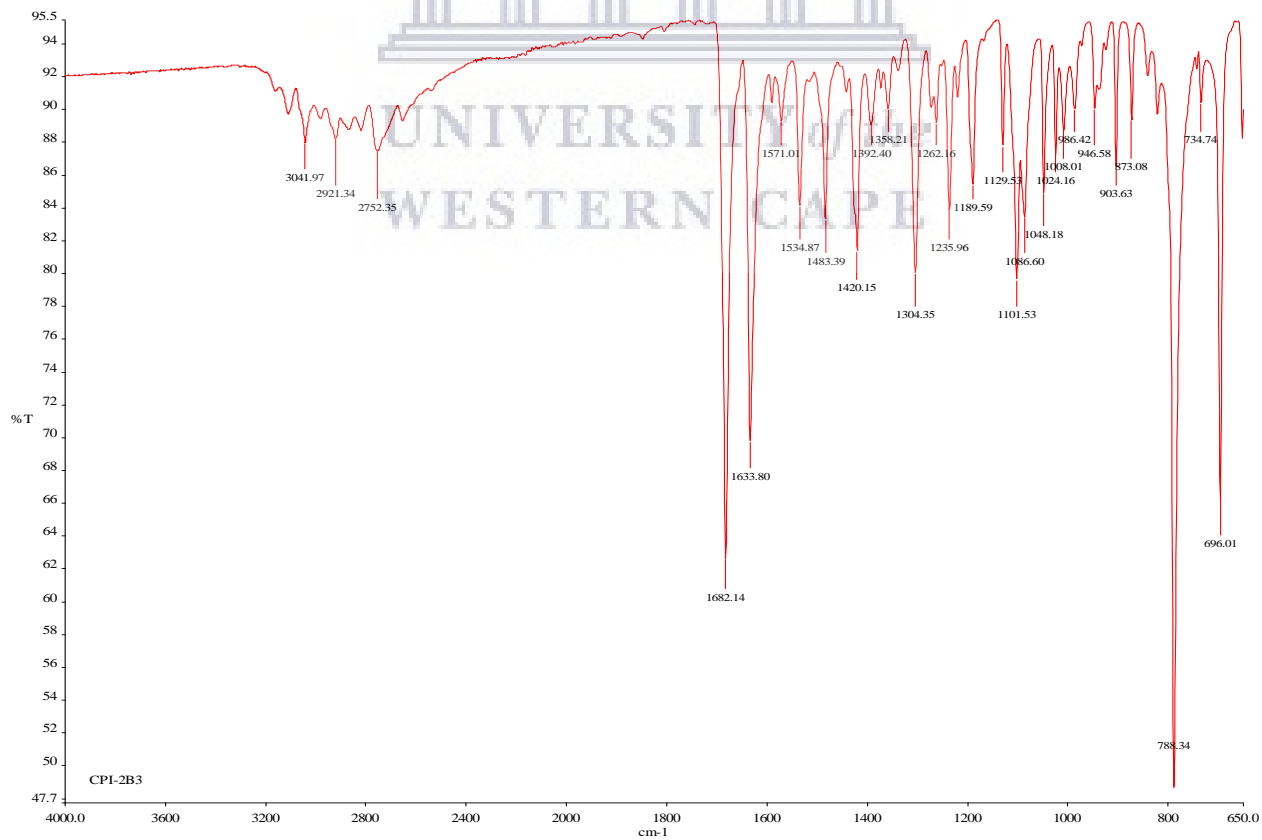


Figure S4.111: ^1H NMR spectrum of compound **4.33c** (400 MHz, DMSO-d_6)

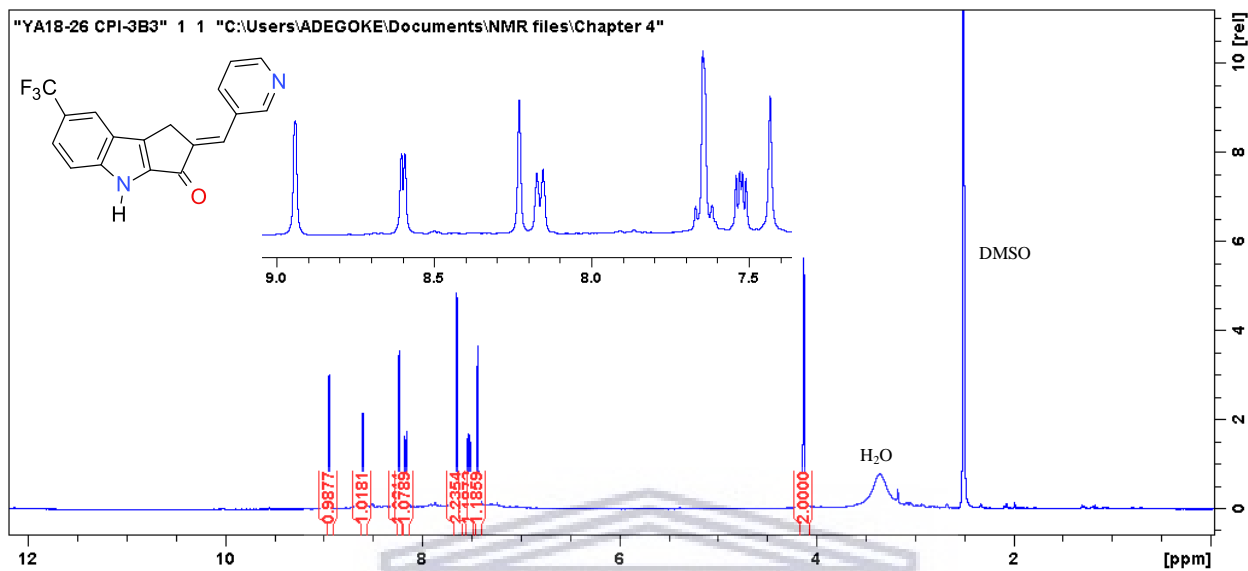


Figure S4.112: ^{13}C NMR spectrum of compound **4.33c** (100 MHz, DMSO-d_6)

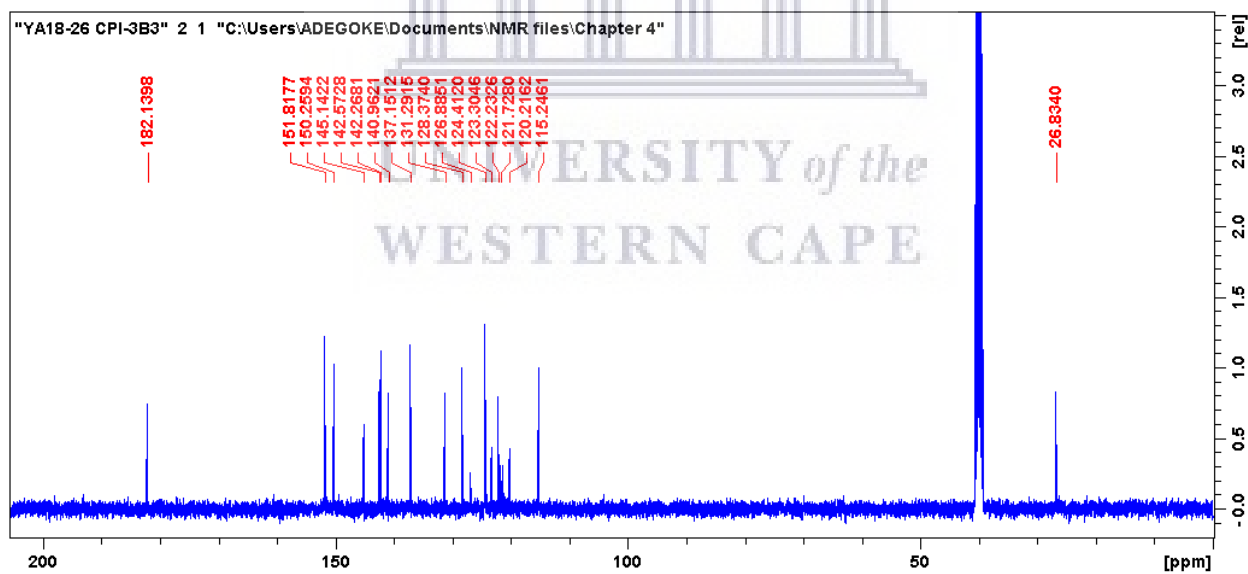


Figure S4.113: HRMS spectrum of compound 4.33c

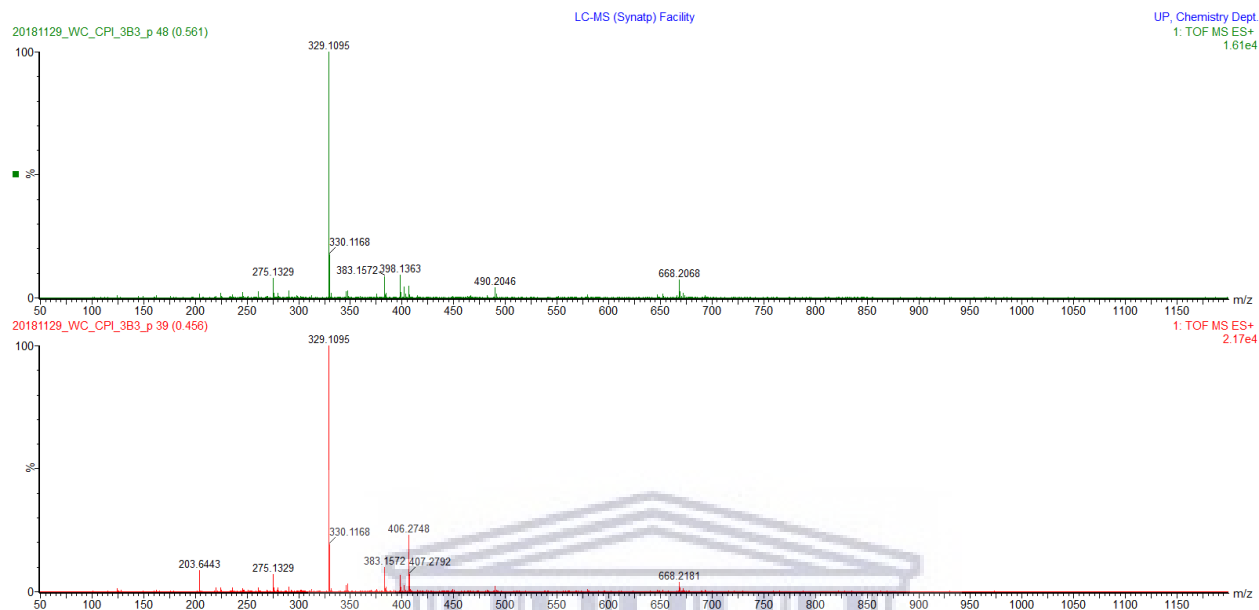


Figure S4.114: IR spectrum of compound 4.33c

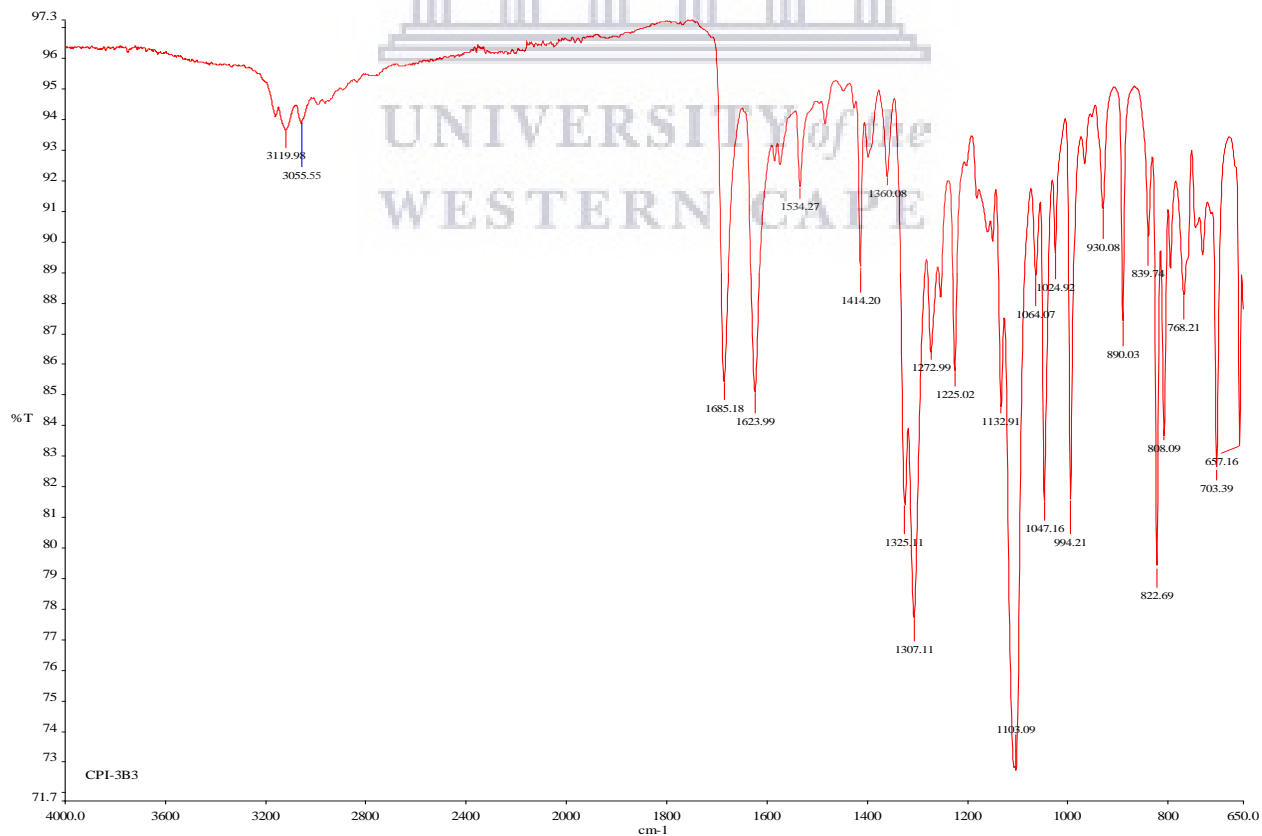


Figure S4.115: COSY NMR spectrum of compound 4.33d

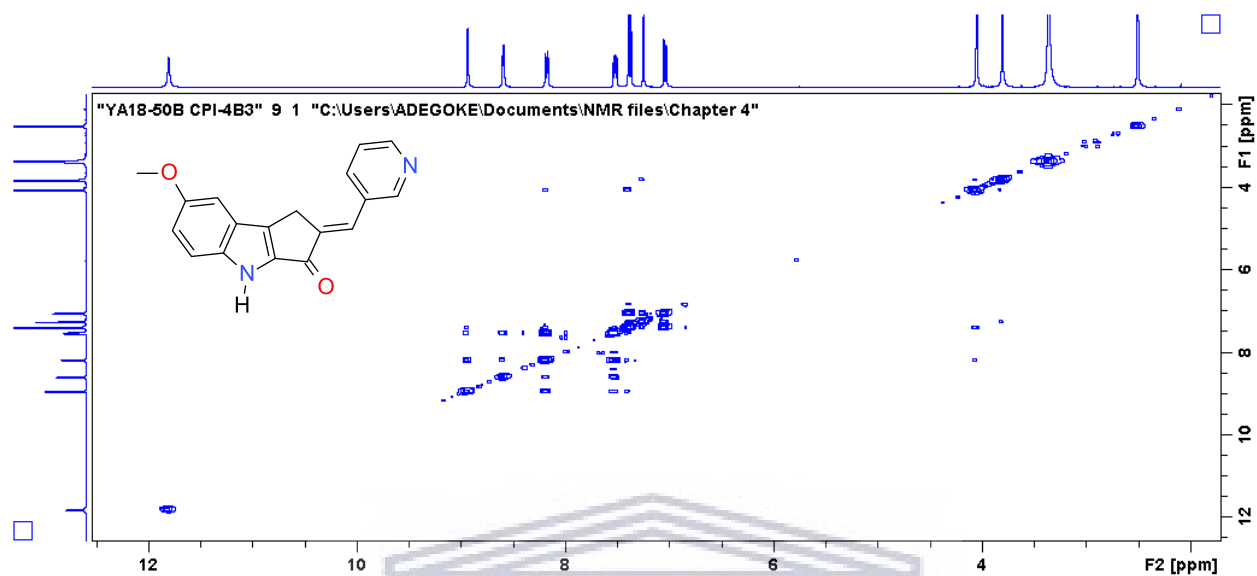


Figure S4.116: HSQC NMR spectrum of compound 4.33d

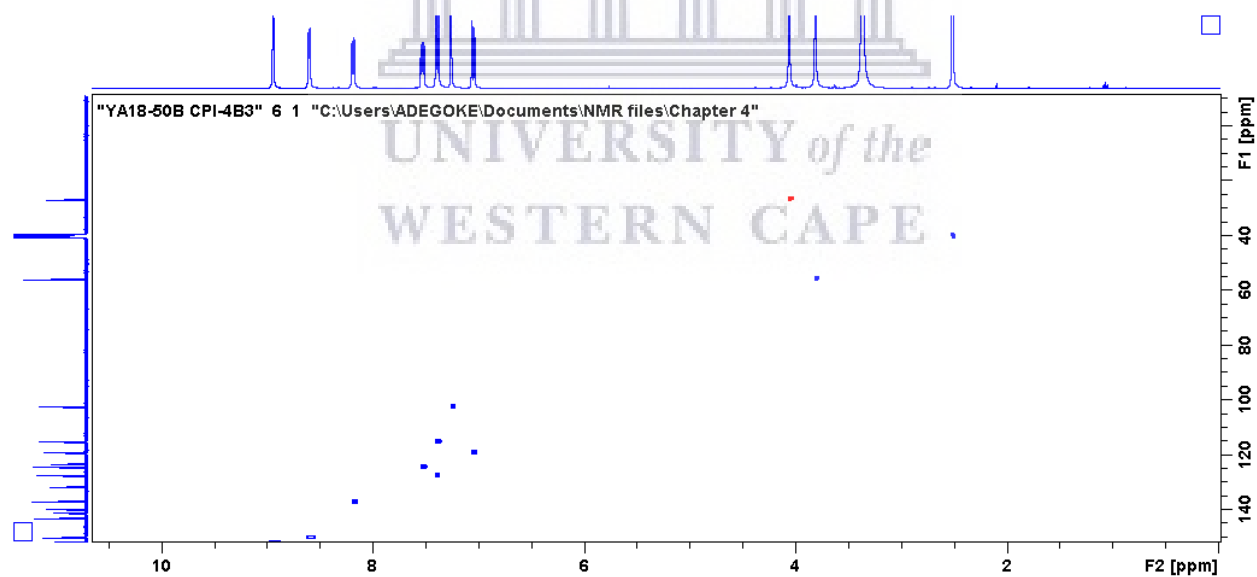


Figure S4.117: HMBC NMR spectrum of compound 4.33d

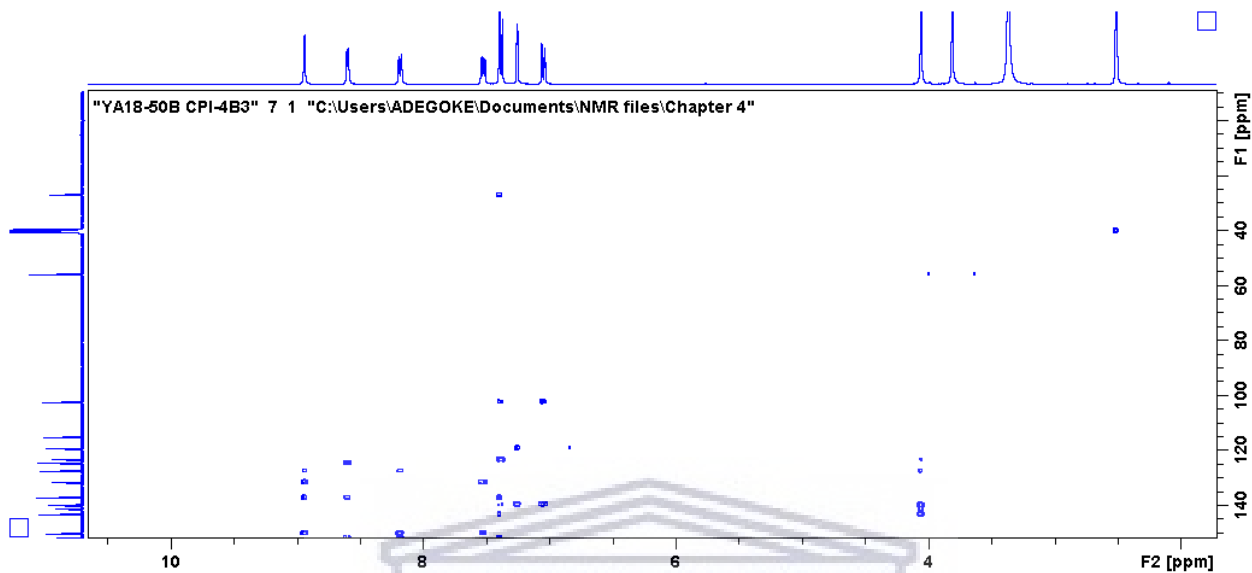


Figure S4.118: HRMS spectrum of compound 4.33d

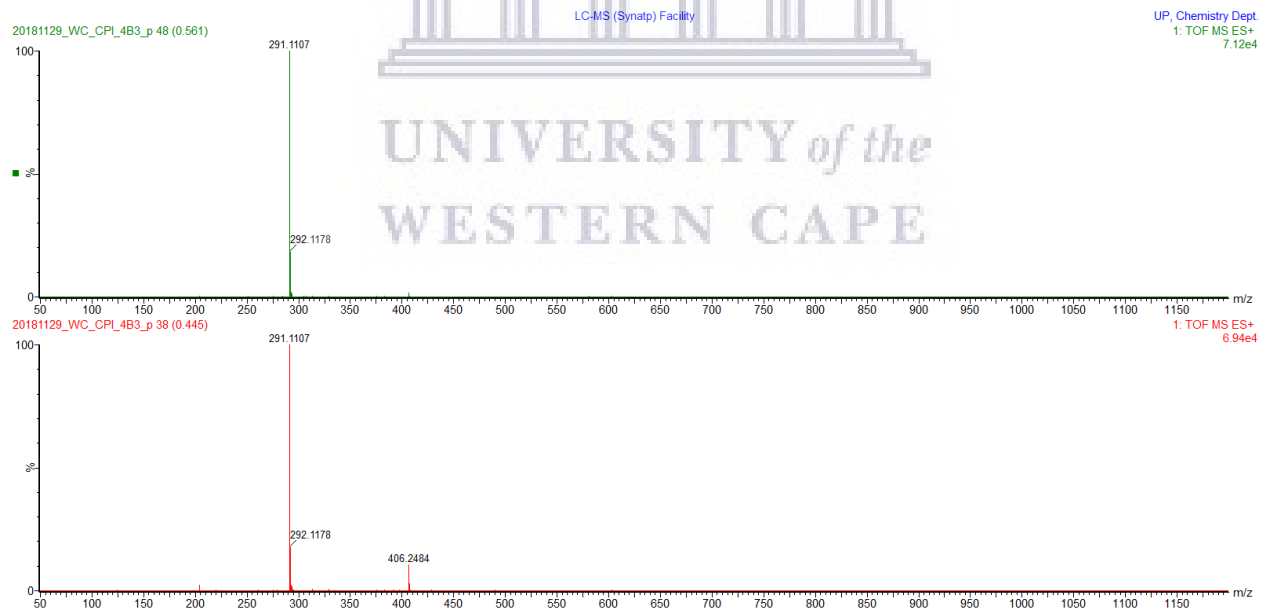
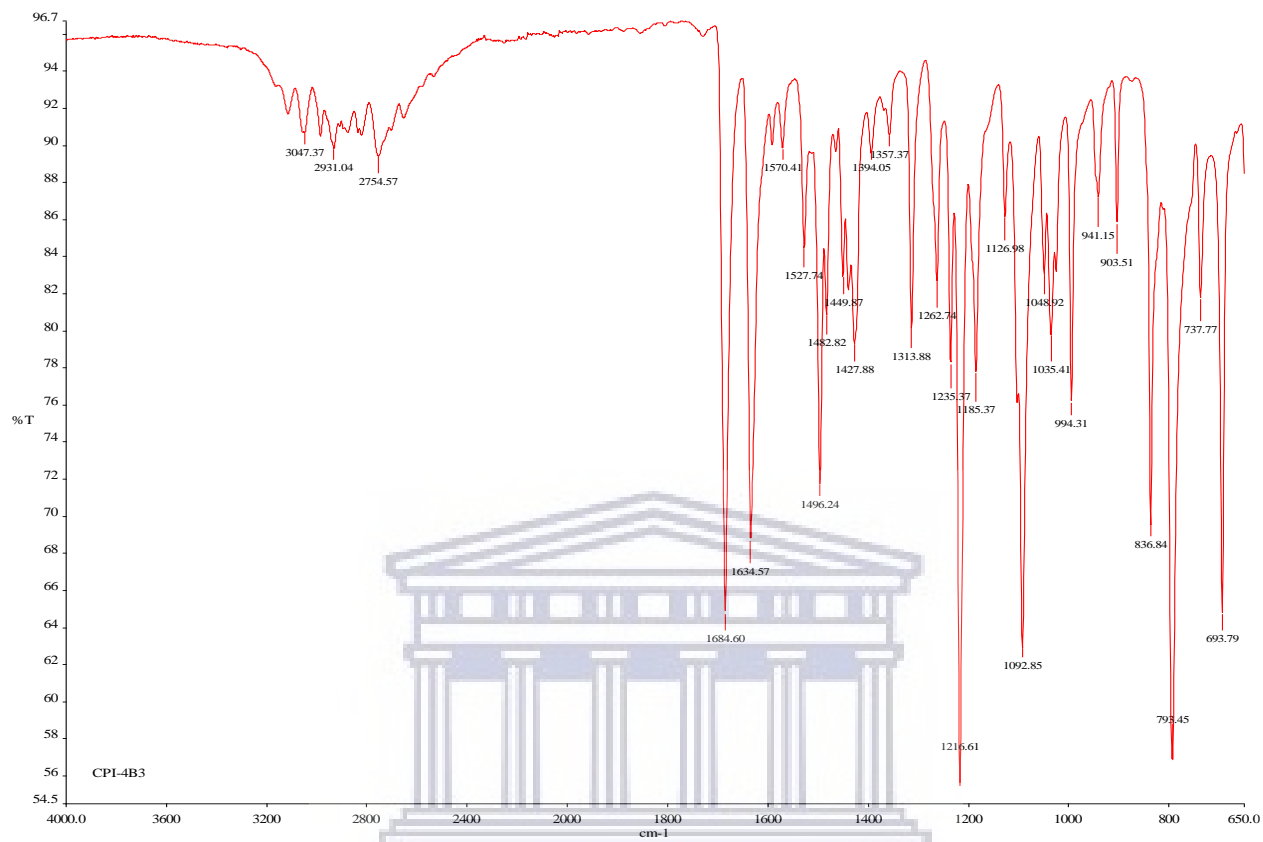


Figure S4.119: IR spectrum of compound 4.33d



UNIVERSITY of the
WESTERN CAPE

Figure S4.120: ^1H NMR spectrum of compound **4.33e** (400 MHz, DMSO-d_6)

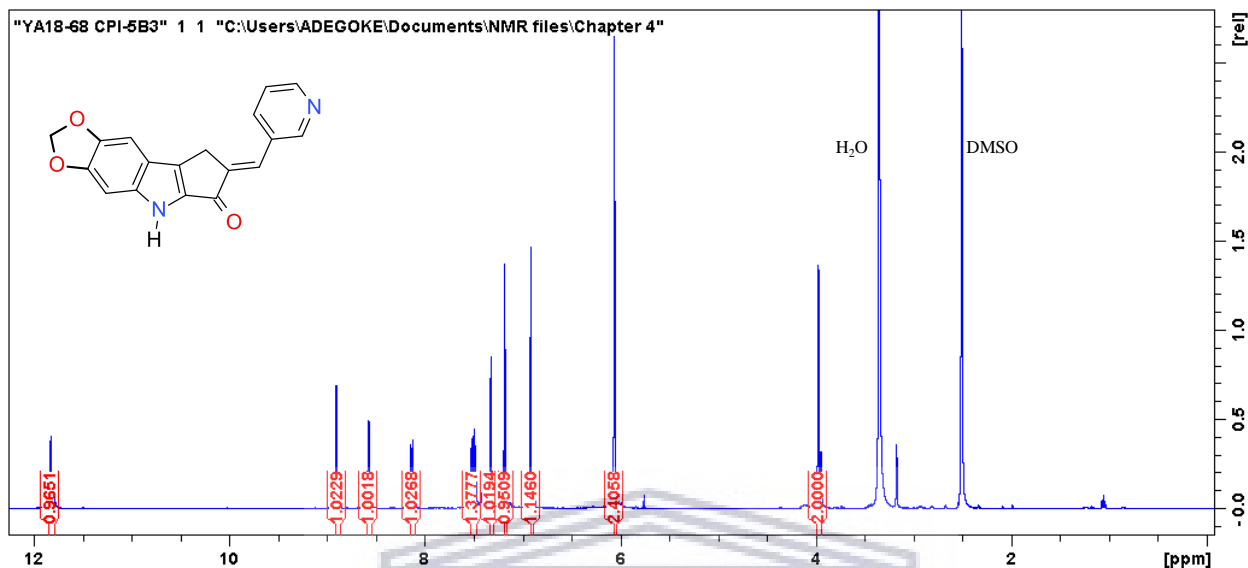


Figure S4.121: ^{13}C NMR spectrum of compound **4.33e** (100 MHz, DMSO-d_6)

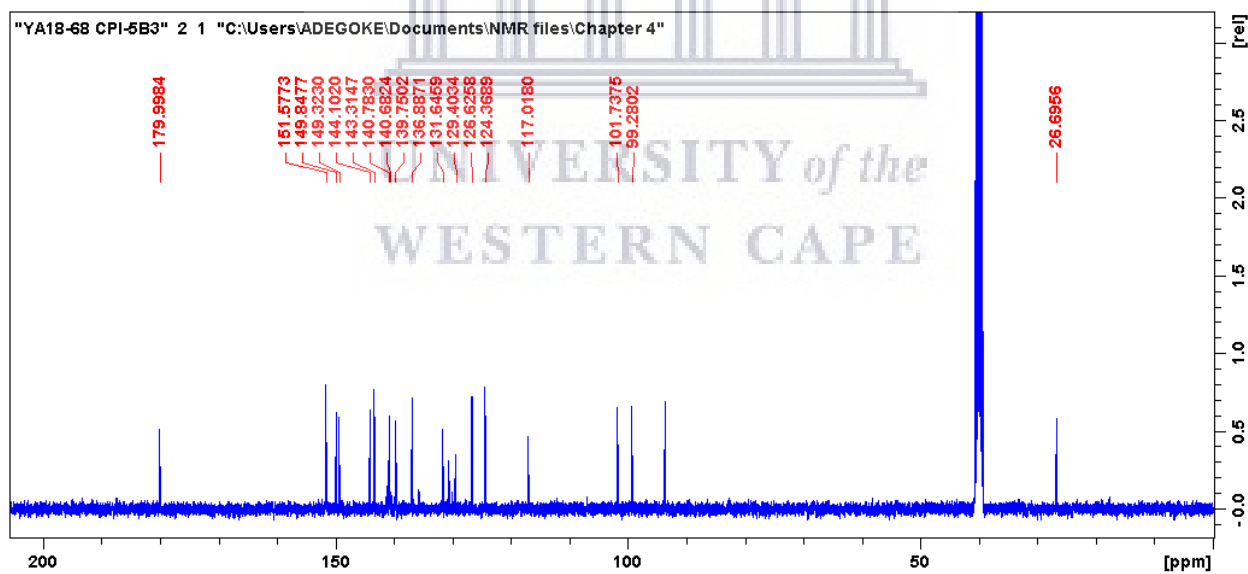


Figure S4.122: HRMS spectrum of compound **4.33e**

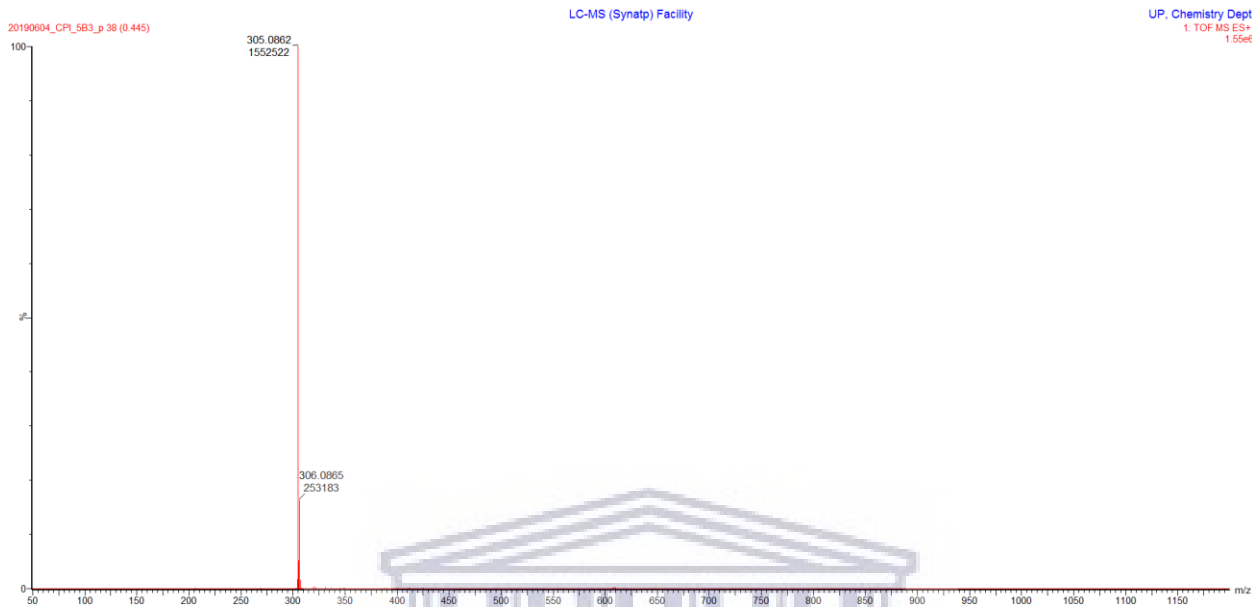


Figure S4.123: IR spectrum of compound **4.33e**

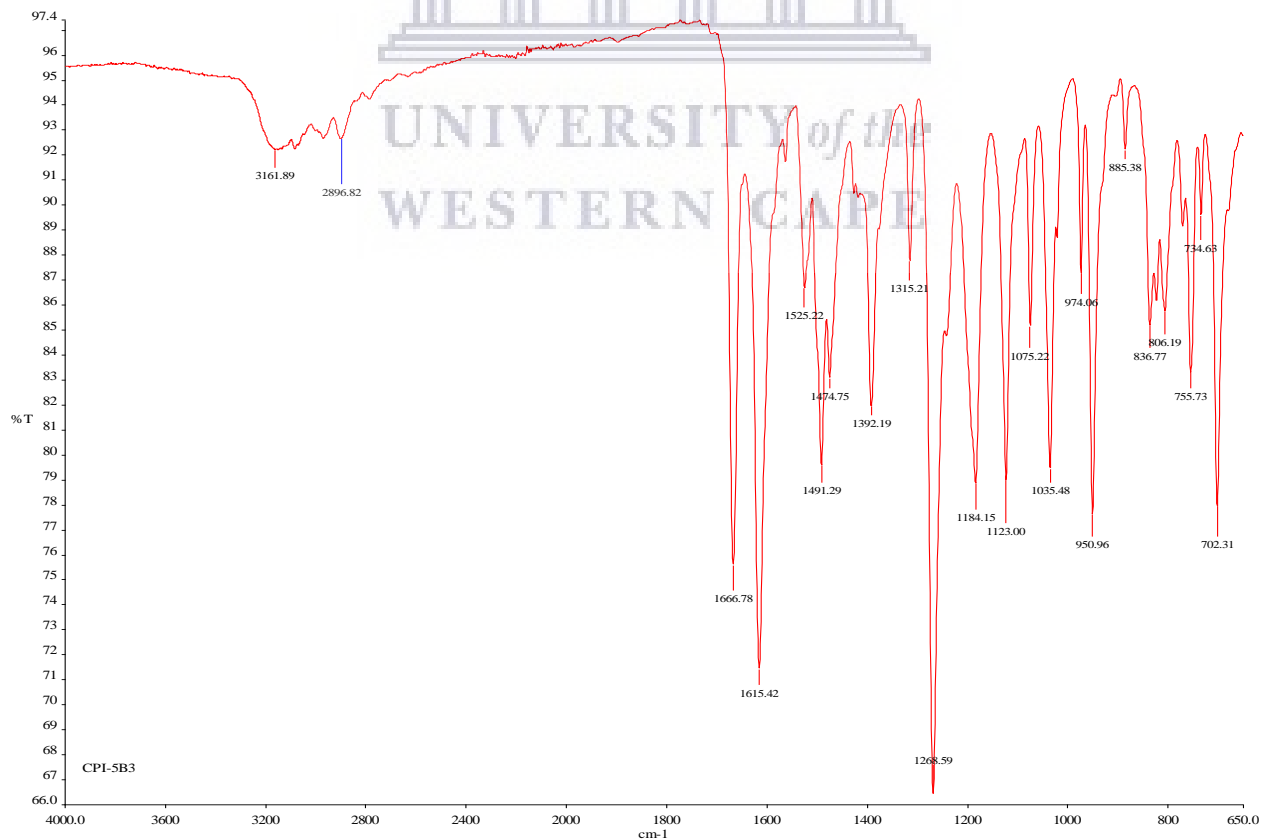


Figure S4.124: ^1H NMR spectrum of compound **4.33f** (400 MHz, DMSO- d_6)

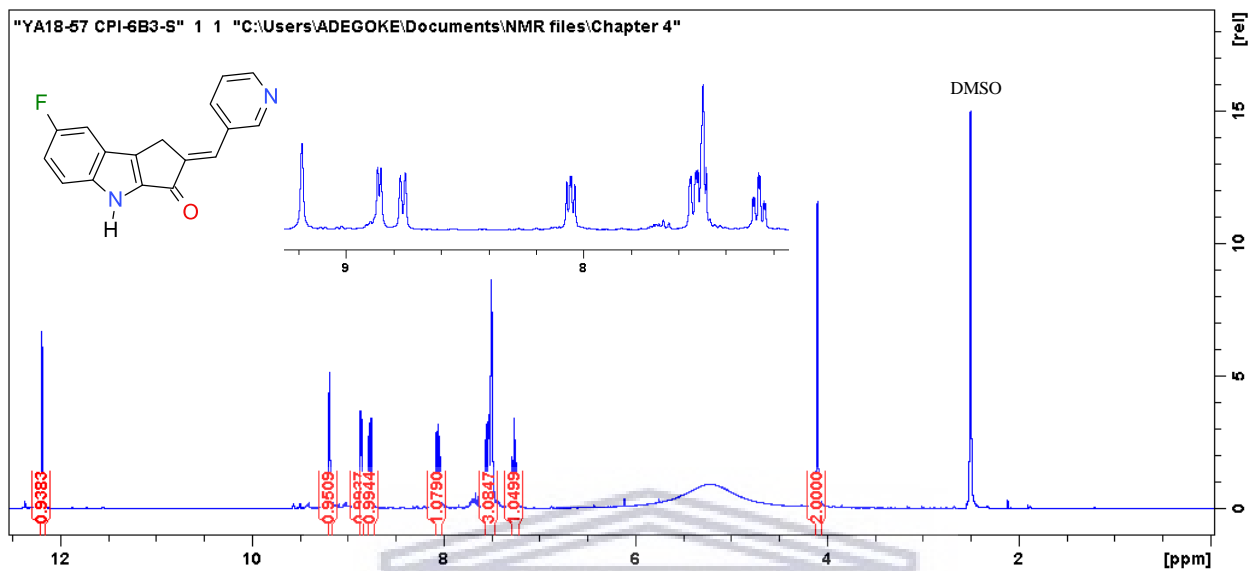


Figure S4.125: ^{13}C NMR spectrum of compound **4.33f** (100 MHz, DMSO- d_6)

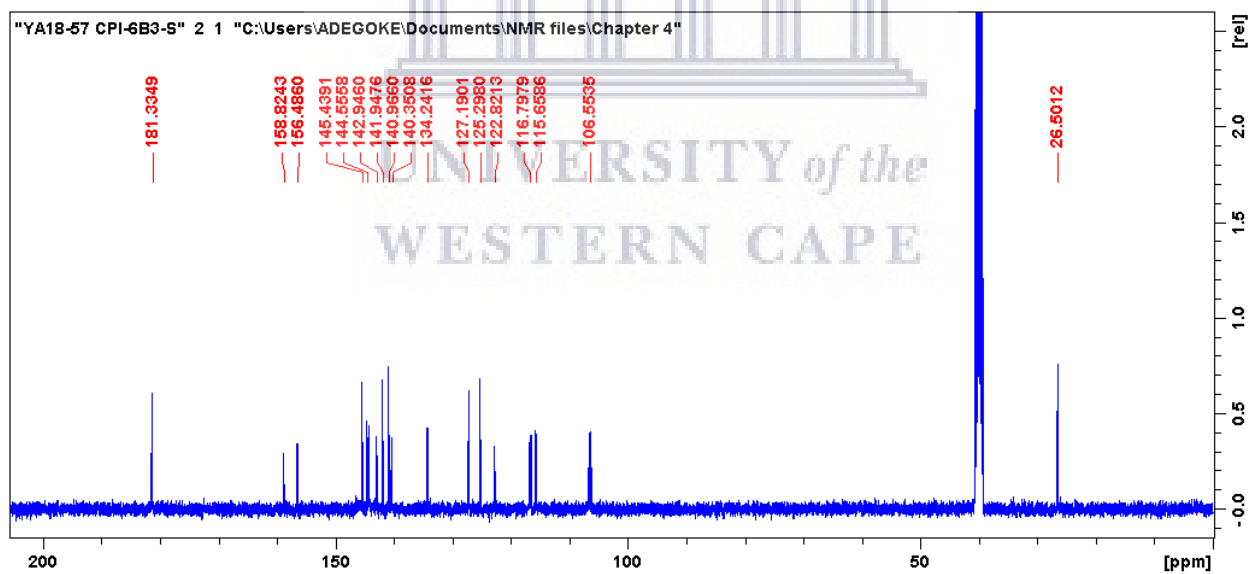


Figure S4.126: HRMS spectrum of compound 4.33f

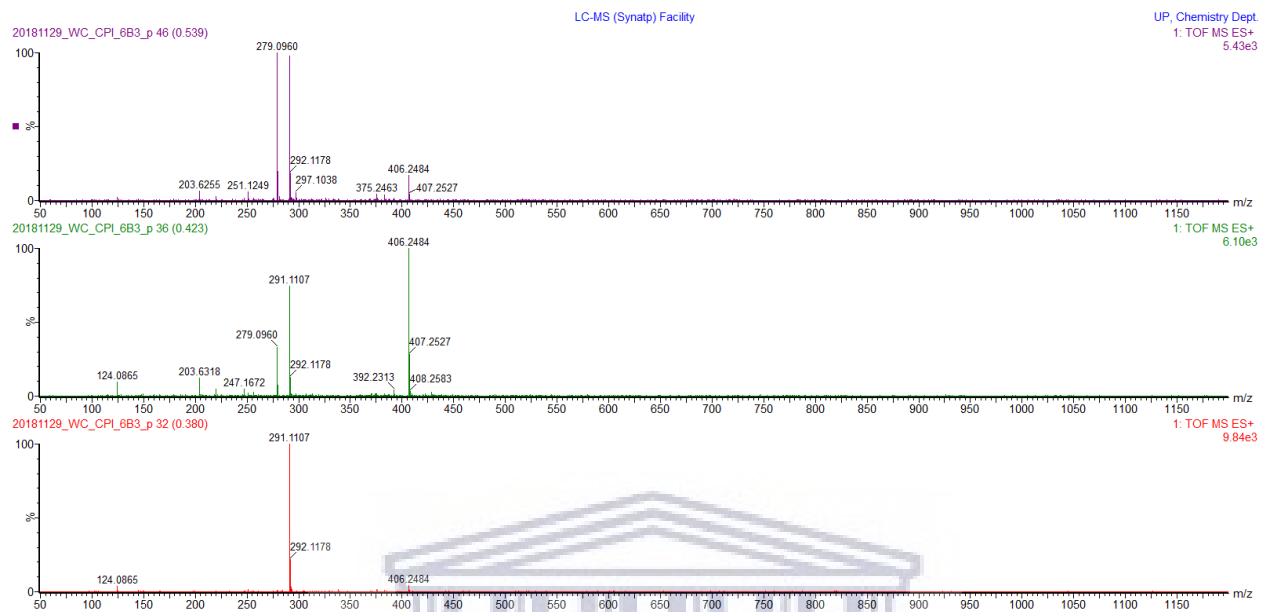


Figure S4.127: IR spectrum of compound 4.33f

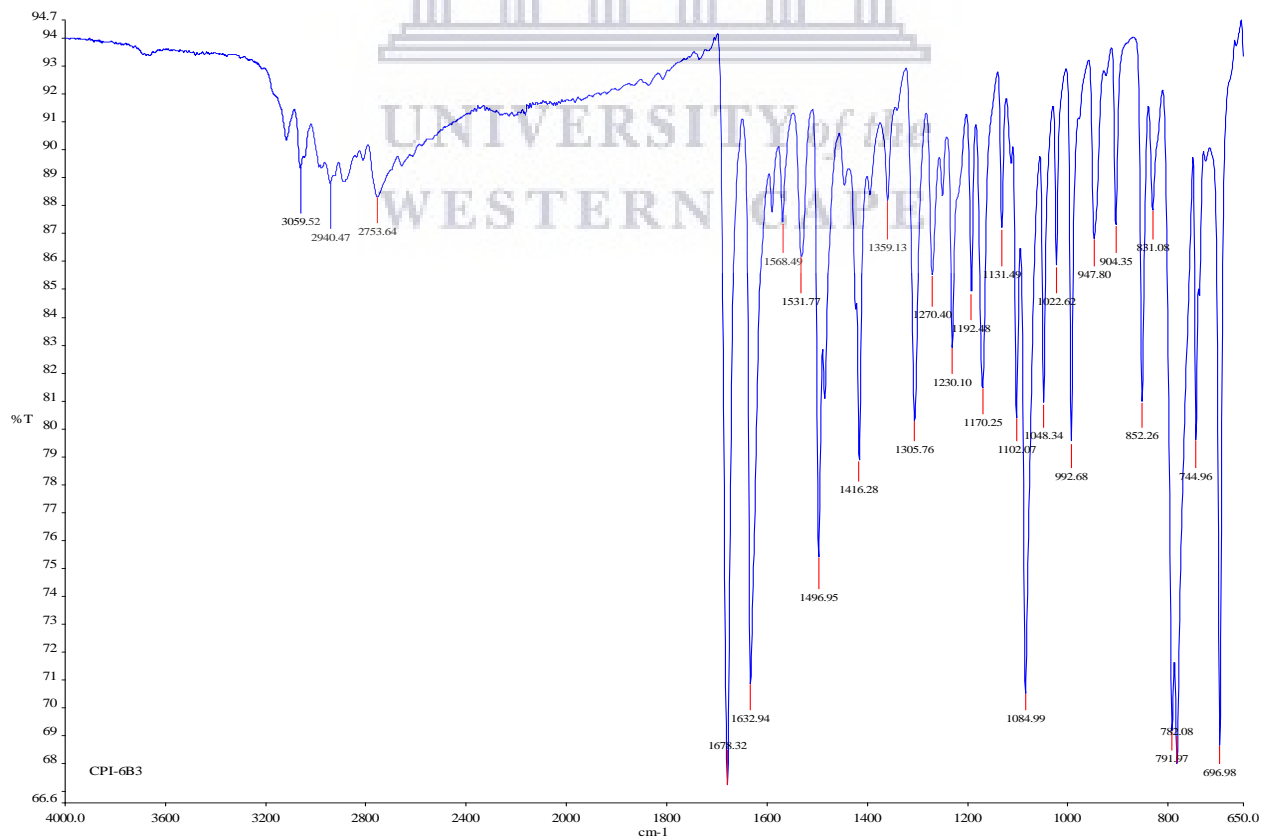


Figure S4.128: ^1H NMR spectrum of compound **4.33g** (400 MHz, DMSO- d_6)

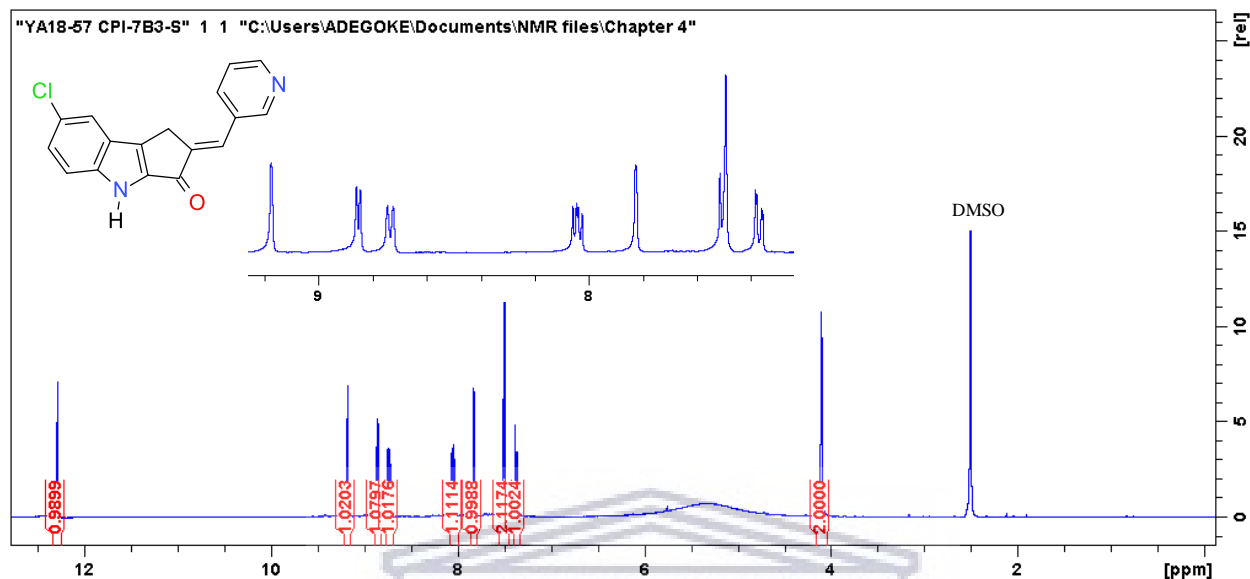


Figure S4.129: ^{13}C NMR spectrum of compound **4.33g** (100 MHz, DMSO- d_6)

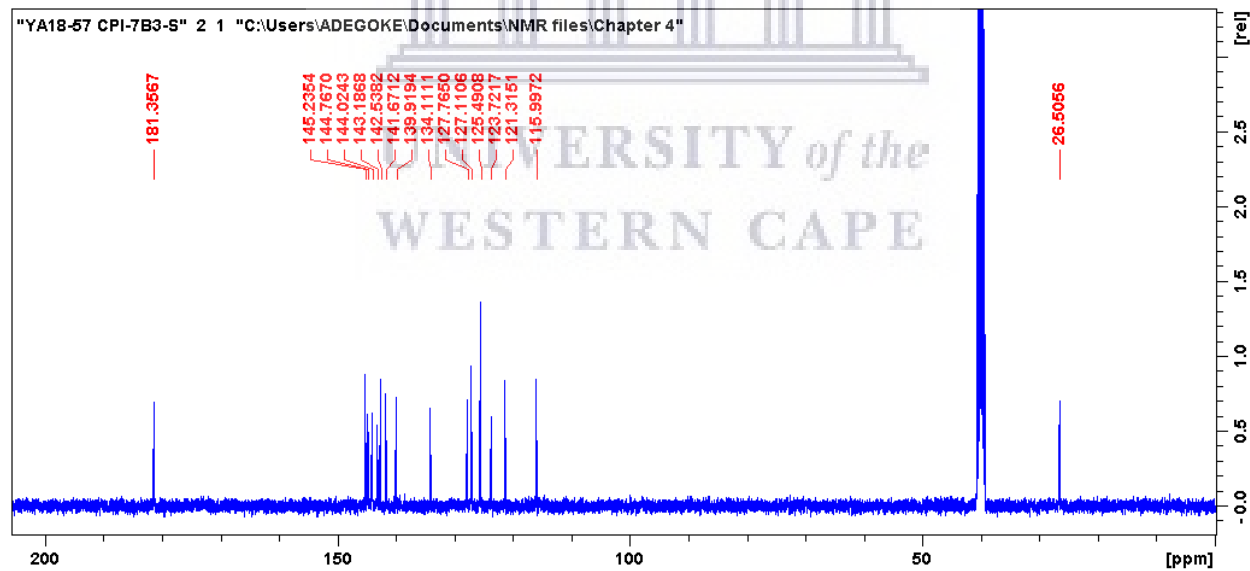


Figure S4.130: HRMS spectrum of compound 4.33g

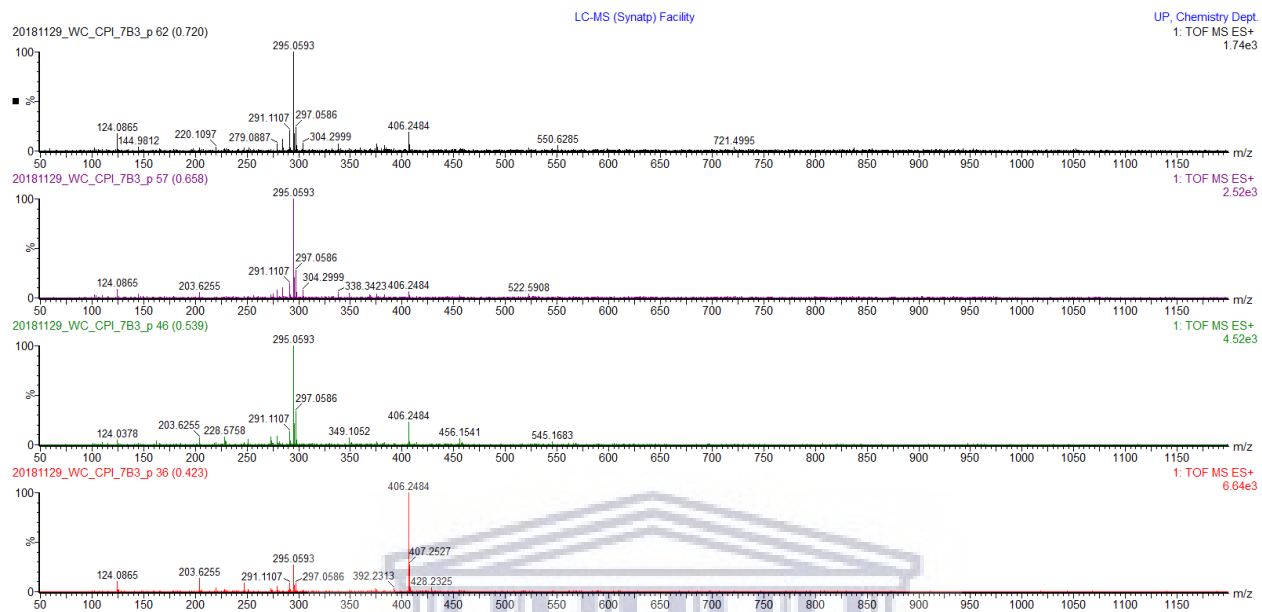


Figure S4.131: IR spectrum of compound 4.33g

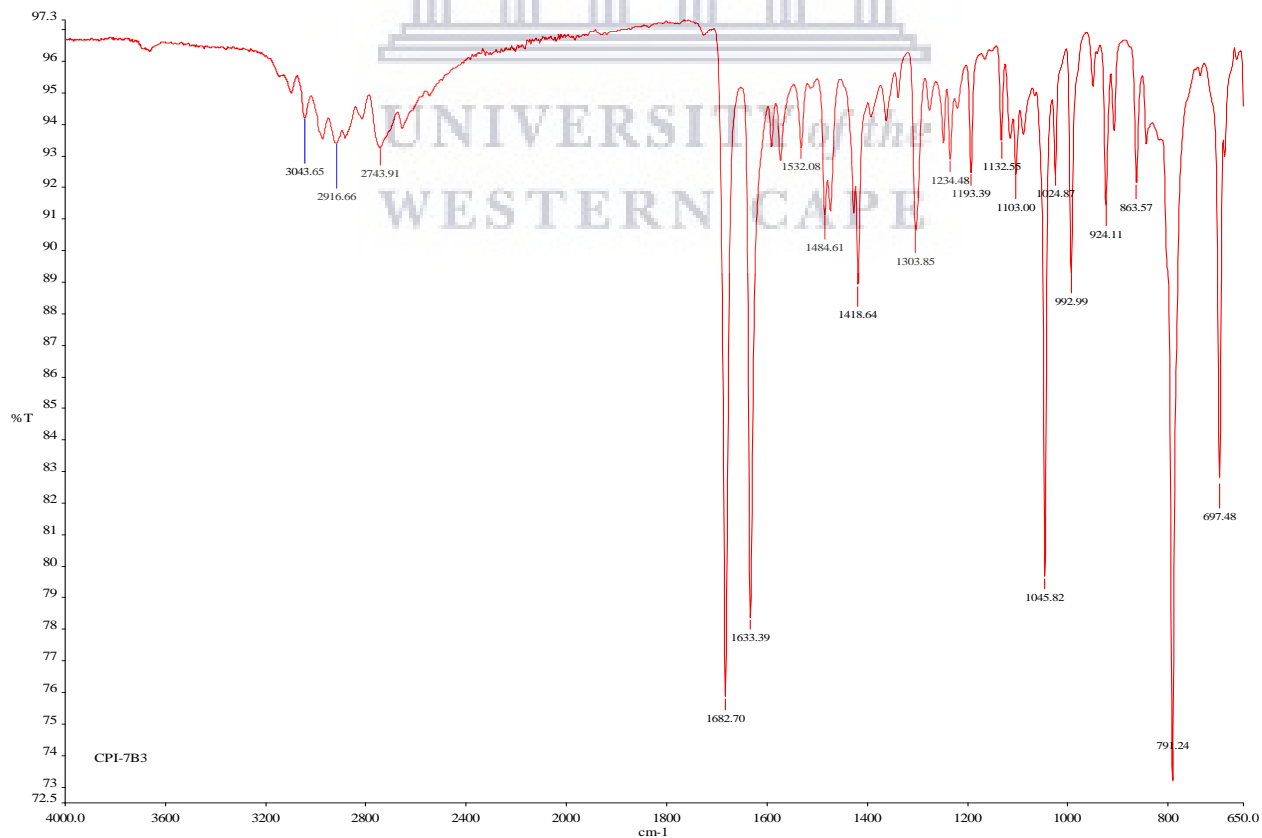


Figure S4.132: ^1H NMR spectrum of compound **4.33h** (400 MHz, DMSO-d_6)

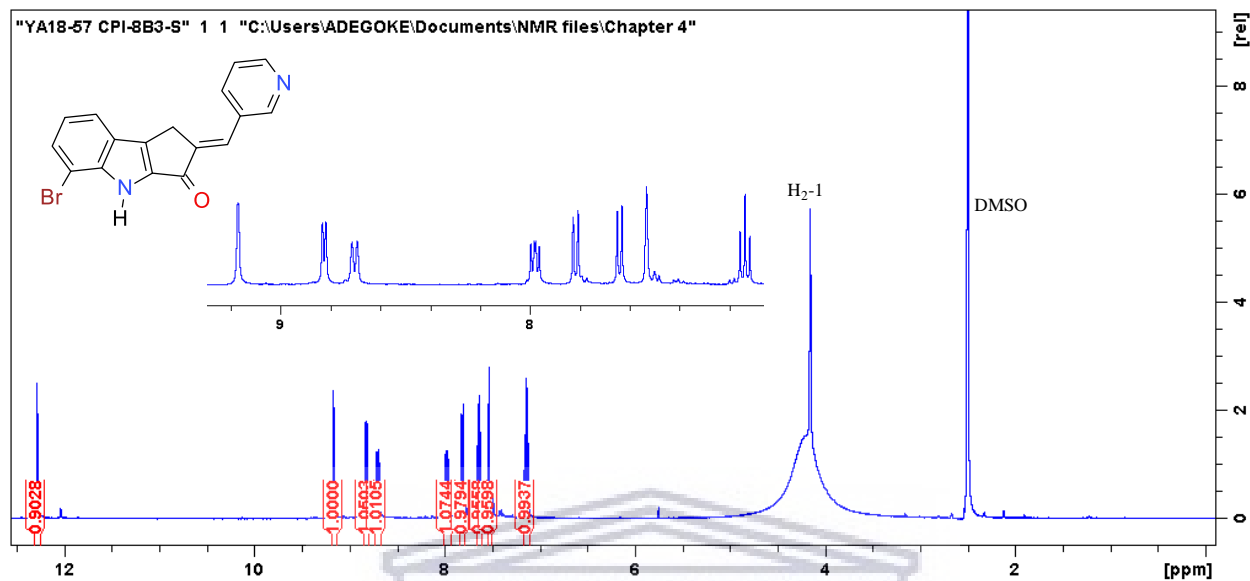


Figure S4.133: ^{13}C NMR spectrum of compound **4.33h** (100 MHz, DMSO-d_6)

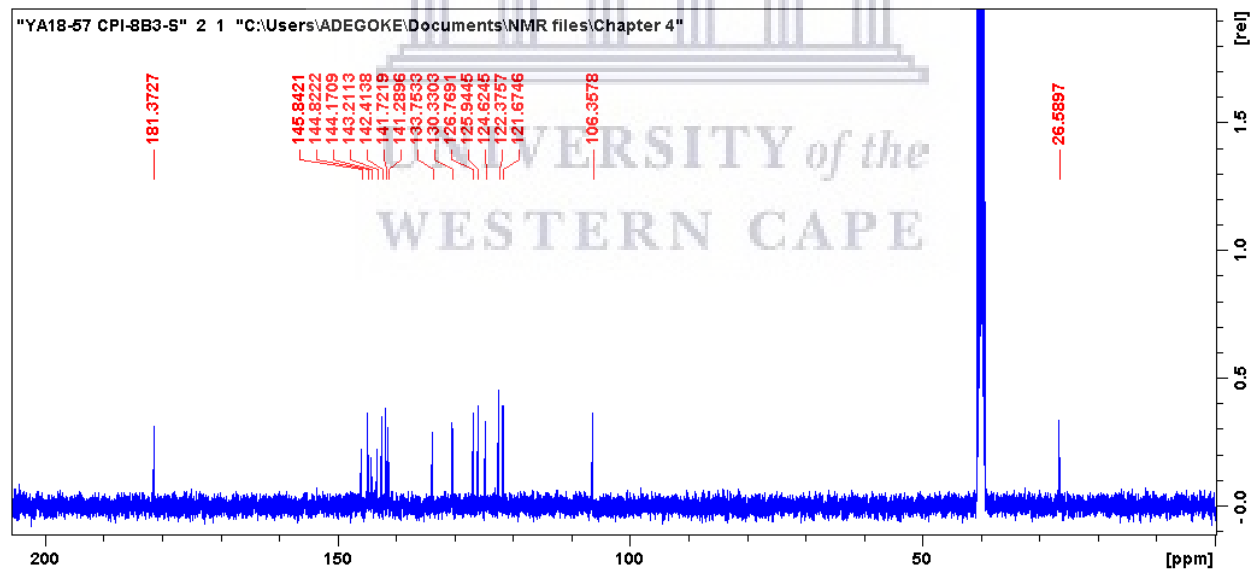


Figure S4.134: HRMS spectrum of compound 4.33h

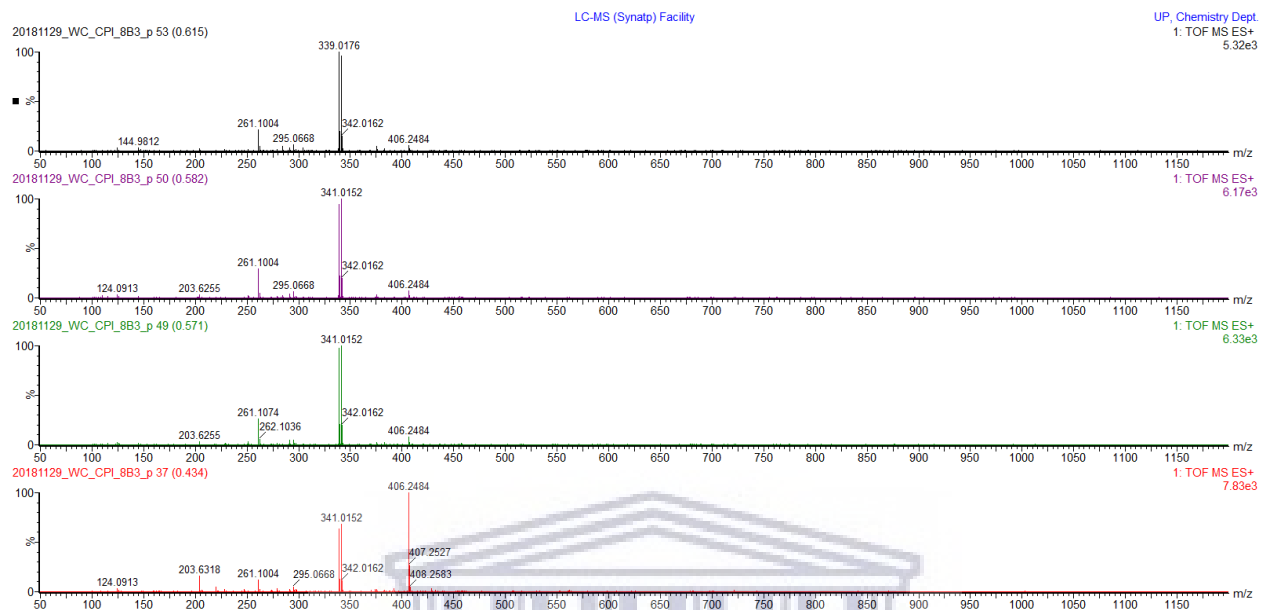


Figure S4.135: IR spectrum of compound 4.33h

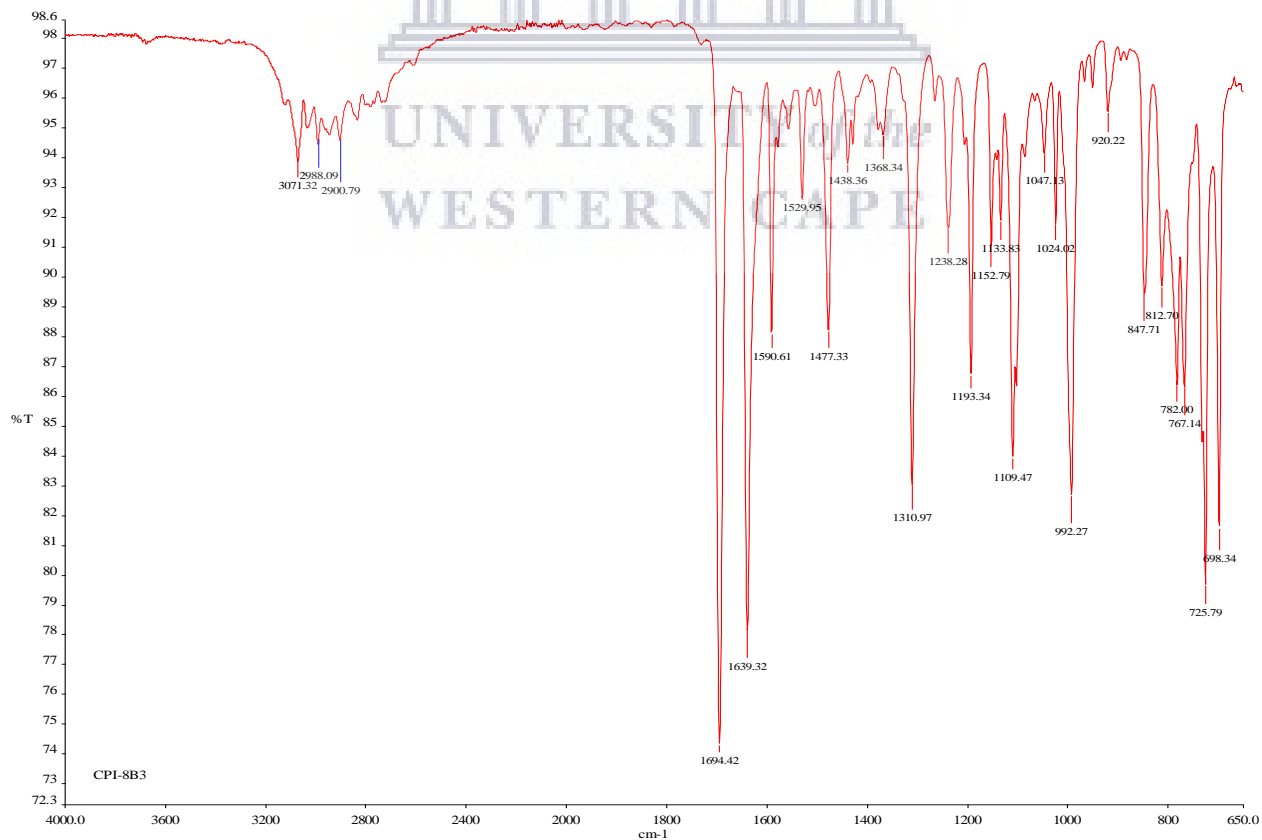


Figure S4.136: ^1H NMR spectrum of compound **4.33i** (400 MHz, DMSO- d_6)

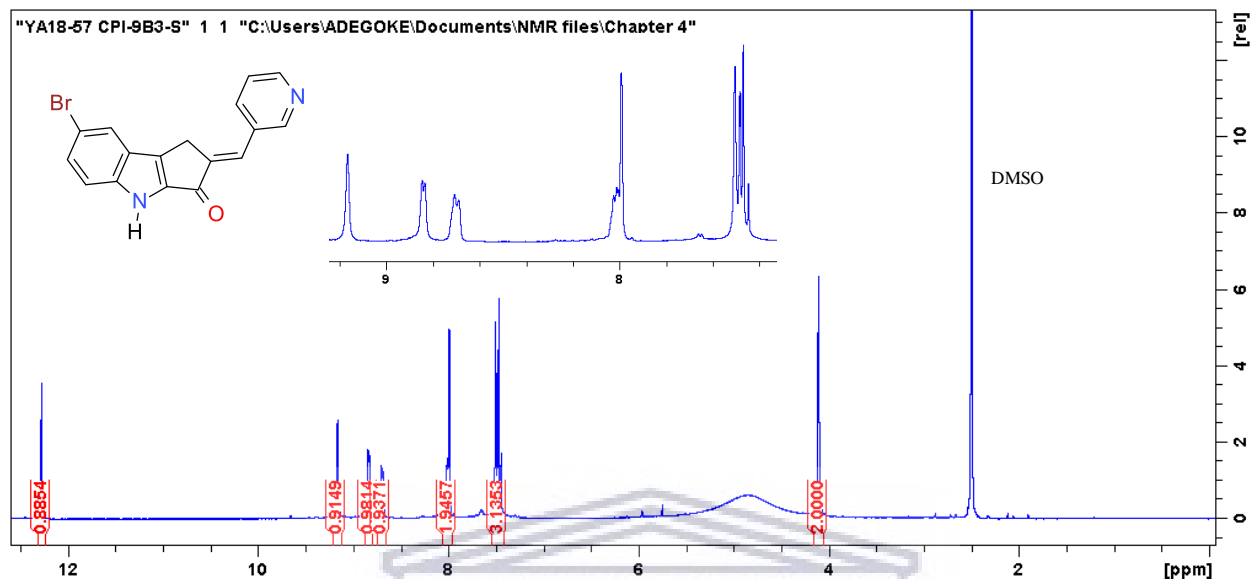


Figure S4.137: ^{13}C NMR spectrum of compound **4.33i** (100 MHz, DMSO- d_6)

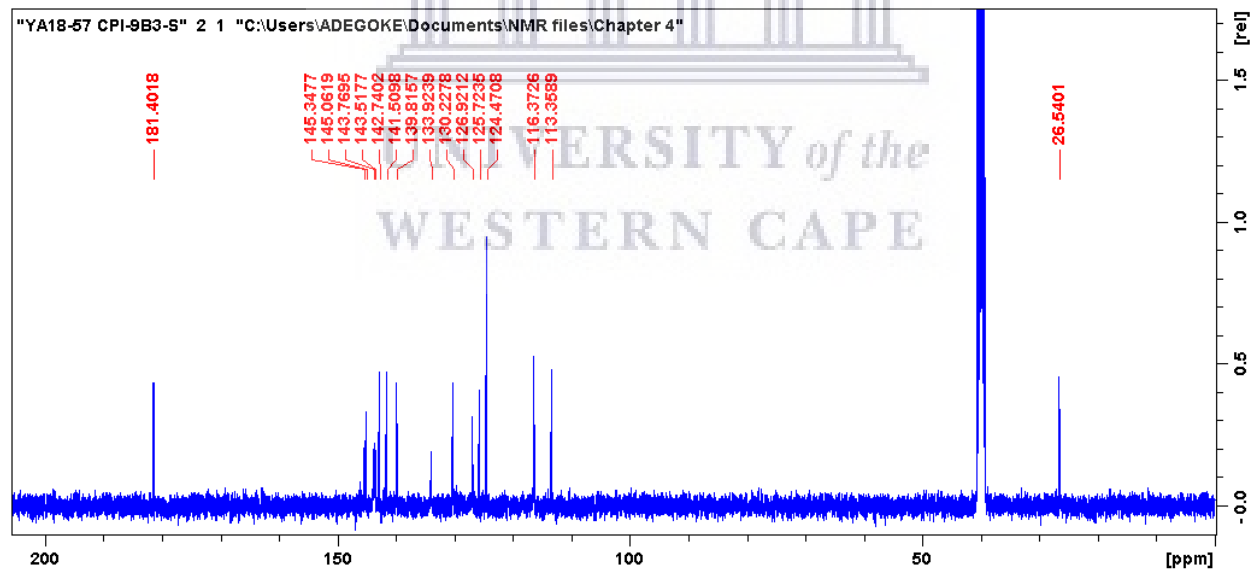


Figure S4.138: HRMS spectrum of compound **4.33i**

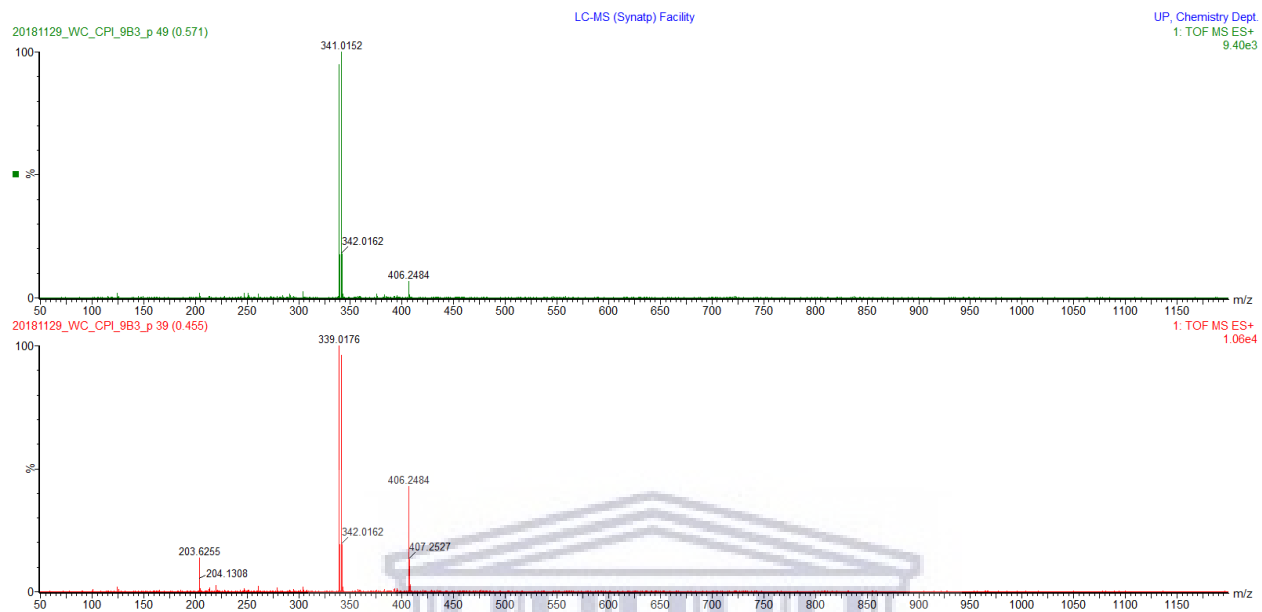


Figure S4.139: IR spectrum of compound **4.33i**

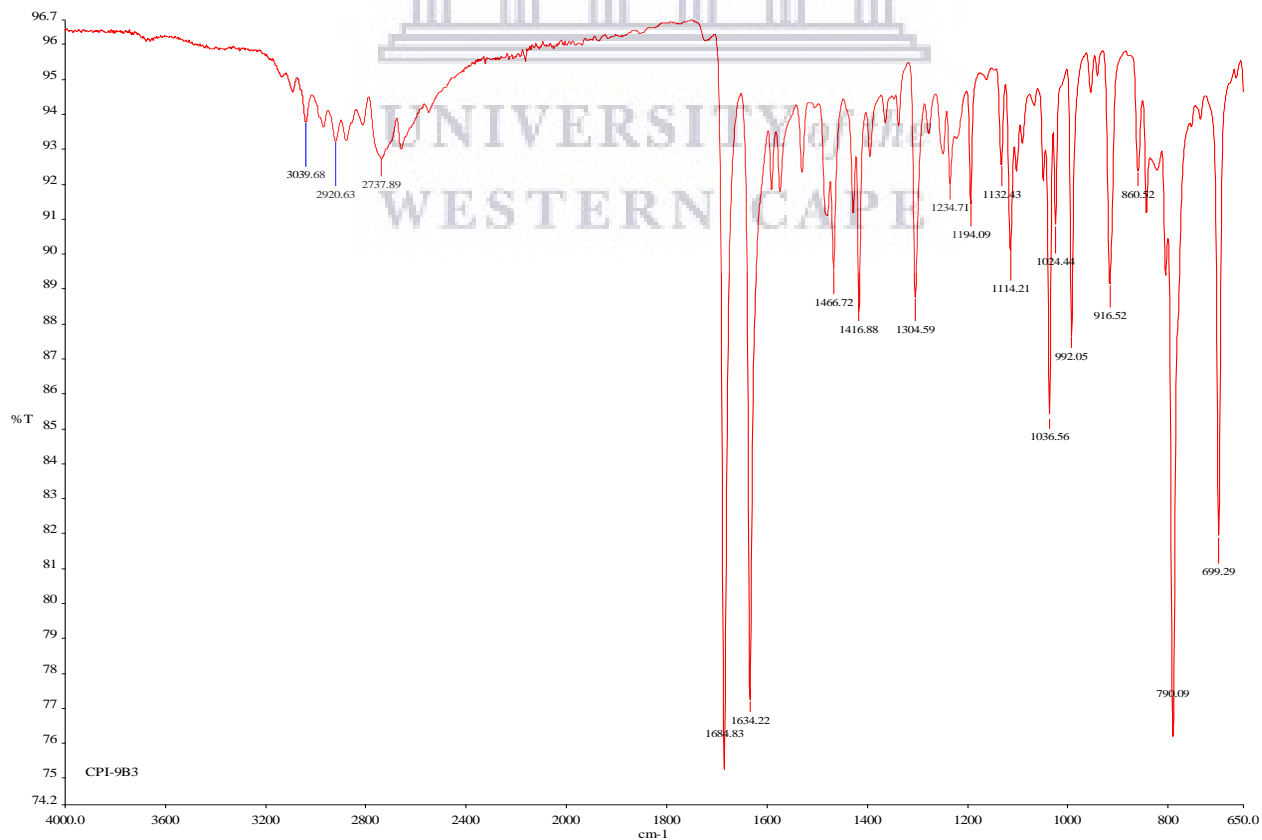


Figure S4.140: ^1H NMR spectrum of compound **4.33j** (400 MHz, DMSO-d_6)

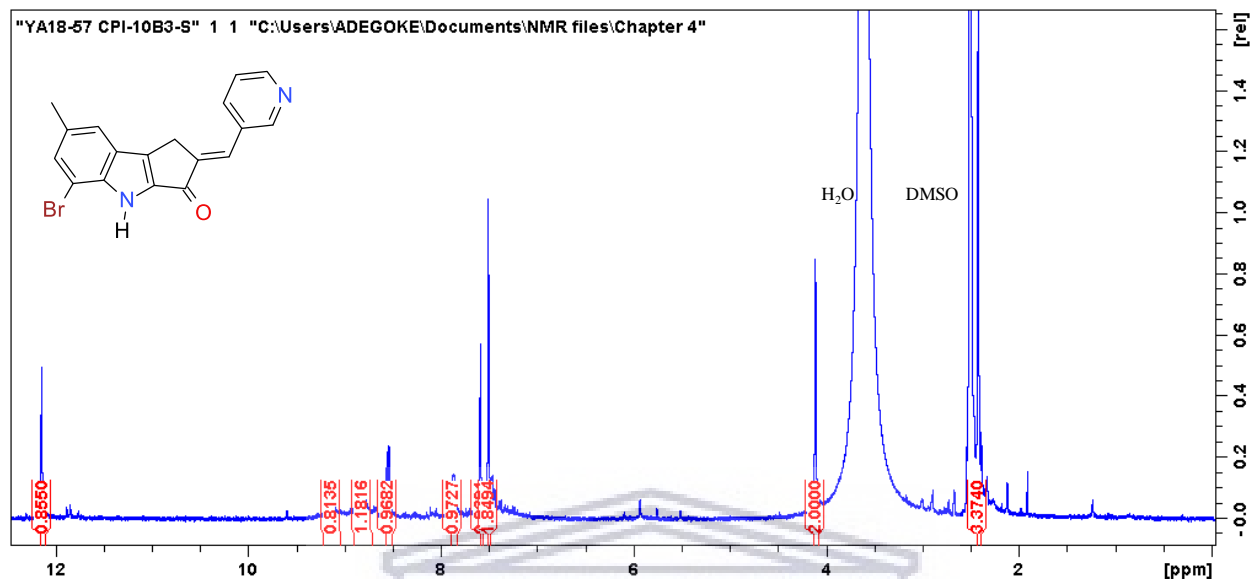


Figure S4.141: HRMS spectrum of compound **4.33j**

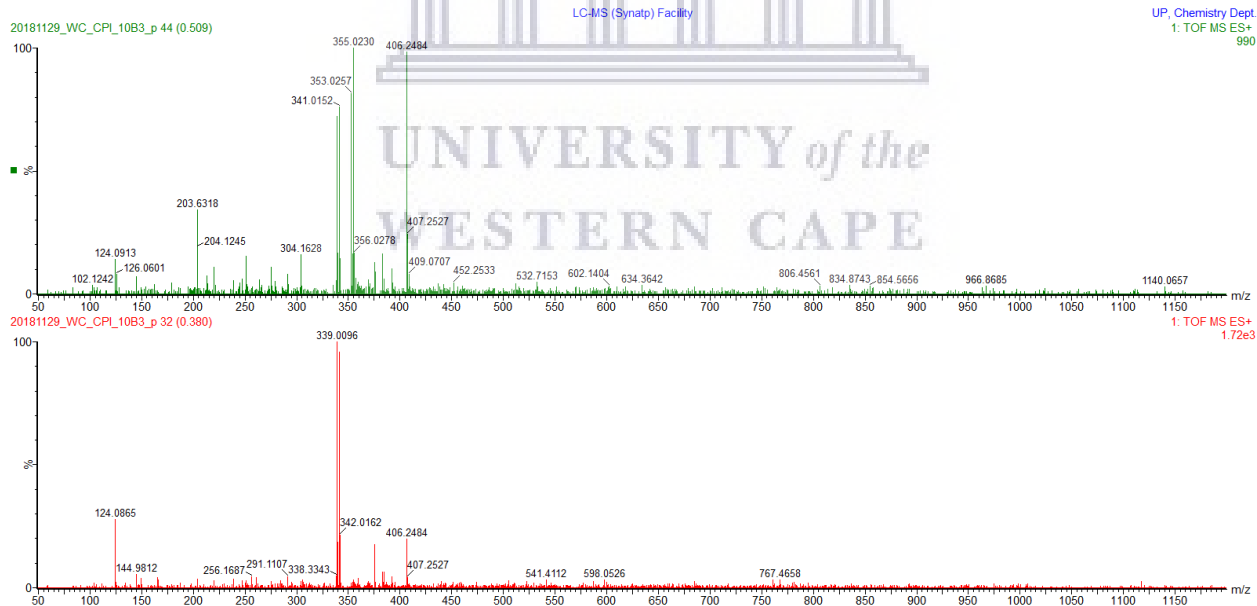


Figure S4.142: IR spectrum of compound **4.33j**

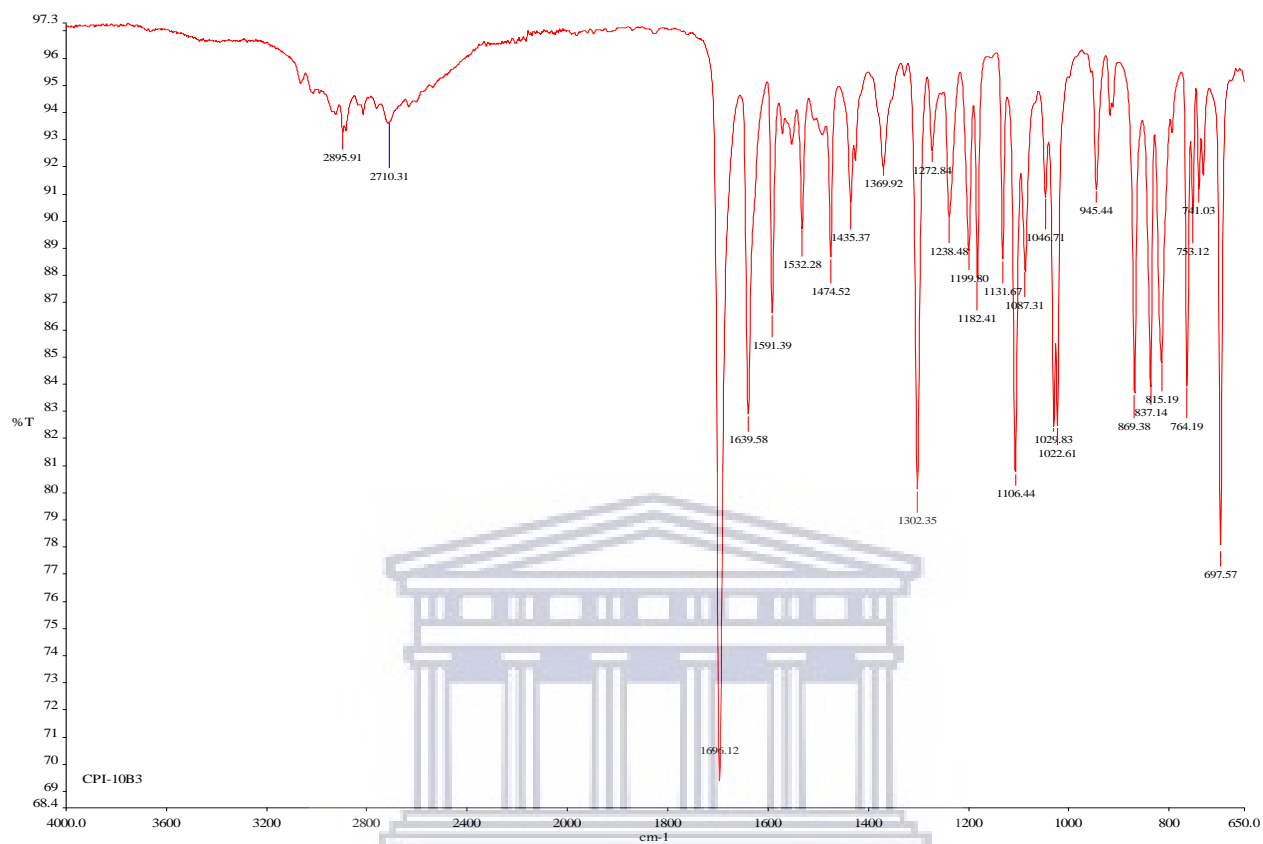


Figure S4.143: ^1H NMR spectrum of compound **4.33k** (400 MHz, DMSO-d_6)

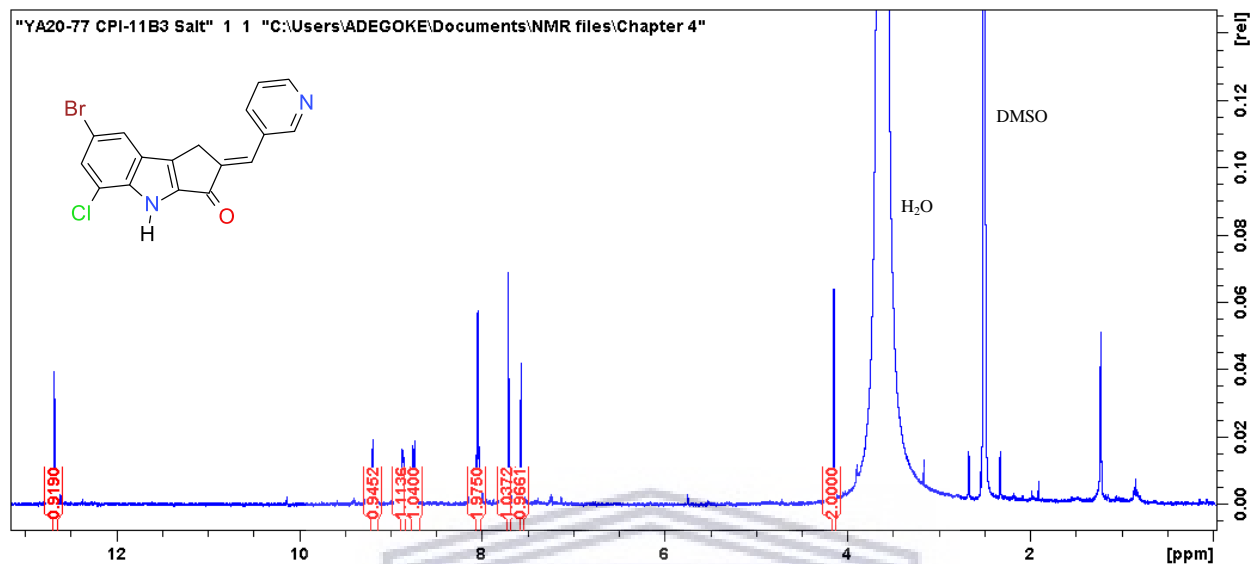


Figure S4.144: HRMS spectrum of compound **4.33k**

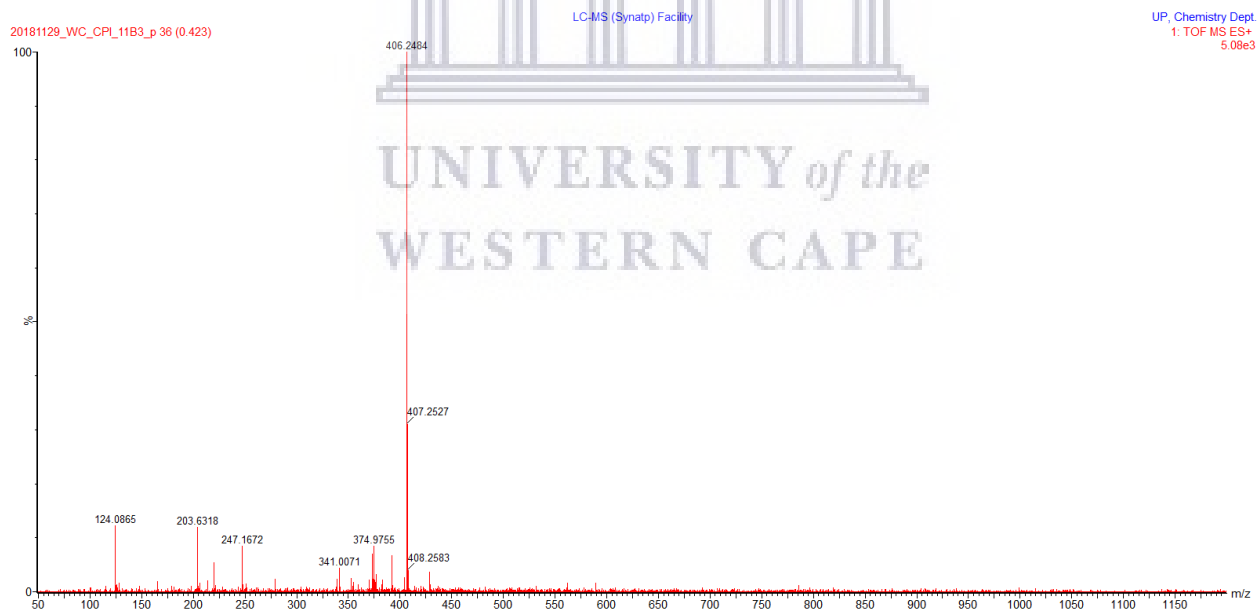
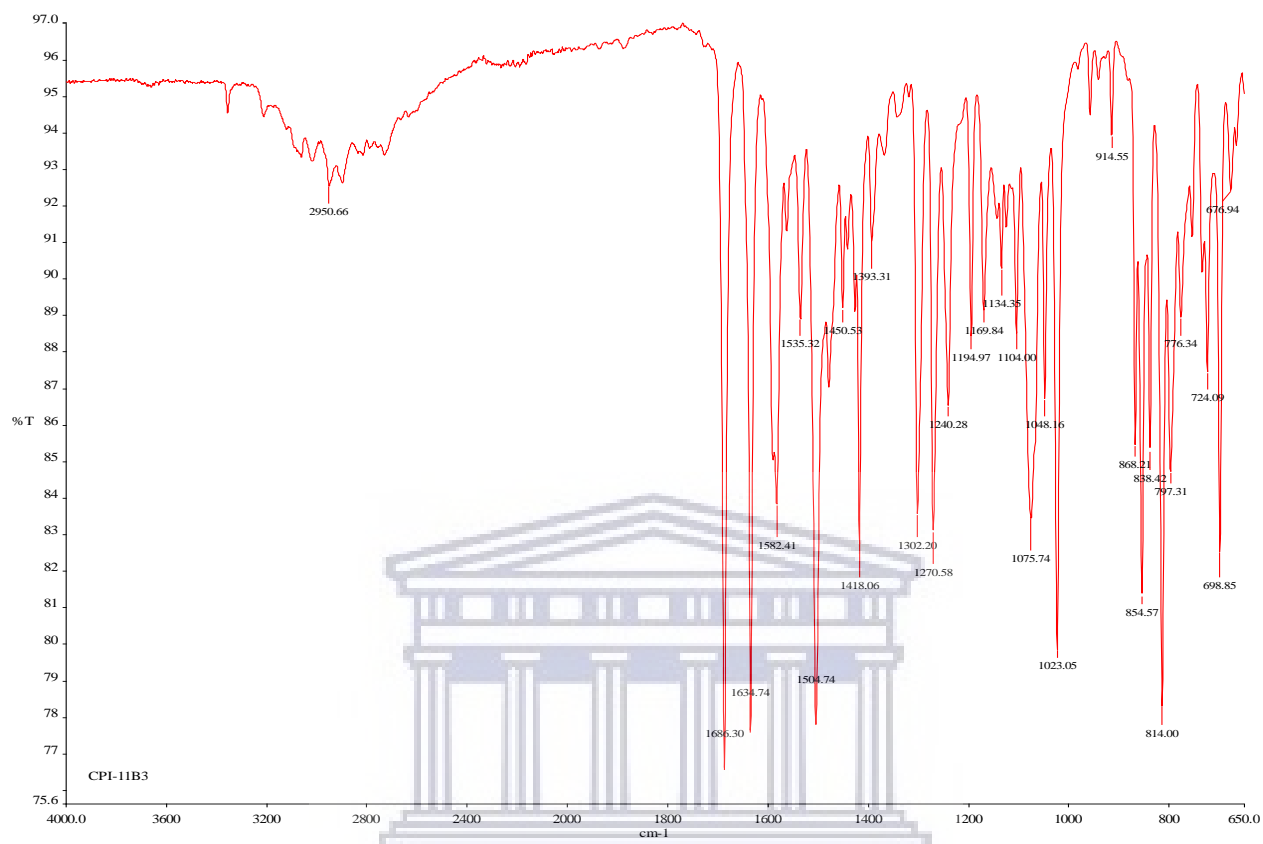


Figure S4.145: IR spectrum of compound **4.33k**



UNIVERSITY of the
WESTERN CAPE

Figure S4.146: ^1H NMR spectrum of compound **4.331** (400 MHz, DMSO- d_6)

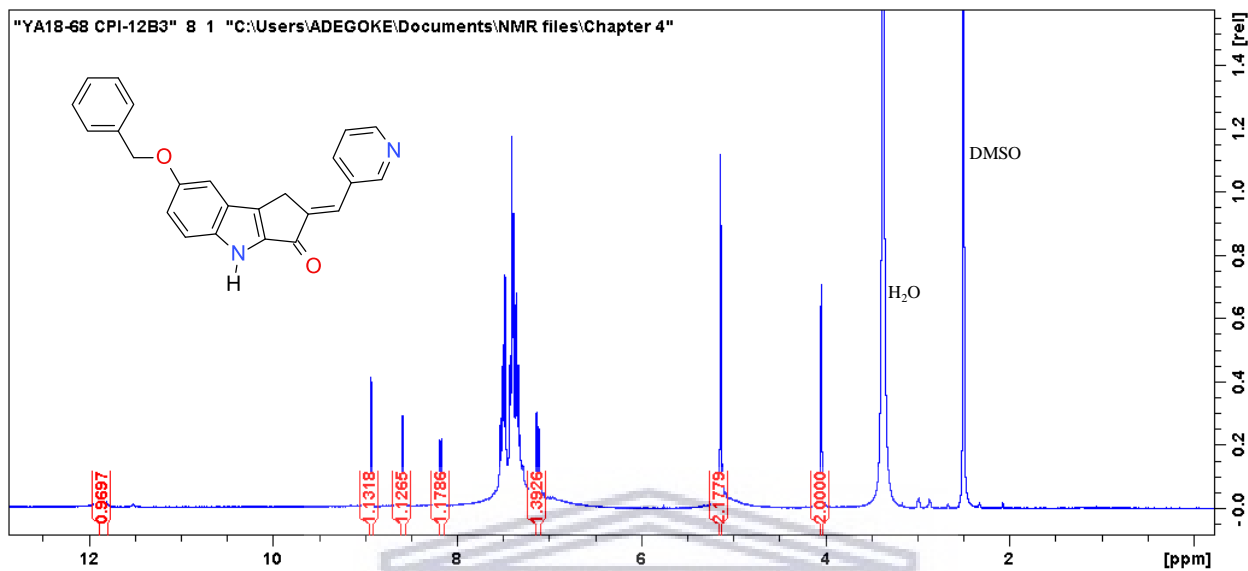


Figure S4.147: ^{13}C NMR spectrum of compound **4.331** (100 MHz, DMSO- d_6)

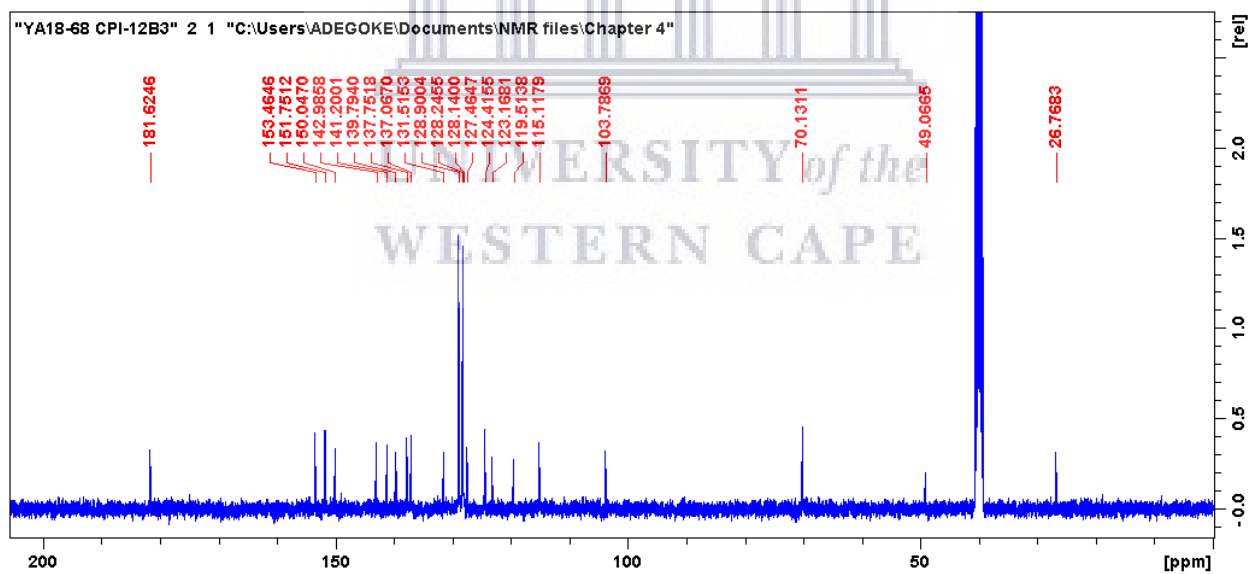


Figure S4.148: HRMS spectrum of compound **4.331**

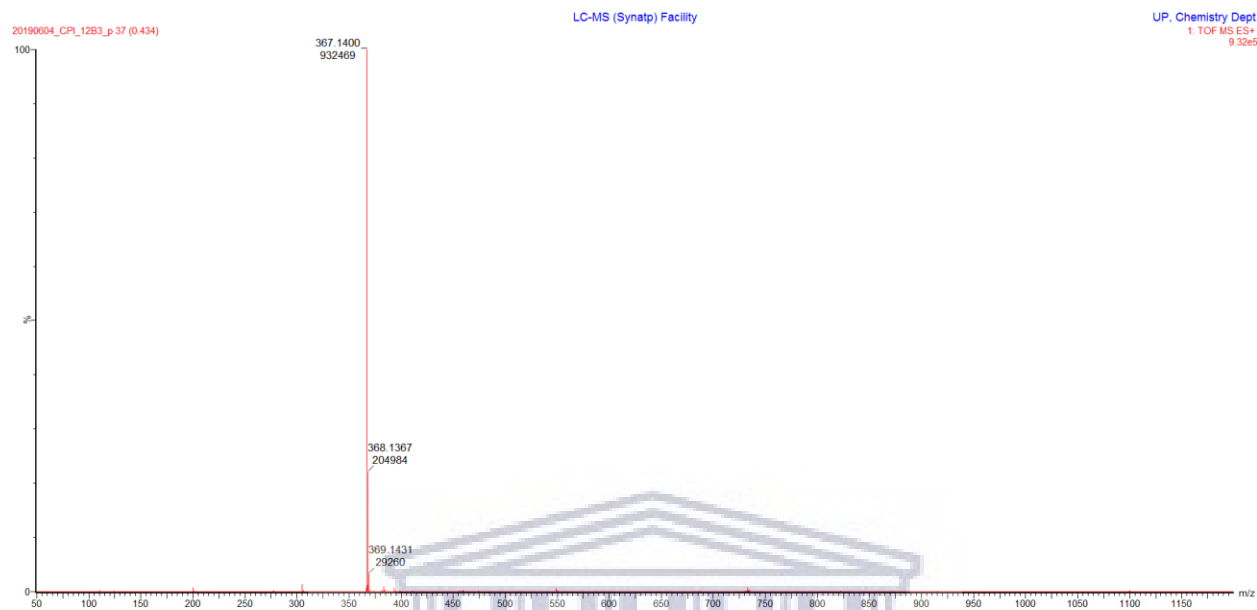
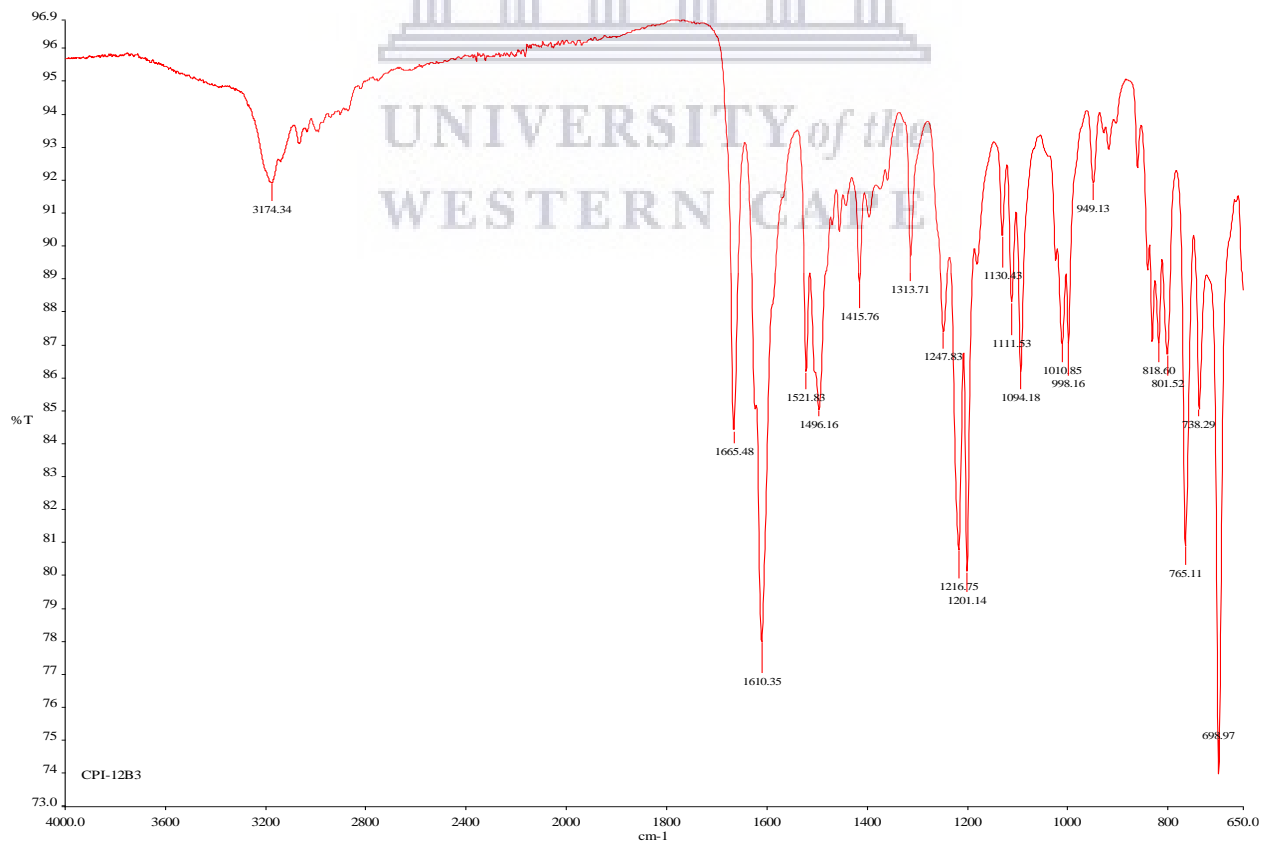


Figure S4.149: IR spectrum of compound **4.331**



Chapter 5

Figure S5.1: ^1H NMR spectrum of compound **5.4** (400 MHz, CDCl_3)

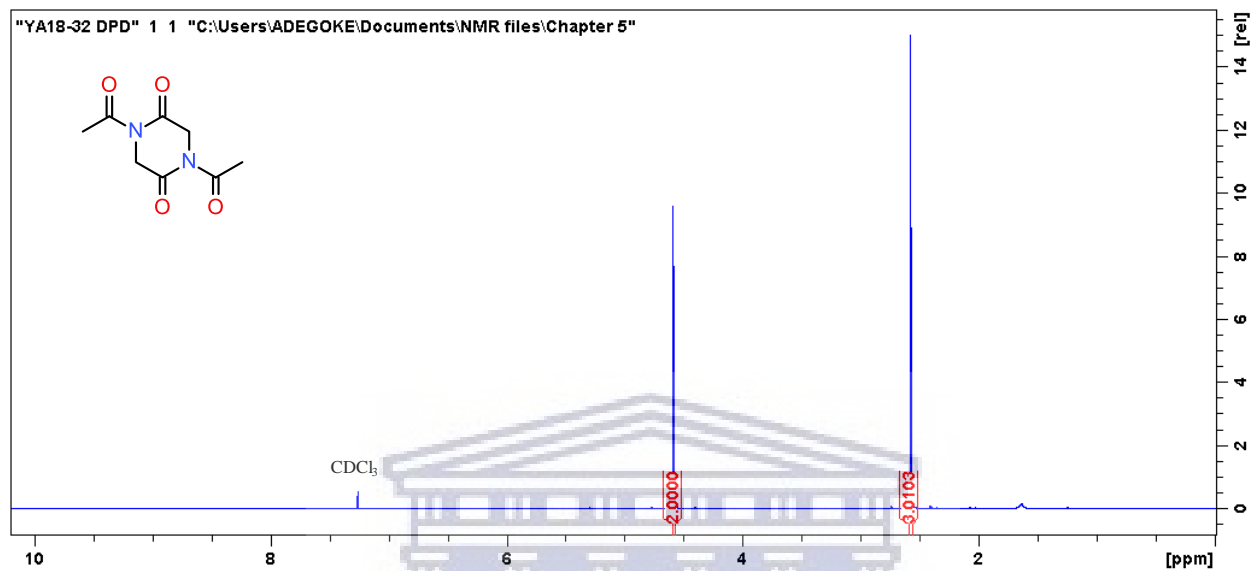
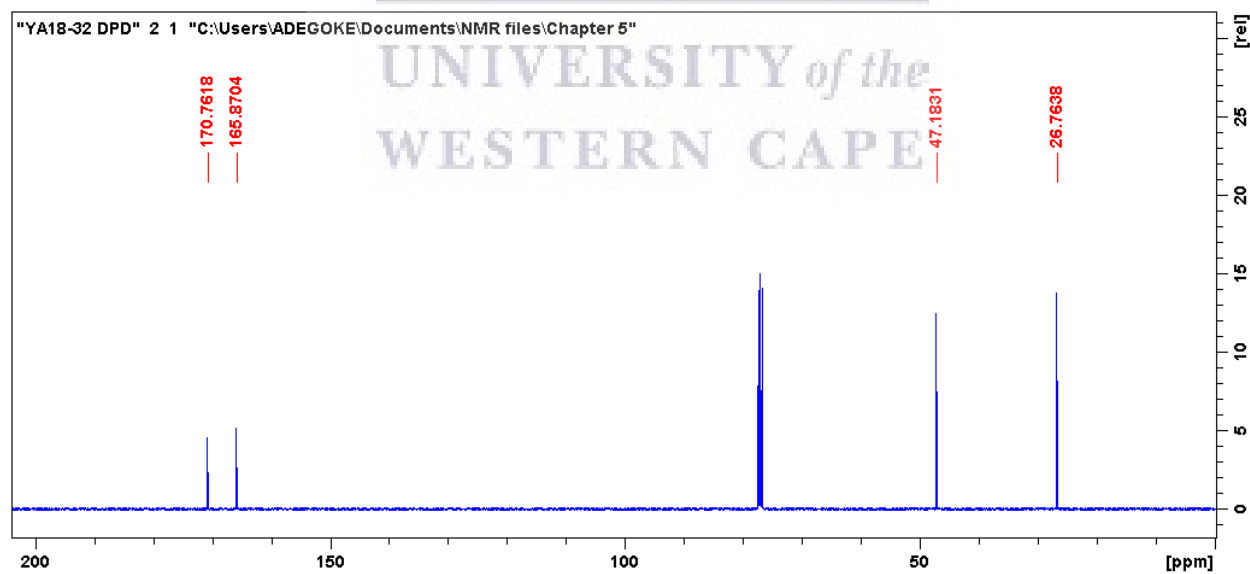


Figure S5.2: ^{13}C NMR spectrum of compound **5.4** (100 MHz, CDCl_3)



Diketopiperazine derivatives 5.4(a-f)

Figure S5.3: ^1H NMR spectrum of compound 5.4a (400 MHz, CDCl_3)

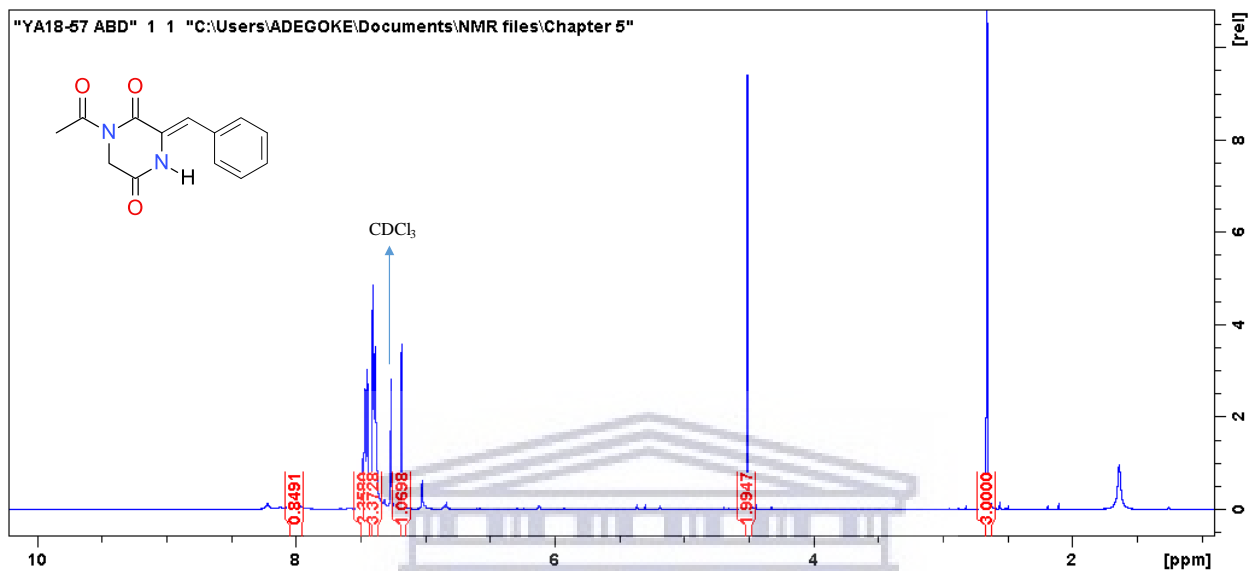


Figure S5.4: ^{13}C NMR spectrum of compound 5.4a (100 MHz, CDCl_3)

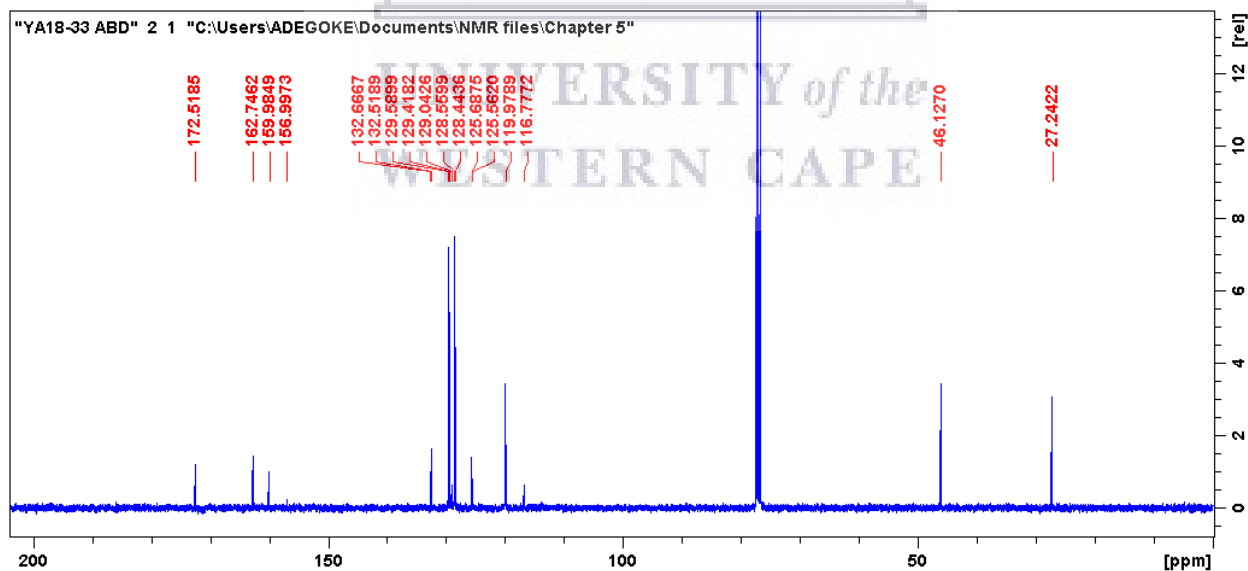


Figure S5.5: HRMS spectrum of compound **5.4a**

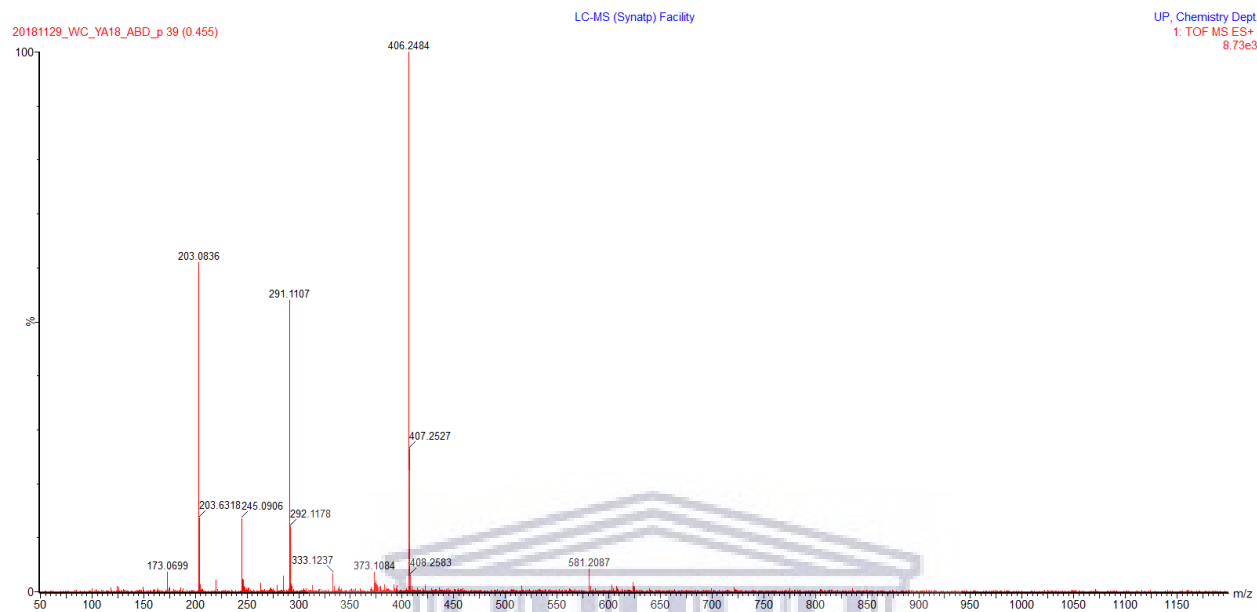


Figure S5.6: IR spectrum of compound **5.4a**

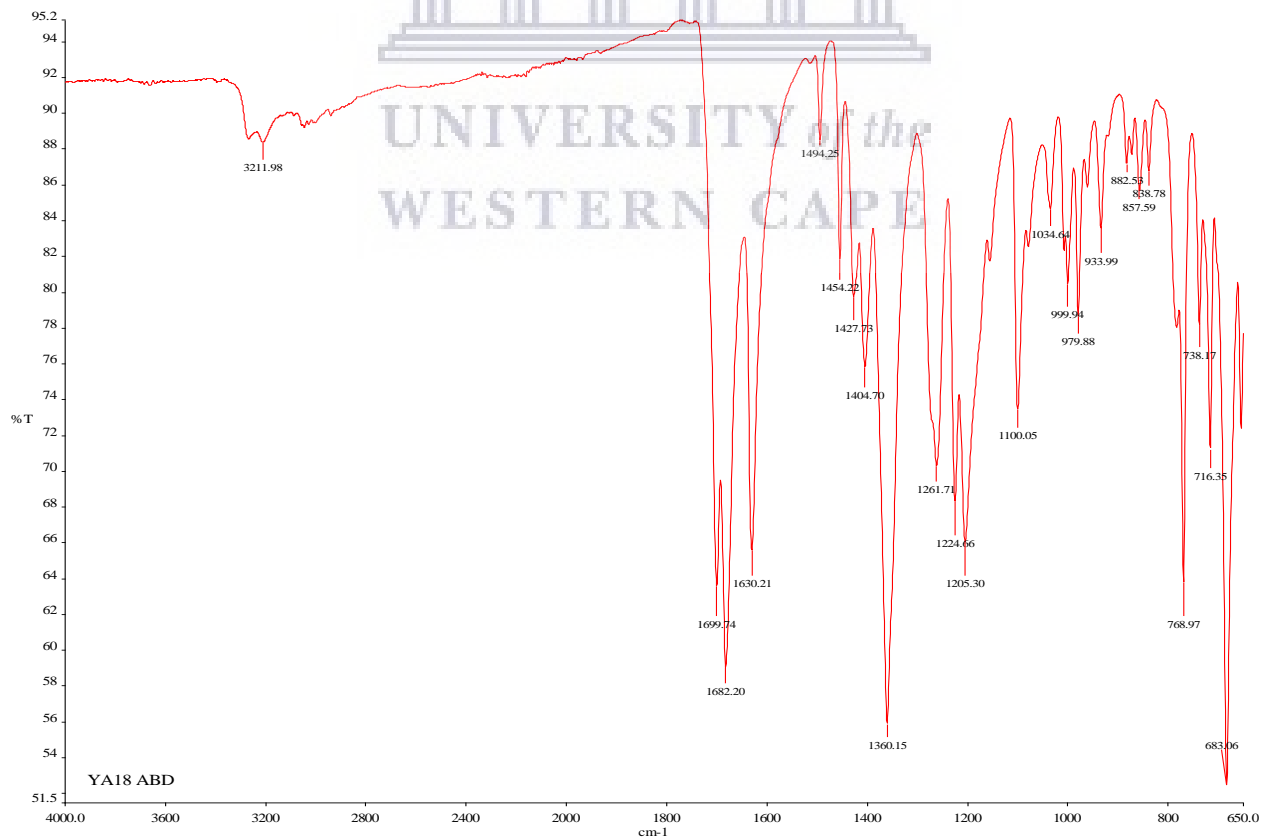


Figure S5.7: ^1H NMR spectrum of compound **5.4b** (400 MHz, CDCl_3)

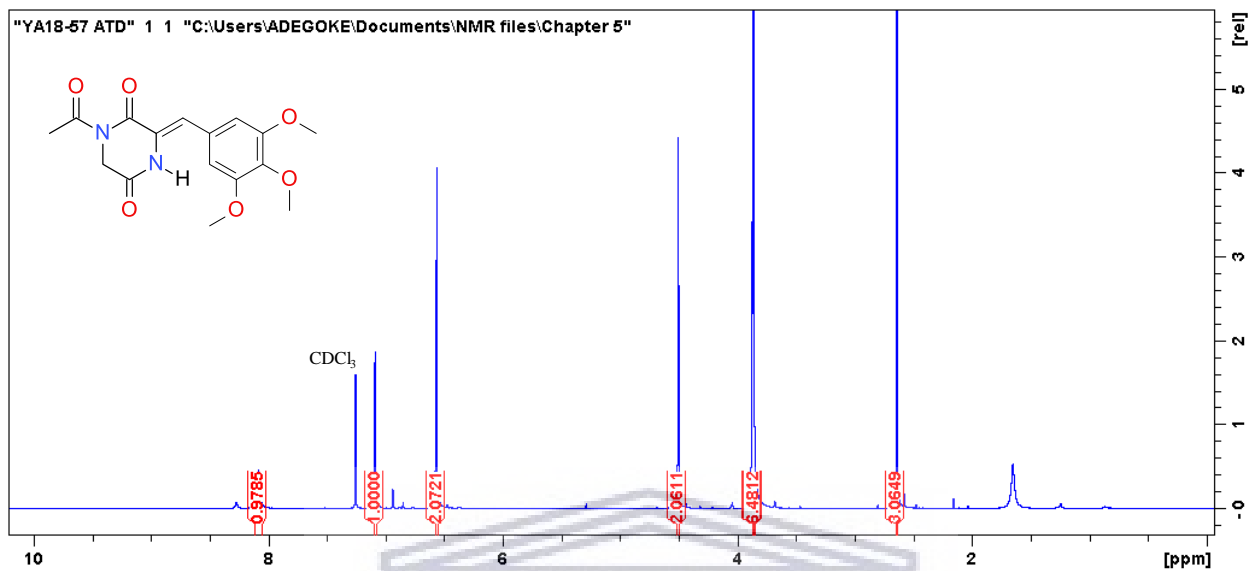


Figure S5.8: ^{13}C NMR spectrum of compound **5.4b** (100 MHz, CDCl_3)

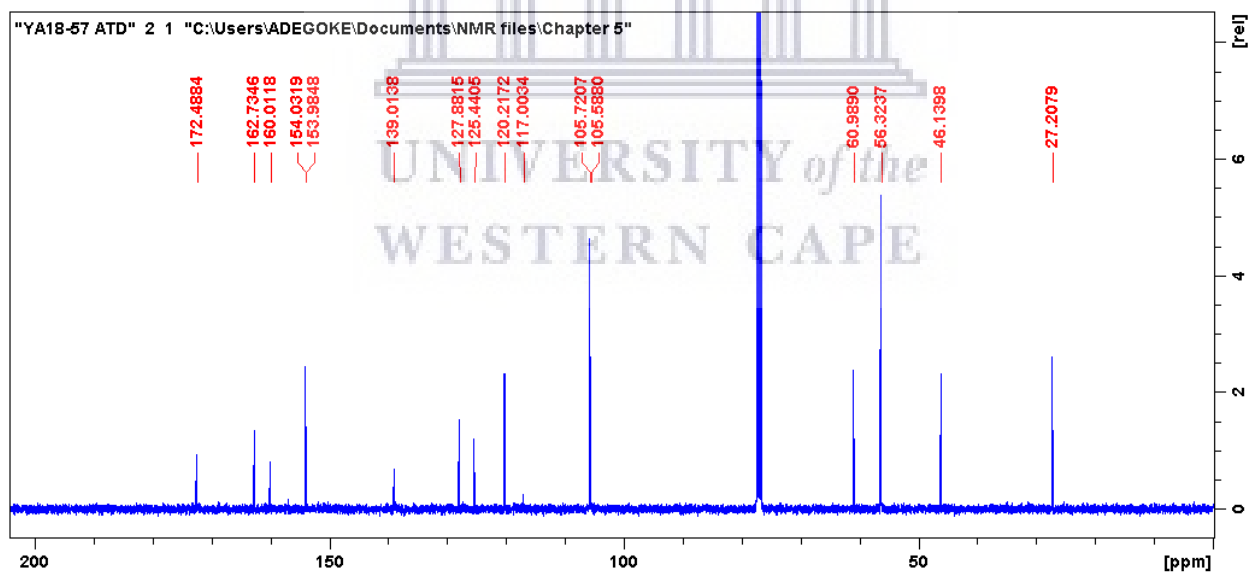


Figure S5.9: HRMS spectrum of compound **5.4b**

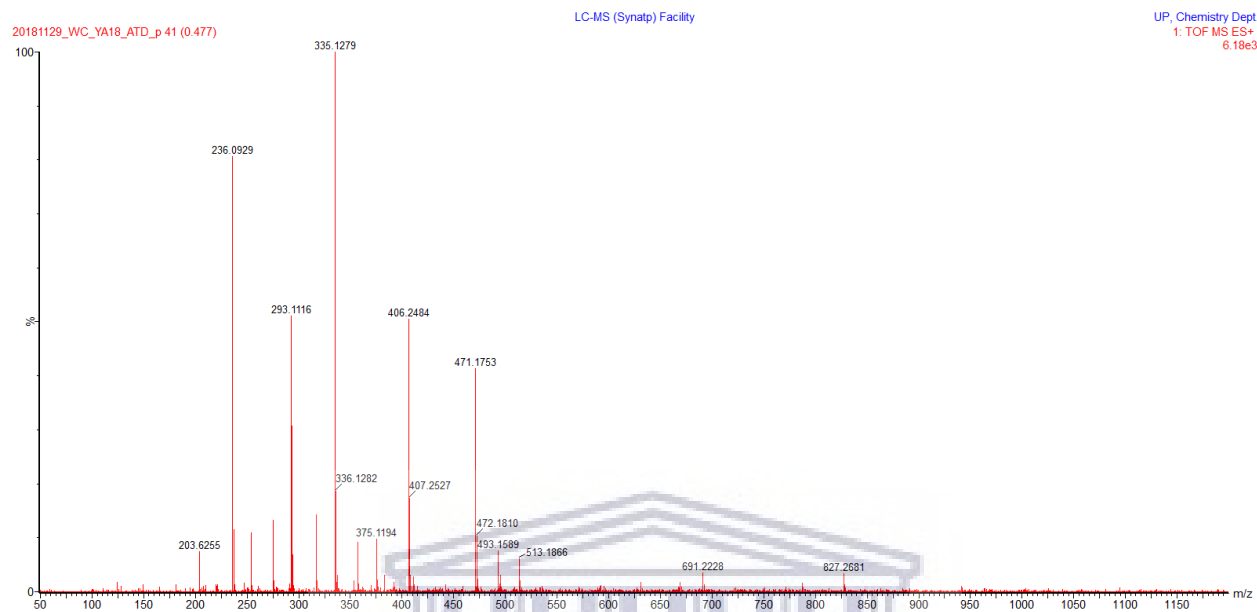


Figure S5.10: IR spectrum of compound **5.4b**

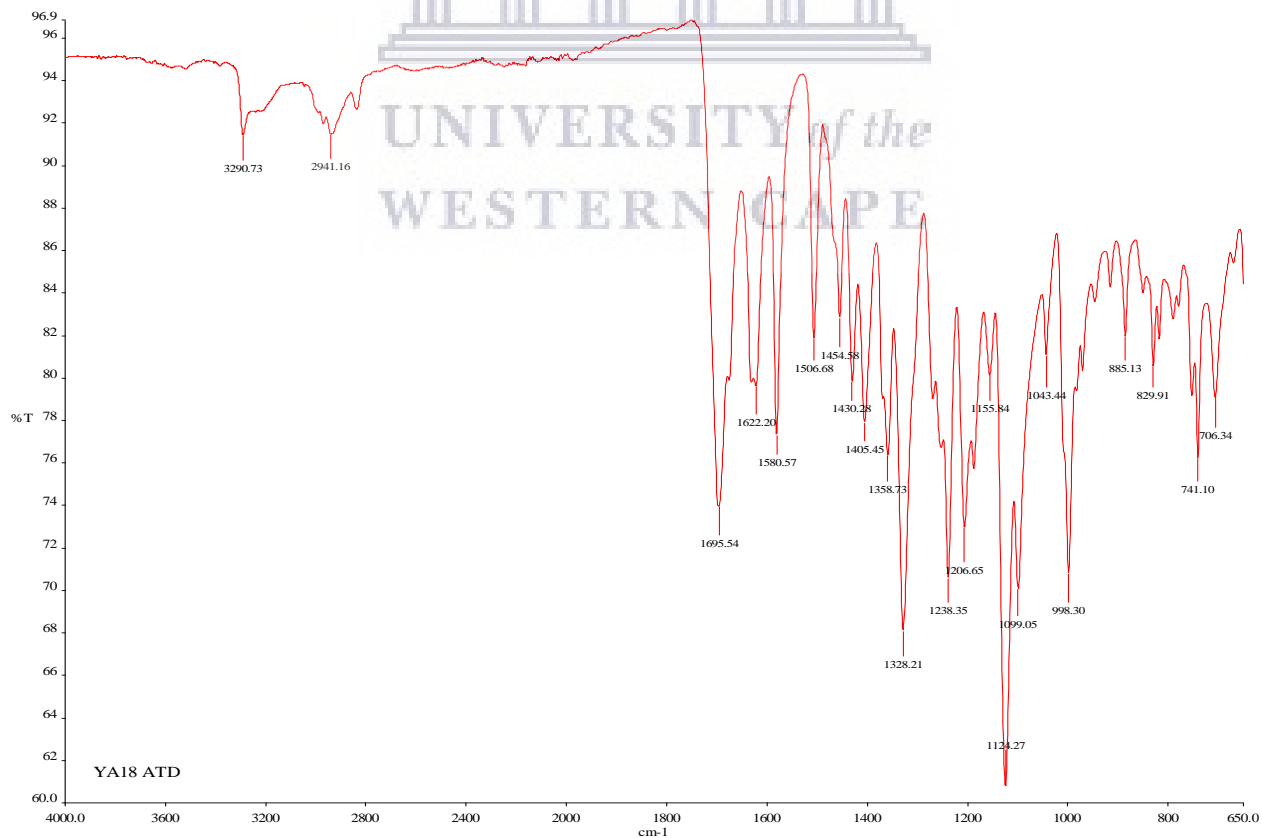


Figure S5.11: DEPT-135 NMR spectrum of compound 5.4c

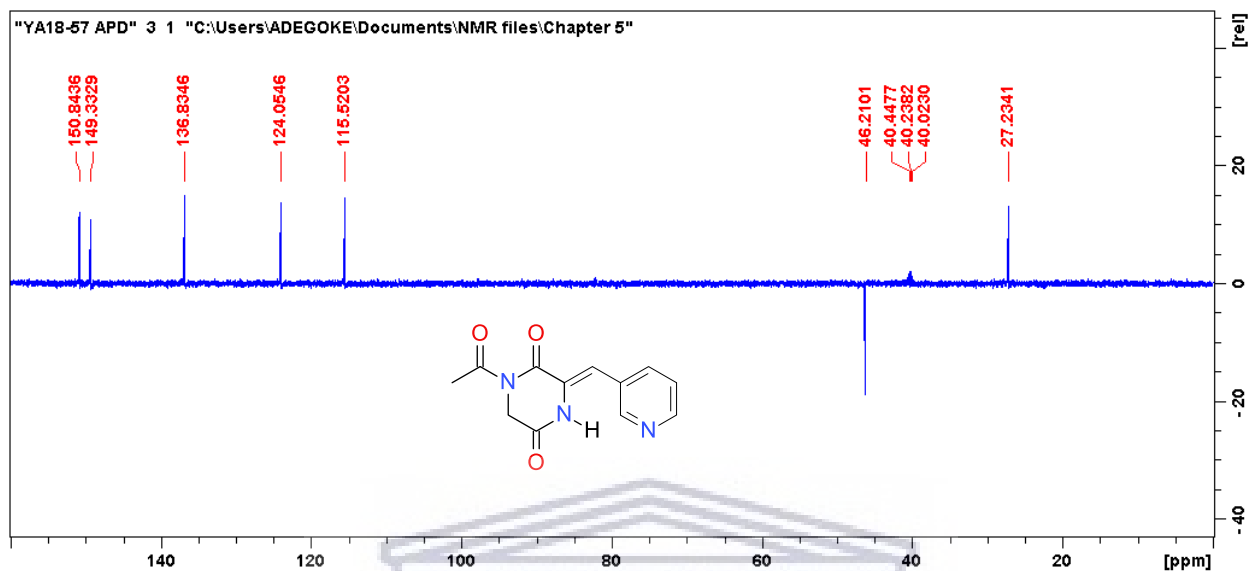


Figure S5.12: COSY NMR spectrum of compound 5.4c

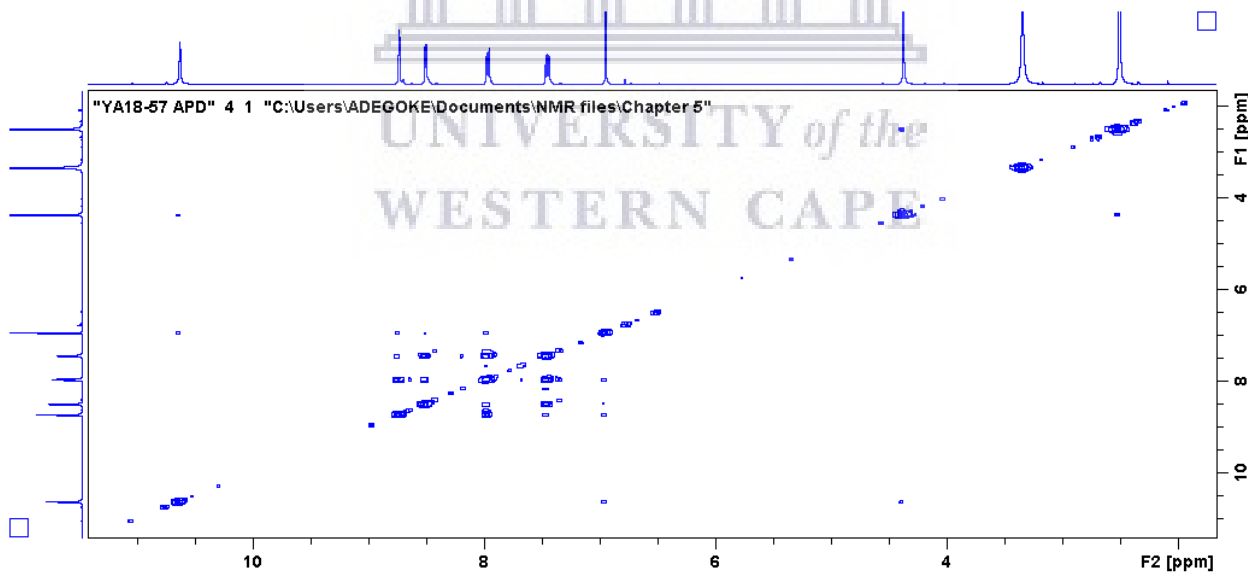


Figure S5.13: HMBC NMR spectrum of compound **5.4c**

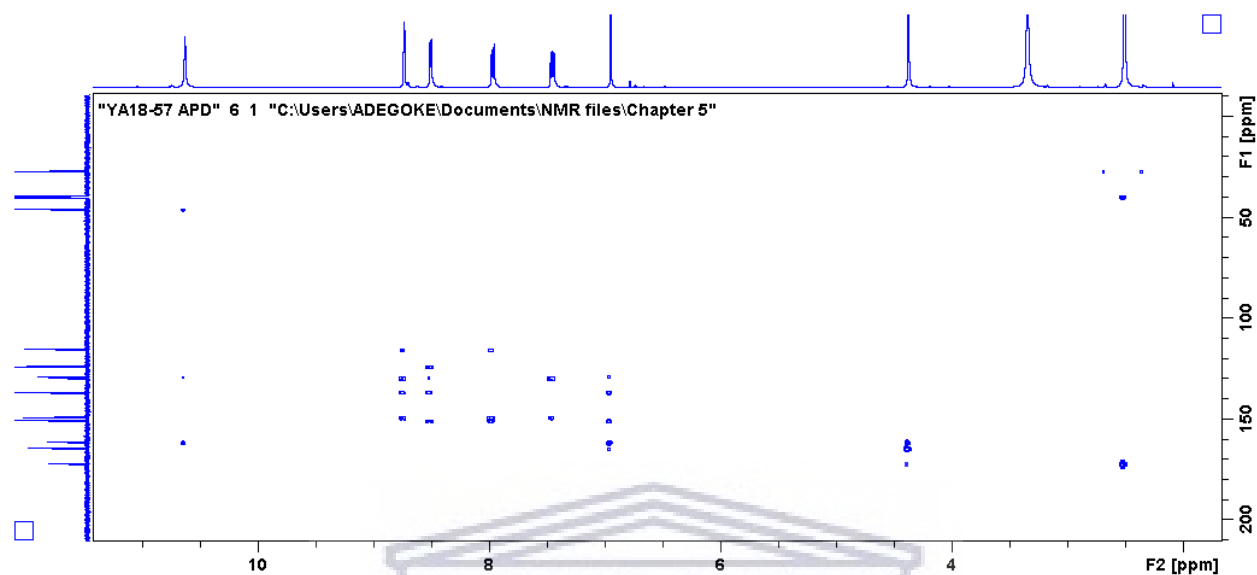


Figure S5.14: HRMS spectrum of compound **5.4c**

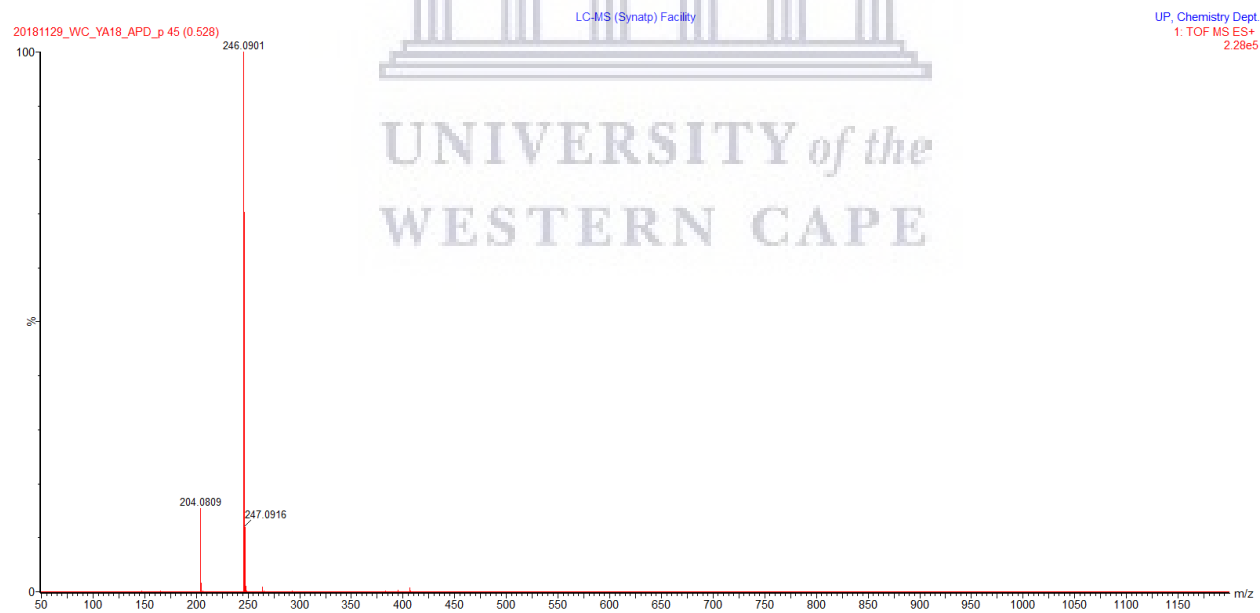
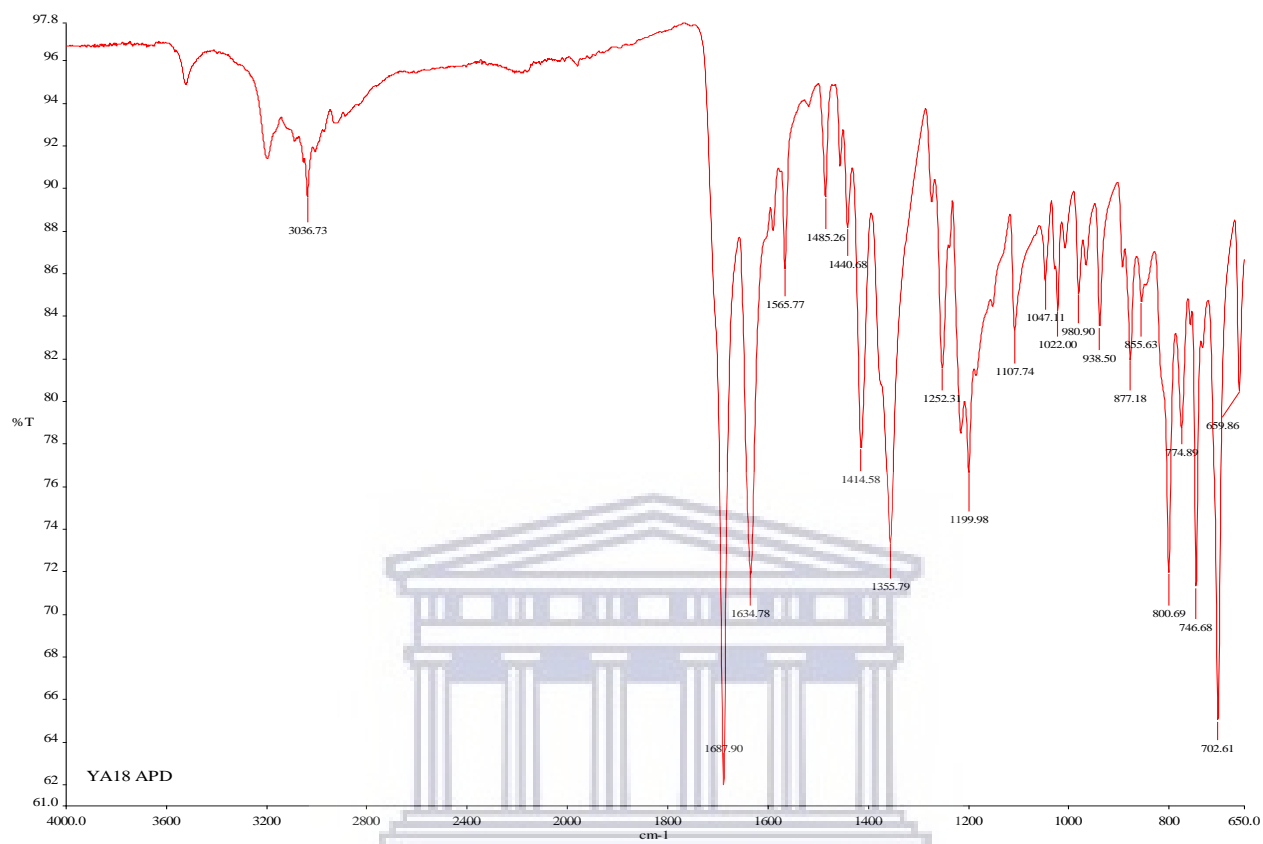


Figure S5.15: IR spectrum of compound **5.4c**



UNIVERSITY of the
WESTERN CAPE

Figure S5.16: ^1H NMR spectrum of compound **5.4d** (400 MHz, DMSO-d_6)

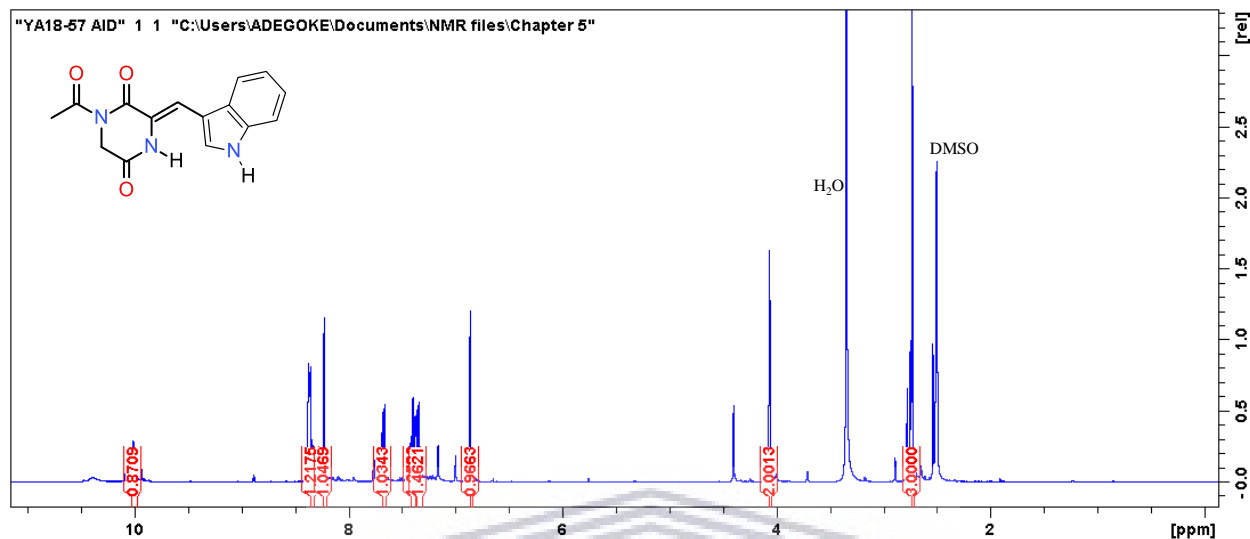


Figure S5.17: ^{13}C NMR spectrum of compound **5.4d** (100 MHz, DMSO-d_6)

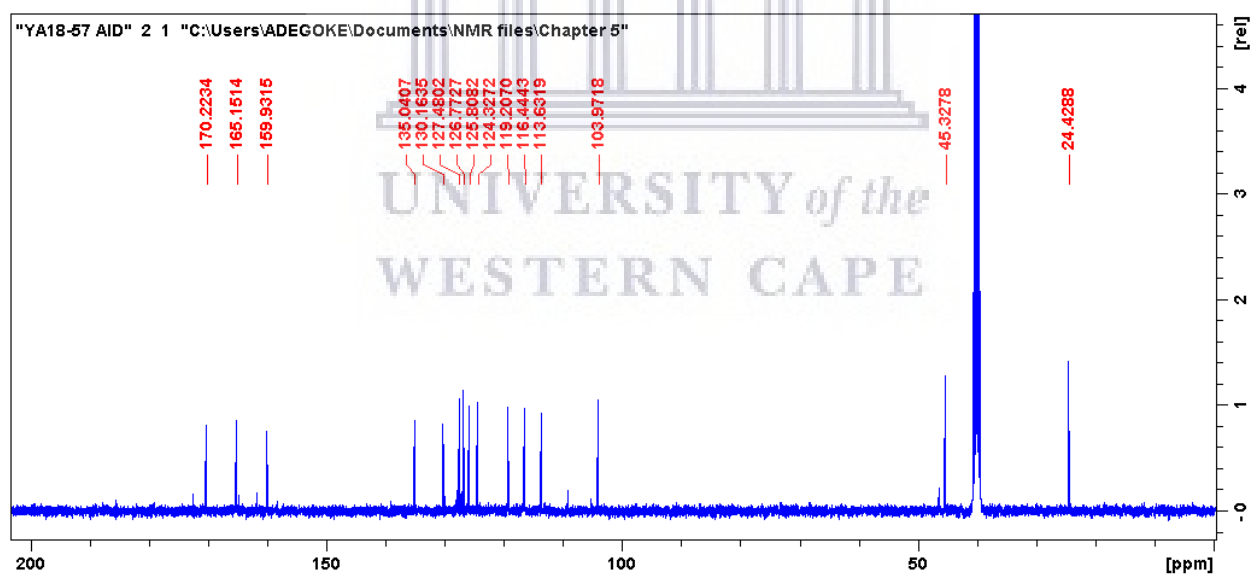


Figure S5.18: HRMS spectrum of compound **5.4d**

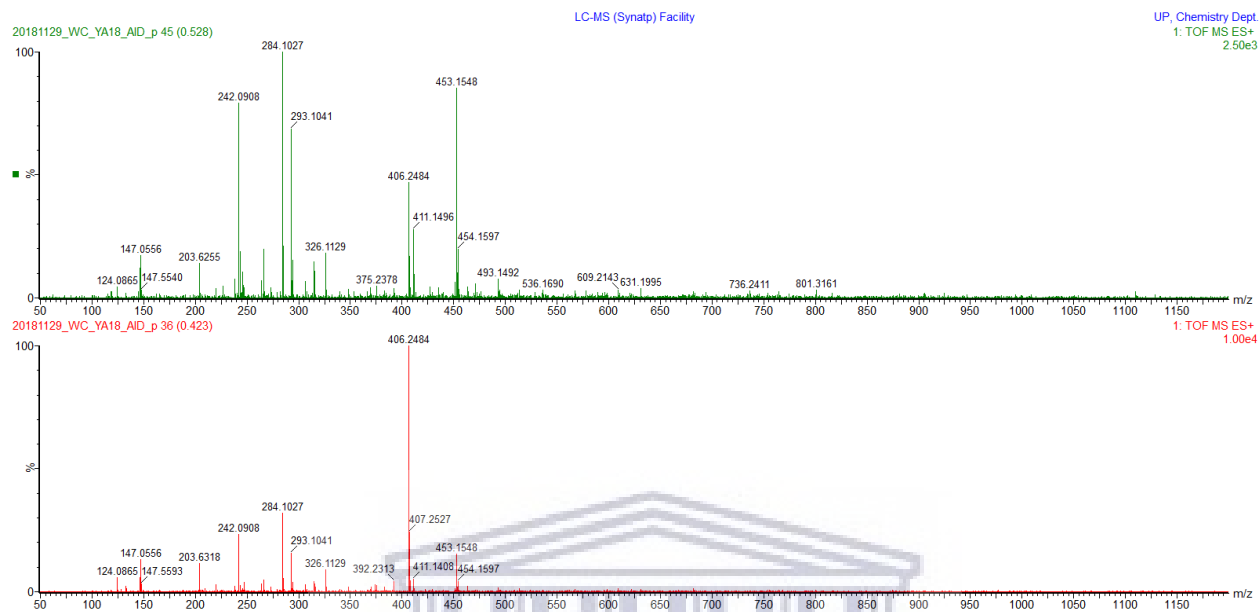


Figure S5.19: IR spectrum of compound **5.4d**

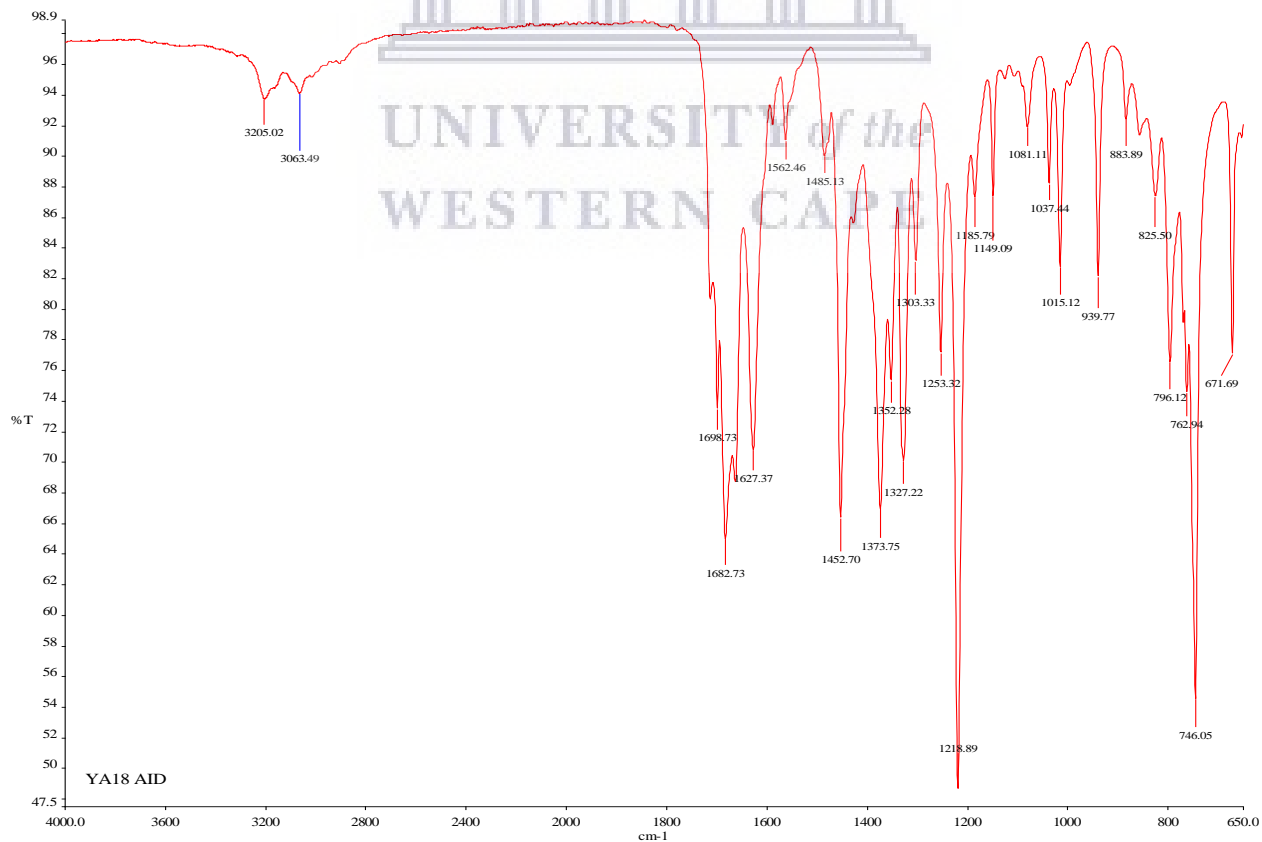


Figure S5.20: ^1H NMR spectrum of compound **5.4e** (400 MHz, CDCl_3)

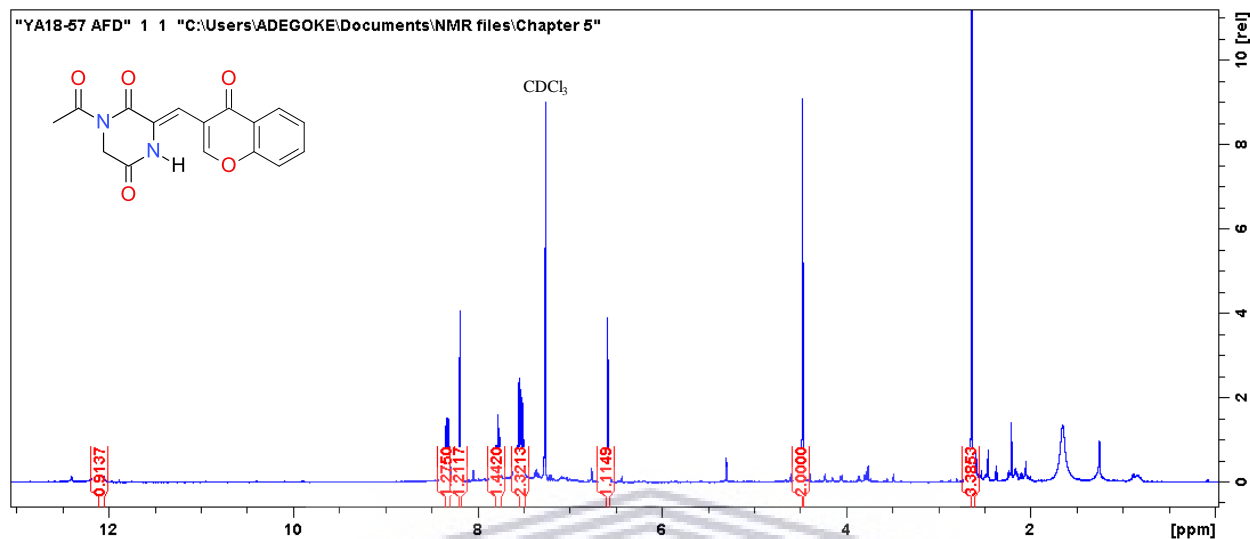


Figure S5.21: ^{13}C NMR spectrum of compound **5.4e** (100 MHz, CDCl_3)

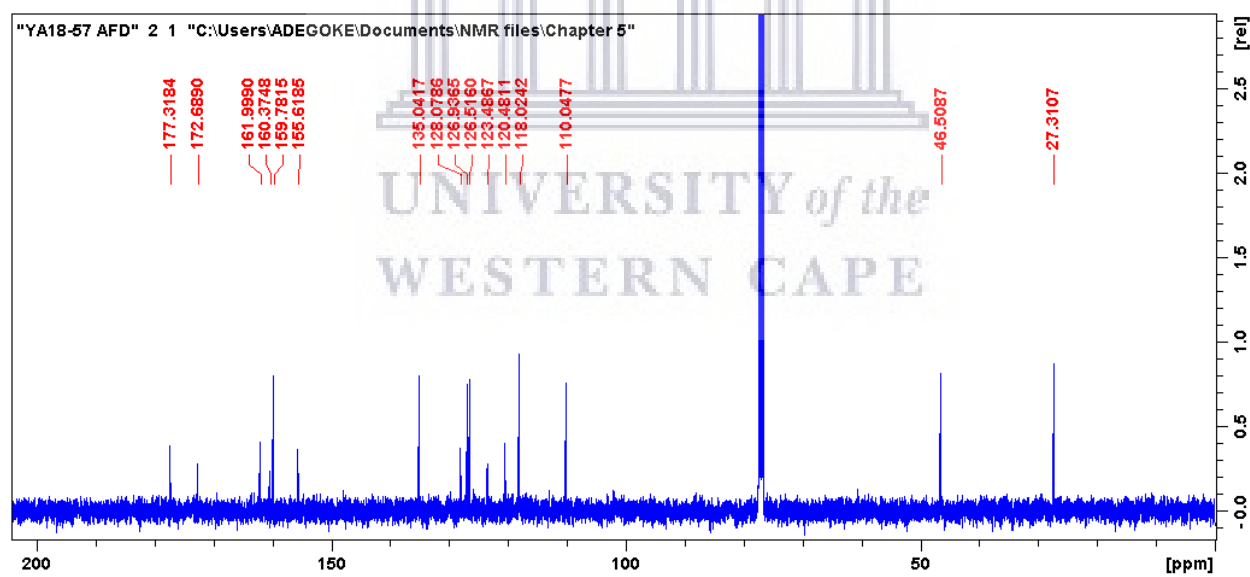


Figure S5.22: HRMS spectrum of compound **5.4e**

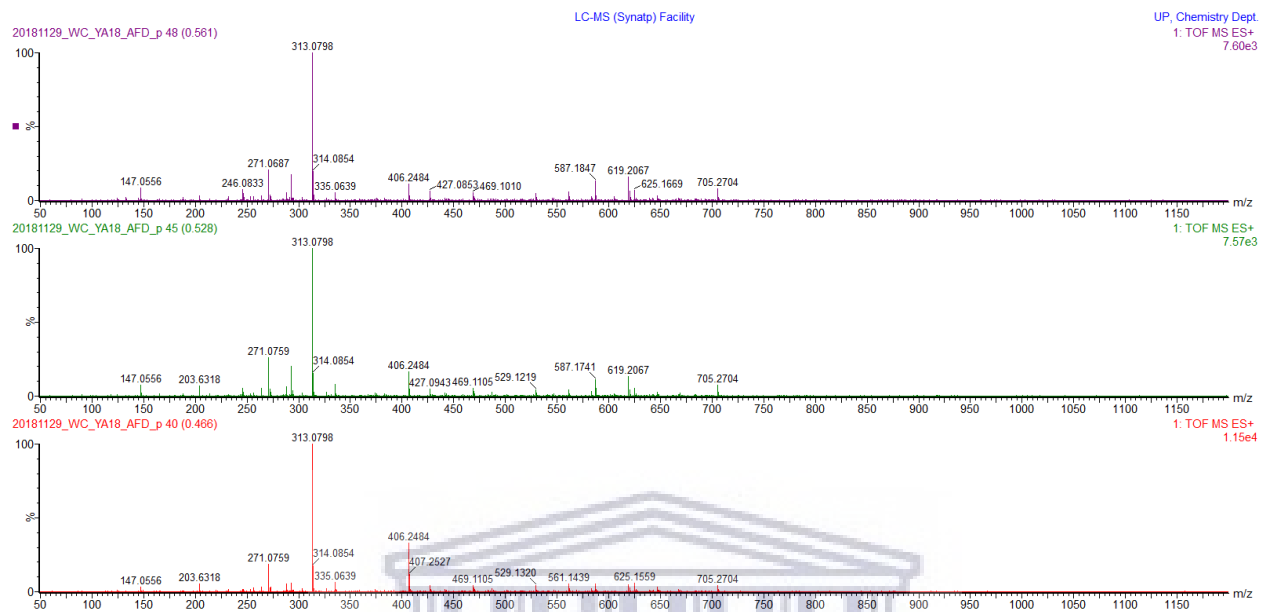


Figure S5.23: IR spectrum of compound **5.4e**

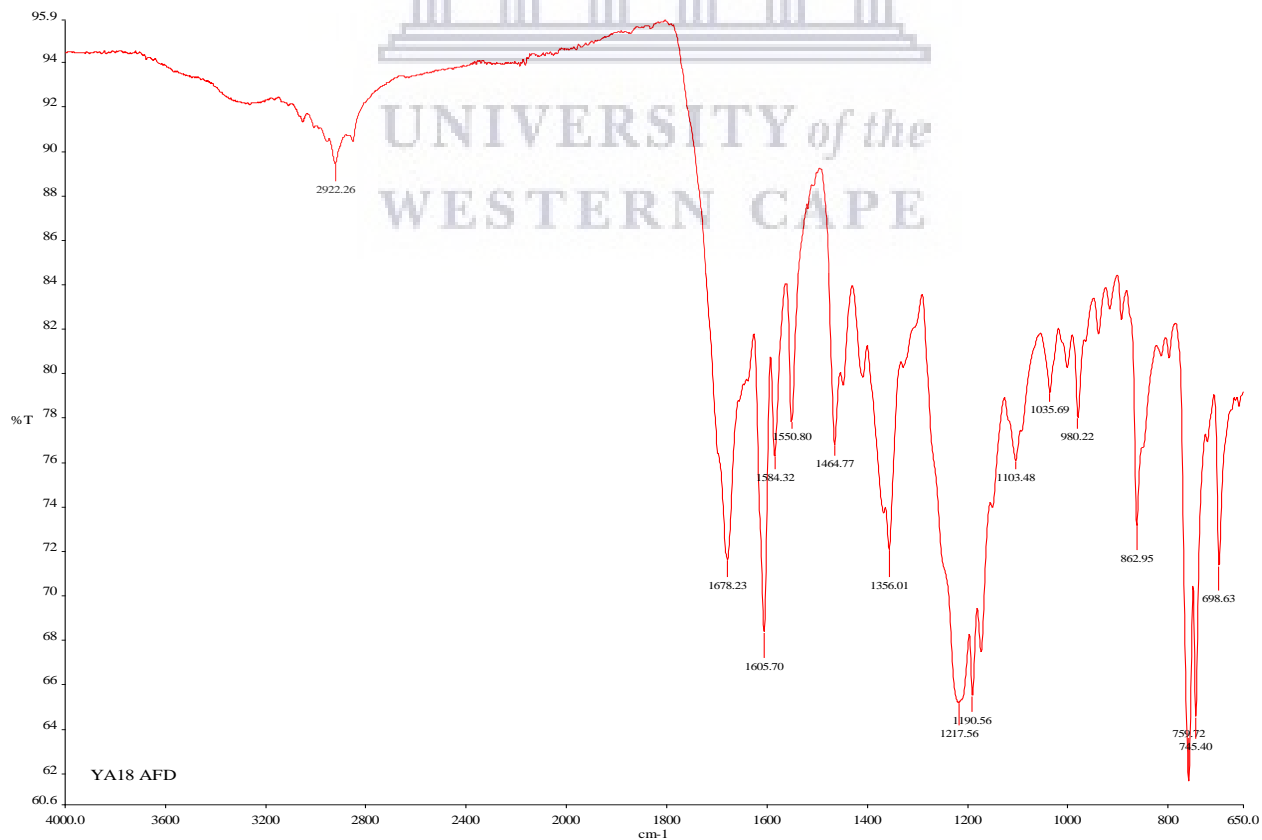


Figure S5.24: ^1H NMR spectrum of compound **5.4f** (400 MHz, CDCl_3)

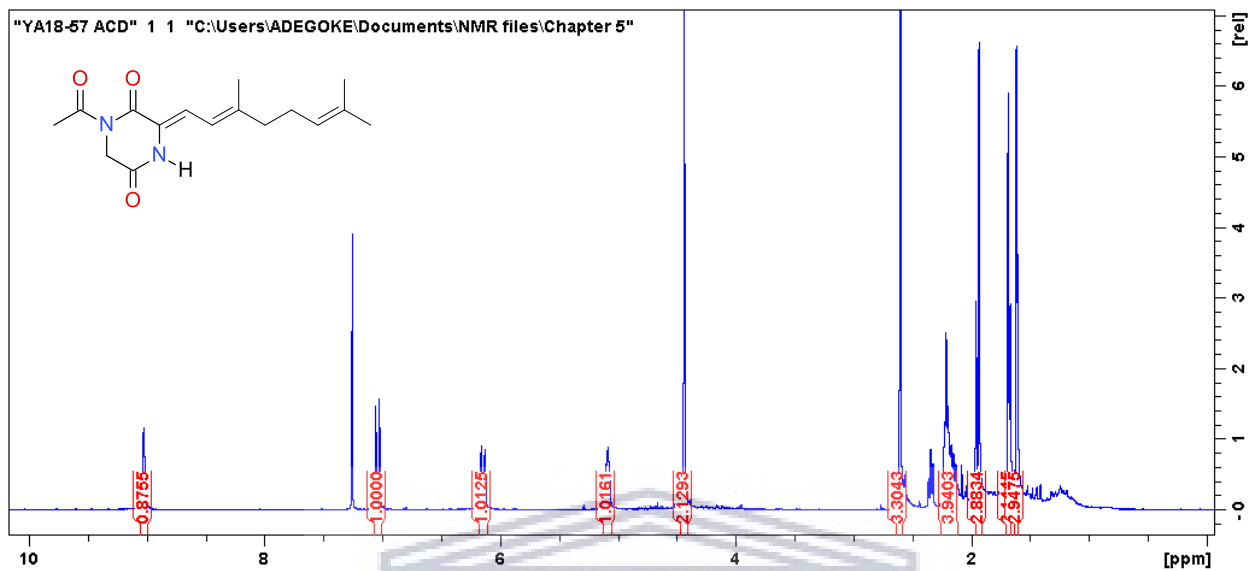


Figure S5.25: ^{13}C NMR spectrum of compound **5.4f** (100 MHz, CDCl_3)

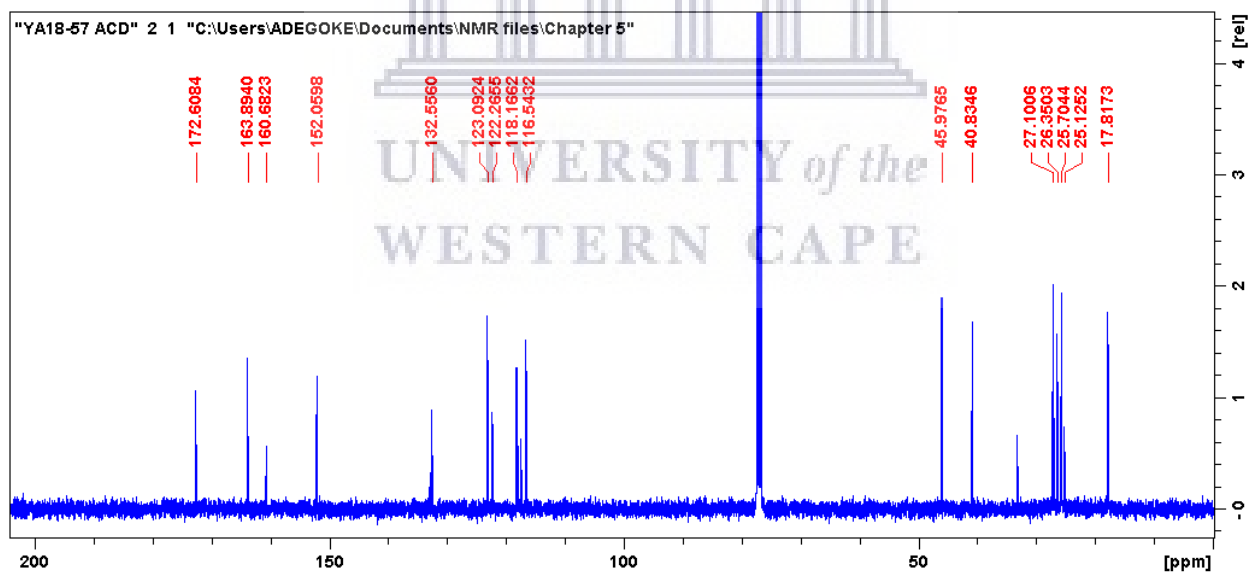


Figure S5.26: HRMS spectrum of compound 5.4f

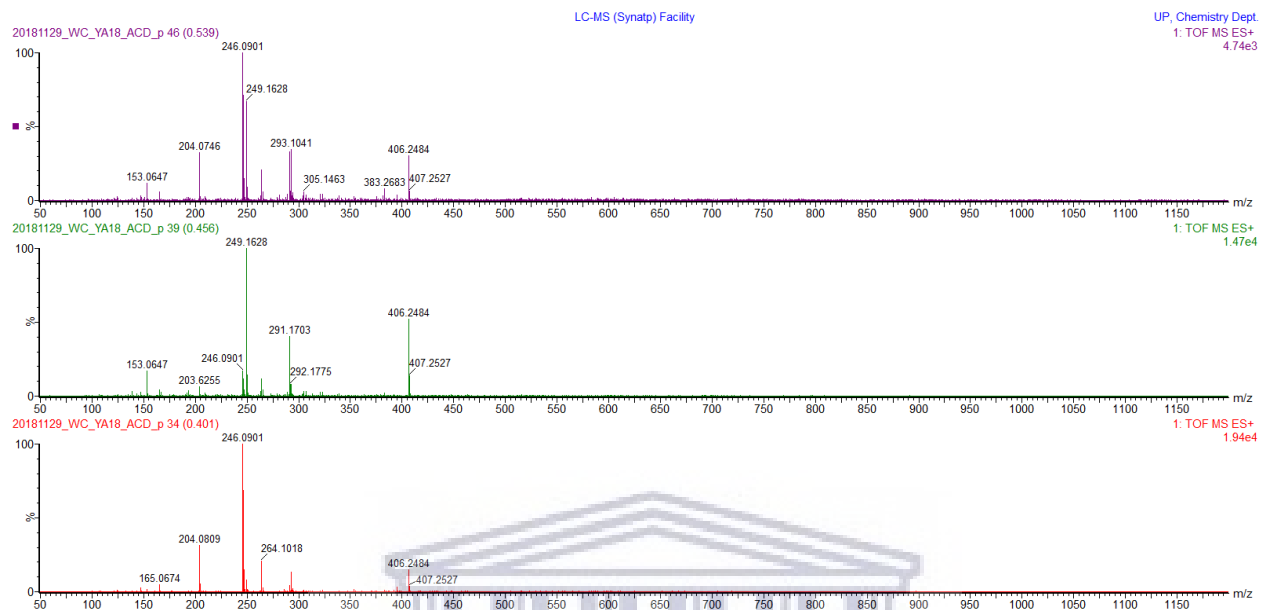
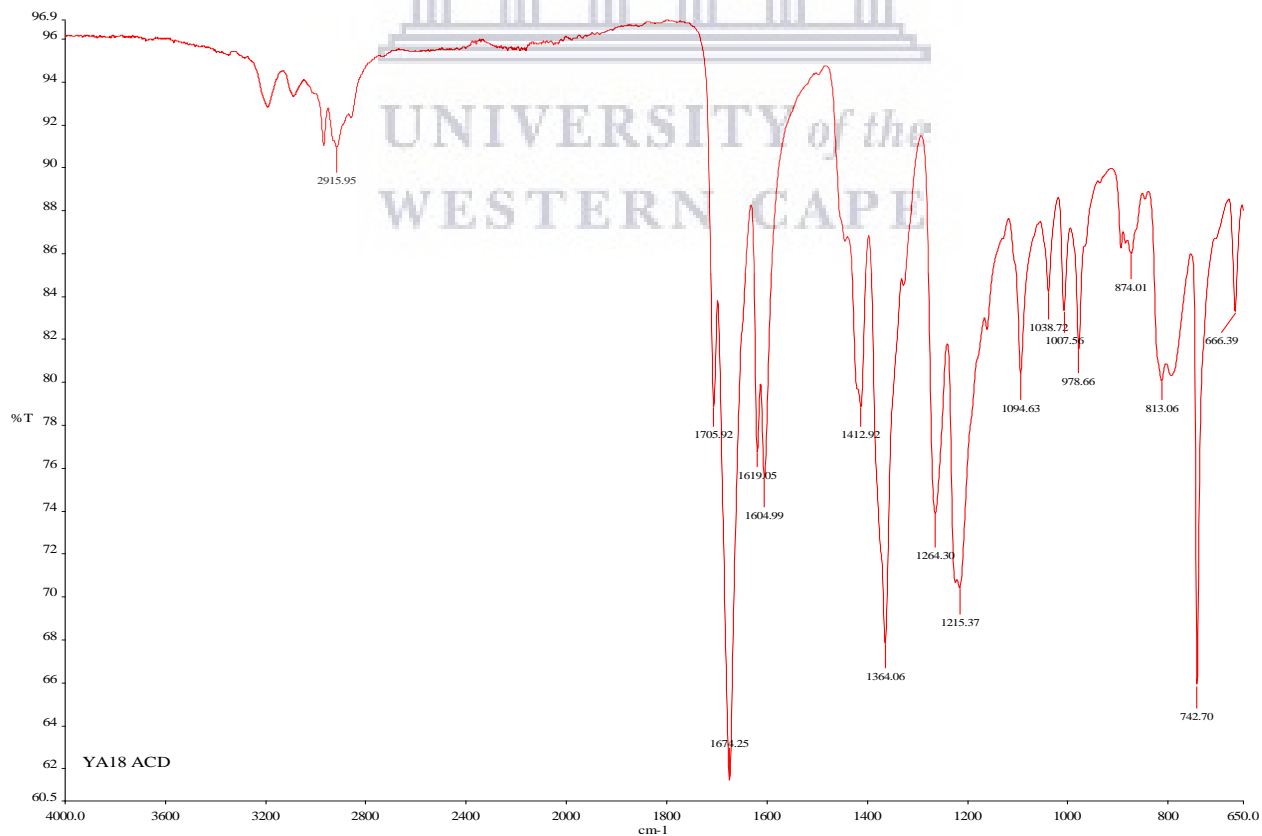


Figure S5.27: IR spectrum of compound 5.4f



Barbituric acid derivatives 5.6(a-f)

Figure S5.28: ^1H NMR spectrum of compound 5.6a (400 MHz, DMSO- d_6)

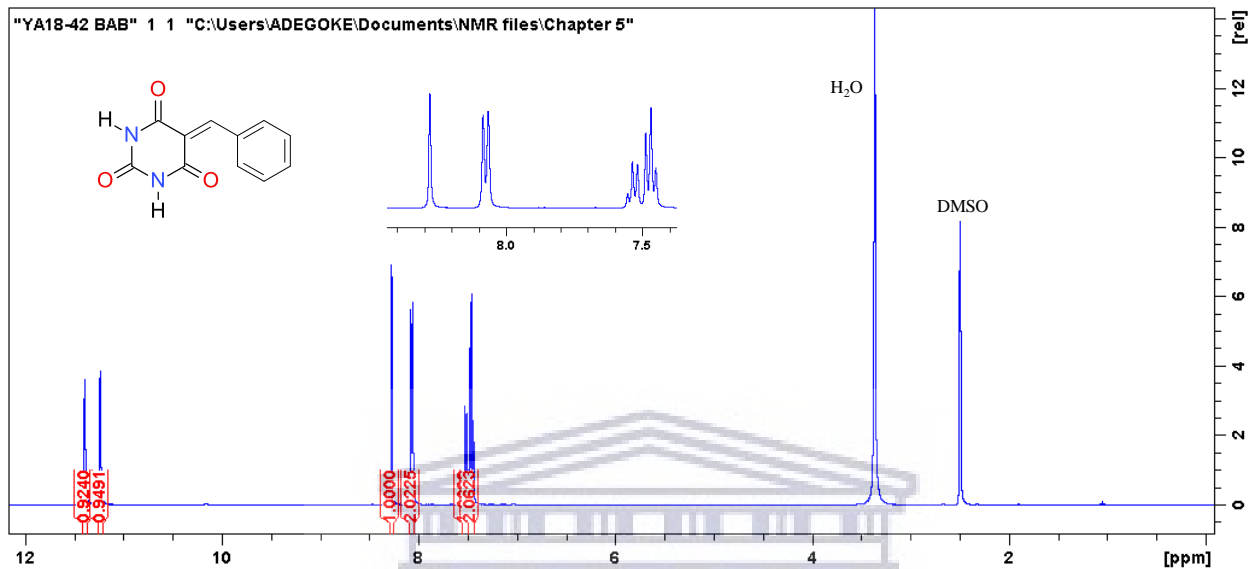


Figure S5.29: ^{13}C NMR spectrum of compound 5.6a (100 MHz, DMSO- d_6)

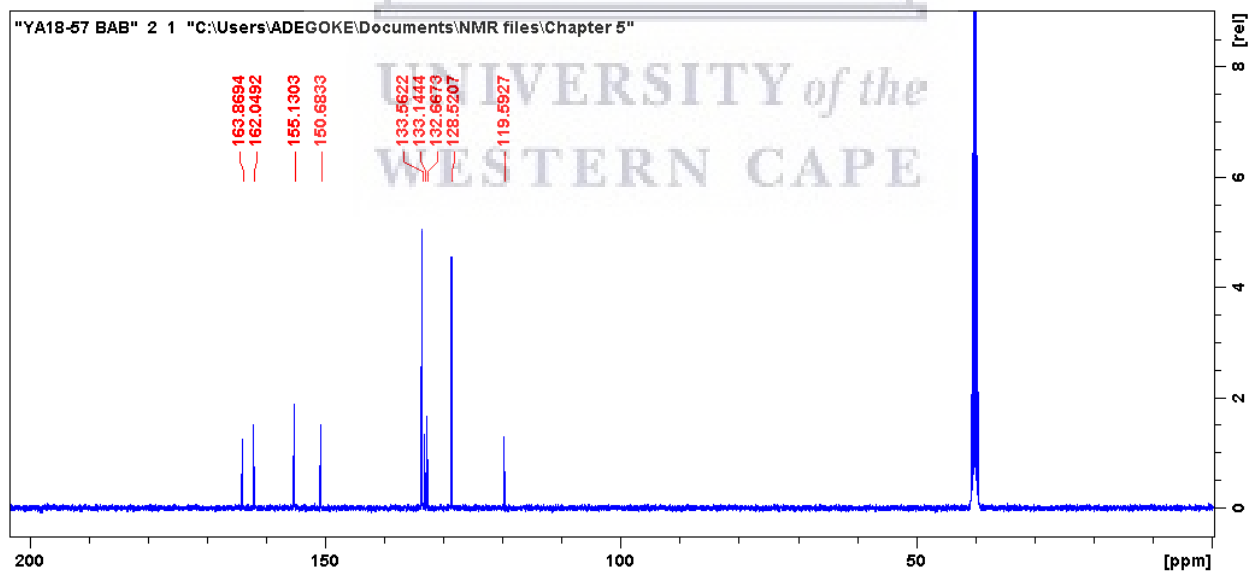


Figure S5.30: HRMS spectrum of compound **5.6a**

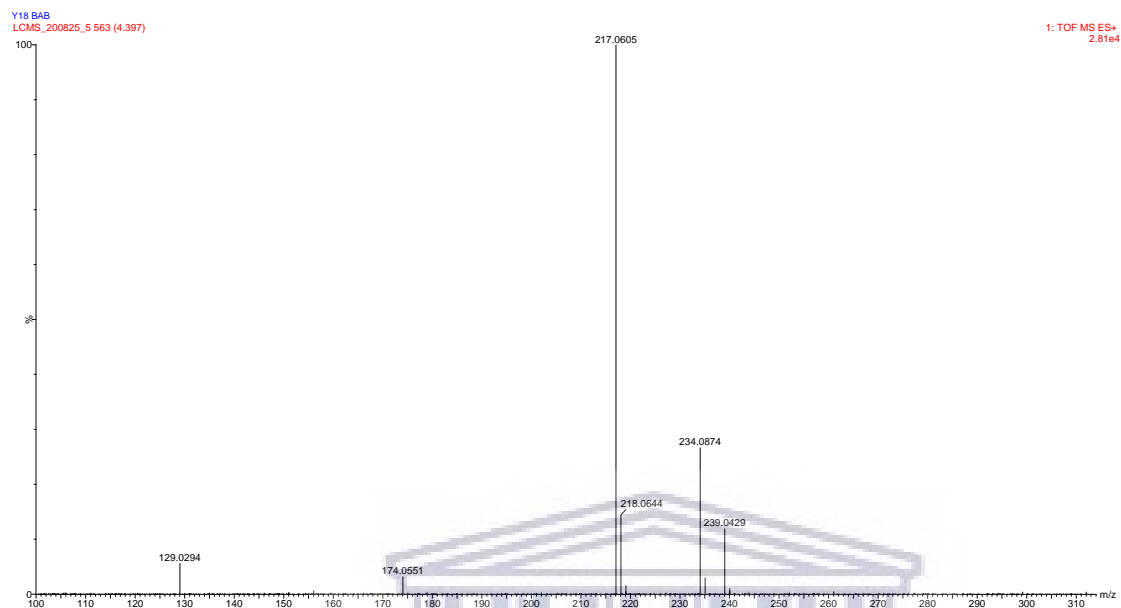


Figure S5.31: IR spectrum of compound **5.6a**

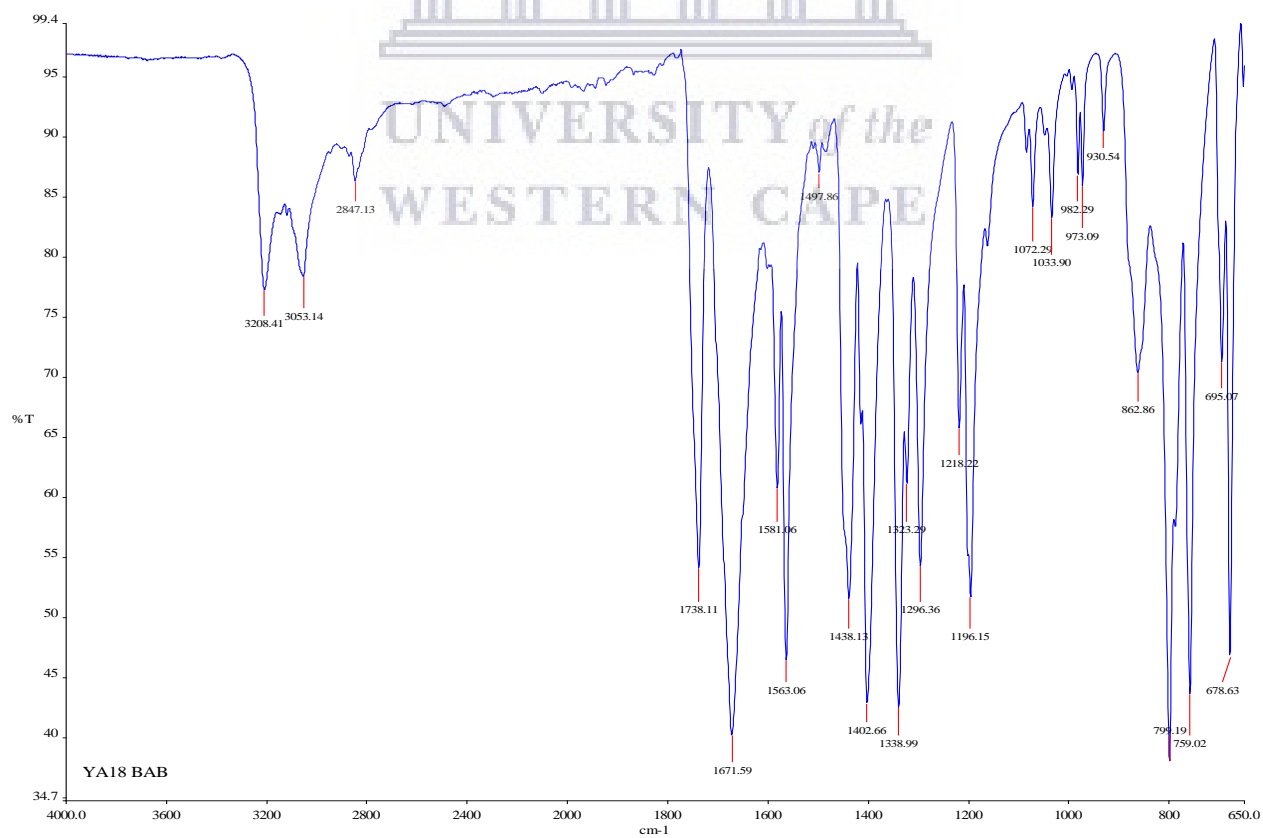


Figure S5.32: ^1H NMR spectrum of compound **5.6b** (400 MHz, DMSO- d_6)

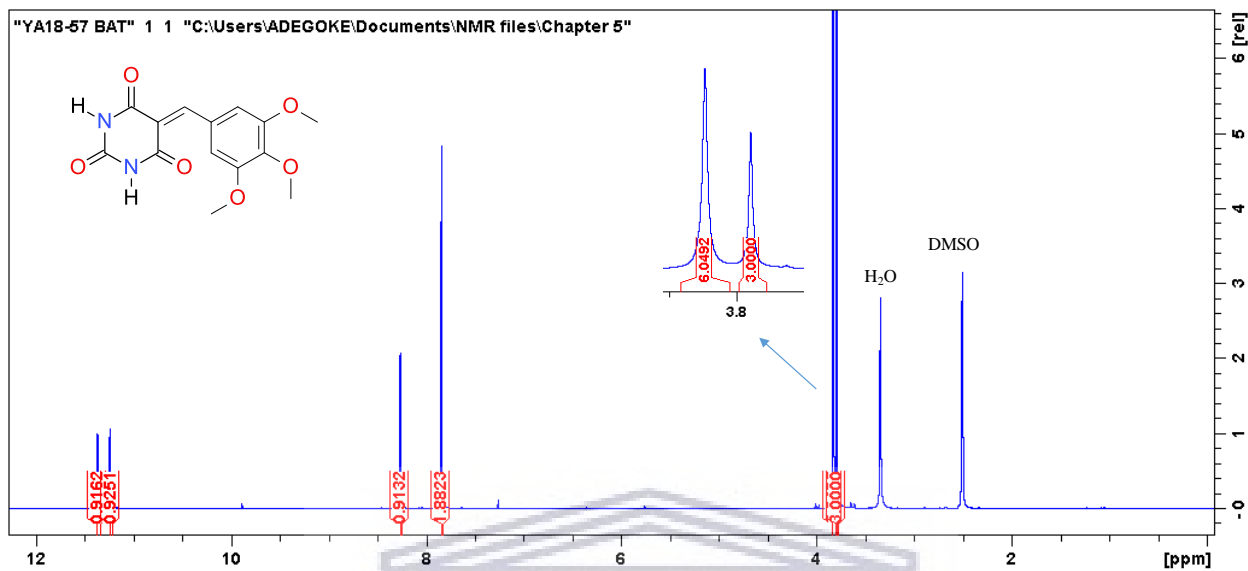


Figure S5.33: ^{13}C NMR spectrum of compound **5.6b** (100 MHz, DMSO- d_6)

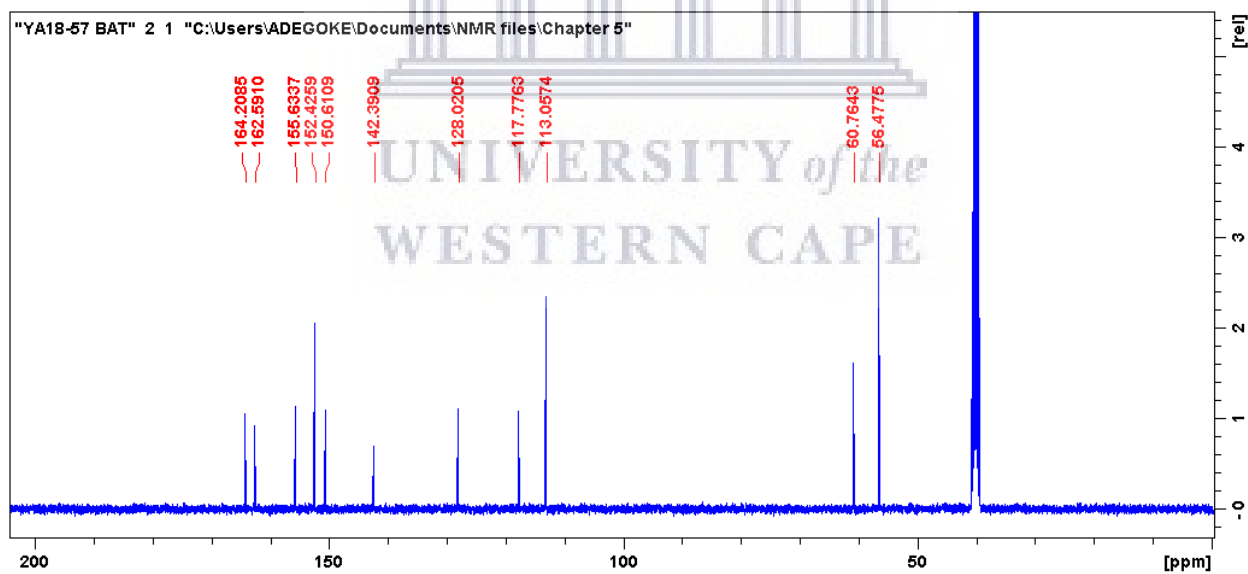


Figure S5.34: HRMS spectrum of compound **5.6b**

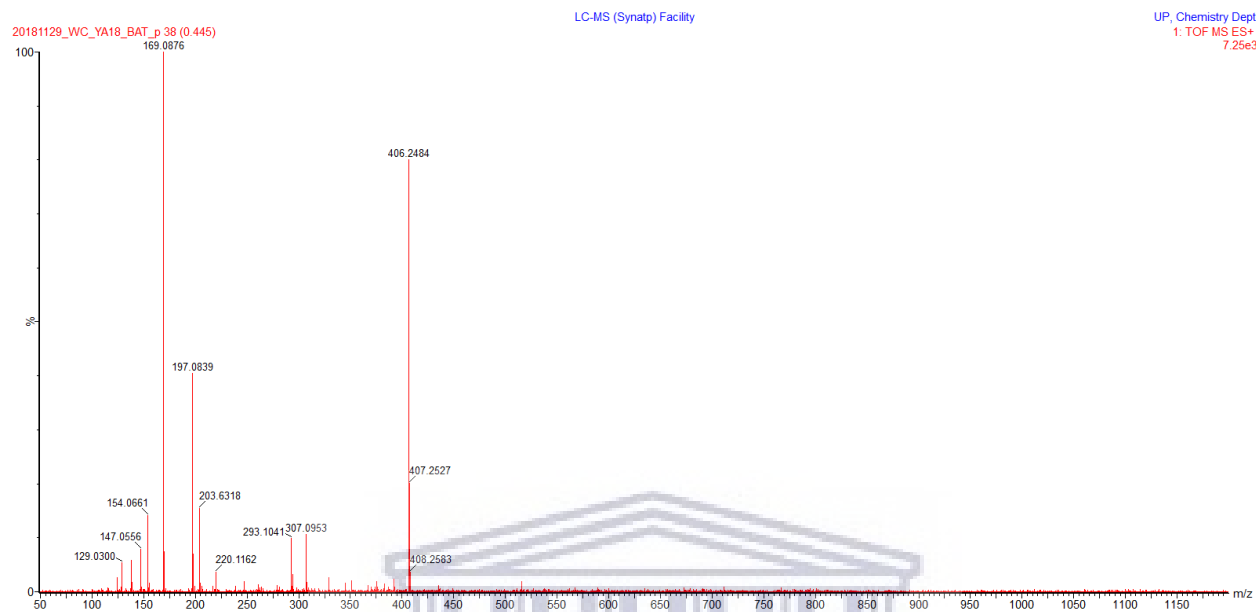


Figure S5.35: IR spectrum of compound **5.6b**

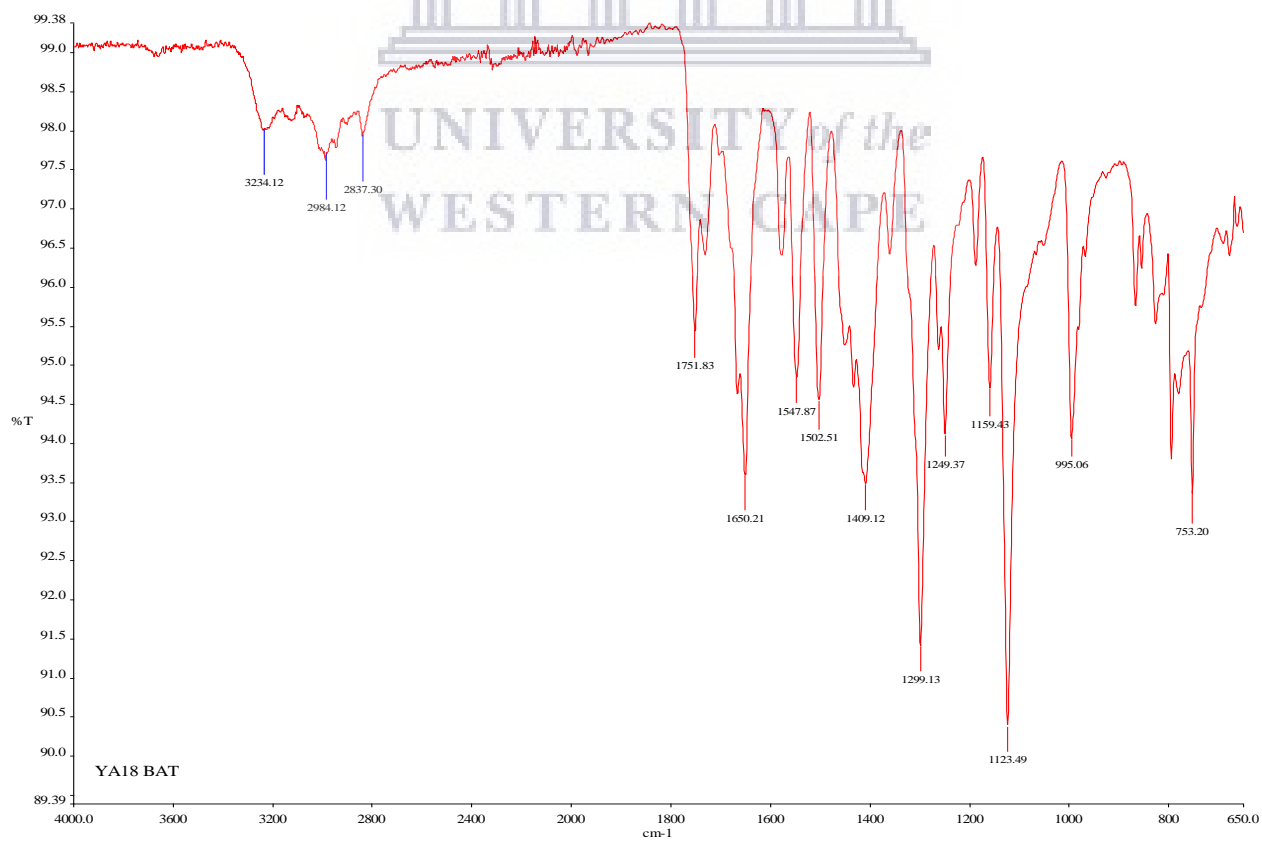


Figure S5.36: ^1H NMR spectrum of compound **5.6c** (400 MHz, DMSO-d_6)

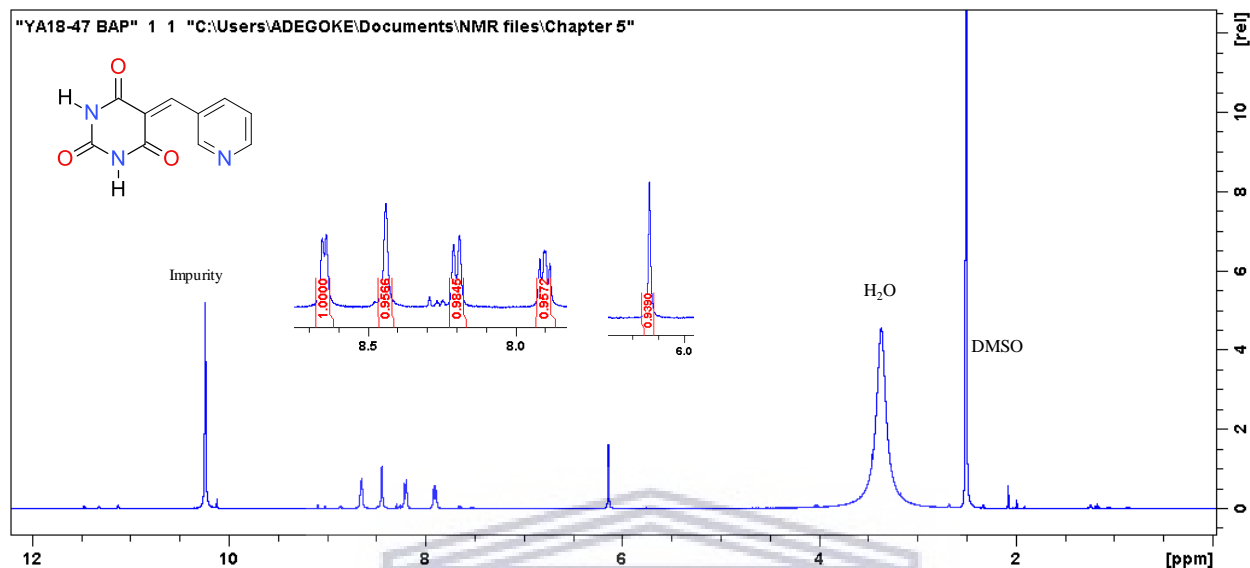


Figure S5.37: ^{13}C NMR spectrum of compound **5.6c** (100 MHz, DMSO-d_6)

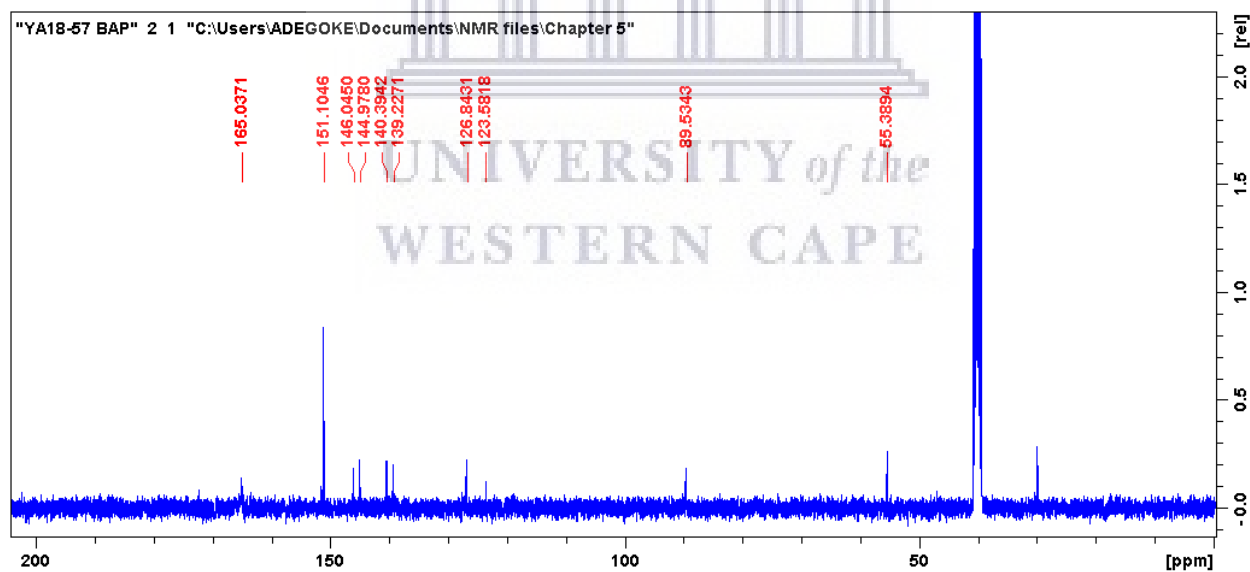


Figure S5.38: HRMS spectrum of compound 5.6c

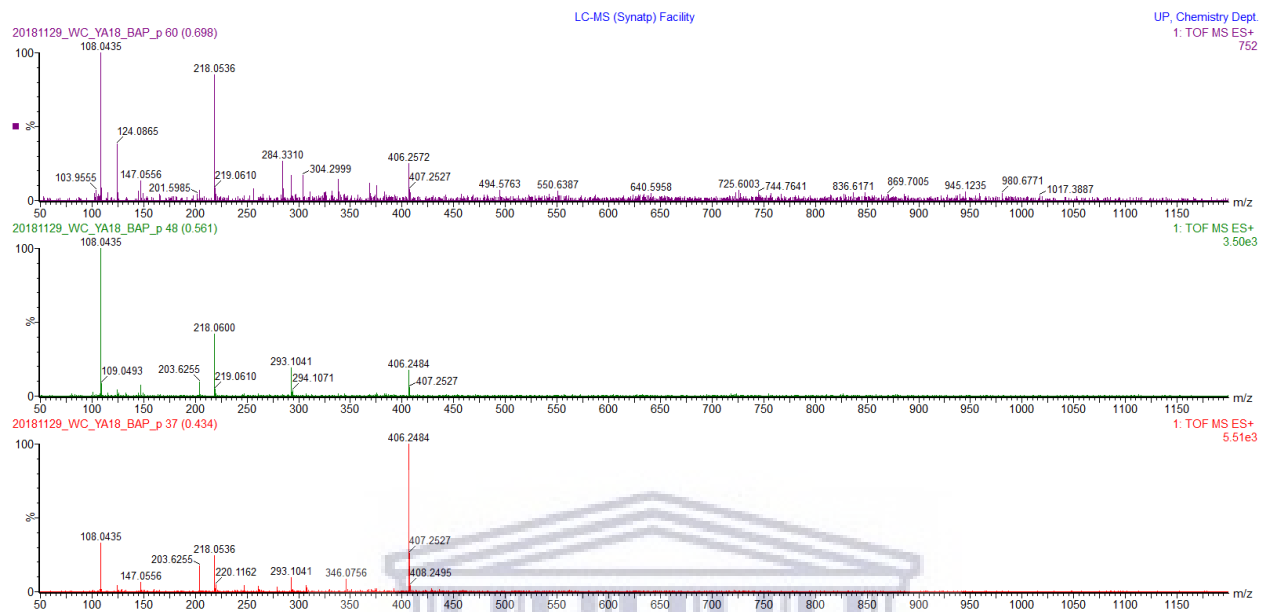


Figure S5.39: IR spectrum of compound 5.6c

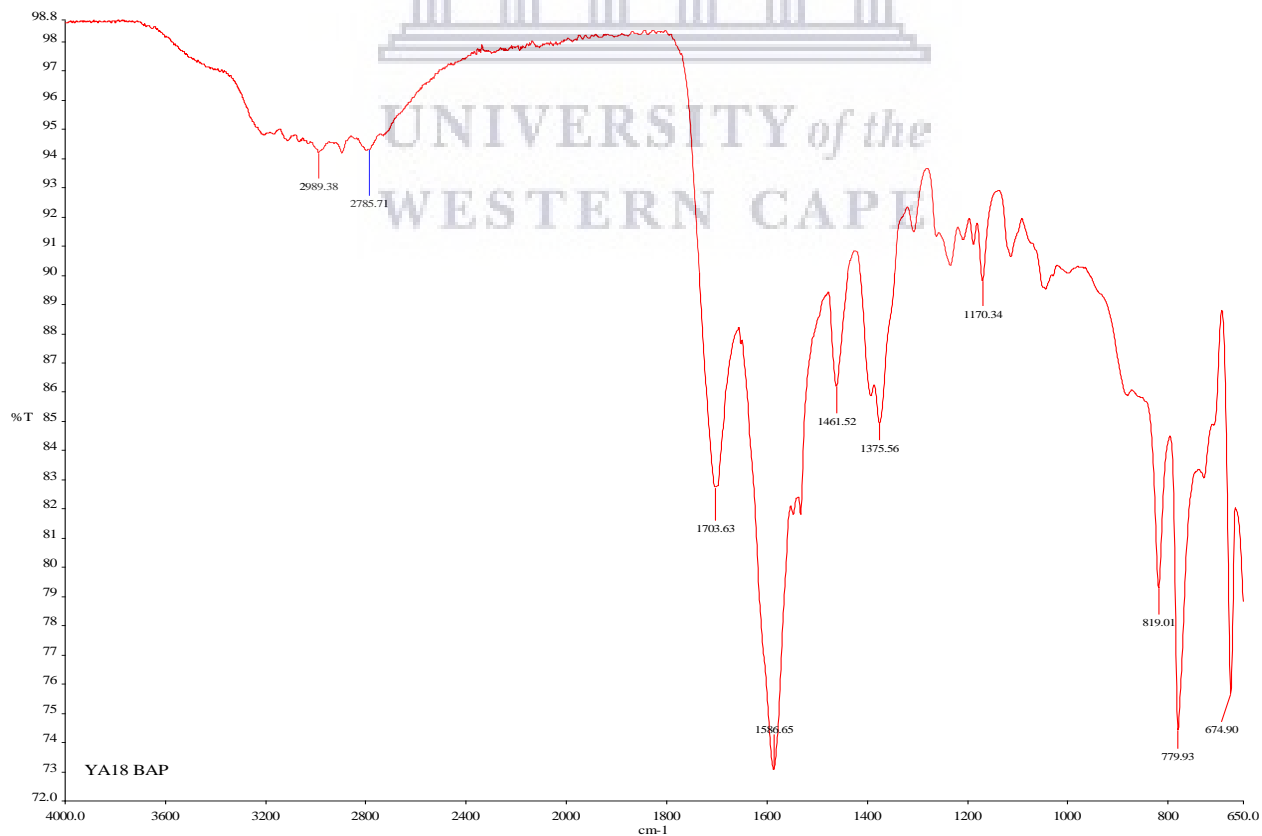


Figure S5.40: ^1H NMR spectrum of compound **5.6d** (400 MHz, DMSO-d_6)

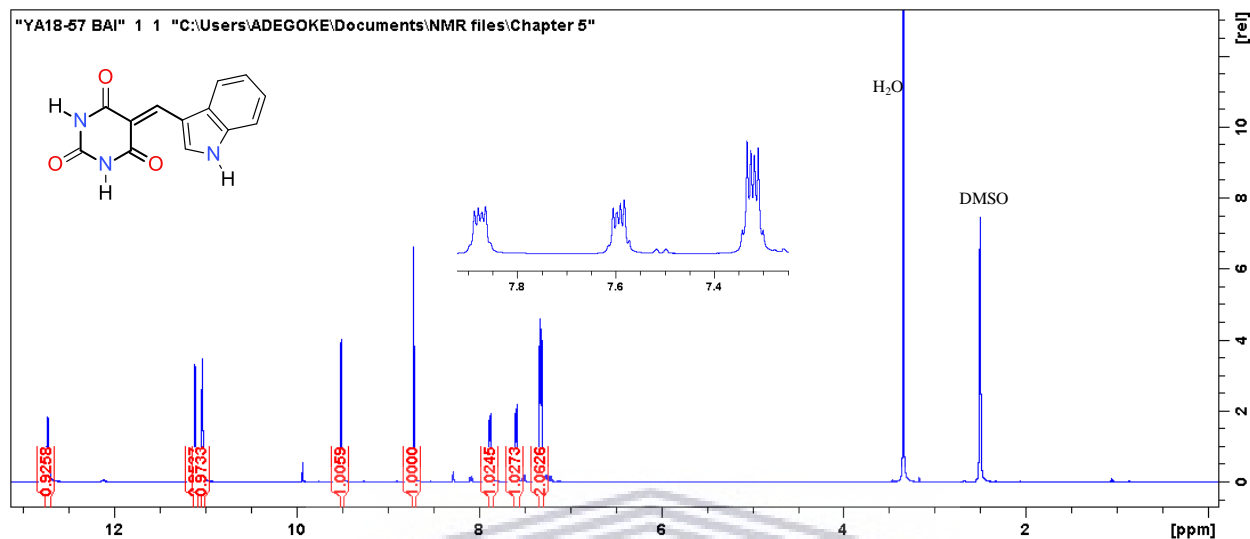


Figure S5.41: ^{13}C NMR spectrum of compound **5.6d** (100 MHz, DMSO-d_6)

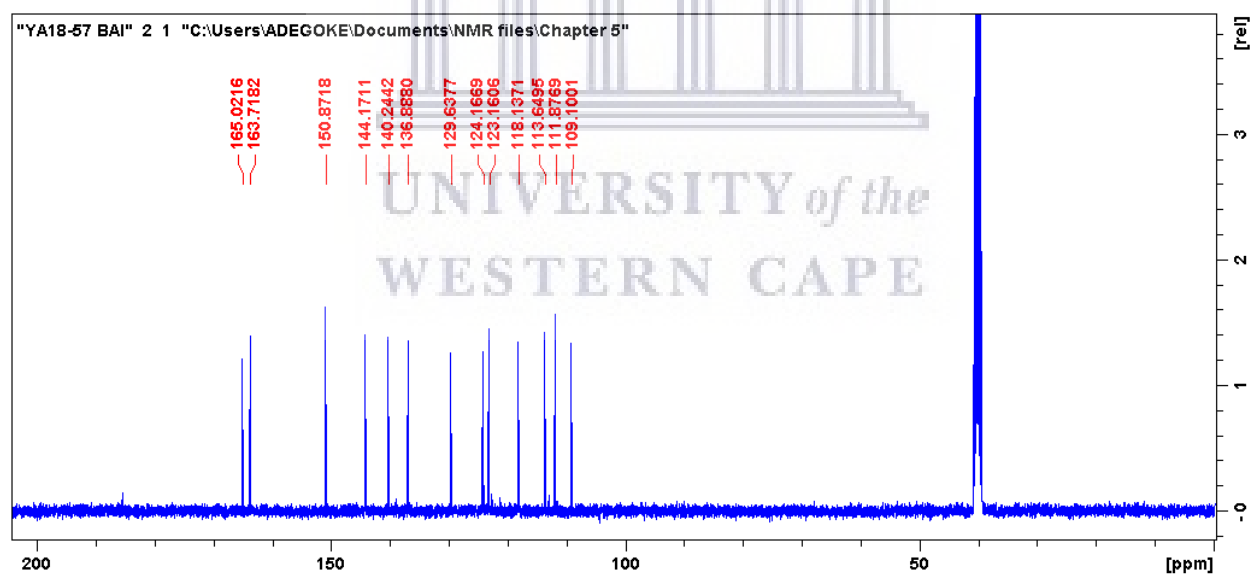


Figure S5.42: HRMS spectrum of compound **5.6d**

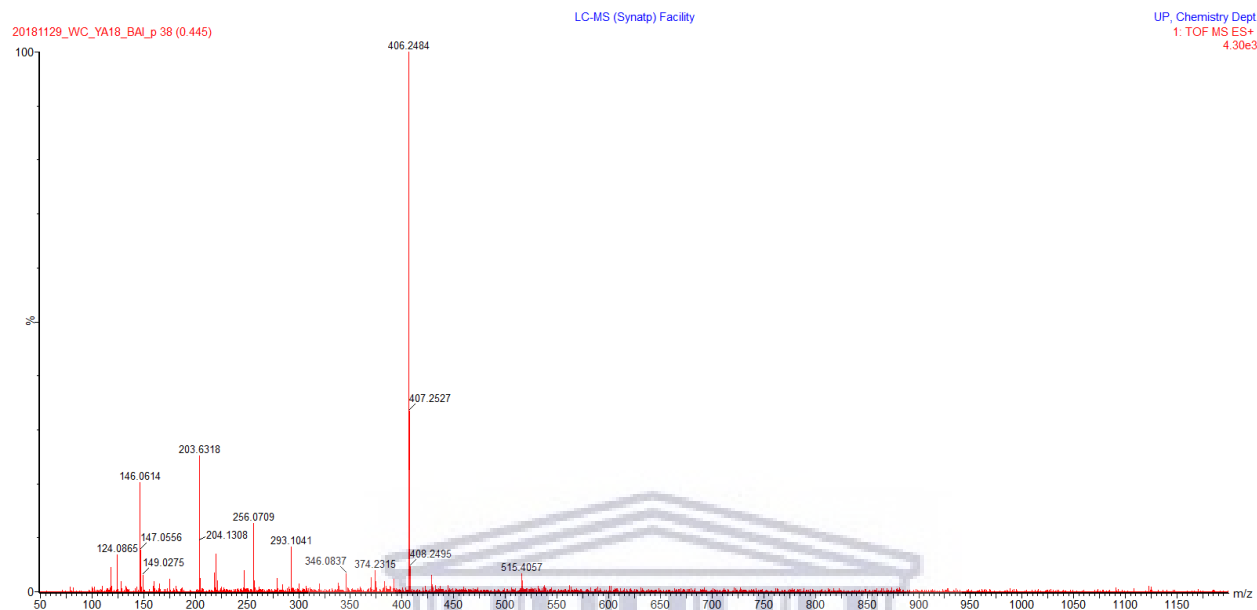


Figure S5.43: IR spectrum of compound **5.6d**

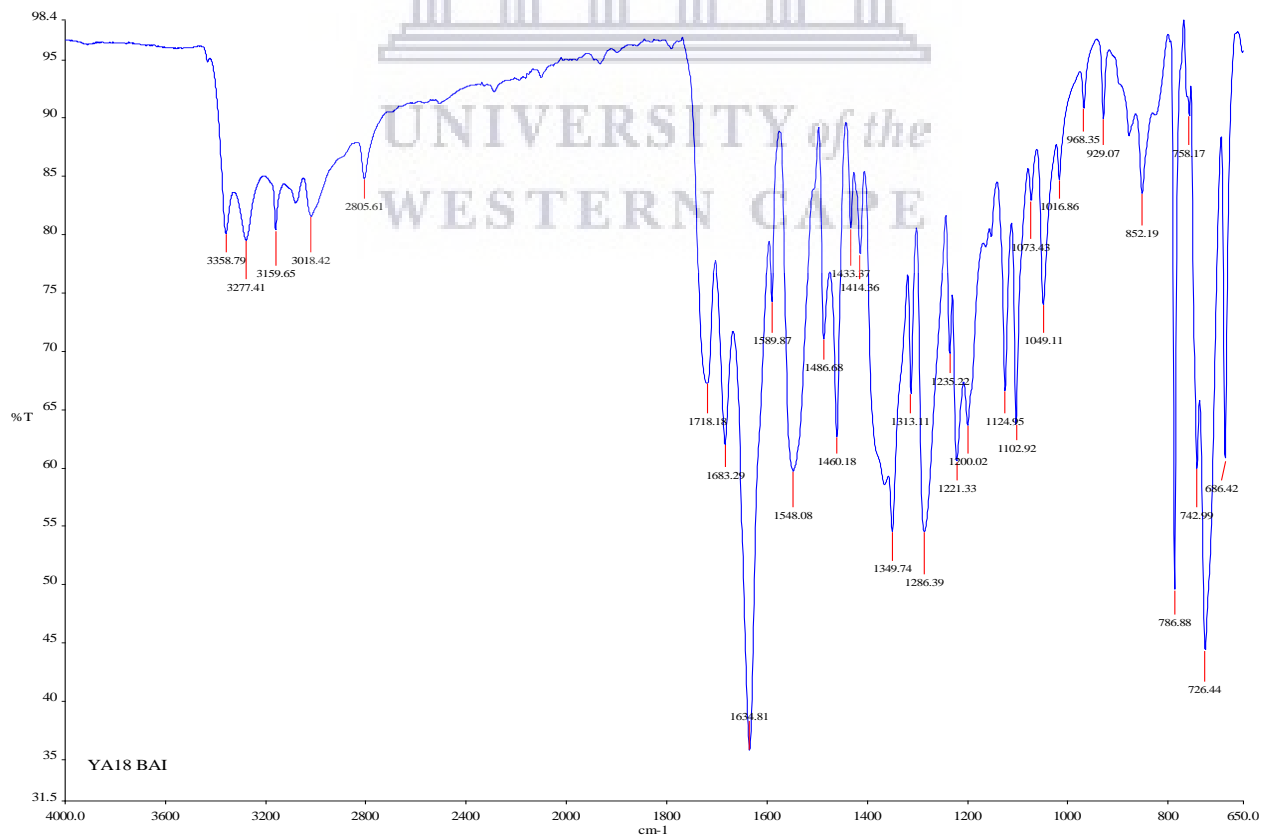


Figure S5.44: DEPT 135 NMR spectrum of compound **5.6e**

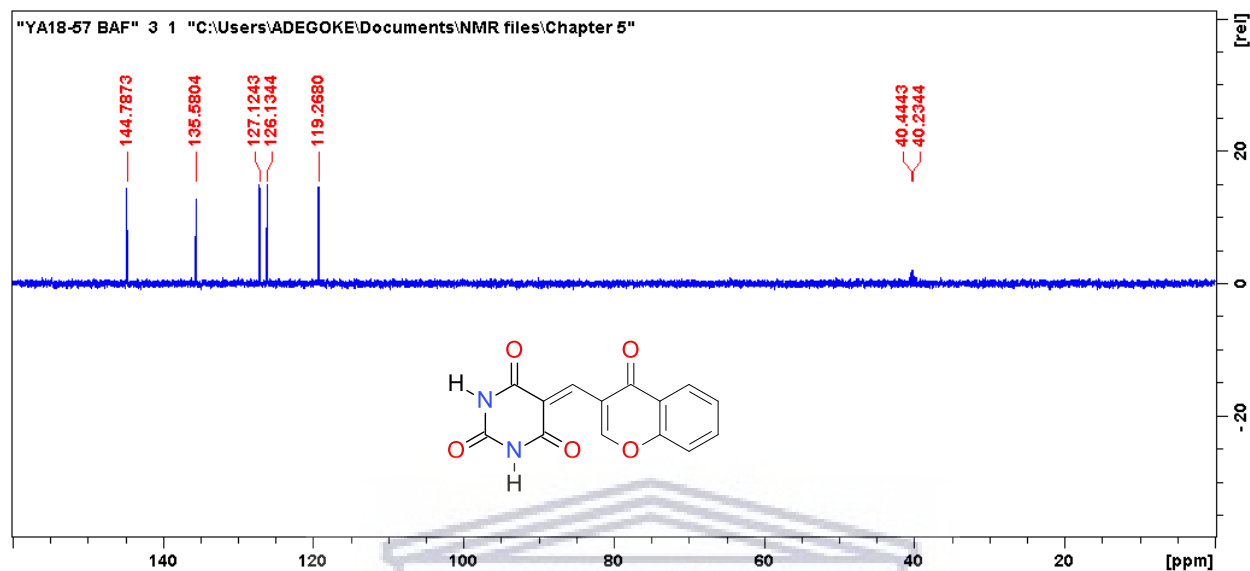


Figure S5.45: COSY NMR spectrum of compound **5.6e**

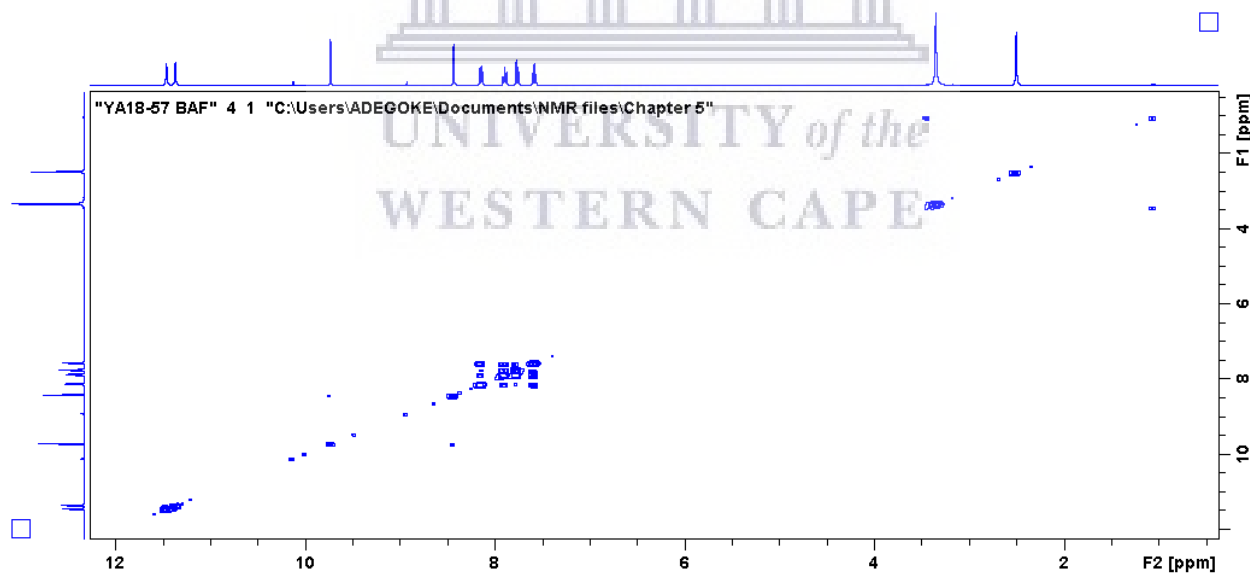


Figure S5.46: HMBC NMR spectrum of compound 5.6e

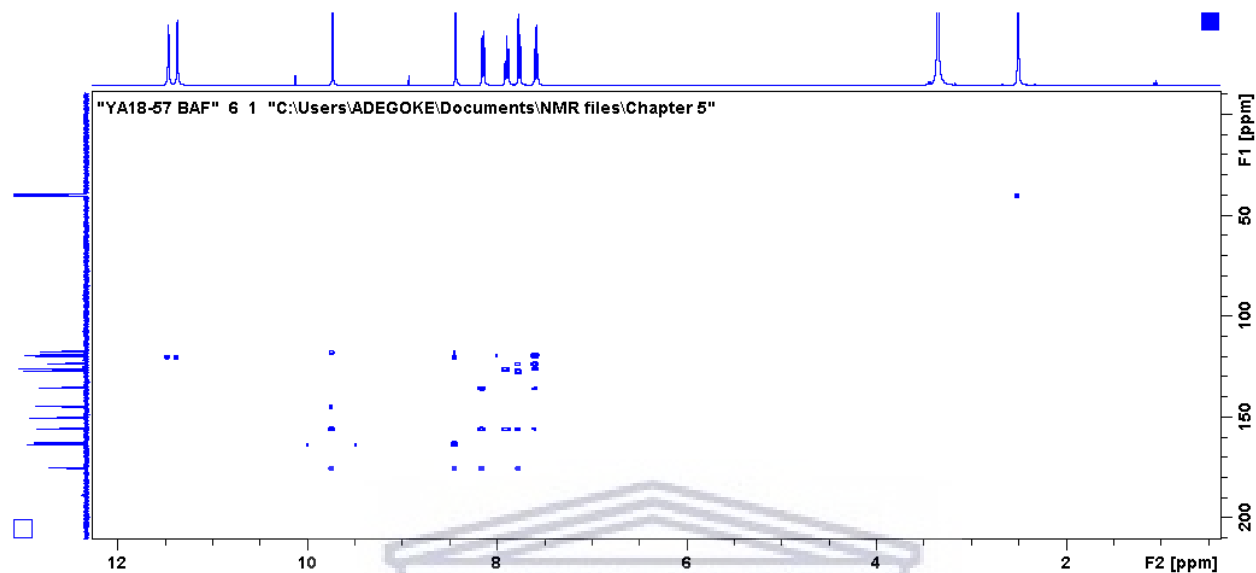


Figure S5.47: HRMS spectrum of compound 5.6e

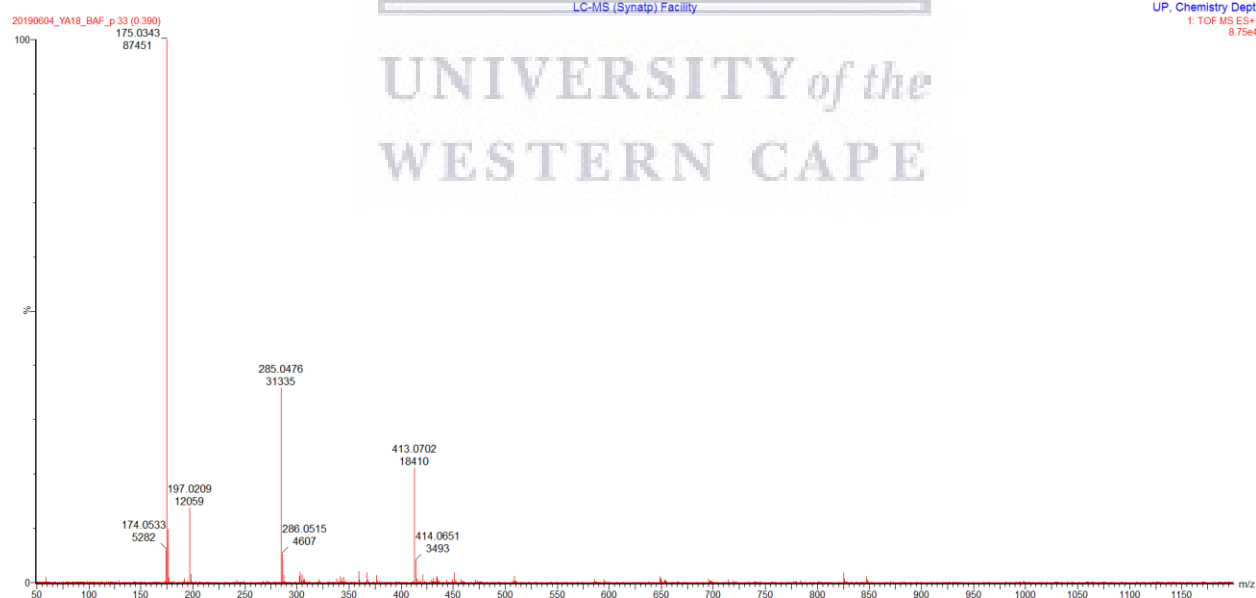


Figure S5.48: IR spectrum of compound **5.6e**

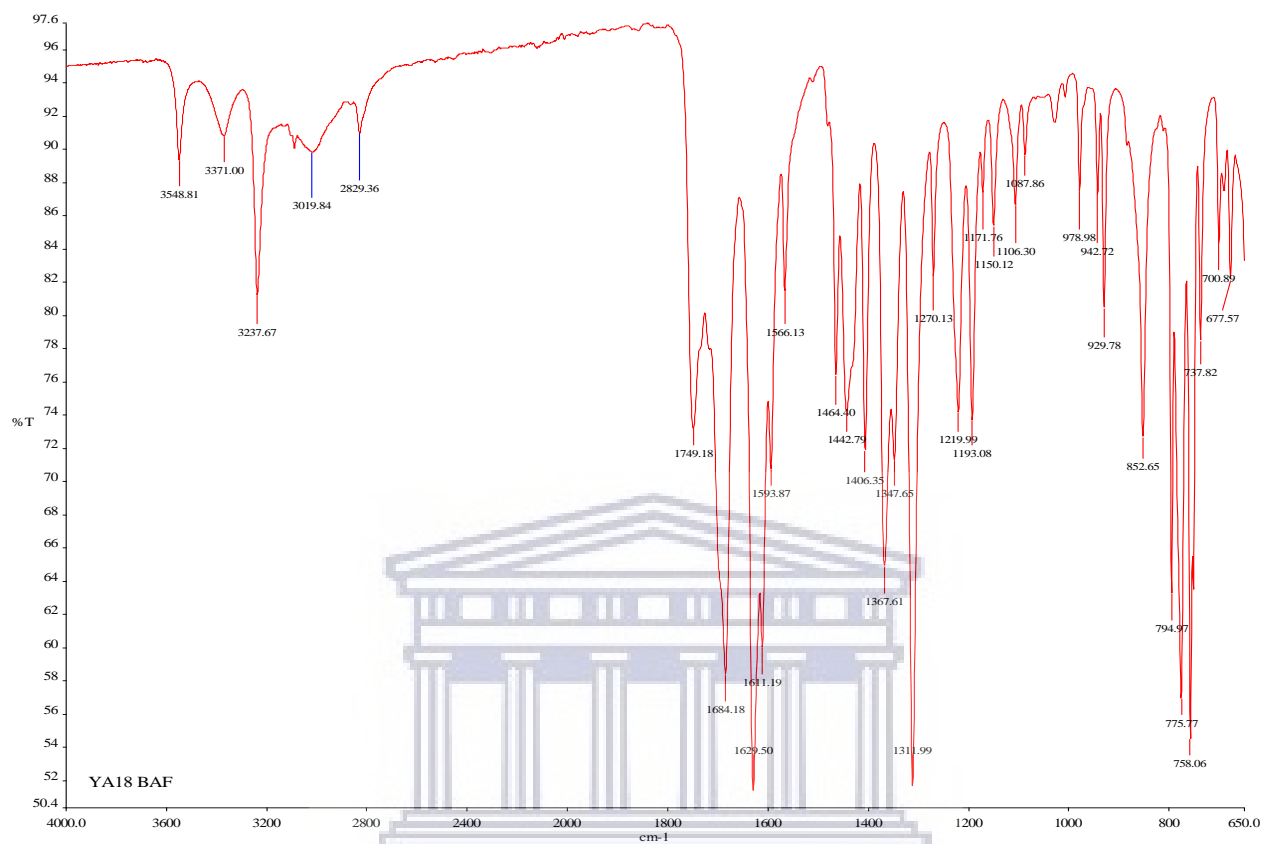


Figure S5.49: ^1H NMR spectrum of compound **5.6f** (400 MHz, DMSO-d_6)

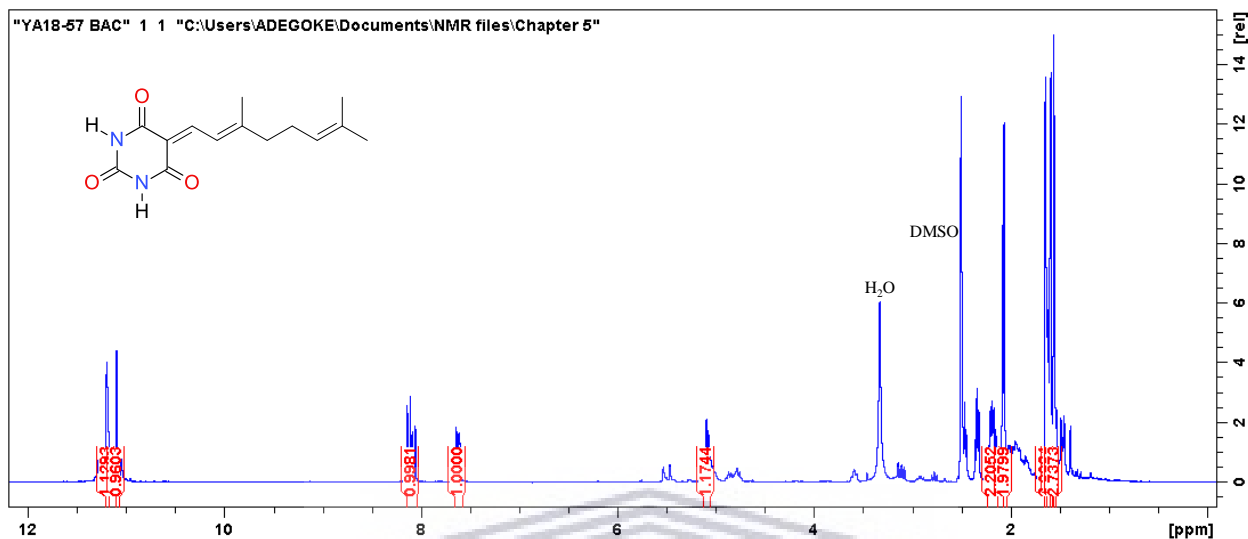


Figure S5.50: ^{13}C NMR spectrum of compound **5.6f** (100 MHz, DMSO-d_6)

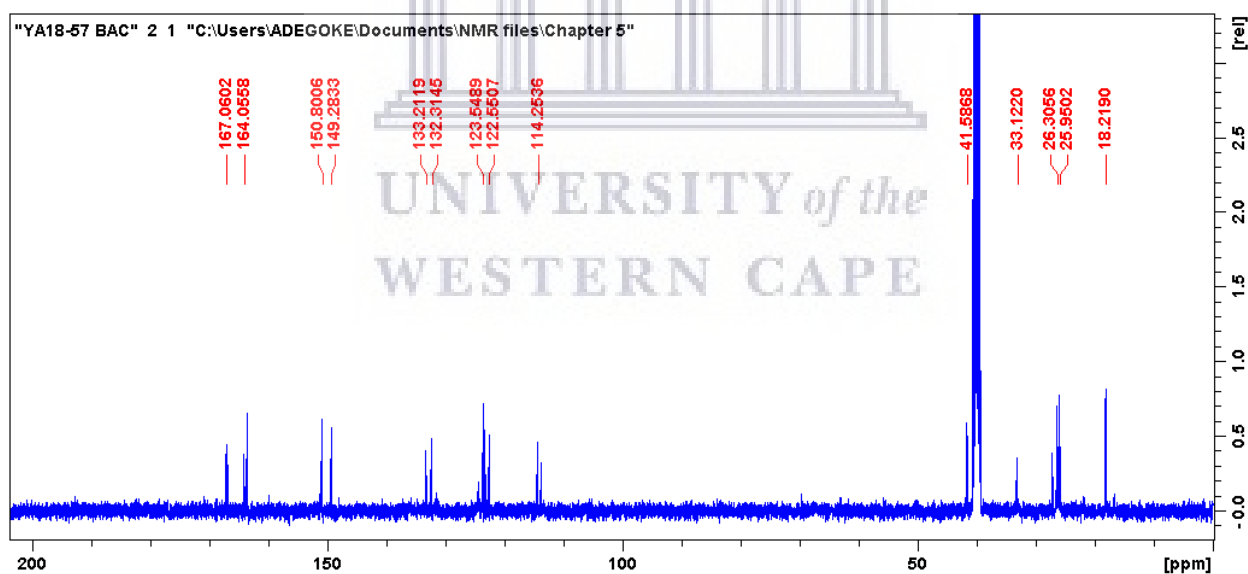


Figure S5.51: HRMS spectrum of compound **5.6f**

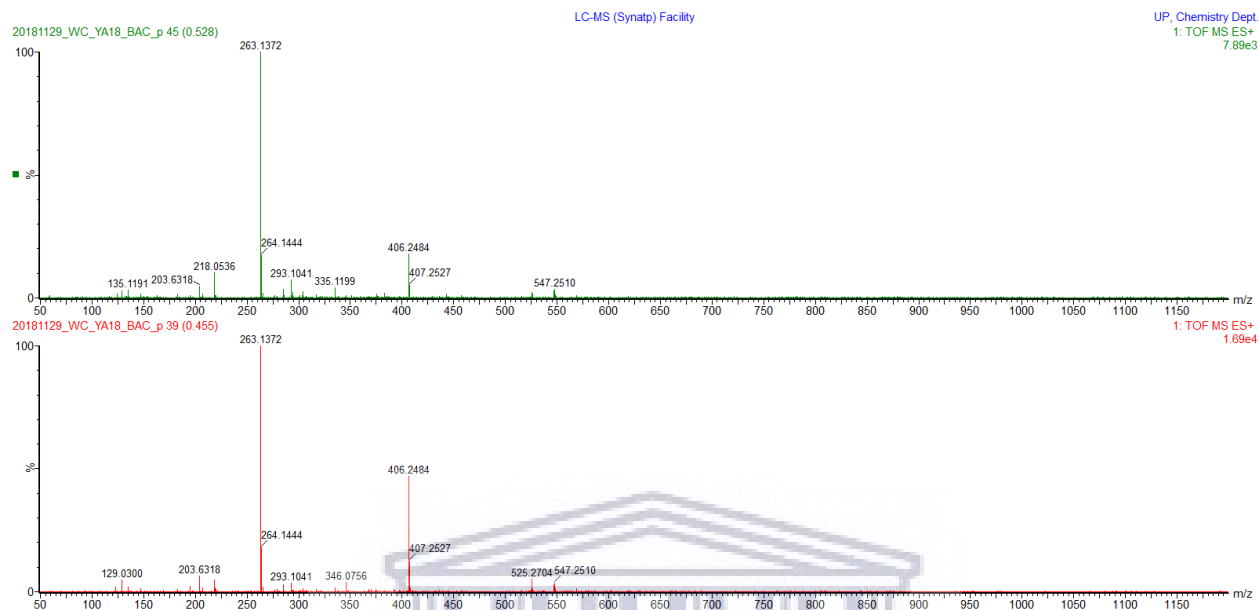
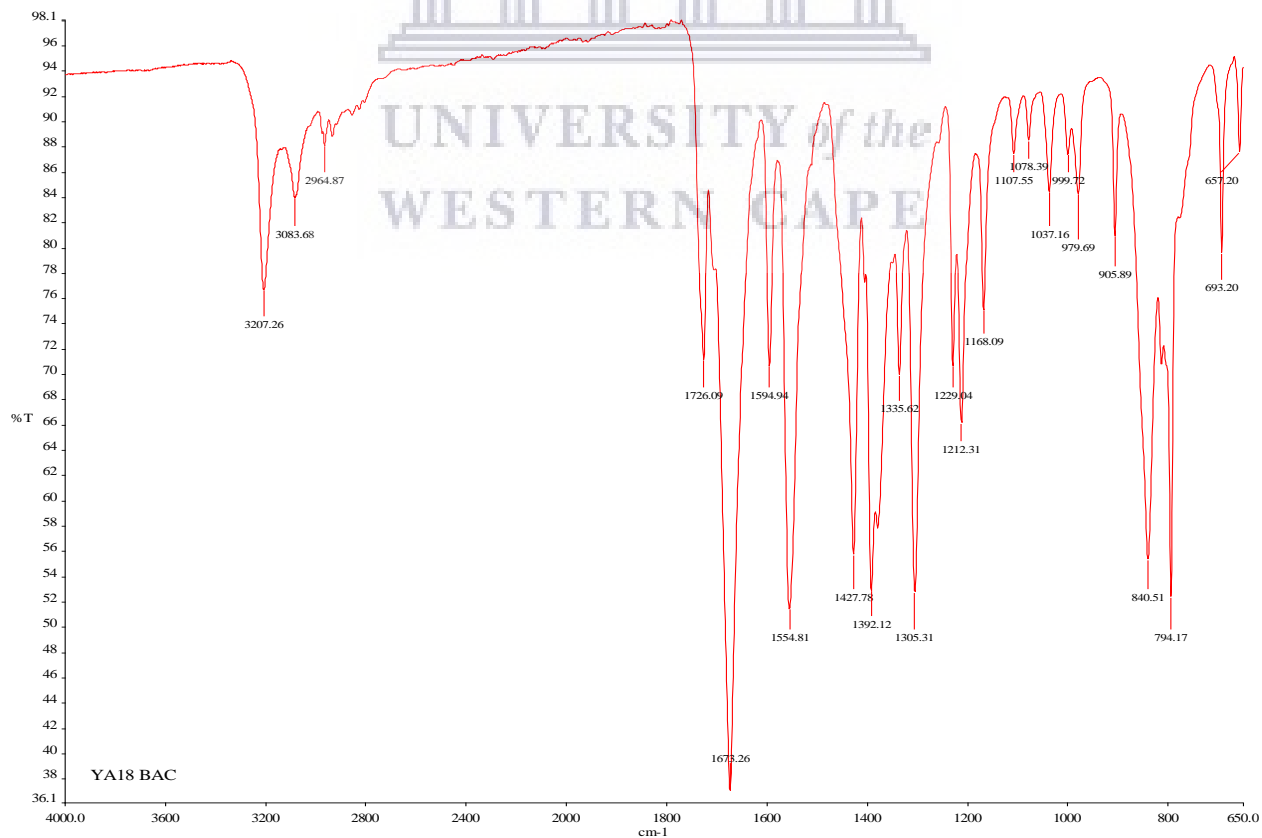


Figure S5.52: IR spectrum of compound **5.6f**



Theophylline derivatives 5.9(a-d)

Figure S5.53: ^1H NMR spectrum of compound 5.9a (400 MHz, CDCl_3)

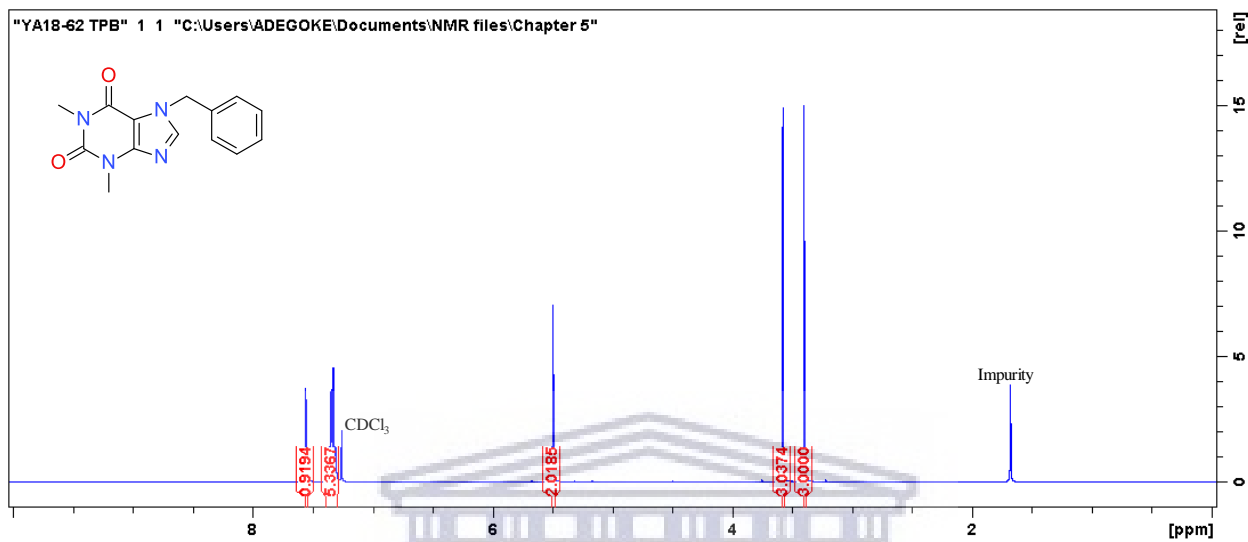


Figure S5.54: ^{13}C NMR spectrum of compound 5.9a (100 MHz, CDCl_3)

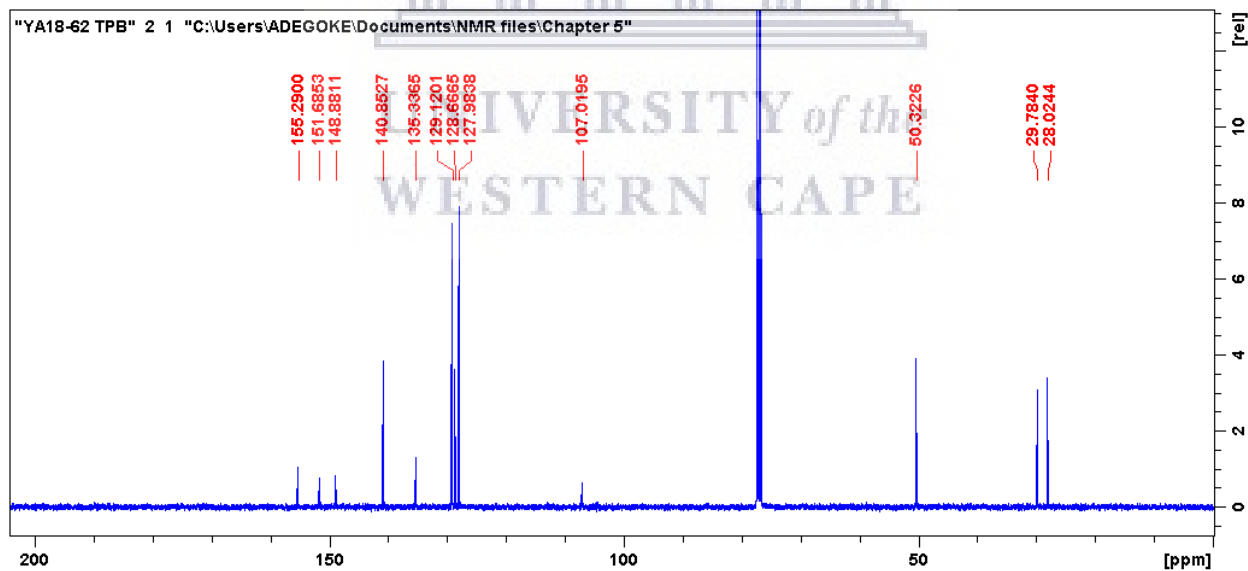


Figure S5.55: HRMS spectrum of compound **5.9a**

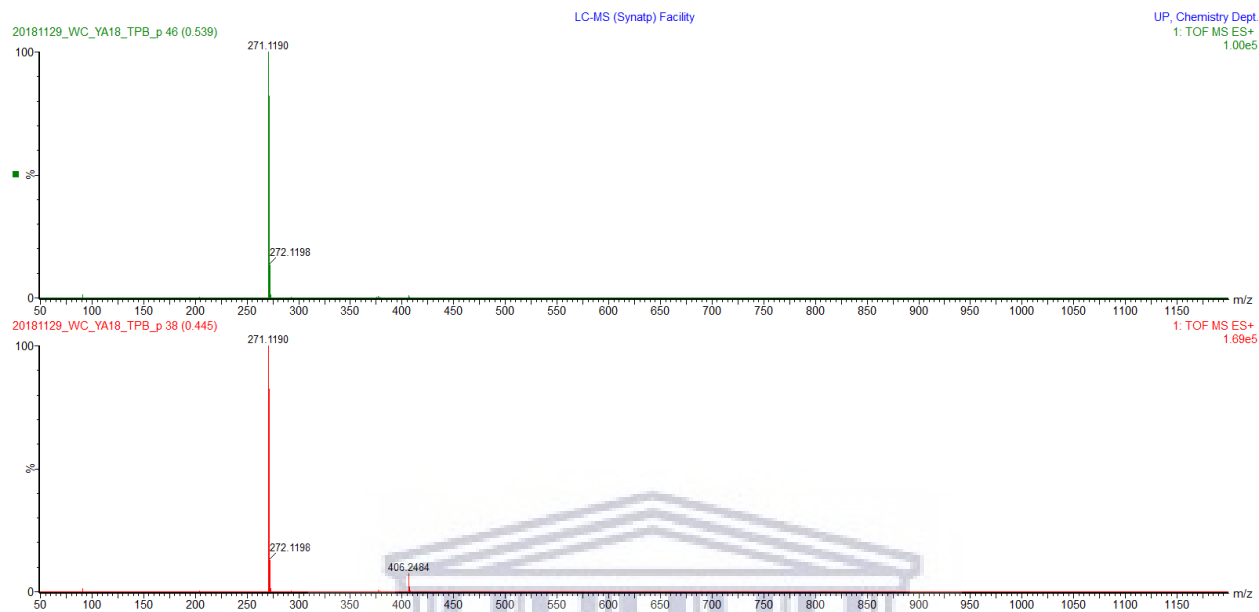


Figure S5.56: IR spectrum of compound **5.9a**

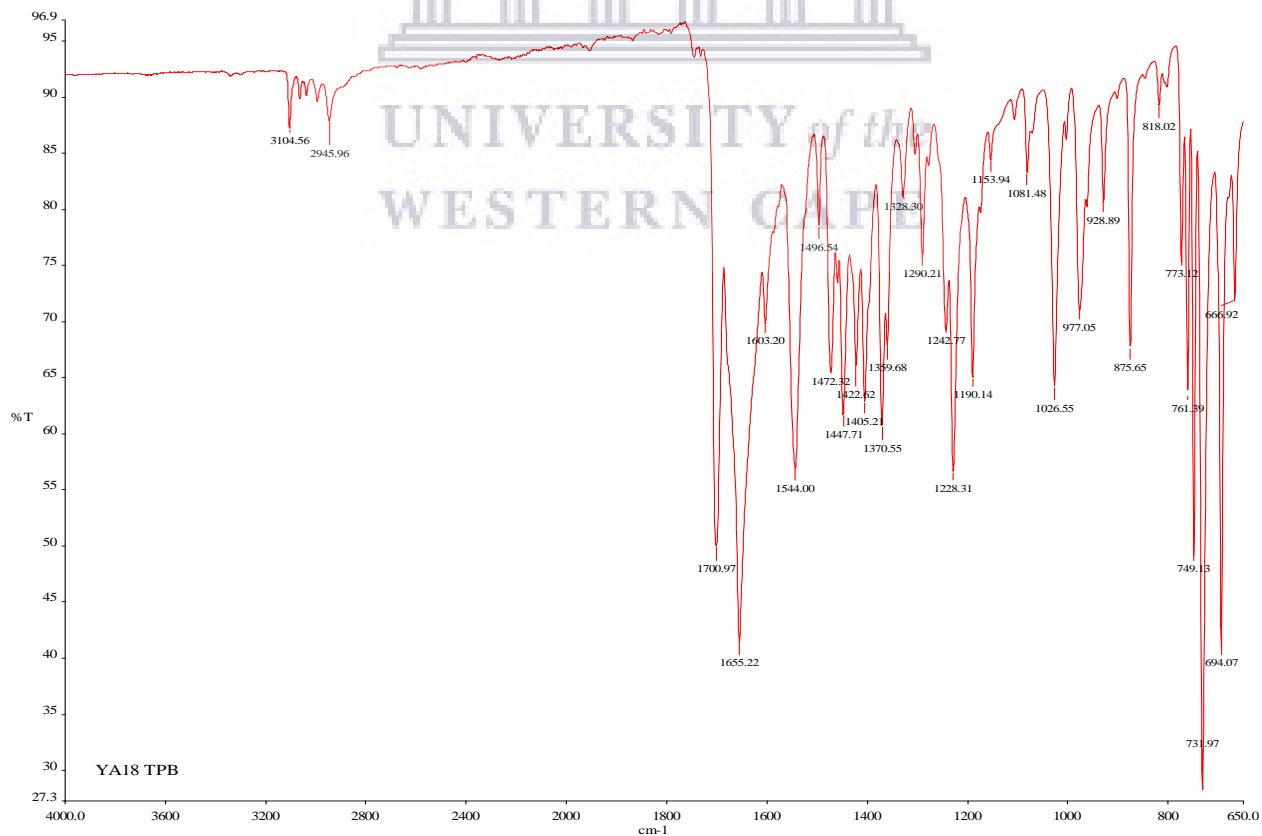


Figure S5.57: ^1H NMR spectrum of compound **5.9b** (400 MHz, CDCl_3)

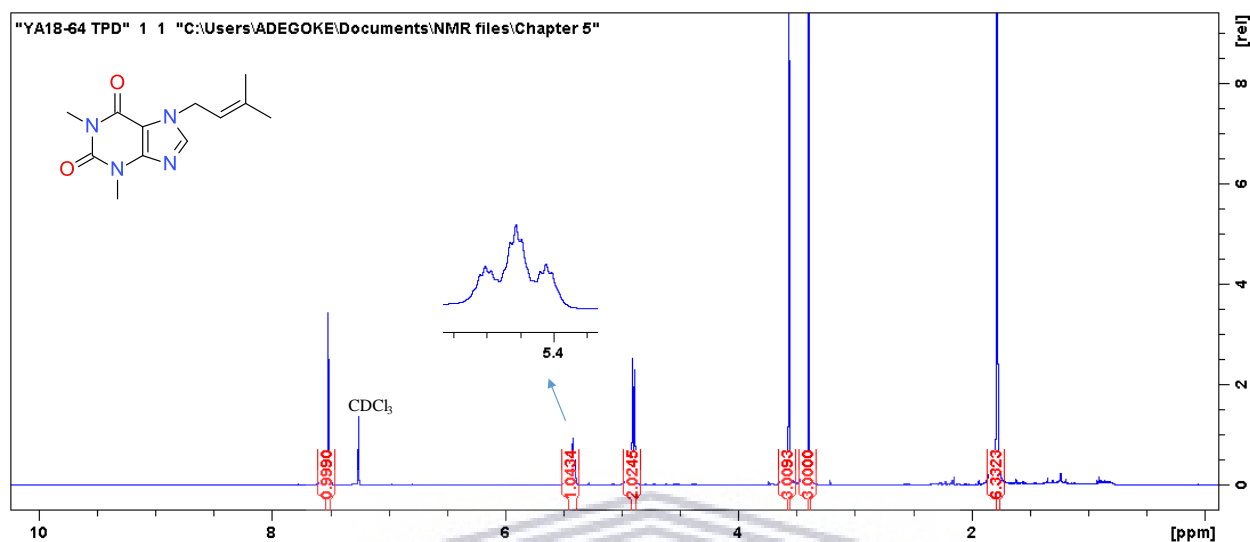


Figure S5.58: ^{13}C NMR spectrum of compound **5.9b** (100 MHz, CDCl_3)

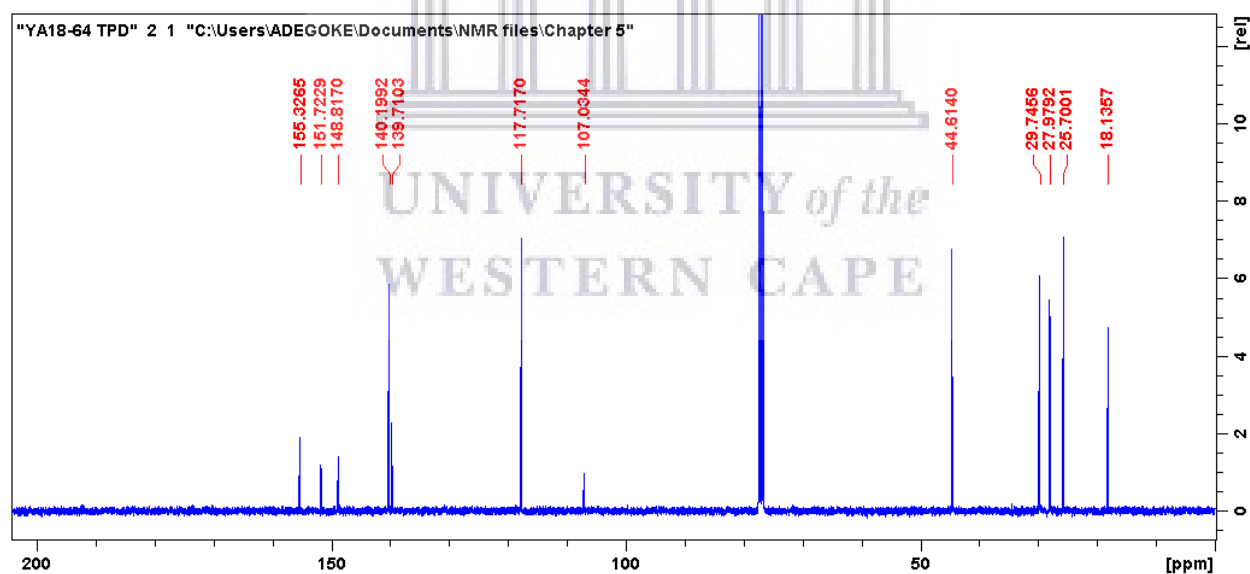


Figure S5.59: HRMS spectrum of compound **5.9b**

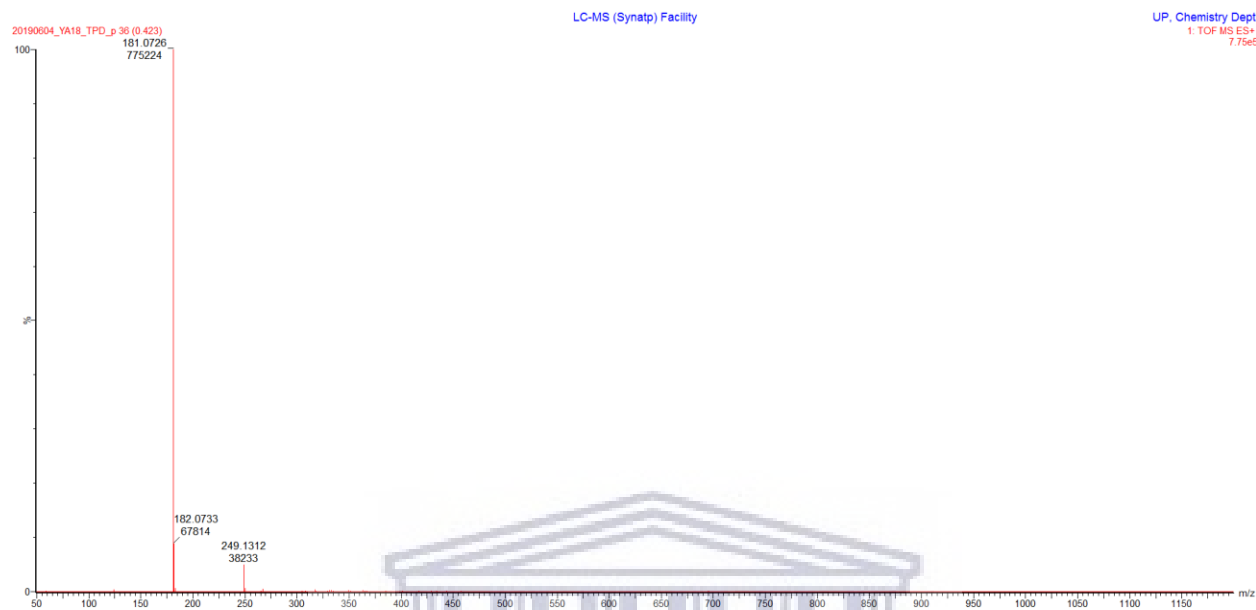


Figure S5.60: IR spectrum of compound **5.9b**

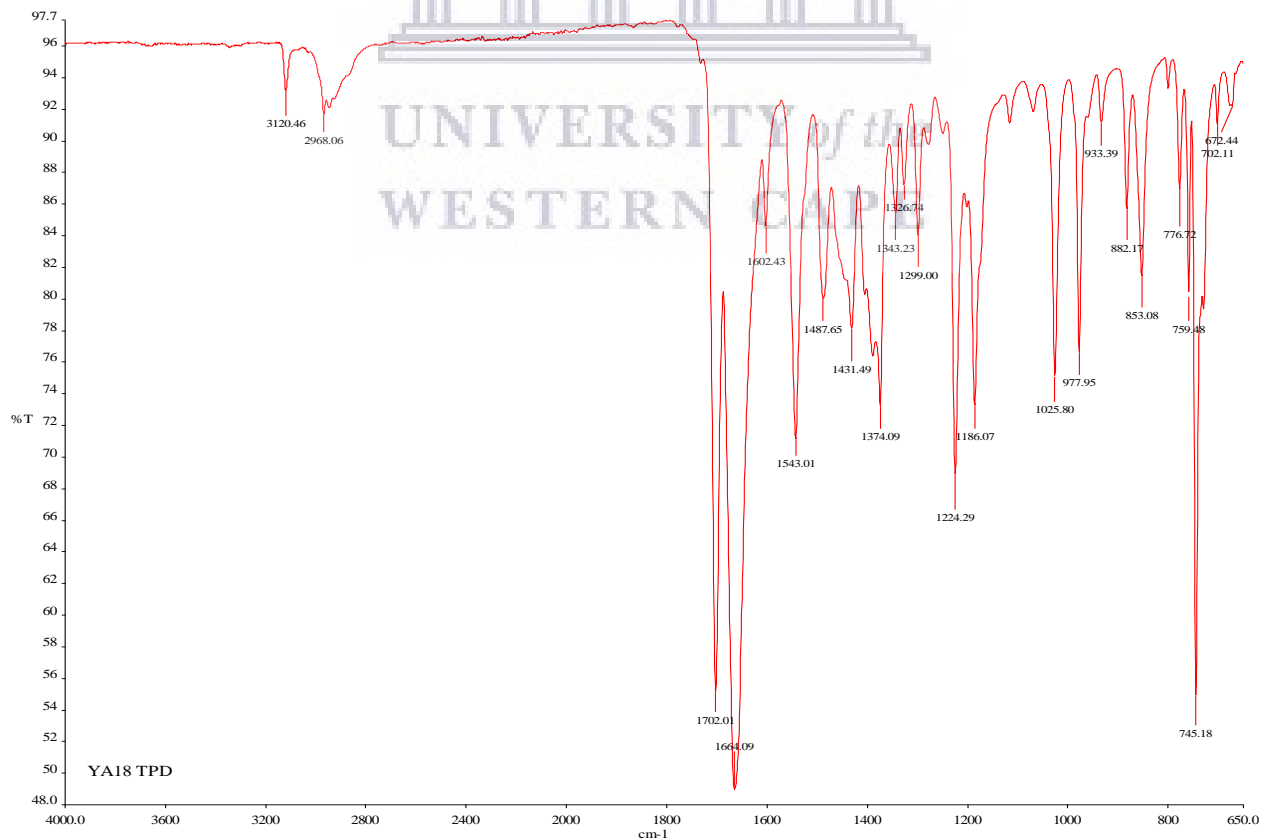


Figure S5.61: ^1H NMR spectrum of compound **5.9c** (400 MHz, CDCl_3)

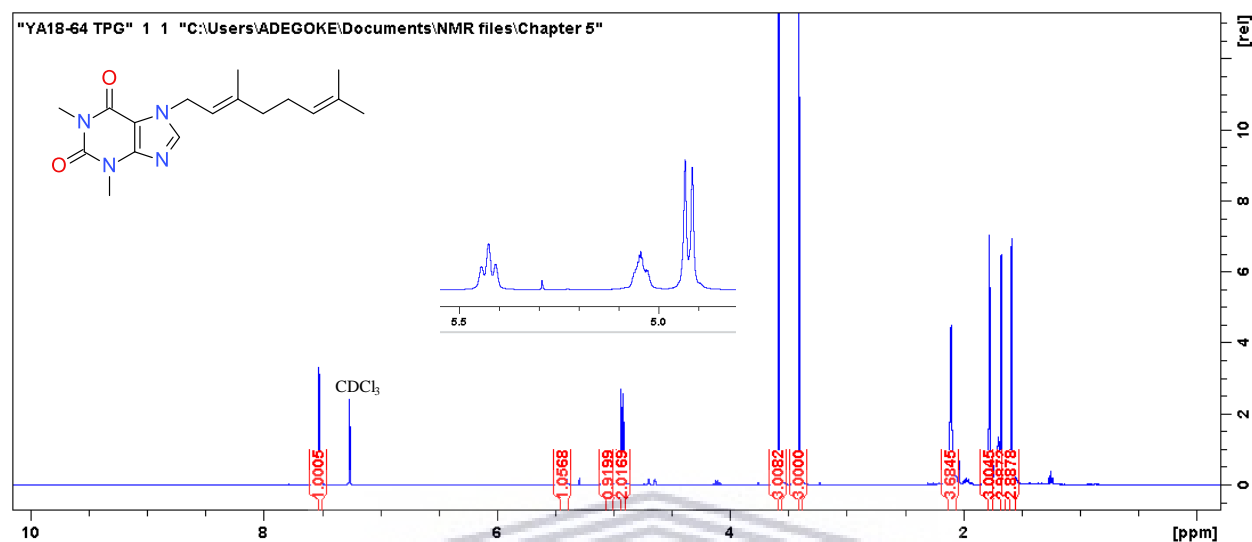


Figure S5.62: ^{13}C NMR spectrum of compound **5.9c** (100 MHz, DMSO-d_6)

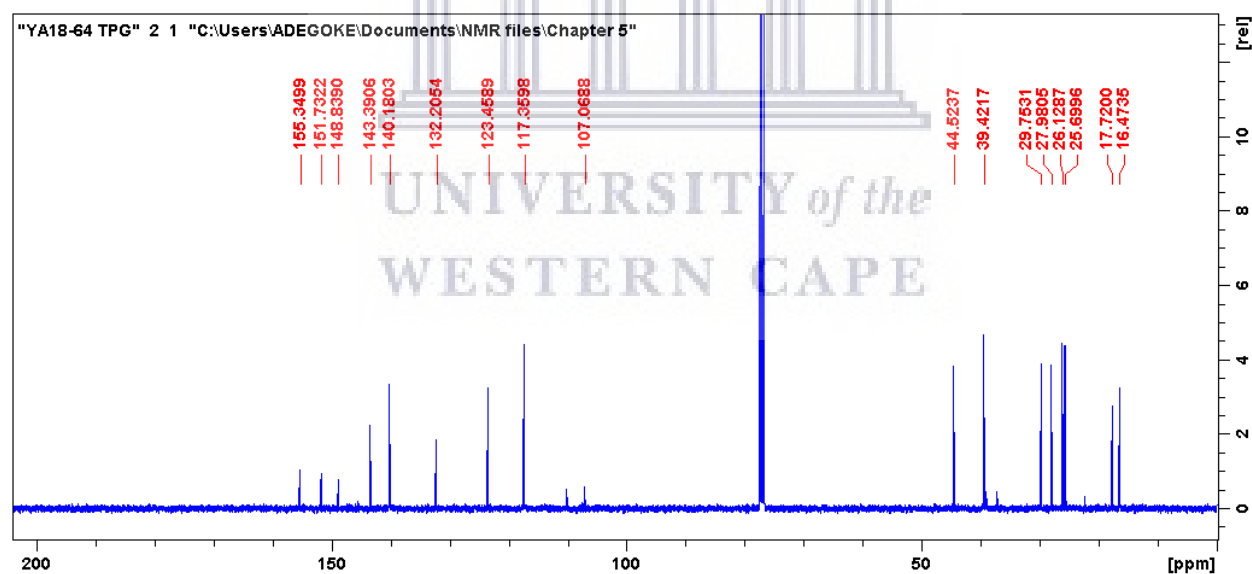


Figure S5.63: HRMS spectrum of compound **5.9c**



Figure S5.64: IR spectrum of compound **5.9c**

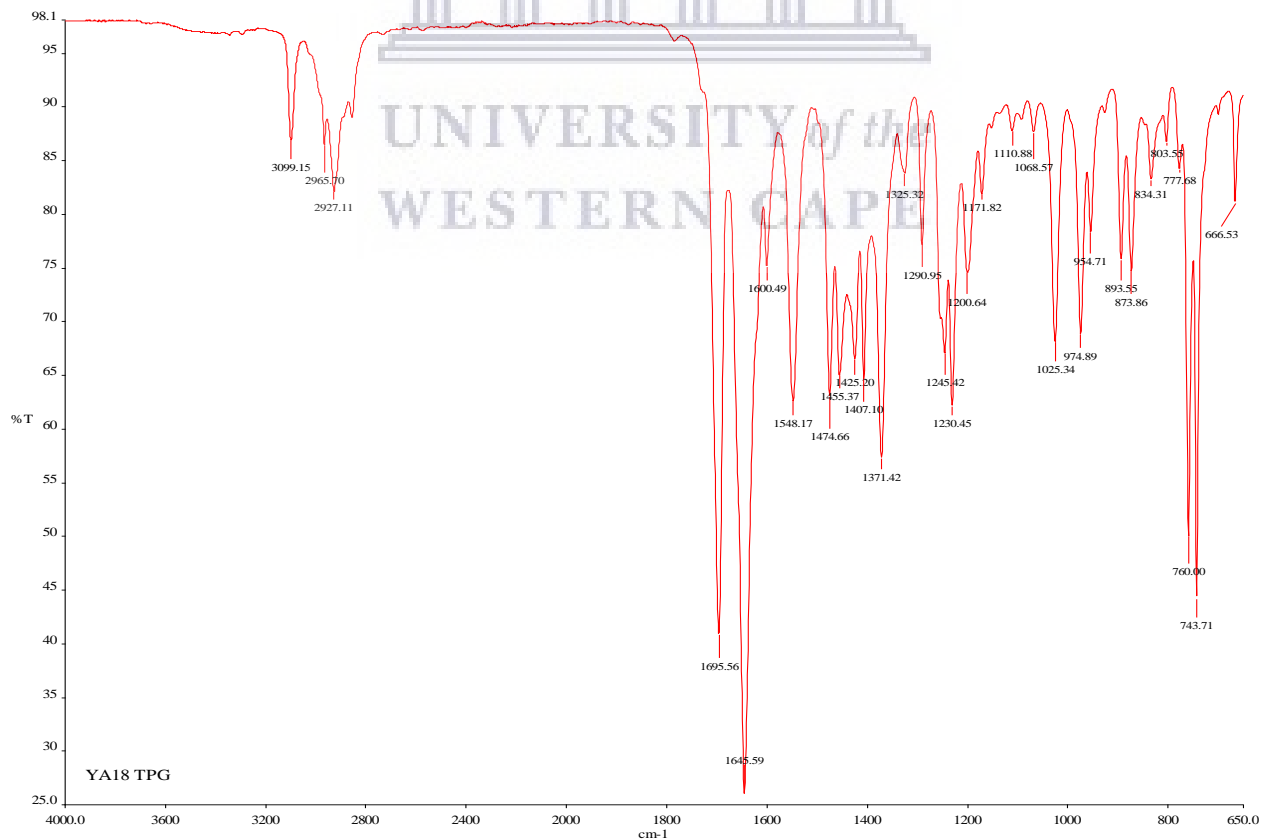


Figure S5.65: DEPT-135 NMR spectrum of compound 5.9d

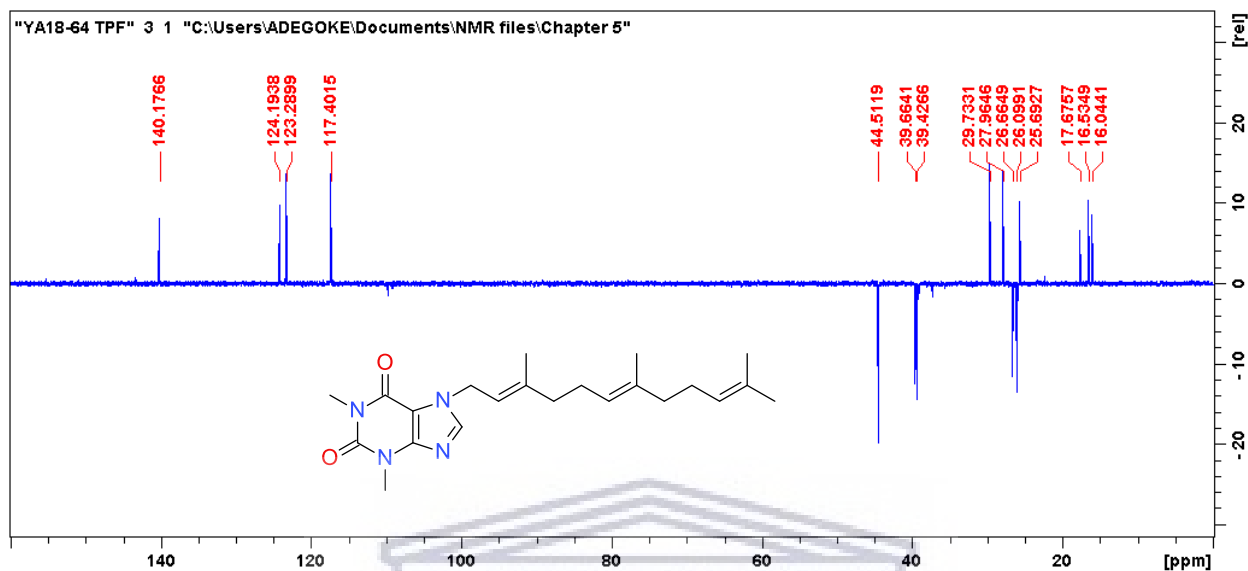


Figure S5.66: COSY NMR spectrum of compound 5.9d

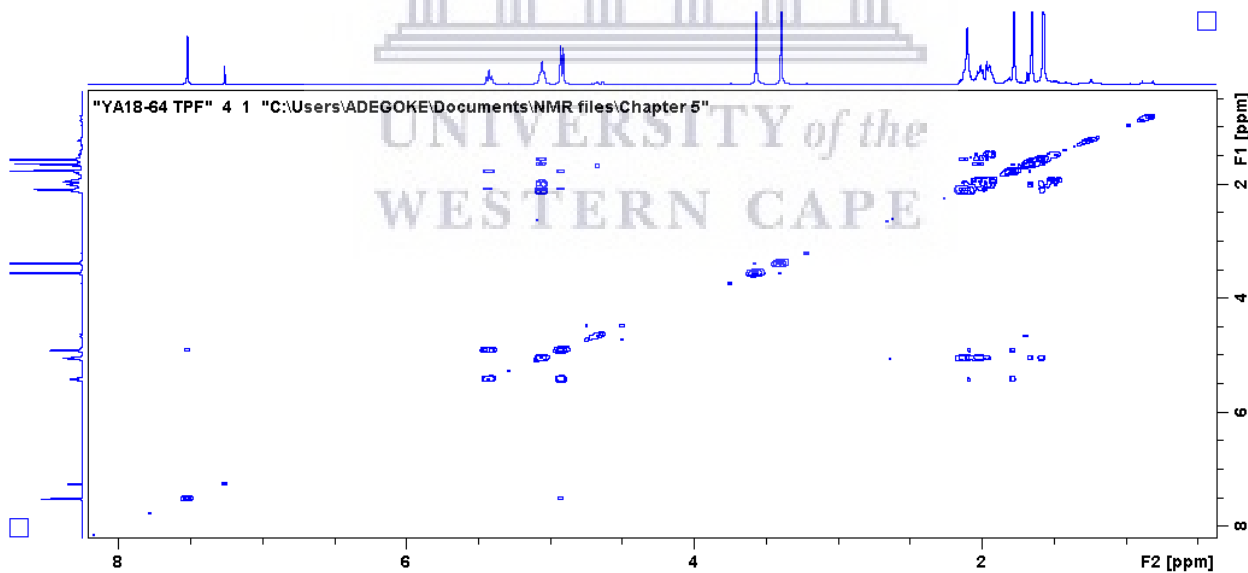


Figure S5.67: HMBC NMR spectrum of compound **5.9d**

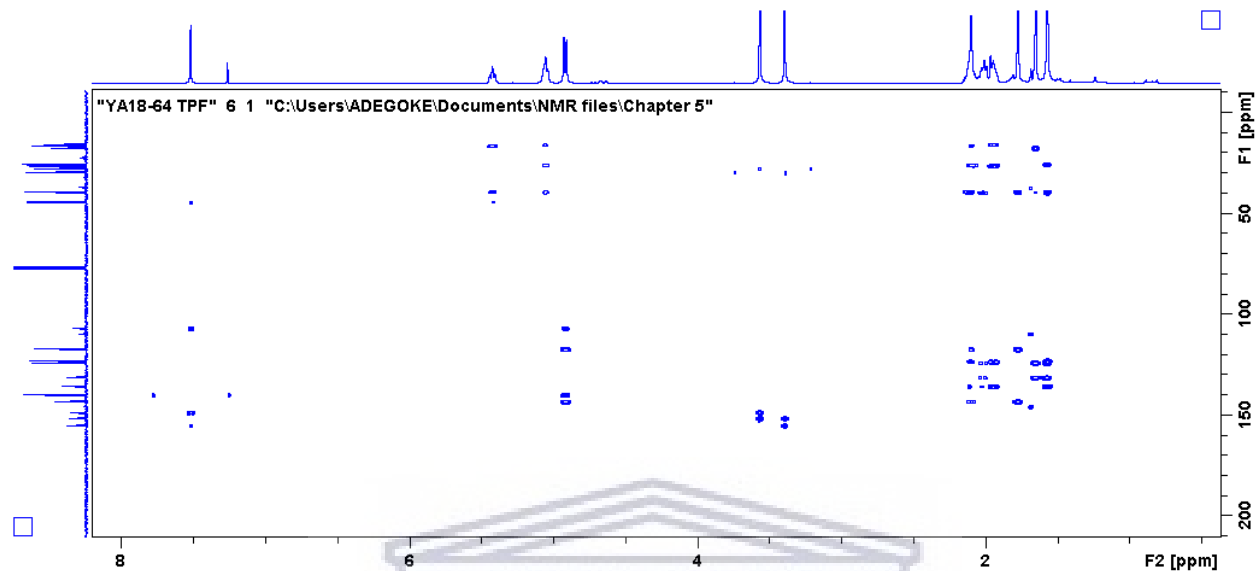


Figure S5.68: HRMS spectrum of compound **5.9d**

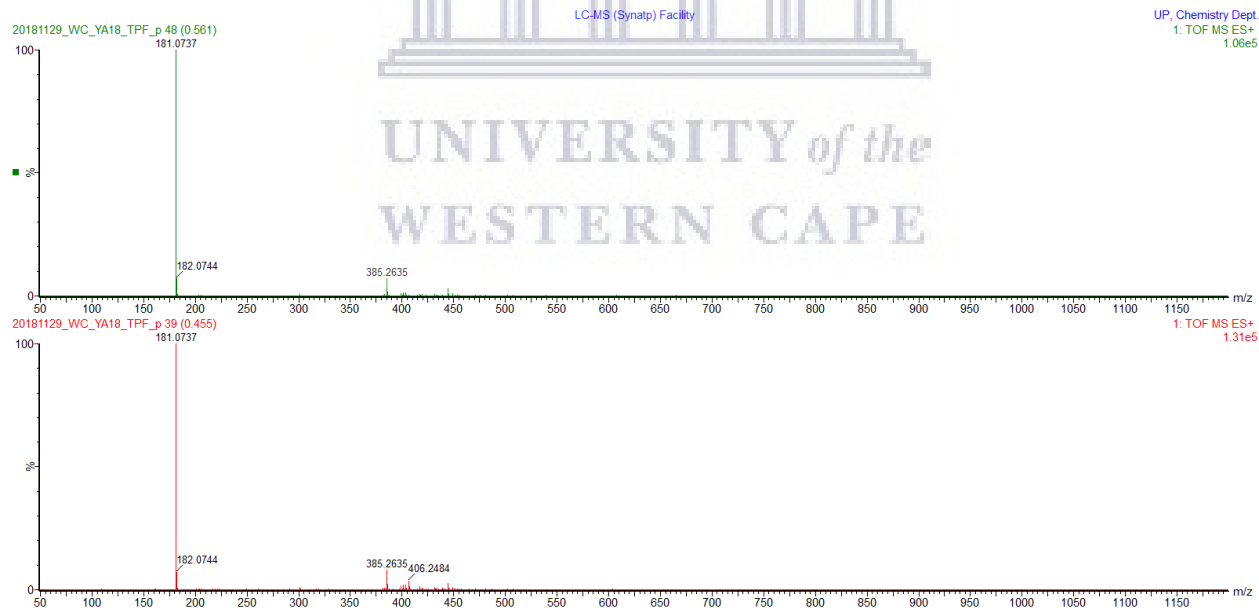
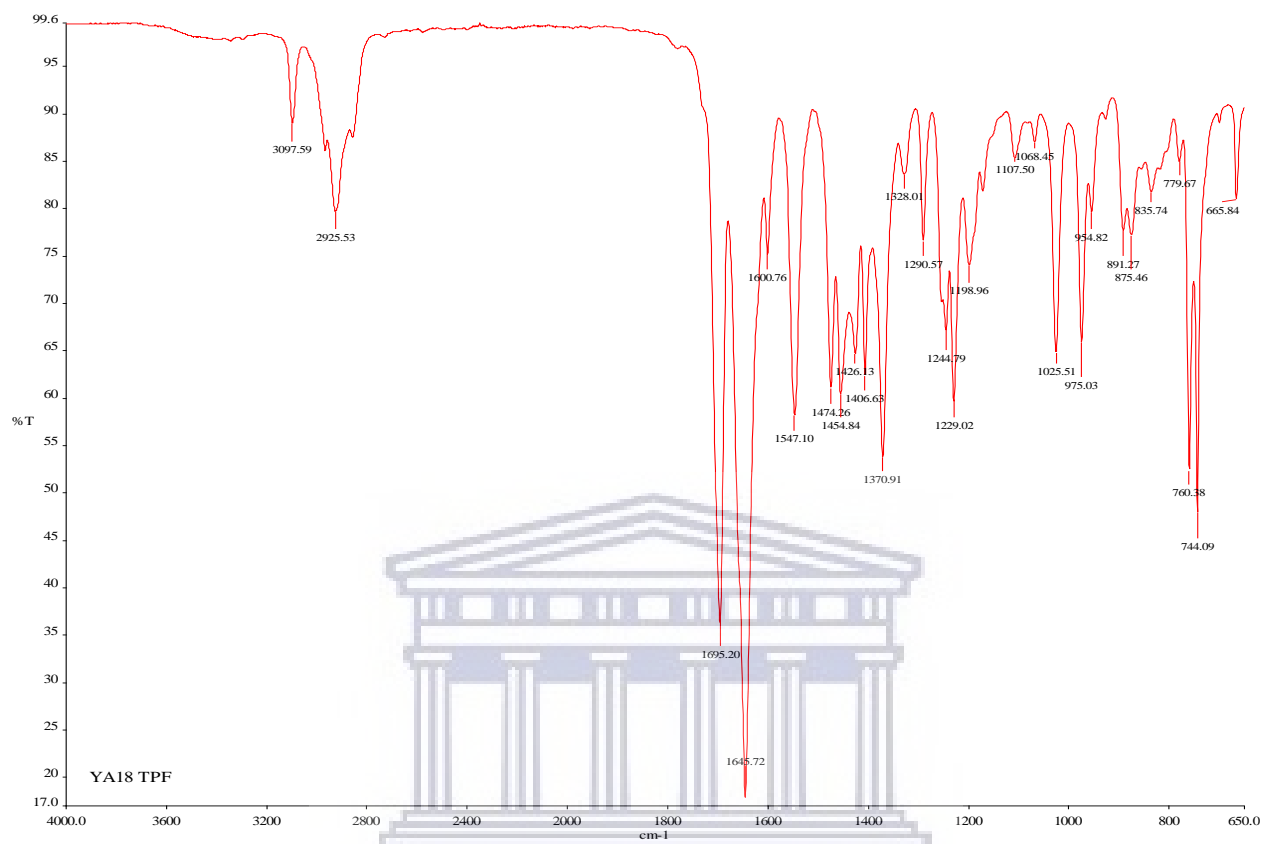


Figure S5.69: IR spectrum of compound **5.9d**



UNIVERSITY of the
WESTERN CAPE